Hydrothermal Carbonisation: A Sustainable Alternative to Versatile Carbon Materials

Habilitationsschrift

zur Erlangung des akademischen Grades

Doktor rerum naturalium habilitatus

(Dr. rer. Nat. habil.)

in der Wissenschaftsdisziplin Materialchemie

eingereicht an der

Mathematisch-Naturwissenschaftlichen Fakultät

der Universität Potsdam

von

Dr. Maria-Magdalena Titirici

Geboren am 24.3.1977 in Bukarest

Potsdam, im Novemberm 2012

for Renatto and Martahon

"Life exists in the universe only because the carbon atom possesses certain exceptional properties"

Sir James Jeans, The Mysterious Universe, 1930

Acknowledgements

methane oxidation, John Texter (Eastern Michigan University) for thermal and electronic conductivity of latex-N-doped carbon dispersions, Dolores Lozano-Castello, Diego Cazorla and Emillia Morallon (University of Alicante) for help with supercapacitors and activated carbons, Noriko Yoshizawa (AIST, Japan) and Jane Howe (Oak Ridge National Lab) for some help with HRTEM, Julian Tornow (FHI) for characterisation of our LiFePO4 system and many other researchers with whom I have exchanged valuable ideas during the past years.

Many thanks also to my group leader colleagues at the MPIKG with whom I have worked during all this time. Especially Jens Weber is aknowdleged for his enormous love for adsorption and all the help with porosity measurements. I thank Klaus Tauer for very interesting scientific and non.scientific discussions and providing me latex nanoparticles. Andreas Taubert is also acknowdleged for his cooperation on ionothermal carbonisation.

I would like to tank all the technicians at MPIKG for their constant help with various measurements. Thanks to Rona Pitschke for the SEM/TEM measurements, Sylvia Pirok for the elemental analysis and especially to Regina Rothe for all her help during all these years with ordering, organisation and many other things. Also thanks to Marlies Gräwert for her help with solving HPLC related problems.

It was also a great pleasure to meet all the guest professors at the MPIKG. I had a lot of fun with a lot of them discussing science as well as doing other activities. Thanks to John Texter for coming to my birthday party in the very underground Berlin and dancing with me electro-minimal. Thanks to Yusuf Yagci for the nice dinners with his wonderful family. Many thanks to Luis Marzan for various dinners with his nice family and for running a half marathon with me. Definitely marathon running with you Marek and your son was great fun.

During these seven years obviously I developed a lot of friendships and met great people from all over the place. Again mentioning all of them here would be simply impossible.

However I need to mention the "golden times" and all my friends from the beginning of my MPI career. Ana, Jelena, Miles, Pedro, Moon, Philipp, Micha, Erwan, Fix, Mr. Berg, Elodie ,Mattij. We definitely rocked and our friendships will be everlasting.

My running partners of course need to be acknowledged. Helena, Fred, Silke, Philippe, Zoe, Alfonso. Running with you in Golm was fun! Here I also need to comment on the biking trips from various places in the middle of nowhere in Germany back to Berlin with Zoe, Fonsi, Camillo and Filipe. That was also something I really enjoyed. Thanks also to Camillo for our bike rides from Golm back to Berlin.

The new people: Thanks to "my frau" Clara for everything including her PA job, to Vasana for being a great office mate and a great friend, to Jens "darling" for the friendship and all the help with German language and solving my tax and cancelation issues.

Many thanks also to Filipe for becoming my office mate again after 8 years of absence and some great Berlin action together, to Hiro for cooking me tasty meals and

all the travels we have done together and to Carla for various cultural events, loads of cafes and loads of chatting.

I can also not forget my Romanian family in Berlin. Thanks to the bunch of crazy guys that add some "slat" in my boring scientist life. In particular Stefan, George, Pilo and Raluca.

Finally many thanks to Renatto for his patience all these past years and to our crazy cat Martahon.

Table of Contents

Preface

To cure from our dependence on fossil fuels and consequently reduce the risks of completely destroying the planet, humanity seeks novel and sustainable technologies. Scientists have the duty to provide solutions and create new materials without using scarce elements but those precursors generously provided by Nature at no cost.

Applications wise, Carbon played and will continue to play a very important role in our daily life. In Nature, Carbon can adopt many different forms. Although known since ancient times as a natural product of biomass coalification, today it is mostly manufactured using fossil based precursors. This should no longer be the case as fossil fuels are diminishing at a rapid rate and they are generating huge amounts of CO_2 in the Earth´s atmosphere extinguishing our ecosystem.

New and sustainable carbon materials are therefore of upmost importance. This thesis presents a novel technology able to produce carbon materials from biomass in water at low temperatures. It mimics the natural process of coal formation (from hundred million years) in the synthetic laboratory (to a few hours). This technology is called Hydrothermal Carbonisation (HTC).

The process of Hydrothermal Carbonisation has been firstly reported by Bergius in 1913 (Nobel Prize winner) and recently re-discovered as an alternative aqueous solution to modern carbon materials by the scientists working at the Max-Planck Institute of Colloids and Interfaces.

Dr. Titirici, the author of this Habilitation Thesis, was the scientist in charge for the development of this technology into novel and exiting materials for very important and timely applications. She was leading of a group of young and highly motivated researchers who during a period of only six years made the Hydrothermal Carbon Technology (HTC) an important addition to Carbon science.

HTC is now a well-established and recognised technology, embraced by many other research groups and with many different products and important applications.

The **first chapter** offers an overview on the state of art of various green carbon materials, from carbon nanotubes to graphene, activated carbons, starbons, ionic liquid derived carbons to HTC including also a brief history of the Hydrothermal Carbonisation Process.

Various HTC precursors of increasing structural complexity are compared in **Chapter 2**: monosaccharaides, water soluble polysaccharides, cellulose and finally raw lignocellulosic biomass. The similarities and differences between the resulting HTC materials are discussed in terms of formation mechanism, final chemical structure, surface groups, morphological features, and porosity.

Chapter 3 describes various possibilities of introducing porosity in such Hydrothermal Carbon Materials in a broader context of Porous Carbon Materials in general. These include the use of structural directing agents such as "soft" or" hard" templates, as well as bio-inspired approaches to generate porosity. The use of hydrothermal carbons as precursors for producing activated carbons is also discussed in detail.

Functionalisation is a challenging task in Carbon science. However this is not the case in Hydrothermal Carbonisation. The low temperatures utilised in hydrothermal carbons allow easy functionalisation either in one step or using post-synthetic strategies. In addition, Hydrothermal Carbonisation can be elegantly used to produce valuable carbon hybrid materials. All these are described in **Chapter 4**.

Maybe one of the most impressive developments of HTC materials is their wide range of applications, often outperforming other fossil derived carbon nanomaterials. **Chapter 5** is dedicated to the utilisation of HTC materials in various important areas. For most of these applications a brief state of art is also provided. Topics such as renewable energy (rechargeable batteries, supercapacitors), electrocatalysis (fuel cells), heterogeneous catalysis, photocatalysis, gas storage, water purification, sensors and medical applications are discussed.

The thesis is mainly focused around the scientific results that emerged from Dr. Titirici research group during the past 6 years. However, a comprehensive state of art is provided in addition to own discoveries in order to provide a complete overview on the current HTC technology. It also needs to be mentioned that parts of this "Habilitation Thesis" will become the subject of a book to be published by Wiley in 2013 entitled: "**Back to Black: Green Carbon Materials via Hydrothermal Carbonization of Biomass**" edited by Dr. Titirici.

1 Green Carbon Materials

1.1 Introduction

In the early part of the 20th century, many industrialised materials such as solvents, fuels, synthetic fibers, and chemical products were made from plant/crop-based resources (Figure 1-1).[1-2] Unfortunately, this is no longer the case and most of today´s industrial materials including fuels, polymers, chemicals, carbons, pharmaceuticals, packing, construction and many others are being manufactured from fossil based resources. Humankind is still living in a world where petroleum resources have the absolute power. However crude oil resources are rapidly diminishing. It is predicted that this will lead to serious conflicts in the world related to distribution and control. What it is even of more concern, is that essentially such fossil-fuel derived products eventually end up as CO_2 in the Earth's atmosphere. Several important findings of climate research have been confirmed in recent decades and are finally accepted as facts by the scientific community. These include indeed a rapid increase in the carbon dioxide concentrations in the atmosphere during the last 150 years, from 228 ppm to the 2007 level of 383 ppm. [3] This increase is our own fault and is due to burning of fossil-fuels.

So what will the world look like in 2050? It is believed that if we continue relying on fossil fuels, we may face an ecological collapse of unprecedented scale due to degradation of natural capital and loss in ecosystem services. However, we have the capability to reverse this dark and worring perspective of an ecological fiasco and shape a future where we could live in harmony with nature. For this to happen, scientists have the most important responsibility and joint efforts from multidisciplinary scientific fields are of upmost significance to achieve this goal.

One of the most important issues is the production of renewable energy to cure our addiction to oil. Solar and wind energy are expected to play the most important role in the future. Available solar and wind energy depends strongly on geography and local climate and varies strongly with season, time of day and weather. This creates additional subsidiary challenges of cost efficient energy storage and transportations. This is why high performing materials in smart grids, batteries, fuel cells, solar cells, gas storage, or efficient catalysts to convert renewable resources in transportation fuels need to be developed.

Figure 1-1: a) Raw materials basis of chemical industry in historical perspective (taken with permission from [2]); b) A view on sustainable materials for a sustainable future (taken with permission from [4]).

The paradigm shift from petroleum hydrocarbons to biobased feedstock provides remarkable opportunities for the chemical processing industry and production of sustainable materials able to perform the above mentioned functions strongly linked with a sustainable future. [5]

Nature offers an abundance of opportunities for shaping structural and functional materials in its wide variety of raw materials including carbohydrates, nucleotides, and proteins. In this respect, Koopman et al. emphasized the importance of developing new starting materials from biomass from an industrial point of view. [6] Biomass is the most abundant renewable resource on earth. An approximate estimation of terrestrial biomass growth amounts to 118 billion tons/year, dried. [7] About 14 billion tons of biomass/year are produced in agricultural cycles and out of this about 12 billion tones/year are essentially discharged as waste. Obviously there is enough biomass available at almost no cost to be used in many different ways. I will point out here three directions for biomass transformation into useful products while focusing on the last one.

1. The greatest potential of biomass utilisation is the generation of biofuels as a sustainable alternative for transportation with no CO_2 emissions. This can be achieved either by fermentation [8], gasification [9] or catalytic liquefaction [10].

2. One aspect of green chemistry refers to the use of biomass to provide alternative starting materials for the production of chemicals, vitamins, pharmaceuticals, colorants, polymers, and surfactants. [11] Industrial white biotechnology highlights the use of micro-organisms to provide the chemicals. It also includes the use of enzyme catalysis to yield pure products and consume less energy. [12] Examples using these techniques include composite materials such as polymeric foams and biodegradable elastomers generated from soybean oil and keratin fibers. [13] Plastics such as polylactic acid [14] along with biomass based polyesthers, [15] polyamides [16] and polyurethanes [17-18] have been also developed. The list of such biomass derived products, commercially available or under development is obviously much larger but a comprehensive review is out of the scope of this thesis. [19]

3. Work on conversion of biomass and municipal waste materials into carbon is still rare, but a significantly growing research topic. This is not surprising given the enormous potential of carbon to solve many of the challenges associated with sustainable technologies described earlier and outlined in Figure 1-1 b.

Carbon (meaning "coal" in Latin) is one of the most spread and versatile element in nature and responsible for our existence today. Humans have been using carbon since the beginning of our civilization. Carbon exists in nature in different allotrope forms from diamond to graphite and amorphous carbon. With the development of modern technology and the need of better preforming materials, a larger number of new carbon materials with well-defined nanostructures have been synthesised by various physical and chemical processes, such as fullerenes, carbon nanotubes (CNTs), graphitic onions, carbon coils, carbon fibers, and others. Carbon materials have been awarded three times in the last 15 years: fullerenes, the 1996 Nobel Prize in Chemistry; CNTs, the 2008 Kavli Prize in Nanoscience; graphene, the 2010 Nobel Prize in Physics. To date, it is probably fair to say that researches on carbon materials are encountering the most rapid development period which I would like to call "**The Back to Black"** period.

Despite its wide spreading and naturally occurrence on Earth, carbon has been mainly synthesised from fossil based precursors with sophisticated and energy consuming methodologies, having as a consequence the generation of toxic gases and chemicals. Pressures of an evolving sustainable society are encouraging and developing awareness amongst the materials science community of a need to introduce and develop novel media technology in the

most benign, resource efficient manner possible. Especially the preparation of porous carbon materials from renewable resources is a quickly recognised area, not only in terms of application/economic advantages but also with regard to a holistic sustainable approach to useful porous media synthesis. Carbon has been created from biomass form the very beginning, throughout the process of coal formation. Nature is mastering the production of carbon from biomass and we only need to translate it into a synthetic process. Therefore we need to reinvent the **"Green Carbon"** period.

Within this first chapter I will like first to provide a short overview on the state of art concerning the production of green carbon materials materials and finally a short history of the **Hydrothermal Carbonisation Technique** which is the main focus of this habilitation thesis.

1.2 Green Carbon Materials

By green carbon I mean materials that are synthesised from renewable and highly abundant precursors using as little energy consumption as possible (e.g. low temperatures) and avoiding the use and generation of toxic and polluting substances. In addition they should perform important technological tasks. These prerequisites are not trivial to achieve. Below I will provide some examples from the literature where the synthesis was such materials was targeted.

1.2.1 Carbon Nanotubes and Graphitic Nanostructures

Many potential applications have been proposed for carbon nanotubes, including conductive and high-strength composites, energy storage and energy conversion devices, sensors, field emission displays and radiation sources, hydrogen storage media, and nanometer-sized semiconductor devices, probes, and interconnects. [20] Some of these applications are now realized in products. Others are demonstrated in early to advanced devices, and one, hydrogen storage, is clouded by controversy. Nanotube cost, polydispersity in nanotube type, and limitations in processing and assembly methods are important barriers for some applications.

The demand for this raw material in the nanotechnology revolution is rising explosively. As this trend continues and nanomaterials become simple commodities, mundane production issues, such as the limitation of available resources, the cost of production materials, and the amount and cost of energy used in nanomaterial synthesis, will become the key cost drivers and bottlenecks. Many efforts have been made to find simple technologies for the mass production of CNTs at low cost.

A review on this topic has been recently published by Dang Sheng Su. [21] For mass production, the catalyst is considered the key factor for CNT growth. Transition metals, Fe, Co, Ni, V, Mo, La, Pt, and Y, are active for CNT synthesis. [22] Any effective production process that leads to a large reduction in costs will lead to a breakthrough of CNT applications. Investigations into new inexpensive feedstocks as well as more efficient catalyst/support combinations suitable for the mass production of CNTs are required.

In one example, Mount Etna lava was used as a catalyst and support for the synthesis of nanocarbon. [23] The main component is Si (SiO_2, 48 wt%), while the total amount of iron as Fe_2O_3 is as high as 11 wt%, distributed among silicate phases and Fe–Ti oxides (Figure 1-2). The presence of iron oxide particles in the porous structure of Etna lava make these materials promising for the growth and immobilisation of CNFs. For the CVD growth (700 °C), the crushed lava powder was introduced into a horizontal quartz reactor and reduced with hydrogen prior to CVD treatment. Ethylene was used as a carbon source. A mixture of CNFs and CNTs grown on lava rock was obtained (Figure 1-2) the nanofibers being dominate. TEM analysis revealed that the CNFs and CNTs obtained on lava exhibited a graphitic wall structure. The diameter distribution of the obtained CNTs and CNFs was broad, ranging from a few nanometers to several micrometers.
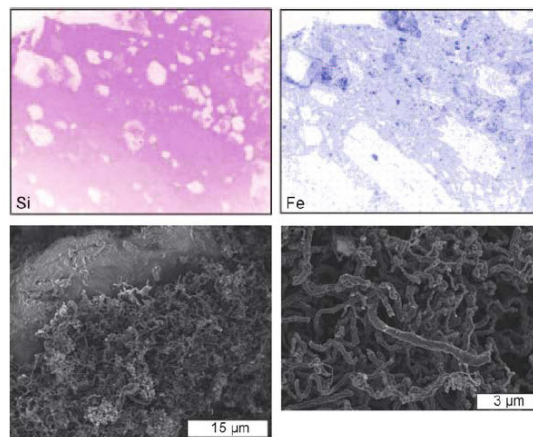
Figure 1-2: SEM images showing the elemental distribution of Si and Fe in lava stone granulate (top) and CNFs grown on lava (bottom) (taken with permission from [21]).

Although the estimated the volume of emitted lava was about 10–11 million cubic meters there are still issues associated with the global availability of such catalyst. The advantage of using lava, which avoids the wet chemical preparation of an iron catalyst, is also challenged by issues such as collection, transportation, and purification that may consume additional energy.

In another example, the same group used a special type of red soil from Croatia as a catalyst support for the synthesis of nanocarbons. The composition of the soil was a mixture of Al, Fe, Si, Ca and Mg oxides. Ethylene was used as carbon source for the CNT growth through a CVD process. CNFs grown on the red soil were found to exhibit a broad diameter distribution. The quality of the CNFs was comparable to that produced using lava rock as the catalyst/support reported above. [21]

Endo and his group used garnet sand pulverised from natural garnet stones (Ube Sand Kogyo, 1.4 $ US dollars per kg), as a catalyst and support and cheap urban household gas (1.1$ m^{-3}) as carbon source for the CVD process. [24] After CVD, the 200 mm-sized granulates of garnet powder (Figure 1-3a) were coarsened to about 400 mm (Figure 1-3b) and were covered with CNTs (Figure 1-3 c and d). About 25–30% of the weight from the sand-CNT composite corresponded to the CNTs. The produced CNTs had diameters typically in the range of 20–50 nm and exhibited well-ordered structures with large-diameter hollow cores (Figure 1-3e and f). The graphitisation degree of the walls was much higher than that of the CNFs prepared with lava and soil catalysts and in addition the resulting CNTs can be very easily separated from the garnet sand, simply by an ultrasonic bath in a water suspension.

Other low cost natural catalysts used in the production of CNTs were bentonite [25] natural minerals such as forsterite, disposide, quartz, magnesite, and brucite [26] or biomass-derived activated carbons previously modified with Fe by an impregnation method. [27-28] The later method resulted in hierarchically structured carbon, consisting of CNFs supported on activated carbon.
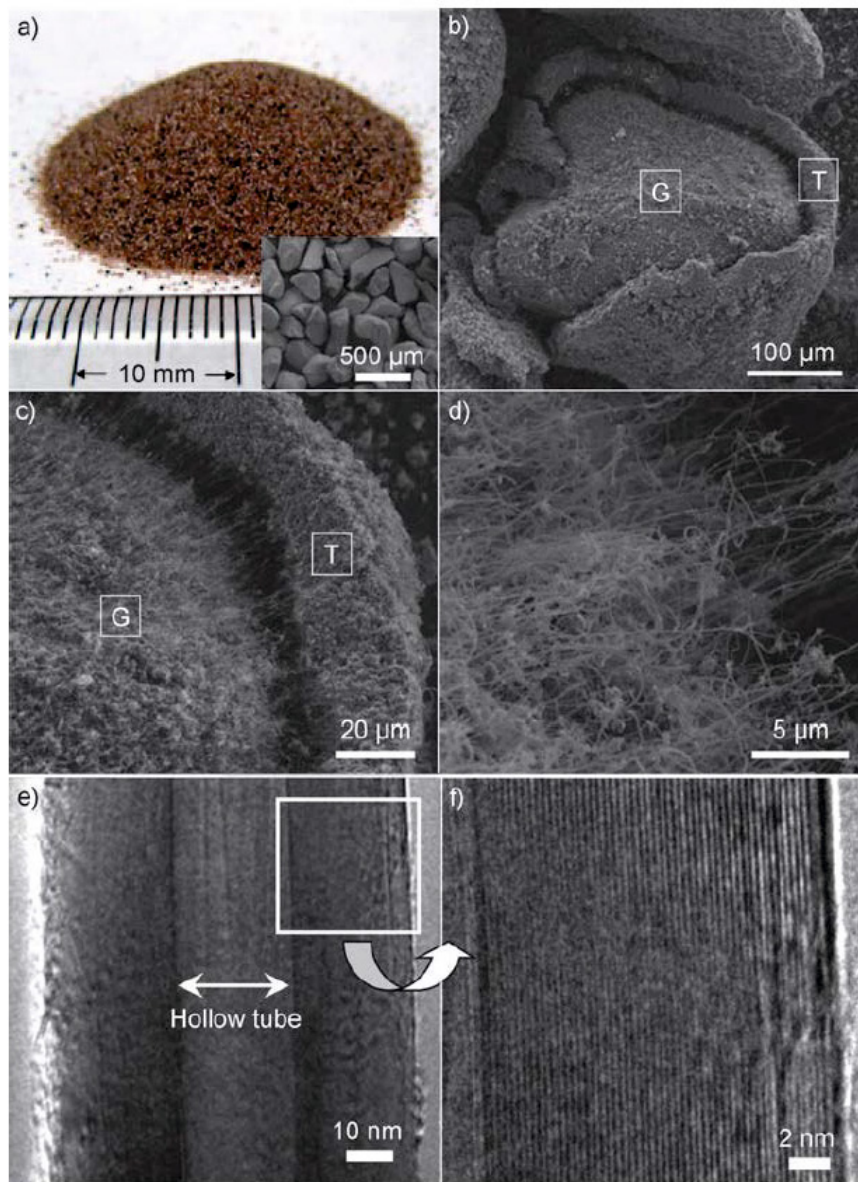
Figure 1-3: a) Photograph of the garnet sand used to produce nanotubes; the inset is an SEM image showing the average diameter of the sand particles (average size ca. 200 mm). b–d) SEM images of the CNTs grown on the surface of the garnet sand particles (in parts b and c, G and T indicate the garnet particle and CNT, respectively; part d corresponds to the CNTs only). e, f) TEM images showing the central hollow core of a typical as-grown CNT(e) and the highly linear and crystalline lattice of the wall (f) (reprinted with permission from Ref [24]).

In another study, the intrinsic iron content of biomass-derived ACs (especially from palm kernel shell, coconut, and wheat straw) was directly used as a catalyst for CNF synthesis. [29] The step

involving preparation of Fe particles on the activated carbon was circumvented and the overall process was simplified.

So far, only examples of how low cost and naturally abundant catalysts have been successfully integrated in the production of carbon nanotubes were presented. However the precursors used were gases of fossil fuel origin. The natural materials originating from biomass, such as coal, natural gas, or biomass itself, can be also used as a carbon source for greener nanocarbon synthesis.

The feasibility of producing CNTs and fullerenes from Chinese coals has been investigated. [30] When used as carbon source camphor ($C_{10}H_{16}O$), a botanical carbon material, was reported to be a highly efficient CNT precursor requiring an exceptionally low amount of catalyst in a CVD process. [31] CNTs can be also obtained by heating grass in the presence of a suitable amount of oxygen. [32] Fabrication of CNTs with carbohydrates could be expected when all the other possibilities have been tested. It is interesting that the well-known formation mechanism of CNTs (i.e., generating active carbon atomic species followed by assembling them into CNTs), cannot be applied here. Tubular cellulose in grass is directly converted into CNTs during the heat treatment.

In respect with developing different methods than CVD for the CNTs production, hydrothermal treatment represents a "greener" solution to nanotubes production, [33] provided that the precursors belong also the same category. Calderon Moreno at al used the hydrothermal process to reorganise amorphous carbon at moderate temperature 600°C and pressures of 100 MPa into nano-graphitic structures such as nanotubes and nanofibers. They provided evidence that carbon atoms rearrange to form curved graphitic layers during hydrothermal treatment. The growth of graphitic multiwall structures in hydrothermal conditions takes place by different mechanisms than in the gas-phase. Hydrothermal conditions provide a catalytic effect caused by the reactivity of hot water that allows the graphitic sheets to growth, move, curl and reorganise bonds at much lower temperatures than in the vapour phase in inert atmospheres. Such reorganisation is induced by the physical tendency to reach a more stable structure with lower energy, by reducing the number of dangling bonds in the graphitic sheets. The mechanism by which amorphous carbon rearranges into curled graphitic cells in the hot hydrothermal fluid is complex and involves the debonding of graphitic clusters from the bulk carbon material in hydrothermal conditions. Closed

graphitic lattices can be favoured at increasing temperatures or more chemically reactive environments.
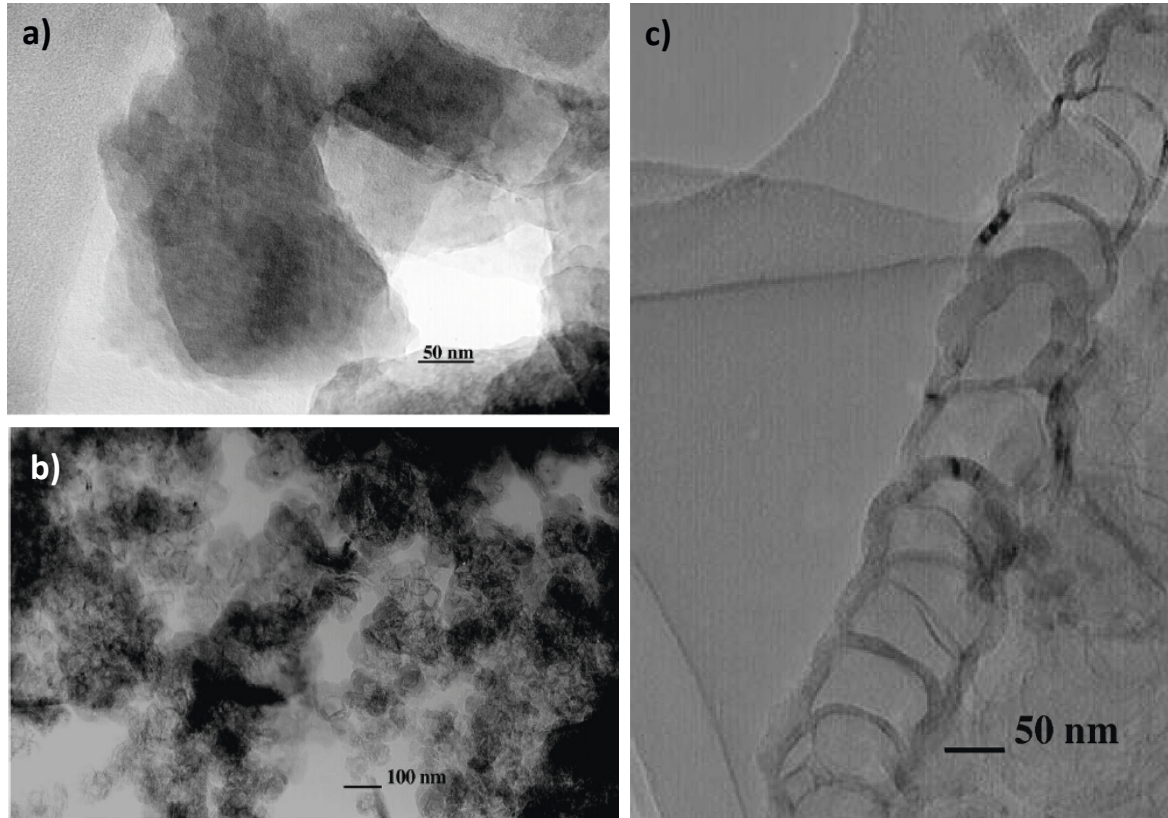
Figure 1-4: a) HRTEM micrograph of the amorphous carbon particles used as starting material; b) HRTEM micrograph of the bulk microstructure after hydrothermal treatment, showing the interconnected nanocells formed by curled graphitic walls; c) a chain of connected cells illustrating how the graphitic carbon form a single interconnected structure with multiple individual nanocells (taken with permission from [34]).

An interesting and low cost approach to high quality multiwall carbon nanotubes is reported by Pol et al who described a solvent-free process that converts polymer wastes such as low density and high-density polyethylene into multi-walled carbon nanotubes *via* thermal dissociation in the presence of chemical catalysts (cobalt acetate) in a closed system under autogenic pressure. [35] The readily available used/waste high density polyethylene is introduced for the fabrication of the MWCNTs. The digital image of such feedstock is shown Figure 1-5a.
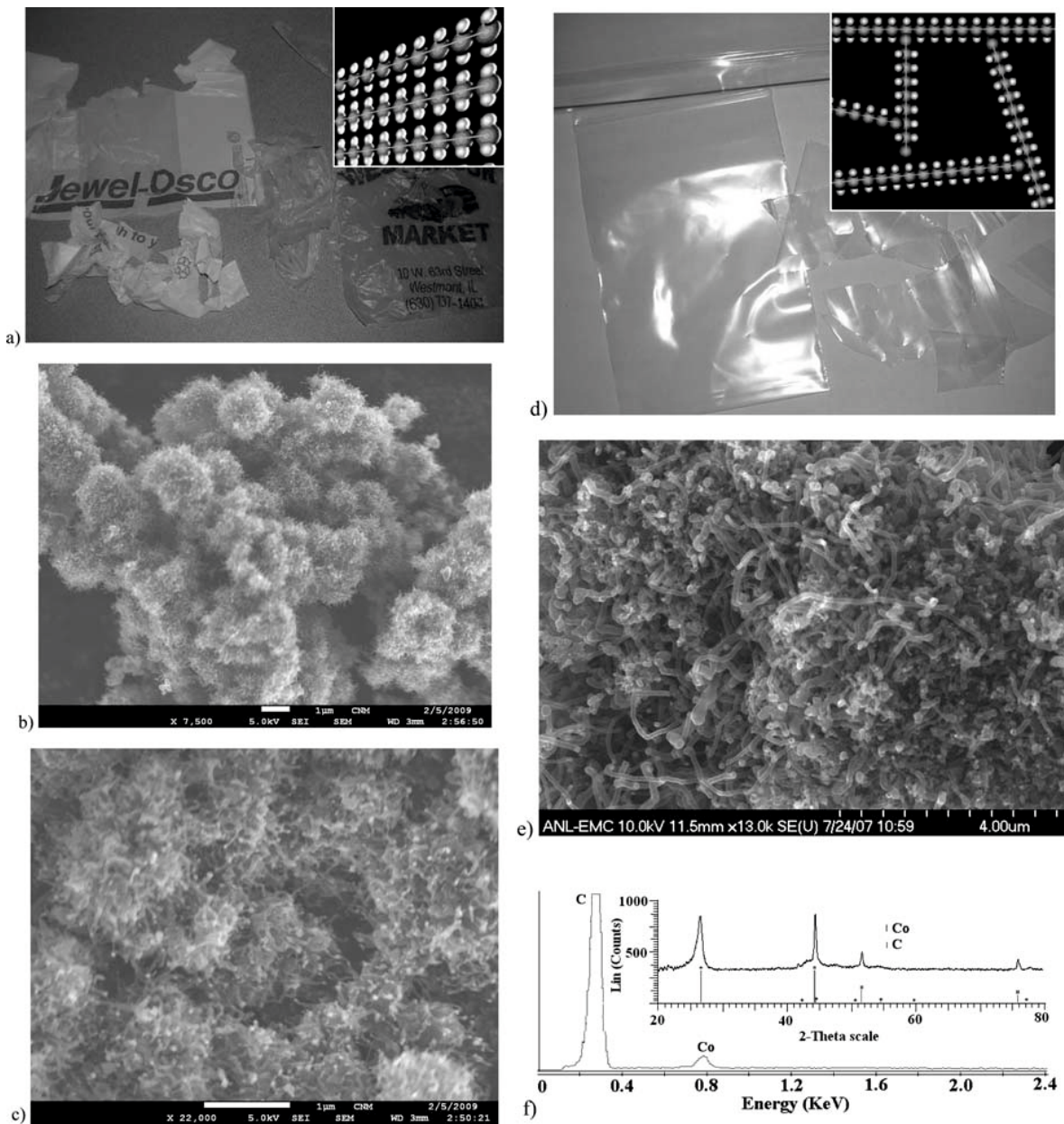
Figure 1-5: (a) Digital image of HDPE (inset the arrangement of PE groups) polymer wastes; (b) field emission scanning electron microscope (FE-SEM) image; (c) HRSEM image of as-prepared MWCNTs using a mixture of high density polyethylene and CoAc; (d) digital image of low density polyethylene (inset shows the arrangement of PE groups) polymer wastes; (e) FE-SEM of MWCNTs prepared from low density polyethylene; and (f) energy dispersive spectroscopy (EDS) measurements of as-prepared MWCNTs fabricated from low density polyethylene with CoAc catalyst (inset shows powder X-ray diffraction [XRD] pattern; taken with permission from [35])

The grocery bags are extruded from a machine that works in the following manner: for the length of the bag, polyethylene molecules (inset Figure 1-5a) are arranged in the long chain direction, allowing maximum lengthwise stretch and possessing greater strength. As shown in Figure 1-5b, the MWCNTs grew outwards forming bunches of 2–3 mm size. Each bunch is comprised of hundreds of MWCNTs growing outwards. Under the above mentioned experimental conditions, polyolefins will reduce to carbon, further producing MWCNTs around the cobalt nanocatalyst obtained from the dissociation of CoAc. The diameters of the MWCNTs are 80 nm; a length of more than a micron (Figure 1-5c) is observed within 2 h of the initial reaction time; thus, the growth of MWCNTs is a function of reaction time. A higher percentage of low density polyethylene was used for making soft, transparent grocery sacks (Figure 1-5d), shrink/stretch films, pond liners, construction materials, and agriculture film. In low density polyethylene, the molecules of polyethylene are randomly arranged (inset Figure 1-5 d). The as formed MWCNTs obtained from the thermolysis of waste low density polyethylene in the presence of CoAc catalyst in a closed system are shown in Figure 1-5e. The MWCNTs were randomly grown during 2 h of reaction time, not analogous to high density polyethylene. The dissociation of low density polyethylene with CoAc catalyst also created ~1000 psi pressure. In both cases, the grown MWCNTs were tipped with nanosized metallic Co particles. Transmission electron micrographs further confirmed the hollow tubular structures of MWCNTs. The energy dispersive spectroscopy (EDS) (Figure 1-5f) and X-ray diffraction (XRD) pattern (inset Figure 1-5f) of MWCNTs prepared from the mixture of low density polyethylene and CoAc confirmed that the MWCNTs are comprised of graphitic carbon and trapped cobalt. It needs to be mentioned that in the absence of the catalysts mocromreter-sized hard spheres were obtained instead. [36]

Given that polyethylene-based used plastics need hundreds of years to degrade in atmospheric conditions and innovative solutions are required for polymer waste, this technology represents a very environmentally friendly and low cost method to produce carbon nanotubes.

Graphitic carbon nanostructures have been synthesised from cellulose by Sevilla *via* a simple methodology that essentially consists of: (i) hydrothermal treatment of cellulose at 250 °C and (ii) impregnation of the carbonaceous product with a nickel salt followed by thermal treatment at 900°C. [37] The formation of graphitic carbon nanostructures seems to occur by a dissolution–precipitation mechanism in which amorphous carbon is dissolved in the catalyst nanoparticles and then reprecipitated as graphitic carbon around the catalyst particles. The subsequent removal

of the nickel nanoparticles and amorphous carbon by oxidative treatment leads to graphitic nanostructures with a coil morphology. This material exhibits a high degree of crystallinity and large and accessible surface area (Figure 1-6).
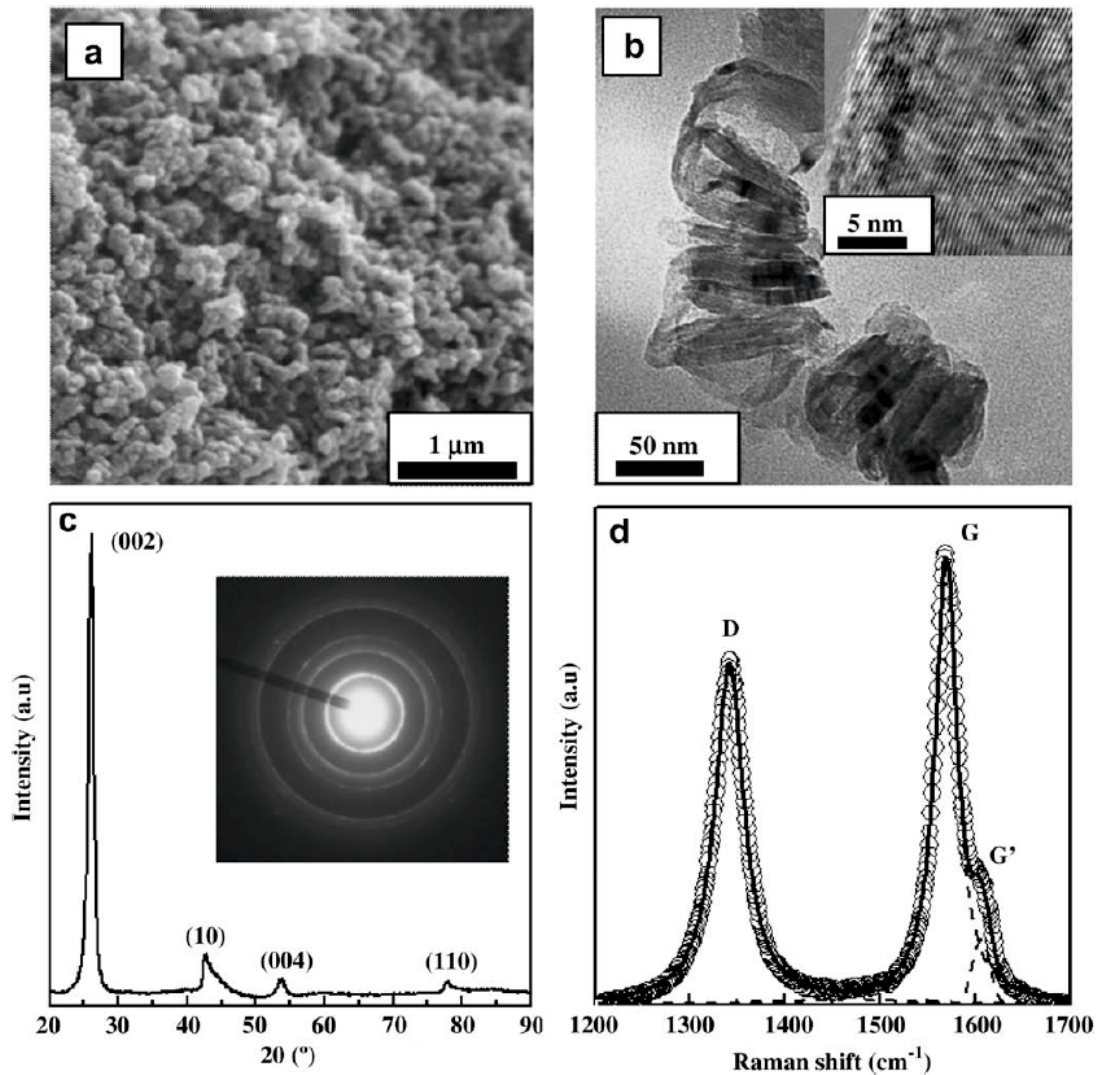
Figure 1-6: Structural characteristics of the graphitic carbon nanostructures obtained from the cellulose-derived hydrochar sample. (a) SEM microphotograph, (b) TEM image (Inset: HRTEM image), (c) XRD pattern (inset: selected area electron diffraction pattern) and (d) first-order Raman spectrum. (Taken with permission from [37])

Ashokkumar at al recently produced onion-like nitrogen doped graphitic structures by simple high carbonisation of collagen, a waste derivative from leather industries (Figure 1-7). Leather industry generates voluminous amounts of protein wastes at a level of 600 kg per ton of

14

skins/hides processed, as leather processing is primarily associated with purification of a multi-component skin to obtain a single protein, collagen. This synthetic route from bio-waste raw material provides a cost-effective alternative to the existing chemical vapour deposition methods for the synthesis of functional nanocarbon materials. [38]
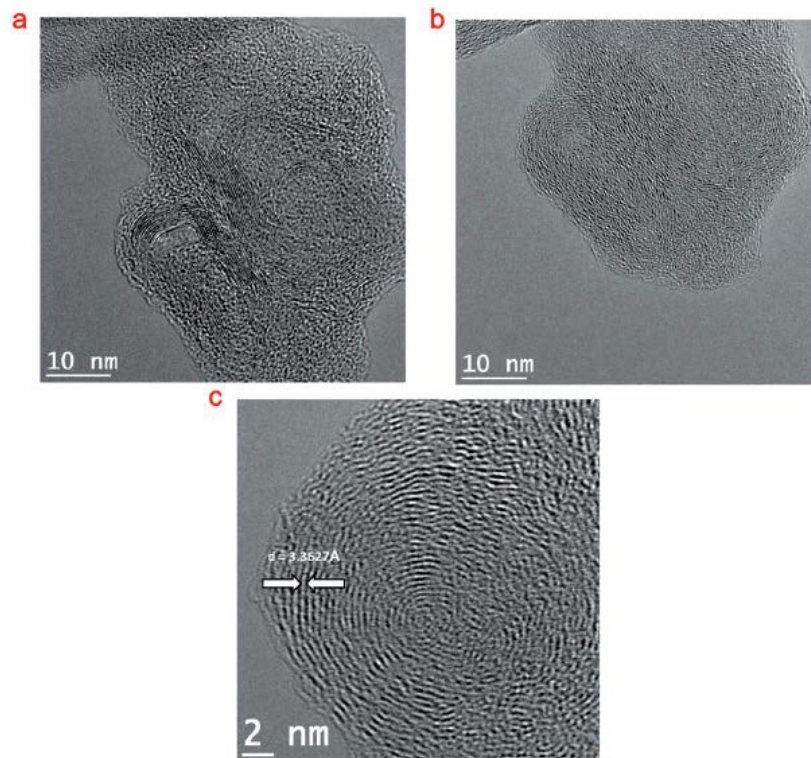
Figure 1-7: HRTEM images of the carbon material derived from collagen waste by treating at 1000 °C for 8 h. (a, b) Polyhedral and spherical onion like nanostructures showing the presence of graphitic layers with significant defects. (c) Spherical carbon nanoonion structure showing highly defective shells separated by 0.3363 nm (taken from [38]).

To summarise this subsection, some progress has been achieved in the synthesis of CNTs and graphitic nanostructures using either natural catalysts and/or natural precursors. Several studies have shown that natural materials can be used for the synthesis of nanomaterials, aimed at developing low cost, environmentally benign, and resource-saving processes for large-scale production. Catalysts free CNTs have been also successfully synthesised from amorphous carbon under hydrothermal conditions. The examples provided show promising potential and interesting perspective on nanocarbon syntheses using these inexpensive resources. Unfortunately when using such low cost technologies, uniform diameters and homogeneous structures are difficult to

achieve. Although the investigations were performed to look for a cost-effective method for mass production of CNTs, studies regarding the sustainability of using such natural organic materials are still required.

1.2.2 Graphene, Graphene Oxide and Highly Reduced Graphene Oxide

Since Nobel Prize winning in 2010, Graphene is the new star of carbon science. Obviously graphene is not a new material and it is known to form graphite by parallel stacking, as well as fullerenes and carbon naotubes by rolling into 2D nanostructures. The delay in it discovery as an individual material can be partially attributed to the single-atom-thick nature of the graphene sheet, which was initially thought to be thermodynamically unstable. [39] However, graphene is not only stable but also exhibits impressive electronic and mechanical properties (charge-carrier mobility= 250 000 cm^2 V^{-1} s^{-1} at room temperature, [40] thermal conductivity =5000W m^{-1} K^{-1}, [41] and mechanical stiffness = 1 TPa. [42]

Chemical exfoliation strategies such as sequential oxidation–reduction of graphite often result in a class of graphene-like materials best described as highly reduced graphene oxide (HRG), [43-44] with graphene domains, defects, and residual oxygen-containing groups on the surface of the sheets. Indeed, none of the currently available methods for graphene production yields bulk quantities of defect-free sheets.

In general, methods for producing graphene and HRG can be classified into five main classes: 1) mechanical exfoliation of a single sheet of graphene from bulk graphite using Scotch tape, [45-46] 2) epitaxial growth of graphene films, [47] 3) chemical vapour deposition (CVD) of graphene monolayers, [48] 4) longitudinal ''unzipping'' of CNTs, [41] [49] and 5) reduction of graphene derivatives, such as graphene oxide and graphene fluoride, [50,51] which in turn can be obtained from the chemical exfoliation of graphite.

Among all these methods, chemical reduction of exfoliated graphite oxide (GO), a soft chemical synthesis route using graphite as the initial precursor is the most efficient approach towards the bulk production of graphene-based sheets at low cost. Stankovich *et al*. [50,52] and Wang *et al*. [53] were among the first to carry out the chemical reduction of exfoliated graphene oxide sheets with hydrazine hydrate and hydroquinone as the reducing agents, respectively.

Since these first reports a significant effort has been made to find greener technologies to reduce exfoliated graphene oxide sheets to defect free graphene. Xia et al reported an electrochemical method as an effective tool to modify electronic states *via* adjusting the external power source to change the Fermi energy level of electrode materials surface. This represents a facile and fast approach to the synthesis of high quality graphene nanosheets in large scale by electrochemical reduction of the exfoliated GO at a graphite electrode, while the reaction rate can be accelerated by increasing the reduction temperature. [54]

Other sustainable methods for the reduction of GO involved photochemical, [55, 56] sugars, [57] iron, [58], Zn powder, [59], vitamin C [60], microwave [61], baker´s yeast, [62] phenols from tea [63], bacteria, [64,65] gelatin, [66] supercritical alchools [67] and others.

Despite all these milder ways towards GO reduction and although it could become an industrially important method to produce graphene, until now the quality of this liquid exfoliated graphene is still lower than mechanically exfoliated graphene due to the destruction of the basal plane structure during the oxidation and incomplete removal of the functional groups. In addition the oxidation of graphite is a tedious method involving very aggressive substances such as $KMnO_4$, $NaNO_3$, H_2SO_4.

Recently, many research groups have published several CVD methods for growing large-sized graphene on wafers. For the growth of epitaxial graphene on single-crystal silicon carbide (SiC), [47] the cost of this graphene is high due to the price of the 4H-SiC substrate. Also, metals such as copper, [68] nickel, [69] [48] iron, [70] cobalt, [71] and platinum [72] have been used as catalytic substrates to grow mono-, bi-, or multilayer graphene. The CVD method is limited to fossil-based gaseous carbon sources such as methane or acetylene.

The group of Tour has come up with a solution to the use of gas precursors and showed that large area, high quality graphene with controllable thickness can be grown from different solid carbon sources, such as polymer films or small molecules, deposited on a metal catalyst substrate at temperatures as low as 800 °C. Both pristine graphene and doped graphene were grown with this one-step process using the same experimental setup. [73] The same group expanded this concept to any solid precursor such as waste food and insects (e.g. cookies, chocolate, grass, plastics, roaches, and dog feces) to grow graphene directly on the backside of a Cu foil at 1050 °C under H_2/Ar flow (Figure 1-8). [74] The nonvolatile pyrolysed species were easily removed by etching

away the front side of the Cu. Analysis by Raman, XPS, UV and TEM indicates that the monolayer graphene derived from these carbon sources is of high quality. Through this method, low-valued foods and negative-valued solid wastes are successfully transformed into high valued graphene which brings new solutions for recycling of carbon from impure sources.

Hermenegildo García and co-workers showed that chitosan, a N-containing biopolymer can form high-quality films on glass, quartz, metals and other hydrophilic surfaces. Pyrolysis of chitosan films under argon at 800 °C and under inert atmosphere gives rise to high-quality single layer N-doped graphene films (over 99% transmittance) as evidenced by XPS, Raman spectroscopy, and TEM imaging. [75]
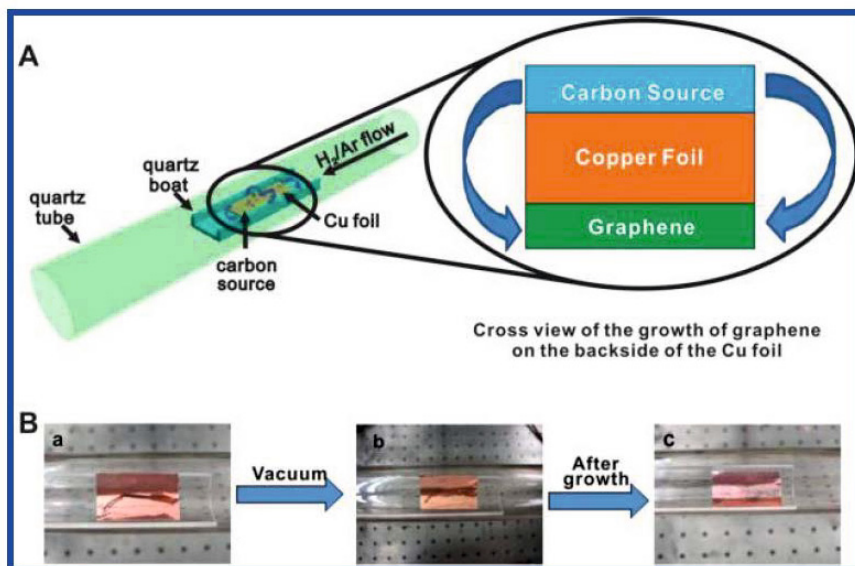
Figure 1-8: A) Diagram of the experimental apparatus for the growth of graphene from food, insects, or waste in a tube furnace. On the left, the Cu foil with the carbon source contained in a quartz boat is placed at the hot zone of a tube furnace. The growth is performed at 1050 °C under low pressure with a H2/Ar gas flow. On the right is a cross view that represents the formation of pristine graphene on the backside of the Cu substrate. (B) Growth of graphene from a cockroach leg. (a) One roach leg on top of the Cu foil. (b) Roach leg under vacuum. (c) Residue from the roach leg after annealing at 1050 °C for 15 min. The pristine graphene grew on the bottom side of the Cu film (not shown; taken from [74]).

Ruiz-Hitzky et al demonstrated the possibility of preparing graphene-like materials from natural resources such as sucrose (table sugar) and gelatin assembled to silica-based porous solids without a requirement for reducing agents. The resulting materials showed interesting

characteristics, such as simultaneous conducting behaviour afforded by the sp^2 carbon sheets, together with chemical reactivity and structural features, provided by the silicate backbone, which are of interest for diverse high-performance applications. The formation mechanism of supported graphene is still unclear, with further studies being needed to optimise its preparation following these green processes. [76]

Much progress has been done to date in the synthesis of sustainable graphene-derived materials. Given that the filed is relatively new, it is expected that new synthetic breakthroughs are soon to come for the large scale low cost synthesis of defect free graphene. It is my personal believe that graphene will continue pay an important role in materials science when associated with applications related to its exceptional physical properties. However for many of the applications described lately in the literature such as adsorption, catalyisis or energy storage, graphene in its pure form is not necessary and other carbon materials can perform as good or even better. In addition, the word "graphene" is too easy used in many of the recent publications for structures that are in fact just disordered graphite and are known in the literature since many years.

1.2.3 Activated Carbons

So far we discussed crystalline forms of carbons such as carbon nanotubes and graphenes. Activated carbons belong to the amorphous carbon category. Activated carbons are by far the oldest and most numerous materials prepared from renewable resources. A comprehensive description is behind the scope of this chapter. Many reviews exist in the literature on this topic. [77] In addition, Chapter 3 provides some information related to activated carbons. Activated carbons are prepared either by chemical or physical activation from biomass or waste precursors at temperatures between 600-900°C. They are microporous and used mainly for adsorption processes (i.e. water purification) and recently in supercapacitors [78] and gas storage. [79] One main disadvantage of activated carbons is the impossibility to predict their resulting porosity and to control their pore properties. I will not say more here and send the interested reader to chapter 3 which is dedicated to porous hydrothermal carbons and includes a section on chemical activation.

1.2.4 Starbons

The "Starbon" technology was developed in the group of Prof. James Clark at the University of York and it is based on the transformation of nanostructured forms of polysaccharide biomass into more stable porous carbonaceous forms for high value applications. [80] This approach opens new routes to the production of porous materials and represents a green alternative to traditional materials based on templating methods. The principle of this methodology relies on the generation of porous polysaccharide precursors which can then be carbonised to preserve the porous structure.

This synthetic strategy was initially focused on the use of mesoporous forms of the polysaccharide starch (from where the name is derived), but evolved into a generic tunable polysaccharide-based route. The technology involves: 1. Native polymer expansion *via* polysaccharide aqueous gel preparation; 2. Production of solid mesoporous polysaccharide, *via* solvent exchange/drying; 3. Thermal carbonisation

The resulting carbon-based materials are highly porous and mechanically stable in the temperature preparation range from 150 to 1000 °C. At temperature above 700 °C the carbonisation process leads to the synthesis of robust mesoporous carbons with a wide range of technologically important applications, including heterogeneous catalysis, water purification, separation media, as well as potential future applications in energy generation and storage applications.

The three main production stages are shown in Figure 1-9. Starch (typically from high amylose corn starch) is transformed into a gel by heating in water. The resulting viscous solution is cooled to 5 °C for typically one to two days to yield a porous gel. Water in the gel is then exchanged with the lower surface tension solvent ethanol. The resulting material is then filtered and may be oven dried to yield a predominantly mesoporous starch with a surface area of typically 180–200 $m^2 g^{-1}$. [81] [82] In the final stage, the mesoporous starch can be doped with a catalytic amount of an organic acid (e.g. p-toluenesulfonic acid).
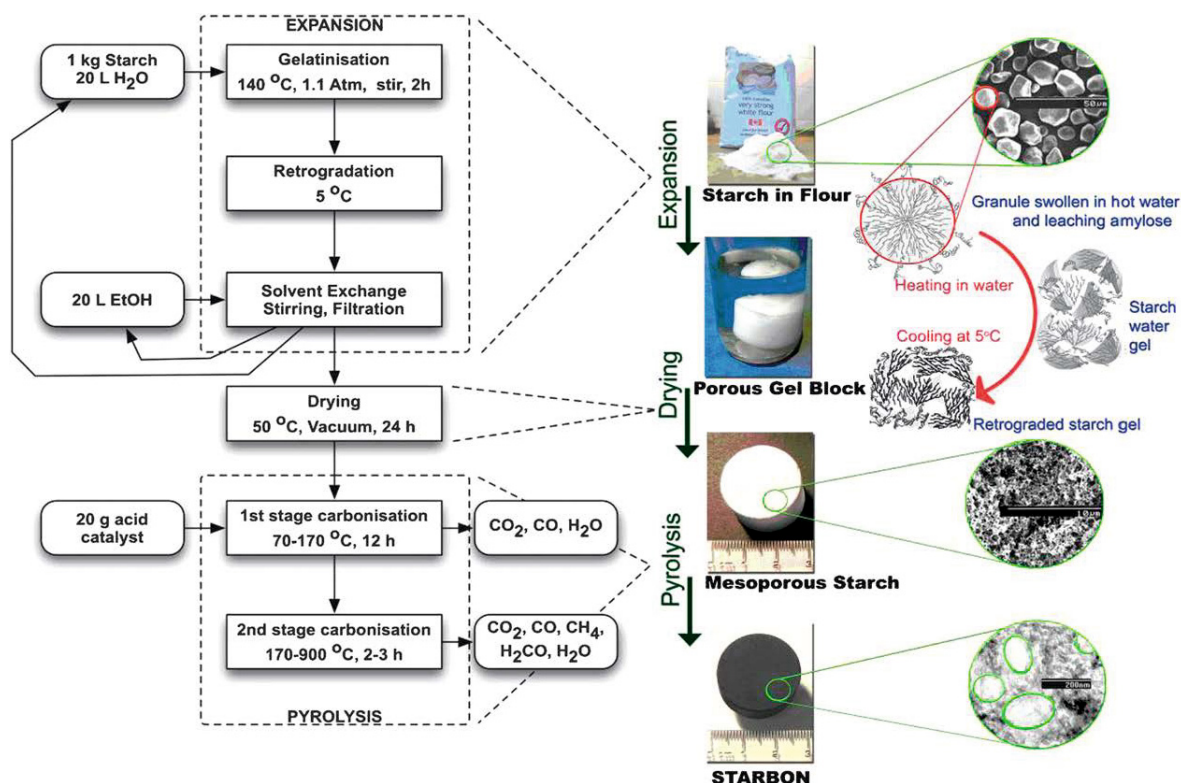
Figure 1-9: Diagrammatic representation of the main processing steps in the production of starch-derived Starbons materials (taken from ref 29).

The surface area of the as prepared materials increased with increasing the carbonisation temperature form 293 m^2/g at 300°C up to 600 m^2/g to 800°C. A nice aspect of this technology, similarly to hydrothermal carbons, is the fact that the surface polarity and the porosity can be nicely modulated with temperature.

Inspired from systematic studies on the starch system the same authors investigated the use of other linear polysaccharides in the preparation of second generation Starbons materials. It was anticipated that the utilisation of differing polysaccharide structures and functionality, may allow access to materials with differing textural properties and nano-morphological properties compared to the original starch-derived materials. Other two polysaccharides investigated were alginic acid and pectin.

Alginic acid is a complex seaweed-derived acidic polysaccharide with a linear polyuronide block copolymer structure. Non-porous native alginic acid may be transformed into a highly mesoporous aerogel (S_{BET} ca. 320 m^2 g^{-1}; V_{meso} ca. 2.50 cm^3 g^{-1}; pore size ca. 25 nm), presenting

21

an acidic accessible surface using the same methodology employed for the preparation of porous starches. [83] N_2 sorption analysis of alginic acid-derived Starbons demonstrated the highly mesoporous nature of these materials particularly at low carbonisation temperatures. Isotherms presented type IV reversible hysteresis while mesoporous volumes contracted with increasing carbonisation temperatures up to 500 °C, where porous properties were stabilised and maintained to 1000 °C (Figure 1-10E). TEM images (Figure 1-10 A-D) demonstrate the organisation of a rod-like morphology into mesoscale sized domains, generating the large mesopore volumes observed from N_2 sorption studies. Materials could also be prepared up to 1000 °C with no decrease in the quality of the textural properties or alteration in the structural morphology. This approach to the generation of second generation Starbons materials used no additive catalyst and simply relied on the decomposition of the acidic polysaccharide itself to initiate the carbonisation process.

Pectin, an inexpensive, readily available and multifunctional polyuronide, occurs as a major cell wall component in land plants. Common commercial sources include fruit skins, a major commercial waste product. Gelation of native citrus pectin in water and subsequent recrystallisation yielded a semi-transparent gel, which was converted to the porous aerogel via solvent exchange/drying outlined above. [84] Supercritical CO_2 extraction of ethanol was found to yield a low density ($\rho = 0.20$ g cm^{-1}), highly porous powder aerogel (Figure 1-11, PI-powder). Addition of hydrochloric acid yielded a viscous solution which could be poured into any desired shaped vessel and cured at room temperature to yield a very dimensionally strong gel, which upon water removal (*via* solvent exchange/ supercritical CO_2 drying) yielded extremely low density materials ($\rho = 0.07$ g cm^{-3}, Figure 1-11 PMI-monolith).

Direct heating of the pectin aerogels under an inert atmosphere allowed direct access to the carbonaceous materials. Promisingly, the resulting Starbons-type materials prepared from the two different pectin aerogel precursors, presented significantly different textural and mesoscale morphologies compared to materials prepared from either alginic acid or acid-doped starch.
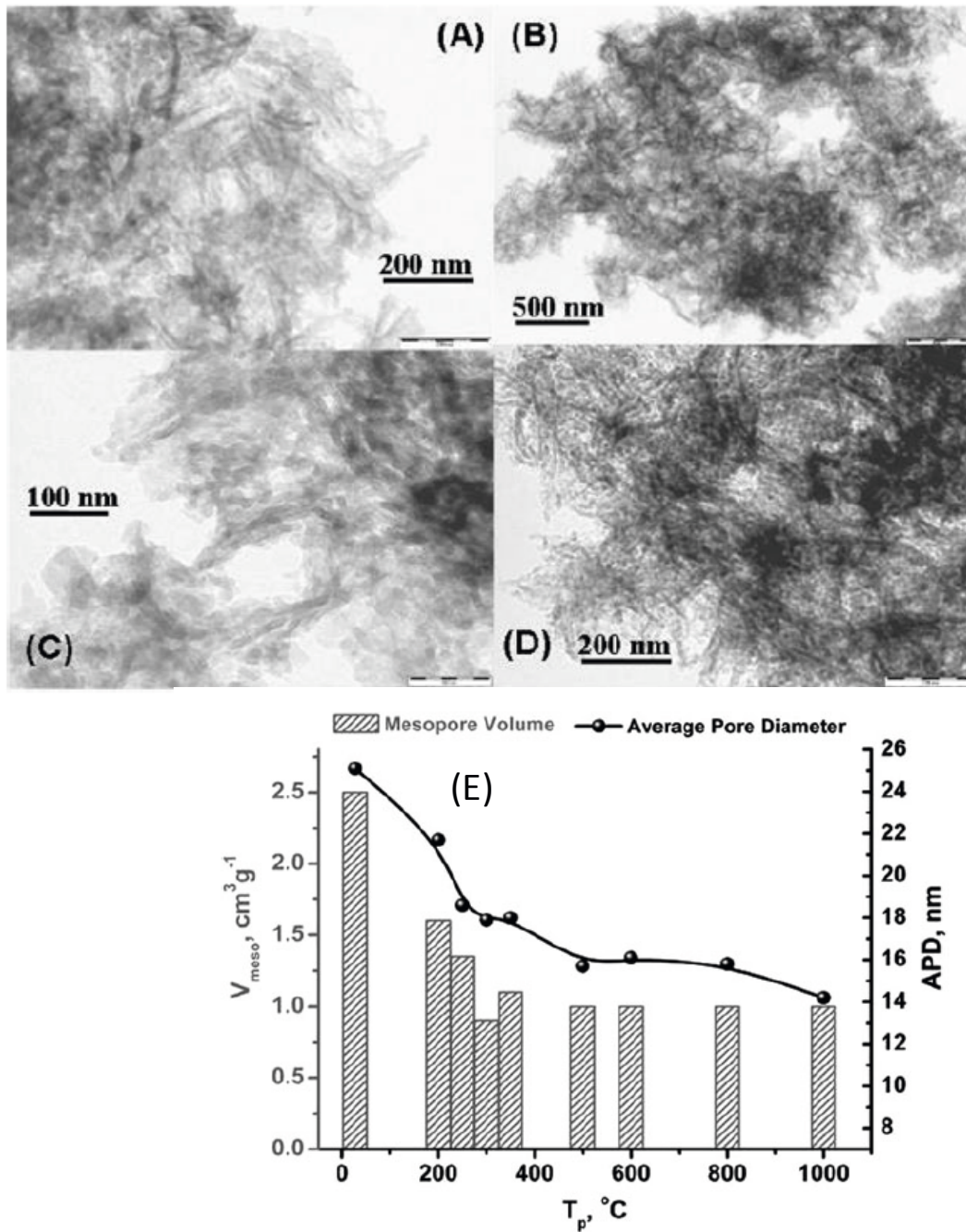
Figure 1-10: TEM images of Alginic acid (AS1)-derived Starbons materials at Tp = (A) 300 °C, (B) & (C) 500 °C, and (D) 1000 °C. (E): Impact of increasing carbonisation temperature on the mesoporous properties of alginic acid-derived Starbons materials (taken with permission from [83]).

Pectin-derived Starbons materials, demonstrate the flexibility of this material synthesis approach in terms of textural and morphological properties, and also further exemplifies the impact of

polysaccharide structure and the metastable gel state, necessary to generate the mesoporosity in these materials. The utilisation of pectin provides two extra routes (excitingly here from the same polysaccharide) for the production of second generation Starbons materials with not only differing porous properties, but with remarkably variable mesoscale morphology, accessible *via* a simple change in the gelation route and the resulting chemical modification of polysaccharide structure (Figure 1-11).
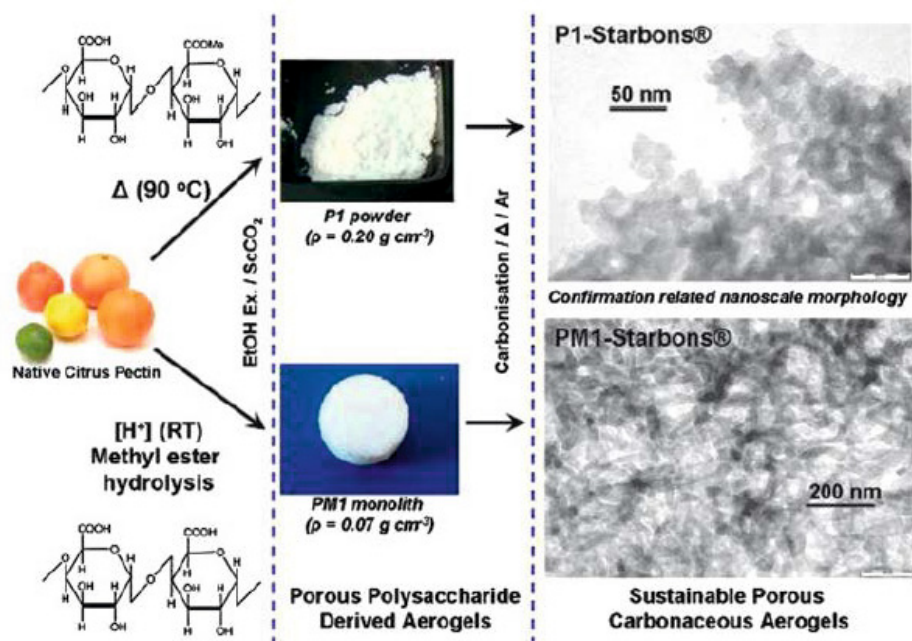
Figure 1-11: Representation of routes to porous polysaccharide derived materials from pectin, and the corresponding TEM images of pectin-derived Starbons-type materials (taken with permission from [84]).

Thus, using various polysacchardide precursors from plat material, Clark, White and co-workers successfully prepared well defined porous carbon materials with tunable porosity, morphology and surface groups. This of course opens the doors to many different applications.

Starbon materials have been intensively applied as heterogenous catalysts. The ability to adjust the surface properties and hydrophobicity/hydrophilicity balance of mesoporous

Starbons give the possibility to achieve highly active, selective and reusable water-tolerant solid acids. Thus, using Strbons as solid catalysis modified with sulphonic groups, the researchers from York successfully esterified various substrates (e.g. succinic (SA), fumaric, levulinic and itaconic

acids) in aqueous ethanol, providing high conversions and selectivities to their respective esters. [85] The rates of esterification of diacids (succinic, fumaric and itaconic) were found to be between 5–10 times higher for our Starbons acids compared to those of commercial solid acids (e.g. zeolites, sulfated zirconias, acidic clays and resins) or microporous commercial sulfonated carbons. (DARCOs and NORITs).

Starbons acids were also found to have a temperature dependent optimum of catalytic activity (that could be controlled by the preparation temperature of the parent Starbons and consequently by modification of its surface properties) as well as a substrate dependent catalytic activity maximum. Starbons acid activities peaked at ca. 400, 450 and 550 °C for succinic, fumaric and itaconic acids, respectively, with sharply reduced activities below or above this preparation temperature.

The same sulphonated carbons proved also to be efficient catalysts for preparation of aromatic amides *via* N-acylation of amines under microwave irradiation. [86] Quantitative conversions of starting material were typically achieved in 5–15 min with very high selectivities to the target product, applicable to a wide range of compounds (including aromatic and aliphatic amines), substituents and acids. Starbons acids provided starkly improved activities compared to other acid catalysts including zeolites, Al-MCM-41 and acidic clays.

The resulting Starbon materials have been also successfully hybridised with various nanoparticles and applied in heterogenous catalysis for various applications. A comprehensive review on this topic is found in [87]

Another very interesting and important application is the application of the alginc acid derived materials prepared at 1000°C as stationary phase in liquid chromatography for the separation of a mixture of carbohydrates. [83] The separation potential was demonstrated for the representative highly polar neutral sugars glucose (mono-), sucrose (di-), raffinose (tri-), stachyose (tetra-) and verbascose (pentasaccharide). This allowed the generation of designer PGC-type stationary phases, whereby the surface polarity could be moderated by selecting the carbonisation temperature employed to control the degree or extent of the graphitic structure development.

Starbons technology provides a useful and sustainable route to highly mesoporous carbonaceous materials. Flexibility in terms of preparation temperature provides carbonaceous materials with

tunable surface chemistry properties, arguably a material feature not accessible *via* conventional hard or soft template routes. By selection of gelation conditions, polysaccharide type and carbonisation temperature, a wide range of carbonaceous materials may be synthesised using inexpensive and readily available renewable sugar-based precursors. Drawbacks of this technology are the lack of well-defined pore size, most of the materials exhibiting broad pore size distributions. In addition the pore properties are unpredictable as in the case of activated carbons. This should be in principle overcome by the use of either hard or soft templates (preferably also derived from biomass) which should lead to hierarchically porous materials.

Another disadvantage of this technology is that it is limited to the use of polysaccharides in their pure form which requires additional isolation and purification from the derived biomass parent material.

1.2.5 The use of Ionic Liquids in Carbon Material´s Synthesis

Recently, it has been shown that carbon materials can also be obtained by the direct carbonisation of some particular ionic liquids (ILs). Thus, Paraknowitsch et al. designed a set of ILs entirely composed of C, N, and H atoms using a combination of nitrogen-containing cations (i.e. 1-ethyl-3-methylimidazolium –EMIm ⁻ or 3-methyl-1-butylpyridine – 3-MPB) and anions (i.e. dicyanamide – dca). [88] Within the same context, Lee et al. designed ILs composed of different cations that contained imidazolium groups (not only EMIm but also 1-butyl-3 methylimidazolium – BMIm – and 1,3-bis(cyanomethyl)imidazolium – BCNIm) and anions that contain nitrile groups (e.g. $[C(CN)_3]$-) (Figure 1-12). [89]
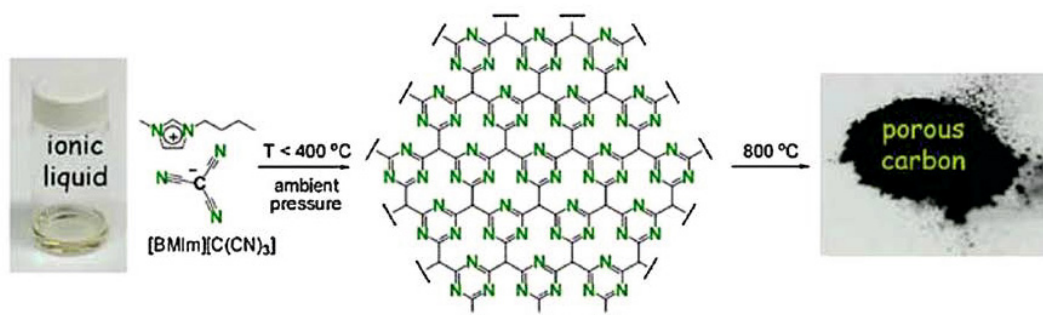
Figure 1-12: Reaction scheme of the trimerization of a nitrile-containing anion, leading to the formation of an extended framework (reproduced with permission from ref. [89])

The nitrogen rich character of these ILs allowed, by direct combustion, obtain nitrogen-doped carbons with remarkable nitrogen contents of up to 18 at%. [89] Interestingly, the authors demonstrated that the carbonisation yield depended on the nitrile character of the anions so that the resulting carbon network can be cross-linked *via* both cations and anions.

This approach based on the use of ILs as carbonaceous precursors was also applied to the preparation of porous carbons with high surface area. Kuhn et al. first reported on an ionothermal polymerisation method using a molten salt ($ZnCl_2$) and simple aromatic nitriles (e.g. 4,4-dicyanobiphenyl and 4-cyanobiphenyl), which provided carbonaceous polymer networks with well-defined bimodal micro- and (nonperiodic) mesoporosity. [90] Later on, Lee et al. used ILs composed of nitrile-functionalized imidazolium-based cations (e.g. $[BCNIm]^+$ or 1-cyanomethyl-3-methylimidazolium – $[MCNIm]^+$) and non-nitrile functionalized anions (e.g. $[Tf2N]^-$ and $[beti]^-$), with surface areas of up to 780 m^2 g^{-1}. [91] Obviously, anions release was detrimental in terms of both carbonisation yields and nitrogen contents.

Textural properties without compromising nitrogen contents can be also obtained with the aid of traditional structural directing agents. The use of porous silica nanoparticles promoted more so than a 10-fold increase in the surface area of the resulting carbons as compared to the ones obtained in the absence of templates [88] (ca. 1500 versus 70 m^2 g^{-1}, respectively).

More intriguing is the use of ILs as solvents for the formation of a silica gel from either hydrolysis or condensation of regular orthosilicate precursors (e.g. TEOS) or by coagulation of LUDOX-silica nanoparticles. Upon carbonisation of the ILs and subsequent silica dissolution hierarchical porous (with pores at both the nano- and microscale) carbon monoliths could be obtained (Fig. 12). [88, 92, 93] The application of this approach to ILs composed of dca (as anion) and a long-alkyl-chain pyridinium derivative (as cation) has recently resulted in the formation of composite (silica and nitrogen doped carbon) microparticles with a well-defined mesoporous structure. [94]
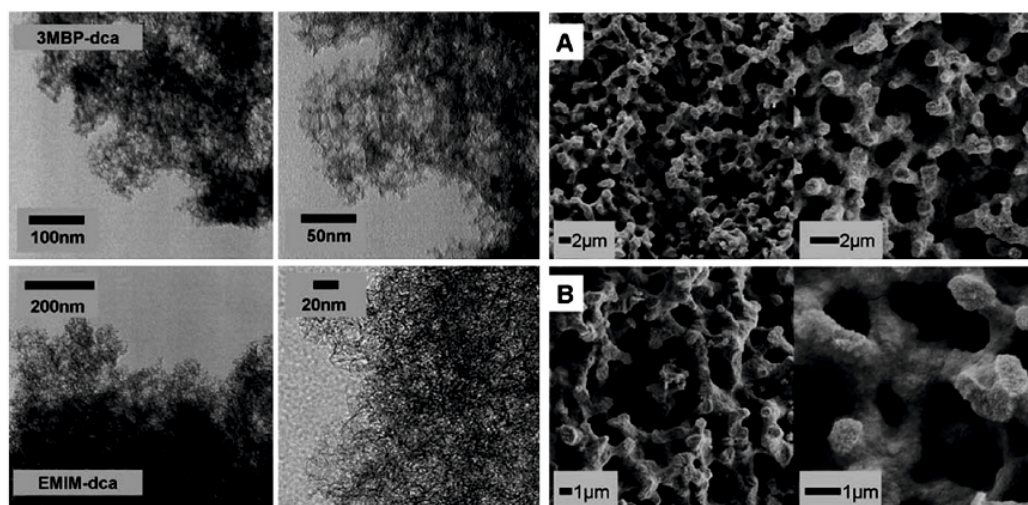
Figure 1-13: Left: TEM-images of Ludox-templated IL-derived materials. (Top) 3MBP-dca, (bottom) EMIM-dca. Right: SEM images of (A) silica monolith template and (B) N-doped carbon monolith (reproduced with permission from ref. [93])

However the "green" character of burning ionic liquids is questionable. Even if such materials showed good properties for various applications especially related to energy storage, the high cost of the precursor does not really pay off.

More valuable methodologies are those in which the ion liquids can be used as recyclable solvents. The lack of vapour pressure that characterises ILs is what provides their "green" character and makes them interesting alternatives for replacing highly volatile organic solvents in synthetic processes. Besides, their excellent solubilisation properties especially for biomass derived components, should make them very suitable for the production of various materials from biomass. All these, in combination with their very high thermal stability should make them ideal "solvents" for high temperature carbonisation reactions in ionic liquids.

Cooper et al. [95] was the first who reported a new type of solvothermal synthesis in which ILs were used as both the solvent and the structure directing agent in the synthesis of zeolites. This methodology has been termed ionothermal synthesis and, since then, this methodology has become one of the most widely used synthetic strategies among the zeolite community. It was also extended to the synthesis of metal-organic-frameworks (MOFs), covalent organic

frameworks (COFs), polymer organic frameworks (POFs), porous silicas, nanoparticles, polymers and others. For more details see ref [96-99].

In the context of this chapter, ionic liquids have been also used for "ionothermal carbonisation". Titirici and Taubert reported that metal containing ILs can play simultaneous the role of structural directing agent, catalyst for carbonisation and solvent. [100] Interestingly, the ionic liquids can be fully recovered at the end of each carbonisation process without any effect on their chemical structure. A variety of carbohydrates were used as a carbon source (i.e. D-glucose, D-fructose, D-xylose, and starch) while 1-butyl-3-methylimidazolium tetrachloroferrate(III), [Bmim][FeCl$_4$] as a reusable solvent and catalyst. The carbon materials derived from these different carbohydrates were similar in terms of particle size (Figure 1-14) and chemical composition, possessing relatively high surface areas from 44 to 155 m^2 g^{-1} after ionothermal processing, which could be significantly increased to >350 m^2 g^{-1} by further thermal treatment (e.g. post-carbonisation at 750 °C). CO$_2$ and N$_2$ sorption analysis, combined with Hg intrusion porosimetry, revealed a promising hierarchical pore structuring to these carbon materials. The ionic liquid [Bmim][FeCl$_4$] has a triple role: it acted as both a soft template to generate the charaterised pore structuring, solvent and as a catalyst resulting in enhanced ionothermal carbon yields. Importantly from a process point of view, the ionic liquid could be successfully recovered and reused.

The group of Dai et al used a protic ionic liquid [DMFH][Tf$_2$N], (*N*,*N*-dimethyl-*N*-formylammonium bis(trifluoromethylsulfonyl)imide) for the synthesis of ionothermal carbons from glucose and fructose at low temperature and ambient pressure. The observed results were similar with those of Titirici where the ionic liquid induces porosity in the resulting carbons while the carbonisation yield is significantly increased. [101]

Although only these two publications exist currently in the literature, this methodology could represent an interesting direction for the synthesis of sustainable carbon materials. The carbonisation can take place at atmospheric pressure in a standard flask while real biomass precursors can be employed. Especially cellulose is known to be solubilised by protic ionic liquids. In addition it was already reported that the ionic liquids can efficiently catalyse the production of hydroxymethyfurfural from biomass. [102] Thus, the HTC yield could be significantly increased.
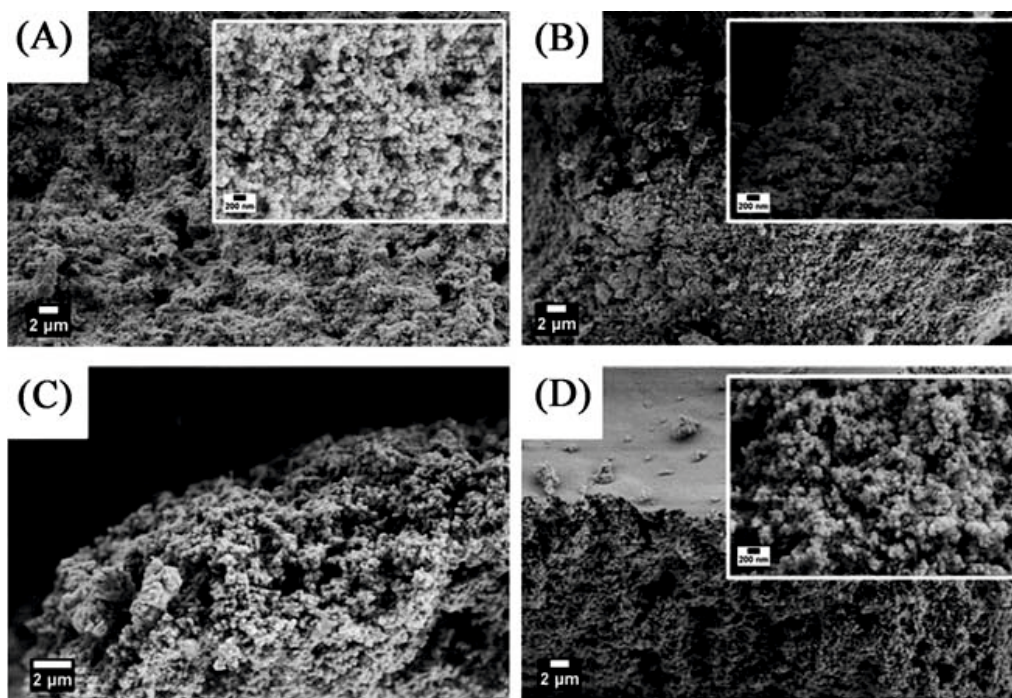
Figure 1-14: SEM micrographs of as-synthesised ionothermal carbons: (A) C-glucose,(B) C-fructose, (C) C-xylose and (D) C-starch (the scale bar in the inset is 200 nm, from ref 100).

By designing tailor-made ionic liquids it should be possible to control the porosity as well as introduce various functions into the resulting ionocarbons. Metal containing ionic liquids should offer the possibility to produce various interesting nanocomposites under the appropriate synthetic conditions. Furthermore, the use of ionic liquids will be far more justified in such a procedure compared with their irreversible conversion in various materials (i.e carbons, polymers).

A related class of ionic liquids named deep-eutectic solvents (DESs) are obtained by complexion of quaternary ammonium salts with hydrogen bond donors. [103] DESs share many characteristics of conventional ILs (e.g. non-reactive with water, non-volatile and biodegradable) while offer certain advantages. For instance, the preparation of eutectic mixtures in a pure state is accomplished more easily than for ILs. There is no need of post-synthesis purification as the purity of the resulting DES will only depend on the purity of the individual components. The low cost of those eutectic mixtures based on readily available components [104, 105] makes them particularly desirable (more than conventional ILs) for large-scale synthetic applications. However, a close inspection of recent literature revealed that their use in materials synthesis is

sporadic compared to ILs. This situation is currently slightly changing and different authors consider DESs as the next generation of ILs. They can act as true solvent-template-reactant systems, where the DES is at the same time the precursor, the template and the reactant medium for the fabrication of a desired material with a defined morphology or chemical composition. A comprehensive review on the topic was recently published by the group of Francisco del Monte. [106]

Carriazo et al. reported the preparation of a DES based on the mixture of resorcinol and choline chloride. Polycondensation with formaldehyde, resulted in the formation of monolithic carbons with a bimodal porosity comprising of both micropores and large mesopores of ca. 10 nm (Figure 1-15). [107] The morphology of the resulting carbons consisted of a bicontinuous porous network built out of highly cross-linked clusters that aggregated and assembled into a stiff, interconnected structure. This morphology is typical for carbons obtained *via* spinodal decomposition. [108] Carriazo et al. hypothesized that one of the components forming the DES (e.g. resorcinol) is acting as a precursor of the polymer phase whereas the second one (e.g. choline chloride) acts as a structural directing agent following a synthetic mechanism based on DES rupture and controlled delivery of the segregated SDA into the reaction mixture.

The wide range of DESs that can be prepared provides a remarkable versatility to this synthetic approach. For instance, Carriazo et al. also reported the use of ternary DESs composed of resorcinol, urea and choline chloride for the synthesis of carbons with surface areas up to 100 m^2 g^{-1} , which are higher than those of carbons obtained from binary DESs composed of resorcinol and choline chloride described above. Urea was here partially incorporated into the resorcinol–formaldehyde (RF) network (upon its participation in polycondensation reactions), the release of which (during carbonisation) resulted in the above-mentioned increase in the surface area.

The same group used DESs composed of resorcinol, 3-hydroxypyridine and choline chloride. [109] In this case, DESs played multiple roles in the synthetic process; liquid medium ensuring reagents homogenisation; structural directing agent responsible for the achievement of the hierarchically porous structure; source of carbon and nitrogen (Figure 1-16).
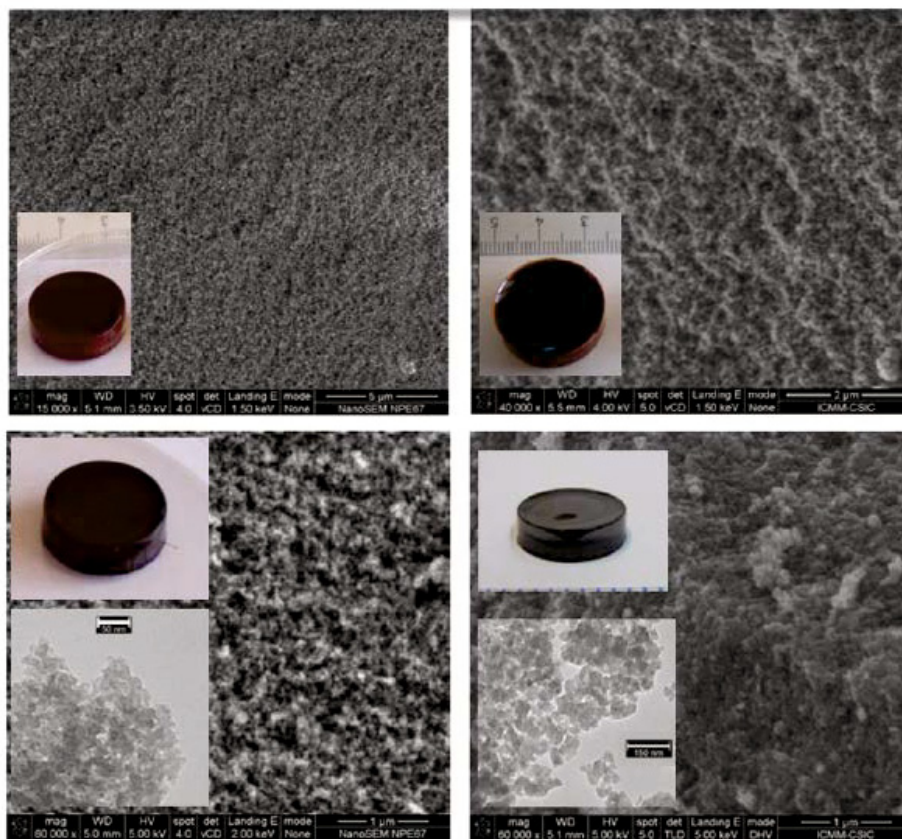
Figure 1-15: Top panel: SEM micrographs of RFRC-DES (left, bar is 5 mm) and RFRUC-DES (right, bar is 2 mm) gels. Insets show a picture of the monolithic RF gels. Bottom panel: SEM micrographs of CRC-DES (left, bar is 1 mm) and CRUC-DES (right, bar is 1 mm) monoliths. Insets show a picture of the respective monolithic carbons and TEM micrographs of CRC-DES (left, bar is 50 nm) and CRUC-DES (right, bar is 150 nm; reprinted with permission from ref. [107] where R=resorcinol; C= chlorine chloride; U= urea; F= formaldehyde)

The formation of a polymer rich phase upon resorcinol and 3-hydroxypyridine polycondensation promotes DES rupture and choline chloride segregation into a spinodal-like decomposition process. Interestingly, the resulting carbons exhibited a combination of surface areas and nitrogen contents (from ca. 550 to 650 m^2 g^{-1} and from ca. 13 to 5 at% for carbonisation temperatures ranging from 600 to 800 1C, respectively) that, unless traditional SDAs are also used, had never been attained by synthetic processes carried out in ILs.
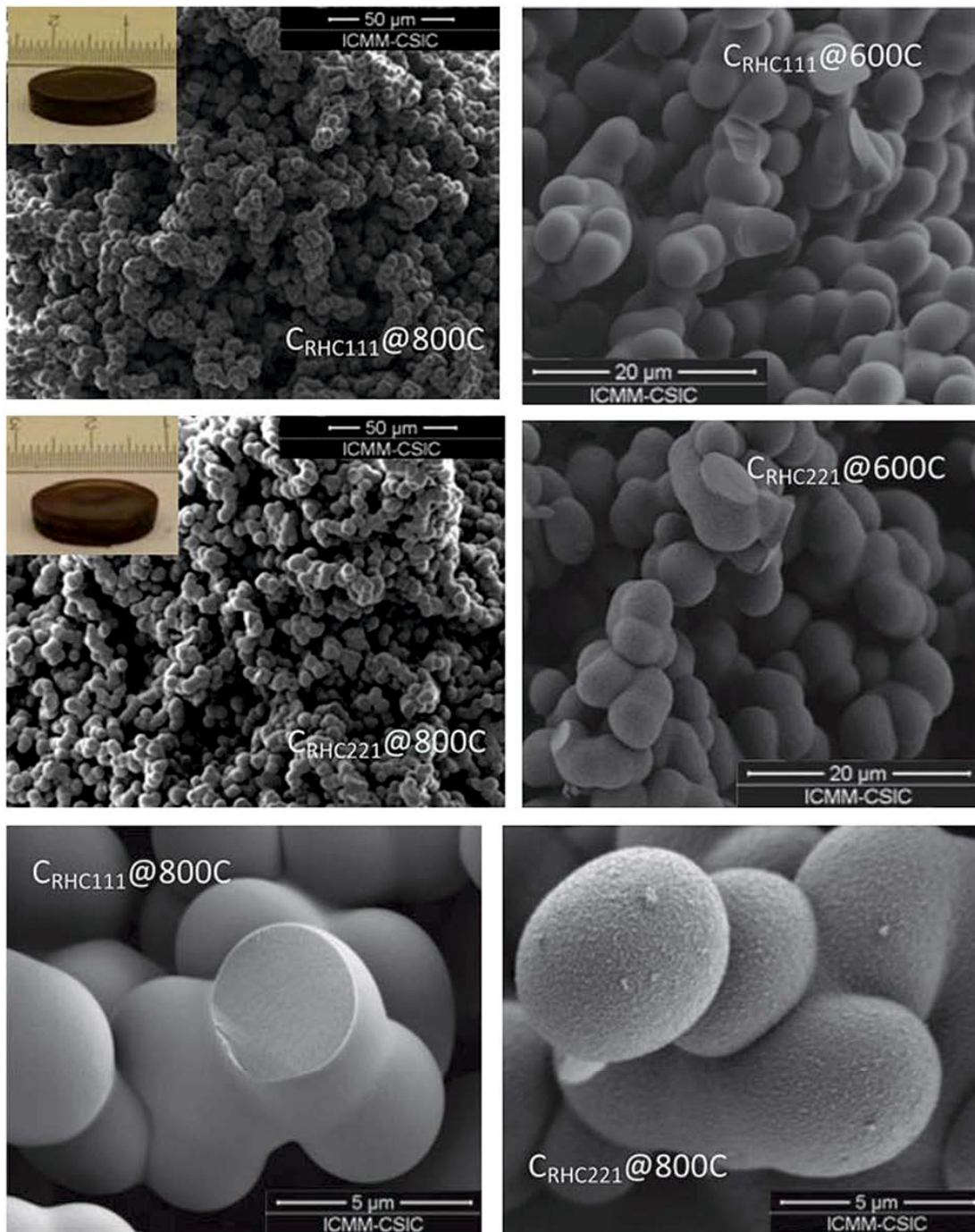
Figure 1-16: SEM micrographs of CRHC-DES and CRHC-DES obtained after thermal treatments at 600 and 800 °C. Insets show pictures of the CRHC-DES and CRHC-DES monoliths obtained after thermal treatment at 800 °C. C=chlorine chloride; R= resorcinol; H=3-hydroxypyridine (taken with permission from [109]).

It is finally worth noting the "green" character of this process because of the absence of residues and/or byproducts eventually released after the synthetic process; i.e. one of the components forming the DES (e.g. resorcinol, mixtures of resorcinol and hydroxypyridine or urea, and furfuryl alcohol) becomes the material itself with high yields of conversion (within the 60–80% range) whereas the second one (e.g. single choline chloride in resorcinol-based synthesis) is fully recovered and can be reused in subsequent reactions.

However, using DES based on carbohydrates (see ref [110]) should improve even further the green character of this methodology for the future production of carbon materials. Such DESs were found to serve some basic function in living cells and organisms. They include sugars, some amino acids, choline, and some organic acids such as malic acid, citric acid, lactic acid, and succinic acid. Looking at plant metabolomics data that Verpoorte and co-workers have collected over recent years, one could clearly see similarities with the synthetic ILs. Such plat major cellular constituents are perfect candidates for making ILs and DES. The authors made various combinations of these candidates (Table 1). [110] Such "natural deep eutectic solvents" (NADES) could be a potential interesting source for new and existing sustainable carbon materials which will be surely exploited in the near future.

Table I. *List of natural ILs and DES*

Combination	Molar Ratio
Citric acid:choline chloride	1:2, 1:3
Malic acid:choline chloride	1:1, 1:2, 1:3
Maleic acid:choline chloride	1:1, 1:2, 1:3
Aconitic acid:choline chloride	1:1
Glc:choline chloride:water	1:1:1
Fru:choline chloride:water	1:1:1
Suc:choline chloride:water	1:1:1
Citric acid:Pro	1:1, 1:2, 1:3
Malic acid:Glc	1:1
Malic acid:Fru	1:1
Malic acid:Suc	1:1
Citric acid:Glc	2:1
Citric acid:trehalose	2:1
Citric acid:Suc	1:1
Maleic acid:Glc	4:1
Maleic acid:Suc	1:1
Glc:Fru	1:1
Fru:Suc	1:1
Glc:Suc	1:1
Suc:Glc:Fru	1:1:1

1.2.6 Hydrothermal Carbonisation

The last procedure to produce green carbon materials is "Hydrothermal Carbonisation" and this makes the subject of this thesis. Its versatility, end-products, applications and limitations will be described within the following chapters. In my opinion, it is by far the most suitable and up-scalable technology at the moment to process waste biomass and transform it into end-products with remarkable properties.

Before going deeper into the secrets of HTC materials some important advantages of this unconventional carbonisation technique should be already underlined here:

(1) Carbonisation temperatures are low—typically in the range 130–250°C.

(2) Carbonisation takes place in water under self-generated pressures thus avoiding precursors drying costs.

(3) Typically spherical micro-sized particles are generally obtained.

(4) Controlled porosity can be easily introduced using nanocasting procedures, natural templates, or activation procedures/thermal treatments. (see Chapter 3)

(5) Carbonaceous materials can be combined with other components, e.g., inorganic nanoparticles to form composites with special physicochemical properties. (see Chapter 4)

(6) The resulting carbon particles have (polar) oxygenated groups residing at the surface which can be in turn used in post functionalisation strategies. (see Chapter 4)

(7) The surface chemistry and electronic properties can be easily controlled via additional thermal treatment, while the morphology and porosity are maintained. (see Chapter 2)

(8) The materials have wide range of timely technological applications (see Chapter 5)

(8) The synthesis can be described as ''carbon negative'', meaning that it has the potential to bind the CO_2 fixed by from original plant precursor.

In this first chapter I will provide a short history of the Hydrothermal Carbonisation Technology.

1.3   Brief History of HTC

As early as 1911 Friedrich Bergius was researching topics that are in our days of extreme importance for finding alternative fuels to the fossil based ones. Back then, Bergius was convinced that it should be possible to carry out the "water gas reaction" and produce hydrogen gas according to the formula $C + 2H_2O = CO_2 + H_2$, if the right temperature and pressure conditions are satisfied.[111] The aim was to inhibit the troublesome formation of carbon monoxide. In order to achieve such goals, Bergius was working at temperatures below 600°C, at which steam practically ceases to act on coal. His intention was to discover whether, the reaction velocity might be increased sufficiently to adjust the equilibrium. Indeed, Bergius managed to oxidise coal when liquid water was reacting with it at 200 bars producing carbon dioxide and hydrogen, in particular when transitional metal catalysts were present in the system. However, oxidation velocities, which would have made such reaction of commercial interest, failed to be achieved.

On the other hand, another very important observation was made: when peat was used as coal material, it was observed that exceptionally large amounts of carbon dioxide formed, and that the carbonaceous residue remaining in the vessel had the same elemental composition of natural coal. This observation prompted Bergius to study the decomposition process of plant substances more closely. He thought the process will be similar to the process of metamorphism which such plant-based compounds undergo in nature in the course of millions of years during their gradual transition into coal.

In those times, many researchers had already attempted to convert biomass, i.e. wood, which contains apart from cellulose lignin, into coal by heating, however the cellulose was decomposed. What Bergius and his co-workers did differently was that they managed to prevent super-heating and thus prevented the decomposition of cellulose by introducing steam. The resulting carbonisation products had a very similar composition with the natural coal. [112]

The secret that Bergius discovered was that the biomass precursor had to be in intimate contact with the liquid water which, at those mild temperatures (200°C) in the high-pressure vessel, could not decompose into gases.

The apparatus that Bergius used to produce the very first hydrothermal carbon ever is presented in Figure 1-17 . The temperatures were between 200-330°C in the presence of liquid water at pressures up to 200 bars.

The first report about the formation of what today I call hydrothermal carbon, citing was " per 2 parts cellulose, there were formed 2 parts carbon dioxide and 5 parts water, and a powdery substance which corresponded approximately to $C_{10}H_8O$ [112]."
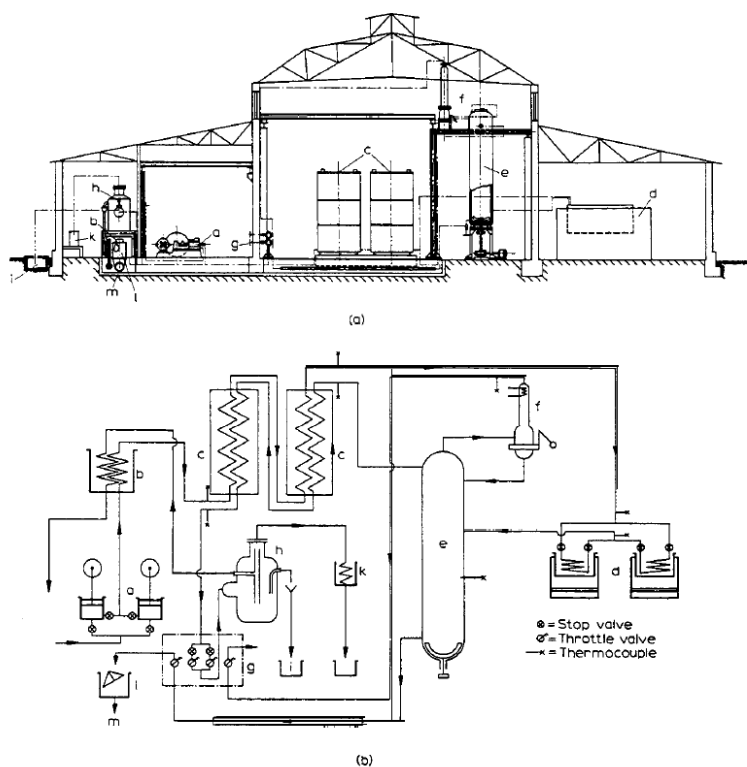
Figure 1-17: **Diagram of cellulose effluent decarbonisation: a) pump; b) pre-heater; c) heat exchanger, d) lead bath furnace; e) reaction vessel, f) column; g) control post, h) tar separator/ tar receiver; k) cooler for alcohol vapour; l) scales for coal slurry; m) screw conveyor(** *Taken from: Chemical reactions under high pressure, Nobel Lecture, May 21, 1932 by Friedrich Bergius***)**

This important discovery was followed by numerous studies of Bergius and his assistant Hugo Specht on the hydrogenation of this artificial coal. [113] Their experiments become the basis for the production of liquid and soluble compounds from coal, a process which they named "coal liquefaction". [114]

For all his studies on the production of synthetic coal as well as hydrogenation studies and his contributions in general to high-pressure reactions, [115] Bergius was awarded the Nobel Prize in 1931.

The enormous discovery of Bergius was followed later on by other studies. For example Berl and Schmidt in 1932 varied the biomass source and treated the different samples, in the presence of water, at temperatures between 150 and 350°C. [116] The latter authors summarised, *via* a series of papers in 1932, the knowledge of those days about the emergence of coal. [117] Later, Schuhmacher et al. analyzed the influence of pH on the outcome of the HTC reaction and found serious differences in the decomposition schemes, as identified by the C/H/O composition. [118] A review of the current knowledge on coal structure and its origin is found in ref. [119]

A renaissance of such experiments started with reports on the low temperature hydrothermal synthesis of carbon spheres (~200°C) using sugar or glucose as precursors in 2001. [120] [121] At the same time, Antonietti and Shu Hong Yu found that the presence of metal ions can effectively accelerate the hydrothermal carbonisation of starch, which shortened the reaction time to several hours and directed the synthesis towards various metal/carbon nanoarchitectures, such as Ag@carbon nanocables, [122] carbon nanofibers[123] and spheres [119].

This was the state of art in 2005, when I have joined the Max-Planck Institute firstly as a post-doctoral fellow and later on as a group leader. Ever since, myself together with a team of very talented PhD students and postdocs worked intensively on this technique, its fundamentals, the production of porous HTC carbons, hybrid materials and their applications.

It has to be mentioned that today the hydrothermal carbonisation is a very well established technique. Many research groups embarked on discovering and revealing new secrets this method still has to offer. Besides the academic interest, several private companies have started large scale HTC production. This is because the resulting char has coal-like properties and is expected to exhibit favourable behaviour with respect to combustion, gasification, and other thermal conversion processes for decentralized applications. [124]

Maybe one of the most appealing large scale applications of HTC process is, as suggested by , Seifritz in a pioneering dissertation in 1993 [125] , the fact that anthropogenic CO_2 emissions could be mitigated by converting biomass into charcoal. Thus, converting fast growing biomass

into HTC the CO_2 bound in the parent biomass will be no longer liberated *via* the photosynthesis process or atmospheric decomposition of the biomass residue but bound to the final solid carbonaceous structure. This represents an efficient way of taking the CO_2 out of the carbon cycle and thus a solution for reducing the already alarming amounts of CO_2 present in the atmosphere, known to be responsible for the climate change. The concept of biochar as an approach to carbon sequestration as well as increasing soil fertility, raise agricultural productivity and reduce pressure on forests in becoming increasingly attention over the past few years. [126] Several papers have been already published where the tremendous potential of HTC as a CO_2 negative solution for soil improvement is discussed. [127-129]

Besides the applications of HTC associated with large cost production, HTC can be used on a much lower scale in nanotechnology for energy and environmental related applications (Chapter 5). This is the author´s filed of expertise as well as the main focus of this thesis. For such applications, laboratory scale production of HTC (500 g -5kg) in commercially available reactors is sufficient.

Weather this technology will really represent one solution to the many of the problems our society is confronted these days regarding depletion of resources, global warming and energy is still be find out in the next coming years.

1.4 References

[1]   J. P. H. van Wyk, *Trends in Biotechnology* **2001**, *19*, 172-177.
[2]   F. W. Lichtenthaler, S. Peters, *Comptes Rendus Chimie* **2004**, *7*, 65-90.
[3]   Rahmstort S, Morgan J, Levermann A, Sach K., in *Global Sustainability-a Nobel Cause* (Ed.: M. M. Schellnhuber H. J, Stern N, Huber V, Kadner S), Cambridge University Press, **2010**, p. 68.
[4]   *MRS Bulletin* **2012**, *37*.
[5]   M. L. Green, L. Espinal, E. Traversa, E. J. Amis, *MRS Bulletin* **2012**, *37*, 303-309.
[6]   R. J. Koopmans, *Soft Matter* **2006**, *2*, 537-543.
[7]   O. Bobleter, *Progress in Polymer Science* **1994**, *19*, 797-841.
[8]   aK. A. Gray, L. S. Zhao, M. Emptage, *Current Opinion in Chemical Biology* **2006**, *10*, 141-146; bA. T. W. M. Hendriks, G. Zeeman, *Bioresource Technology* **2009**, *100*, 10-18; cJ. Lee, *Journal of Biotechnology* **1997**, *56*, 1-24; dY. Lin, S. Tanaka, *Applied Microbiology and Biotechnology* **2006**, *69*, 627-642; eL. R. Lynd, *Annual Review of Energy and the Environment* **1996**, *21*, 403-465; fL. R. Lynd, W. H. van Zyl, J. E. McBride, M. Laser, *Current Opinion in Biotechnology* **2005**, *16*, 577-583; gL. R. Lynd, P. J. Weimer, W. H. van Zyl, I. S. Pretorius, *Microbiology and Molecular Biology Reviews* **2002**, *66*, 506-+; hM. Ni, D. Y. C. Leung, M. K. H. Leung, *International Journal of Hydrogen Energy* **2007**, *32*, 3238-3247; iO. J. Sanchez, C. A. Cardona, *Bioresource*

Technology **2008**, *99*, 5270-5295; jY. Sun, J. Y. Cheng, *Bioresource Technology* **2002**, *83*, 1-11; kC. E. Wyman, *Annual Review of Energy and the Environment* **1999**, *24*, 189-226; lJ. Zaldivar, J. Nielsen, L. Olsson, *Applied Microbiology and Biotechnology* **2001**, *56*, 17-34.

[9]   aA. V. Bridgwater, *Fuel* **1995**, *74*, 631-653; bA. Demirbas, *Progress in Energy and Combustion Science* **2007**, *33*, 1-18; cL. Devi, K. J. Ptasinski, F. Janssen, *Biomass & Bioenergy* **2003**, *24*, 125-140; dY. Matsumura, T. Minowa, B. Potic, S. R. A. Kersten, W. Prins, W. P. M. van Swaaij, B. van de Beld, D. C. Elliott, G. G. Neuenschwander, A. Kruse, M. J. Antal, *Biomass & Bioenergy* **2005**, *29*, 269-292; eP. McKendry, *Bioresource Technology* **2002**, *83*, 37-46; fP. McKendry, *Bioresource Technology* **2002**, *83*, 55-63; gA. A. Peterson, F. Vogel, R. P. Lachance, M. Froeling, M. J. Antal, Jr., J. W. Tester, *Energy & Environmental Science* **2008**, *1*, 32-65; hD. Sutton, B. Kelleher, J. R. H. Ross, *Fuel Processing Technology* **2001**, *73*, 155-173.

[10]   aD. M. Alonso, J. Q. Bond, J. A. Dumesic, *Green Chemistry* **2010**, *12*, 1493-1513; bY.-C. Lin, G. W. Huber, *Energy & Environmental Science* **2009**, *2*, 68-80; cP. S. Nigam, A. Singh, *Progress in Energy and Combustion Science* **2011**, *37*, 52-68; dR. C. Saxena, D. Seal, S. Kumar, H. B. Goyal, *Renewable & Sustainable Energy Reviews* **2008**, *12*, 1909-1927; eA. Sivasamy, K. Y. Cheah, P. Fornasiero, F. Kemausuor, S. Zinoviev, S. Miertus, *Chemsuschem* **2009**, *2*, 278-300; fX. Tong, Y. Ma, Y. Li, *Applied Catalysis a-General* **2010**, *385*, 1-13; gS. Van de Vyver, J. Geboers, P. A. Jacobs, B. F. Sels, *Chemcatchem* **2011**, *3*, 82-94; hM. M. Yung, W. S. Jablonski, K. A. Magrini-Bair, *Energy & Fuels* **2009**, *23*, 1874-1887.

[11]   P. T. Anastas, M. M. Kirchhoff, *Accounts of Chemical Research* **2002**, *35*, 686-694.

[12]   aM. Adamczak, U. T. Bornscheuer, W. Bednarski, *European Journal of Lipid Science and Technology* **2009**, *111*, 800-813; bH. W. Blanch, B. A. Simmons, D. Klein-Marcuschamer, *Biotechnology Journal* **2011**, *6*, 1086-1102; cS. P. S. Chundawat, G. T. Beckham, M. E. Himmel, B. E. Dale, in *Annual Review of Chemical and Biomolecular Engineering, Vol 2, Vol. 2* (Ed.: J. M. Prausnitz), **2011**, pp. 121-145; dI. A. Hoell, G. Vaaje-Kolstad, V. G. H. Eijsink, in *Biotechnology and Genetic Engineering Reviews, Vol 27, Vol. 27* (Ed.: S. E. Harding), **2010**, pp. 331-366.

[13]   C. K. Hong, R. P. Wool, *Journal of Applied Polymer Science* **2005**, *95*, 1524-1538.

[14]   K. M. Nampoothiri, N. R. Nair, R. P. John, *Bioresource Technology* **2010**, *101*, 8493-8501.

[15]   S. Gharbi, J. P. Andreolety, A. Gandini, *European Polymer Journal* **2000**, *36*, 463-472.

[16]   A. Mitiakoudis, A. Gandini, *Macromolecules* **1991**, *24*, 830-835.

[17]   S. Boufi, M. N. Belgacem, J. Quillerou, A. Gandini, *Macromolecules* **1993**, *26*, 6706-6717.

[18]   C. Pavier, A. Gandini, *European Polymer Journal* **2000**, *36*, 1653-1658.

[19]   aA. Brandelli, D. J. Daroit, A. Riffel, *Applied Microbiology and Biotechnology* **2010**, *85*, 1735-1750; bC. Briens, J. Piskorz, F. Berruti, *International Journal of Chemical Reactor Engineering* **2008**, *6*; cR. Fischer, N. Emans, *Transgenic Research* **2000**, *9*, 279-299; dR. Harun, M. Singh, G. M. Forde, M. K. Danquah, *Renewable & Sustainable Energy Reviews* **2010**, *14*, 1037-1047; eA. S. Mamman, J.-M. Lee, Y.-C. Kim, I. T. Hwang, N.-J. Park, Y. K. Hwang, J.-S. Chang, J.-S. Hwang, *Biofuels Bioproducts & Biorefining-Biofpr* **2008**, *2*, 438-454; fA. Pandey, C. R. Soccol, *Brazilian Archives of Biology and Technology* **1998**, *41*, 379-389; gO. Pulz, W. Gross, *Applied Microbiology and Biotechnology* **2004**, *65*, 635-648; hR. R. Singhania, A. K. Patel, C. R. Soccol, A. Pandey,

Biochemical Engineering Journal **2009**, *44*, 13-18; iD. Sipkema, R. Osinga, W. Schatton, D. Mendola, J. Tramper, R. H. Wijffels, *Biotechnology and Bioengineering* **2005**, *90*, 201-222; jY. Tokiwa, B. P. Caiabia, *Canadian Journal of Chemistry-Revue Canadienne De Chimie* **2008**, *86*, 548-555.

[20] R. H. Baughman, A. A. Zakhidov, W. A. de Heer, *Science* **2002**, *297*, 787-792.

[21] D. S. Su, *Chemsuschem* **2009**, *2*, 1009-1020.

[22] A.-C. Dupuis, *Progress in Materials Science* **2005**, *50*, 929-961.

[23] D. S. Su, X.-W. Chen, *Angewandte Chemie* **2007**, *119*, 1855-1856.

[24] M. Endo, K. Takeuchi, Y. A. Kim, K. C. Park, T. Ichiki, T. Hayashi, T. Fukuyo, S. Linou, D. S. Su, M. Terrones, M. S. Dresselhaus, *Chemsuschem* **2008**, *1*, 820-822.

[25] A. Rinaldi, J. Zhang, J. Mizera, F. Girgsdies, N. Wang, S. B. A. Hamid, R. Schlogl, D. S. Su, *Chemical Communications* **2008**, 6528-6530.

[26] S. Kawasaki, M. Shinoda, T. Shimada, F. Okino, H. Touhara, *Carbon* **2006**, *44*, 2139-2141.

[27] D. S. Su, X. Chen, G. Weinberg, A. Klein-Hofmann, O. Timpe, S. B. A. Hamid, R. Schlögl, *Angewandte Chemie International Edition* **2005**, *44*, 5488-5492.

[28] X.-W. Chen, D. S. Su, S. B. A. Hamid, R. Schlögl, *Carbon* **2007**, *45*, 895-898.

[29] X. W. Lou, J. S. Chen, P. Chen, L. A. Archer, *Chemistry of Materials* **2009**, *21*, 2868-2874.

[30] aA. Dosodia, C. Lal, B. P. Singh, R. B. Mathur, D. K. Sharma, *Fullerenes Nanotubes and Carbon Nanostructures* **2009**, *17*, 567-582; bQ. Jieshan, L. Yongfeng, W. Yunpeng, W. Tonghua, Z. Zongbin, Z. Ying, L. Feng, C. Huiming, *Carbon* **2003**, *41*, 2170-2173; cR. B. Mathur, C. Lal, D. K. Sharma, *Energy Sources Part a-Recovery Utilization and Environmental Effects* **2007**, *29*, 21-27; dJ. S. Qiu, Y. F. Li, Y. P. Wang, W. Li, *Fuel Processing Technology* **2004**, *85*, 1663-1670; eJ. S. Qiu, F. Zhang, Y. Zhou, H. M. Han, D. S. Hu, S. C. Tsang, P. J. F. Harris, *Fuel* **2002**, *81*, 1509-1514; fJ. S. Qiu, Y. Zhou, L. N. Wang, S. C. Tsang, *Carbon* **1998**, *36*, 465-467; gJ. S. Qiu, Y. Zhou, Z. G. Yang, D. K. Wang, S. C. Guo, S. C. Tsang, P. J. F. Harris, *Fuel* **2000**, *79*, 1303-1308; hJ. S. Qiu, Y. Zhou, Z. G. Yang, L. N. Wang, F. Zhang, S. C. Tsang, P. J. S. Harris, *Molecular Materials* **2000**, *13*, 377-384; iM. Z. Wang, F. Li, *New Carbon Materials* **2005**, *20*, 71-82; jM. A. Wilson, H. K. Patney, J. Kalman, *Fuel* **2002**, *81*, 5-14; kX.-f. Zhao, J.-s. Qiu, Y.-x. Sun, C. Hao, T.-j. Sun, L.-w. Cui, *New Carbon Materials* **2009**, *24*, 109-113; lW. Zhi, W. Bin, G. Qianming, S. Huaihe, L. Ji, *Materials Letters* **2008**, *62*, 3585-3587.

[31] M. Kumar, T. Okazaki, M. Hiramatsu, Y. Ando, *Carbon* **2007**, *45*, 1899-1904.

[32] Z. H. Kang, E. B. Wang, B. D. Mao, Z. M. Su, L. Chen, L. Xu, *Nanotechnology* **2005**, *16*, 1192.

[33] Y. Gogotsi, J. A. Libera, M. Yoshimura, *J. Mater. Res.* **2000**, *15*, 2591-2594.

[34] J. M. Calderon Moreno, T. Fujino, M. Yoshimura, *Carbon* **2001**, *39*, 618-621621.

[35] V. G. Pol, P. Thiyagarajan, *Journal of Environmental Monitoring* **2010**, *12*, 455-459.

[36] S. V. Pol, V. G. Pol, D. Sherman, A. Gedanken, *Green Chemistry* **2009**, *11*, 448-451.

[37] M. Sevilla, A. B. Fuertes, *Chemical Physics Letters* **2010**, *490*, 63-68.

[38] M. Ashokkumar, N. T. Narayanan, A. L. Mohana Reddy, B. K. Gupta, B. Chandrasekaran, S. Talapatra, P. M. Ajayan, P. Thanikaivelan, *Green Chemistry* **2012**, *14*, 1689-1695.

[39] N. D. Mermin, *Physical Review* **1968**, *176*, 250-254.

[40]   M. Orlita, C. Faugeras, P. Plochocka, P. Neugebauer, G. Martinez, D. K. Maude, A. L. Barra, M. Sprinkle, C. Berger, W. A. de Heer, M. Potemski, *Physical Review Letters* **2008**, *101*, 267601.

[41]   A. A. Balandin, S. Ghosh, W. Bao, I. Calizo, D. Teweldebrhan, F. Miao, C. N. Lau, *Nano Letters* **2008**, *8*, 902-907.

[42]   C. Lee, X. Wei, J. W. Kysar, J. Hone, *Science* **2008**, *321*, 385-388.

[43]   S. Park, J. An, I. Jung, R. D. Piner, S. J. An, X. Li, A. Velamakanni, R. S. Ruoff, *Nano Letters* **2009**, *9*, 1593-1597.

[44]   S. Park, J. An, R. D. Piner, I. Jung, D. Yang, A. Velamakanni, S. T. Nguyen, R. S. Ruoff, *Chemistry of Materials* **2008**, *20*, 6592-6594.

[45]   K. S. Novoselov, D. Jiang, F. Schedin, T. J. Booth, V. V. Khotkevich, S. V. Morozov, A. K. Geim, *Proceedings of the National Academy of Sciences of the United States of America* **2005**, *102*, 10451-10453.

[46]   K. S. Novoselov, A. K. Geim, S. V. Morozov, D. Jiang, Y. Zhang, S. V. Dubonos, I. V. Grigorieva, A. A. Firsov, *Science* **2004**, *306*, 666-669.

[47]   C. Berger, Z. Song, X. Li, X. Wu, N. Brown, C. Naud, D. Mayou, T. Li, J. Hass, A. N. Marchenkov, E. H. Conrad, P. N. First, W. A. de Heer, *Science* **2006**, *312*, 1191-1196.

[48]   K. S. Kim, Y. Zhao, H. Jang, S. Y. Lee, J. M. Kim, K. S. Kim, J.-H. Ahn, P. Kim, J.-Y. Choi, B. H. Hong, *Nature* **2009**, *457*, 706-710.

[49]   L. Jiao, L. Zhang, X. Wang, G. Diankov, H. Dai, *Nature* **2009**, *458*, 877-880.

[50]   S. Stankovich, D. A. Dikin, R. D. Piner, K. A. Kohlhaas, A. Kleinhammes, Y. Jia, Y. Wu, S. T. Nguyen, R. S. Ruoff, *Carbon* **2007**, *45*, 1558-1565.

[51]   L. J. Cote, F. Kim, J. Huang, *J. Am. Chem. Soc.* **2008**, *131*, 1043-1049.

[52]   S. Stankovich, R. D. Piner, X. Chen, N. Wu, S. T. Nguyen, R. S. Ruoff, *Journal of Materials Chemistry* **2006**, *16*, 155-158.

[53]   G. Wang, J. Yang, J. Park, X. Gou, B. Wang, H. Liu, J. Yao, *The Journal of Physical Chemistry C* **2008**, *112*, 8192-8195.

[54]   H. L. Guo, X. F. Wang, Q. Y. Qian, F. B. Wang, X. H. Xia, *ACS Nano* **2009**, *3*, 2653-2659.

[55]   Y. H. Ding, P. Zhang, Q. Zhuo, H. M. Ren, Z. M. Yang, Y. Jiang, *Nanotechnology* **2011**, *22*.

[56]   X.-H. Li, J.-S. Chen, X. Wang, M. E. Schuster, R. Schlögl, M. Antonietti, *Chemsuschem* **2012**, *5*, 642-646.

[57]   C. Z. Zhu, S. J. Guo, Y. X. Fang, S. J. Dong, *ACS Nano* **2010**, *4*, 2429-2437.

[58]   Z.-J. Fan, W. Kai, J. Yan, T. Wei, L.-J. Zhi, J. Feng, Y.-m. Ren, L.-P. Song, F. Wei, *ACS Nano* **2011**, *5*, 191-198.

[59]   Y. Liu, Y. Li, M. Zhong, Y. Yang, Y. Wen, M. Wang, *Journal of Materials Chemistry* **2011**, *21*, 15449-15455.

[60]   Z. Sui, X. Zhang, Y. Lei, Y. Luo, *Carbon* **2011**, *49*, 4314-4321.

[61]   W. Kai, F. Tao, Q. Min, D. Hui, C. Yiwei, S. Zhuo, *Applied Surface Science* **2011**, *257*, 5808-5812.

[62]   P. Khanra, T. Kuila, N. H. Kim, S. H. Bae, D.-s. Yu, J. H. Lee, *Chemical Engineering Journal* **2012**, *183*, 526-533.

[63]   Y. Wang, Z. Shi, J. Yin, *Acs Applied Materials & Interfaces* **2011**, *3*, 1127-1133.

[64]   G. Wang, F. Qian, C. W. Saltikov, Y. Jiao, Y. Li, *Nano Research* **2011**, *4*, 563-570.

[65]   E. C. Salas, Z. Sun, A. Lüttge, J. M. Tour, *ACS Nano* **2010**, *4*, 4852-4856.

[66]   K. Liu, J.-J. Zhang, F.-F. Cheng, T.-T. Zheng, C. Wang, J.-J. Zhu, *Journal of Materials Chemistry* **2011**, *21*, 12034-12040.

[67]   E. B. Nursanto, A. Nugroho, S.-A. Hong, S. J. Kim, K. Y. Chung, J. Kim, *Green Chemistry* **2011**, *13*, 2714-2718.

[68]   X. Li, W. Cai, J. An, S. Kim, J. Nah, D. Yang, R. Piner, A. Velamakanni, I. Jung, E. Tutuc, S. K. Banerjee, L. Colombo, R. S. Ruoff, *Science* **2009**, *324*, 1312-1314.

[69]   A. Reina, X. Jia, J. Ho, D. Nezich, H. Son, V. Bulovic, M. S. Dresselhaus, J. Kong, *Nano Letters* **2008**, *9*, 30-35.

[70]   Kondo. D, Sato. S, Yagi. K, Harada. N, Sato. M, Nihei. M, Y. N, *Appl. Phys. Express* **2010**, *3*, 025102.

[71]   H. Ago, Y. Ito, N. Mizuta, K. Yoshida, B. Hu, C. M. Orofeo, M. Tsuji, K.-i. Ikeda, S. Mizuno, *ACS Nano* **2010**, *4*, 7407-7414.

[72]   B. J. Kang, J. H. Mun, C. Y. Hwang, B. J. Cho, *Journal of Applied Physics* **2009**, *106*, 104309-104301-104309-104306.

[73]   Z. Sun, Z. Yan, J. Yao, E. Beitler, Y. Zhu, J. M. Tour, *Nature* **2010**, *468*, 549-552.

[74]   G. Ruan, Z. Sun, Z. Peng, J. M. Tour, *ACS Nano* **2011**, *5*, 7601-7607.

[75]   A. Primo, P. Atienzar, E. Sanchez, J. M. Delgado, H. Garcia, *Chemical Communications* **2012**, *48*, 9254-9256.

[76]   E. Ruiz-Hitzky, M. Darder, F. M. Fernandes, E. Zatile, F. J. Palomares, P. Aranda, *Adv. Mater.* **2011**, *23*, 5250-5255.

[77]   aT. Ahmad, M. Rafatullah, A. Ghazali, O. Sulaiman, R. Hashim, *Journal of Environmental Science and Health Part C-Environmental Carcinogenesis & Ecotoxicology Reviews* **2011**, *29*, 177-222; bY. Chen, Y. Zhu, Z. Wang, Y. Li, L. Wang, L. Ding, X. Gao, Y. Ma, Y. Guo, *Advances in Colloid and Interface Science* **2011**, *163*, 39-52; cA. Demirbas, *Journal of Hazardous Materials* **2009**, *167*, 1-9; dO. Ioannidou, A. Zabaniotou, *Renewable & Sustainable Energy Reviews* **2007**, *11*, 1966-2005; eS.-H. Lin, R.-S. Juang, *Journal of Environmental Management* **2009**, *90*, 1336-1349; fM. Mayhew, T. Stephenson, *Environmental Technology* **1997**, *18*, 883-892; gA. R. Mohamed, M. Mohammadi, G. N. Darzi, *Renewable & Sustainable Energy Reviews* **2010**, *14*, 1591-1599; hG. Rodriguez, A. Lama, R. Rodriguez, A. Jimenez, R. Guillen, J. Fernandez-Bolanos, *Bioresource Technology* **2008**, *99*, 5261-5269; iG. Skodras, I. Diamantopouiou, A. Zabaniotou, G. Stavropoulos, G. P. Sakellaropoulos, *Fuel Processing Technology* **2007**, *88*, 749-758; jY. Uraki, S. Kubo, *Mokuzai Gakkaishi* **2006**, *52*, 337-343; kH. Yu, G. H. Covey, A. J. O'Connor, *International Journal of Environment and Pollution* **2008**, *34*, 427-450.

[78]   aE. Frackowiak, F. Beguin, *Carbon* **2001**, *39*, 937-950; bA. G. Pandolfo, A. F. Hollenkamp, *Journal of Power Sources* **2006**, *157*, 11-27; cP. Simon, Y. Gogotsi, *Nature Materials* **2008**, *7*, 845-854; dL. L. Zhang, X. S. Zhao, *Chemical Society Reviews* **2009**, *38*, 2520-2531.

[79]   aS. Choi, J. H. Drese, C. W. Jones, *Chemsuschem* **2009**, *2*, 796-854; bD. Lozano-Castello, J. Alcaniz-Monge, M. A. de la Casa-Lillo, D. Cazorla-Amoros, A. Linares-Solano, *Fuel* **2002**, *81*, 1777-1803.

[80]   R. J. White, V. Budarin, R. Luque, J. H. Clark, D. J. Macquarrie, *Chemical Society Reviews* **2009**, *38*, 3401-3418.

[81]   V. L. Budarin, J. H. Clark, R. Luque, D. J. Macquarrie, R. J. White, *Green Chemistry* **2008**, *10*, 382-387.

[82]   V. Budarin, J. H. Clark, J. J. E. Hardy, R. Luque, K. Milkowski, S. J. Tavener, A. J. Wilson, *Angewandte Chemie International Edition* **2006**, *45*, 3782-3786.

[83]   R. J. White, C. Antonio, V. L. Budarin, E. Bergstroem, J. Thomas-Oates, J. H. Clark, *Advanced Functional Materials* **2010**, *20*, 1834-1841.

[84]   R. J. White, V. L. Budarin, J. H. Clark, *Chemistry-a European Journal* **2010**, *16*, 1326-1335.

[85]   V. Budarin, R. Luque, D. J. Macquarrie, J. H. Clark, *Chemistry – A European Journal* **2007**, *13*, 6914-6919.

[86]   R. Luque, V. Budarin, J. H. Clark, D. J. Macquarrie, *Green Chemistry* **2009**, *11*, 459-461.

[87]   R. J. White, R. Luque, V. L. Budarin, J. H. Clark, D. J. Macquarrie, *Chemical Society Reviews* **2009**, *38*, 481-494.

[88]   J. P. Paraknowitsch, J. Zhang, D. Su, A. Thomas, M. Antonietti, *Adv. Mater.* **2010**, *22*, 87-+.

[89]   J. S. Lee, X. Wang, H. Luo, S. Dai, *Adv. Mater.* **2010**, *22*, 1004-1007.

[90]   P. Kuhn, A. Forget, J. Hartmann, A. Thomas, M. Antonietti, *Adv. Mater.* **2009**, *21*, 897-901.

[91]   J. S. Lee, X. Wang, H. Luo, G. A. Baker, S. Dai, *J. Am. Chem. Soc.* **2009**, *131*, 4596-4597.

[92]   X. Wang, S. Dai, *Angewandte Chemie International Edition* **2010**, *49*, 6664-6668.

[93]   J. P. Paraknowitsch, A. Thomas, M. Antonietti, *Journal of Materials Chemistry* **2010**, *20*, 6746-6758.

[94]   J. P. Paraknowitsch, Y. Zhang, A. Thomas, *Journal of Materials Chemistry* **2011**, *21*, 15537-15543.

[95]   E. R. Cooper, C. D. Andrews, P. S. Wheatley, P. B. Webb, P. Wormald, R. E. Morris, *Nature* **2004**, *430*, 1012-1016.

[96]   E. R. Parnham, R. E. Morris, *Accounts of Chemical Research* **2007**, *40*, 1005-1013.

[97]   A. Taubert, Z. Li, *Dalton Transactions* **2007**, 723-727.

[98]   R. E. Morris, *Chemical Communications* **2009**, 2990-2998.

[99]   Z. Ma, J. Yu, S. Dai, *Adv. Mater.* **2010**, *22*, 261-285.

[100]   Z.-L. Xie, R. J. White, J. Weber, A. Taubert, M. M. Titirici, *Journal of Materials Chemistry* **2011**, *21*, 7434-7442.

[101]   J. S. Lee, R. T. Mayes, H. Luo, S. Dai, *Carbon* **2010**, *48*, 3364-3368.

[102]   aJ. B. Binder, R. T. Raines, *J. Am. Chem. Soc.* **2009**, *131*, 1979-1985; bS. Hu, Z. Zhang, Y. Zhou, B. Han, H. Fan, W. Li, J. Song, Y. Xie, *Green Chemistry* **2008**, *10*, 1280-1283; cC. Lansalot-Matras, C. Moreau, *Catalysis Communications* **2003**, *4*, 517-520; dC. Moreau, A. Finiels, L. Vanoye, *Journal of Molecular Catalysis a-Chemical* **2006**, *253*, 165-169; eH. Zhao, J. E. Holladay, H. Brown, Z. C. Zhang, *Science* **2007**, *316*, 1597-1600.

[103]   A. P. Abbott, G. Capper, D. L. Davies, R. K. Rasheed, V. Tambyrajah, *Chemical Communications* **2003**, 70-71.

[104]   A. P. Abbott, D. Boothby, G. Capper, D. L. Davies, R. K. Rasheed, *J. Am. Chem. Soc.* **2004**, *126*, 9142-9147.

[105]   C. A. Nkuku, R. J. LeSuer, *The Journal of Physical Chemistry B* **2007**, *111*, 13271-13277.

[106]   D. Carriazo, M. C. Serrano, M. C. Gutierrez, M. L. Ferrer, F. del Monte, *Chemical Society Reviews* **2012**, *41*, 4996-5014.

[107]   D. Carriazo, M. a. C. Gutiérrez, M. L. Ferrer, F. del Monte, *Chemistry of Materials* **2010**, *22*, 6146-6152.

[108]   M. Takenaka, T. Izumitani, T. Hashimoto, *Journal of Chemical Physics* **1993**, *98*, 3528-3539.

[109]   K. Katuri, M. L. Ferrer, M. C. Gutierrez, R. Jimenez, F. del Monte, D. Leech, *Energy & Environmental Science* **2011**, *4*, 4201-4210.

[110]   Young Hae Choi, Jaap van Spronsen, Yuntao Dai, Marianne Verberne, Frank Hollmann, Isabel W.C.E. Arends, Geert-Jan Witkamp, R. Verpoorte, *Plant Physiol* **2011**, *156*, 1701-1705.

[111]   F. Bergius, *Zeitschrift fur Komprimierte und Flussige Gase* **1915**, *17*.

[112]   F. Bergius, *Naturwissenschaften* **1928**, *16*, 1-10.

[113]   F. Bergius, *Journal of the Society of Chemical Industry* **1913**, *32*.

[114]   F. Bergius, *Zeitschrift Des Vereines Deutscher Ingenieure* **1925**, *69*, 1359-1362.

[115]   F. Bergius, *Zeitschrift fur Elektrochemie* **1912**, *18*.

[116]   E. Berl, A. Schmidt, *Justus Liebigs Annalen Der Chemie* **1928**, *461*, 192-220.

[117]   E. Berl, A. Schmidt, H. Koch, *Angewandte Chemie* **1932**, *45*, 517-519.

[118]   aJ. P. Schuhmacher, H. A. Vanvucht, M. P. Groenewege, L. Blom, D. W. Vankrevelen, *Fuel* **1956**, *35*, 281-290; bJ. P. Schuhmacher, F. J. Huntjens, D. W. Vankrevelen, *Fuel* **1960**, *39*, 223-234.

[119]   M. W. Haenel, *Fuel* **1992**, *71*, 1211-1223.

[120]   H. L. Qing Wang, Liquan Chen, Xuejie Huang, *Carbon* **2001**, *39*, 2211-2214.

[121]   X. Sun, Y. Li, *Angewandte Chemie International Edition* **2004**, *43*, 597-601.

[122]   S. H. Yu, X. J. Cui, K. L. L. L. Li, B. Yu, M. Antonietti, H. Colfen, *Adv. Mater.* **2004**, *16*, 1636–1640

[123]   H. S. Qian, S. H. Yu, L. B. Luo, J. Y. Gong, L. F. Fei, X. M. Liu, *Chem. Mater.* **2006**, *18*, 2102.

[124]   S. K. Hoekman, A. Broch, C. Robbins, *Energy Fuels* **2011**, *25*, 1802-1810.

[125]   W. Seifritz, *Int. J. Hydrogen Energ* . **1993**, *18(5)*405.

[126]   aK. Y. Chan, L. Van Zwieten, I. Meszaros, A. Downie, S. Joseph, *Australian Journal of Soil Research* **2007**, *45*, 629-634; bY. Kuzyakov, I. Subbotina, H. Chen, I. Bogomolova, X. Xu, *Soil Biology & Biochemistry* **2009**, *41*, 210-219; cD. D. Warnock, J. Lehmann, T. W. Kuyper, M. C. Rillig, *Plant and Soil* **2007**, *300*, 9-20.

[127]   M. Sevilla, J. A. Macia-Agullo, A. B. Fuertes, *Biomass and Bioenergy, 35*, 3152-3159.

[128]   J. A Libra, K. S Ro, C. Kammann, A. Funke, N. D Berge, Y. Neubauer, M-M. Titirici, C. Fühner, O. Bens, J. Kern, K-H. Emmerich, *Biofuels* **2011**, *2(1)*, 89-124.

[129]   M. M. Titirici, A. Thomas, M. Antonietti, *New J. Chem.* **2007**, *31*, 787-789.

2 Structural Characterisation of Hydrothermal Carbons

2.1 Introduction

In the concept of biorefineries, in which transportation fuels and chemicals are produced from biomass instead of fossil resources, as well as in HTC, the transformation of sugars, especially glucose, plays an important role. [1] Both processes (biorefinery and HTC) are extremely important since they represent an efficient way to use residual biomass, transforming it on one hand into ecologically friendly fuels and on the other hand into carbon materials with numerous applications in our daily lives.

While sugars can be produced directly from biomass, such as from saccharose present in sugarcane or sugar beet, or semi-directly from hydrolysis of starch, which is present in corn and other crops, there is concern that such processes may compete with the food supply. Glucose can alternatively be obtained from cellulose present in lignocellulosic biomasses such as wood, straw, grass, municipal solid waste, and crop residues. These materials are complex mixtures of natural polymers—cellulose (35–50 %), hemicelluloses (25–30 %), and lignin (15–30 %)—tightly bonded by physical and chemical interactions. [2]

Since cellulose is the major component of lignocellulosic materials, efficient processes for hydrolysis/hydrothermal treatment of cellulose seem to be interesting entry points for the production of both biofuels and HTC materials. However, the chemical transformation of lignocellulosic biomasses presents serious challenges. This is due to complex structure of cellulose being recalcitrant towards efficient chemical and biological transformations.
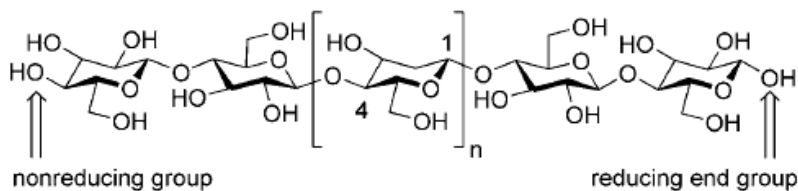
Figure 2-1: Structure of cellulose. [3]

Chemically, cellulose is a linear and syndiotatic polymer of β-$_D$-glucose where the anhydroglucose units (AGU) are bonded to each other through a glycosidic linkage at positions 1 and 4 (Figure 2-1). [3] A relatively dense network of intermolecular H bonds is established between the cellulose units. Consequently, cellulose has a very high resistance against chemical and biological transformations, and insolubility in most of the common solvents.

The two processes, biomass to biofuels and biomass to HTCs have as common path the hydrolysis of cellulose. Bergius, the discoverer of HTC, [4] was one of the first to perform studies on cellulose hydrolysis in the 30s. [5] In his process, the hydrolysis of cellulose was carried out in 40 wt% HCl at room temperature. Under these conditions, cellulose and hemicellulose were solubilised in the reaction medium, whereas lignin remains insoluble. Cellulose breaks downs into oligosaccharides and glucose within a few hours with the formation of large amounts of dehydration products, such as 5-hydroxymethylfurfural and levulinic acid. Hemicellulose is also hydrolyzed, producing mannose, xylose, galactose, glucose, and fructose, mainly as oligomers. Since this pioneering work, many other processes for cellulose hydrolysis, based on the same principle have been reported. [6-9] Many of these processes employ hydrothermal conditions. This allows adjusting the ionic product and dielectric constant of water over a wide range by means of pressure and temperature. The critical parameters for water are 374.2 °C and 22.1 MPa, which signifies that depending on the conditions, water is in the sub or supercritical regime. [10] Water in such "overheated" state is a very acidic and reactive substance, permitting chemical reactions such as cellulose hydrolysis and biomass refining in general without the addition of strong acids.[11]

The transformation of cellulose into its glucose monomers and of biomass in general into easily hydrolysable carbohydrates is a crucial prerequisite for both biofuels and HTC formation. Under hydrothermal conditions, the dehydration of glucose and other sugars is in general is favoured. [12] Hydroxymethylfurfural (HMF) and furfural are the resulting dehydration products of sugars. [13] Furfural is generated from pentoses, such as xylose and ribose, whereas HMF is built from hexoses, such as glucose, fructose and mannose. With increasing persistence time in aqueous medium, HMF successively decomposes into levulinic acid (LA) and formic acid (FA) on the one hand and into polymeric carbonaceous material on the other hand (Figure 2-2). [14]

While other researchers tried to avoid the formation of a solid during such processes by polymerisation of HMF, my research group and others rediscovered these processes in the sense of Bergius for the production of green and valuable carbon and carbon hybrid materials. [4] [15] [16] [17] [18] Mostly depending on the applied conditions i.e. the grade of carbonisation the products are called humines, [19] hydrothermal carbons [20] or hydrochars.[21]
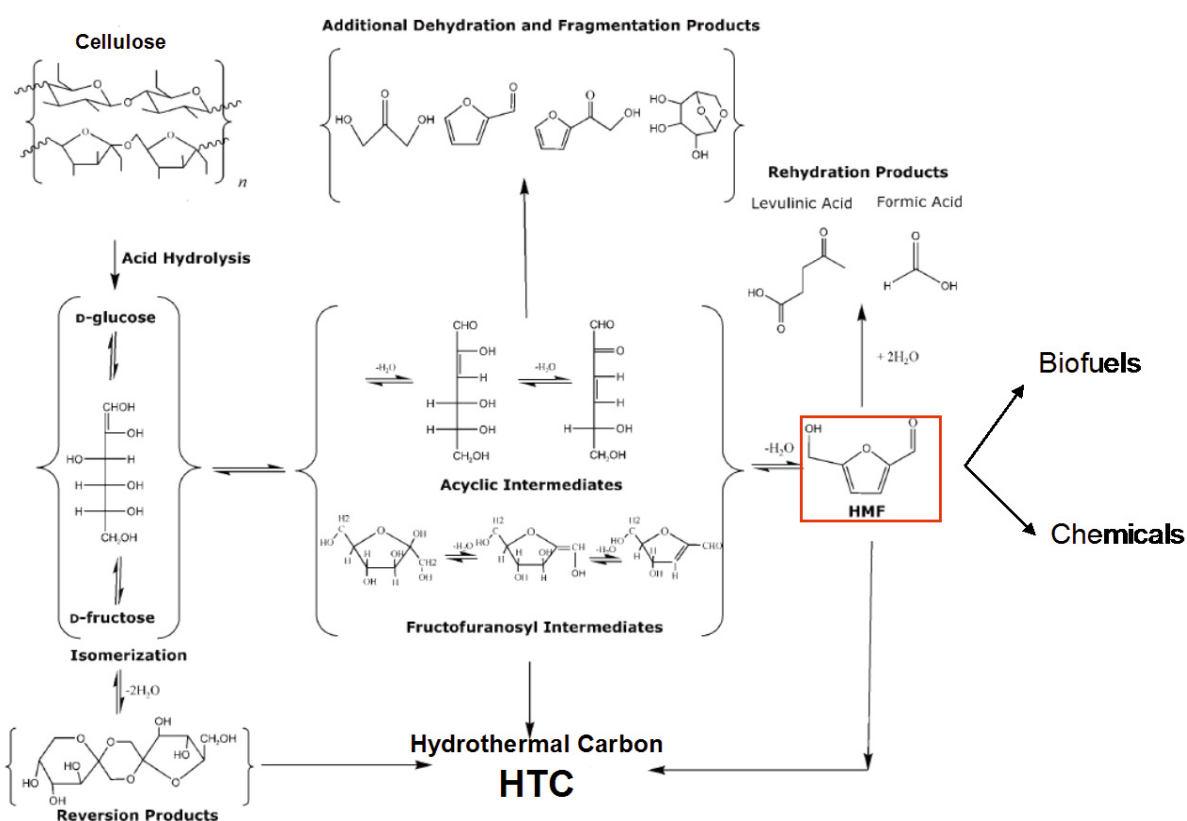
Figure 2-2: Reaction pathways for acid-catalyzed dehydration of polysaccharides (containing hexose monomer units) to 5-hydroxymethylfurfural (HMF). Structures in brackets correspond to representative species.

On the other hand, if isolated and extracted before further polymerisation or rehydration, HMF is the most important biomass derivative for the future productions of biofuels [22-23] and renewable chemicals. [24]

In this chapter I will present a detailed characterisation study of HTC materials. First, glucose will be employed as a model system to better understand the properties and the final chemical structure of HTC materials. ^{13}C-solid state NMR is a crucial charaterisation technique for the accomplishment of this task. Once the structure of glucose-derived HTC materials will be elucidated, I will compare the properties of HTC materials derived from various precursors including water soluble polysaccharides, cellulose and real biomass.

2.2 Glucose: a Model Study Precursor for HTC

Since glucose is the most abundant sugar unit in biomass and the major product of acidic hydrolysis of carbohydrate biomass, [12] considered not to compete with food supplies, we choose it as a model system for understanding its transformation mechanism into HTC as well as the final chemical structure of glucose-derived HTCs.

Under hydrothermal conditions (180-280°C; self-generated pressure) the isomerisation of glucose into fructose appears according to the Lobry de Bruyn-Alberta van Ekstein rearrangement (Figure 2-2). [25] It is considered, that HMF is derived from dehydration of fructose and not from glucose directly. [26] Once HMF is formed, it is *in situ* "polymerised/resinified" to form hydrothermal carbon. [19] What we wanted to understand in this study is why do we obtain micrometer-sized spherical particles, how does the HMF polymerisation occurs and what is the final chemical structure of the as-formed material. A correlation between HTC chemical structure obtained using ^{13}C solid state NMR with other data acquired using a variety of characterisation techniques will be presented in this subchapter.

2.2.1 Nucleation during the Hydrothermal Treatment of Glucose

In order to understand the nucleation in HTC, we started investigating the morphology of the glucose-derived HTC spheres at different temperatures and residence times. Figure 2-3 shows the morphology of the HTC spheres derived from hydrothermal carbonisation of 10 wt% glucose solution for 12h at different temperatures. It can be observed that the temperature affects both the carbonaceous particle average diameter as well as the size distribution: higher temperatures (280°C) lead to larger particles and a more homogeneous average size.
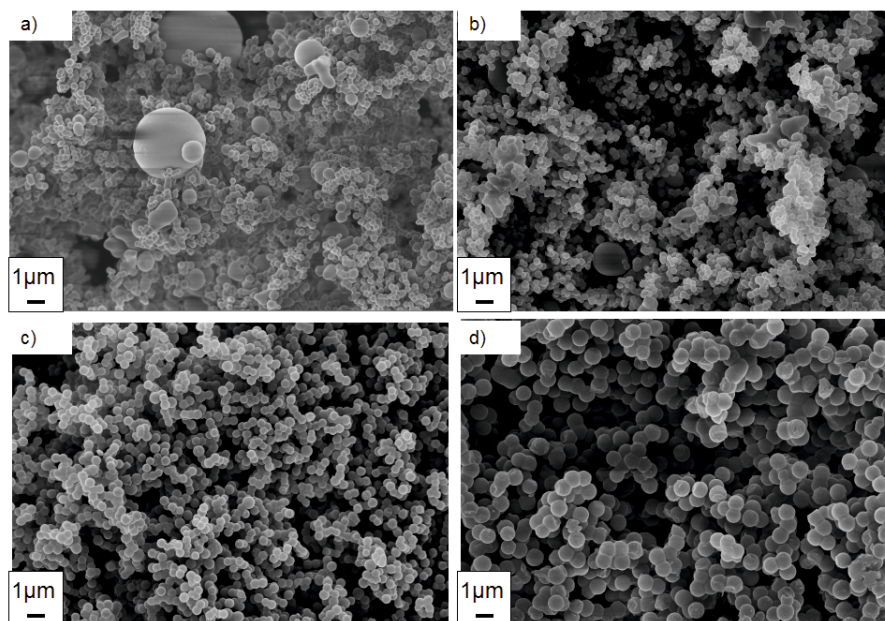
Figure 2-3: Scanning electron micrographs of hydrothermal carbon materials obtained from 10 wt% glucose for 12h at: a) 160°C; b) 180°C; c) 200°C; d) 280°C (taken from [27]).

This observation was also confirmed by dynamic light scattering (DLS) measurements. In the case of the material prepared at 160°C, an average particle hydrodynamic radius of 474 nm was measured, while for the 280°C samples the mean value was 685 nm. For samples prepared at higher temperatures, the correlation between DLS and SEM measurements is reasonable. On the other hand, for the materials prepared at 160°C, the measured values using DLS is higher than the ones observed in the SEM pictures. This might be due to the wider size distribution of this sample and therefore to the presence of very large particles, which could affect the overall diameter obtained from light scattering and therefore increase the average error. Another factor that can possibly contribute to the value mismatch might be the presence of particles aggregates in the 160°C sample, which could increase the value of the measured hydrodynamic particle radius. However, although the DLS measurements do not allow determining a precise estimate of the particle size for the sample processed at lower temperature, it is important to underline that they quantitatively confirm the increase in the average particle diameter as the HTC processing temperature becomes higher, which could be observed from SEM measurements.
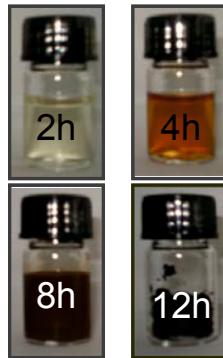
Figure 2-4: Changes in 10 wt% glucose solutions upon HTC at 180°C.
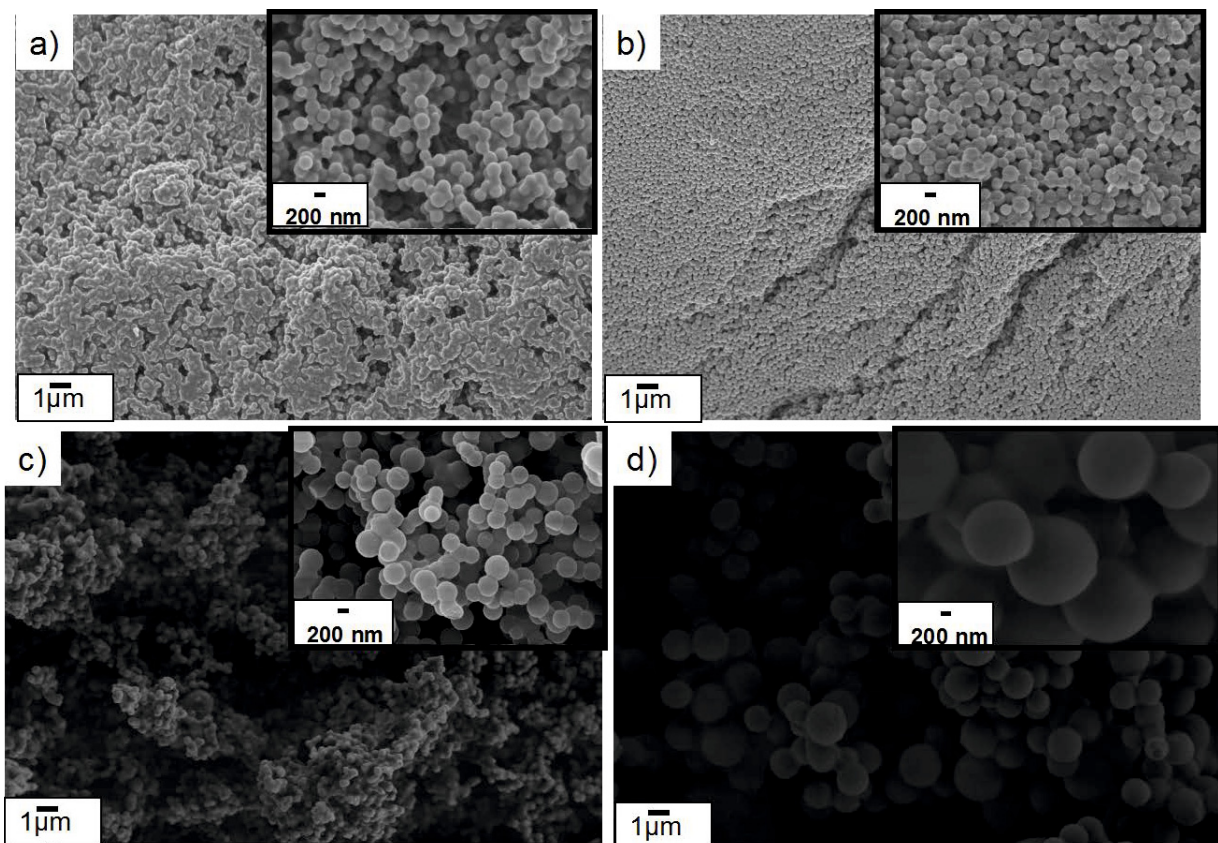
Figure 2-5*: **Scanning electron micrographs of hydrothermal carbon materials obtained from 10wt% glucose at 180° after: a) 5h; b) 8h; c) 12h; d) 20°C.**

The next parameter we have changed was the residence time while keeping constant the concentration of glucose solution (10 wt%) and temperature (180°C, Figure 2-4). Nothing happens after a hydrothermal treatment of 2h. After 4h, the colour of the solution becomes dark orange suggesting that a polymerisation-aromatisation occurred. Past 5h, the first solid precipitate is observed. A closer look at this precipitate using SEM (Figure 2-5 a) reveals the tendency to aggregate and form spherically shaped nuclei of about 150 nm. After additional 8h of hydrothermal treatment a brown colloidal dispersion is formed. Examining the newly formed solid with SEM, we clearly see a homogenous burst of nucleation with monodisperse particles of ~200 nm being formed. Leaving the reaction proceed further (12h) leads to the formation of a final black-brown precipitate (Figure 2-4).

The solid formed after 12h consist of spherically shaped particles of around 500 nm, aggregated together (Figure 2-5 c). The size of the particles increases even further (~ 1.5μm) if the hydrothermal treatment is continued for longer times (Figure 2-5 d). We need to mention that these experiments were done in the absence of any catalyst known to accelerate the HTC process such as acids or Fe ions. [28]

According to these microscopy data we can assume that the up to 2h the dehydration of glucose into HMF occurs *via* the previously mentioned Lobry de Bruyn-Alberta van Ekstein rearrangement. [25] This has been also confirmed by GC-MS experiments of the 10 wt% solution after 2h hydrothermal treatment at 180°C (Figure 2-6) showing indeed the formation of HMF together with his rehydration products levulinic acid, dihydrohyacetone, acetic acid and formic acid. The inevitable rehydration of HMF to levulinic and formic acid (Figure 2-2) lowers the pH of the solution to a value of~ 3. Thus, the *in situ* formed organic acids catalyse the dehydration and further polymerisation of HMF. A GC-MS of the same residual solution obtained upon the hydrothermal treatment of 10 wt% glucose at 180°C for 20h, after the filtration of the black precipitate, shows that at this stage there is no residual HMF left. HMF has been transformed *via* a cascade of chemical reactions into HTC with the spherical morphology depicted in Figure 2-5 d.
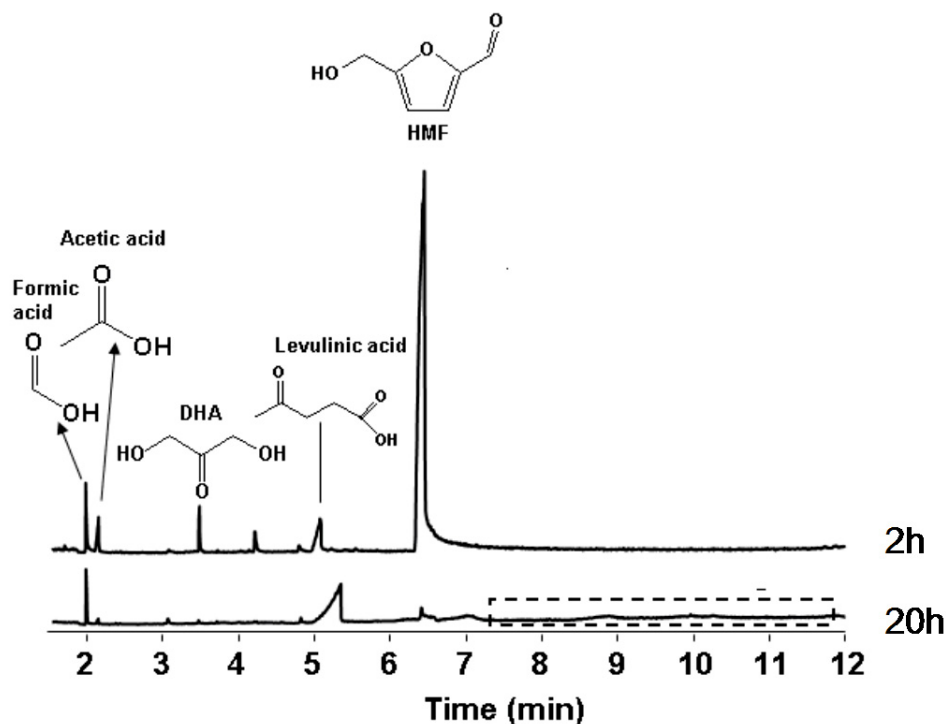
Figure 2-6: GC experiments on residual liquors from hydrothermal treatment of glucose.

It is extremely difficult to determine exactly which chemical reactions take place in the autoclave during the HTC formation and I will come back to this point later on in section 2.2.7 [29] Once such polymeric species are formed (after ~ 5h) they precipitate out of the aqueous solution leading to the morphology shown in Figure 2-5 a. Upon chemical reactions occurring *in situ* in the autoclave these resulting nuclei grow to a uniform size (Figure 2-5 b). The more complex the reactions become inside the autoclave upon increasing the residence time, the growth of the particles occurs heterogeneously resulting in rather polydisperse and agglomerated particles. The growth process continues until all the monomer (HMF) has reacted and the final particles attain a final particles size of ~1.5 μm after 20 h [29]. According to our experimental results, the growth of carbon spheres seems to conform to the LaMer model [30] as shown schematically in Figure 2-7. No carbon spheres formed when a 10 wt% glucose solution was hydrothermally treated below 160 °C. However, the orange or red colour and increased viscosity of the resulting solutions

53

indicate that some aromatic compounds and oligosaccharides are formed, [31] in what has been denoted the "polymerisation" step. When the solution reached a critical supersaturation (e.g., 10 wt%, 160°C, 5 h), a short single burst of nucleation resulted.
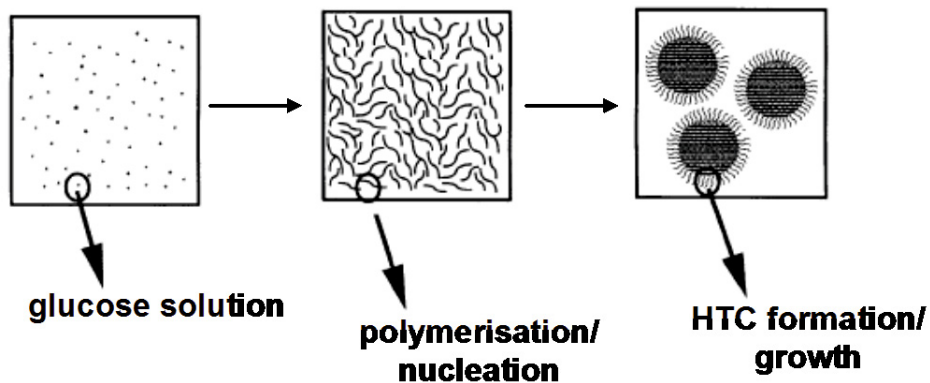
Figure 2-7: Schematic representation of nucleation-growth process for the glucose HTC spheres (adapted from [15]).

Unfortunately it is very difficult to monitor *in situ* the nucleation-growth process during the HTC process due to the relatively high temperatures and pressures inside the autoclaves. Yet in 2009 Iversen and co-workers reported a high temperature high pressure study on the hydrothermal formation of zirconia nanoparticles by time-resolved *in situ* synchrotron X-ray diffraction.[32] We are currently in contact with the authors for a future collaboration on hydrothermal carbonisation of glucose using the high temperature and pressure set-up and Small Angle X-Ray Scattering (SAXS) instead, since our materials are not crystalline. However, until these interesting experiments will be conducted, we can only assume a nucleation-growth in HTC as described above.

2.2.2 Yields and Elemental Composition:

The glucose HTC yields are calculated using the following formula:

$$HTC\_yield\% = \frac{amount\_of\_re\operatorname{cov}ered\_solid\_after\_HTC(g)}{initial\_amount\_of\_biomass(g)}$$

The HTC yield of glucose is 0 below a certain temperature threshold, because no appreciable amount of solid is formed and can be recovered under these conditions.

Two important conclusions can be withdrawn looking at the yield versus temperature plot in the case of hydrothermally treated glucose (Figure 2-8): 1. A minimum temperature threshold for the HTC formation from glucose exists at ~150-160°C. Below this value no measurable quantity of solid residue can be recovered. 2. The process can be tuned to optimise hydrothermal carbon yield. The maximum yield is achieved at 200°C, after which it starts a gradually decline. An explanation for this downward trend is due competitive gasification reactions at higher temperatures. [33] However it must be kept in mind that the theoretical HTC yield, that is achievable when glucose is used as a starting material, is 60% (grey dotted line in Figure 2-8 a). This value can be easily derived from the mechanism of 5-HMF formation, since from each molecule of glucose, which is firstly converted to 5-HMF and then reacts to form HTC carbon, four water molecules (40% of the starting mass) are eliminated. These represent an unavoidable yield loss, which must be taken into account.

The change in carbon content for glucose-derived HTC material as a function of temperature is shown in Figure 2-8. a. A constant and gradual increase is observed as the reaction temperature enhanced. The only noticeable difference (~20%), is observed between the carbon content of raw glucose and the one of the HTC carbon produced at the lowest possible conversion temperature (160°C). The explanation for this abrupt change is the dehydration step of glucose to HMF in the early stages of hydrothermal carbonisation.

Combining the calculated yields at different temperatures with the elemental analysis results it is possible to investigate the mass loss upon temperature increase as a function of chemical composition (Figure 2-8 b). Thus, between 200-250°C the decrease of the HTC yield is majorly due to oxygen loss. The carbon content undergoes an initial sharp decrease, presumably due to the conversion of glucose into water soluble degradation products, such as levulinic acid, dihydroxyacetone and formic acid (Figure 2-2) after which it remains relatively constant within temperature range 200-250°C. The carbon efficiency starts diminishing more rapidly above 250°C due to simultaneous gasification reactions.
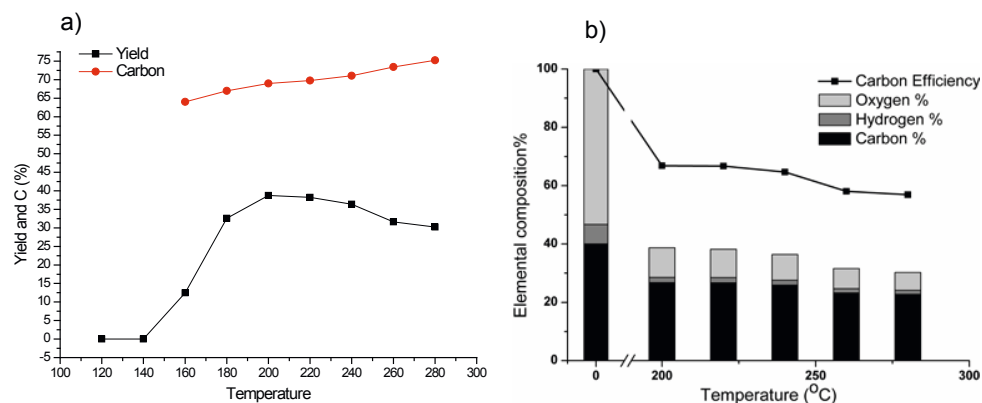
Figure 2-8 a) Calculated hydrothermal carbon yield (black) and carbon content (red) obtained from chemical analysis of HTC material obtained from glucose at different processing temperatures (raw glucose % C = 40 wt%); b) HTC yield normalised elemental composition of hydrothermal carbon obtained from glucose at different processing temperatures (temperature 0 corresponds to raw glucose whose HTC yield is taken as 100%) and carbon efficiency. $\left(\dfrac{amount\_of\_carbon\_in\_the\_product}{initial\_amount\_of\_carbon} \right)$ **(adapted from [27]).**

2.2.3 FT-IR

FT-IR spectroscopy on the glucose-derived HTCs at different processing temperatures, shows hydrophilic surfaces with a distribution of –OH (ϑ = 3500-3700 cm^{-1}) and –C=O groups (ϑ = 1700 cm^{-1}). The relative intensity of the 1700 cm^{-1} peak, corresponding to C=O vibration increases sharply until 200-220$^{\mathrm{o}}$C, but then it levels off as temperature increases in good agreement with yield and elemental analysis (Figure 2-9). In addition, at 1620-1680 cm^{-1} stretching vibrations corresponding to C=C bonds are observed, indicating the presence of aromatic units in the final HTC structure. The inset shows the FT-IR spectra of the row glucose material for a better understanding of the transformations underwent upon hydrothermal treatment. Therefore we can conclude from FT-IR studies that the glucose-derived HTC contain both oxygen-rich polar functionalities as well as aromatic divisions.
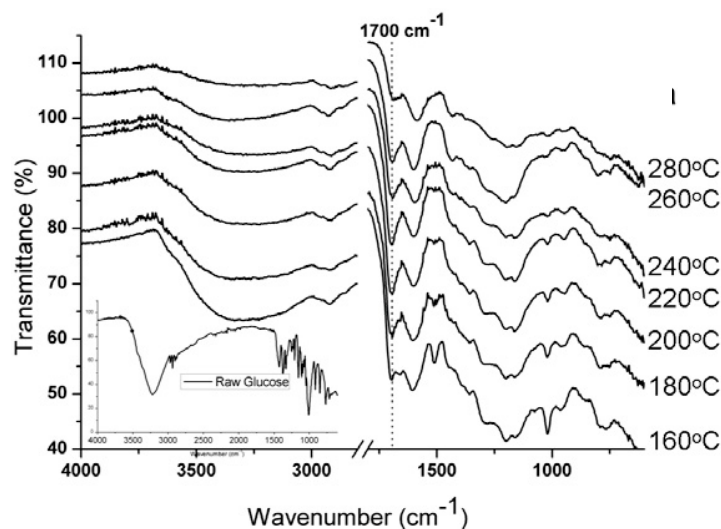
Figure 2-9: FTIR spectra of hydrothermal carbon obtained from glucose at different temperatures.

2.2.4 Thermal Behaviour and Porosity Evolution:

During HTC formation, side products such as levulinic acid or formic acid coexist (Figure 2-2) and are generally physosorbed onto the resulting carbons. The normal employed procedure is simple washing with water and ethanol after the synthetic step. However, this may not be an efficient procedure to completely remove such products. The subsequent release of such compounds may lead to undesired structural changes (e. g. microporosity development) or negative performance for specific applications (e.g. analyte contamination upon using HTC as a stationary phase in chromatography).

In order to ascertain the possible presence of entrapped molecules within the glucose derived HTC structure   at 180°C, a comparative analysis between washed HTC (normal synthetic procedure) and Soxhlet extracted HTC (with ethanol, hexane and THF), is presented in this following section. TGA-IR was used to analyse the thermal decomposition behaviour of both samples (Figure 2-10 and Figure 2-11). The thermal decomposition of the non-extracted sample is composed of two relative broad events (160 – 270 ^{o}C and 350 – 600 ^{o}C; (Figure 2-10a), whilst in the case of the extracted HTC carbon, only one main event between 350 and 600 ^{o}C is observable (Figure 2-10 b).
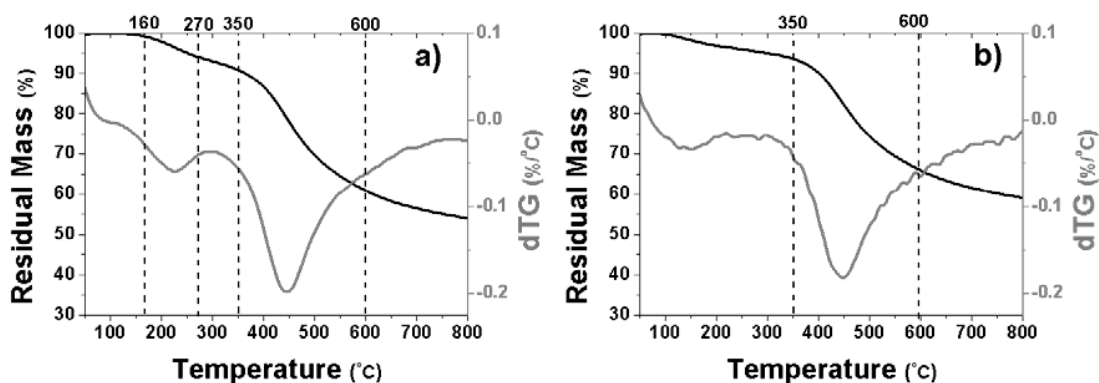
Figure 2-10: Thermogravimetric analysis of glucose derived HTC carbon at 180oC a) before extraction and b) after three consecutive extractions with ethanol, hexane and THF (*NB: The first peak between 100 - 180 ^{o}C is ignored, as it is attributed to removal of residual extraction solvent and physisorbed water*; from [34]).

The first event (160-270°C) of the non-extracted sample is attributed to the thermal evolution of levulinic acid, embedded within the highly cross-linked HTC structure. Several evidences support this observation. First of all the peak appears at the levulinic acid boiling point range (i.e. 245-246°C). GC-MS analysis of the extracted ethanol fraction demonstrates the presence of levulinic acid confirming its removal upon Soxhlet extraction (Figure 2-11 a-b). This explains the absence of the 160 - 270 ^{o}C dTG peak in the TGA curve of the extracted sample. Furthermore gas phase IR analysis of the evolved species during the thermal degradation of HTC carbon indicates that over the temperature range 160 - 270 ^{o}C, the detected peaks are all ascribable to levulinic acid (Figure 2-11b). In particular, extract gas phase IR traces at 1770 and 1740 cm^{-1} correspond to the carbonyl stretching of ketones and carboxylic acids. Such traces are not detected during the thermal decomposition of the extracted sample.
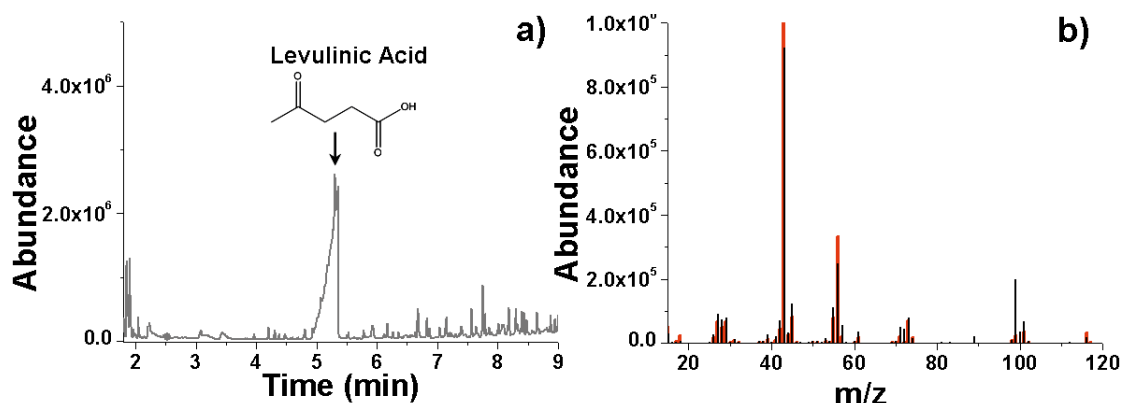
Figure 2-11: a) Gas chromatograph of the extract obtained after Soxhlet extraction with ethanol of glucose derived HTC carbon at 180°C. b) Mass Spectrum of the peak indicated in (a) (red – literature data, [35] black – experimental data-from [34]).

The decomposition event over the range $350 - 600\ °C$ is observed for both samples. This indicates a restructuring of the carbon motifs with simultaneous loss of volatile species, as supported by the corresponding IR analysis of the evolved gases (Figure 2-12). At 400 °C the peakes with the strongest intensities correspond to traces of CO_2 and CO. Subsequently at ~ 450 °C, methane evolution is detected and the intensity of its corresponding peak increases until 550 °C. Above this temperature threshold all the detected signals fade away at different rates.
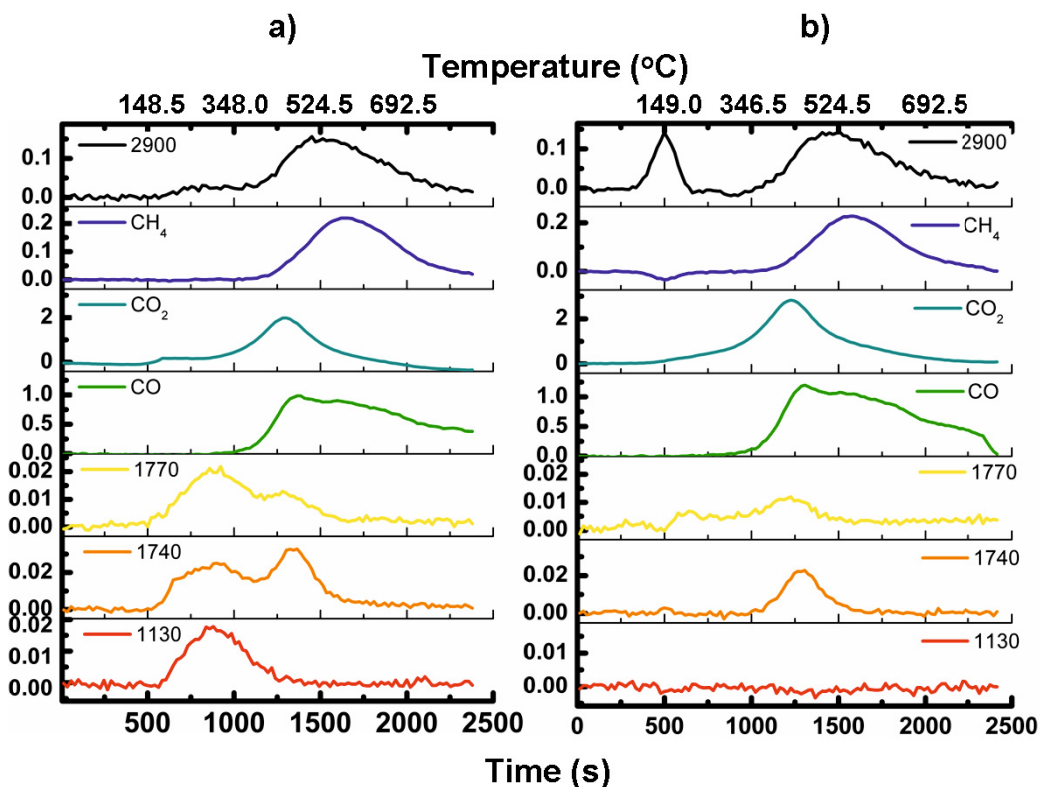
Figure 2-12: Extracted traces from TG-IR analysis at selected wavenumbers (cm^{-1}) for a) HTC synthesised at 180°C and b) HTC synthesised at 180°C after extraction with EtOH, hexane and THF. The legend shows either the name of the gas, the trace can be attributed to, or the wavenumber, the gas is detected at (from [34]).

The development of porosity in glucose-derived HTC carbons, after Soxhlet extraction or further pyrolysis at 600 ^{o}C was monitored using N_2 sorption (Figure 2-13). 600 ^{o}C was chosen as processing temperature, since at this temperature the main decomposition events have already occurred. N_2 sorption isotherms of the as-synthesised and extracted HTC carbons show negligible gas uptake indicating the absence of any developed internal porosity (Figure 2-13.a) This is rather surprising for the latter sample, since the removal of the levulinic acid upon extraction was expected to create some voids within the HTC carbon structure. This might be due to the fact that the carbon synthesised at 180 ^{o}C possesses still a relatively "soft" or "polymeric-like" structure. It is well known from material science templating strategies that porosity (microporosity in particular) can be induced within an organic polymeric structure only if the

60

overall scaffold has a certain degree of rigidity to counterbalance the polymer chains tendency to pack closely together once the template is removed. [36]
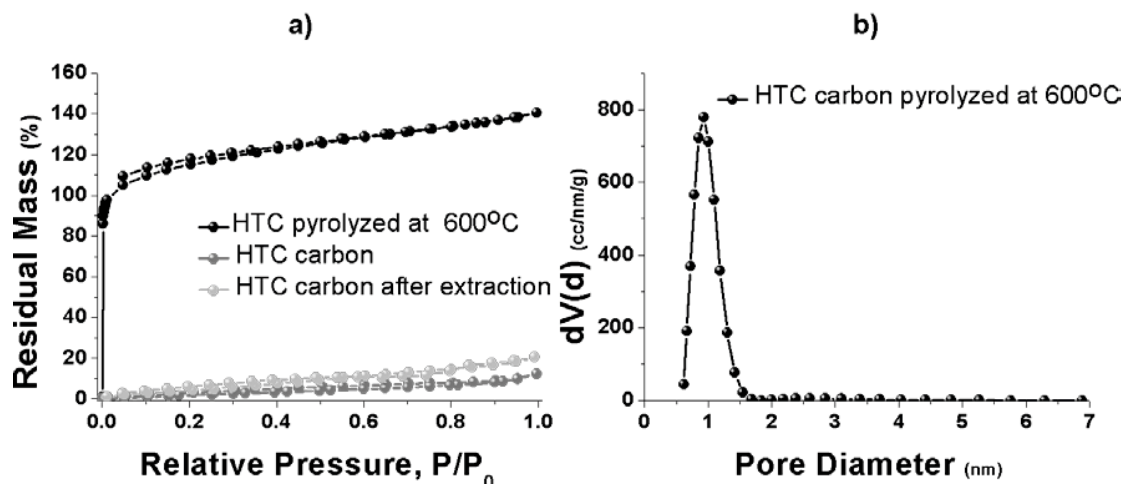
Figure 2-13: (a) N_2 **sorption isotherms of glucose-derived HTC carbon at 180 ^{o}C and then pyrolysed at 600 ^{o}C; and (b) QSDFT PSD adsorption for glucose-derived HTC carbon at 180 ^{o}C pyrolysed at 600 ^{o}C.**

A type I isotherm characterises the N_2 uptake of the HTC carbon further treated at 600 ^{o}C (Figure 2-13. a). The high adsorption capacity at low relative pressures ($P/P_0 < 0.05$) and the relatively sharp knee of the isotherm curve are indicative of a predominantly microporous material and a narrow pore size distribution (PSD). Using Quenched Solid Density Functional Theory (QSDFT) [37] a more precise estimate of the PSD was obtained (Figure 2-13.b). It is evident that the material porosity is predominantly due to pores with an average diameter of *ca*. ~ 1 nm, with a relatively narrow PSD. Even though the QSDFT data indicates a well-defined PSD, the accuracy is questionable since N_2 sorption analysis suffers from several limitations when employed to characterise microporous materials. I will come back to this issue later on in section 2.3.8 where I will present a careful porosity analysis of HTC materials using both N_2 and CO_2 as probing gases.

The formation of microporosity during the thermal degradation of HTC carbon is due to the combined effects of volatile species elimination (e.g. CO, CO_2 and CH_4) and formation of condensed aromatic intermediates. Both these processes lead to the development of voids (i.e. pores) between the isotropic pre-graphinic structures, present at this stage.
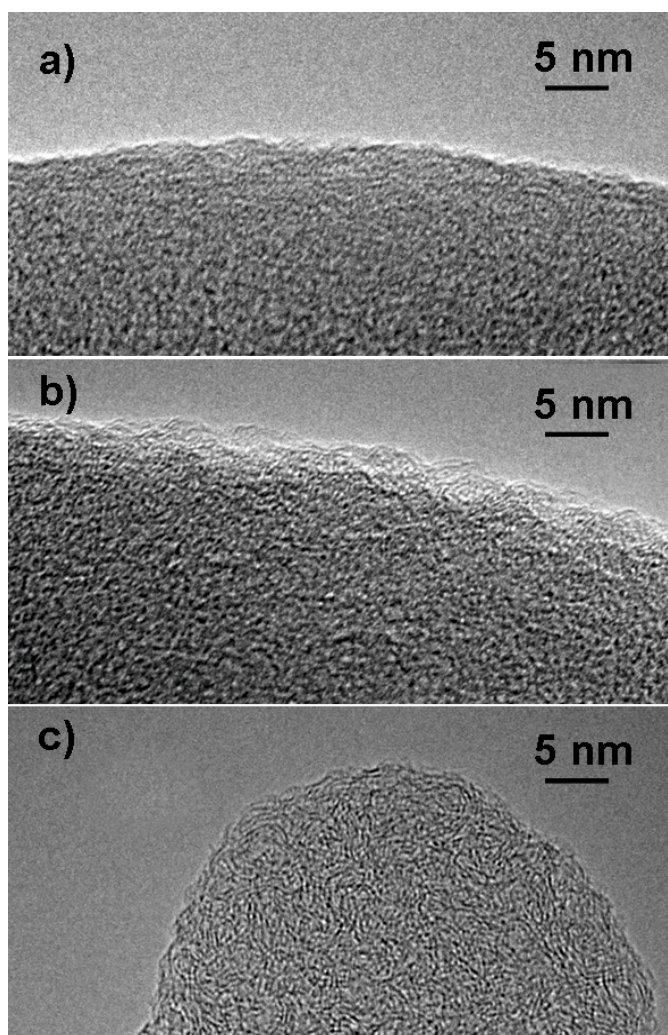
Figure 2-14: High resolution TEM of glucose derived HTC synthesised at 180°C a) before and after pyrolysis at b) 600 °C and c) 900 °C (taken from [34]).

The effects of pyrolysis on the structural texture of HTC carbons were also investigated using HR-TEM (Figure 2-14). The surface of the 600°C post-pyrolised sample appears rougher in comparison to the one of standard HTC-G-180°C. This can be associated with the formation of short and highly curved aromatic pre-graphinic domains leading to micropore formation within the carbon structure. An additional increase in the pyrolysis temperature (900 °C) leads to cross-linking between the intermediate aromatic structures (Figure 2-14.c). A highly curved profile and

isotropic orientation is still observed related to a partial closure of the structural voids developed during the thermal degradation of the HTC carbon.

2.2.5 XRD and Raman Spectroscopy:

The XRD pattern of the 180°C glucose-derived materials (Figure 2-15.a) shows broad, disordered peaks at d =3.41A°and d = 2.02 A° indicating an amorphous nature. Naturally, these peaks become much more intense upon further carbonisation at higher temperatures under N_2 atmosphere, corresponding to an increased degree of local order.
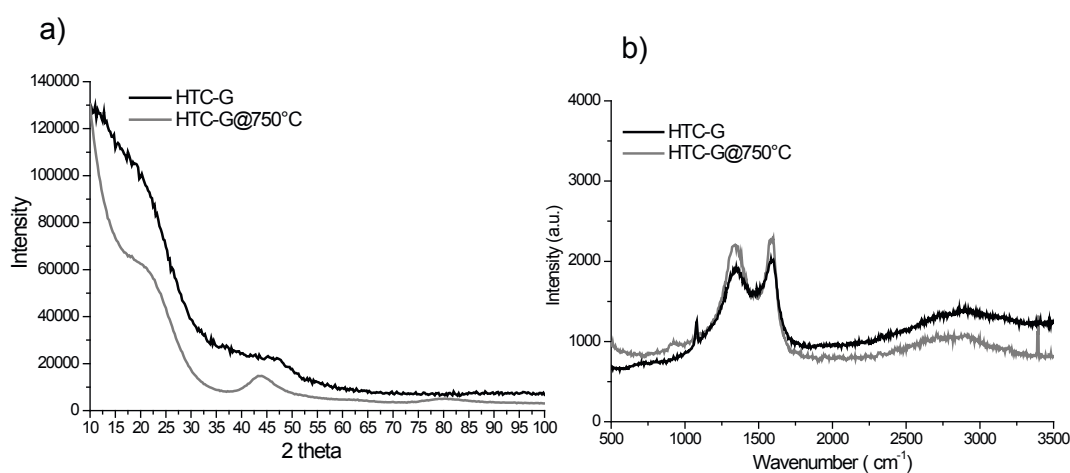
Figure 2-15: a) XRD pattern and b) Raman Spectra of glucose derived HTC material (180°C) and after pots calcination at 750°C.

The Raman spectrum of the glucose-HTC material at 180°C as well as of the material after further calcination at 750°C (Figure 2-15. c) contains wide D and G bands around 1360 and 1590 cm^{-1}, respectively, that are characteristic for amorphous carbons or disordered graphite. A peak at 2908 cm^{-1} was assigned to a combination of the graphitic and a disorder mode (G+D). The large value of the ratio of peak intensities (ID/IG = 0.8) indicated the low graphitic degree in the hydrothermal carbon material. Although there is a slight change in the peak intensities upon further calcination, I have to mention that Raman is not a very accurate characterisation technique for HTC materials as they "*in situ*" graphitise under the laser beam. The main conclusion from

both Raman and XRD is that we are dealing with amorphous carbonaceous materials which upon further thermal treatment became aromatic "graphitic-like" however still with very disordered structure.

2.2.6 Chemical Structure of Glucose derived HTC –a Solid State ^{13}C-NMR Study:

So far we have looked at the structure, functionalities and porosity of glucose-derived hydrothermal carbons formed during the hydrothermal carbonisation of glucose with a combination of characterisation techniques such as FT-IR, XRD, Raman, Electron Microscopy, TG-IR and N_2 adsorption. All these results suggest a material with polar oxygenated functionalities coexisting with an aromatic amorphous type of carbon structure. Upon further thermal treatment the functionalities are slowly lost resulting in a slight increase in microporosity. As a consequence the level of structural order of the pyrolysed HTC materials increases at the same type as the functional groups disappear. (see section 2.3.7 for more details)

For these specific materials, solid state NMR provides a better spectral resolution with respect to FT-IR or XPS, which are otherwise important for the characterisation of HTC but cannot asses the chemical environment. The possibility of using selective pulse sequences in ^{13}C-NMR leads to the identification of separate chemical species without ambiguity. In addition, the poor spectral resolution of FT-IR and XPS does not allow a reliable quantification of the carbon species while ^{13}C NMR should be able to provide much better results from this point of view.

Glucose offers the possibility of ^{13}C isotopic enrichment for ^{13}C solid state NMR studies which were performed in collaboration with a specialised group in Paris, in particular with Dr. Niki Baccile and Florence Babonneau. [38] The goal of this study was to show that hydrothermal carbon from ^{13}C isotopically enriched D-(+)-glucose is a good model to analyse the chemical connection motifs of HTCs. This objective was achieved by combining ^{13}C solid-state MAS (Magic Angle Spinning) NMR methods, such as one-dimensional (single-pulse, cross polarisation-magic angle spinning CP-MAS, inversion recovery cross-polarisation IRCP, through bond C-H filtering, insensitive nuclei enhanced by polarisation transfer INEPT) and two-dimensional experiments (^{13}C-^{13}C exchange spectroscopy and through-space ^{13}C homonuclear double-quantum-single-quantum correlation).

Solid-state NMR studies on a large variety of carbonaceous materials, especially in soils and sediments, have already been performed to identify chemical species and to refine carbon structures. [39] The most common experiments use the ^{1}H to ^{13}C cross-polarisation (CP) technique coupled to magic-angle spinning (MAS). They have the advantage of signal enhancement leading to reasonable acquisition times with respect to ^{13}C single-pulse MAS NMR experiments. Unfortunately, quantification using CP is more challenging than in a single-pulse experiment due to the more complicated spin dynamics. On the contrary, single-pulse (SP) experiments, which are preferred over CP for quantification, are generally time consuming. Extensive signal broadening coming from the potential presence of paramagnetic centers can also be a complicating factor, but this has not really prevented deep investigations of coals or chars by solid-state NMR. [40] Cross polarisation at one single contact time is, in general, the fastest approach to obtain preliminary information about chemical composition. [41-42]

The average chemical composition in weight percent of a resulting glucose HTC at 180°C is 62% C; 4 % H and 34% O which corresponds to the molar formula $CH_{0.77}O_{0.41}$. The large H content will be favourable to ^{1}H-^{13}C through-space (CP) or through-bond (INEPT) heteronuclear polarisation transfer NMR experiments that will help in the identification of the various sites.

Figure 2-16 shows the ^{13}C solid-state CP-MAS NMR spectra of hydrothermal carbon samples obtained from pure glucose (HTC-G0), a mixture of pure (20%) and fully enriched glucose (80%) (HTC-G80), and a mixture of pure (80%) and selectively enriched glucose (20%) (HTC-G20) recorded using a contact time of 3 ms. A primary qualitative attribution based on literature can be proposed for each spectral domain. Region I (0-100 ppm) is characteristic of sp^3 carbon atoms, indicating the presence of a broad distribution of CHx (x=1-3) sites. Region II (100-160 ppm) is characteristic of sp^2 carbon atoms in C=C double bonds with signals between 140 and 160 ppm, more specifically due to oxygen bound, O-C=C, sp^2 carbons. In region III (170-225 ppm), C=O groups in either carboxylic acid moieties (175 ppm) or ketones and aldehydes (200-220 ppm) resonate. Finally, a peak at 75 ppm, whose intensity largely varies among all materials, corresponds to residual glucose.
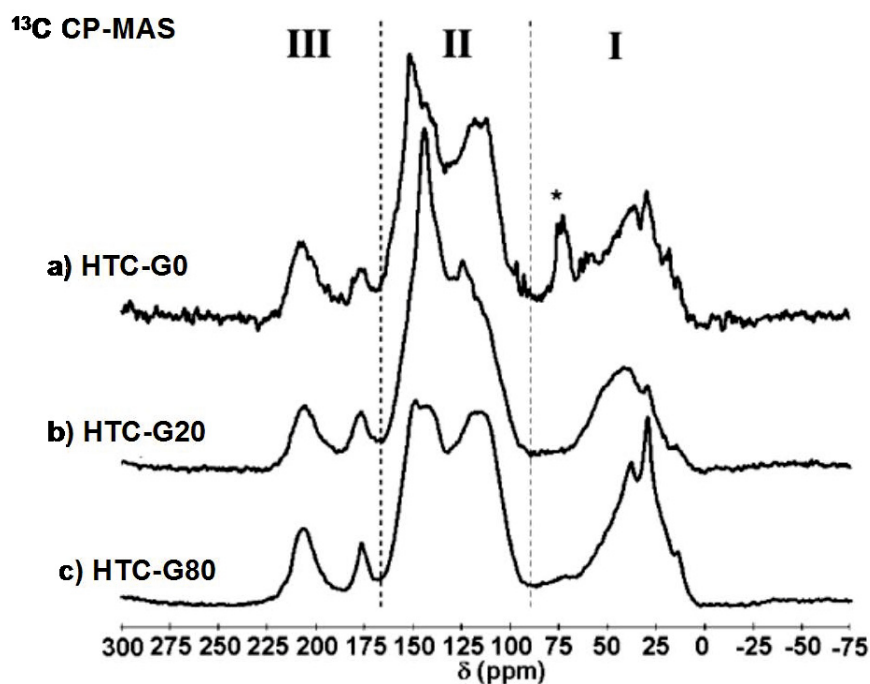
Figure 2-16: Carbon-[13]CP-MAS NMR experiments of samples (a) HTC-G0, (b) HTC-G20, and (c) HTC-G80 obtained with contact time tCP =3 ms (taken from [38]).

To contribute to a better understanding of the reaction mechanism, which transforms glucose into functionalised carbonaceous powders, a selectively ^{13}C-enriched glucose molecule in position 1 (sample HTC-G20) was used to promote amplification of specific signals, especially in the carbonyl region. However, all the spectra in Figure 2-16 look similar, which demonstrates that the ^{13}C, initially in position 1, was abundantly reshuffled through the complete structure. Even if a closer observation of the spectra, nevertheless, shows some slight differences in the relative intensities of several peaks, we exclude the employment of specific isotope labelling for a more refined investigation of the chemical condensation mechanism.

As expected, comparison between HTC-G0 (acquisition time =5500 s) and HTC-G80 (acquisition time =70 s) shows that isotopic enrichment is extremely useful in terms of sensitivity. In addition, despite the high level of enrichment, peak broadening due to [13]C

66

homonuclear dipolar couplings is not observed, showing that a MAS rate of 14 kHz is sufficient to efficiently average out the ^{13}C homonuclear dipolar interactions, which are expected to range between 2 and 7 kHz depending on C-C distances.

Such a high-quality response allowed recording quantitative single-pulse (SP) MAS experiments on sample HTC-G80 (Figure 2-17, spectrum a). Very few differences can be noticed when comparing the SP to the CP-MAS spectrum recorded with a long contact time of 3 ms (Figure 2-17, spectrum b) due to the large proton content (H/C = 0.77) and the presence of strong ^{1}H homonuclear dipolar coupling giving rise to efficient ^{1}H spin-diffusion processes. Slight differences are mainly concentrated in the C=O region, where the two signals around 176 and 210 ppm are clearly multicomponents: (1) a sharp peak centered at 210.0 ppm is present in the SP spectrum but hardly detected by CP; (2) similarly, the signal at 176.5 ppm in the SP spectrum reveals the presence of a sharp peak overlapping a broader signal.
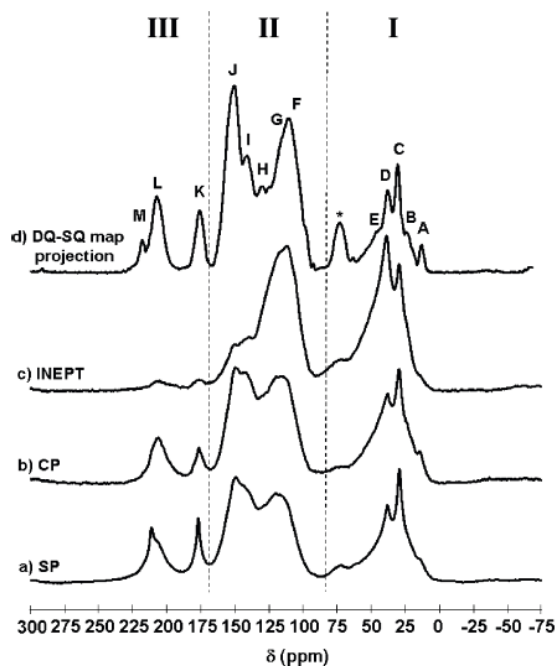
Figure 2-17: Carbon-13 MAS NMR spectra of sample HTC-G80 recorded with various sequences: (a) SP, (b) CP, and (c) INEPT. (d) Skyline projection of the 2D [13]C-^{13}C DQ-SQ experiment shown in Figure 2-22 (taken from [38]).

It is clear so far that ^{13}C NMR spectra suggest a complex nature of the final hydrothermal carbon with the presence of a larger variety of carbon sites. In the following section, the ^{13}C resonance assignments have been refined combining several ^{13}C NMR techniques. The insensitive nuclei enhanced by polarisation transfer (INEPT) technique gives a straight-forward interpretation on protonated carbon sites, as carbon signals are filtered *via* the through-bond *J*-coupling. Cross-polarisation experiments have been performed at different contact times ranging from 35 μs to 7 ms. We have found that this approach provides selective pieces of information mainly in region II characteristics of aromatic peaks. Insensitive nuclei enhanced by polarisation transfer (IRCP) experiments were also performed at several inversion times (from 1 to 500 μs), and they were extremely useful in the spectral resolution of the complex multicomponent aliphatic region. Finally, the 2D [13]C-^{13}C DQ-SQ correlation spectrum was very powerful to finely resolve most of the carbon species and to establish their connectivities. Our indexation (peaks A-M in Figure 2-22 spectrum d, and Table 2-1) is based on this 2D DQ-SQ correlation experiment and all techniques cited above. The decomposition of the skyline projection is shown in Figure 2-21 a.

A detailed description of each experiment used to investigate the structure of the carbonaceous material is given in the following paragraphs.

Table 2-1: Peak assignment for the HTC-G80 after decompositions of 13C DQ-SQ, CP, and IRCP experiments. Percentage of each carbon group was obtained by decomposition of the HTC-G80 SP spectrum

spectral domain	CP/IRCP	INEPT (x= 1-3)	peak	$\delta(^{13}C)$ (ppm)	percentage
		Mobile CH$_3$	CH$_x$	A	13.9	
		Rigid CH$_2$	CH$_x$	B	23.9	
		Rigid CH$_2$	CH$_x$	C	28.7	
I sp^3 C		Mobile CH$_3$	CH$_x$	C	29.6	23
		Mobile CH$_2$	CH$_x$	D	38.3	
		CH	CH$_x$	E	50.5	
		CH	CH$_x$	*b*	73.4	
	β-C	CH	CH$_x$	F	110.0	29
	β-C	C	CH$_x$	G	118.2	
II sp^2 C	–	C	C	H	131.2	35
	α-C	C	C	I	140.7	
	α-C	C	C	J	148-156	
III C=O		-	CH$_x$	K	175-179	4
			C	L	202-207	9
		-	C	M	218.4	

2.2.6.1 Insight on Protonated Carbons by INEPT Experiments:

As shown in Figure 2-17 c, definite proof of the identification of protonated carbon sites is provided by the refocused INEPT-MAS experiment which allows probing ^{1}H-^{13}C through-bond (J-coupled) connectivities. Nevertheless, this experiment confirms the existence of protonated carbons in region I (10-50 ppm). The broad signal between 110 and 130 ppm (sp^2 sites) demonstrates that the majority of the sites contributing to the signal centered at 150 ppm are actually nonprotonated. This is an important piece of information since it strongly suggests that the signals at 110-130 and 150 ppm can be mainly assigned to furanic -O-C=CH- and O-C=CH- sites, respectively. Indeed, similar chemical shift values are observed for ά-positions (161.8 and 152.3 ppm, Figure 2-18) and β-positions (111.4 and 127.3 ppm Figure 2-18) in HMF, as shown in Figure 2-16
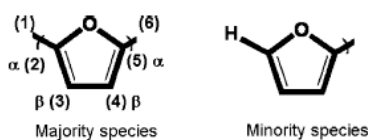
Figure 2-18: Furan ring with the ά-position (or positions 2; 5) and β-Positions (or positions 3;4) highlighted.

In agreement with the known chemical steps that transform glucose into HMF [25], we believe that this compound reacts further so that the furan ring may constitute the majority of the carbonaceous scaffold, in agreement with CP, IRCP, and DQ-SQ experiments shown later.

Finally, the two low-intensity signals at 176.5 and 208 ppm suggest the presence of a small amount of aldehydes with respect to typical non-protonated carbonyl sites detected in the same chemical shift range, such as ketones and carboxylic acids, indicating the aldehyde as a preferred reaction site. Nevertheless, the presence of residual aldehyde groups was also proved by^{1}H-^{13}C CP HETCOR experiments performed at a relatively short contact time of 500 μs (result not shown) showing a correlation peak between the C=O signal at 176.5 pp and a proton resonance at 9.0 ppm. One should remark that no cross-peak was detected at 211.0 ppm, corroborating the CP data and confirming the assignment of this signal to a ketone group.

2.2.6.2 *Insight on Aromatic Carbons using ^{1}H-^{13}C CP Experiments:*

Figure 2-19 a shows ^{1}H-^{13}C CP-MAS spectra recorded at various contact times from very short (t_{CP} = 35 μs) to long values (t_{CP} =10 ms). The spectrum recorded at t_{CP} = 35 μs mainly reveals aliphatic and β carbons and looks very similar to the INEPT spectrum. This is expected since, for a short contact time, magnetisation transfers only occur across strong dipolar couplings corresponding to short C-H distances characteristic of C-H$_x$ bonds. [43] The aliphatic zone (10-80 ppm) of the CP-MAS spectra shows a very complex shape composed of several unresolved resonances for which more insight will be provided by the IRCP experiments as shown next. However, interesting insights can be actually gained in the aromatic region (100-160 ppm, region II). Five main peaks (F, G, H, I, J) are evidenced, and the corresponding evolution of the integrated area of peaks F, G, J, and I as a function of cross-polarisation time is shown in Figure 2-19 b. Interestingly, peaks G, I, and J show the same polarisation behaviour, typical of a quaternary carbon (as compared to the behaviour of the ketone L peak at 208 ppm, reported on the graph for comparative purposes), whereas peak F shows a very fast increase in intensity, which is typical of a protonated carbon. Therefore, CP-MAS experiments clearly show that peak G, which was expected to have a chemical nature similar to that of peak F on the basis of their very close ^{13}C chemical shifts, could not be assigned to protonated carbon as peak F and is dominated by quaternary species. We will use this important piece of information to depict the exact nature of the carbon sites related to peaks F and G after the analysis of the 2D DQ-SQ map. One important remark: CP behaviour of peak H at 131.2 ppm reveals to be typical of a quaternary carbon. This piece of information will provide valuable insights about the nature of this resonance in conjunction with the DQ-SQ experiment.
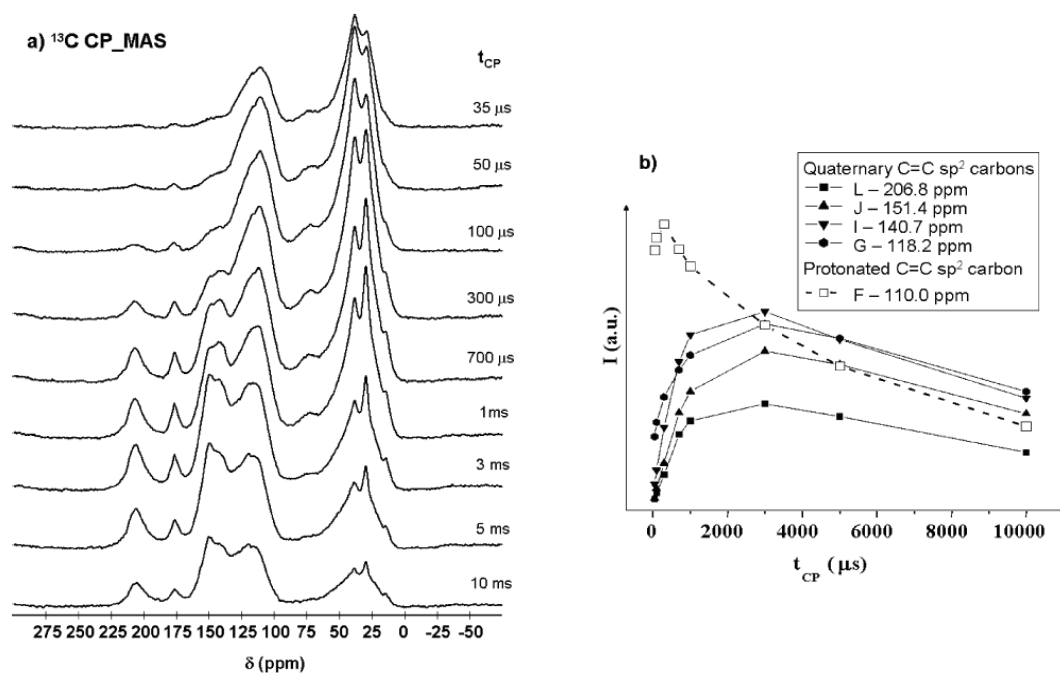
Figure 2-19: Evolution of ^{13}C CP-MAS spectra recorded on HTC-G80 for different contact times (a) and variation of peak intensities of aromatic region (b) as a function of the contact time (taken from [38])

2.2.6.3 Insight on the Aliphatic Region using ^{1}H-^{13}C IRCP Experiments:

For a detailed and complete analysis of the aliphatic region where a strong overlapping of signals is observed, IRCP is a better approach than simple CP-MAS. Inversion recovery cross-polarisation (IRCP) experiments are generally selective to rigid CH_2 and CH sites as their normalised intensity signal tends, respectively, to a negative value (-1/3) or to 0 as a function of t_i. On the contrary, the signal of mobile CH_3 and/or quaternary carbons remains positive. Figure 2-20 a. shows some IRCP experiments for the aliphatic region at selected inversion times; after 100 μs, the broad signal inverts, with the exception made for two sharp components within peaks at 29.6 and 38.3 ppm. Decomposition of the IRCP spectra is shown in Figure 2-21 b; typically, the set of peaks A-E from DQ-SQ projection (Figure 2-21. a) was used for some selected IRCP spectra. Finally, the evolution of the integrated normalised intensity as a function of the inversion time for some peaks is presented in Figure 2-20 b. Negative intensity values occur for CH_2 groups whose peaks are at 23.9 (B), 28.7 (C), and 38.3 (D) ppm; stars show the typical behaviour

71

for mobile CH_3 species, as confirmed for peak A at 13.9 ppm and sharp peak C at 29.6 ppm belonging to CH_3 groups. Finally, intensity variation for peak E at 50.5 ppm shows the expected behavior for CH groups as also confirmed by comparison to the behavior of the peak labeled (*) due to the CH of glucose (73.4 ppm), acting as an internal CH standard. Table 2-1 summarizes the main families of CHx groups (peaks A-E), but one should notice that peaks C and D are certainly multicomponents, resulting from the DQ-SQ projection (Figure 2-21. a) and the cross-peaks in the 2D map.
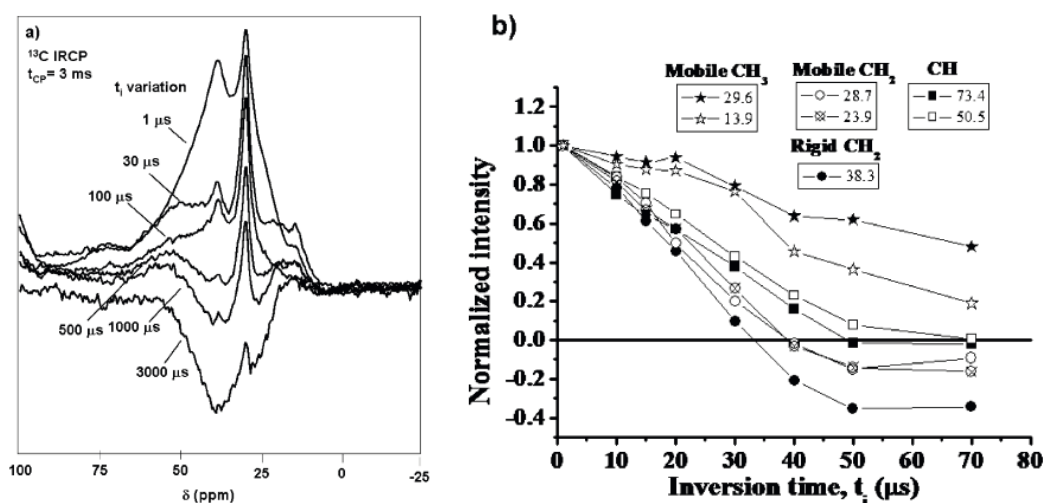
Figure 2-20: (a) IRCP spectra recorded at various inversion times in the aliphatic region for sample HTC-G80. (b) Evolution of IRCP peak intensity for selected decomposed peaks belonging to various CH, CH_2, and CH3 groups (taken from [38]).

2.2.6.4 Insight on Spatial Connectivity using ^{13}C Homonuclear DQ-SQ Correlation Experiments:

The experiments previously performed allowed identification of the different functions present in the carbonaceous samples but did not provide information about close spatial proximities between the various carbon groups. Indeed, several NMR methods exist to visualize short-range connectivities *via* either through-bond or through space techniques: for example, the group of Emsley used double-quantum excitation (INADEQUATE [44]) to probe carbon-carbon connectivities in biomass. [45]

For our study, we strongly preferred the use of double-quantum excitation; in fact, the signals lying on the diagonal in a 2D DQ-SQ experiment provide crucial pieces of information about connectivity among equivalent sites.
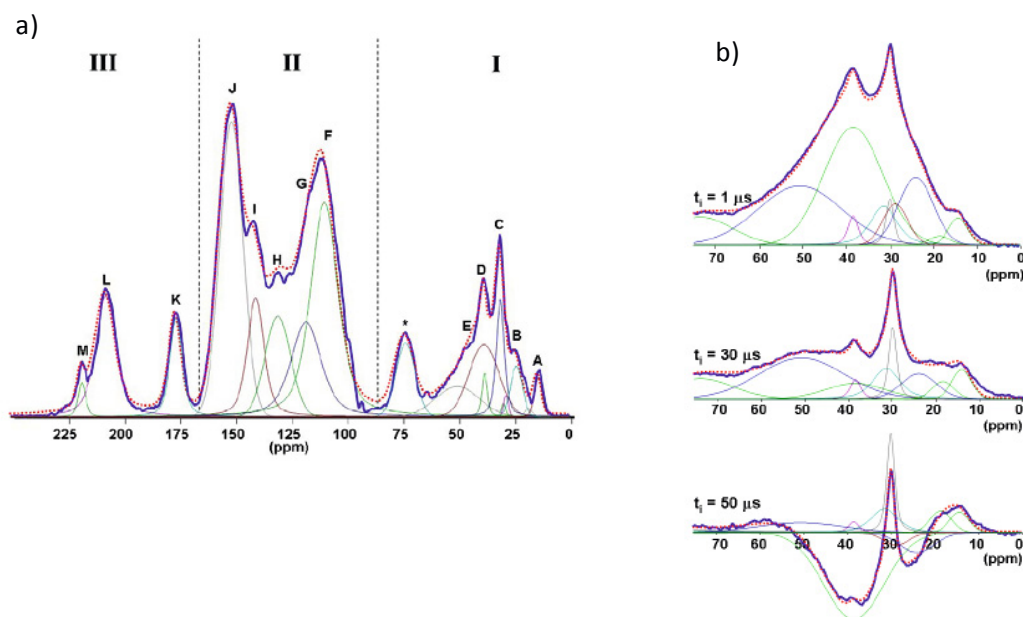
Figure 2-21: a) Simulation (violet) of the 2D ^{13}C-13C DQ-SQ projection (blue); b) Simulation (violet) of the aliphatic region of several IRCP spectra (blue) at different inversion times (taken from [38]).

Since we were unable to optimise a high-quality INADEQUATE experiment on our samples, probably due to the low values and dispersion of J-coupling values for sp^2 and sp^3 carbon sites, we performed a two-dimensional (2D) ^{13}C homonuclear double-quantum-single-quantum (DQ-SQ) MAS experiment using the SC14 sequence. [46] This experiment allows the double-quantum recoupling of dipolar-coupled spin pairs and results in a 2D spectrum (with a direct SQ MAS dimension and an indirect DQ dimension for which the frequency corresponds to the sum of the two individual chemical shifts of the pair of coupled spins), allowing one to trace out the C-C proximities between both inequivalent and equivalent sites. In the case of uniformly ^{13}C-labeled samples, the DQ-SQ correlation spectra are dominated by the direct (one-bond) strong couplings

due to dipolar truncation effects, [46] and the longer-range C-C proximities are evidenced through indirectly correlated peaks of lower and negative intensities. [47]

To avoid the presence of the indirectly correlated peaks and only observe correlation peaks reflecting the one bond C-C strong coupling, we have used short DQ excitation and reconversion times (corresponding to two rotor periods) to record the 2D CP-filtered DQ-SQ correlation spectrum of sample HTC-G80, which has a high ^{13}C enrichment level. Crosspeaks (93.2-72.7 and 97.0-75.1 ppm) relate to the DQ excitation of C1-C2 groups in the α- and β-pyranose forms of glucose (whose presence was highly abundant also in the mother liquors). This is very important as glucose acts as the internal standard proving that the SC14 sequence under the employed conditions is selective to one C-C bond length.

The main and most important result of the 2D DQ-SQ^{13}C-^{13}C map is the visualisation of the subtle connectivity among all species shown *via* the numerous cross-peaks, revealing the complexity of the carbon skeleton; however, they can be grouped in five different categories (symbolysed by dashed rectangles in Figure 2-22 a), depending if they relate two carbon sites from the same spectral region (I-I and II-II) or from two different regions (I-II, I-III, and II-III). The most intense correlation peaks belong to the II-II region, revealing strong homonuclear ^{13}C-^{13}C dipolar interactions between those sp^2 C sites. Peaks in the I-I region are less intense, but the dipolar coupling between sp^3 C is expected to be lower (longer C-C distance and possible internal mobility). As expected, no crosspeak relates two C=O sites from region III. Then, the most intense cross-peaks relating C sites from two different spectral regions are found in region I-III, showing that the C=O groups are mostly bonded to sp^3 C sites. Fewer and less intense cross peaks are found in regions I-II and II-III, suggesting the existence of spatially distinct domains that discriminate the sp^2 C sites from the others.

A closer look to the various regions will help in proposing some structural motifs for the carbonaceous scaffold. (For a clear trace of the connectivity on the 2D DQ-SQ map, one should refer to Figure 2-22 b.)

Aromatic core (region II-II): As established earlier by CP and INEPT experiments, region II corresponds primarily to R-substituted furanic rings where peak F originates from protonated β-

carbons and peaks I and J are related to non-protonated ά-carbons. For this spectral range, the DQ-SQ map shows four diagonal autocorrelation peaks (F-F, G-G, H-H, and I-I) and three partly overlapping off-diagonal cross-correlation peaks (F-J, F-I, and G-J).

The cross-correlation peaks F-J clearly suggest connectivity between the ά-carbons of two furanic rings through a C=C double bond, as shown in Scheme 2-1 a structure b whereas the correlation peak I-I reveals a direct furanic connection, as depicted in Scheme 2-1. a structure c. The auto-G-G and cross-correlation peaks G-J and F-B indicate that quaternary β-carbons F and G also constitute an important site for extra-furanic connectivity, as shown in Scheme 2-1 a structures d-f. To this regard, due to the equivalent amount of protonated and quaternary β-carbons (peaks F and G) as observed in SP MAS spectrum, one β-carbon out of two throughout the whole material is cross-linked. Finally, peak H at 131.2 ppm, given its chemical shift (typical for extended aromatic networks), its quaternary nature (as seen by CP behaviour as a function of contact time), and the presence of an auto- H-H cross-peak (though of low intensity), describes the existence of spurious domains of arene-like aromatic units (Scheme 2-1a structure a).

Due to the intensity of the cross-peaks depicted in region II-II and the nature of the identified chemical species we believe that the core of the carbonaceous material is mainly composed of cross-linked furanic species. The chemical nature of the cross-links, spacers, and possible end functions, which are directly bonded to the furanic rings, is described below after analysing the correlation peaks between regions I-I, I-II, I-III, and II-III.

Cross-links between furanic groups (regions II-I and II-III): Chemical functions that are directly connected to ά-carbons are shown in Scheme 2-1b and are related to off-diagonal cross-peak signals found in regions II-I and II-III of the DQ-SQ map of Figure 2-22 a. Signal B identifies a wide distribution of R-CH$_2$ groups, which can be, in turn, connected to either a second furan ring (Scheme 2-1. b structure a) or to a carbonyl C=O group (signal M, Scheme 2-1 b-structure b), which can be interpreted as either an aldedhyde or a ketone group connected to an E site at 50.5 ppm, most likely a CH group (see IRCP). At a lower extent, a carbonyl C=O group can be directly bonded to ά-carbons (Scheme 2-1b-structure c).
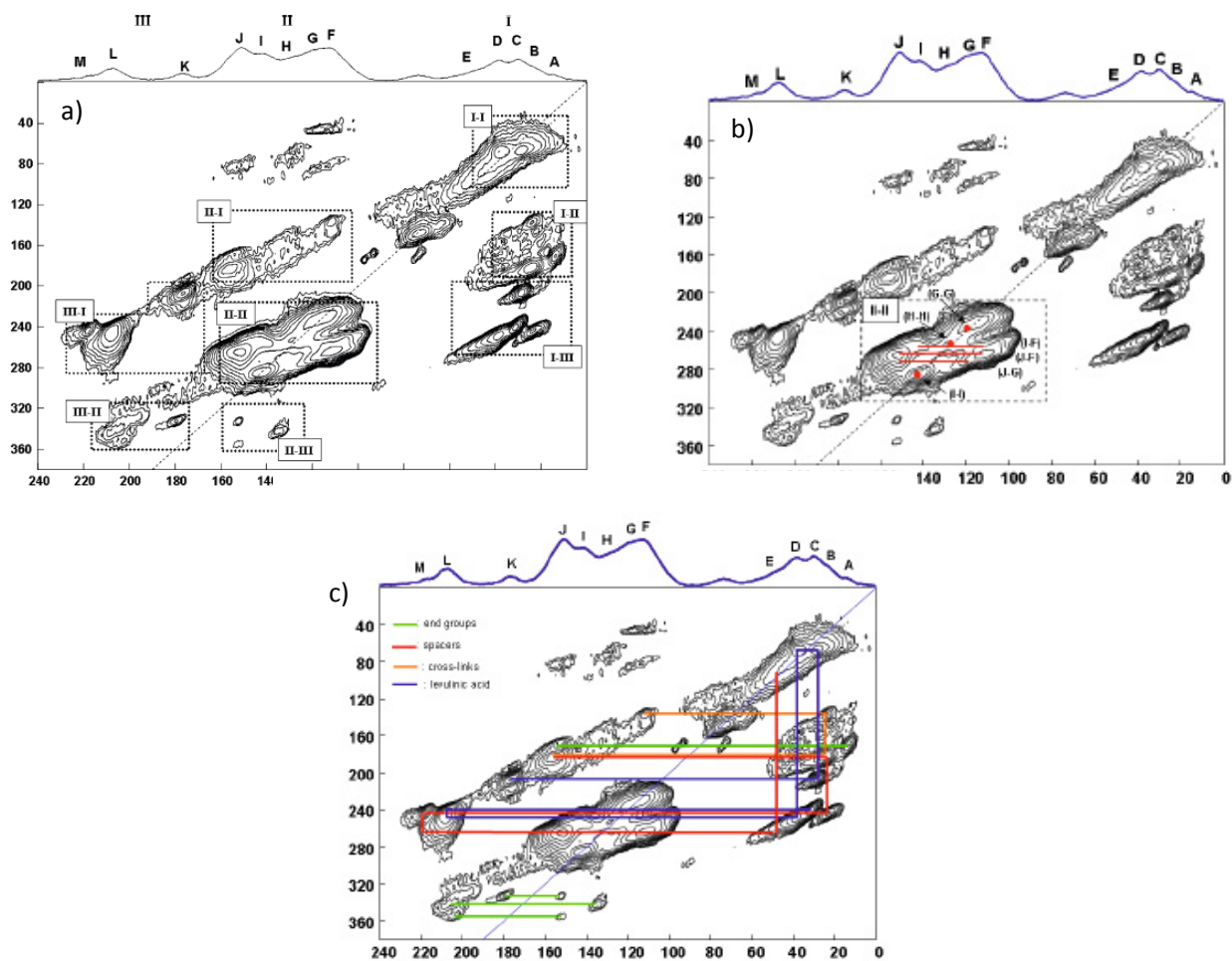
Figure 2-22: a) Two-dimensional ^{13}C DQ-SQ MAS NMR correlation spectrum recorded on sample HTC-G80 with $\tau_E = \tau_R = 285.3$ μs. Insights on the connectivity scheme are provided in b and c); b) Highlight of connectivity pathways for the aromatic region; c) Highlight of connectivity pathways (refer to coloured legend for details) between aliphatic and carbonyl C=O, aromatic and aliphatic, aromatic and carbonyl C=O regions (taken from [38]).

.
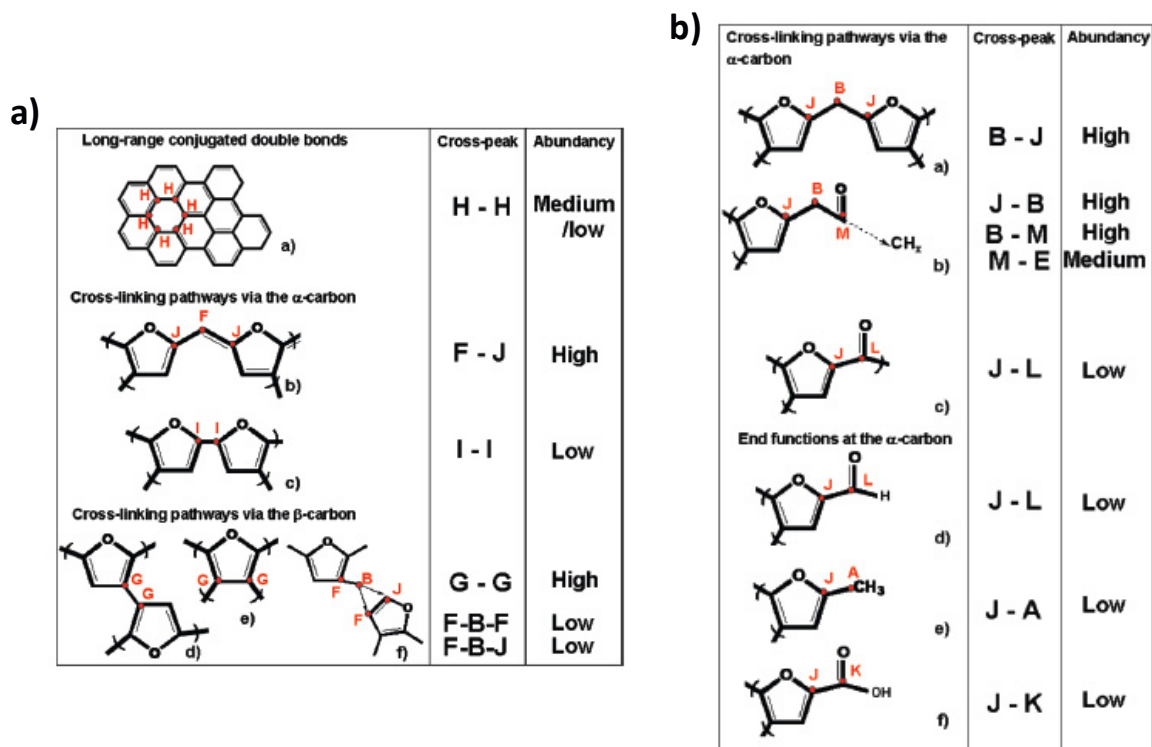
Scheme 2-1: a) Structural motifs identified in region II-II from the 2D DQ-SQ [13]C-^{13}C correlation Spectrum; b) Cross-links between furanic rings and end functions at the á-carbon identified from the 2D DQ-SQ [13]C-13C correlation spectrum (taken from [38]).

End functions. A low amount of direct functional groups directly linked to the furanic rings is evidenced on the 2D correlation spectrum, as depicted in Scheme 2-1. b- structures d-f.

Typically, aldehydic (Scheme 2-1. b-structure d), methyl (Scheme 2-1. b.-structure e), and carboxy (Scheme 2-1. b.- structure f) groups bonded to the R-carbon are evidenced through the off-diagonal J-L, J-A, and J-K cross-correlation peaks, respectively.

Interestingly, the connection between the arene-like peak H and the rest of the material is allowed by a keto group (cross-peak H-L).

Cross-linking (regions III-I and I-I). These regions mainly show the interactions among carbons that compose the linkers between furanic moieties. Peak B identifies CH_2 (see IRCP) cross-links between furanic species (peaks F and J):$C_{\acute{a}}$-CH_2-$C_{\acute{a}}$ (J-B-J, high intensity); $C\beta$-CH_2-

77

Cβ (F-B-F, but very weak intensity); and C$_{\acute{\alpha}}$-CH$_2$-Cβ (J-B-F, of weak intensity). Peak E at 50.5 ppm is a CH group according to IRCP experiments. The corresponding cross-peak is very broad and difficult to analyse as it mainly connects to ketones E-L even if CH-CH (E-E) or CH-CH$_2$ (E-D) self-correlation may also be possible.

Levulinic acid (LA). All correlation peaks that have been discussed above are related to the structure of the furanic network. However, several additional intense cross-correlation peaks between regions I and III are also clearly observed on the 2D correlation spectrum. This concerns the K-C cross correlation peaks at about 176.5 (K) and 28.7 (C) ppm in the SQ dimension, the C-D cross-correlation peaks at 28.7 (C) and 38.3 (D) ppm, the D-L cross correlation peaks at 38.3 (D) and 208 (L) ppm, and, finally, the L-C correlation peaks at 208 (L) and 29.6 (C) ppm. First, this set of correlation peaks clearly indicates that the C peak contains two distinct components (which overlap completely in the 1D MAS and CP-MAS spectra) with isotropic chemical shifts very similar to those reported for the CH$_3$ (29.7 ppm) and CH$_2$ (27.9 ppm) groups of levulinic acid in CDCl$_3$ solution. Second, it shows a K-C-D-L-C connectivity pattern that is characteristic for levulinic acid. The presence of levulinic acid was confirmed by an additional 2D ^{13}C homonuclear proton-driven magnetisation exchange experiment realised with a mixing time of 150 ms without the classical ^{1}H-^{13}C CP step (result not shown). This approach allows the detection of all mobile species whose sensitivity is very low using a common CP approach due to molecular mobility. We were able to visualise the same connectivity pattern, 29.6-210.0-38.3-28.7-176.5 ppm, typical for the levulinic acid molecule. Meanwhile, sharp signals at 210.0 and 176.5 ppm, which were lost after CP treatment, were recovered and found to be coherent with peak attribution and connection related to levulinic acid. This additional experiment shows that part of LA exists in a free form within the material core and it is in good agreement with our TG-IR analysis. So if one wishes to have levulininc acid free HTC a Soxhlet extraction is necessary. (see section 2.2.4)

One final remark: the four well-defined, but weak, cross-peaks at 75 ppm (marked by an asterisk) and (93, 97) ppm can be attributed to the unreacted $\acute{\alpha}$- and β-glucopyranose forms of glucose, as pointed out before, existing in spurious amounts (Scheme 2-2).

It is clear from the 2D experiment that glucose does not correlate with any other carbon in the sample, suggesting its simple entrapment in the carbonaceous matrix. All data support the idea that the main structural motif is the furan ring directly coming from HMF, the dehydration product of glucose. The very intense cross-peaks J-F provide the main spectroscopic evidence for this assumption: the amount of C=C-O and C=C is close to one-to-one. Any interpretation including widespread graphene sheets decorated with OH groups is not consistent with our data because an intense peak at 130 ppm, in addition to the resonance above 140 ppm, would be otherwise expected. This idea was also corroborated by the fact that direct carbonisation of HMF provides a material whose chemical characteristics are very close to a glucose-synthesised carbon, as it will be shown by solid-state NMR experiments in the following section.

However, the final product of thermally treated biomass is not just a simple polyfuran, and the obtained material is quite complex, as suggested by the combination of coexisting structures depicted in Figure 2-18. Clearly, HMF units merge together mainly *via* ά-carbons, causing the long-range conjugated double bonded network, but ramification from *β*-positions is also very common as one *β*-carbon out of two is actually cross-linked. Even if the presence of furan moieties in the structure of carbonaceous materials was very seldom highlighted, we believe that this is actually the only coherent explanation to our data.

To have a picture of how the internal structure of the carbonaceous powder is disposed, one should consider several points:

(1) The dimension of each particle ranges between 0.5 and 2 μm (Figure 2-3)

(2) ^{13}C-^{13}C DQ-SQ experiments show that most of the furan rings are strongly mutually connected, suggesting their very close spatial proximity;

(3) Quantitative data indicate that a fairly high amount of carbon signal (>20%), excluding free levulinic acid) comes from aliphatic carbons, and through space connectivities show that most of those groups play a crosslinking role between carbonyls and furans.

These considerations clearly exclude a long-range furanic network whose external surface is decorated with aliphatic chains and carbonyl groups, but it rather leads us toward an

interpretation in which the micrometer-sized carbon particle is actually composed of many interconnected (through short keto-aliphatic spacers) nanosized domains in which an arbitrary combination of structures proposed in Scheme 2-1 coexist together. The model as described above is visualized in Scheme 2-2

Analysis of the overall intensity of the SP spectrum (Table 2-1) of HTC-G80 lets us attribute 13% of carbon to C=O containing groups, ca. 64% to sp^2 C=C carbons (in particular, about 29% to ά-carbons, 29% to β-carbons, and 6% to arene sheets) and around 23% to sp^3 carbons.
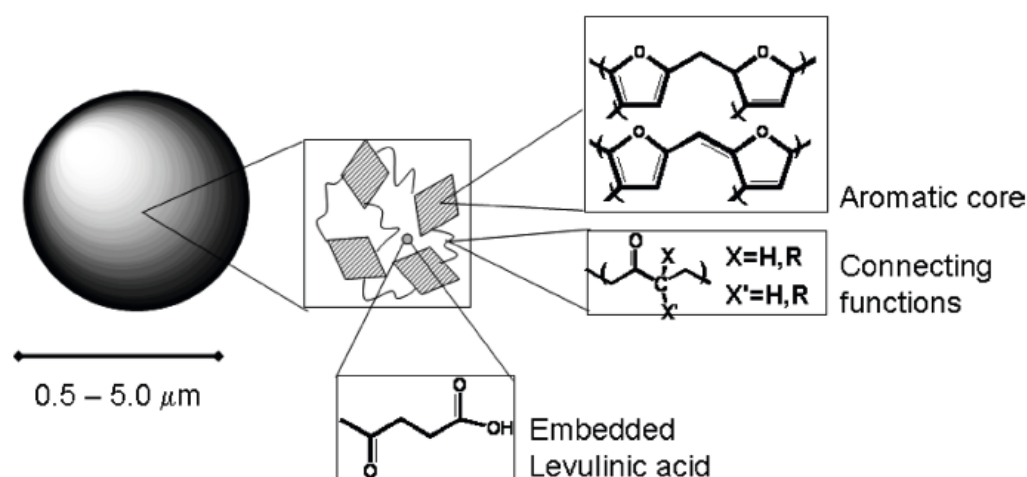
Scheme 2-2: Proposed structural model of 180°C glucose-derived HTC particle (taken from [38]).

2.2.7 Potential Chemical Reactions involved in the HTC Formation Mechanism

^{13}C- Solid state NMR proved to be a very powerful technique in the determination of the final structure of HTC materials using here glucose as a model system. However, we still do not know what are the chemical reactions occurring in the autoclave during HTC which lead to the formation of such a polyfuranic-based carbonaceous material.

Since HMF is considered the main precursor for the generation of HTC, in order to get an idea of reactions, which are likely to occur it is worth to have a look at the respective chemistry.

Figure 2-23 gives an overview on the reaction pathways. Furan is a five-membered heterocyclic aromatic compound. The ring is composed of one oxygen and four carbon atoms. The aromatic resonance energy is low compared to benzene and the electron density within the ring exceeds the one of benzene due to the electron-donating effect of the oxygen. Consequently, furan shows high reactivity (10^{11} times higher than benzene) towards electrophilic aromatic substitution reactions, which are preferred in the 2,5-position (Figure 2-23/I). The high electron density and low resonance stabilisation lead to manifold electrophilic addition and ring-opening reactions compared to other aromatic compounds. As acid catalysed ring-opening reaction lead to diketones, furans can be seen as masked diketones, as well (Figure 2-23/II). Diketones, possessing α-hydrogens can easily undergo inter- and intramolecular aldol-type reactions due to the keto-enole tautomerism.
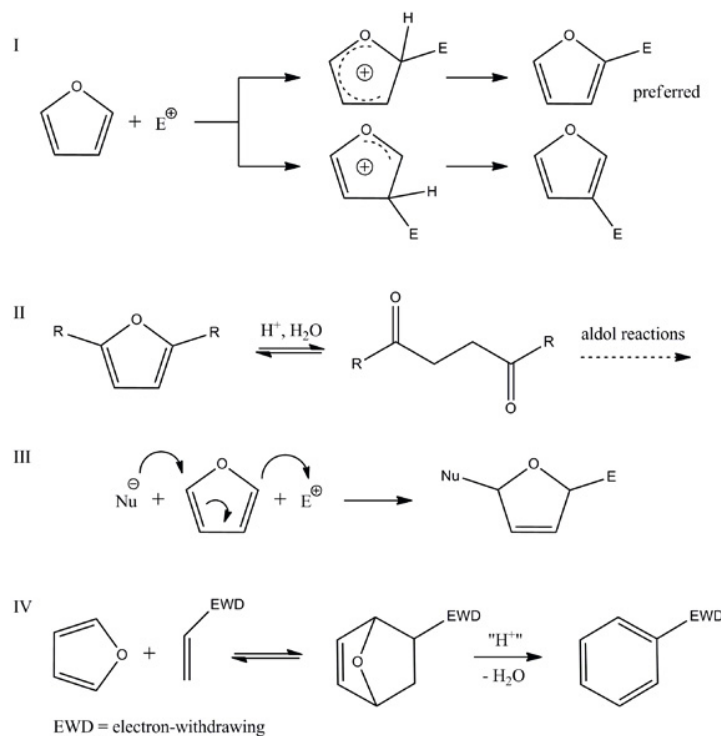
Figure 2-23: Possible chemical reactions of furan ring (taken from [48]).

Because of the rather weak conjugation of the oxygen atom, furans can also undergo nucleophilic addition reactions, behaving like a 1,3-butadiene (Figure 2-23/III). The resulting adducts can be

easily converted by nucleophilic substitution. Additionally, the 1,3-diene substructure is fixed in the ring, perfectly arranged as diene component in Diels-Alder reactions (Figure 2-23/IV). Diels-Alder products can be transformed into classical aromatic compounds.

Regarding the chemistry of HMF, mainly reactions on the hydroxymethyl group (esterification, etherification and oxidation) and the formyl group (reduction, oxidation, aldol reactions and aldol-like reactions) are mostly investigated with the aim to produce symmetric compounds for the use as monomers in sustainable polymers. [49]

To distinguish HMF from furan and get some insights into the hydrothermal carbonisation, first the respective chemistry of the functional groups has to be considered. Typical reactions are shown in Figure 2-24. The very reactive formyl group can be attacked by several nucleophiles. One of the most important reactions of aldehyds is the aldol condensation with α-carbonyl compounds, such as diketones (Figure 2-24/A). In the presence of alcohols aldehyds are transferred into acetals (Figure 2-24/B). Interestingly, the acetalisation changes the reactivity of the furan ring in HMF, as it blocks the electron-withdrawing mesomeric effect of the formyl group and therefore increases the electron-density within the ring.

The hydroxyl group within the hydroxymethyl substituent can undergo simple nucleophilc substitution being a good leaving group (Figure 2-24/C), as well as etherification/esterification in the presence of alcohols/carboxylic acids (Figure 2-24/D). Dissociation of the hydroxy group gives reactive carbocations (Figure 2-24/E), which can undergo electrophilic substitution reactions at nucleophilic furan rings (Figure 2-24/F).
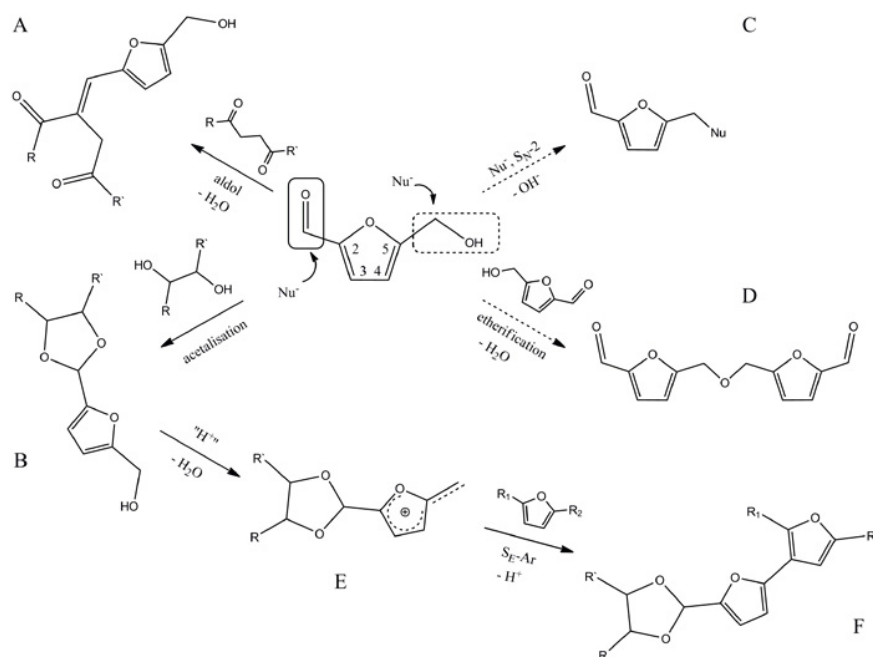
Figure 2-24: Selection of possible HTC-relevant reactions at the substituents of HMF and acetal-protected HMF (taken from [48]).

Second, substituents also change the chemistry of the ring (Figure 2-25). The electron-withdrawing substitutes will reduce electrophilic attacks on the ring (Figure 2-25/I). This is especially the case as the hydroxymethyl- and the formyl-group in HMF are located at the preferred 2,5-positions. Nucleophilic addition reactions are more favoured due to the already mentioned resonance effect with the formyl group, instead (Figure 2-25/II). However, the substituents are even more reactive in that sense and also lead to sterical hindrance at the 2,5-position.

The addition of water and subsequent ring-opening leads to the formation of levulinic acid (LA) and formic acid (FA) in hydrothermolysis (Figure 2-25/III). This indicates the strong involvement of such ring-opening reactions, which can convert furans into diketones.[50] α-H-diketones give rise to versatile aldol chemistry (Figure 2-25/III).
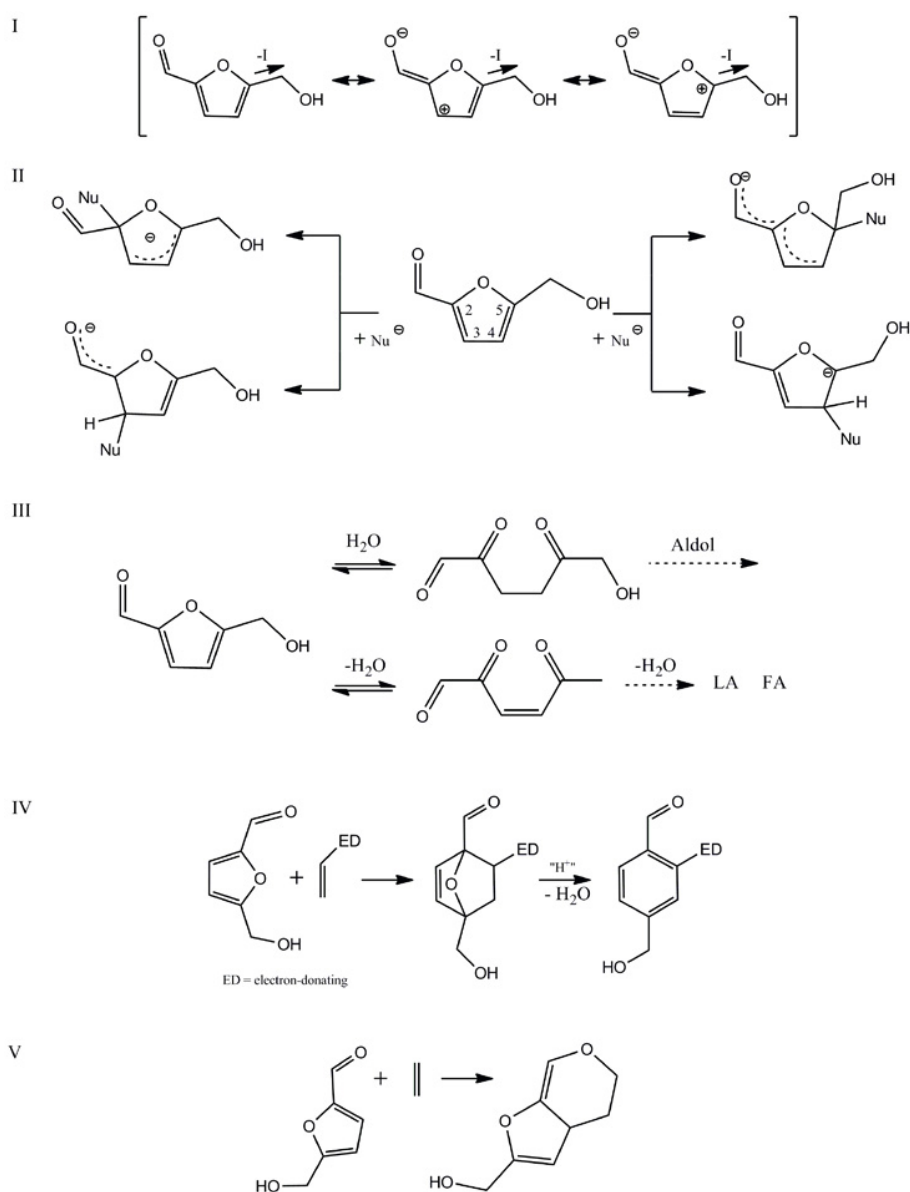
Figure 2-25: Selection of possible HTC-relevant reactions at the ring of HMF (taken from [48]).

In context with Diels-Alder reactions, the diene substructure of HMF changes from an electron-rich diene like furan, to an electron-poor diene, which consequently prefers the reaction with electron-rich dienophils (Figure 2-25/IV). Notably, the formyl-group in HMF is located in α-ene position and therefore creates another diene substructure, which might also undergo Diels-Alder reaction (Figure 2-25/V). Pressure and temperature can influence the reactivity, especially in

Diels-Alder reactions, which are exothermic and have a negative reaction volume. Water, as the solvent, can be favourable for Diels-Alder reactions of rather hydrophobic reactants and it also accelerates reactions with ionic transition states like aldol reactions.

The chemistry of mono-substituted furans, which either possess the hydroxymethyl- (furfuryl alcohol) or the formyl-function (furfural) is well-investigated. Self-condensation, sometimes called resinification, of furfural and fururyl alcohol is also reported. Gandini et al., who contributed a lot to furan-based polymerisation, explains the difficulties in understanding the mechanism of poly-furfuryl alcohol with two side reactions namely hydride abstraction and intramolecular Diels-Alder reactions. [51] Succeeding H^-/H^+ abstraction cycles at methylene bridges of the oligo(furfurylalcohol) lead to a conjugated linear polymer. Dihydrofuran moieties are then likely to react as dienophils with the diene substructure of furans to produce the typical cross-linked resins. With this model Gandini et al. also explained the colour generation of the branched polymer by highly conjugated sections within the resin.[51] The proposed polymerisation and cross-linking scheme is presented in Figure 2-26/A. The resinification of furfuryl alcohol under acidic and aqueous conditions probably also possesses diketone formation within the polymer chain. This happens *via* ring-opening reactions, which are thermodynamically slightly favoured. [52] Attention has to be drawn on the possibility to convert the ether bridge in oligo-/poly(furfuryl alcohol) into a methylene bridge by the release of formic acid. Estherification (Figure 2-24/D), is expected from HMF as well. Therefore this mechanism is also likely to contribute to the formation of HTC. However, due to the formyl group the reactivity of HMF should be closer to furfural, where the "resinification" is even more complicated and less investigated. Different resin precursors, shown in Figure 2-26/B were found by simple thermal degradation of furfural at 100-250 °C. Both together lead to cross-linked precipitates. It is proposed that again charge stabilisation in the conjugated systems may lead to the dark colour. Radical reactions as well as reactions involving the release of hydride ions have to be considered. Nevertheless, it is reported that HMF, which does not posses a free 2- or 5-position, is hardly sensitive to this reaction.[51b] Additionally, the presented "resinification" products are clearly to be distinguished from the respective hydrothermal carbon as ring-opening reactions were avoided by anhydrous conditions.
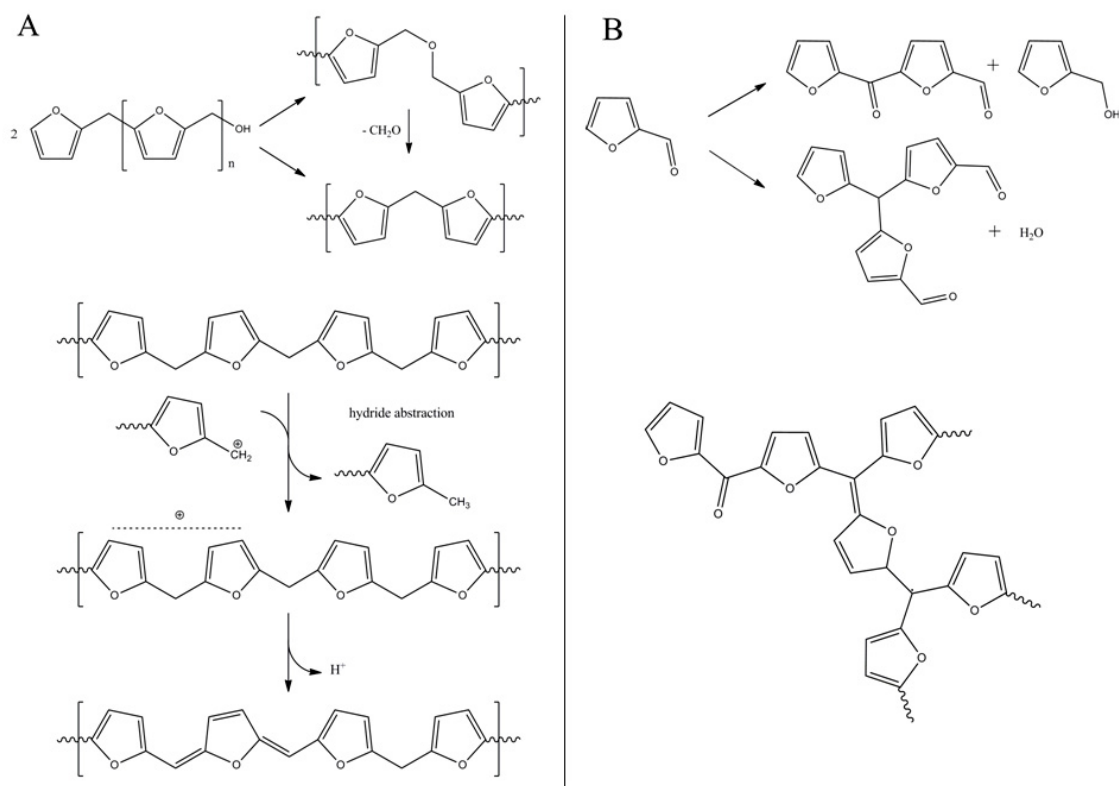
Figure 2-26: Resinification schemes of A) furfuryl alcohol and B) furfural (taken from [48]).

To summaries, acetal formations from HMF with glucose as well as intermediate diols are very likely to be formed during the HTC process. As mentioned before, the acetalisation reduces the reactivity of HMF due to the protection of the aldehyde group. The increased electron density of the ring increases the reactivity of the hydroxyl group, which can or undergo etherification or dissociates leading to substitution in the 3,4-position of other furans. Ring-opening reactions create diketones like LA, which can easily undergo aldol condensations. Horvat et al, who studied the formation of levulinic acid, pointed out that instead of 2,3-addition of water, which finally leads to levulinic acid, the 4,5-water addition should also occur. They proposed that this pathway, most likely producing 2,5-dioxo-6-hydroxohexanal (Figure 2-25/III), for the formation of polymeric species.[53] Together substitution and condensation are polymerisation reactions.

The NMR experiments indicate the furans to be mostly 2,5-substituted, therefore aldol condensation can be considered to be indeed one of the most important occurring reaction. This was also confirmed in a recent experiment by Patil and co-workers who compared the structural features of HTC materials formed from glucose, fructose and HMF. [54] Therein, diketones will react with the very reactive aldehyde function of HMF and with other diketones. Like reported for poly(furfurylalcohol), loss of formaldehyde converts ether-bridges into methylene bridges. Deprotonation and dehydroxylation can create conjugated networks, which can explain the dark colour of HTC. The involved dehydrofurans and double bond give rise to Diels-Alder reactions with the inherent diene substructure of furanes creating further cross-linking and additionally aromatic structures observed in a very small percentage from NMR (structure Scheme 2-1 a). Formation of the abundant CH_2 groups acting as linkers between furan rings (see section 2.2.6.3) may originate from nucleophilic addition after possible elimination of the hydroxyl group on HMF. The nucleophilic attack on the aldehyde group of HMF from a second furanic unit may lead to hydroxyl species that can, in turn, be eliminated with subsequent electron rearrangement and formation of a sp^2 CH carbon between two furan moieties (Scheme 2-1.a.-structure b). The formation of specific CH_3 and COOH ending groups (from Cά of furan ring) was previously reported. [55]

We believe that such a complex HTC structure is the result of a cascade of coexisting reaction paths of interfurfural polymerisation and aldol condensation reactions involving both the furan motif and dehydrated glucose-based products, such as levulinic acid. This more vinylic, aliphatic structure explains many of the properties of hydrothermal coal, such as rather high combustion value [56], high chemical reactivity, reductive properties, and high ion binding capacity and wettability. Summarised we can speak of a set of dehydration, polymerisation i.e. condensation and addition and aromatisation reactions, which lead to the final chemical structure of HTC.

From NMR we found that about 60% of the carbon atoms belong to a cross-linked furan-based structure. Furan moieties are directly linked either *via* the R-carbon or *via* sp^2- or sp^3-type carbon groups, where cross-linking can occur. Additional cross-linking sites are located at the β carbons of the furan ring. In good agreement with TG-IR (Figure 2-10) we found that levulinic acid, one

of the decomposition products of hydroxymethylfurfural (HMF), is highly abundant in the final material as embedded molecule.

It is indeed very challenging to fully understand the chemistry behind the formation of HTC materials. As in the case of nucleation, *in situ* monitoring of the reaction using NMR or LC-MS are alternatives. However, these are difficult to achieve because of the very severe conditions inside the autoclave. In this respect the use of ^{13}C solid state NMR on ^{13}C labelled glucose derived materials together with revising furan chemistry helped us to propose a potential mechanism and a final chemical structure of HTC materials (Scheme 2-2)

2.3 Structural Differences between HTC Materials from Different Hydrolysable Carbohydrates

After determining the final structure of the glucose based HTCs we embarked on a comparative structural study of hydrothermally synthesised carbon materials obtained from different saccharides classified according to their number of carbons (pentoses *vs.* hexoses) and growing complexity (mono vs. di- vs. polysaccharides). [57] In this subchapter I will compare such materials in terms of morphology, functional groups, crystalinity, porosity as well as chemical structure using the combination of techniques previously described for glucose. In addition, the effect of post calcination at different temperatures on the HTC materials will also be presented. [34]

I will show that all materials obtained from hexoses-based mono- (glucose, HMF), di- (maltose, sucrose) and polysaccharides (amylopectin, starch) have the same chemical nature in terms of atom percentage and functional groups, as verified by ^{13}C solid-state cross polarisation (CP) NMR analysis , scanning electron microscopy (SEM), FT-IR and others. On the other hand, pentose-based (xylose, furfural) carbonaceous materials clearly showed interesting morphological and chemical differences with respect to hexose-based ones. This work also clearly underlines that no substantial difference exists between monosaccharide- and polysaccharide derived carbons, suggesting that the complexity of polysaccharides (not including cellulose, section 2.4) hardly has any influence on the material-forming mechanisms. This is important as it indicates that basic studies performed on simple test molecules, like glucose, have broader validity and that

irrespective of the complexity of the saccharide source, the final materials have very similar local functionalities and connection patterns.

2.3.1 Morphology:

Particle dispersions of carbonaceous materials were prepared from saccharides at 180°C in water in a closed autoclave. The dried HTC powders were thereafter calcined at different temperatures (350, 550, 750 and 950 °C) under a constant flow of N_2 gas at a heating rate 5 °C/min below 350 °C and 2 °C/min above 350 °C and then kept at the desired temperature for 2 h. We denoted the materials HTC-X-Y where X represents the name (or initial) of the precursor and Y represents the post-calcination temperature. Ex: HTC-Glucose is the hydrothermal carbon from glucose (180 °C) while HTC-Glucose-350 is the same material after post-calcination at 350 °C.

Despite the similar chemical nature of the employed sugars, the first being a hexose and the second a pentose, the final materials have remarkably different shapes Figure 2-27. The decomposition of xylose leads to separated carbon spheres with a diameter between 100 and 500 nm while glucose-based carbon is characterised by a mixture of spheres whose size varies between 500 nm and 1 mm, randomly dispersed inside an interconnected matrix of smaller particles (<200 nm).

It needs to be mentioned that the particle size and homogeneity can be further controlled by temperature, time and concentration (see section2.2.1). The morphology of HTC carbon materials, no matter of the precursor and temperature, does not change upon further thermal treatment Figure 2-29.

SEM micrographs of carbon materials from disaccharides (maltose, sucrose) and polysaccharides (amylopectin, starch) are depicted in Figure 2-28. HT*C*-maltose and HT*C*-sucrose are composed of interconnected particles, in coexistance with domains (larger in *C*-maltose) where aggregation occurs. *C*-maltose is composed of a larger number of small (200–500 nm) particles in co-existence with larger spheres (2 mm). By contrast, *C*-sucrose is composed of spherical particles whose size vary between 700 nm and 2 mm. Strong similarities are found for *C*-maltose and *C*-

glucose materials, both caracterised by isolated large spherical particles within a large matrix of interconnected small particles with ill-defined shape.
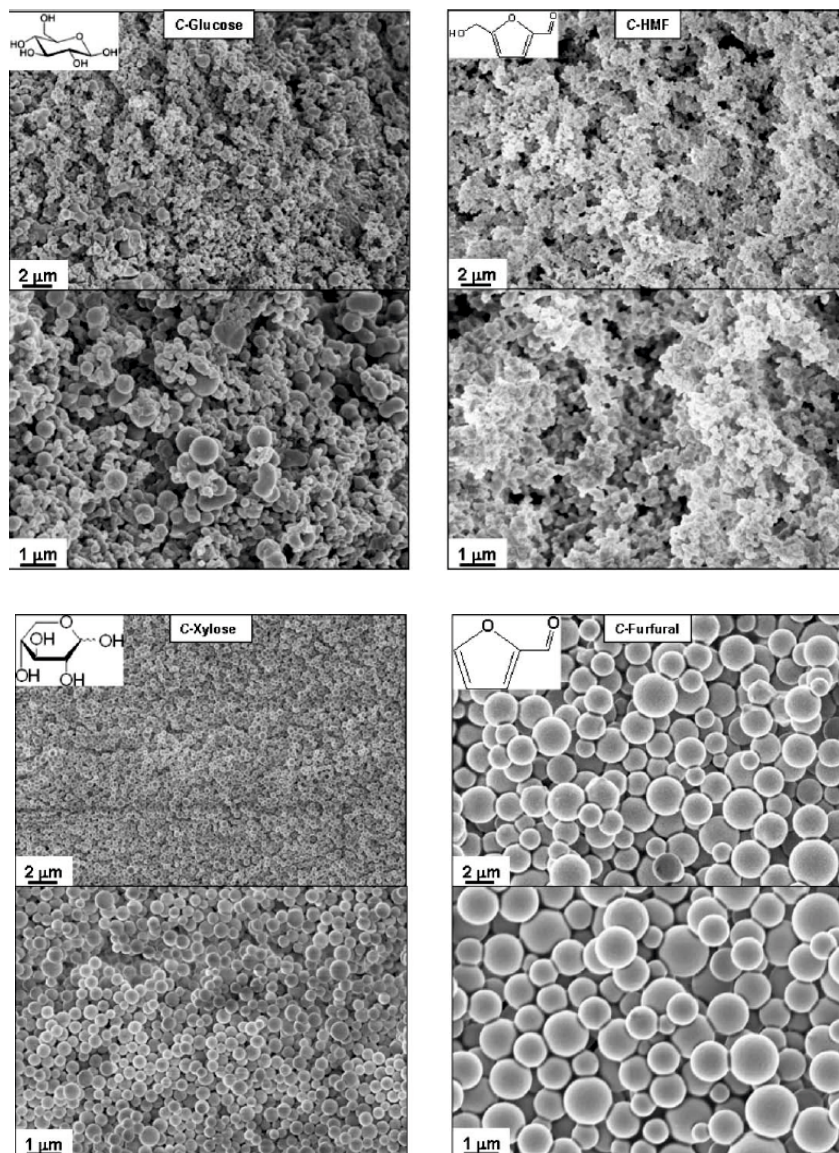
Figure 2-27: SEM images of samples HTC-Glucose, C-HMF, C-Xylose and C-furfural (taken from [57]).

Polysaccharides including amylopectin and starch, whose SEM images Figure 2-28 show interconnected spherical particles ranging from 700 nm to 2 mm, provide very similar dispersion patterns despite their low solubility in water at room temperature. When one compares SEM structures of final carbons to original saccharides (micrographs not shown-see ref. 57), the

restructuring process which took place during HTC and transformed the original disordered bulky materials into micrometer-sized particles and/or spheres is self-evident. As described for the case of glucose, HTCs form by the decomposition of hexoses to HMF and pentose to furfural followed by a cascade of chemical reactions such as dehydration, polymerisation i.e. condensation and addition and aromatisation reactions. Nicely dispersed, separated spherical particles are found for xylose and furfural derived HTC (Figure 2-27). An explanation for this may probably come from the limited water solubility of furfural (< 8.5 m/v%), which tends to emulsify in solution, and carbonisation may only take place inside droplets. In the case of hexose-based carbohydrates the morphology is rather similar. Of course the higher is the complexity of the carbohydrate (monosaccharide < disaccharide < polysaccharide) the higher is the polydispersity of the resulting HTCs. This might be due to the different hydrolysis and dehydration rates. In the case of polysaccharides and disaccharides, they are firstly hydrolyzed to the monosaccharide units (i.e. glucose) and s further dehydrated to HMF *via* the Lobry de Bruyn-Alberta van Ekstein rearrangement. [25]
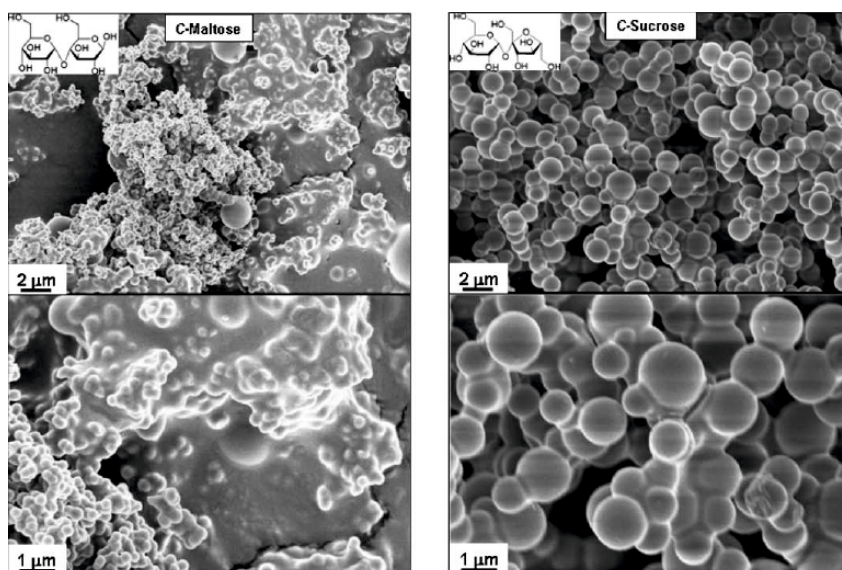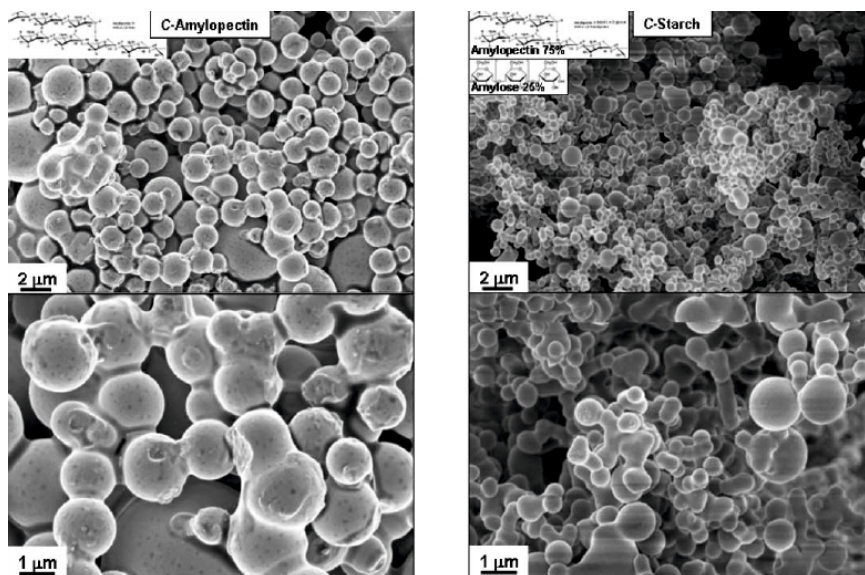
Figure 2-28: SEM images of samples C-sucrose, C-maltose, C-starch and C-amylopectin.
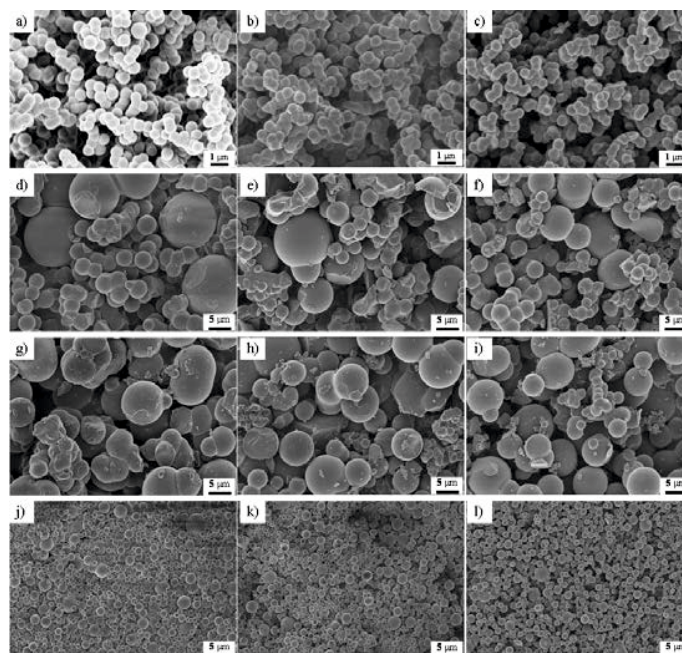
Figure 2-29: SEM images of HTC and post-calcined carbons. a) HTC-Glucose; b) HTC-Glucose-550; c) HTC-Glucose-950; d) HTC-Sucurose; e) HTC-Sucurose-550; f) HTC-Sucurose-950; g) HTC-Starch; h) HTC-Starch-550; i) HTC-Starch-950; j) HTC-Xylose; k) HTC-Xylose-550; and l) HTC-Xylose-950 (taken from [34]).

2.3.2 Elemental Composition:

Elemental analysis of the HTC carbons calcined at different temperatures Table 2-2 shows major compositional changes in the temperature interval 350 - 750 °C, where carbon content increases from ~70% to ~95% while the H and O contents are markedly reduced. Increasing calcination temperature to 950 °C has a continuous effect on the HTC carbon elemental composition, but this time, the rate of change with temperature is small. These findings suggest the critical temperature region for HTC carbon thermal decomposition is lower than 750 °C which is consistent with the TGA that the main decomposition event is over the range 350 - 600 °C (Figure 2-10.)

The chemical composition also largely changed during the hydrothermal process: saccharides turn into dark brown or black powders with a carbon content increasing from the original 40 wt% to 64–70 wt% meanwhile, the oxygen presence is reduced from 53 wt%, as found in, *e.g.*, glucose, to 27–30 wt% for carbon powders. Looking at the elemental composition data in Table 2-2 we can observe that HTC-xylose has higher carbon content (68% C) as compared with the other samples with similar values (~ 66% C). This is explained by the fact that xylose forms HTC *via* furfural resulting in a more condensed carbon network. Nonetheless, the oxygen level remains quite high even in C-xylose (25.4%) meaning that the conjugated C=C network is always accompanied by larger quantities of functional groups (C=O, COOH), furan rings and ethers.

Upon further thermal treatment the values between the different precursors are very similar. Obviously, the higher the post-treatment temperature, the higher is the carbon content and the less the oxygen. This suggests that an aromatisation process occurs with the elimination of polar functional groups.

Table 2-2: Elemental analysis data of HTC and post-calcined carbons:

Samples	C (wt%)	H(wt%)	O (wt%)	Samples	C (wt%)	H(wt%)	O (wt%)
HTC-G	66.77	4.358	28.872	HTC-St	66.1	4.487	28.413
HTC-G-350	68.29	4.169	27.541	HTC-St-350	68.91	4.187	26.903
HTC-G-550	82.71	3.089	14.201	HTC-St-550	83.5	3.484	13.016
HTC-G-750	94.04	1.668	4.292	HTC-St-750	95.02	1.103	3.877
HTC-G-950	96.42	0.509	3.071	HTC-St-950	96.14	0.406	3.454
HTC-Su	66.77	4.431	28.799	HTC-X	68.51	4.05	25.44
HTC-Su-350	69.84	4.265	25.895	HTC-X-350	69.63	4.021	26.349
HTC-Su-550	87.07	2.99	9.94	HTC-X-550	83.64	3.497	12.863
HTC-Su-750	93.03	1.657	5.313	HTC-X-750	95.66	1.241	3.099
HTC-Su-950	95.22	0.41	4.37	HTC-X-950	97.21	0.416	2.374

2.3.3 FT-IR

The FT-IR spectra of the HTC carbons as well as the ones obtained after calcination at various temperatures are shown in Figure 2-30 for four precursors. Abundant functional groups can be observed on all HTC carbons. A broad absorption band between 3700 and 3100 cm^{-1} corresponds to O-H (bonded) stretching vibration. The band at $\sim$ 2925 cm^{-1} indicates the presence of methylene-type groups (e.g., ν(C-H)$_{stretch}$). The bands at ~1700 and ~1600 cm^{-1} are attributed to C=O and C=C stretching vibrations, respectively, support the concept of aromatisation of biomass during hydrothermal treatment. [15] While these characters are the same for all the four HTC carbons, independent on the used precursors, there are also some differences especially in the case of xylose (HTC-X). The two weak bands in the 1520 – 1450 cm^{-1} region for HTC-X, which can be attributed to aromatic ring stretching vibration,[58] differ from the other three HTC carbons, which only have one band each. A stronger aromatic characters for HTC-X, as shown by the more resolved bands at 880 and 752 cm^{-1} (δ(C-H)$_{oop\ (out\ of\ plane)}$), is also suggested.[59] These differences are again related to the fact that xylose is a 5C sugar and the formation of HTC takes place *via* the formation of furfural and not HMF. Therefore, a more condensed structure with a slightly more "aromatic" character is obtained upon HTC. This is clearly confirmed by the ^{13}C-solid state NMR experiments (Figure 2-34).

The carbons calcined at 350 °C have the similar spectra with the hydrothermally carbonised materials. This is in good agreement with the TGA data (Figure 2-10) which shows that the main decomposition event (for glucose) starts only above 300°C.
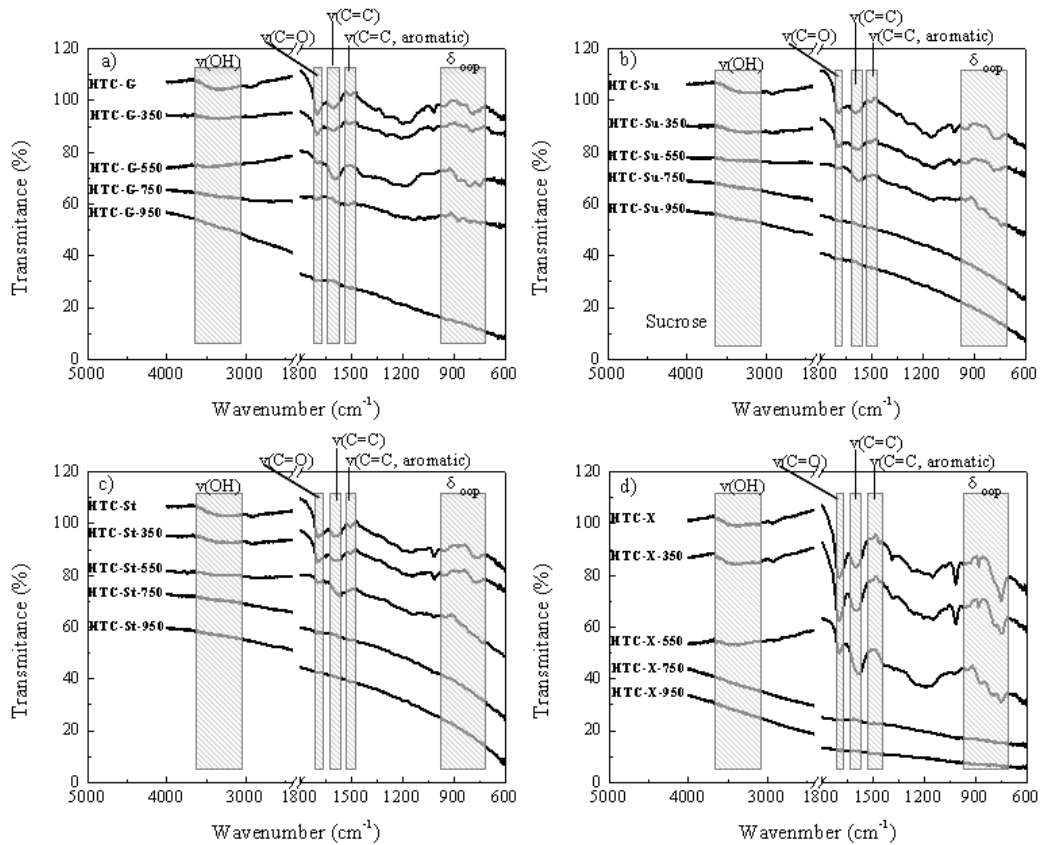
Figure 2-30: FT-IR spectra of the HTC and post-calcined carbons, derived from a) glucose, b) sucrose, c) starch, and d) xylose (taken from [34]).

Increasing the post-calcination temperature to 550 °C, the intensity of most oxygen-containing related bands decrease, while the C=C band becomes of stronger intensity. Some new bands corresponding to aromatic features such as bands at 876, 814 and 748 cm^{-1}(δ(C-H)$_{oop}$) appear at 550. [59] These are due to further dehydration and condensation reactions towards arene-like aromatic domains. [60] As the temperature further increases to 750 °C and 950°C the degree of carbonisation increases, therefore no adsorption bands can be detected and the spectra become smooth.

95

2.3.4 XPS

XPS offers information about the surface functional groups and for all the investigated HTC and pots-carbonised HTC materials. The XPS spectra show tow peaks corresponding to C1s and O1 (Figure 2-31, Table 2-3). The high resolution C1(s) envelope of glucose and xylose derived HTC carbons are characterised by three main contributions, at 285.0 eV (**C1**, C-C and C-H$_x$), 286.3/286.6 eV (**C2**, C-O-H (hydroxyl), C-O-C (ether)) and 287.9/288 eV (**C3**, C=O (carbonyl)) with a minor shoulder at 289.3/289.44 eV (**C4**, O=C-O (acid or ester)). The relatively high intensity of the peaks at **C2** and **C3** indicates the presence of a considerable amount of oxygenated functionalities mostly related to the furan and carbonyl moieties present in the HTC carbon structure.[60] Pyrolysis at 550 °C causes a major reduction of the oxygen related contributions indicating the loss of such functionalities and a resultant increase of surface hydrophobicity. The residual **C3** peaks can be attributed to the presence of phenolic groups forming during the pyrolysis process as confirmed by ^{13}C solid state NMR.[60] The peak at 290.1 eV (**C4(b)**) for the glucose derived carbon is attributed to adsorption of CO_2.

Increasing the temperature to 950 °C leads to a further loss of oxygenated functional groups present at this stage only in minor quantities. In addition the simultaneous increase of the peak at 291.1 eV (**C5**) for xylose derived carbon, corresponding to $\pi \rightarrow \pi^*$ shake up satellites, suggests the presence of extended pre-graphinic polyaromatic domains as the major building unit of the carbon scaffold. The peak at 290.4 eV (**C4(b)**) for glucose derived carbon is also attributed to adsorption of CO_2.

In good agreement with elemental composition the HTC from glucose contains less sp^2 graphitic carbon and more carbon bound to oxygen then the xylose material. Once the materials are calcined at higher temperatures the differences between them become neglectable.

Table 2-3: Experimental C1s / Binding energy B.E. (eV)/ Chemical state assignments for glucose and xylose derived carbons

Samples	C1 Sp2-Graphitic or C-C/C-H$_x$	C2 C-O	C3 C=O	C4 O=C-O	C4(b) Carbonate	C5 π-π* Shake up Satellite
HTC-G-180	285/69.4%	286.3/22.5%	287.9/6.4%	289.3/1.7%	X	X
HTC-G-550	285/82.5	286.4/11.6	288/3.3%	X	290.1/2.6%	X
HTC-G-950	285/85.1%	286.54/7.3%	288/4.2%	X	290.4/3.4%	X
HTC-X-180	285/74.4%	286.6/18%	288/4.7%	289.44/2.8%	X	X
HTC-X-550	285/78.9	286.3/16.3	287.9/2.1%	289.4/2.8%	X	X
HTC-X-950	285/81.4%	286.33/10%	288/3.8%	289.5/2.1%	X	291.1/2.7%
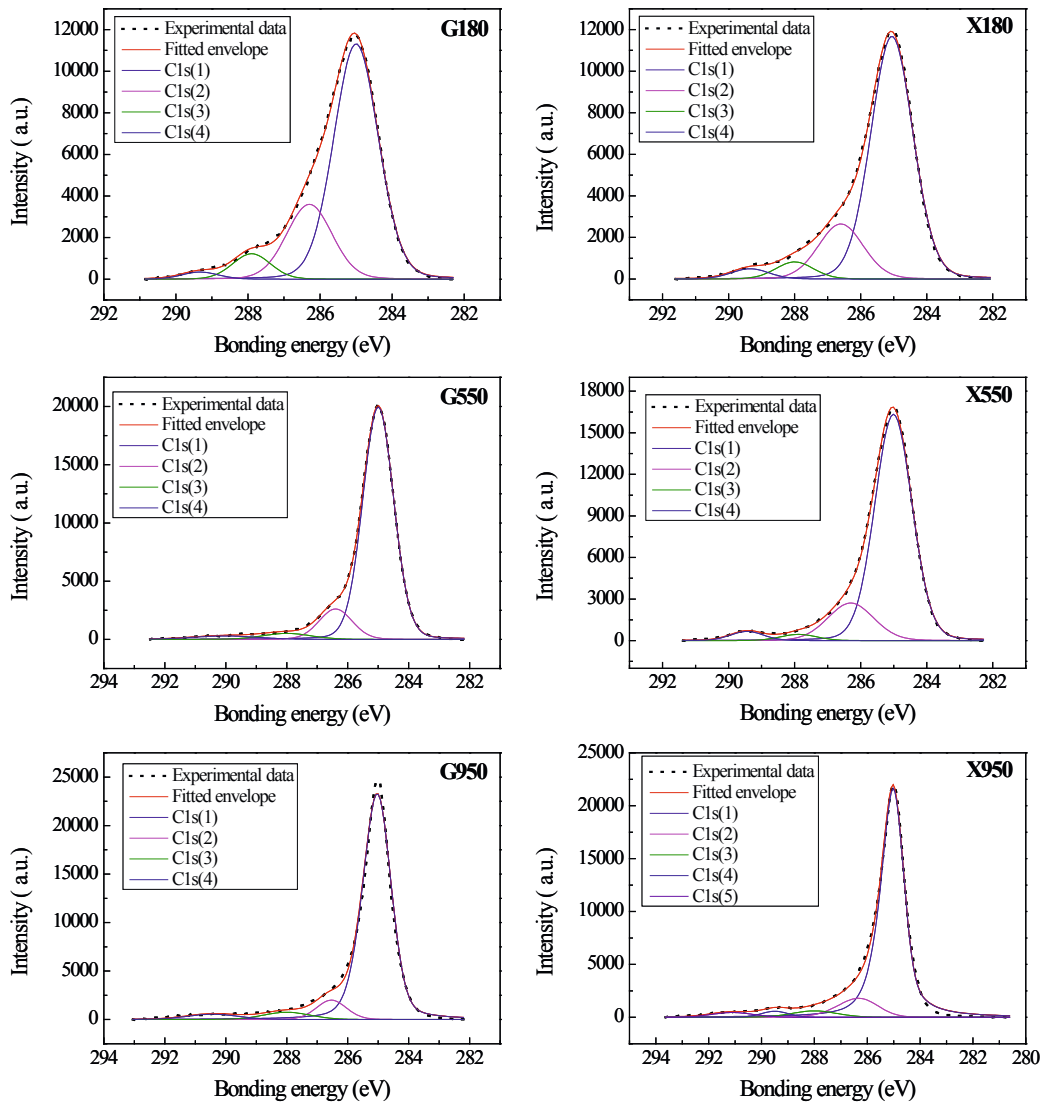
Figure 2-31: High-resolution XPS scans of C1 (s) photoelectron envelope for the HTC and post-calcined carbons derived from glucose and xylose (taken from [34]).

2.3.5 Zeta Potential: Surface Charge:

Zeta potential measurements (Figure 2-32) support very well the conclusions withdrawn from the FT-IR and XPS experiments. The surface charge of the materials is in all cases negative over all the chosen pH range. This is expected for HTC materials due to the acidic oxygenated groups on

the surface. [61] It can be clearly observed that the materials obtained after hydrothermal carbonisation have highly negative zeta potential values similar to the ones further calcined at 350 °C. Upon further heat treatment at 550 °C there is a significant increase in the zeta potential value in good agreement with the TGA profile as well as FT-IR experiments. This is due to the loss of functional groups as described before. This effect is even more pronounced upon further thermal treatment at even higher temperatures although not such great differences in the zeta potential values are noticed between 550 °C and 950 °C. This is because at 550 °C almost all the functional groups have been lost. The values are still negative due to the acidic character of the carbon materials with still some oxygen atoms incorporated in the final structure.[61]
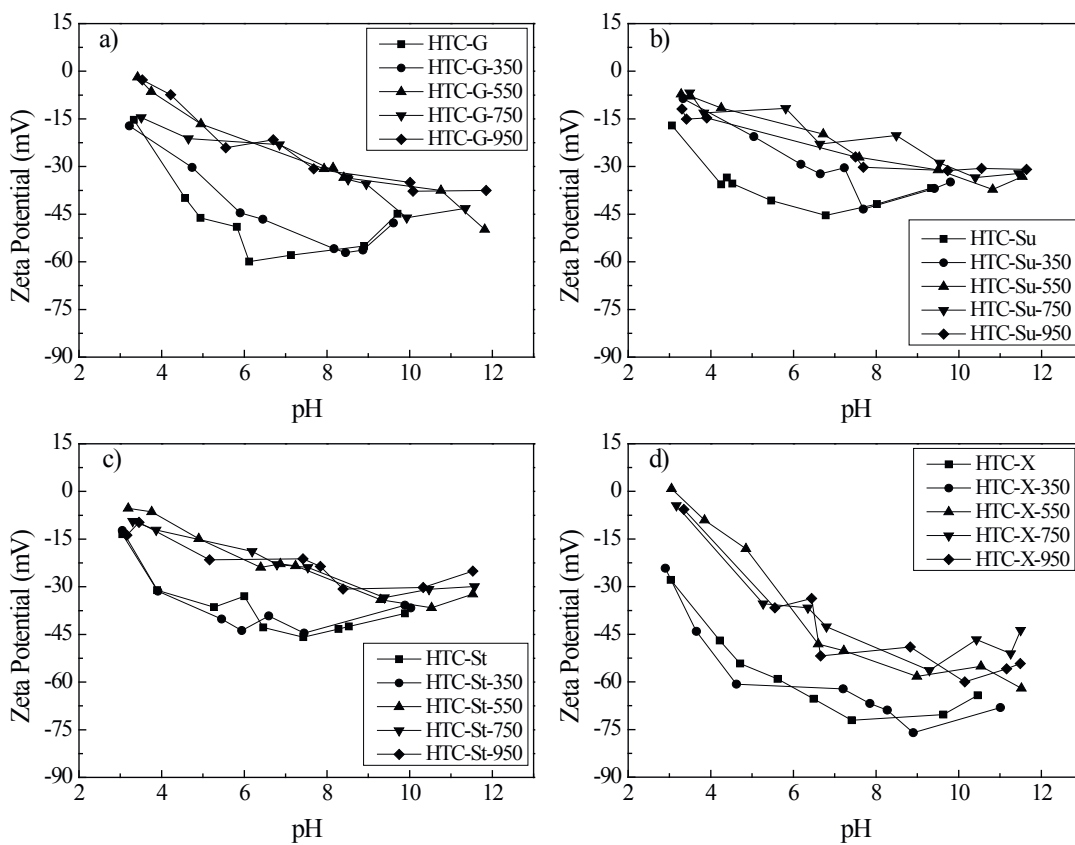
Figure 2-32: Zeta potential as a function of pH for HTC and post-calcined carbons, derived from a) glucose, b) sucrose, c) starch, and d) xylose (taken from [34]).

2.3.6 XRD

The observed X-ray reflections for all HTC materials are very broad, suggesting that the materials are very disordered and amorphous structures. The reflection at higher scattering angles is typically found in amorphous materials (e.g. polymers) and might reflect the average separation distance (4.0–4.5 Å) between segments.
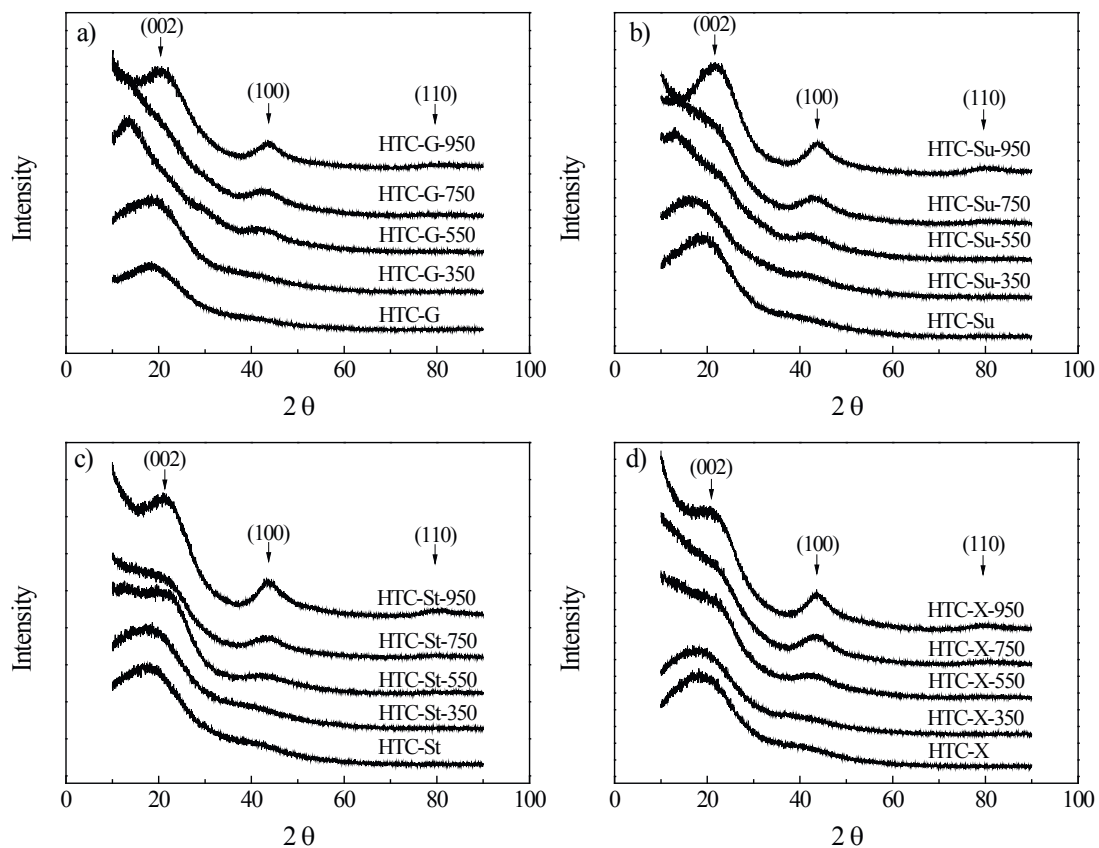
Figure 2-33: XRD patterns of of the HTC and post-calcined carbons, derived from a) glucose, b) sucrose, c) starch, and d) xylose (taken from [34]).

The reflection could also be related to a highly disturbed (002) interlayer carbon packing. Interestingly, these carbonaceous materials also present a reflection at lower scattering angles, potentially originating from either intramolecular repeat distances or large inter-segmental distances. The presence of these two reflections is analogous to observations on some

intrinsically microporous polymers [62], and is in accordance with the observation of microporosity in the carbonaceous materials. Upon increasing the temperature, the level of structural order increases which suggests that indeed aromatisation towards a more-turbostatic-like structure occurs. Starting with 750°C the 002 reflection corresponding to the interlayer scattering as well as the intralayer 100 reflection become obvious, as a proof of aromatisation/pre-graphitisation. There are no visible differences in XRD patterns between different precursors, all indicating the same general trend.

2.3.7 ^{13}C-Solid State NMR: Chemical Structure of HTC materials

Figure 2-34 shows ^{13}C solid state CP-MAS NMR spectra of HTC-glucose and HTC-xylose (highlighted in gray for convenience).
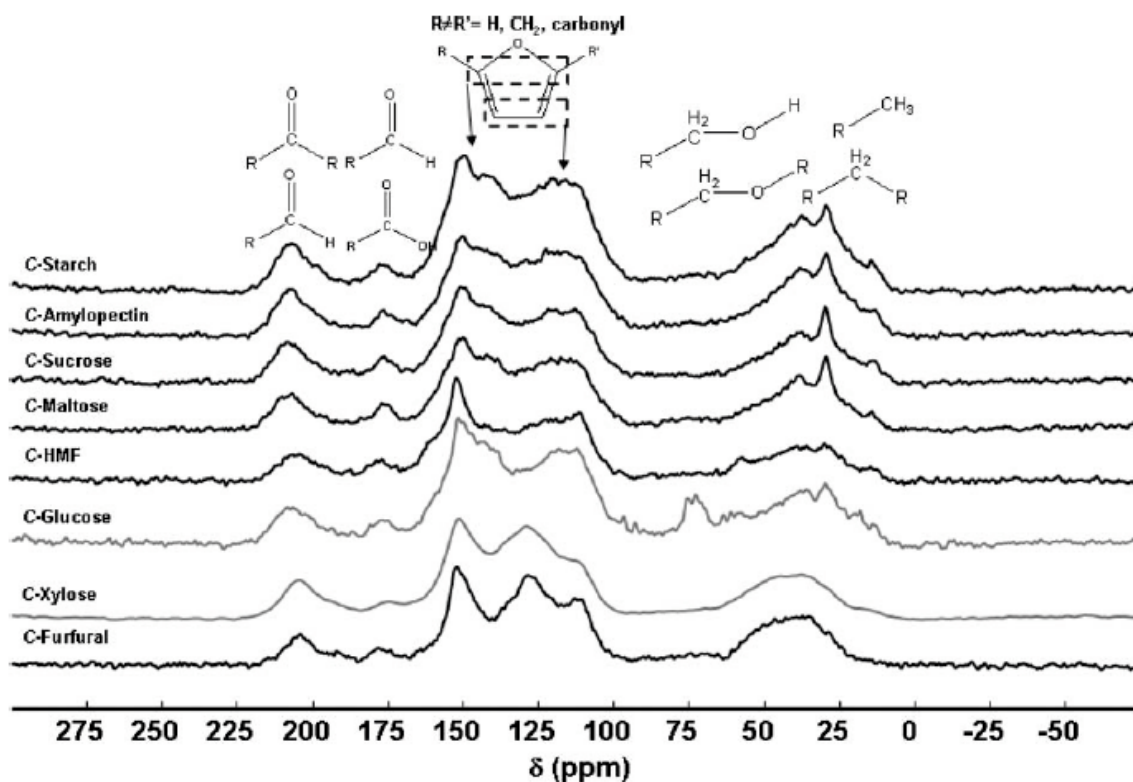
Figure 2-34: ^{13}C solid-state CP-MAS NMR spectra (t_{CP}= 3 ms) of HTC-starch, HTC-amylopectin, HTC-sucrose and HTC-maltose, HTC-HMF, HTC-glucose, HTC-xylose and HTC-furfural (taken from [57]).

^{13}C NMR spectra present some common peaks at 208 ppm (though a difference in 4 ppm at higher fields is observed for HT*C*-xylose), 175 ppm, 150 ppm and 40 ppm. On the other side, significant differences occur in the regions between 130 and 110 ppm, at 75 ppm and between 40 and 20 ppm. These observations show that similarities can be related to acomparable amount of carbonyl groups (aldehydes, ketones and carboxylic acids at chemical shifts between 210 and 170 ppm) as well as to the presence of oxygen-substituted protonated and non-protonated C=C bonds resonating at 150 ppm. By contrast, the peak at 129 ppm, which is generally attributed to aromatic carbons, as it is typical for graphitic structures or long-range conjugated double bonds, indicates the higher aromatic character of HT*C*-xylose carbon with respect to HT*C*-glucose. The peak at 75 ppm is indicative of the presence of hydroxylated methylene groups, which constitute an important part of HT*C*-glucose, while almost no hint of such groups is observed in HTC-xylose. Finally, at low chemical shifts, HT*C*-xylose seems to be dominated by aliphatic groups resonating in the 40–50 ppm region while HT*C*-glucose shows an additional contribution of methylene between 20 and 40 ppm.

Overall, it seems that carbon material obtained from xylose has a higher aromatic character than *HTC*-glucose, and its higher carbon content (68.5%) as well as XPS and FT-IR supports this observation. To reveal further details of this difference, we hydrothermally carbonise the known intermediates of dehydration, HMF and furfural under the same carbonisation conditions. The analysis of local chemical environments around carbon atoms probed by ^{13}C NMR also reveals some astonishing similarities between HT*C*-glucose and HT*C*-HMF and between HTC-xylose and HTC-furfural, respectively. The characteristic aromatic peak at 129 ppm is clearly prominent only in the pentose-derived carbon samples. ^{13}C solid-state NMR spectra from HTC-maltose, HTC-sucrose, HTC-amylopectin and HT*C*-starch show exactly the same characteristics already observed for HTC-glucose and HTC-HMF. The materials can be considered as chemically equivalent, in good agreement with the elemental analysis, where the carbon content for all hexose-based carbons is 64% ± 1% (Table 2-2). Our previous experiments for glucose (see section 2.2.6) strongly suggest that these furans are also the reacting species for carbon material. In fact, the morphologies and chemical structures of carbons obtained from saccharides are directly related to those of carbons obtained from pure furans according to the following parallelism: HTC-hexoses ~ HTC-HMF and HTC-pentoses ~ HTC-furfural (Figure 2-27).

Additionally, intermediate molecules derived from saccharide dehydration (levulinic acid, dihydroxycetone, formic acid, acetic acid, formaldehyde, pyruvaldehyde, *etc.*) [63] coexist with furans and they can probably be responsible for particle size, powder texture and aggregation discrepancies. The striking similarities of NMR fingerprint spectra between all hexose-based carbons and HTC-HMF, or between HTC-xylose and HTC-furfural clearly prove that chemical complexity, the usual problem as an educt for materials chemistry, is indeed essentially resolved throughout hydrothermal carbonisation by driving all saccharides (except cellulose-see section 2.4) only through two main reaction pathways: from sugar to furan-based (furfural or HMF) intermediate and from the furan to carbon.

Additionally, we have to mention that the amount of final carbon powder from glucose and any other hexose-derived carbohydrates is about 1.5 times higher than carbon obtained from xylose. This is probably not a big surprise as it is known from furan chemistry that furfural, the dehydration product of xylose, is a low reactive compound due to the joint stabilising effects of furan aromatic ring and carbonyl function [55] with respect to polycondensation. On the other hand, even if general knowledge about the reactivity of HMF itself is smaller, its molecular similarity to furfuryl alcohol, a widely studied and highly reactive modified furan, may justify its higher reactivity as described previously in section 2.2.7. [55]

The intense peak at 129 ppm observed for xylose and furfural derived materials, typical for aromatic C=C sites, is most presumably indicative for a higher degree of self-reaction between furfural molecules within the droplets *via* the unprotected, highly reactive, 5-position. By contrast, ^{13}C solid-state NMR spectra and elemental analysis data for HTC-hexoses and HTC-HMF are remarkably similar, thus indicating that the system most presumably has to pass the same reaction pathway *via* the hydroxymethylfurfural stage and before carbonisation can take place.

Finally, the fact that no substantial difference exists between all hydrothermal hexose carbons also shows that glucose can be safely used as a model molecule for the understanding of the formation of these materials as described in section 2.2.6.

Figure 2-35 makes a summary of the main results obtained from ^{13}C-NMR studies on the HTC carbons from various precursors indicating that all hexoses (including their dehydration product, HMF) lead to the same type of material, while pentoses lead to a different type of carbon.
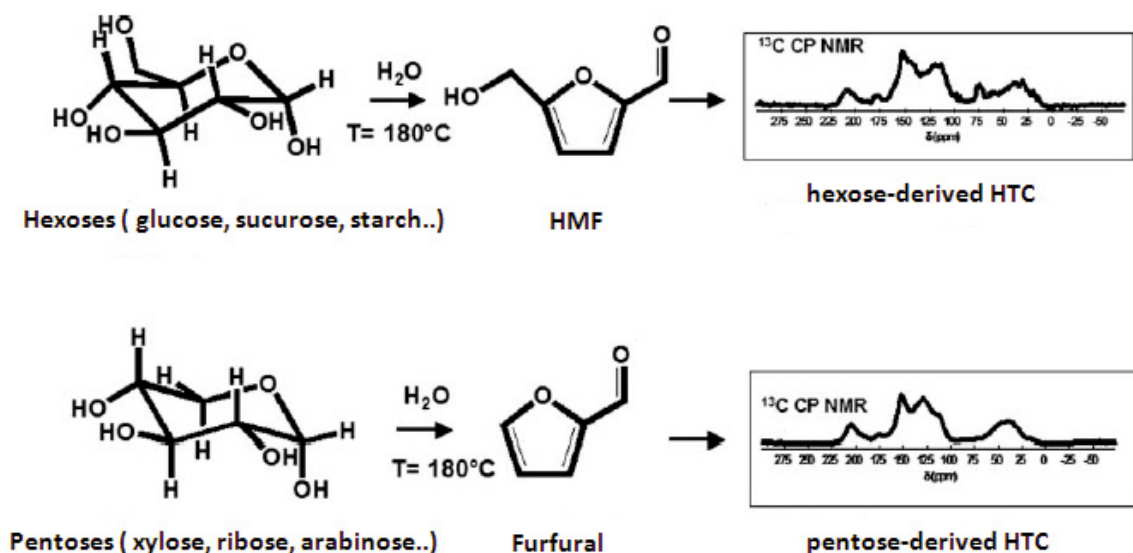
Figure 2-35: Reaction pathways encountered in the formation of hydrothermal carbons from hexose and pentose sources, leading to the differently structured and shaped materials (taken from [57]).

In order to better understand the effect of further thermal treatment of the structure of HTC carbons, we recorded the ^{13}C-NMR spectra of glucose post-calcined at various temperatures (Figure 2-36). [60]
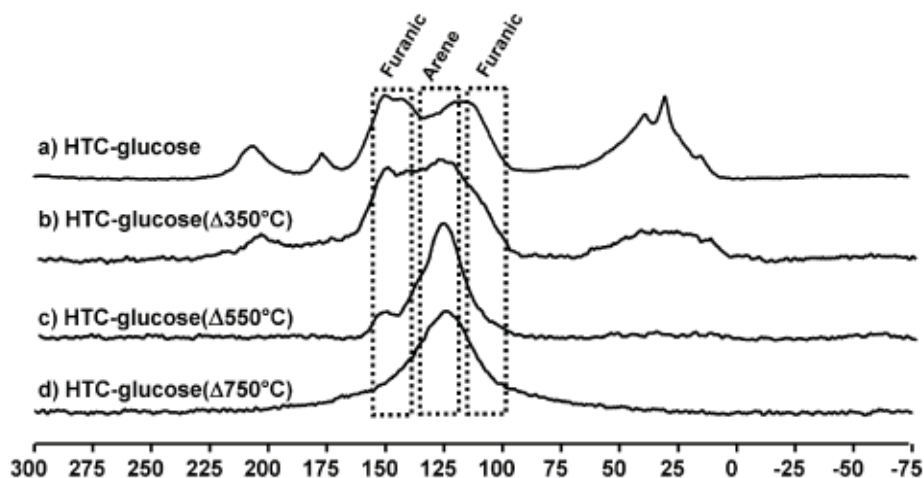
Figure 2-36: Single-pulse MAS ^{13}C-NMR experiments performed on the sample "HTC-glucose" as a function of calcination temperature. All samples were obtained from a ^{13}C-rich glucose source (see 2.2.6; taken from [57]).

Elemental analysis of the hydrothermal carbons pyrolysed at different temperatures (Table 2-2) together with TGA analysis (Figure 2-10) reveals major compositional changes in the temperature interval 350 -550°C, where the C content increases to approximately 85% while the H and O contents are markedly reduced. Increasing temperature to 750 ^{o}C has a similar effect on the HTC carbon elemental composition, although this time the rate of change of the carbon content with temperature is less steep. These findings suggest that 350 - 550°C interval is the critical temperature region for HTC carbon thermal decomposition. Presumably at temperatures > 550°C, the occurring carbonisation can be described as a charring process. Although EA, FT-IR, XRD do not show major differences between HTC and HTC-G-350°C (Table 2-2), the aromatic regions (δ = 105-155 ppm) of these carbons do differ significantly from each other, as observed *via* ^{13}C solid state NMR analysis (Figure 2-36). [60] HTC-G-350°C presents an enhanced level of aromatisation, demonstrated by an increased intensity of the central resonance at δ =125-129 ppm and partial loss of the furanic shoulder at δ = 110 - 118 ppm, as compared to the parent HTC material. Likewise, and in agreement with EA results, increasing the temperature from 350 to 550°C results in the disappearance of furanic associated resonances, as polyaromatic arene-like species become the most dominant structural motif. Increasing the temperature further to 750 ^{o}C

105

leads to enhanced aromatisation of the HTC carbon, as indicated by the drifting of the central aromatic resonance to a lower chemical shift (δ = 125 ppm) and by the broadening of its profile. Both features are indicative of an extended delocalized π- system and of a reduced mobility of the carbon species. [64] As may be anticipated, increasing the temperature over this range (i.e. 350 – 750°C) also leads to the loss of the thermally unstable aliphatic groups, as observed from the progressive disappearance of resonances in the δ = 10-60 ppm region (Figure 2-36).

This ^{13}C NMR analysis of thermal treated HTC samples emphasises how examination of the aromatic resonances provides a very useful analytical handle on the development of the carbon structure as a function of pyrolysis temperature. To provide more details on such structures, 2D DQ-SQ ^{13}C NMR experiments were designed to investigate these structural changes. As shown in section 2.2.6, solid state NMR technique provides a greater degree of information regarding molecular connectivity of the different species within the carbon chemical structure.
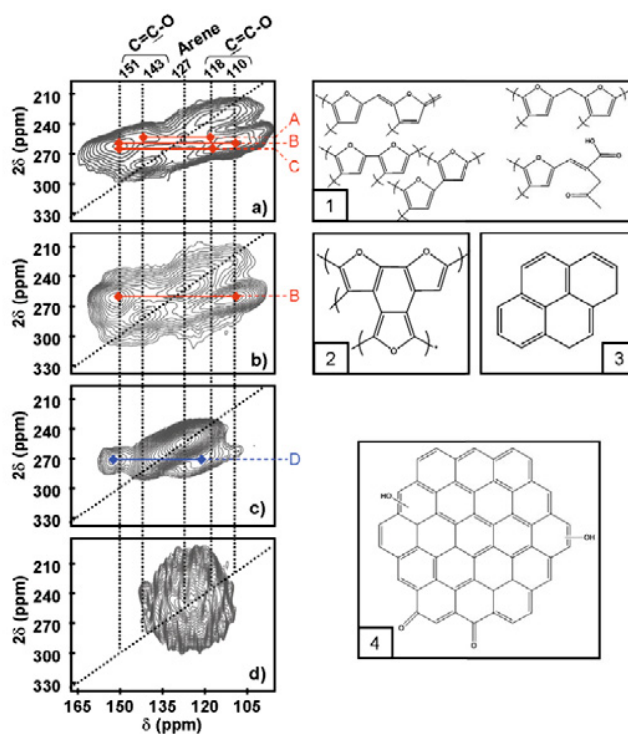
Figure 2-37: Aromatic region (δ = 100 – 160 ppm) of the ^{13}C spectra obtained with ^{13}C-^{13}C DQ-SQ experiments (CP filtered) performed on HTC carbons obtained from a) glucose at 180°C and then thermal treated (Δ) at b) 350°C, c) 550°C and d) 750°C (taken from [60])

As initial point of examination, a 2D spectrum of the aromatic region of glucose-derived HTC carbon (prepared at 180 ^{o}C) was obtained (Figure 2-37a). As explained in section 2.2.6 , the *on* (δ =110, 118 and 143 ppm) and *off* (A, B and C) diagonal cross peaks are characteristic of a carbon framework mostly composed of highly crosslinked furan moieties (Figure 2-37; Figure 2-22). Upon first inspection, pyrolysis of the HTC carbon at 350 ^{o}C does not result in major modifications of the 2D aromatic spectrum (Figure 2-37 b). However the persistence of crosspeak **B** is noteworthy and strongly supports the evidence that furan units are still present within the carbon framework at this pyrolysis temperature. At the same time the near complete disappearance of the on and off diagonal crosspeaks (A and C), related to the resonance at δ = 118 ppm, suggests that the bonding patterns involving the cross-linked 3 and 4 furan carbons have changed. The coupled increased intensity of the on diagonal δ = 127 ppm crosspeak implies that such carbons are now part of a more extended, conjugated aromatic structure, resulting in the observed peak shifts. Such structures (a reference example model is given in Figure 2-37 structure 2) may arise due to condensation reactions, leading to the formation of a more cross-linked and thermally stable aromatic network. Similar trends have been observed during the pyrolysis of polyfurfuryl alcohol (PFA) derived furan-rich resins.[65] The strong relative intensity of the δ = 127 ppm on-diagonal crosspeak cannot be solely justified by the presence of such structural motifs (Figure 2-37 structure 2.) Further peak deconvolution / refinement and assignment of the aromatic region highlights the multi-component nature of the resonance at δ = 127 ppm, which is found to be the sum of two distinct contributions at δ = 131 and δ = 125 ppm (Figure 2-38-a). Additional CP experiments at variable contact times (i.e. t_{CP}) indicate the protonated nature of the δ = 125 ppm component, since its intensity rapidly increases upon CP (Figure 2-38-b). All these results are indicative of the presence of both protonated and non-protonated sp^2 aromatic carbons within the material structure. Therefore, based on these evidences, it is not possible to exclude the presence of small arene-like aromatic structures in the HTC carbon scaffold prepared at 350°C (Figure 2-37-structure 3).

The complete loss of the furanic-based network only occurs after further thermal treatment at 550°C, as confirmed by the loss of the crosspeak **B** (Figure 2-37-c). Conversely, the aromatic region of the 2D spectrum is now characterised by a stronger cross peak at δ = 127 ppm, representative of a very well developed polyaromatic arene-like scaffold.
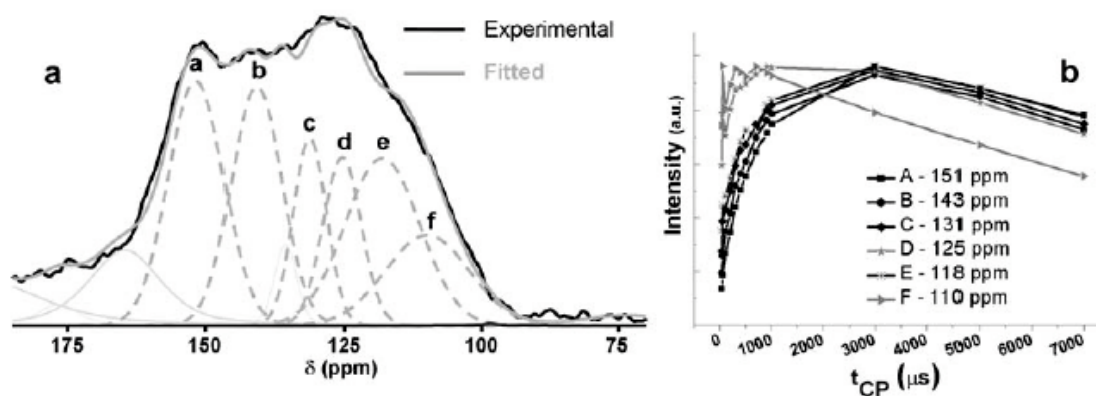
Figure 2-38: a) Peak deconvolution and assignment of the aromatic region for the HTC sample thermal treated at 350 °C. b) Contact time (t_{CP}) dependence of the peak intensity according to the deconvolution shown in a (taken from [60]).

The additional crosspeak D is instead attributed to phenolic carbons close to quaternary and protonated sp^2 carbons. These experimental results are verified by comparison with literature studies on the pyrolysis / thermal treatment of PFA-derived furan-rich resins. Furan ring opening is expected between 300 and 500 °C, resulting in oxygen elimination, [66-67] whilst polyaromatic arene-like domains are spontaneously formed from the furan units fragments. [68] Therefore the total disappearance of the furanic-related cross peaks in the pyrolysis temperature range 350 - 550 °C and the dramatic intensity increase of the $\delta = 127$ ppm on diagonal cross peak are presumably the result of such thermal decomposition processes.

The disappearance of the crosspeak **D,** together with the drifting of the $\delta = 127$ ppm crosspeak to a lower chemical shift value ($\delta = 125$ ppm), suggests that a further increase in the post treatement temperature to 750 °C leads to additional aromatisation of the carbon framework and loss of the hydroxyl groups belonging to the phenolic moieties. As a result, the material is at this stage composed of extended aromatic domains (Figure 2-37-structure 4). However EA of HTC-Δ750 suggests that the presence of residual oxygenated functionality, presumably at the polyaromatic domain edges, cannot be totally discarded (Table 2-2; Figure 2-37-structure 4). These moieties are not detectable and therefore not visible in the 2D spectra, because of their low relative abundance.

All the presented NMR data fit very well with the TG-IR experiments on HTC glucose (section 2.2.4) as well as with the XPS data (section 2.3.4).

2.3.8 Porosity of HTC Carbons

We performed a careful analysis of the pore properties of HTC materials using both N_2 (77 K) as well as CO_2 (273 K) sorption. [34] N_2 sorption at 77 K can give information about a broad size range of micro- and mesopores.[69] However, for ultramicroporous materials, the measurement may have kinetic restrictions and could not achieve to equilibrium in an acceptable measurement time.[70] Thus the measurement may provide erroneous determination of the sorption isotherms.[70a]

This was exactly the case when measuring the porosity of HTC and HTC calcined materials using N_2 (77 K) as an adsorbate. This is related to the ultramicroporos nature of these materials. Figure 2-39 shows the N_2 isotherms (77 K) of the glucose (a) and xylose (b) derived carbons. The corresponding Non-Linear Density Function Theory (NLDFT) PSDs and porosity data are shown in Figure 2-39 c, d and Table 2-4 respectively. The N_2 isotherms of the hydrothermal treated and 350 °C calcined samples show negligible N_2 uptakes resulting in almost no pore volumes by the NLDFT model as shown in Table 2-4.

Table 2-4: N_2 sorption porosity data of the HTC and calcined carbons derived from glucose and xylose

Samples	N$_2$ sorption			
	NLDFT model			S_{BET} (m^2/g)
	V_{total} (cm^3 g^{-1})	V_{micro} (cm^3 g^{-1})	D (nm)	
HTC-G	0.012	0	3.03	7.9
HTC-G-350	0.009	0	2.796	7.1
HTC-G-550	0.04	0.027	1.614	19.8
HTC-G-750	0.197	0.171	1.289	428
HTC-G-950	0.168	0.142	1.475	352

HTC-X	0.009	0	2.769	5.7
HTC-X-350	0.006	0.001	2.769	5.0
HTC-X-550	0.126	0.126	1.614	298
HTC-X-750	0.179	0.162	1.41	432
HTC-X-950	0.163	0.156	1.475	389
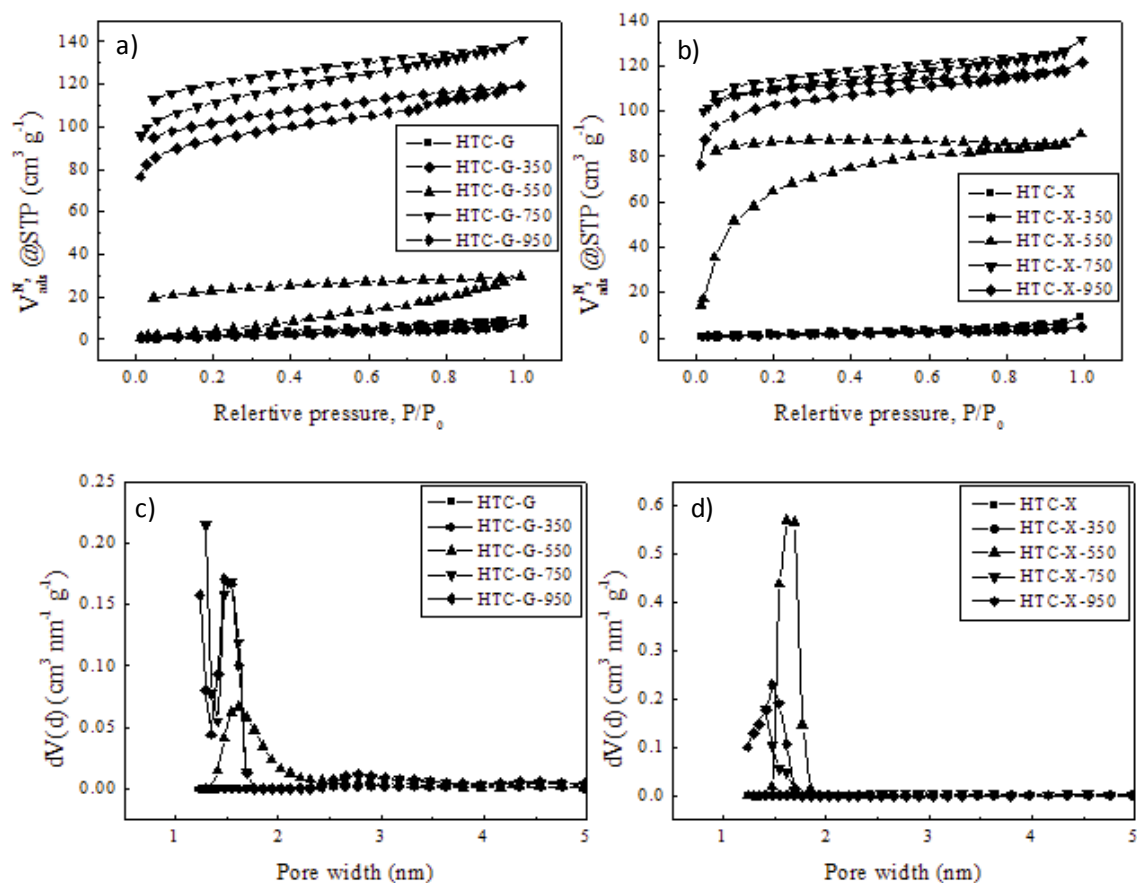
Figure 2-39: a) N_2 sorption isotherms (77 K) of glucose derived HTCs; b) N_2 sorption isotherms (77 K) of xylose derived HTCs; c) NLDFT PSDs of glucse-derived HTCs; d) NLDFT PSDs of xylose-derived HTCs (taken from [34]).

Although still in the low range, Grand Canonical Monte Carlo method (GCMC) used for pore size and pore volume determination using CO_2 sorption shows, much higher pore volumes of $0.06 - 0.08$ cm^3/g (Table 2-5). This supports well the fact that the N_2 sorption measurements are kinetically restricted. The poor charaterisation power of N_2 adsorption especially for the HTC materials might be due to the fact that the carbon synthesised at 180 ^{o}C and 300°C possesses still a relatively "soft" or "polymeric" like structure. It is well known from material science templating strategies that porosity (microporosity in particular) can be induced within an organic polymeric structure only if the overall scaffold has a certain degree of rigidity to counterbalance the polymer chains tendency to pack closely together once the template is removed. [71]

All of the samples calcined at 550, 750 and 950 °C show significantly higher N_2 uptakes because of the development of microporosity upon heat treatment related to the elimination of gasses and other volatile compounds (Figure 2-10). All the isotherms present however extensive pressure hysteresis, which may be caused by very narrow pores and/or swelling effects.[72]

As N_2 adsorption at 77.3 K presented kinetic restrictions, CO_2 sorption at 273 K turned out to be a much more appropriate methodology to determine the microporosity of HTC carbons and the post calcined counterparts. This is because of the smaller kinetic diameter of CO_2 ($D_{CO_2} = 0.33$ nm, $D_{N_2} = 0.36$ nm) and the higher measurement temperature of 273 K (higher thermal energy). Besides, the influence of the high quadrupole moment of CO_2 should also be taken account of, because it makes the adsorption isotherm very sensitive to the presence of functional groups and may lead to a higher CO_2 uptake than N_2 as described later. [70b, 73]

Figure 2-40 and Figure 2-41 show CO_2 (273 K) adsorption isotherms and GCMC PSDs for the HTC and post-calcined carbons. All of the isotherms show no hysteresis, indicating good adsorption kinetics as compared to N_2 adsorption. The porosity continuously develops upon increasing the post-calcination temperature as shown by the continuous increase in gas uptake. This increase in gas uptake is limited for the 180 °C and 350 °C materials. Again this is in good agreement with TG-IR which shows that the elimination of volatiles starts above 350 °C. For the 550 °C materials, we noticed a leap in gas uptake. This can be correlated with the elimination of volatile species and the formation of the condensed aromatic intermediates during thermal decomposition. [60] Both processes lead to the development of microvoids between the aromatic

pre-graphinic structures. There is another significant increase in gas uptake observed for the 750 °C materials, which is due to the elimination of all volatile compounds up to that temperature. At higher temperatures, the creation of additional porosity is neglectable. PSDs show pore size in the same range (mainly 0.35-0.8 nm). While the amount of supermicropores (<0.8 nm), is almost constant no matter of the temperature applied, the fraction of ultramicropores grows significantly with increasing calcination temperature. The pore volumes and surface areas obtained using CO_2 sorption and GCMC model for all the materials are listed in

Table 2-5. Even though the pore volumes of the HTC carbons are low, they exhibit ~200 m^2/g surface areas because of the ultramicroporosity of these materials. For the carbons calcined at 950 °C, the surface areas are as high as 650 - 750 m^2/g.

Table 2-5: Porosity data (obtained by CO2 adsorption at 273 K) of the HTC and post-calcined carbons

Samples	CO$_2$ sorption (GCMC model)		Samples	CO$_2$ sorption (GCMC model)	
	V_p (cm^3 g^{-1})	S_{GCMC} (m^2 g^{-1})		V_p (cm^3 g^{-1})	S_{GCMC} (m^2 g^{-1})
HTC-G	0.066	183	HTC-St	0.063	189
HTC-G-350	0.068	202	HTC-St-350	0.068	208
HTC-G-550	0.146	442	HTC-St-550	0.117	379
HTC-G-750	0.19	657	HTC-St-750	0.179	646
HTC-G-950	0.216	735	HTC-St-950	0.195	700
HTC-Su	0.067	173	HTC-X	0.07	224
TC-Su-350	0.068	212	HTC-X-350	0.076	244
HTC-Su-550	0.147	485	HTC-X-550	0.119	393
HTC-Su-750	0.182	631	HTC-X-750	0.188	662
HTC-Su-950	0.2	682	HTC-X-950	0.195	681
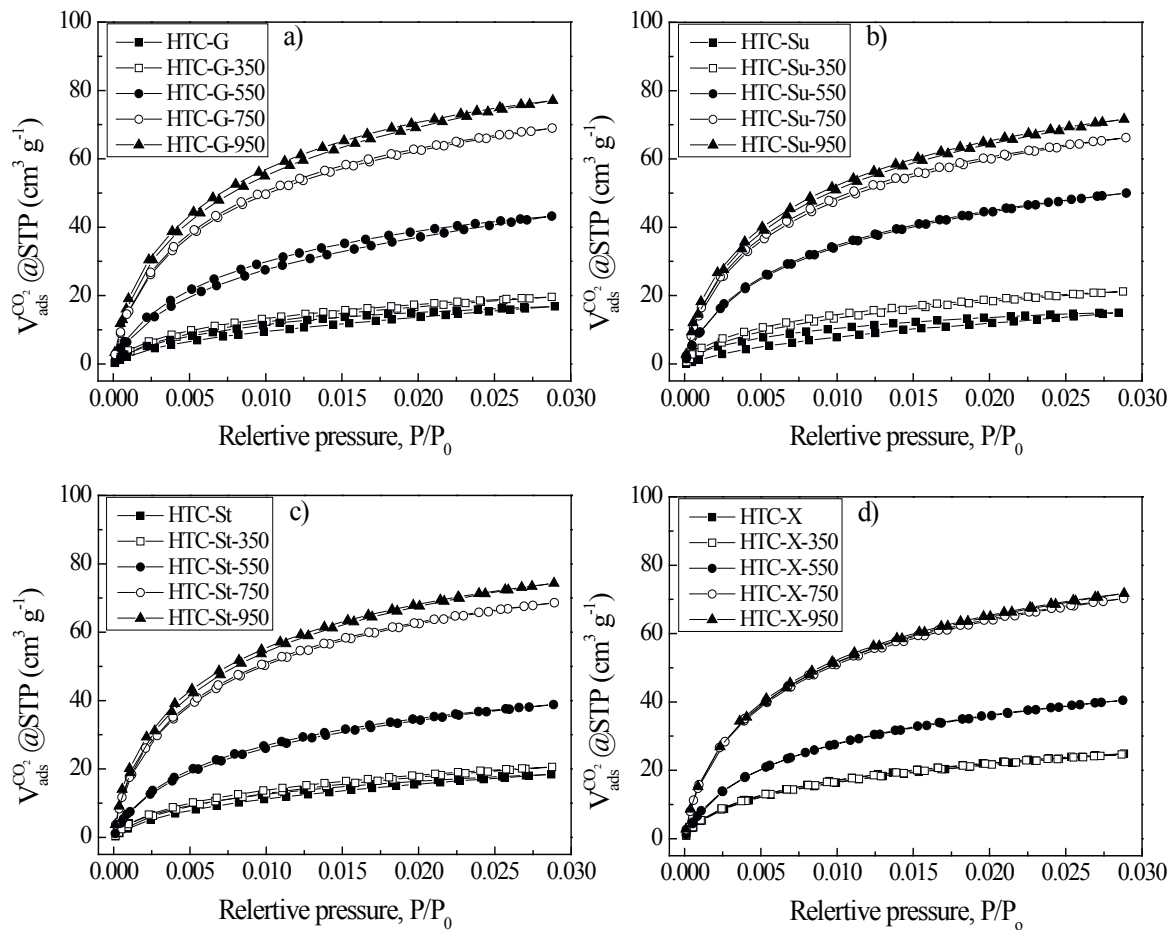
Figure 2-40: CO_2 adsorption/desorption isotherms (273 K) of HTC and post-calcined carbons, derived from a) glucose, b) sucrose, c) starch, and d) xylose (taken from [34]).
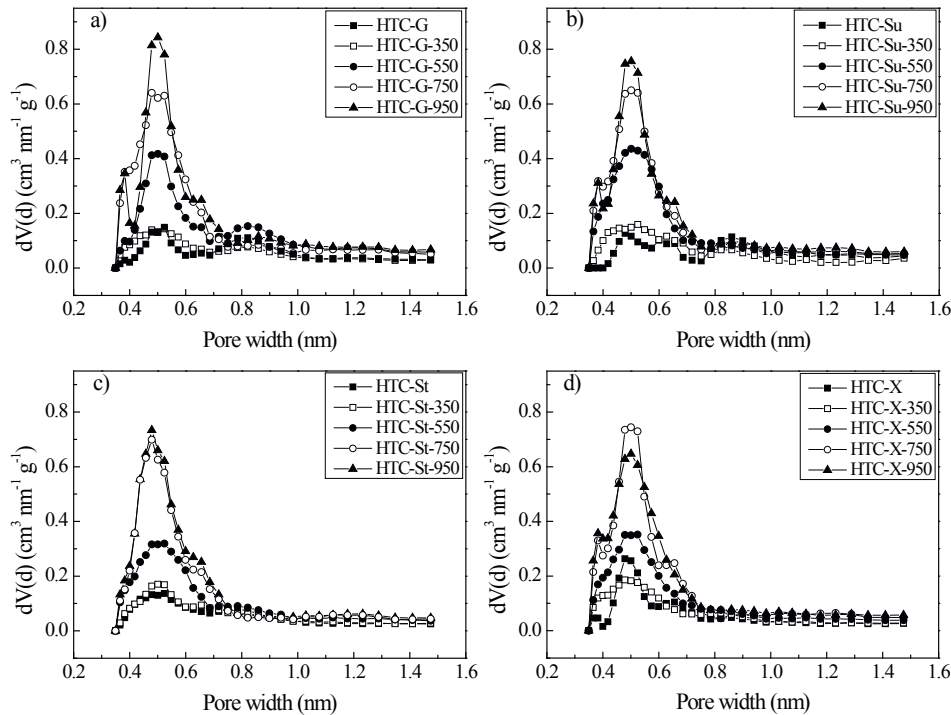
Figure 2-41: PSDs (calculated from the CO_2 adsorption isotherms by the GCMC method, assuming carbon slit pores) of HTC and calcined carbons corresponding to Fig. 2-40, derived from a) glucose, b) sucrose, c) starch, and d) xylose (taken from [34]).

2.4 HTCs from Lignocellulosic Biomass

2.4.1 Morphology

Thus far I have presented fundamental charaterisation data regarding the morphology, porosity and chemical structure of HTC materials derived from simple carbohydrates. The next challenging step in HTC is the effective exploitation of lignocellulosic biomass as carbon precursors, which would guarantee a readily accessible and carbon negative feedstock supply.

Considering the energy shortage, environmental crisis and the increasingly customer demands, the discovery of facile, low-cost, environmentally friendly and nontoxic routes to produce novel valuable carbon materials is a key issue in today's society. Lignocellulosic biomass, in particular

plant cell wall-based cellulose, is the most abundant and renewable resource on earth. It can serve as a source for both energy (biofuels) and carbon.

Lignocellulosic biomass is composed of three main components: cellulose, hemicellulose and lignin. The relative proportion of cellulose varies according to the biomass origin from 20% to 45% for agricultural wastes.[74] The structure of cellulose is shown in Figure 2-1 and it is insoluble in most of the common solvents. Hemicellulose, the second biomass component contains many different sugar monomers, has a random structure, is amorphous and easy hydrolysable. Unlike carbohydrate based cellulose and hemicellulose, lignin is a complex, cross-linked, 3D biopolymer with phenyl propane units and hydrophobic properties. Lignin is concentrated between the outer layers of the biomass fibres leading to structural rigidity and holding the polysaccharide fibres together. The decomposition and degradation of lignin and hemicelluloses is much easier than for cellulose. [75-76] Based on this different reactivity it is feasible to separate cellulose and hemicelluloses from lignin, especially using alkaline treatments. [77-78] Lignin can be further processed to obtain important phenol-derived chemicals used in various chemical industries. [79-80]

The elaboration of a general reaction mechanism for the HTC of lignocellulosic biomass is crucial since only a complete understanding of the chemical transformations occurring during the HTC process will allow control over morphology, porosity and functionality in a similar fashion to the one obtained when using simple carbohydrates as precursors. For the purpose of this investigation a relatively low lignin content biomass was chosen: rye straw (cellulose: hemicellulose: lignin = 41.2:21.2:19.5). This raw material is an agricultural waste product; therefore, it is available at costs well below petrochemical based chemicals.

In order to get useful insights on the transformation mechanism of rye straw into HTC materials, we studied individually the HTC mechanism of pure cellulose and alcell lignin by analysing how the chemical nature and morphology of the produced HTC carbon change in relation to the processing temperature and time. [27] The obtained results were then compared to glucose (see section 2.2), which was used as a reference model.

This study allowed us to highlight and discuss the probable differences in the HTC mechanism of each raw material and to determine the role of lignin in the hydrothermal carbonisation of lignocellulosic biomass. [27]

The morphology of HTC spheres when using glucose as a precursor at different carbonisation temperatures has been already shown in Figure 2-3. The morphology of cellulose derived HTC carbons is shown in Figure 2-42. At low HTC processing temperatures (Figure 2-42 a–b), cellulose is resistant to hydrothermal treatment. Its fibers are still intact and arranged in the characteristic cellulose network. [81] On the other hand, as observed in Figure 2-42 c–d, upon increasing the HTC temperature, spherical particles start forming, which is similar to the HTC materials obtained from glucose. However, the overall morphology is not as homogeneous as for simple sugars (Figure 2-3; Figure 2-27; Figure 2-28).
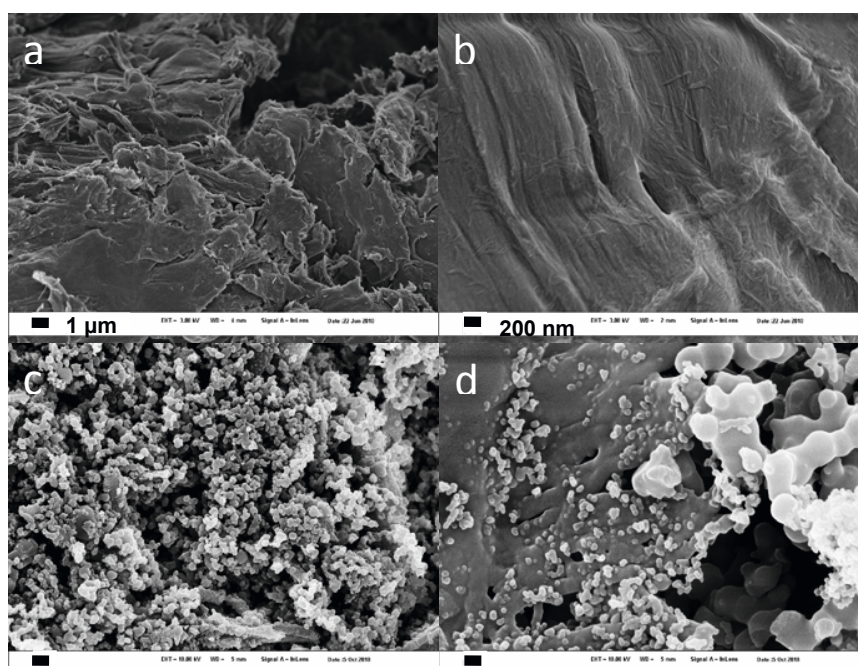
Figure 2-42: Scanning electron micrographs of hydrothermal carbons obtained from cellulose at 160°C (a, b) and 220°C (c, d) (taken from [27]).

Combining these observations with results shown in Figure 2-43, a remarkable difference in the mechanism of particle formation can be noticed between glucose and cellulose. In the former

case, particles form through a nucleation step from a homogeneous solution upon formation and polymerisation of hydroxymethylfurfural. [15] Initially, their diameter is approximately in the 100–200 nm range (Figure 2-43a). As the residence time increases, they keep on growing until they reach their final size, which depends upon the HTC processing temperature (Figure 2-3).

On the other hand, in the case of cellulose, upon increasing the temperature the fibrous network starts to be disrupted at several points (Figure 2-42, Figure 2-43b), leading to the formation of nano/micro-sized cellulose fragments, which, not being soluble in water, adopt a spherical shape to minimize their contacting interface with the surroundings.
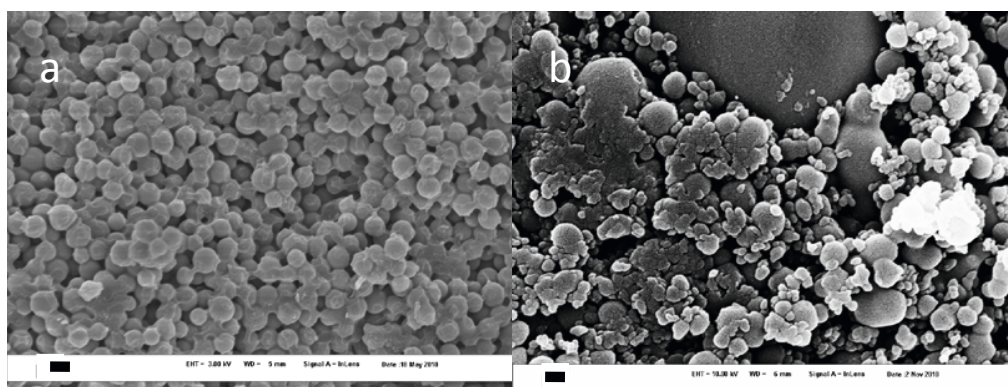
Figure 2-43: Scanning electron micrographs of hydrothermal carbons obtained from a) glucose at 180°C, b) cellulose at 240°C for 6h (taken from [27]).

After investigating the hydrothermal transformation of cellulose and comparing it to the reference glucose-derived HTC, we proceeded with hydrothermal carbonisation of rye straw, an agricultural biowaste. The SEM micrographs in Figure 2-44 show that the morphological transformations of rye straw after hydrothermal treatment are very similar to the ones of cellulose. The lignocellulosic biomass does not undergo any structural disruption at low (T= 180°C) temperatures (Figure 2-44 a-b) and the rye straw fibrous structure is maintained intact. When the biomass is hydrothermally treated at higher temperatures (T= 240°C), its fibrous network is disrupted and spherical particles start forming similarly to what has been previously described for cellulose (Figure 2-44 c, d).

In addition, Figure 2-44 c clearly shows that part of the biomass natural macrostructure persists even after the spherical particles start forming. It can be seen that the particles formation takes place on the surface of the rye straw fibers, which overall still maintain their original structural scaffold.
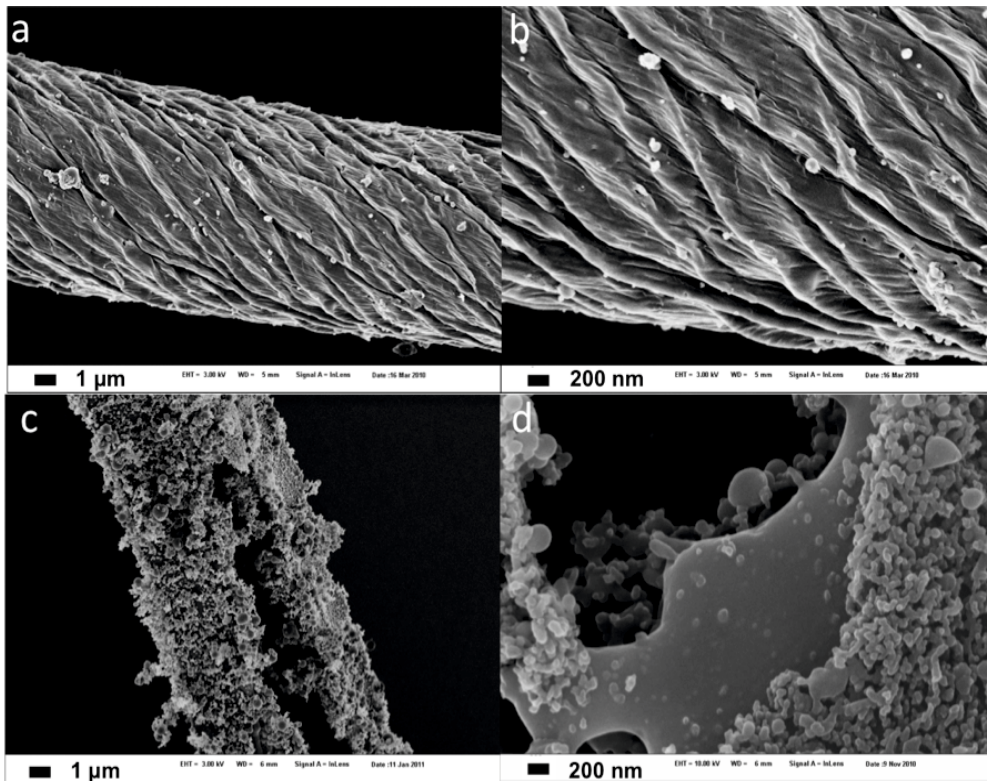
Figure 2-44: Scanning electron micrographs of hydrothermal carbon materials obtained from hydrothermal carbonisation of rye straw at 160°C (a, b) and 240°C (c, d) (taken from [27]).

2.4.2 Yields and Elemental Composition

In section 2.2.2 the formula for calculating the yields for glucose derived HTCs was presented:

$$HTC\_yield\% = \frac{amount\_of\_recovered\_solid\_after\_HTC(g)}{initial\_amount\_of\_biomass(g)}$$

Figure 2-45 a compares the yields obtained upon hydrothermal carbonisation of glucose, cellulose, lignin and rye straw at different temperatures. Here we need to point out that, contrary to water-soluble glucose where the yield is 0 at low processing temperatures, for all the other raw materials (cellulose, lignin and rye straw), the HTC yield gradually decreases from an initial value of 100% due to the increasing extents of liquefaction and gasification of the biomass at higher temperatures values, which are parallel reactions to the process of HTC formation. [82]
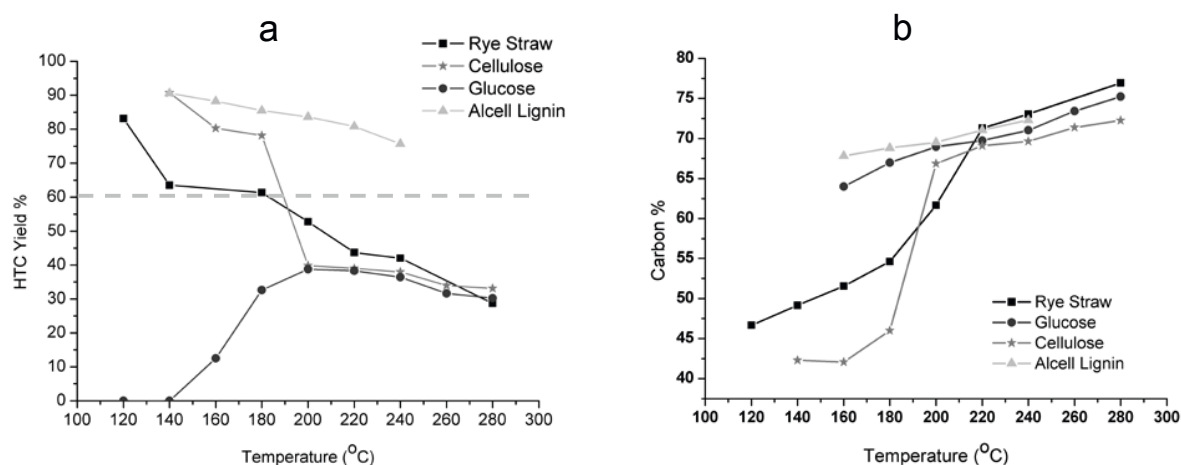
Figure 2-45: a) Calculated hydrothermal carbon yields and b) carbon content obtained from chemical analysis of HTC material obtained from glucose, cellulose, alcell lignin and rye straw at different processing temperatures. The carbon w% for the raw materials are respectively: Glucose = 40%, Cellulose = 41.75%, Alcell Lignin = 66.10% and Rye Straw = 45.86% (taken from [27]).

Figure 2-45 underlines a very interesting feature of cellulose HTC behaviour. Both the HTC yield and carbon content can be observed to undergo only minor changes within the low temperature range (140-180°C). On the other hand, between 180 and 200°C, a sharp transition takes place. The HTC yield and the carbon content respectively become approx. 37% and 65%. After reaching this critical point, the changes are no longer so drastic and only small variations occur. The presence of this sharp transition supports the idea of the existence of a well-defined temperature threshold, above which cellulose structure is disrupted. The disruption then generates the morphology that was observed during the microscopy analysis of the cellulose derived HTC material at relatively high processing temperatures (Figure 2-42 c-d). This finding is additionally

119

well supported by XRD measurements of raw and hydrothermally treated cellulose at different temperatures (data not shown). It can be observed that between 180 and 200°C the peaks, corresponding to crystalline cellulose [83], disappear. The structure of the material corresponds now to amorphous carbon with almost no noticeable long range ordering.

Similarly to cellulose, abrupt changes in both the HTC yield and the carbon content are observed during hydrothermal carbonisation of rye straw at different temperatures. However there are two main differences that need to be underlined:

1. Rye straw is more sensitive to hydrothermal treatment in the low temperature range (120-180°C). A probable explanation for this observation is the presence of hemicellulose and xylose-based polysaccharides within the rye straw. These biopolymers are known to be less stable than cellulose when hydrothermally treated; as a consequence they can undergo hydrothermal carbonisation in a lower temperature range with a consequential yield loss due to formation of liquid and volatile side products. [84].

2. The changes in HTC yield and carbon content are less sharp than in the case of cellulose in the region immediately above 180°C and they appear to be slightly shifted to higher temperature values. The lignin, present within the lignocellulosic biomass, could be the cause of such differences. As it can be observed in Figure 2-45, this compound is affected by hydrothermal treatment to a very limited extent. As a consequence its presence might cause the HTC yield of rye straw to decrease less abruptly as temperature increases. Furthermore, since lignin acts as support within the plant wall, [85] it might stabilize the cellulose and prevent its crystalline structure disruption at lower temperatures.

The data regarding yields and elemental analysis highlight an interesting feature, which is common to all the investigated precursors: they all follow similar trends for both the HTC yield and carbon content for temperature values, which are above 220 °C. This might be due to the fact that above this temperature value all substrates follow similar chemical reaction pathways. This

120

hypothesis, as it will be seen in the next section, is supported as well by ^{13}C solid state NMR studies.

2.4.3 ^{13}C-Solid State NMR studies-Chemical Structure of biomass derived HTCs

As previously reported in section Section 2.2.6 and 2.3.7 the HTC carbons synthesised at 180°C were found to be majorly composed of highly cross-linked furanic-type units and characterised by oxygen containing functionalities (i. e. ketones and carbonyl groups).

Here the aim was to obtain more insights on the bulk chemical structure of HTC carbons from glucose, cellulose and rye straw as a function of processing temperature and reaction time.

In the case of glucose (Figure 2-46) , increasing the HTC temperature leads to a HTC carbon with a higher degree of aromatisation, as indicated by a major decrease in the relative intensity of the peaks at $\delta = 150$ ppm and $\delta = 110$ -118 ppm, respectively corresponding to carbons 2,5 and 3,4 of the furanic ring, and the simultaneous increase in relative intensity of the peak at $\delta = 125$ - 129 ppm, ascribable to sp^2 aromatic carbons relating to more condensed aromatic arene-like structures. The behaviour of the resonance at $\delta = 208$ ppm also shows the high dependence of the oxygenated functionalities content (i.e. ketones) on the processing conditions. Increasing the HTC temperature leads to the loss of such moieties and a consequential oxygen content decrease, as suggested by the progressive disappearance of the $\delta = 208$ ppm peak. In addition, the relative intensity of resonances associated with aliphatic-type groups is fairly constant for samples prepared at T = 180, 200 and 240 °C whilst, at higher HTC temperatures (i.e. 280 °C), it significantly decreases indicating the loss of these less thermally stable species which are either converted to volatile products through gasification reactions or to increasingly more condensed sp^2 aromatic species. This observation is in agreement with the carbon efficiency decrease observed in the previous section during HTC of glucose at temperatures higher than 250 °C. (see section 2.2.2)
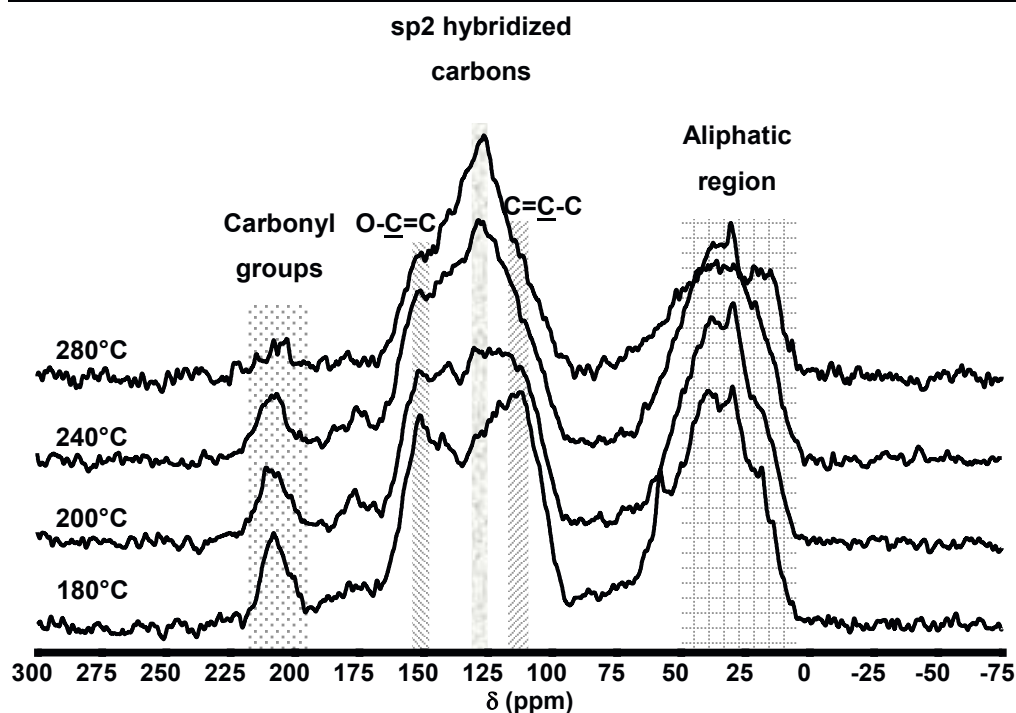
Figure 2-46: ^{13}C CP MAS NMR spectra of glucose-derived HTC carbons prepared at increasing processing temperatures (taken from [27]).

In a second set of experiments, glucose-derived HTC carbons (T = 240 °C) were synthesised at different reaction times and characterised by ^{13}C ssNMR (Figure 2-47 a). An analysis of the aromatic region (i.e. δ = 105 - 155 ppm) reveals that the central resonance at δ = 125 - 129 ppm is not visible in the early stages of the reaction (i.e. 2h). The entire region of the spectrum is characterised predominantly by the presence of two resonances corresponding to furanic rings (i.e. δ = 150 and 110 - 118 ppm). As the HTC reaction time is increased, the relative intensity of these latter peaks diminishes, while the central resonance at δ = 125 - 129 ppm becomes increasingly more prominent. From these observations, it is evident that under more severe HTC processing conditions (i.e. HTC T > 200°C, long reaction time) the cross-linked furanic structures, comprising the HTC carbon obtained at 180 °C, react further *via* intramolecular condensation, dehydration and decarbonylation reactions to create more condensed aromatic arene-like carbon environments. This mechanistic speculation is also supported by further evidences obtained after repeating the same time experiments at lower HTC processing temperature (i.e. 180 °C) (Figure 2-47 b). In this case, all spectra maintain an NMR profile

122

predominantly characterised by carbon resonances related to furanic ring structures (δ = 150 and 110 - 118ppm). This finding, coupled to the evident lack of a predominant resonance at δ = 125 - 129 ppm, suggests that when the HTC is performed at relatively low processing temperatures (e.g. T $\leq$ 180°C), the initial furan rich carbon structure is maintained regardless of the reaction time.
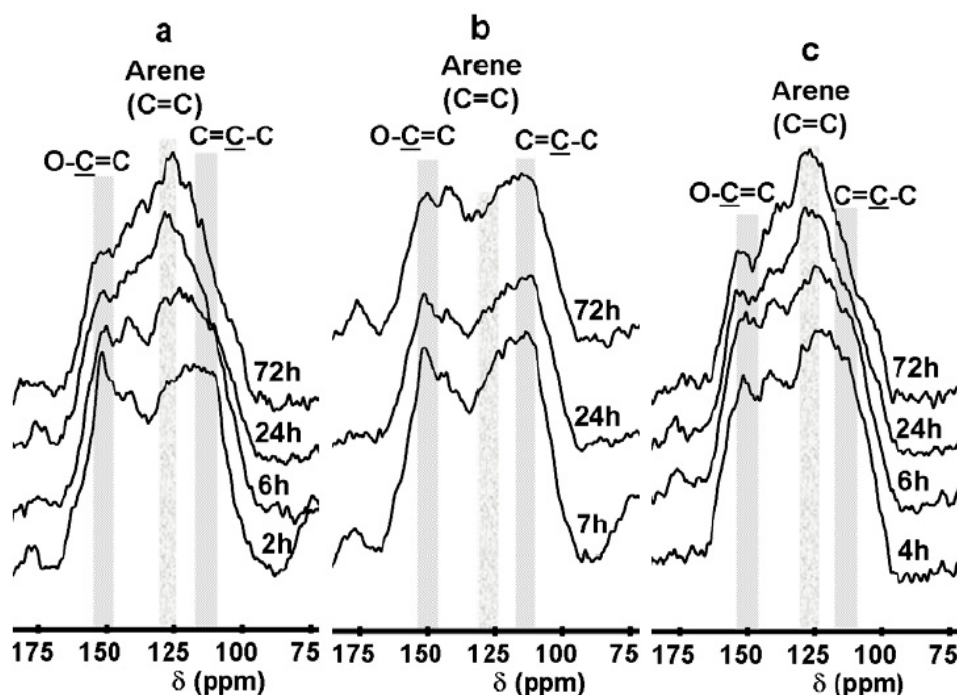
Figure 2-47: **^{13}C CP MAS NMR spectra of HTC carbon obtained from a) glucose at 240 °C, b) glucose at 180 °C and c) cellulose at 240 °C prepared at increasing reaction / HTC treatment times (taken from [27]).**

In order to highlight potential differences with glucose HTC, the same temperature dependent experiments were also repeated, using cellulose as the HTC precursor (Figure 2-48). In accordance with the findings of the previous sections, the obtained ^{13}C NMR spectra demonstrate that when T = 180°C, cellulose is still unaffected by hydrothermal treatment. The characteristic resonances (i.e. δ = 65, 72,75, 84, 89 and 105 ppm) [86] are still present and well resolved in the NMR spectrum, while no resonances are observed in the aromatic region indicating no major HTC carbon formation. As the processing temperature is raised to 200 °C, dramatic differences

are observed in the NMR spectrum. All characteristic cellulose resonances disappear, whilst a new broad resonance centred at δ = 125-129 ppm emerges. Furthermore, as observed for glucose, cellulose-derived HTC carbon shows a similar reduction in the relative intensities of resonances associated with oxygenated functional groups and an increase in the aromatic character at progressively higher temperatures, as respectively indicated by the disappearance of the peak at δ = 208 ppm and the relative increase of resonances in the region δ = 125 - 129 ppm. These findings highlight that glucose- and cellulose-derived HTC carbons show identical peak evolution patterns for temperature values higher than 200°C, indicating the similar nature of the chemical transformations characterizing the HTC of both substrates above this temperature threshold.
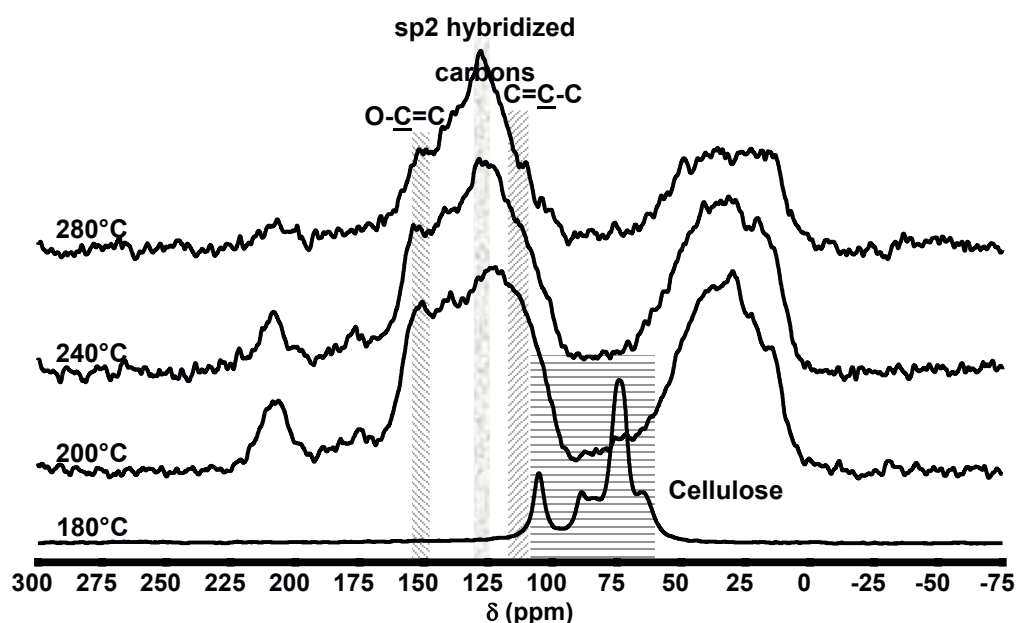
Figure 2-48: ^{13}C CP MAS NMR spectra of cellulose-derived HTC carbons prepared at increasing processing temperature (taken from [27]).

However the ^{13}C NMR spectra of cellulose derived HTC carbon, synthesised at different reaction times, highlight a remarkable difference between the HTC mechanism of glucose and cellulose (Figure 2-47 c). All carbon samples obtained from cellulose are characterised by the presence of the central resonance at δ = 125 – 129 ppm. This feature is present since the early stages of the reaction contrarily to what was observed for the treatment of glucose as a function of time

(Figure 2-47 a) at the same temperature. This finding suggests that the hydrothermal carbonisation of cellulose does not proceed solely through a furanic composed intermediate (i.e. HMF), as observed in the case of the model monosaccharide (i.e. glucose). The major conversion mechanism is instead thought to be the direct transformation of the cellulosic substrate into a final carbonaceous material composed of polyaromatic arene-like networks, presumably involving reactions that are normally characteristic of the pyrolysis process. During cellulose pyrolysis, the char formation is attributed to a manifold of reactions leading to cellulose intramolecular rearrangement and formation of a cellulose-derived polymeric compound, referred to as *intermediate cellulose*. This reaction intermediate then converts to aromatic network structures at extended reaction times. [87] [88] This mechanistic speculation is well supported by the similar ^{13}C NMR profiles of cellulose-derived HTC carbon and char obtained from lignocellulosic biomass pyrolysis. [89] [90]

In the case of rye straw-derived HTC carbons, it is evident that the spectra evolution, as a function of temperature, follows a similar pattern for cellulose except for two major differences (Figure 2-49). First of all, resonances related to cellulose are still present in the sample synthesised at T = 200 °C. This observation is in good agreement with SEM and yield analysis, with the higher temperature-resistance of rye straw to HTC processing, attributed to the presence of lignin stabilising the cellulose fraction of the biomass. Secondly, the rye straw derived HTC carbons spectra are characterised by two additional resonances (δ = 56 and 145-148 ppm) corresponding to the methoxy functional groups (-OCH3) and to aromatic carbons bounded to such moieties in lignin, as indicated by ^{13}C CP NMR investigations of an alcell lignin sample. The near complete disappearance of such resonances in HTC carbon synthesised at T = 280 °C, marks the loss of these functional groups at such processing conditions presumably *via* demethanation reactions.
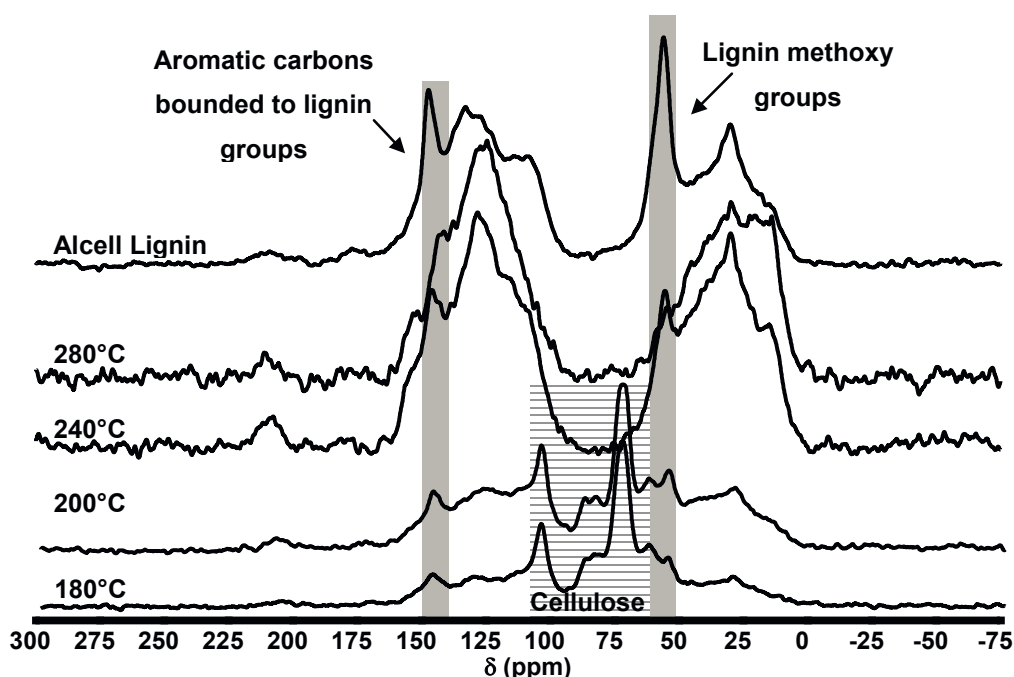
Figure 2-49: Solid state ^{13}C CP NMR spectra of hydrothermal carbon obtained from rye straw at different temperatures (taken from [27]).

2.4.4 Mechanistic insights on cellulose/biomass conversion into HTC

Overall the results of the previous analysis suggest a different conversion pathway for cellulose, when HTC processing is performed under mild conditions. At $T \geq 180$ °C, rather than the hydrolysis of the polysaccharide into glucose and its subsequent conversion into a furan rich HTC carbon, cellulose undergoes a disruption of its fibrous network leading to the formation of nano/micro sized cellulose fragments, as initially observed *via* SEM image analysis. These fragments adopt a spherical shape in order to minimise the contacting interface with the surrounding water and hence reduce the chances of hydrolysis of the glycosidic bond. At this point, the cellulosempresent in the bulk is likely to be exposed to a comparatively homogeneous thermal environment resembling the one of pyrolytic processes. Under these conditions, the cellulosic substrate undergoes intramolecular condensation, dehydration and decarbonylation reactions leading to the production of a hydrothermal carbon structurally composed of a more condensed polyaromatic arene-like carbon domains. [91] A very limited degree of hydrolysis and consequential glucose formation most likely takes simultaneously place at the envelopes

126

interface, where cellulose is in contact with water. However this reaction route accounts only for a minor extent of cellulose conversion (Figure 2-50)
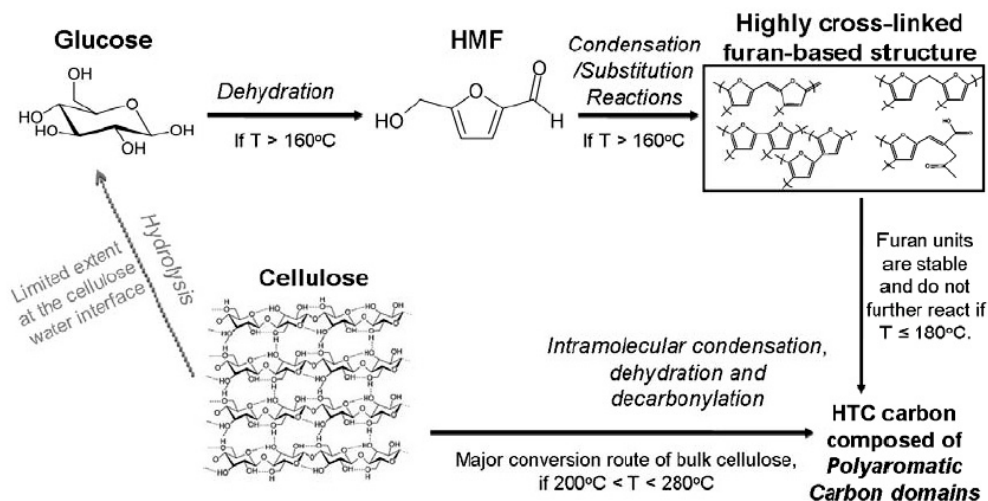
Figure 2-50: Proposed model for cellulose conversion during hydrothermal treatment under mild processing conditions (180 °C < T < 280 °C). (NB: Dotted lines represent minor reaction routes; taken from [27]).

This mechanistic scheme is well supported by the evidence that other non-reducing carbohydrates, such as starch, contrarily to cellulose, do yield furan-rich HTC carbon. In particular hydrothermal carbonisation of amylose rich starch (Hylon VII, 70% amylose) is a pertinent example, since its chemical composition is identical to cellulose. However this biopolymer is soluble in water when heated at relatively mild temperatures (60-70°C), as previously explained.
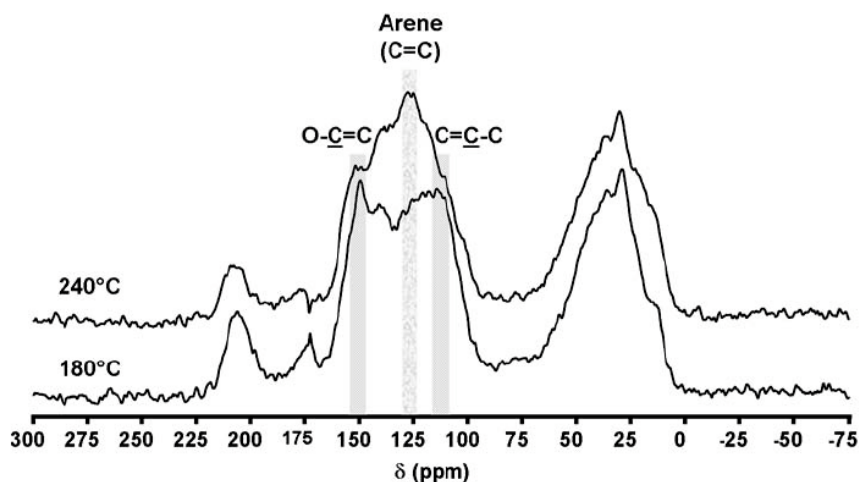
Figure 2-51: **^{13}C CP MAS NMR spectra of amylose (Hylon VII) derived HTC carbons at different processing temperatures (taken from [92]).**

Therefore amylose is more likely than cellulose to hydrolyse under mild hydrothermal treatment. This hypothesis is confirmed by ^{13}C NMR experimental evidences (Figure 2-51) Resonances corresponding to furan moieties (δ= 110 – 118 ppm and δ = 151 ppm) characterise the amylose-derived HTC carbon produced at 180°C. On the other hand increasing the processing temperature leads to the development of resonances in the region δ = 125-129 ppm, as observed in glucose-derived HTC carbon. These findings are indicative of amylose hydrolysis into glucose and consequential HTC formation, contrarily to what observed for cellulose.

In order to enhance the extent of cellulose hydrolysis to glucose at milder temperature values (i.e. 180 °C), HTC experiments in the presence of strong mineral acids (i.e. H_2SO_4) were performed (Figure 2-52). The obtained ^{13}C NMR spectra show that at relatively low pH (i.e. 1) cellulose fully reacts at 180 °C . Nonetheless resonances corresponding to furanic moieties are not the dominant features of the NMR spectra, as it would be expected at this processing temperature value. The NMR spectrum for cellulose at pH = 1, shows a well-developed polyaromatic arene-like carbon resonance with a major shoulder at δ = 151 ppm, indicative of oxygenated sp^2 hybridised carbon environments. These features also characterise the NMR spectra of glucose-derived HTC carbon prepared at different pH. As a consequence, these results demonstrate the

128

dependence of the chemical structure of HTC carbon upon the initial reaction mixture pH. Strong acidic solutions lead preferentially to the development of polyaromatic carbon species probably due to a higher extent of formation of furan degradation products (e.g. levulinic acid) [93] reacting *via* aldol condensation and increasing the degree of conjugation of the carbon framework. [19]
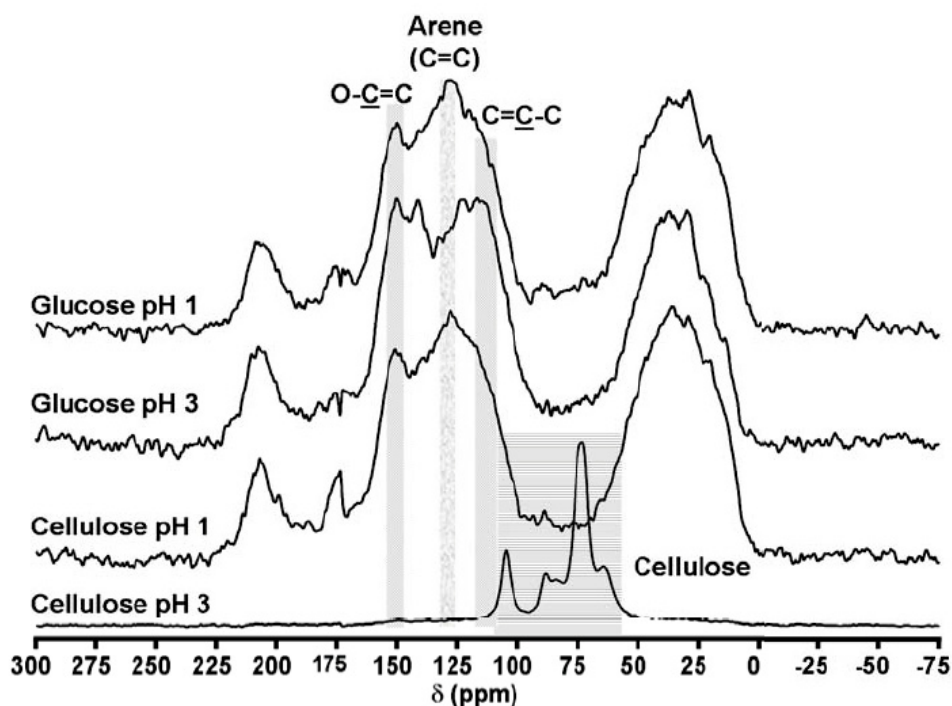
Figure 2-52: ^{13}**C CP MAS NMR spectra of hydrothermal carbon obtained from glucose and cellulose at different initial pHs (taken from [92]).**

The developed model also applies to lignocellulosic biomass. As previously observed, the hydrothermal carbonisation of rye straw is majorly governed by the reactivity of its cellulosic fraction, which is shifted to higher temperatures (i.e. T = 240 °C) compared to pure cellulose (i.e. T = 200 °C). Despite this increase, it is interesting to notice how under hydrothermal conditions the cellulose present in lignocellulosic biomass fully reacts over a lower temperature range than during pyrolysis. [94] A possible explanation for such a difference is the partial hydration of cellulose chains under HTC processing conditions, which can destabilise the hierarchical cellulosic structure and cause its disruption in this lower temperature range. The enhanced

129

reactivity of crude biomass during HTC is further supported by the loss of lignin methoxy groups, which under hydrothermal conditions takes place between 240 – 280 °C, while during pyrolysis it is not observed before 350 °C.

2.5 Conclusions and Perspectives

This chapter presented a comprehensive study of the properties of hydrothermal carbons. Firstly glucose was used as a model system to understand the properties and the final composition of HTC materials. Upon hydrothermal carbonisation glucose forms spherically shaped particles. Their size and homogeneity can be controlled with reaction time, temperature and concentration. We and others [15] have assumed a "La Mer" nucleation model [95] although here there are some doubts which need to be further clarified in the near future. This could be in principle done employing "*in situ*" characterisation techniques to better understand nucleation in HTC.

^{13}C-solid state NMR proved to be one of the most useful techniques to understand the final chemical structure of HTC materials. All data support the idea that the main structural motif is the furan ring directly coming from HMF, the dehydration product of glucose. A series of oxygenated groups and aliphatic functions are interconnected with furans and with a small fraction of arne-like motifs at 180°C. Further calcination of HTC carbons from glucose lead to an increase in the aromaticity level and arene function. Other employed charaterisation techniques (FT-IR, XRD, XPS, etc) nicely confirm such findings.

Overall the detailed ^{13}C ssNMR study of the HTC carbon, developed by our group highlights the high abundance of cross-linked furan units within the carbon framework structure. However, as confirmed by the complexity of the 2D ^{13}C homonuclear spectrum, it also shows a high heterogeneity of bonding patterns arising from the several reactions (e.g. self-condensation, substitution aldol condensation, etherification) that 5-HMF may undergo under hydrothermal conditions. Although some possible reactions have been described in section 2.2.7 at this stage it is not exactly clear what happens inside the autoclave during the HTC of glucose. Again, it will be very useful to use "*in situ*" techniques such as Mass Spectroscopy combined with Liquid and Solid State NMR to fully understand the reactions involved in the final chemical structure of HTC.

When we compared various HTC materials produced from several water soluble polysaccharides we realised that the chemical structure is very similar. Slight differences in morphology, functionality and chemical composition are encountered between hexoses and pentoses. In addition the more complex is the polysaccharide is, the more difficult is the morphological control of the resulting HTC material.

Finally we have compared the structure of HTC carbons from glucose with the one of HTC carbons from cellulose and with a real lignicellulosic biomass, rice straw. The main differences between HTC carbons derived from cellulose and glucose have been analysed, based on the effects of HTC temperature and reaction time on the morphology and chemical structure of the synthesised samples. In the latter case, it was observed that HTC temperature is a powerful tool that allows tuning the chemical structure of the synthesised material. At relatively low temperatures (i.e. 180 °C) glucose-derived HTC carbon was majorly composed of highly cross-linked furan units, as seen in the previous chapter. However increasing the HTC temperature led to the formation of condensed polyaromatic carbon domains possessing an increasingly hydrophobic character. In the case of cellulose-derived HTC carbon, the furan rich structure could not be isolated at any of the investigated processing conditions. The chemical structure of the synthesised samples was always characterised by a prevalent polyaromatic nature, as suggested by ^{13}C ssNMR experiments. These evidences were indicative of a different HTC conversion mechanism for cellulose, involving reactions that are commonly observed during pyrolytic processes. The low water solubility of cellulose was identified as the cause of such difference, since it hindered the hydrolysis of the glycosidic bond and resultant formation of glucose. This mechanistic speculation was supported by the evidence that amylose, a glucose polymer soluble in water at relatively low temperature (i.e. 60-70 °C), did produce furan rich HTC carbon.

These reactivity patterns observed for cellulose were also reflected in the rye straw-derived HTC carbon, indicating the main role of the cellulose fraction during the HTC processing of lignocellulosic biomass. Furthermore, in the case of rye straw, the cellulose conversion to HTC carbon was observed to shift to a higher temperature range (i.e. 220 - 240 °C) presumably due to the presence of lignin hindering its disruption. However, its full conversion into a final

carbonaceous material still took place in a lower temperature range than during pyrolysis (ca. 350°C) providing potential advantages from an energetic point of view.

In addition we have also looked at the porosity of the resulting HTC materials from the hydrothermal carbonisation of monosaccharides, polysaccharides or lignocellulosic biomass. Unfortunately independent of the precursor used such materials are literally non-porous. A slight amount of micropores could be introduced into these materials upon further calcination to higher temperatures (i.e. 500-1000°C) as determined by CO_2 adsorption in the detriment of functional groups. Interestingly, such a low amount of micropores is enough to induce selective adsorption of CO_2 over N_2. Details regarding this discovery are provided in Chapter 5, with some potential use in gas separation.

However other possibilities need to be researched to produce porous HTC materials for important applications. This has been successfully achieved by our group during the past years of intensive HTC research and the next chapter (chapter 3) is dedicated to this matter, while chapter 5 will present a huge variety of HTC applications in many very important areas.

2.6 References

[1]   aY. Roman-Leshkov, C. J. Barrett, Z. Y. Liu, J. A. Dumesic, *Nature* **2007**, *447*, 982-985; bG. W. Huber, J. N. Chheda, C. J. Barrett, J. A. Dumesic, *Science* **2005**, *308*, 1446-1450.
[2]   R. Rinaldi, F. Schüth, *Energy Environ. Sci* **2009**, *2*, 610-626.
[3]   D. Klemm, B. Heublein, H.-P. Fink, A. Bohn, *Angew. Chem.* **2005**, *117*, 3422 –3458.
[4]   F. Bergius, *Naturwissenschaften* **1928**, *16*, 1-10.
[5]   F. Bergius, *Industrial and Engineering Chemistry* **1937**, *29*, 247-253.
[6]   E. E. Harris, E. Beglinger, US Department of Agriculture, Forest Service, Forest Products Laboratory, Madison, Wisconsin, **1946**.
[7]   J. Kusama, Tokyo, **1960**.
[8]   D. R. Thompson, H. E. Grethlein, *Ind. Eng. Chem. Prod. Res. Dev.* **1979**, *18*, 166-169.
[9]   R. Erckel, R. Franz, R. Woernle, T. Riehm, in *US Patent 4 556431*.
[10]   D. Bröll, C. Kaul, A. Krämer, P. Krammer, T. Richter, M. Jung, H. Vogel, P. Zehner, *Angewandte Chemie International Edition* **1999**, *38*, 2998-3014.
[11]   F. Jin, H. Enomoto, *Bioresources* **2009**, *4*, 704-713.
[12]   J. N. Chheda, Y. Roman-Leshkov, J. A. Dumesic, *Green Chemistry* **2007**, *9*, 342-350.
[13]   B. L. Scallet, J. H. Gardner, *Journal of the American Chemical Society* **1945**, *67*, 1934-1935.
[14]   F. S. Asghari, H. Yoshida, *Industrial & Engineering Chemistry Research* **2007**, *46*, 7703.
[15]   X. Sun, Y. Li, *Angewandte Chemie International Edition* **2004**, *43*, 597-601.

[16]   M.-M. Titirici, A. Thomas, M. Antonietti, *Advanced Functional Materials* **2007**, *17*, 1010-1018.

[17]   M. Antonietti, A. Thomas, M. Titirici, *Physical Chemistry Chemical Physics* **2007**, *9*, T45-T45.

[18]   M. M. Titirici, A. Thomas, M. Antonietti, *New J. Chem.* **2007**, *31*, 787-789.

[19]   S. K. R. Patil, C. R. F. Lund, *Energy & Fuels* **2011**, *25*, 4745-4755.

[20]   R. D. Cakan, M.-M. Titirici, M. Antonietti, G. Cui, J. Maier, Y.-S. Hu, *Chemical Communications* **2008**, 3759-3761.

[21]   A. B. Fuertes, M. C. Arbestain, M. Sevilla, J. A. Macia-Agullo, S. Fiol, R. Lopez, R. J. Smernik, W. P. Aitkenhead, F. Arce, F. Macias, *Australian Journal of Soil Research*, *48*, 618-626.

[22]   M. Chidambaram, A. T. Bell, *Green Chemistry* **2010**, *12*, 1253-1262.

[23]   J. P. Lange, R. Price, P. M. Ayoub, J. Louis, L. Petrus, L. Clarke, H. Gosselink, *Angew. Chem.-Int. Edit.* **2010**, *49*, 4479-4483.

[24]   X. Tong, Y. Ma, Y. Li, *Applied Catalysis A: General*, *385*, 1-13.

[25]   S. J. Angyal, in *Glycoscience: epimerisation, isomerisation and rearrangement reactions of carbohydrates*, Springer-Verlag, Berlin, **2001**, pp. 1-14.

[26]   X. Qi, M. Watanabe, T. M. Aida, R. L. Smith, Jr., *Catalysis Communications* **2008**, *9*, 2244-2249.

[27]   C. Falco, N. Baccile, M.-M. Titirici, *Green Chemistry* **2011**, *13*, 3273-3281.

[28]   S. H. Yu, X. J. Cui, K. L. L. L. Li, B. Yu, M. Antonietti, H. Colfen, *Adv. Mater.* **2004**, *16*, 1636–1640

[29]   A. Chuntanapum, Y. Matsumura, *Industrial & Engineering Chemistry Research* **2009**, *48*, 9837-9846.

[30]   V. K. LaMer, *Ind. Eng. Chem.* **1952**, *44*.

[31]   T. Sakaki, M. Shibata, T. Miki, H. Hirosue, N. Hayashi, *Bioresource Technology* **1996**, *58*, 197-202.

[32]   M. Bremholm, J. Becker-Christensen, B. B. Iversen, *Advanced Materials* **2009**, *21*, 3572-3575.

[33]   S. K. Hoekman, A. Broch, C. Robbins, *Energy Fuels* **2011**, *25*, 1802-1810.

[34]   L. Yu, C. Falco, J. Weber, R. J. White, J. Y. Howe, M.-M. Titirici, *Langmuir* **2012**, *28*, 12373-12383.

[35]   http://webbook.nist.gov/cgi/cbook.cgi?ID=C123762&Mask=200#Mass-Spec.

[36]   A. Thomas, F. Goettmann, M. Antonietti, *Chem. Mater.* **2008**, *20*.

[37]   http://www.auts.edu.cn/

[38]   N. Baccile, G. Laurent, F. Babonneau, F. Fayon, M.-M. Titirici, M. Antonietti, *The Journal of Physical Chemistry C* **2009**, *113*, 9644-9654.

[39]   P.F. Barron, M. A. Wilson, *Nature* **1981**, *289*.

[40]   M. Bardet, S. Hediger, G. Gerbaud, S. Gambarelli, J. F. Jacquot, M. F. Foray, A. Gadelle, *Fuel* **2007**, *86*, 1966.

[41]   M. J. Sullivan, G. E. Maciel, *Anal. Chem.* **1982**, *54*, 1608.

[42]   L. P. dela Rosa, M.; Lang, D.; Gerstein, B.; Solomon, P., *Energy Fuels* **1992**, *6*.

[43]   L. B. Alemany, D. M. Grant, R. J. Pugmire, T. D. Alger, K. W. Zilm, *J. Amer. Chem. Soc.* **1983**, *105*, 2133.

[44]   A. Lesage, C. Auger, S. Caldarelli, L. Emsley, *J. Amer. Chem. Soc.* **1998**, *120*, 9059.

[45]   A. Lesage, M. Bardet, L. Emsley, *J. Amer. Chem. Soc.* **1999**, *121*, 10987.
[46]   A. Brinkmann, M. M. Eden, M. H. Levitt, *J. Chem. Phys.* **2000**, *112*, 8539.
[47]   M. Hohwy, C.M. Rienstra, C. P. Jaroniec, R. G. Griffin, *J. Chem.Phys.* **1999**, *110*, 7983.
[48]   Fellinger T. P, PhD thesis, (University of Potsdam), **2011**.
[49]   A. A. Rosatella, S. P. Simeonov, R. F. M. Frade, C. A. M. Afonso, *Green Chemistry* **2011**, *13*.
[50]   H. E. van Dam, A. P. G. Kieboom, H. van Bekkum, *Starch - Stärke* **1986**, *38*, 95-101.
[51]   aM. Choura, N. M. Belgacem, A. Gandini, *Macromolecules* **1996**, *29*, 3839-3850; bA. Gandini, M. N. Belgacem, *Progress in Polymer Science* **1997**, *22*, 1203-1379; cA. Gandini, *Polymer Chemistry* **2011**, *1*, 245-251.
[52]   T. Kim, R. S. Assary, C. L. Marshall, D. J. Gosztola, L. A. Curtiss, P. C. Stair, *ChemCatChem* **2011**, *3*, 1451-1458.
[53]   J. Horvat, B. Klaic, B. Metelko, V. Sunjic, *Tetrahedron Letters* **1985**, *26*, 2111-2114.
[54]   S. K. R. Patil, J. Heltzel, C. R. F. Lund, *Energy & Fuels* **2012**, *26*, 5281-5293.
[55]   A. Gandini, M. N. Belgacem, *Prog. Polym. Sci.* **1997**, *22*, 1203.
[56]   A. Funke, F. Ziegler, *Biofuels, Bioprod. Bioref* **2010**, *4*, 160-177.
[57]   M.-M. Titirici, M. Antonietti, N. Baccile, *Green Chemistry* **2008**, *10*, 1204-1212.
[58]   M. M. Titirici, A. Thomas, M. Antonietti, *Journal of Materials Chemistry* **2007**, *17*, 3412-3418.
[59]   R. J. White, C. Antonio, V. L. Budarin, E. Bergstroem, J. Thomas-Oates, J. H. Clark, *Advanced Functional Materials* **2010**, *20*, 1834-1841.
[60]   C. Falco, F. Perez Caballero, F. Babonneau, C. Gervais, G. Laurent, M.-M. Titirici, N. Baccile, *Langmuir* **2011**.
[61]   N. Baccile, M. Antonietti, M. M. Titirici, *Chemsuschem* **2010**, *3*, 246-253.
[62]   M. A. N. Ritter, A. Thomas, I. Senkovska, S. Kaskel , J. Weber, *Macromolecules* **2009**, *42*, 8017–8020.
[63]   M. J. Antal, W. S. L. Mok, G. N. Richards, *Carbohydr. Res* **1990**, *199*.
[64]   J. C. C. Freitas, F. G. Emmerich, G. R. C. Cernicchiaro, L. C. Sampaio, T. J. Bonagamba, *Solid State Nuclear Magnetic Resonance* **2001**, *20*, 61-73.
[65]   C. L. Burket, R. Rajagopalan, A. P. Marencic, K. Dronvajjala, H. C. Foley, *Carbon* **2006**, *44*, 2957-2963.
[66]   X. Zhang, D. H. Solomon, *Chemistry of Materials* **1999**, *11*, 384-391.
[67]   H. Eckert, Y. A. Levendis, R. C. Flagan, *The Journal of Physical Chemistry* **1988**, *92*, 5011-5019.
[68]   A. Shindo, K. Izumino, *Carbon* **1994**, *32*, 1233-1243.
[69]   aJ. Silvestre-Albero, A. Silvestre-Albero, F. Rodríguez-Reinoso, M. Thommes, *Carbon* **2011**; bR. V. R. A. Rios, J. Silvertre-Albero, A. Sepulveda-Escribano, M. Molina-Sabio, F. Rodriguez-Reinoso, *Journal of Physical Chemistry C* **2007**, *111*, 3803-3805.
[70]   aF. Rodriguez Reinoso, J. D. Lopez Gonzalez, C. Berenguer, *Carbon* **1982**, *20*, 513-518; bN. Ritter, I. Senkovska, S. Kaskel, J. Weber, *Macromolecules* **2011**, *44*, 2025-2033; cJ. Jagiello, M. Thommes, *Carbon* **2004**, *42*, 1227-1232.
[71]   A. Thomas, F. Goettmann, M. Antonietti, *Chemistry of Materials* **2008**, *20*, 738-755.
[72]   N. Ritter, I. Senkovska, S. Kaskel, J. Weber, *Macromolecular Rapid Communications* **2011**, *32*, 438-443.

[73]   S. J. Gregg, K. S. W. Sing, *Adsorption, Surface Area and Porosity*, 2nd ed. ed., Academic Press INC., London, **1982**.

[74]   P. Kumar, D. M. Barrett, M. J. Delwiche, P. Stroeve, *Ind. Eng. Chem. Res* **2009**, *48*, 3713–3729

[75]   M. P. Pandey, C. S. Kim, *Chem. Eng. Technol.* **2011**, *34(1)*, 29-41.

[76]   Y. S. Sun, X. B. Lu, S. T. Zhang, R. Zhang, X. Y. Wang, *Bioresource. Technology.* **2011**, *102* 2936–2294.

[77]   H. D. Willauer, J. G. Huddleston, M. Li, R. D. Rogers, *J. Chromatogr. B.* **2000**, *743(1–2)*, 127–135.

[78]   M. Kim, G. Aita, D. F. Day, *Appl Biochem Biotechnol* **2010**, *161*, 34-40.

[79]   N. E. El Mansouri, J. Salvado, *Industrial Crops and Products* **2006**, *24*, 8-16.

[80]   G. Ward, Y. Hadar, C. G. Dosoretz, *Journal of Chemical Technology and Biotechnology* **2003**, *78*, 1239-1245.

[81]   A. C. O'Sullivan, *Cellulose* **1997**, *4*, 173-207.

[82]   A. Kruse, A. Gawlik, *Ind. Eng. Chem. Res* **2003**, *42(2)*, 267-279.

[83]   M. L. P. Mansikkamaki, K Rissanen, *Carbohydrate Polymers* **2007**, *68*, 235-241.

[84]   W.S.L. Mok, M.J Antal, *Ind. Eng. Chem. Res* **1992**, *31*, 1157-1161.

[85]   P. Kumar, D.M.Barrett, M.J.Delwiche, P.Stroeve, *Ind .Eng. Chem. Res* **2009**, *48*, 3713-3729

[86]   S. Link, S. Arvelakis, H. Spliethoff, P. De Waard, A. Samoson, *Energy & Fuels* **2008**, *22*, 3523-3530.

[87]   J. Pastorova, R. E. Botto, P. W. Arisz, J. J. Boon, *Carbohydrate Research* **1994**, *262*, 27.

[88]   J. B. Wooten, J. J. Seeman;, M. R. Hajaligol, *Energy & Fuels* **2004**, *18*.

[89]   M. Bardet, S. Hediger, G. Gerbaud, S. Gambarelli, J. F. Jaquot, M. F. Foray;, A. Gadelle, *Fuel* **2007**, *86*, 1966.

[90]   K. David, Y.Q. Pu, M. Foston, J. Muzzy, A. Ragauskas, *Energy & Fuels* **2009**, *23*, 498.

[91]   C. Liu, J. Huang, X. Huang, H. Li, Z. Zhang, *Computational and Theoretical Chemistry* **2011**, *964*, 207-212.

[92]   C. Falco, PhD Thesis thesis, (University of Potsdam), **2012**.

[93]   N. S. Mosier, C. M. Ladisch, M. R. Ladisch, *Biotechnology and Bioengineering* **2002**, *79*, 610-618.

[94]   K. David, Y. Pu, M. Foston, J. Muzzy, A. Ragauskas, *Energy & Fuels* **2008**, *23*, 498-501.

[95]   V. K. LaMer, R. H. Dinegar, *Journal of the American Chemical Society* **1950**, *72*, 4847-4854.

3 Porous Hydrothermal Carbons

3.1 Introduction

Beginning from the use as adsorbents for decolourisation of alcohol, water and sugar or for the removal of moisture from the architectures in ancient times, porous carbon materials have been widely used in our society. [1] More recent applications are dedicated to the use in industry as adsorbents (e.g. activated carbon) for drinking water, wastewater and gas purification or as catalysts or catalyst supports. [2-5] The well-developed surface area and porosity of such materials are critical to these application typically enhancing the adsorption capacity/selectivity or catalytic activity. Porous carbon materials are becoming of increasing interest to the developing application fields of energy storage [6] (e.g. electrodes for Li ion batteries or supercapacitors), fuel cells (e.g. novel catalysts or catalyst supports for the oxygen reduction reaction) [7-9] or chromatography technologies, [10-12] which is expected to amount as much as 90-billion-dollar market in the year 2013 (Figure 3-1). [13] When compared to conventional electrolytic capacitors or to batteries, carbon-based supercapacitors offer good specific energy (1-10 Wh kg^{-1}), as recently demonstrated, for example, by carbon aerogels with high porosity and surface area (> 50 %, 400 - 1000 m^{2}g^{-1}). [14]
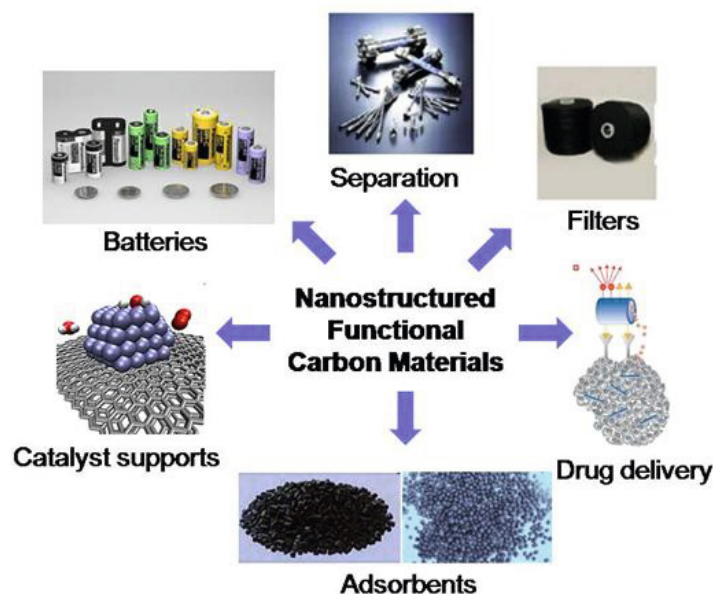
Figure 3-1: Schematic representation of the main application fields of porous carbon materials

Due to the extreme versatility of carbon materials available (e.g. crystalline, amorphous, bulk, nanostructured, activated, functionalised), a great deal of literature research has discussed the use of various electrodes configurations for supercapacitors or secondary batteries (please see for example reference [6]). This is a good example of how material porosity directly affects the electrochemical performance. In order to improve even further the performance of carbon materials, novel synthetic approaches as well as a developed fundamental understanding of their properties are strongly desirable from materials chemistry point of view.

In this context, as we have learned in the previous chapters, hydrothermal carbonisation process (HTC) can be considered as a very interesting, green and versatile technique to produce carbon materials. [15-16] However, as they are synthesised directly from biomass or carbohydrates at low temperatures (130-250°C), they essentially present very limited surface area and pore volumes (see Chapter 2, analysis of porosity section) therefore inhibiting use in the aforementioned application fields.

This chapter focuses on the development of synthetic routes to introduce well-defined porosity into hydrothermal carbons. In the this chapter, various synthetic routes towards porous hydrothermal carbon materials or composites will be introduced and discussed, focusing on the synthesis of different pore systems and morphologies directed by the presence of various structure directing agents (e.g. organic and inorganic templates). Attention will also be applied to the utilisation of naturally occurring biomcomposites (e.g. crustacean shells) and their use in the preparation of porous HTC materials. Chemical activation will also be discussed as a possibility to produce HTC microporous materials.

The presented methods allow tailoring of the final structure *via* the tools of colloid and polymer science, leading to selectable material morphology for a wide range of applications.

3.2   Templating – an Opportunity for Pore Morphology Control

In relation to the introduction of porosity into carbon materials, Knox *et al.* (1986) was one of the first to synthesise nanoporous carbon materials with a variety of pore structures using the appropriate nanostructured silica materials as sacrificial templates. [10] This procedure reflects the "hard templating (or exo-templating)" approach to structure replication. [17-18] Generally, in hard templating, a carbon precursor (e.g., phenol – formaldehyde resin) infiltrates a sacrificial hard

template structure and is carbonised within the pores (normally at high temperatures; e.g. > 700 ^{o}C). The template is then removed to give the inverse nanostructures of the original inorganic templates (Figure 3-2 a)
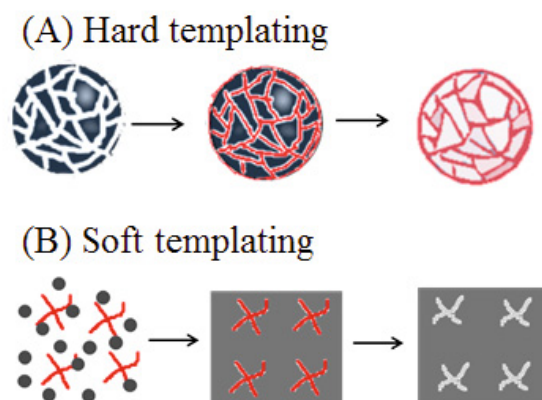
Figure 3-2: Schematic drawing of (A) hard templating and (B) soft templating approach to synthesise porous and high-surface area materials. For endo (hard) templating, the templating species are occluded in the forming solid, for exo (soft) templating, a rigid porous solid is infiltrated with the precursor for another solid. Endo templates as well as exo templates are removed from the composite to yield the porous or high-surface area materials (adapted with permission from [17]) .

More recently, Zhao *et al.* and Dai *et al.* have independently demonstrated that under the correct synthesis conditions, the use of a sacrificial inorganic template is not required, demonstrating a direct route to ordered porous carbon materials *via* the self-assembly of block copolymers and suitable aromatic carbon precursors (e.g. phloroglucinol or resorcinol-formaldehyde). [19-24] This method, widely recognised as one of the classical methods to produce inorganic porous materials by sol-gel chemistry, is called soft templating or endo-templating (Figure 3-2 b).

The hydrothermal process has clear advantages when compared to the classical carbonisation method (e.g., pyrolysis) since it takes place in the aqueous phase and thus can, in principle, be easily combined with classical templating procedures. Pure carbohydrates are in this case the most convenient precursors since they are easily dissolved in water. Additionally, polar functionalities are present on the materials surface allowing relatively facile further modification to be performed, which is somewhat difficult in the case of carbon materials with highly developed aromatic / graphitic character usually obtained from the conventional carbonisation procedure (e.g. synthesised using a phenol formaldehyde resin precursor). [16] The surface

138

chemistry of the resulting HTC materials can also easily be controlled and in turn carbon condensation / aromaticity (e.g. by post thermal treatment), offering the opportunity to direct surface or pore wall chemistry for specific application needs.

3.2.1 Hard Templating in HTC

Following the same principle as the structural replication presented by Knox *et al*., [10] mesoporous hydrothermal carbons have been produced by conducting HTC at 180°C in the presence of nanostructured sacrificial silica bead templates (LiChrospher® Si100, average particle size 10 μm, pore size 10 nm). [25]
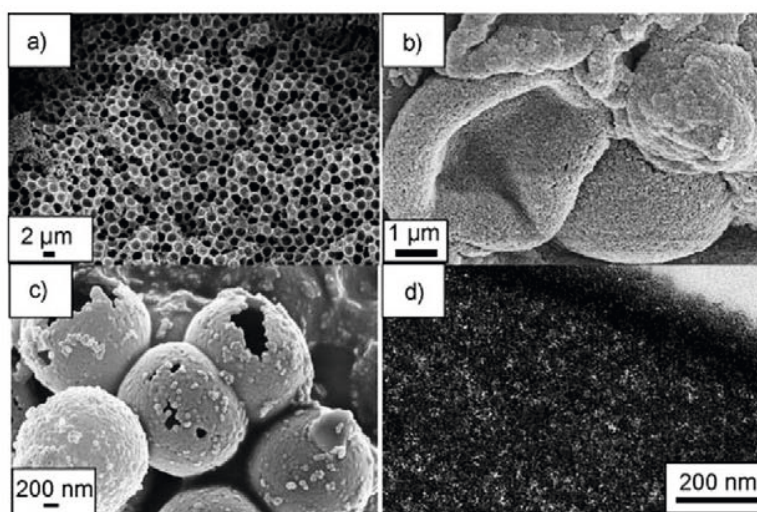
Figure 3-3: Morphologies obtained *via* HTC of 2-furaldehyde in the presence of silica templates with different polarities. (A) Macroporous carbon cast obtained in the presence of nonporous silica with a very hydrophobic surface, (B) mesoporous-shell hollow spheres obtained from mesoporous silica templates with moderate hydrophobicity, (C) hollow spheres obtained using nonporous silica spheres with moderate hydrophobicity, and (D) mesoporous hydrothermal carbon replica obtained using a calcined mesoporous silica template. (taken with permission from 25)

Significantly, it was found that it is important to match the template surface polarity with that of the carbon precursor. Hydrophobisation of the silica template can be performed *via* methylation or thermal treatment. A variety of morphologies are obtained using silica templates with different polarities and 2-furaldehyde as a carbon source (Figure 3-3). The use of silica templates with a very hydrophobic surface character leads to the generation of macroporous carbon casts (Figure 3-3 (a)), whereas hollow carbon spheres are produced when using a moderately hydrophobic surface (Figure 3-3 (b)). Dehydroxylated silica templates filled with 60 wt% 2-furaldehyde

resulted in mesoporous carbonaceous microspheres (Figure 3-3d) thus demonstrating successful templating, whereas application of a 30 wt% carbon precursor gave only small carbon spherules (6 – 10 nm diameter) owing to the lack of interconnectivity between growing particles in the coating. Furthermore, when rehydroxylated silica was used, demixing occurred due to the enhanced hydrophilic character of the template surface essentially inhibiting impregnation of the 2-furaldehyde.

Complete impregnation was achieved by controlling the degree of hydrophobicity of the template and by controlling the concentration of the carbon precursor in an aqueous solution. In addition to the matching of the surface polarities, it was also illustrated that the carbon nanocoating procedure operates in a "patchwise" manner, *via* the generation of stable colloidal intermediates. For nonporous templates, hollow carbonaceous spheres with a robust carbon coating are observed (Figure 3-3 (c)). Further investigation was conducted using mesoporous silica beads LiChrospher® Si300 with the average particle size and pore diameter of 10 μm and 30 nm, respectively to yield spherically shaped carbonaceous particles. [25-26] SEM images of the obtained carbon replica of Si300 reveals that the both particle size (~ 10 μm) and the morphology uniformity were maintained (Figure 3-4 (a) and (b)).

One of the main advantages of the combined HTC - hard templating method is the accessibility of nanostructured materials possessing useful surface functionalities. By further thermal treatment under an inert atmosphere of the obtained composites (i.e. 350, 550, 750 ^{o}C) followed by the template removal, carbon spheres with different surface functionalities and pore properties were obtained. This post-carbonisation treatment had no significant impact on the spherical material morphology (Figure 3-4 (c) and (d)). Elemental analysis (EA), revealed an increase in carbon content of the synthesised materials 64 wt% to 81 wt% (350 to 750 ^{o}C), thus showing increasing carbon-rich material character.
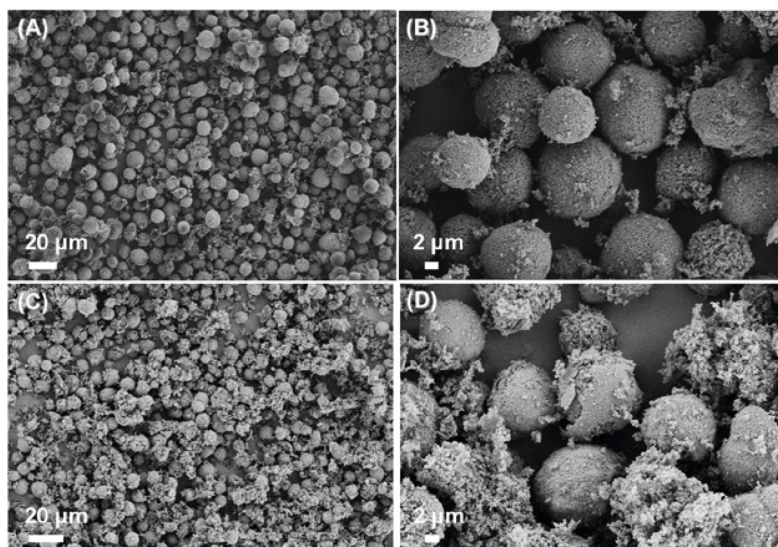
Figure 3-4: SEM micrographs of (A) and (B) an as-synthesised carbon replica (HTC@180°C) and (C) and (D) a carbon replica after post-carbonisation at 750 °C.
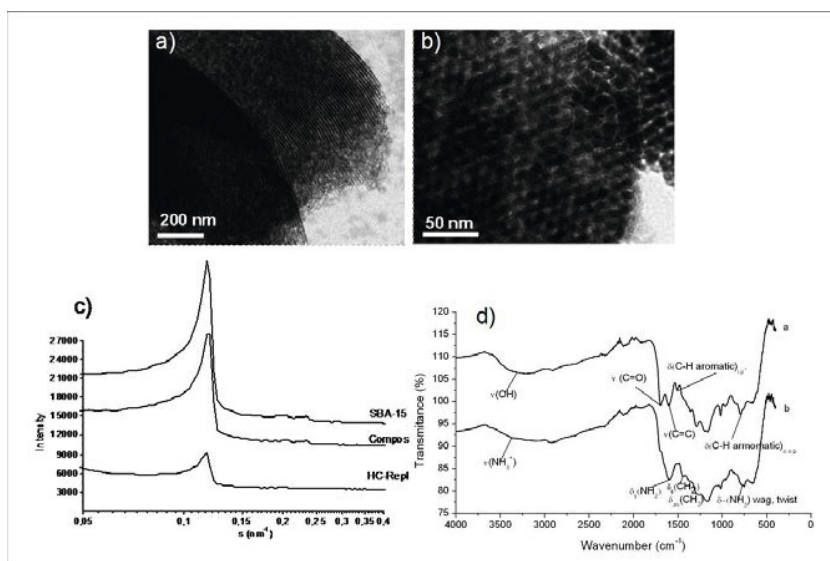
Figure 3-5: (A) and (B) TEM micrographs of the ordered mesoporous carbon obtained by replication of the SBA-15 silica template; (C) SAXS patterns of the silica template, corresponding composites and ordered hydrothermal carbon materials) and (D) FTIR spectra of the ordered carbon replica before and after amino functionalization (taken with permission from 27)

Similarly to the production of CMK type materials pioneered by Ryoo *et al.*, [18] hexagonally ordered mesoporous SBA-15 silica has also been used as a sacrificial inorganic template for the preparation of ordered carbonaceous replicas under hydrothermal conditions. [27] TEM images of the carbonaceous duplication also demonstrates that the ordered hexagonal pattern is maintained

in the carbon product (Figure 3-5 (a) and (b)). SAXS analysis of the carbon replica presented Bragg reflections of (100), (110) and (200), characteristic of the 2D hexagonal arrangement (Figure 3-5 (c)), further confirming the maintenance of the structural regularity. Using the functionality generated by the HTC process, relatively simple chemical modification strategies can employed to further modify the SBA-15 carbon replica pore wall and surface groups. The introduction of surface amino groups was confirmed by EA (~ 4 mmol N/g) and FTIR spectroscopy as indicated by bands at 1615 cm^{-1} at 772 cm^{-1} characteristic of amino (-NH$_2$) groups (Figure 3-5(d)).

Analogous to the structural replication of mesoporous silica, the nanostructure of a macroporous anodic alumina membrane (AAO) was also achieved *via* a combined HTC – hard templating strategy to yield tubular carbons. [28] Again, the surface character of the tubular carbonaceous nanostructure was controlled by employing post-synthesis thermal treatments. TEM images reveal that the micrometre long tubular carbons possess an open ended structure with smooth surfaces constituted of a hollow internal diameter of *ca.* 125 (± 25) nm and *ca.* 40 nm thick carbonaceous tube walls (Figure 3-6), with pore wall thickness observed to marginally decrease as treatment temperature passed 550 $^{\circ}$C (i.e. as the carbon network condenses).

High resolution TEM images of before (Figure 3-6 (e)) and after carbonisation (Figure 3-6 (f)), revealed the level of local order improved with temperature indicative of increasing aromatic / pseudo-graphitic character. In addition, the surface area and the pore volume were observed to increase upon employing higher post carbonisation temperature as was observed in the case of carbon spheres again due to the development of microporosity (see chapter 6 for details). Furthermore the useful material chemistry of these tubular structures can be modified with stimuli responsive polymers for controlled dispersion applications. [28]
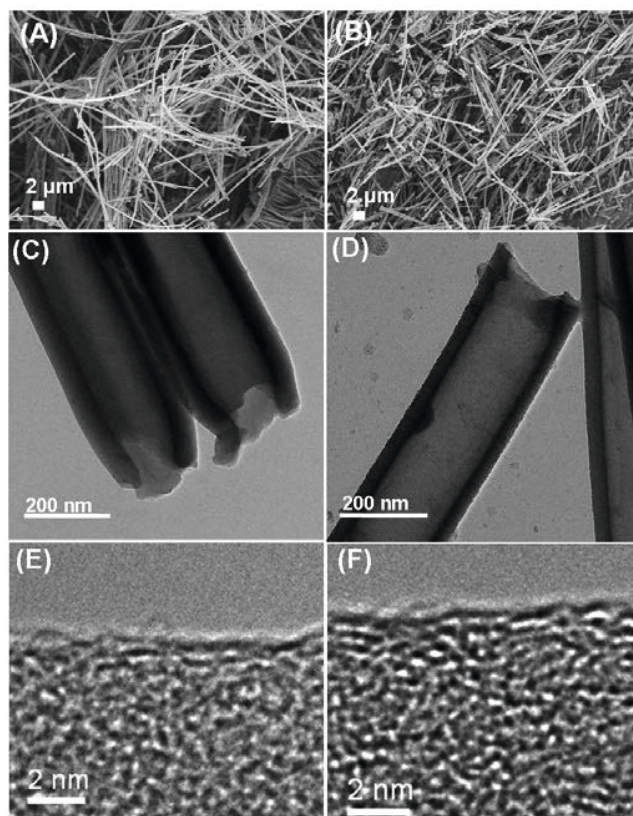
Figure 3-6: SEM micrographs of (A) as-synthesised tubular carbons and (B) tubular carbons post-carbonised at 750 °C; TEM micrographs of (C) as-synthesised tubular carbons and (D) tubular carbons post-carbonised at 750 °C; HRTEM micrographs of (E) as-synthesised tubular carbons and (F) tubular carbons post-carbonised at 750 °C (taken from 28).

3.2.2 Soft Templating HTC

The use of soft, polymeric templates of defined size and shape (e.g. polymer nanoparticles) can also be employed in the synthesis of nanostructured HTC materials. My research group, (Titirici White *et al.)* have used aqueous dispersions of polystyrene latex nanoparticles (PSL) (e.g., D = 100 nm) as a templates to synthesise functional hollow carbon nanospheres (Figure 3-7 (a)). [29] Using the hydrothermal conversion of Glucose at 180 °C in the presence of the PSL template, results in a controllable coating of hydrothermal carbon of the polymer body. Thermal treatment of the resulting composite, above the decomposition point of PSL (e.g., > 500 °C) results in formation of hollow carbonaceous nanospheres. Latex nanoparticles of any desired diameter and narrow size distribution can be readily prepared allowing in principle subtle control of the hollow carbon nanosphere size over a wide range of diameters.

Thermal treatment at 1000 ^{o}C generate a turbostratic-type carbon layering in the nanospheres wall with a thickness of *ca.* 20 nm (Figure 3-7 (b)) suitable for the application as anode materials in Li$^+$ [30], Na$^+$ [31] as well as cathode in Li-S batteries, [32] which will be discussed Chapter 5 dedicated to the applications of HTC.
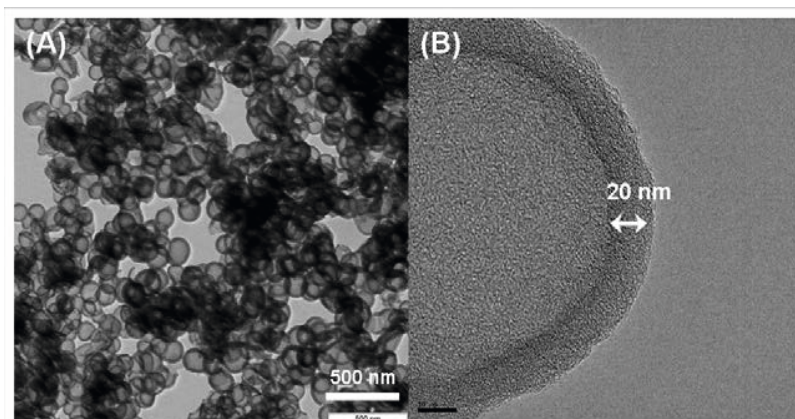
Figure 3-7: (A) TEM images of MPG-C100nm HTC composite material (i.e., before template removal); (B) MPG-C100nm-550°C demonstrating polystyrene latex template removal; (C) and (D) HRTEM images of MPG-C100nm-1000°C. (taken from [29])

It is proposed in materials science that enhanced application performance (e.g. catalysis) can be generated by the synthesis of organised, uniformly sized and shaped material pore texture at nanoscale, in tandem with controlled pore wall chemistry. As mentioned earlier, Zhao *et al*. and Dai *et al*. have recently demonstrated a soft templating route, a direct route to ordered porous carbons *via* organic - organic self-assembly of a block copolymer (e.g. Pluronic$^®$ block copolymers or polystyrene-*b*-poly(4-vinylpyridine)) and a suitable aromatic carbon precursor (e.g. phloroglucinol [20] or phenol-formaldehyde [21-22]). Hydrogen bond interactions play a significant role in orientating the resulting poly-aromatic network, whilst pore structuring was conventionally controlled mainly by polymeric template (e.g. *via* concentration and structure), copolymer - precursor ratio and *p*H. The polymeric template can be then removed either by solvent extraction or heat treatment about its decomposition temperature. Carbons prepared using such strategies, typically present rather chemically condensed (e.g. graphitic-like) pore walls / surfaces due to the high temperature syntheses, which inhibit facile post chemical modification and limits surface hydrophobicity / polarity modification. Therefore, performing the same type of soft templating process under HTC conditions becomes of great interest. One of the main

advantage is the fact it offers direct access to ordered porous carbons with useful surface functionality, whilst it will be a key point and highly challenging to achieve the stable formation of a polymeric template – precursor assembly under HTC conditions. In this context, it was found out that the selection of a suitable carbon precursor and HTC temperature can lead to successful "soft" templating of hydrothermal carbons.

In the first attempt, HTC of D-fructose was performed at 130 $^{\circ}$C in the presence of block copolymer Pluronic$^{\circledR}$ F127 (EO_{106}-PO_{70}-EO_{106}) to yield a carbonaceous precipitate with ordered nanostructure. [33]

This composite was further heat treated under N_2 to 550 $^{\circ}$C, resulting in template removal yielding a carbonaceous product (denoted as C-MPG1-*micro*), composed of 82.6 wt% C, 14.2 wt% O, and 3.2 wt% H, respectively. Here, the use of D-fructose is considered to play a crucial role in successful templating of supramolecular assembly of block copolymer template since it undergoes HTC at 130 $^{\circ}$C; a significantly lower temperature to that previously reported for other sugars (e.g. D-glucose; 180 $^{\circ}$C). [33] Typically, block copolymer micelles are not stable at the high temperature used for the HTC process. [34] Therefore, the use of D-fructose allows access to a more stable micellar phase and opens the opportunity for soft templating. The complete removal of block copolymer species from the template – carbon composite was confirmed by thermogravimetric analysis, representing a significant mass loss regime at ~ 400 $^{\circ}$C (i.e. the F127 decomposition) followed by a smaller secondary charring step at ~ 600 $^{\circ}$C (i.e. further condensation / aromatisation of the carbon structure). SEM image analysis of C-MPG1-*micro* indicated a layer-by-layer growth mode yielding relatively uniform cuboctahedron-like particles in the 1 – 10 μm size range. Whilst of a similar size to non-templated HTC material, particles synthesised *via* this templating approach present a faceted edge / layered morphology, indicative of the growing direction of the hydrothermal carbon network by the templating phase as well as of the formation of near single crystalline particles. TEM image analysis demonstrates the long-range regularly ordered pore structure (Figure 3-8 (a)), whilst synchrotron small angle X-ray scattering (SSAXS) analysis of C-MPG1-*micro* indicates the formation of a near perfect cubic *Im3m* symmetry (Figure 3-8 (b)). Moreover, the obtained 2D scattering pattern (Figure 3-8 (b) insert) is indicative of a single-crystalline nature to this material and presents well resolved peaks at *q*-spacing values of 0.51, 0.72 and 0.87 nm^{-1} respectively, corresponding to a *d*-spacing of 12.3 nm equating to a unit cell parameter of 17.4 nm. The calculated SSAXS unit cell parameter

agrees well with the presented TEM image, while unusually both SSAXS and TEM indicate the generation of a very thick pore wall feature for C-MPG1-*micro* with dimensions of between 7 - 10 nm.
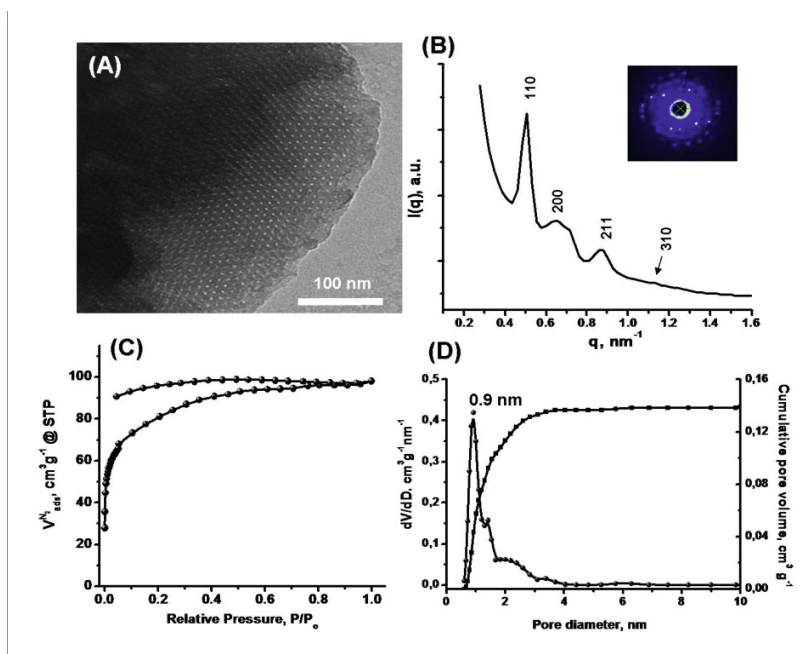
Figure 3-8: (A) TEM, (B) Synchrotron SAXS pattern (right-up; diffraction pattern) (C) N2 sorption isotherm, and (D) pore size distribution (QSDFT) of as-synthesised C-MPG1-micro material (reproduced from reference [33]).

In order to investigate the pore property of the obtained material, N_2 sorption analysis was carried out generating a microporous type I isotherm with a non-reversible nature due to structural changes in pore wall dimensions during sorption processes (Figure 3-8 (c)). [35] Specific surface area and total pore volume were calculated as 257 m^2 g^{-1} and 0.14 $cm^3 g^{-1}$ respectively. The pore size distribution presents a sharp peak at a diameter of 0.9 nm and a less discrete broader shoulder centred around 2 nm (Figure 3-8 (d)). By comparison, the F127 / HTC-carbon composite material presented very limited pore volume and surface area indicating that indeed pores are opened upon removal of the block copolymer template *via* acalcination. TEM image analysis of this composite indicated an F127 micelle diameter of ~ 11 nm and carbon wall thickness of ~ 7 nm (Figure 3-9 (a)). SAXS analysis of the F127 / HTC-carbon composite demonstrated a well-resolved pattern with the *d*-spacing value of the first peak equivalent to 16.8 nm, corresponding to a unit cell parameter of 23.6 nm, which is considerably larger to pore

146

dimensions observed after template removal (Figure 3-9 (b)).

A possible formation mechanism was proposed. It is believed that as HTC proceeds *via* the dehydration/ polycondensation reactions to generate a polyfuran-like network [36] (see details in the solid state NMR sections of chapter 2) the organised block copolymer micellar phase is essentially "templated", whereby in the initial steps D-fructose is absorbed *via* hydrogen bonding interactions into the hydrophilic PEO moiety of the F127. Here, the resulting polyfuran-like network is comparatively hydrophobic and therefore the possibility of "templating" of a reversed phase through a hydrophobic interaction still cannot be discounted. Upon removal of the template at 550 °C, the resulting pores are smaller than that of before template removal due to structural shrinkage (e.g. carbon network condensation) or possible partial carbonisation of the block copolymer.
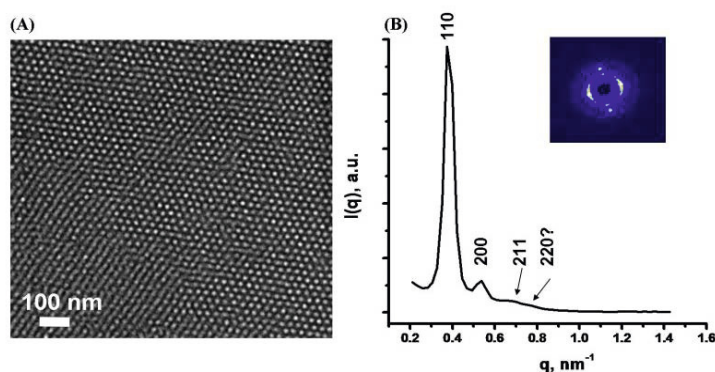
Figure 3-9: (A) TEM micrograph and (B) Synchrotron SAXS pattern of C-MPG1-micro before template removal (insert; 2D scattering pattern reproduced with permission from reference [34]).

Importantly, further work revealed that the ordered pore phase dimensions of this C-MPG1-*micro* material could be shifted into the mesoporous domain by the addition of a pore swelling agent, trimethylbenzene (TMB) to the F127 / D-fructose reaction mixture (denoted as C-MPG1-*meso*). Thermal template removal at 550 °C generates carbonaceous particles again with faceted ages similar in morphology to C-MPG1-*micro*. Close examination of the pore structuring *via* TEM image analysis indicated the maintenance of the well-ordered pore structuring upon addition of the pore swelling agent with a pore diameter and wall thickness of ~5 nm and ~10 nm, respectively (Figure 3-10 (a)). SSAXS analysis of C-MPG1-*meso* presented well resolved peaks at inverse nanometre values of $q = 0.47, 0.65, 0.80$ and 0.94 nm^{-1} and a further peak at higher q

values (Fig. 10(b)), indicative of *Im3m* symmetry and a unit cell of 18.9 nm showing the increased regular unit. The peak at 0.47 nm^{-1} is accompanied with a small shoulder feature indicating some structural heterogeneity (e.g. the presence of a mixed phase) as also demonstrated by the increased polycrystalline nature of this material (2D scattering pattern; Figure 3-10(b) insert).
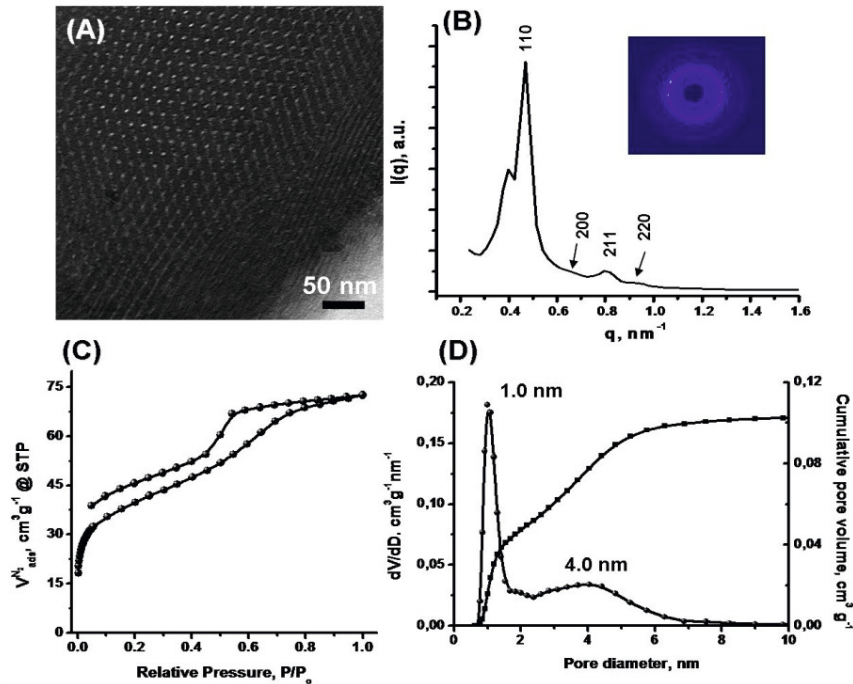
Figure 3-10: (A) TEM, (B) Synchrotron SAXS pattern (right-up; diffraction pattern) (C) N2 sorption isotherm, and (D) pore size distribution (QSDFT) of as-synthesised C-MPG1-meso material (reproduced from reference [33])

The transition from a Type I (i.e. for C-MPG1-*micro*) to a Type IV N$_2$ sorption profile for C-MPG1-*meso* was observed with associated capillary condensation feature at P/P$_o$ ~ 0.45, indicative of a shift in pore structuring into the mesopore domain (Figure 3-10 (c)). Consequently, a reduction in surface area (S$_{BET}$ = 116 m^{2}g^{-1}) and total pore volume resulted (V$_{total}$ = 0.10 cm^{3}g^{-1}). The addition of the swelling agent resulted in a bimodal pore size distribution with a new maximum at 4.0 nm in the mesopore domain and a discrete micropore peak at 1.0 nm (e.g. from template removal in mesopore walls) (Figure 3-10 (d)). Correspondingly, mesopore volume was enhanced as a proportion of the total pore volume, increasing from ~ 20 % in C-MPG1-*micro*, to ~ 60 % upon addition of TMB, for C-MPG1-*meso*.

Mechanistically, the added TMB is believed to interact with hydrophobic PPO moieties, thus swelling the spatial volume of the hydrophobic region, which in turn results in the observed pore expansion into the mesopore range as observed in more classical inorganic templating examples. [37-38]

It is presumed that carbonaceous crystal growth is determined by the rate of hexose dehydration (i.e. the generation of hydroxymethyl furfural (HMF)) and subsequent polymerisation reactions. Relatively slow dehydration and strong hydrogen bonding interactions between HMF and the PEO segments of the F127 template favour the growth of the templated, almost perfect single crystalline carbonaceous structures.

3.2.3 Naturally Inspired Systems: The Use of Natural Templates

The organisation of organic and inorganic matter at the nanometer scale is exemplified best by biological materials systems, and the development of novel materials mimicking or deriving inspiration from these natural systems is a dominant theme in materials chemistry, with one aim to produce material systems the same efficiency and selectivity as those provided by Nature. [39]
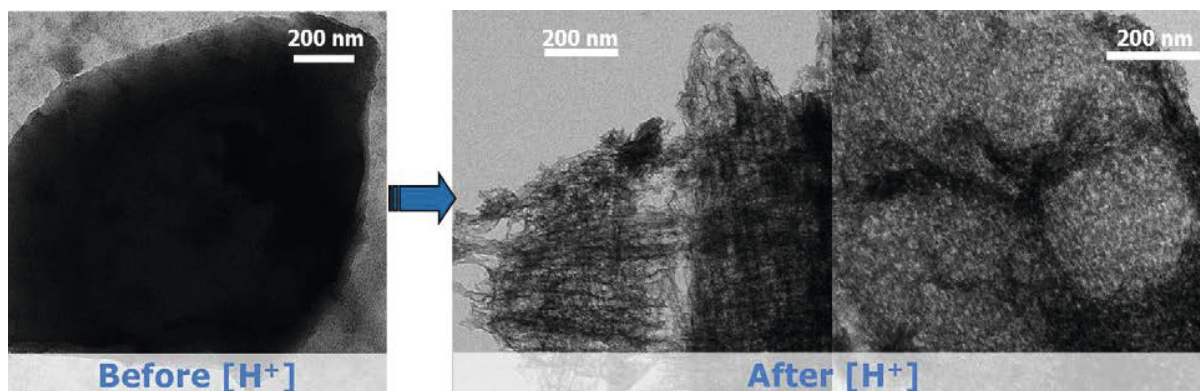
Figure 3-11: Prawn shell-derived carbons *via* HTC processing and post thermal treatment at 750 °C; Acetic Acid [H+] is used to remove the CaCO$_3$ component (reproduced from reference [42]).

In this regard, biominerals are mostly natural inorganic/organic (e.g. polysaccharide) composites that perform as structural supports, mineral storage, and protective surfaces. [40] Self-assembly of polysaccharides into organised structures with a cooperative inorganic partner such as CaCO$_3$, produces lightweight and dimensionally strong natural composites, as demonstrated by the exoskeletons of crustaceans and insects, [41] where the polysaccharide content is sufficiently high to enable a follow-up conversion chemistry. The inorganic and organic components are often

organised into nanoporous sized domains, and replication/mimicking of these systems potentially can lead to the design of novel advanced materials

Our group reported on the hydrothermal carbonisation of crustacean exoskeletons, namely prawn and lobster shells into nanostructured (nitrogen-doped) porous carbonaceous materials (Figure 3-11). [42] Marine derived crustacean shells are composed of the nitrogen containing polysaccharide, chitin (poly-β-(1→4)-N-acetyl-D-glucosamine) and an inorganic component (e.g. $CaCO_3$). Such high volume industry shell waste represents an inexpensive, accessible source of nitrogen-containing biomass that does not directly impact the food chain. These exoskeleton biocomposites represented useful precursor biomasses for the preparation of porous carbons, whereby the organic component is carbonised in the presence of the (structure donating) inorganic component $CaCO_3$, which finally could be removed with the use importantly from a process point, a weak (waste) Brønsted acid, Acetic Acid (e.g. Vinegar). These acids are to be compared to the more aggressive reagents usually employed in inorganic template removal in conventional mesoporous carbon synthesis, for instance HF/NH4F (aq) or caustic NaOH conditions. [43]

The use of nitrogen containing polysaccharide-derived biomass is an important aspect, as it directly allows the preparation of especially useful nitrogen doped carbon materials with improved performance range (e.g. for electrodes for supercapacitors [44] or fuel cells [45]). We will provide detailed aspects of such improved applications in Chapter 4 and especially Chapter 5.
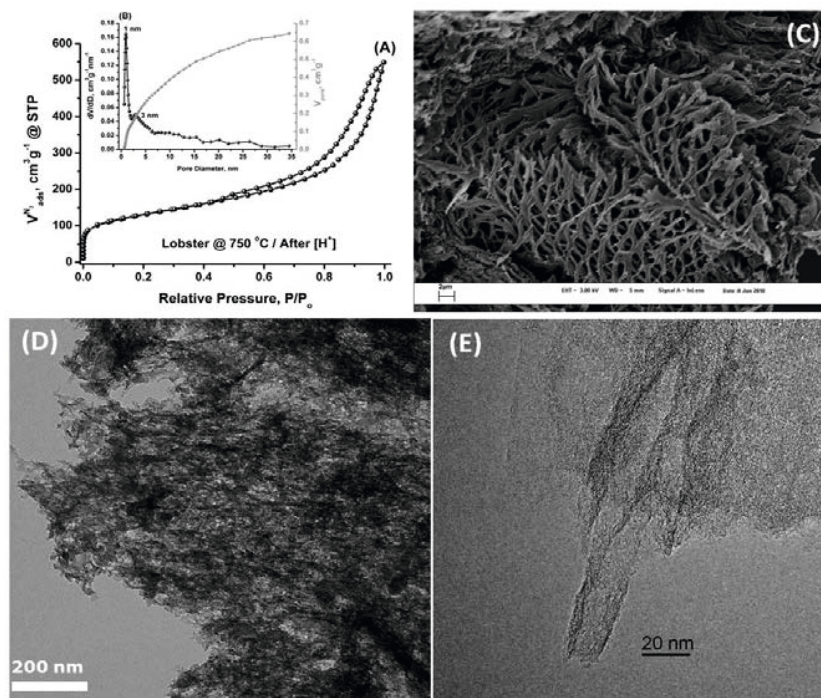
Figure 3-12: Lobster shell-derived HTC materials (and thermal treatment at 750°C); (A) N$_2$ sorption isotherm; (B) corresponding NLDFT pore size distribution; (C) SEM image of the macromorphology; (D) TEM and (E) HRTEM images of the carbon nanostructure (adapted from [46]).

N-doped carbon synthesis from crustacean shells such as for example lobster shells [46] would not only be beneficial from an economic standpoint, but also allow a simple route to the introduction of material dopant within carbon structures that would be almost impossible to reproduce synthetically (Figure 3-12); particularly advantageous in high value end applications. Nitrogen doping of carbons is for instance known to enhance material electrical conductivity, as the introduction of the N heteroatom into the graphitic structure contributes further electron carriers in the conduction band. [47] Further discussion regarding the heteroatom doping of hydrothermal carbon structures will be developed in Chapter 4, while the use of these materials as electrodes in super capacitors or heterogeneous catalyst supports will be discussed in Chapter 5.

3.3 Carbon Aerogels

Aerogels are known in a great variety of compositions and are used in a manifold of high - end applications including chromatography, adsorption, separation, gas storage, detectors, heat insulation, as supports and ion exchange materials. [48-49] Without doubt, silica aerogels are the most prominent and developed materials in this field, as they have revolutionised high pressure

liquid chromatography (HPLC), allowing highest resolution and fast separation at the same time. [50] Silica however also has some chemical disadvantages, and in 1987, Pekala *et al.* described for the first time organic aerogels as an interesting alternative. [51] Aerogels are defined by the *IUPAC* as non‑fluid networks composed of interconnected colloidal particles as the dispersed phase in a gas which is usually air. Typically an aerogel is formed by supercritical drying of the wet colloidal gel. Their characteristics include interconnected large diameter mesopores, low material density ($\rho \sim 0.004 - 0.5 \, \text{g cm}^{-3}$) and high specific surface area. The formation of colloidal gels is a "*bottom up*" synthetic process following the well‑established sol‑gel chemistry where colloidal particles form at first and then are aligned and condensed by thermodynamic forces. [52] Therefore the aerogel synthesis, achieved *via* the HTC processing of sugars, is of significant interest, not only from the viewpoint of green chemistry but also with application potential in mind. [53]

The exciting new HTC system was further investigated, especially in terms of particle size and porosity control. The results should be related to the well‑known trends in the RF system. Hierarchically structured but also inexpensive porous organic aerogels are capable of competing with their inorganic (*e.g.* silica) counterparts in sorption and insulation applications. [53] The most common organic aerogels are the aforementioned RF systems. [52] Here the formation of the gel phase occurs through the catalysed polycondensation of the reactive precursors in water. The whole gel formation can take several days. A well‑developed microstructure is also crucial for the following drying procedure to achieve the organic aerogels. The solvent has to be removed from the pores, while the structure has to withstand capillary forces induced by evaporation. Some investigations on this topic have been summarised by Job *et al.* [54] So far supercritical drying is still the most prominent procedure used to minimise the effects of capillary collapse.

Besides being highly porous and lightweight, another advantage of organic aerogels is the possibility to introduce electric conductivity by converting them into carbon aerogels, thus accessing electrical / electrochemical applications like batteries, [55] supercapacitors, [56] and as conductive supports as cathodes for fuel cell applications. [57] For those applications, it is important to have additional control over micro- and mesoporosity development. As it is possible to subtly influence and design material nanoscale structuring by chemical means, such that carbon aerogels can also be classified as nanostructured carbon. To convert polymers into carbon aerogels, usually pyrolysis is employed (*e.g.* T > 500 °C). The carbonisation process leads to a

loss of oxygen and hydrogen functionalities and therefore more condensed carbon structures. [57] Finally, depending on the pyrolysis temperature and the respective precursor chemistry ("graphitisability") of the former organic structure, an electrically conductive carbon network is achieved and can be used for a wide range of applications. A review article on RF - based organic and carbon aerogels was published by Al - Muhtaseb *et al.* [58] In the following section four promising routes to the formation of HTC aerogel materials are introduced and discussed.

3.3.1 Ovalbumin / Glucose-derived HTC Carbogels

Moving away from the use of templates, the introduction of secondary biomass precursors (e.g. proteins) has been found to have interesting consequences on the porosity, morphology and texture of the resulting HTC materials. Baccile *et al.* first reported that throughout the addition of the glycoprotein, ovalbumin, at variation concentrations, carbonaceous nanoparticles or continuous nanosponges with high specific surface areas can be efficiently produced. [59] Taking this approach one step further, it was found that under the right HTC processing conditions of temperature, time, drying technique (e.g. supercritical CO_2 extraction) and ovalbumin concentrations, it is possible to synthesis highly functional, low density, nitrogen-doped HTC monolith materials; termed *Carbogels* (Figure 3-13) [60] Commonly available inexpensive proteins such as ovalbumin are interesting additives for the HTC process, being H_2O soluble, nitrogen rich and having the potential to act as surface stabilizing / structure directing agents during the formation of the evolving hydrothermal carbon network. After supercritical drying of the recovered gel product, a low density monolith product is produced (Figure 3-13). The material was then characterised by solid state NMR, FT-IR and XPS.

Qualitative bulk ^{13}C NMR analysis indicates distinct resonances in the $\delta = 0 - 60$ ppm region for sp^3 aliphatic "C" and at $\delta = 29.8$ and 52.9 ppm for methyl and/or methoxyester groups, [61] whilst sp^2 "C" resonances ($\delta = 90 - 160$ ppm) are relatively pronounced, indicative of a strong aromatic *Carbogel* character at this low preparation temperature (Figure 3-13(A)). Further resonances at $\delta = 128.8$ and 150.8 ppm relate to all-carbon aromatics and poly(furan)-type networks respectively. [36] The intense resonance at $\delta = 172.9$ ppm for carboxylate-type groups, and partially resolved higher resonances for ketones /aldehydes ($\delta > 200$ ppm) are significantly different to previously reported NMR analyses of hydrothermal carbons. Notably resonances are relatively sharp and decoupled, indicating a rather mobile (polymeric) nature to material structure.
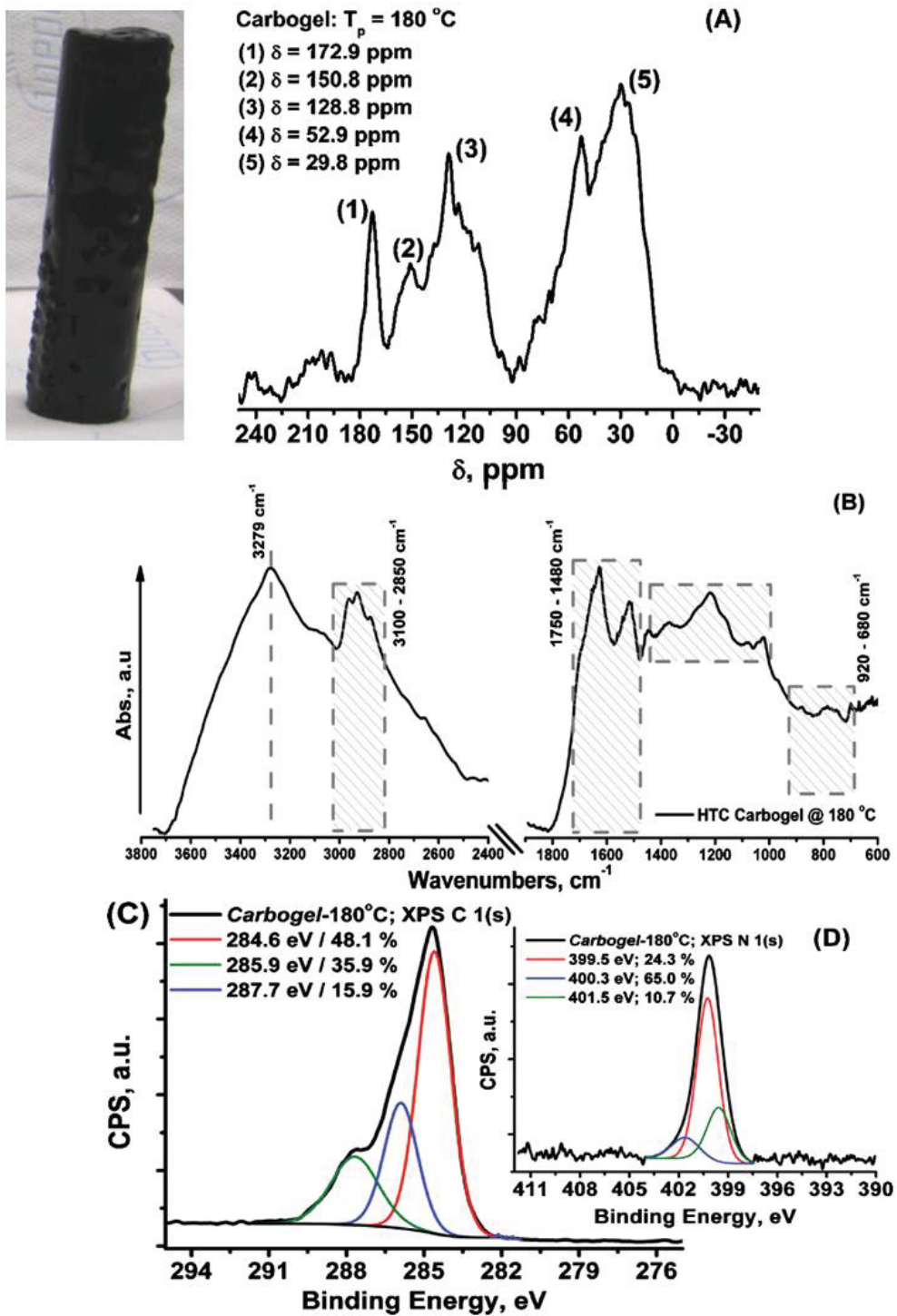
Figure 3-13: Characterisation of hydrothermal Glucose / albumin Carbogel monolith (photograph) product by (A) 13C CPMAS NMR; (B) ATR-FTIR; and high resolution XPS analysis of the (C) C 1(s) and (D) N 1(s) photoelectron envelopes (adapted with permission from [60])

FTIR analysis indicates carbonyl/carboxylic features (at 1750–1480 cm^{-1} (e.g. ν(C=O) ~ 1626 cm-1)) mixed with N-containing groups (e.g. amines at 1580 cm^{-1}) (Figure 3-13 (B)). [62] A band at 1666 cm^{-1} corresponds to amide C=O groups whilst a band at ~ 1076 cm^{-1} is assigned to the C-N bending mode. There are also possible contributions in this region from a variety of pyridinic / pyridonic and pyrrolic-like structures. [63] The band at 1516 cm^{-1} is reflective of conjugated/condensed O-containing groups (e.g. C=C–O; "Furans"). A broad composite spectral band in the 900 – 720 cm^{-1} region, assigned to C–H (out-of-plane) bending modes, reflects a wide range of (N-containing) aromatic groups. [63]

High resolution C 1(s) XPS analysis reveals three distinct binding energies of 284.6 eV (C–C/–CH$_x$; 48.1 % area), 285.9 eV (C–N bond: 35.9 %area) and 287.7 eV (–C=O/–C(O)N– (amide); 15.9 %area) (Figure 3-13 (C)). N 1(s) envelope analysis indicated a high pyrrolic surface character (400.3 eV; 65.0 % area), contributions from 1°/2° amines (399.5 eV; 24.3 % area) and pyridinic/quaternary-type motifs (401.5 eV; 10.7 % area) (Figure 3-13 (D)). [64] Both bulk elemental analysis and surface XPS quantification demonstrate the uniform N incorporation into both the carbon structure and surface (e.g. N% = 7.5 (elemental (combustion) analysis) / 6.8 (XPS survey scan quantification)), whilst SEM images indicate a continuous interlinked N-doped fibrous monolithic macromorphology (Figure 3-14 (A) and (B)). The early onset of aromatization and relative absence of keto-groups was believed to be a consequence of the reaction with protein (e.g. Maillard reaction), significantly altering the chemical hydrothermal charbonisation cascade. Details regarding Maillard chemistry and the reactions occurring during the HTC formation of N-doped carbons will be provided in Chapter 4.
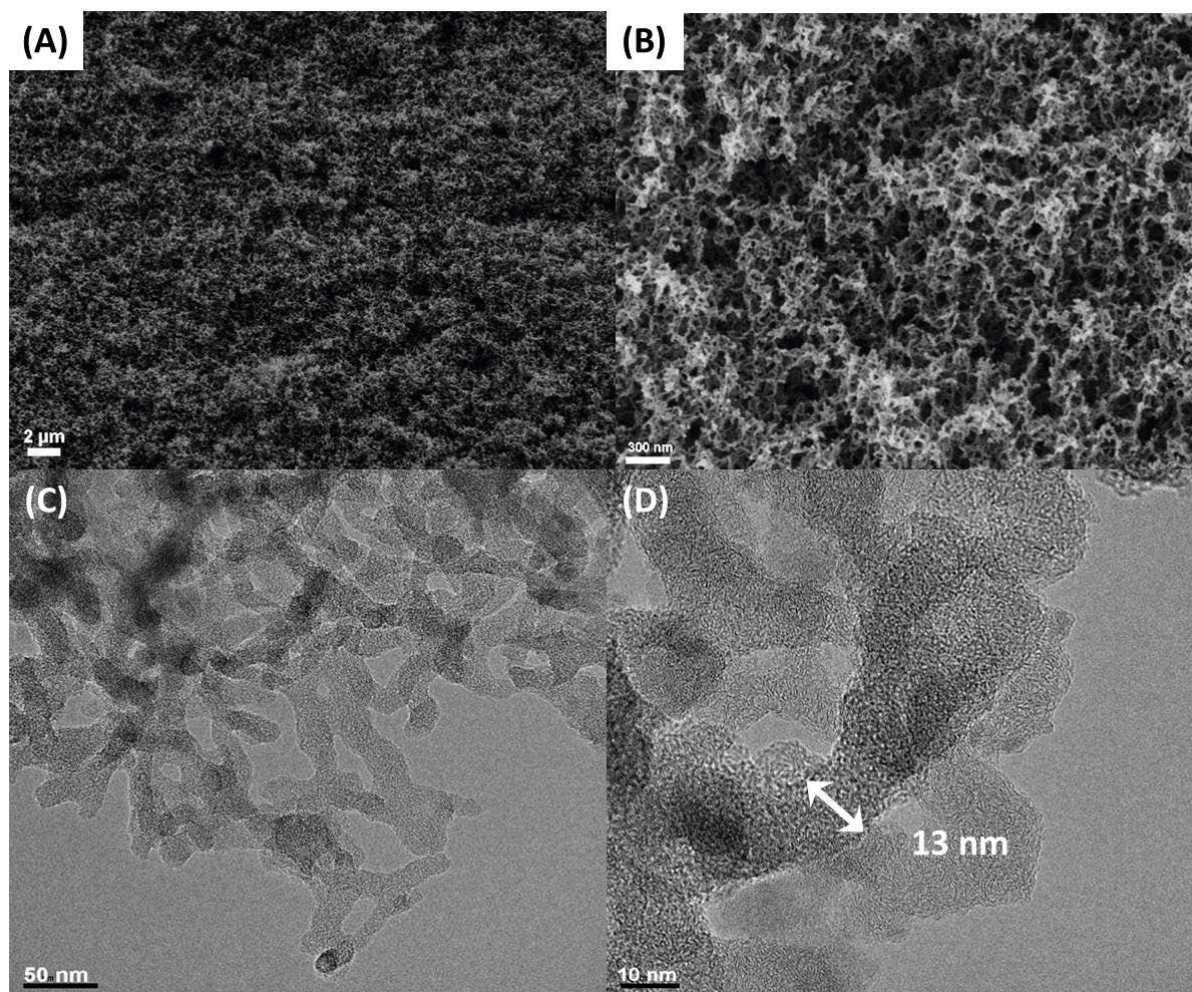
Figure 3-14: (A) and (B) SEM images of the aerogels; (C) and (D) HRTEM images of aerogels thermally treated at 750 and 900 $^{\circ}$C respectively (reproduced from reference [60])

Using the dried hydrothermal Carbogel, derivatives were prepared using thermal charbonisation (T_p) in the 350–900 °C range to manipulate surface chemistry (e.g. C or N condensation state) and demonstrate material flexibility (See Chapter 4 for further discussion relating to heteroatom doping).

The resulting Carbogels presented Type IV/H3 reversible sorption isotherms, where hysteresis loops were found to be limited at low T_p (e.g. $\leq$ 350 °C), developing through the intermediate T_p range, stabilising to a more classical Type IV/H3 profile with a more open hysteresis, at T_p = 900 °C (Figure 3-15).
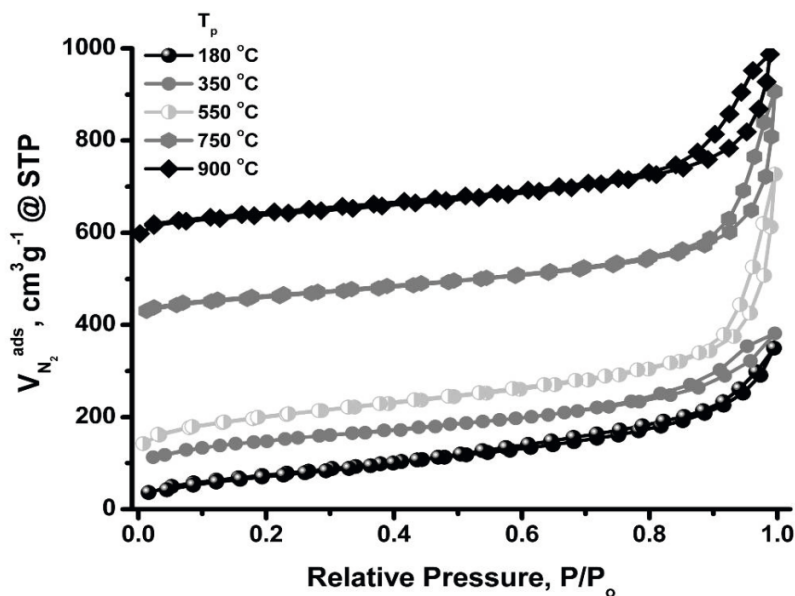
Figure 3-15: N$_2$ sorption isotherms for the Carbogel-180°C and carbonaceous derivative therefrom prepared at increasing carbonisation temperature.

Material surface areas irrespective of T_p are considerably higher (S_{BET} > 240 m^{2}g^{-1}) than those previously reported values for (non-templated) hydrothermal carbon materials (but lower than more traditional carbon aerogels), here passing through a maxima at T_p = 550 °C as strongly micropore-bound decomposition products are thermally removed. A reduction in V_{micro} at higher T_p then occurs as the carbon network undergoes further chemical condensation and micropore closure. Mesoporosity as a proportion of total porosity stabilizes after T_p = 550 °C, the result of network contraction, reaching promising values of V_{meso} > 0.45 cm^{3}g^{-1}. For all materials, broad pore size distributions were observed with partially defined diameter maxima in the micropore range (pore diameter ~ 1 nm) and lower mesopore region (pore diameter ~ 3 nm) although significantly volume contributions are made from all mesopore size domains. High resolution TEM images of the resulting carbonised materials maintained the continuous highly porous nature of the *Carbogel* parent (Figure 3-14 (C) and (D)). Material in all cases presented highly (meso)porous nanomaterial structuring, with image analysis demonstrating elegantly the unusual coral-like continuous carbonaceous hierarchical nano-architecture. The hyper-branched network has walls of disordered graphitic-like sheets of *ca.* 10–15 nm thickness composed of ~2–3 short carbon layers stacking locally in no preferential long range (> 100 nm) orientation.

It is proposed that the protein (and associated Maillard products) act as surface stabilising /

structure directing agent(s) to create a stable heteroatom (N) doped carbon scaffolds possessing co-continuous flexible porosity, tuneable chemistry and structural size (Figure 3-14). The reaction of the reducing sugar and free amino groups of the protein is provided to dramatically alter the HTC cascade reaction, leading to branched Carbogel networks with different morphologies from previously reported HTC materials. Given the structural similarities with corresponding monolithic silicas, [50] it was speculated that a similar underlying formation mechanism resulted in the formation of the continuous porous structure. This involves sugar dehydration, carbon precursors demix from the aqueous phase in a spinodal fashion, which in this case is stopped from further ripening towards droplets by an early and efficient reaction with the water-based proteins. As will be discussed in the next chapter (Chapter 4), material chemistry (e.g. nitrogen bonding motifs) can simply be directed *via* selection of a post-synthesis thermal treatment temperature. The applications of these monoliths in catalysis will be discussed later in this thesis (Chapter 5).

3.3.2 Borax-mediated Formation of HTC Carbogels from Glucose

In the context of appropriate HTC catalysis, borates, (*e.g.* boric acid and borax) are well - known for their strong interaction with vicinal - dihydroxy compounds, such as glucose and fructose. Negatively charged borate - diol and borate - didiol complexes are formed which change the reactivity and physical properties of the sugar solutions. [65] [66] We have recently reported on the exploitation of this interactions for the synthesis of hydrothermal carbonaceous gels. [67] As an example, hydrothermal treatment of 20 ml of 30 % glucose solution with 500 mg of borax at 200 °C for 20 h resulted in the formation of dark brown, mechanically stable monoliths (Figure 3-16). The monoliths are composed of aggregated nanometre sized spherical particles, leading to a colloidal hydrogel. Macro- and mesoporosity can be observed generating a lightweight carbon material exhibiting hierarchical porosity. After purification by extraction with water and ethanol, elemental analysis demonstrated a chemical composition similar to conventional HTC (*i.e.* ~ 64 % C; ~ 5 % H).
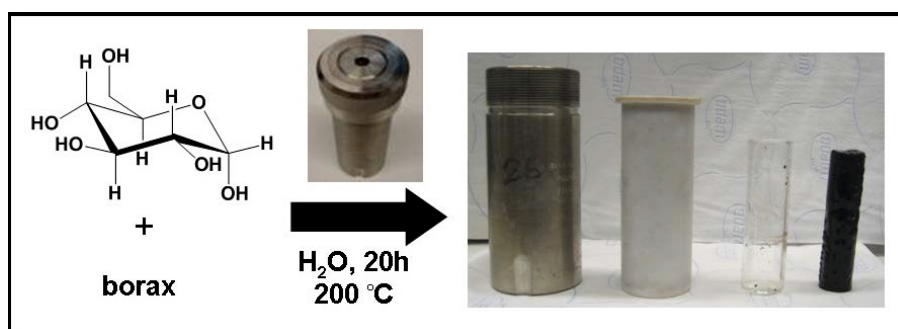
Figure 3-16: Scheme of the hydrothermal reaction of glucose in presence of borax resulting in a black monolith (reproduced from reference [67]).

Since additionally the yield was clearly improved compared to hydrothermal treatment of pure glucose under the same reaction conditions, studies of the reaction time were carried out (solid yield improved from 26 % to 44 %, carbon yield from 42 % to 73 % for the HTC of 20 ml 30 % glucose solution at 200 °C for 19 h). 20 ml of 30 % aqueous glucose solutions with and without 500 mg borax were heat treated at 200 °C for 1, 2, 3, and 4 hours for comparison (Figure 3-17).

Figure 3-17: Comparison of HTC products from glucose with and without the addition of borax after different reaction times. Shown are results from 20 ml glucose solutions (30 %) with (cat.) and without (ref.) the addition of 500 mg of borax for 1, 2, 3 and 4 hours at 200 °C (reproduced from reference [67])

The accelerated carbonisation by borax, (*i.e.* higher yields in shorter times with an onset at lower temperatures), could be explained by catalysis of glucose dehydration. Referring to the reactivity of borax with sugars, [68] [69] one can expect that the interaction of borax with the vicinal diols leads to negatively charged boron - diol or boron - didiol complexes, enhancing the reactivity in the dehydration of glucose to HMF. Concurrently to our research Riisager *et al.* have presented a study describing the impact of boric acid on the hydrothermal dehydration of glucose, confirming the proposition that borax does in fact catalyse the dehydration of glucose. [70] Further studies indicates that catalytic activity may arise from the stabilisation of intermediates appearing within the isomerisation of glucose to fructose mediated by negatively charged boron - diol complexes

with their results correlating with the lowered activation energy to the corresponding coordinated intermediate structures. [68] However, at the conditions used during HTC, the Lobry de Bruyn - Alberda van Ekstein isomerisation already converts glucose into fructose. [69] Compared to the dehydration of fructose, the hydrothermal carbonisation is a rather slow process and therefore should not be affected by the accelerated isomerisation.

To further investigate the role of borax, a HTC system employing borax and fructose as precursor was investigated, whereby 20 ml of 30 % aqueous fructose solutions with and without 500 mg borax were heat treated at 140 °C for 2, 3, and 4 hours for comparison (Figure 3-18). It is clear that in this case, borax also accelerates the hydrothermal carbonisation of fructose. In addition to the improved dehydration of glucose, the subsequent carbonisation / resinification reactions occurring in a later stage are therefore catalysed, as well.

Figure 3-18: Comparison of HTC products from fructose with and without the addition of borax after different reaction times. Shown are results from 20 ml glucose solutions (30 %) with (cat.) and without (ref.) the addition of 500 mg of borax for 1, 2, 3 and 4 hours at 140 °C.

Particle aggregation indicates that borax also promotes cross - linking, which is essential for the gelation process and monolith evolution. It has to be mentioned, that HTC of pure HMF with borax as additive leads to perfect gels as well. Regarding the mechanism of the catalysis, borates are known to catalyse esterification [71] and decarboxylation. [72] However, these properties at least do not obviously affect the HTC reaction pathways. One characteristic, also in the context of HTC, is the formation of boron - dioxo complexes (Figure 3-19). It is proposed that borax coordinates sugars and thereby competes with the aldehyde - protecting acetalisation reaction of sugars with HMF, eventually promoting aldol condensations of the "*free*" HMF.
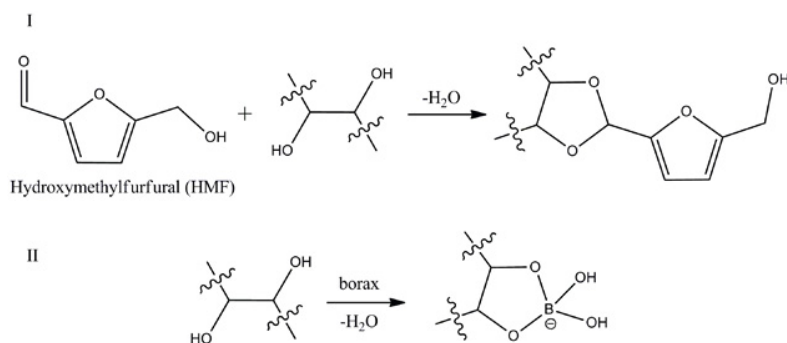
Figure 3-19: Side reactions (I acetalisation; II borate-diol complexation) within the hydrothermal carbonisation of sugar (herein simplified as dioles) in the presence of borax (reproduced from reference [67]).

Representative of our reported system, four *Carbogel* examples were synthesised at different sugar / borax ratios denoted as *Carbogels X*, where *X* corresponds to the used amount of borax in milligrams while the amount of water and glucose was kept the same (20 ml 30 % glucose solutions). The *Carbogels* were produced by hydrothermal treatment of the solutions at 180 °C for 8 hours. Shorter reaction times resulted in the formation of unstable gels or sol - like suspensions. Under the reported reaction conditions, low density (*e.g.* $\rho \sim 0.12$ g cm^{-3}) *Carbogels* were produced of ~ 3.1 g mass with a carbon content of ~ 64 % (thus resulting in 80 % carbon yield with respect to glucose, the volume fraction of pores is $\Phi \approx 0.94$).

SEM and TEM image analysis of the resulting aerogels revealed the presence of very small, spherical HTC nanoparticles, aggregating to create a gel structure with hierarchical porosity. (Figure 3-20). With increasing system borax concentration, the microstructure becomes increasingly finer due to decrease in primary particle size (from A to D in Figure 3-20). The decreasing particle size with decreasing sugar / borax ratio is in accordance to the structure control trends in the classical RF system. Both SEM and TEM images reveal the *Carbogel* network to be composed of uniform sized, aggregated, spherical nanoparticles generating the desired hierarchical porous network. It is worth mentioning that the particle size control is not limited to the sub - 50 nm range. Experiments with less borax and / or longer reaction times lead to gels with particle size bigger than 100 nm range and therefore very likely cover the whole possible range underneath classical HTC particle dimensions.
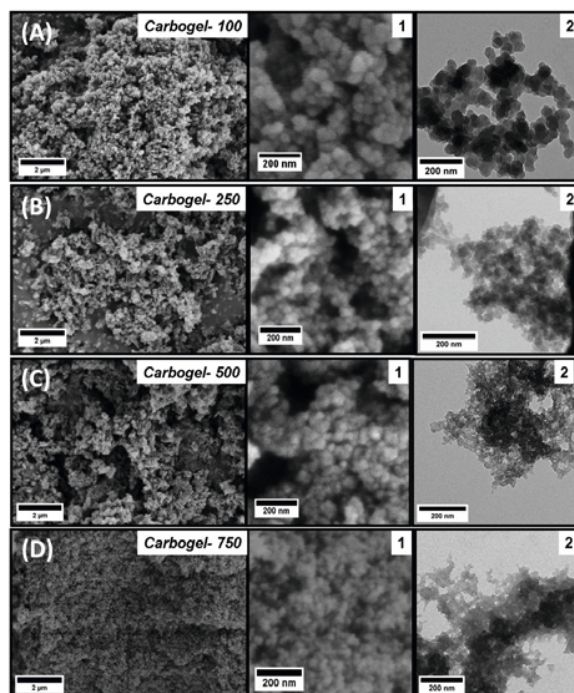
Figure 3-20: SEM and TEM images of Carbogels - X prepared from different amounts X of borax (in mg), with the same amount of water and glucose. SEM overview images are presented on the left side, while higher resolved SEM and TEM images are for each Carbogel indicated as 1 and 2 (reproduced from reference [67]).

Thermal treatment of the dried hydrophilic gels under nitrogen atmosphere at 550 °C and 1000 °C (heating rate = 10 K min^{-1} followed by an isothermal period of 5h) leads to uniform dimensional shrinkage of the monolith macrostructure with preservation of the overall cylindrical shape.

As observed *via* TEM, at higher sugar / borax ratios the local nano- and microstructure in terms of particle shape and connectivity are also retained upon heating to these carbonisation temperatures (Figure 3-21). However, aerogels composed of very fine, sub - 10 nm particles do not completely withstand the carbonisation process and shrink to more condensed systems. Determination of the particle size *via* TEM (Figure 3-21*Carbogel 750@1000 °C*) indicates that also the primary particle size decreases upon carbonisation, in accordance with the mass loss throughout carbonisation.

In addition, nitrogen sorption measurements were carried out to investigate the porosity of the as - formed hierarchical carbon structures (Figure 3-22). With increasing sugar / borax ratio, the aerogels show an increasing gas uptake and a higher specific surface area due to the presence of

smaller primary nanoparticles. *Carbogel - 750* breaks this trend, as the $S_{BET} = 209 \text{ m}^2 \text{g}^{-1}$ is decreased compared to $233 \text{ m}^2 \text{g}^{-1}$ for *Carbogel - 500*. In accordance with the TEM images (Figure 3-21), this reflects the collapse of the very fine structure within the freeze drying process, *i.e.* 7 nm disordered carbon cannot withstand the capillary forces of a pore of similar size. This is well known from corresponding, even rigid polymer structures. [73]
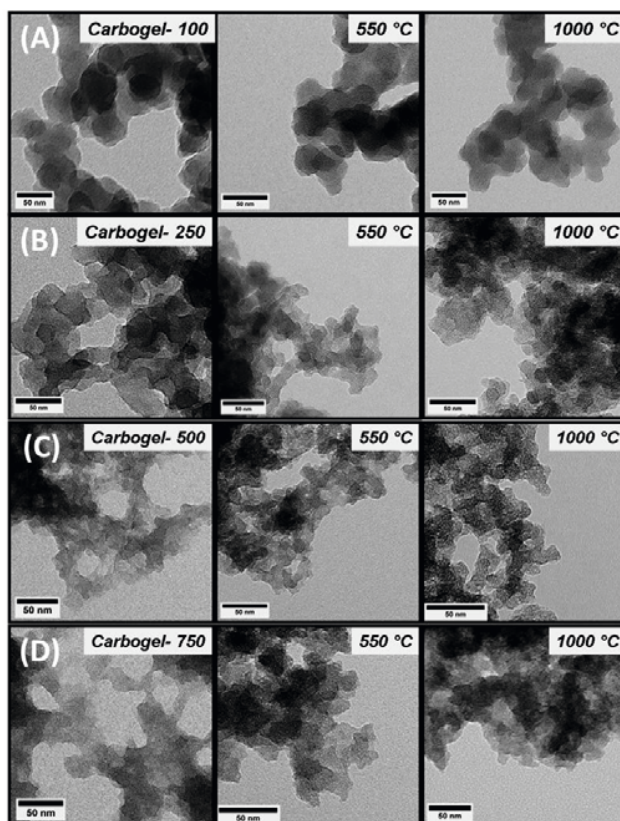
Figure 3-21: Comparison of TEM images of as - prepared Carbogels - X and the respective post - carbonised samples at 550 °C and 1000 °C, where X stands for the used amount of borax within the synthesis protocol (reproduced from reference [67]).

Regarding gas sorption behaviour for the post - carbonised systems, a strong increase of the specific surface area especially after thermal treatment at 550 °C / N_2 is observed. High surface area materials exhibiting $\sim 600 \text{ m}^2 \text{g}^{-1}$ (*Carbogel - 250 @ 550 °C*) are accessible even without chemical activation using the relatively simple synthetic route and conditions. The carbonised *Carbogel - 100* and *Carbogel - 250* samples show a trend of increasing surface area with increasing sugar / borax ratio, the result of a reduction in the primary particle size. The high borax structures are again already too fine to withstand carbonisation completely, resulting in

partial structure collapse and a marked reduction of the accessible surface and overall porosity. The interplay of enhancement of surface area and fragility of the architecture is also nicely reflected in the high temperature data: carbonisation at higher temperatures (*i.e.* 1000 °C) produces lower surface area materials, although the primary particle size has been dramatically decreased.

A more quantitative porosimetry analysis of the so far optimised products, *Carbogel - 250* and the corresponding post - carbonised *Carbogels,* was performed (Figure 3-22). Only marginal hysteresis and lack of defined plateau region as relative pressure reaches unity (*i.e.* $p / p_0 \sim 1$) of the sorption profile, reflects the combination of a slit - type micropore structure combined with a high external surface area due to small, interconnected primary carbon nanoparticles. The "*exploding*" sorption capacity at relative pressures near unity reflects the presence of excessive large diameter mesoporosity and macroporosity, which can be expected from a material with 94 vol. % overall porosity.
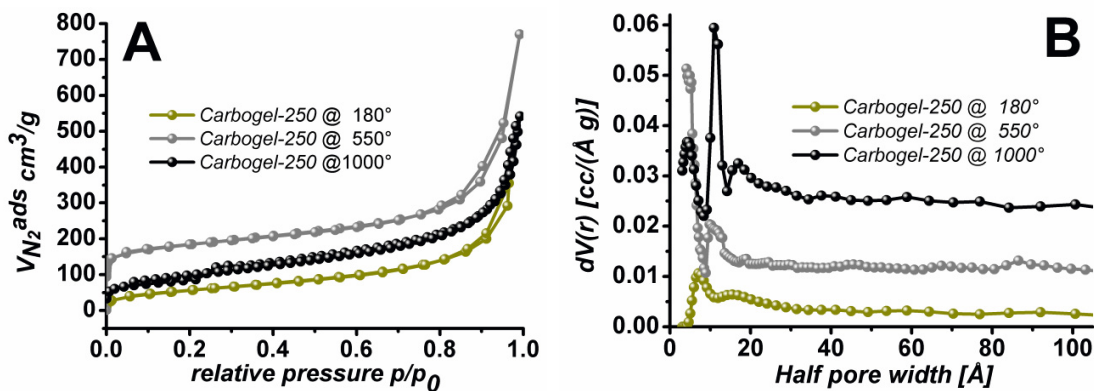
Figure 3-22: Comparison of nitrogen sorption analysis of as - prepared Carbogel - 250 and the respective products from post - carbonisation at 550 °C and 1000 °C. A) Nitrogen sorption isotherms B) Pore size distributions (reproduced with permission from reference [70]).

As - prepared *Carbogels* show in general limited microporosity ($V_{micro} \leq 0.10$ cm^3 g^{-1};), which is very typical for ductile, polymer - like behaviour of the walls. [73] Heat treatment at 550 °C significantly increases this micropore content to about 0.25 cm^{3}g^{-1}, which means that the material now behaves as a rigid carbon scaffold post - carbonised carbon aerogels showing isotherms (left) and pore size distributions (right). Also the mesopore volume is observed to increase nicely upon carbonisation at 550 °C ($V_{meso} > 0.5$ cm^{3}g^{-1} @ 550 °C), most likely as the result of material contraction / condensation processes opening up interstitial porosity between the primary

164

particles, which was closed ahead by ductile deformation. Interestingly, nitrogen sorption at *Carbogel - 250 @ 1000 °C* shows a loss both of micro- and mesoporosity. This means that the structure rearrangements observed by TEM on a larger scale are also found on the molecular and low nanometre scale: the whole structure simply sinters due to temperature induced carbon - carbon rearrangements.

To investigate the applicability in electrochemical applications (*i.e.* as electrode materials in various systems), the electrical conductivities of pulverised and pressed Carbogel - 250 before and after thermal treatment under inert atmosphere was measured. Electrochemical measurements were carried out with Gamry Reference 600 potentiostate (Gamry Instruments) and Gamry EIS 300 / Physical Electrochemistry software. The electrical conductivity was evaluated applying a simple resistor - model on potentiostatic impedance spectroscopy at 1 - 1000 Hz using a two electrode setup. The specific conductivities increase with increasing carbonisation temperature reaching 290 S m^{-1} at 1000 °C. These values are, considering the high porosity of the materials, comparably high and absolutely sufficient to support an electrode application. The hierarchical porosity of the monolithic Carbogels suggest the use of the material as electrodes for fast processes, were mass transport takes a crucial role.

3.3.3 Carbogels from the Hydrothermal Treatment of Sugar and Phenolic Compounds

Ryu *et al.* [74] shown that the hydrothermal charbonisation of sugars, *i.e.* xylose or fructose, in the presence of phenolic compounds can largely enhance the yield of the typical HTC microspheres, up to 20-fold through the addition of phloroglucinol. In this study, the authors suggest a possible mechanism where the phenolic compounds act as a cross-linker, *via* intermolecular condensation with dehydrated sugars, *i.e.* 5-hydroxymethyl-2-furaldehyde (HMF) or furfural, and/or hydrothermal carbon nuclei.[74] The higher reactivity of phloroglucinol, related to its electron density in 2, 4, 6 ring position, seems to involve a more efficient crosslinking without any additive,[74] while the use of resorcinol to design hydrothermal carbon materials implies the presence of a suitable catalyst.[75] According to the investigation by Katsoulidis *et al.*[76] on the solvothermal polymerisation of phloroglucinol and aldehyde derivatives leading to highly microporous polymers, electrophilic aromatic substitutions can also be considered as a possible mechanism pathway. This second route involves the covalent linking of a carbonyl group on

dehydrated sugar with two phloroglucinol moieties by eliminating a water molecule. [76]

Taking this "phenolic-sugar approach" one step further, it has been found that highly porous carbon aerogels can be obtained from phloroglucinol-monosaccharide mixtures without any catalyst or additive in hydroalcoholic media.[77] Since monosaccharides can be isolated from the cellulosic fraction of lignocellulosic biomass and phloroglucinol can be extracted from the bark of fruit trees, this approach constitutes an interesting renewable synthetic pathway.

As shown in Figure 3-23a, after hydrothermal treatment of fructose and phloroglucinol monomers at 180˚C for 20 h, smooth carbon-based wet gels were produced. After further CO_2 supercritical drying, the as-synthesised monolithic brown aerogels (Figure 3-23 b) depict an airy continuous interlinked macro-morphology made of small aggregated particles (Figure 3-23c). Transmission electron micrographs display a consistent hyper-branched structure with pores' diameter up to 100 nm (Figure 3-23d) and walls' thickness of about 15 nm (Figure 3-23e). Nitrogen sorption experiments performed on these aerogels depict consistent mixed isotherms (Figure 3-24). While the first steep rise at low relative pressures (*i.e.* from 0 to about 0.05) is characteristic of microporous materials, the gradual increase in sorption volume from 0.1 suggests a multilayer adsorption within the bigger pores. Since the nitrogen sorption curves show unclear hysteresis, we can assume type IV (H3) / type II mixed isotherms, displaying both adsorption on open surfaces of macropores and volume filling of smaller mesopores, associated with the capillary condensation phenomenon. This feature is in good agreement with TEM observations, highlighting a broad pore size distribution from few nanometers up to 100 nm (Figure 3-23d-e).

Depending on the synthetic pathway, the carbon-based aerogels present different porous characteristics (Figure 3-24). Two categories of aerogels were made. The first category are gels made with a lower amount of phenolic cross-linker and giving poor carbon yields (gels made from glucose or at a low hydrothermal temperature, 130˚C). These aerogels present BET surface areas lower than 610 m^2g^{-1} with a microporous contribution around 300 $m^2.g^{-1}$. Nevertheless, after further thermal treatment under inert atmosphere an increase in the total surface area, mainly related to a large rise in the microporous contribution was systematically noticed.
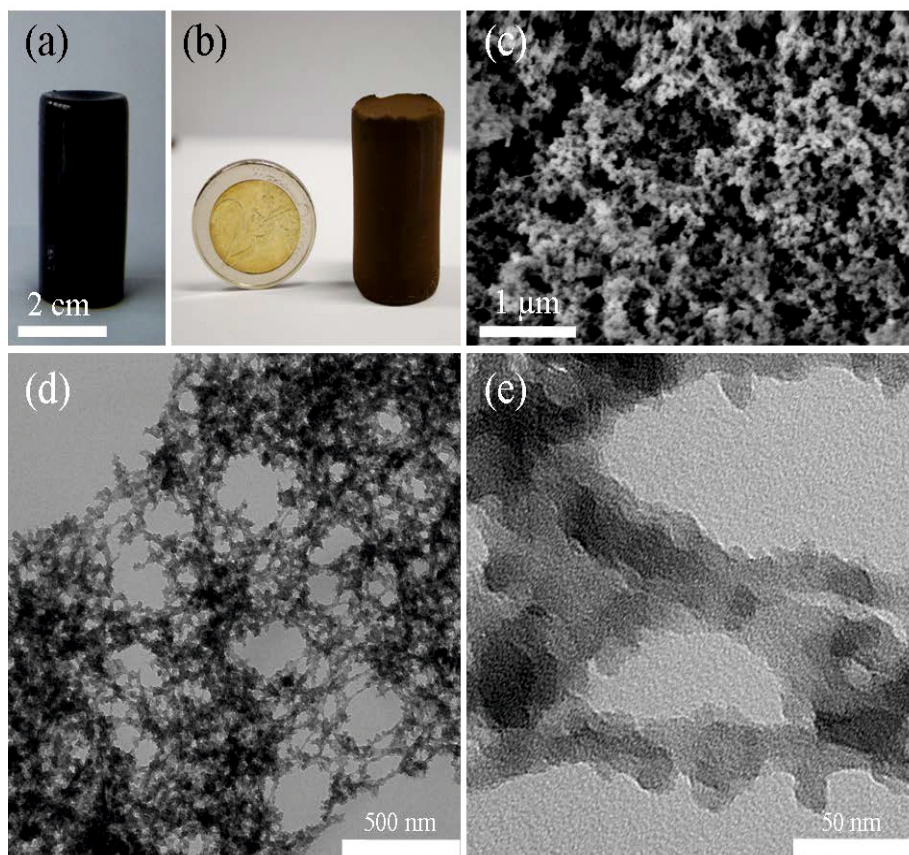
Figure 3-23: Pictures of a gel obtained from a mixture of phloroglucinol and fructose at a molar ratio ½ and HTC temperature of 180˚C, (a) before and (b) after CO2 supercritical drying. (c) SEM micrograph and (d-e) TEM micrographs of the corresponding supercritical-dried aerogel (taken with permission from [32]).

The second category corresponds to materials obtained from highly reactive monosaccharide-phloroglucinol systems (*i.e.*, typically from fructose and xylose made at high hydrothermal temperature, 180˚C). These aerogels exhibited a higher cross-linking level, involving a better preservation of the micro-mesoporous character of the scaffold after supercritical drying, leading to higher specific surface areas (up to 1100 $m^2.g^{-1}$), with a surprisingly high microporous contribution, around 650 m^2g^{-1}. After further thermal treatment a significant drop of the specific surface area can be pointed out, suggesting a large modification of the porous framework. Indeed, the noticeable macroscopic shrinkage of the carbon-based scaffold is also effective at the micro- and mesoscopic levels. After further pyrolysis, most of the shrunk micropores are probably too small to be detected by nitrogen sorption. However, the BET and mesoporous surface areas, about 650 and 150 m^2g^{-1} respectively, are still noteworthy. These carbogels are attractive as potential materials for separation, adsorption or heterogeneous catalysis.
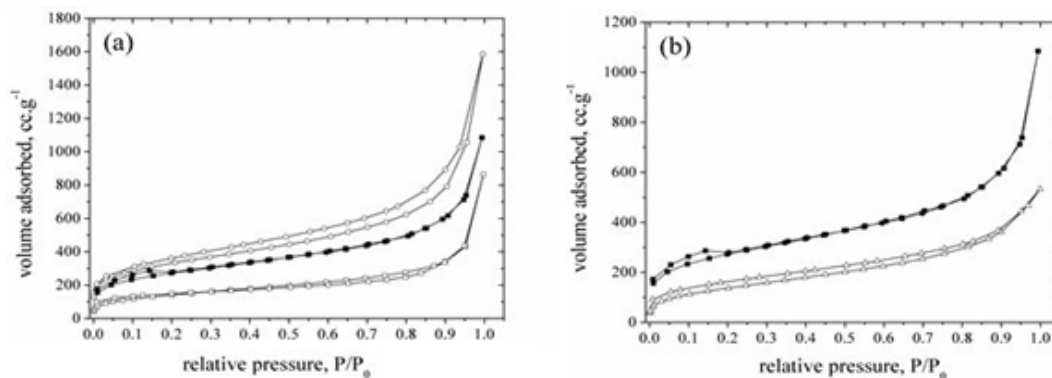
Figure 3-24: (a) Nitrogen sorption isotherms of aerogels obtained from hydrothermal treatment of phloroglucinol-monosaccharide mixture at a molar ratio ½ and temperature of 180˚C from ○ xylose, ■ fructose and □ glucose. (b) Nitrogen sorption isotherms of aerogels obtained from hydrothermal treatment of phloroglucinol-fructose mixture at 180˚C with a molar ratio of ■ 1/2 and Δ 1/7.

3.3.4 Emulsion-Templated "Carbo-HIPEs" from the Hydrothermal Treatment of Sugar Derivatives and Phenolic Compounds

When the aimed application of porous carbons involves the immobilization of bulky catalysts, such as proteins or bacteria, bigger macropores are essential to increase the accessibility of the supported biocatalysts, while reducing the low diffusion kinetics. This need is largely increased when the application involves the use of monolithic supports. [78] A rational pathway to increase pores' diameter of monoliths to the micro- or even millimetric scale is to combine the sol-gel polymerisation with a soft-templating approach, such as air-liquid foaming [79] or liquid-liquid emulsification.[80]

Particularly, the use of High Internal Phase Emulsion (HIPE) as a template to design macroporous polymers has been the center of attention since Barby *et al*.[81] developed the design of polyHIPEs in the early 1980s, from organic monomers such as styrene and divinylbenzene. This formulation involving a water-in-oil concentrated emulsion remains, by far, the most studied. Our research group reported for the first time, polyHIPEs, or more precisely "carbo-HIPEs" (carbo- for carbonised and HIPE for High Internal Phase Emulsion), were prepared from biomass-derivative precursors, *i.e.* furfural and phloroglucinol, using an oil-in-water concentrated emulsion.[82] These foams represent the first emulsion-templated carbo-HIPEs obtained from saccharide derivatives, leaving the beaten path of resorcinol/formaldehyde [83] and

divinylbenzene-based polymers. [84] Considering the hydrothermal charbonisation conditions (T ˚C > 130°C and relatively high pressures, ~ 10 bars), an oil-in-water direct emulsion cannot be stable. A pre-polymerisation of the monomers within the continuous phase was necessary before the hydrothermal treatment, in order to keep the integrity of the liquid-liquid foam. With this aim, phloroglucinol was used as a cross-linking agent, while iron (III) was employed as a Lewis acid catalyst, promoting the polycondensation between phenolic and furanic compounds, following a mechanism similar to the one described previously for the "phenolic-sugar approach". As shown in Figure 3-25 a, after a one-step synthesis, HTC macroporous monoliths were obtained. These materials depict a typical macromorphology made up of aggregated hollow-spheres (Figure 3-25 b), called *cells*. [80a] This macrostructure is directly induced by the polymerisation of the hydroalcoholic continuous phase of the direct emulsion. These *cells*, corresponding to the removed oil droplets, exhibit large diameters from 10 up to 50 μm. Furthermore, due to the interstices left in the continuous phase or by direct contact between two nearby packed oil droplets, these monolithic foams present narrower macropores, called *connecting windows*. [80a] This feature has been underlined both by scanning electron microscopy (Figure 3-25c), showing a highly interconnected macrostructure. Macroscopic pore size distribution obtained by mercury intrusion porosimetry performed on a carbo-HIPE after a further thermal treatment at 950 °C displays a main contribution centred at 3 μm, while two weak contributions, centred at 300 nm and 4 μm, can also be noticed. As a direct consequence of a high connectivity, the carbo-HIPEs depict a large macroporosity of about 98 %, together with total macroscopic cumulative volume and surface area respectively up to 18 cm^3g^{-1} and 300 m^2g^{-1}. [82]
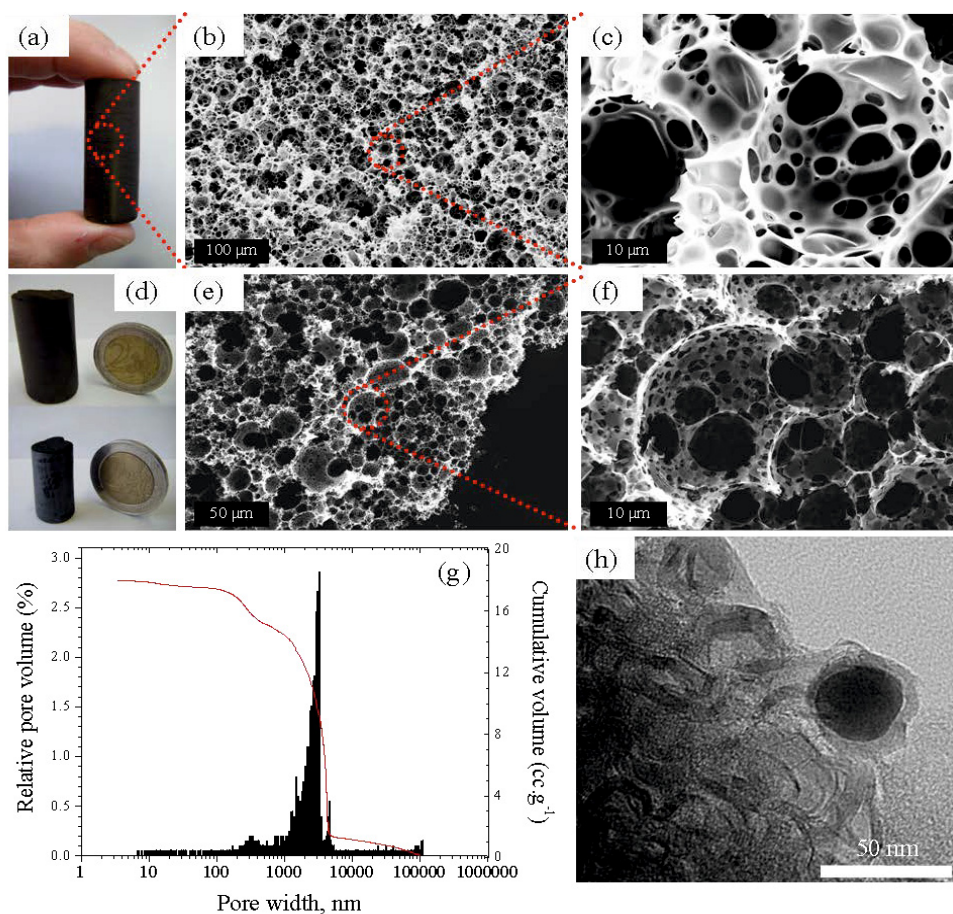
Figure 3-25: (a) Picture of an as-synthesised carbo-HIPE made at 130°C during 24h, after Soxhlet extraction and drying at 80 °C. (b-c) Scanning electron micrographs of a carbo-HIPE made at 130°C during 24h and synthesised with an oil volume fraction of 0.8. The micrograph (c) is an higher magnification of the micrograph (b). (d) Picture of an as-synthesised carbo-HIPE, after Soxhlet extraction and drying at 80 °C (top) and of the same monolith after further thermal treatment at 950 °C under nitrogen (bottom). (e-f) Scanning electron micrographs of a carbo-HIPE after further thermal treatment at 950 °C, synthesised with an oil volume fraction of 0.8. The micrograph (f) is an higher magnification of the micrograph (e). Pore size distribution obtained by mercury intrusion porosimetry (g) and transmission electron micrograph (h) of a carbo-HIPE after further thermal treatment at 950 °C under nitrogen.

Beyond a *cellular* macrostructure, these carbo-HIPEs depict, after further thermal treatment at higher temperature, highly micro- and mesoporous frameworks (Figure 3-26). [82] While the first contribution can be attributed to the physical activation induced by charbonisation, the mesopores contribution is related to the catalytic effect of the iron-based particles toward the graphitisation of amorphous carbons. [85] As shown in Figure 3-25h, at high temperature these metallic nanoparticles diffuse within the carbonaceous framework, while catalysing graphitisation preferentially on their surface, leading to hollow graphitic rings. As a direct consequence,

170

mesopore volumes up to 0.1 cm^3.g^{-1} were determined by the QSDFT theory, and BET surface areas of about 500 m^2.g^{-1} were reached.
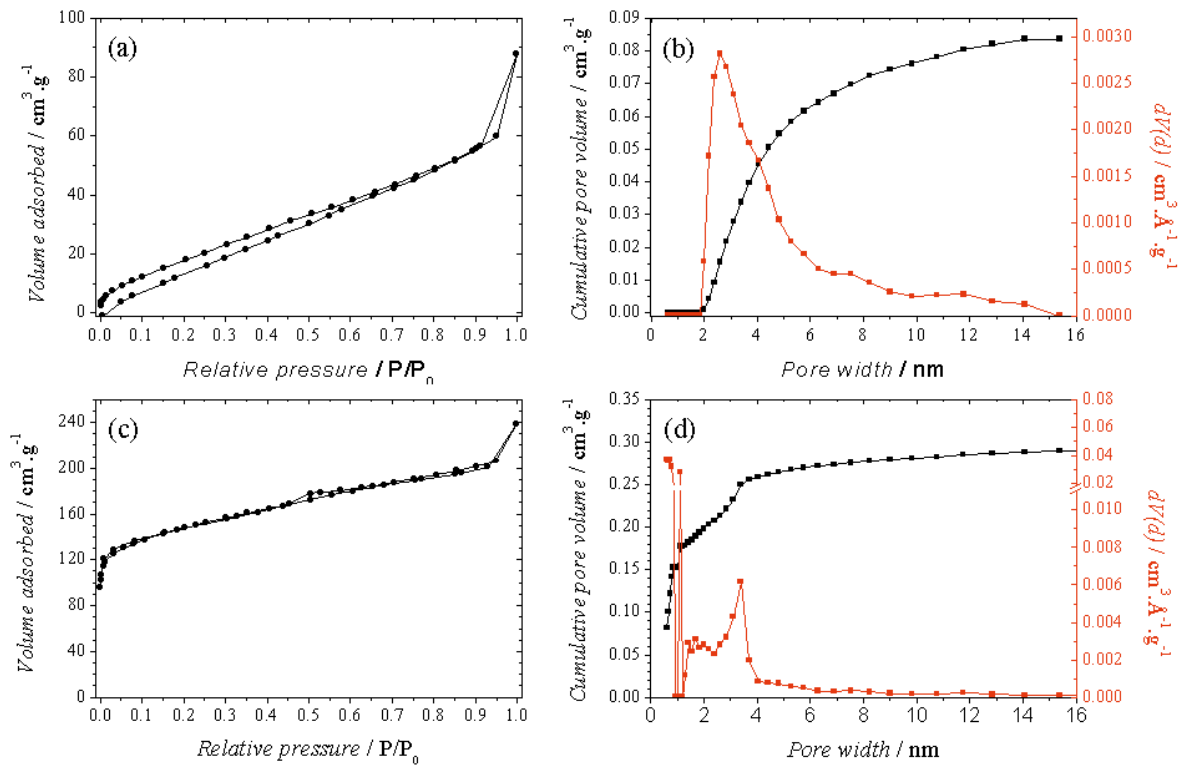
Figure 3-26: Nitrogen sorption isotherms and pore size distribution of carbo-HIPE made at 130°C during 24h, after Soxhlet extraction and drying at 80 °C (a-b) and of the same foam after further thermal treatment at 950 °C under nitrogen (c-d).

Another important feature related to the macrocellular porous structure of the carbo-HIPE foams concerns the mechanical properties. To assess these properties, mechanical tests under compression have been performed (Figure 3-27). The first linear portion of the stress-strain curve (Figure 25b), from 0 to 5 % strain, corresponds to the elastic portion, from which can be extracted the Young's modulus, of about 3 MPa. This Young's modulus is rather low compared with the ones usually obtained for nonreinforced organic PolyHIPEs, [86] from 20 up to 65 MPa, revealing a low cross-linking level. Then, after reaching the yield strength (0.16 MPa), a non-linear plastic behaviour was observed, related to permanent deformations of the material. Finally, a densification of the monolith, typical behaviour of foam, was noticed. Nevertheless, till 60 % strain, the ductile foam did not collapse and kept its monolithic aspect (Figure 3-27 a) together

with its macrocellular morphology. However, the first stress-strain cycle induced a noticeable permanent volume drop of 11 %.
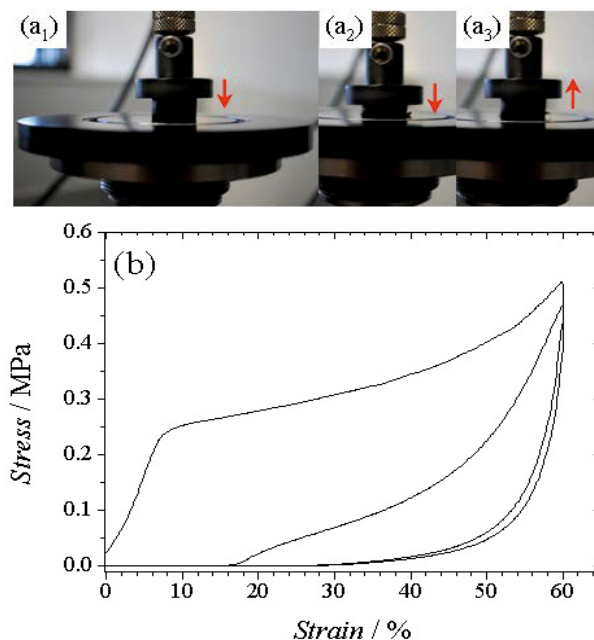
Figure 3-27: (a) Picture of an as-synthesised carbo-HIPE made at 130°C during 24h, after Soxhlet extraction and drying at 80 °C. (b-c) Scanning electron micrographs of a carbo-HIPE made at 130°C during 24h and synthesised with an oil volume fraction of 0.8.

After the immobilisation of a catalytic mixture made of glucose oxidase and redox polymer, these carbo-HIPE foams were successfully used as bioelectrodes for enzymatic fuel cells through the electrooxidation of glucose.[82] These macrocellular foams can be considered as promising candidates in many applications involving the use of continuous flow process, particularly in the field of separation science and heterogeneous catalysis. [78a, 87]

3.4 Chemically Activated HTC

In the case of monosaccharide derived HTC carbons, the lack of porosity has been elegantly overcome by using hard\soft-templating strategies or by addition of structural directing agents as described in the previous pages.[88] Such synthetic routes are effective because of the homogeneous nature of the pre-HTC aqueous reaction mixture. On the other hand, in the case of cellulose and more generally of lignocellulosic biomass, the same synthetic approaches are not that easily feasible because of the insolubility of the cellulosic substrate in water. As a

consequence, in order to introduce porosity in the lignocellulosic biomass derived HTC carbons, post-synthesis methods are required.

Activated carbons (ACs) are highly porous carbon materials, exhibiting appreciable apparent surface area and micropore volume (MPV), which can present a wide variety of pore size distributions (PSD) and micropore size distributions (MPSD). [89-91] They are solids, which can be prepared in different forms, such as powders, granules, pellets, fibres, cloths and others. Due to these features and their special chemical characteristics, they can be used for very different applications, e.g. liquid and gas phase treatments and energy storage. [92-93]

Physical or chemical activation processes are well-known strategies to produce highly porous carbons from coal-derived precursors and it has been largely described in the literature. [94] Their application to lignocellulosic biomass is widely used, but it is not as effective because of poor yields and low porosity development, arising from the excessive degradation of the organic substrate. [95] In this regard the HTC treated biomass is characterised by a more "coal-like" chemical structure, as a consequence it may represent a more suitable precursor for the production of highly porous activated carbons (ACs).

Sevilla et al. were the first to report on the chemical activation of HTC materials as a way to generate highly porous materials. They applied the procedure to HTC materials derived from glucose, starch, cellulose and eucalyptus sawdust achieving large apparent surface areas, up to ~ 3000 m^2/g, and pore volumes in the 0.6-1.4 cm^3/g range. Those materials are further characterised by narrow micropore size distributions in the supermicropore range (0.7-2 nm). Tuning of the PSD was achieved through the modification of the activation temperature (600-850ºC) and the amount of KOH used (KOH/HTC weight ratio = 2 or 4). Applications of these microporous materials for supercapacitors [96], hydrogen storage [97] and CO_2 capture [98].

Our group also prepared nitrogen doped activated carbon from hydrothermal carbons obtained from nitrogen containing precursors using the KOH procedure. [99] However in order to maintain some of the initial nitrogen into the activated carbon, the activation temperatures were low (600°C) which led to low surface areas compared with the values normally encountered in activated carbons (~ 600 m^2/g). These materials were successfully used as electrodes in supercapacitors and this will be in detail described in Chapter 5. [100]

Zhang et al prepared activated carbon-based carbon/carbonaceous composites with different surface functional groups by a hydrothermal carbonisation-deposition method in which commercial activated carbon was exposed to a gaseous mixture of furfural/water or furfural/acrylic acid/water at 180 °C to form the carbon/carbonaceous composites. The results indicate that the surface area and pore volume of the composite can be tailored by tuning the hydrothermal treatment time. More importantly, different functional groups can be anchored onto the composites. Thus, composites with surface hydroxyl or carboxylic or amine groups were prepared. [75]

Carbonaceous monoliths rich in surface sulfonic acid groups were synthesized by one-pot hydrothermal carbonisation of the mixture of p-toluenesulfonic acid/glucose/resorcinol at 180 °C and further carbonized and activated to form monolithic carbons with high surface area and large pore volume. The surface area and pore volume per mass increased with prolonging the activation time (0-6 h) and the best results on 6-h activated samples were 2337 m^2/g and 2.12 cm^3/g. These carbonized and activated samples showed better oxidation resistance than one commercial activated carbon under air. Moreover, the adsorption capacity for dye molecules with different size on these activated samples was significant higher than that on commercial activated carbons and a synthetic ordered mesoporous carbon. [75]

Roman, Nabais and Titirici have recently investigated the hydrothermal carbonisation of various lignocellulosic biomass (walnut shell, sunflower stem and olive stone) as a more energy-efficient tactic as compared with the traditional pyrolysis. The authors discovered that the final yield is higher and the initial hydrothermal treatment allows a better control over the resulting porosity. The produced activated carbons show a higher porosity development when activated with carbon dioxide while the activation with air produced carbon materials with acidic surface chemistry. [101]

However, none of these previous works investigate in detail the effect and influence of the precursor, hydrothermal carbonisation temperature and activation ratio on the porous properties of the resulting activated carbons.

Our group in collaboration with the group of Dolores Lozano Castello and Diego Cazorla studied the KOH chemical activation of HTC carbons obtained from glucose, cellulose and a real lignocellulosic biomass, i.e. rye straw as a function of their chemical structure.

In the next pages, I will present a full characterisation of the developed porosity of activated HTC materials (AC-HTCs) using both N_2 and CO_2 adsorption. When N_2 adsorption was used, two different models were applied to estimate the pore parameters from the gas sorption isotherms: The Dubinin-Radushkevich (DR) model [102] and the Density Functional Theory (DFT) model. [103] CO_2 sorption was used to detect only pores whose diameter is less than 1-1.5 nm (i.e. narrow micropore).[104-105]

The Dubinin-Radushkevich (DR) model best applies to microporous carbons with a narrow PSD. [106] For such materials it is possible to derive a fair estimate of the micropore volumes. On the other hand, the results concerning the PSD are generally considered less reliable. [107] For carbons with broader size distributions, modified versions of the DR equation are necessary, such as the Dubinin-Astakhov or the Dubinin-Stoeckly. However their use is less widespread, because it is much more cumbersome.

For the Density Functional Theory (DFT) model two different models are available: Non-Linear (NLDFT) and Quenched State (QSDFT). The former assumes adsorption taking place on flat, structureless, graphitic pore walls. The latter instead takes into account surface roughness effects. [108] They both yield fairly good estimates of microporous volume and PSD, as confirmed by Monte Carlo Simulation. However, in the case of ACs, generally the values calculated with the QSDFT model tend to be more accurate. [109]

3.4.1 The influence of Hydrothermal Carbonisation Temperature on the Porosity of Chemically Activated Hydrothermal Carbons

For the purpose of this investigation, HTC carbons derived from glucose, cellulose and rye straw were synthesised at different HTC temperatures (sample names *x-y*, *x* is the initial of the carbon precursor and *y* the HTC temperature) and then activated at the same processing conditions (KOH ratio = 3, activation temperature 750 ^{o}C). EA, SEM and N_2-CO_2 gas adsorption were used to characterise the synthesised ACs. The complete porosity analysis is presented only for the activation of glucose derived HTC carbons. For cellulose and rye straw only a summary of the overall results is shown, since their KOH chemical activation follows very similar trends to glucose.

The elemental composition of the HTC carbons derived ACs is characterised by very similar values regardless of the different precursors or HTC synthesis conditions (Table 3-1).

Table 3-1: EA of HTC carbon derived ACs and pyrolysed HTC carbon

Sample	Elemental Composition (wt%)			
	C%	H%	O%	N%
HTC carbons derived ACs[a]	85.0-88.0	1.5-2.1	10.1-12.8	0.1-0.4
HTC-Δ750[b]	94.0	1.7	4.2	0.1

On the other hand, compared to HTC carbons pyrolysed at comparable temperatures (HTC-Δ750), their oxygen content is higher. This difference can be attributed to the higher degree of surface oxidation, which is typically observed after KOH chemical activation. Several oxygen-containing functional groups (e.g. lactone, phenol, quinone) are known to be present on the surface of ACs.[110]

SEM was used to investigate the morphology of AC HTCs derived from glucose, cellulose and rye straw (Figure 3-28). It is evident that for all three precursors the KOH chemical activation leads to a complete morphological change. The spherical micrometer-sized particles, characterising both glucose and cellulose derived HTC carbons (Chapter 2) or the rye straw fibres-like structures (Chapter 2), which are still present after HTC treatment, are not observed anymore. The AC materials are now composed of macrometer-sized monolithic fragments with sharp edges. Furthermore higher magnification SEM micrographs (Figure 3-28b,d,f) show a high level of surface roughness, hinting at the material extensive microporosity.
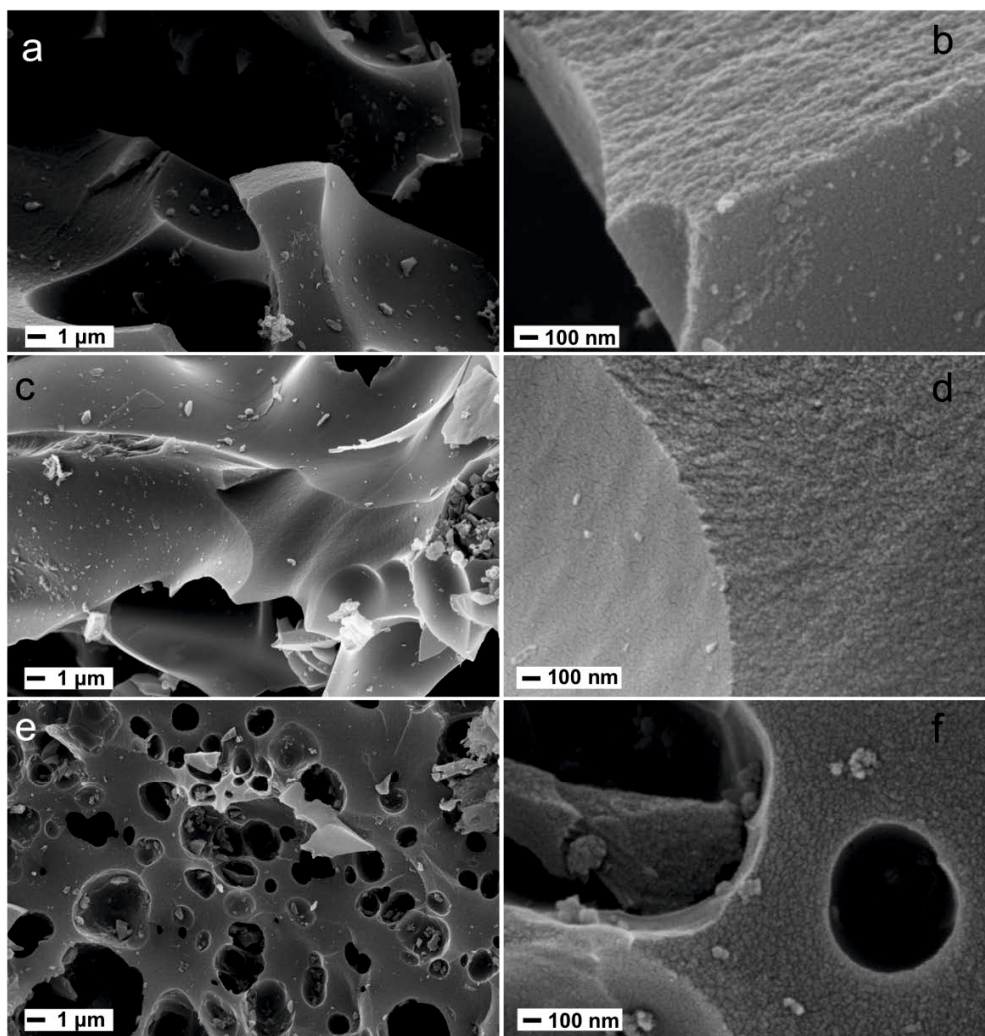
Figure 3-28: SEM images of ACs derived from a), b) glucose (G – 240°C), c), d) cellulose (C – 240°C) and e), f) rye straw (RS – 240°C) HTC carbons.

In order to fully characterise the porosity of microporous materials, it is recommendable to employ both CO_2 and N_2 gas adsorption and to validate the obtained results by analysing them with different isotherms models. For this reason, an analysis based on the combination of the BET, DR and DFT models applied to N_2 and CO_2 isotherms is developed in this section.

All the N_2 isotherms of the ACs, produced from glucose derived HTC carbons, are characterised by a type I profile (Figure 3-29a). A more attentive analysis reveals that G-240°C has the largest N_2 uptake, arising from a higher porosity development than in the cases of G-180°C and G-280°C. Furthermore, interestingly G-280°C N_2 isotherm shows a much sharper knee at low relative pressure than G-180°C and G-240°C. This finding suggests that the pore size distribution

(PSD) of this former sample is much narrower than for the two latter ones. Therefore, it can be deduced that G-180°C and G-240°C have a higher tendency to develop larger pores during chemical activation than G-280°C.

Apart from the total micropore volume applying the DR equation to the N$_2$ isotherms (Figure 3-29 b-c-d) can also provide useful information about the ACs PSD. At low (A/b)^2 values, the deviation of the experimental results curve (grey full dot line) from the linear fit (continuous red line) is an estimate of the PSD of the sample. Larger deviations correspond to samples with a greater pore fraction out of the micropores range (i.e. in the mesopores range). According to this criterion, G-240^{0}C (Figure 3-29c) is characterised by the widest PSD and largest fraction of mesopores. G-180°C (Figure 3-29b) shows a similar trend, although the fraction of mesopores is certainly smaller since the deviation from the linear fit is less pronounced. Contrarily to these first two samples, G-280°C (Figure 3-29c) shows only a negligible deviation from the linear fit suggesting a minor presence of mesopores in this latter sample. The findings, obtained from the DR analysis, are in good agreement with the QSDFT-PSD (Figure 3-29e). The amount of mesopores present in the G-280°C sample, as already mentioned, is negligible. G-180°C and G-240°C are instead characterised by a large fraction of mesopores, with the latter sample exhibiting the highest amount.

In order to assess the pore volume and the PSD of the narrow microporosity region characterising G-180°C, G-240°C and G-280°C, CO$_2$ adsorption was used, since N$_2$ sorption is not as effective in probing this pore range. It is evident from the measured CO$_2$ isotherms (Figure 3-30a), that G-280°C has the largest gas uptake followed by G-240°C and then G-180°C. This trend differs from the one observed in N$_2$ sorption and it suggests that G-280°C generates prevalently micropores (majorly narrow micropores) with a narrower PSD. On the other hand, G-180°C and especially G-240°C have the tendency to generate ACs with a broader PSD. This speculation is also confirmed by the NLDFT PSDs, derived from the CO$_2$ isotherms (Figure 3-30b). Even in the lower micropore range (pore width < 1.0 nm), the PSD of G-280°C is shifted towards smaller pore widths than in the case of G-180°C and G-240°C. All the values pore characteristics are to be found in Table 3-2.

Figure 3-29: a) N$_2$ adsorption isotherms, b), c), d) application of DR equation to N$_2$ adsorption isotherms and e) N$_2$ adsorption QSDFT PSD of ACs (G-180°C, G-240°C, G-280°C)

Table 3-2: Calculated surface area (S) and pore volume (V) using different models (subscript) on either N2 or CO$_2$ isotherms for G-180°C, G-240°C, G-280°C

Sample	$S_{N2-BET \ (m^2/g)}$	$V_{N2-Ex \ (cm^3/g)}$ $^{(a)}$	$V_{N2-DR \ (cm^3/g)}$	$V_{CO2-NLDFT \ (cm^3/g)}$	$V_{CO2-DR \ (cm^3/g)}$
G-180	1859	0.94	0.69	0.34	0.31
G-240	2264	1.21	0.84	0.40	0.35
G-280	1610	0.73	0.66	0.41	0.41

179
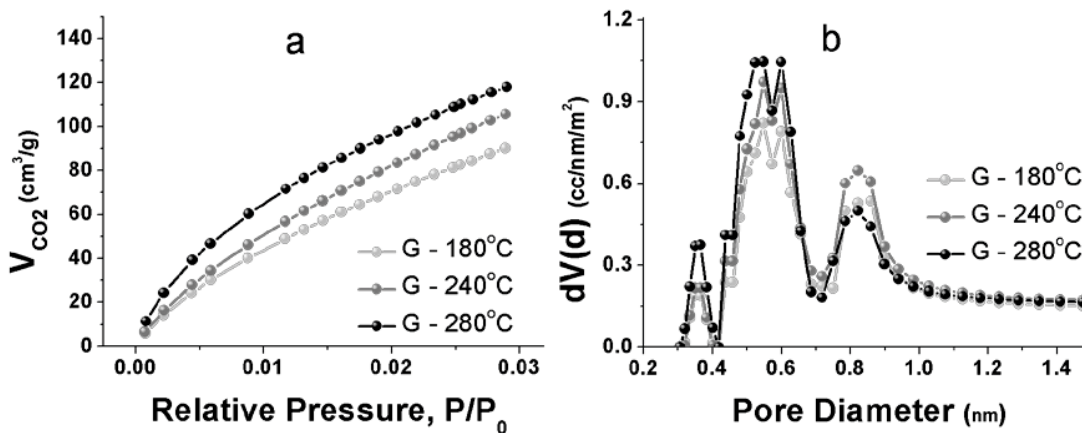
Figure 3-30: a) CO_2 (273 K) isotherms and b) NLDFT PSD of ACs (G-180°C, G-240°C, G-280°C)

Using the previously discussed models, the key parameters defining the porosity of the ACs (i.e. surface area and pore volume) can be calculated (Figure 3-31).

$V_{CO2-NLDFT}$ and V_{CO2-DR} (V_{CO2-DR} is used for the analysis) can be considered as an approximate estimate of narrow micropore volume. V_{N2-DR} and V_{N2-EX} (V_{N2-EX} is calculated from the experimental isotherm) are respectively approximate estimates of the micropore volume and the total pore volume, accessible to N_2 at the measured conditions.

Combining the different pore volume values and the PSDs, obtained by applying the NLDFT and QSDFT models respectively to CO_2 and N_2 isotherms it is possible to obtain a results overview effectively summarising the findings that were highlighted previously.

G-240°C is the sample characterised by the highest porosity development, since it shows the largest total pore volume and surface area (Table 3-2). At the same time, it has the widest PSD, as indicated by the large difference between its total pore volume (i.e. V_{N2-EX}) and narrow micropore volume (i.e V_{CO2-DR}) values. The PSD of G-180°C follows very similar trends to the one of G-240°C. However the extent of porosity development for the former sample is smaller, as indicated by its lower total pore volume and surface area. G-280°C is the case when KOH chemical activation is the least effective. This sample shows the lowest pore volume and surface area. Furthermore, its PSD is much narrower than in the other two samples and is characterised by a very low mesopore fraction, as indicated by the negligible difference between its total pore

volume (V_{N2-EX}) and micropore volume (i.e. V_{N2-DR}) values (≈ 0.05 cm^3/g).

Figure 3-31: Calculated surface area (S) and pore volume (V) using different models (subscript) on either N$_2$ or CO$_2$ isotherms for G-180°C, G-240°C, G-280°C

Using the same analysis framework, the effects of KOH chemical activation on cellulose and rye straw derived HTC carbons can be effectively analysed and compared to the glucose case (Figure 3-32 Figure 3-33 and Figure 3-34). The porosity analysis for the chemical activation of cellulose derived HTC carbons (C-200, C240 and C-280) show very similar trends to the ones observed for glucose. The highest porosity development is observed for the sample synthesised at 240°C (C-240), as indicated by its highest surface area and total pore volume values (Table 3-3).

Table 3-3: Calculated surface area (S) and pore volume (V) using different models (subscript) on either N2 or CO2 isotherms for C-200, C-240, C-280, RS-240 and RS 280

Sample	S_{N2-BET} (m^2/g)	V_{N2-Ex} (cm^3/g)[a]	V_{N2-DR} (cm^3/g)	$V_{CO2-NLDFT}$ (cm^3/g)	V_{CO2-DR} (cm^3/g)
C-200	1827	0.95	0.71	0.39	0.37
C-240	2334	1.26	0.84	0.40	0.38
C-280	1082	0.50	0.45	0.33	0.34
RS-240	2361	1.11	0.93	0.44	0.42
RS-280	1930	0.95	0.82	0.44	0.42

C-200 and C-240 show very similar PSDs, characterised by a significant mesopore fraction (Figure 3-32). On the other hand, the sample synthesised at 280°C (C-280) shows the lowest surface area and total pore volume, indicating a lower extent of activation. Furthermore, its mesopore volume fraction is practically negligible, as it was also observed for G-280. Its PSD is mostly characterised by narrow micropores.

Figure 3-32: Calculated surface area (S) and pore volume (V) using different models (subscript) on either N2 or CO2 isotherms for C-200, C-240, C-280, RS-240 and RS 280
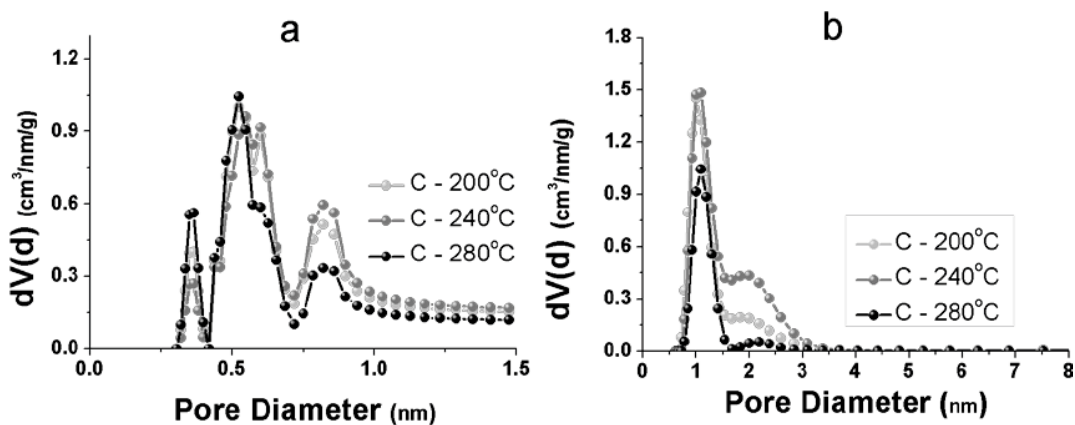
Figure 3-33: a) CO$_2$ NLDFT pore size distribution and b) N$_2$ adsorption QSDFT pore size distribution of C-200°C, C-240°C and C-280°C ACs.

In the case of rye straw derived HTC carbons (RS-240, RS 280), KOH chemical activation also generates high surface area and total pore volume ACs (Figure 3-32 Table 3-3). Once again, the sample synthesised at 240°C is characterised by the highest porosity development. However, this time it can be noticed that the development of mesoporosity is less than for glucose and cellulose (Figure 3-34). Furthermore, as indicated by its relatively high surface area and total pore volume, the sample synthesised at 280°C does not exhibit such a reduced extent of activation as for the other two carbon precursors. These dissimilarities can be explained by taking into account the more heterogeneous composition and structure of rye straw (i.e. lignin presence and fibrous structure), which may still mildly affect the activation process, regardless of the HTC pre-treatment.
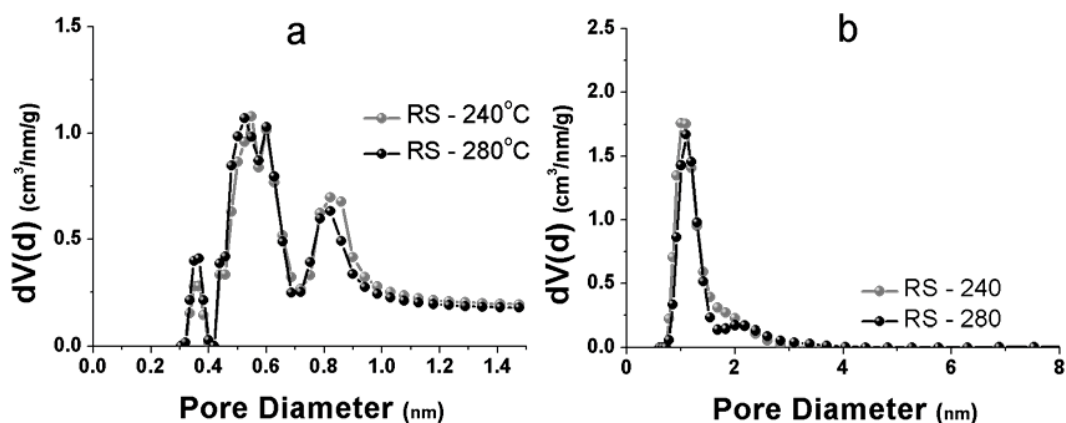
Figure 3-34: a) CO_2 NLDFT pore size distribution and b) N_2 adsorption QSDFT pore size distribution of RS - 240°C and RS – 280°C ACs.

Overall, this analysis highlights that the HTC temperature extensively affects the porosity of the derived ACs. HTC carbons, synthesised at higher temperatures (e.g. 280°C), generate ACs with a lower porosity development and narrower PSDs, whilst the ones, produced at 180-240°C, upon KOH activation, develop a greater porosity characterised by a greater mesopores fraction. These trends can be explained by taking into account the dependence of the chemical structure of HTC carbons upon the synthesis temperature. [111] More severe HTC processing conditions (i.e. higher temperatures) generate HTC carbons with a higher degree of aromatisation, resulting into enhanced chemical stability and structural order. As observed for the hydroxide activation of

several coals, both features are detrimental to the reactivity of the carbon substrate, leading to a reduced porosity development.[112]

3.4.2 The Effect of KOH: HTC Carbon Ratio on the Porosity of Chemically Activated Hydrothermal Carbons

In this section ACs, produced *via* KOH activation of rye straw derived HTC carbons (synthesized at 240°C) at different KOH : Carbon Precursor ratio (KOH ratio = 2:1, 3:1 and 4:1, activation temperature 750°C), are investigated. This parameter (i.e. KOH ratio) is one of the main variables determining the key features of the ACs porous structure (i.e. surface area, total pore volume and micropore volume). As a consequence, it can be employed as a term of comparison to determine the effectiveness of HTC temperature as an additional process variable.
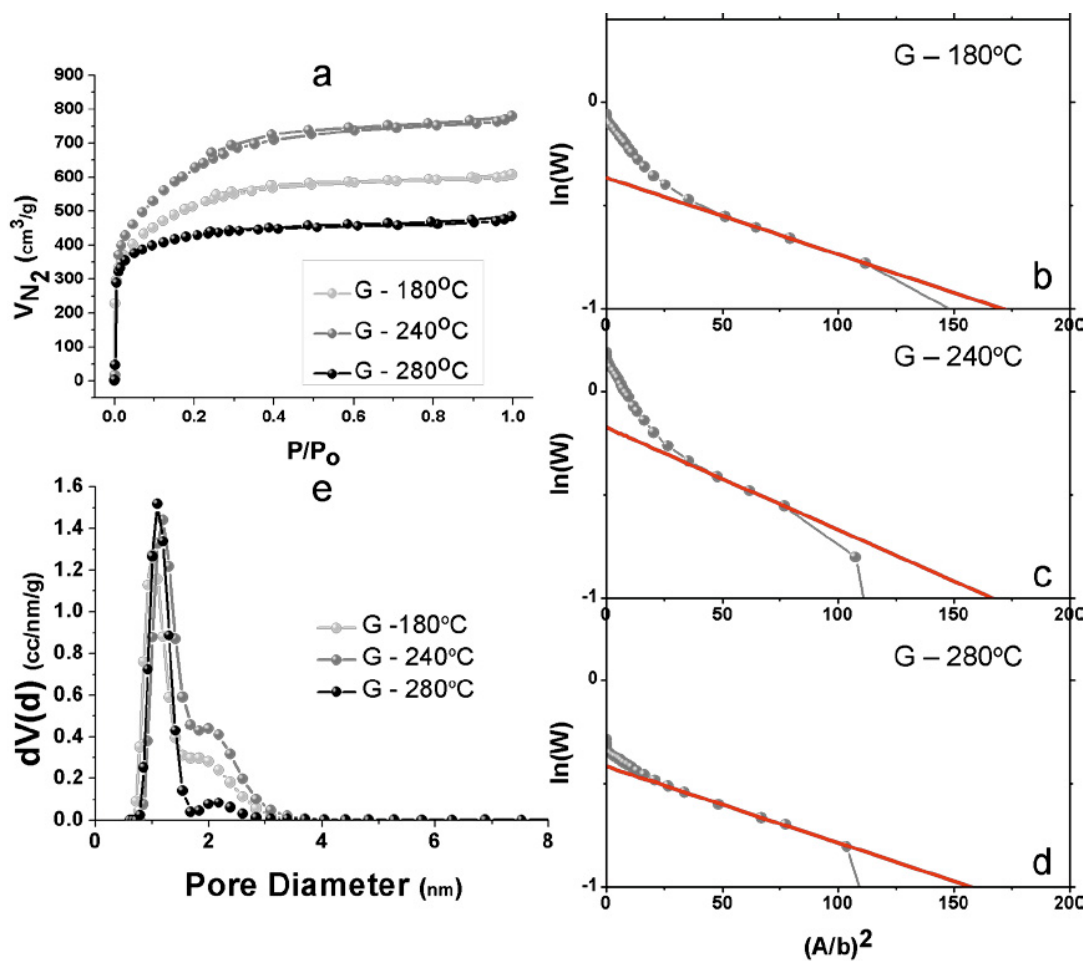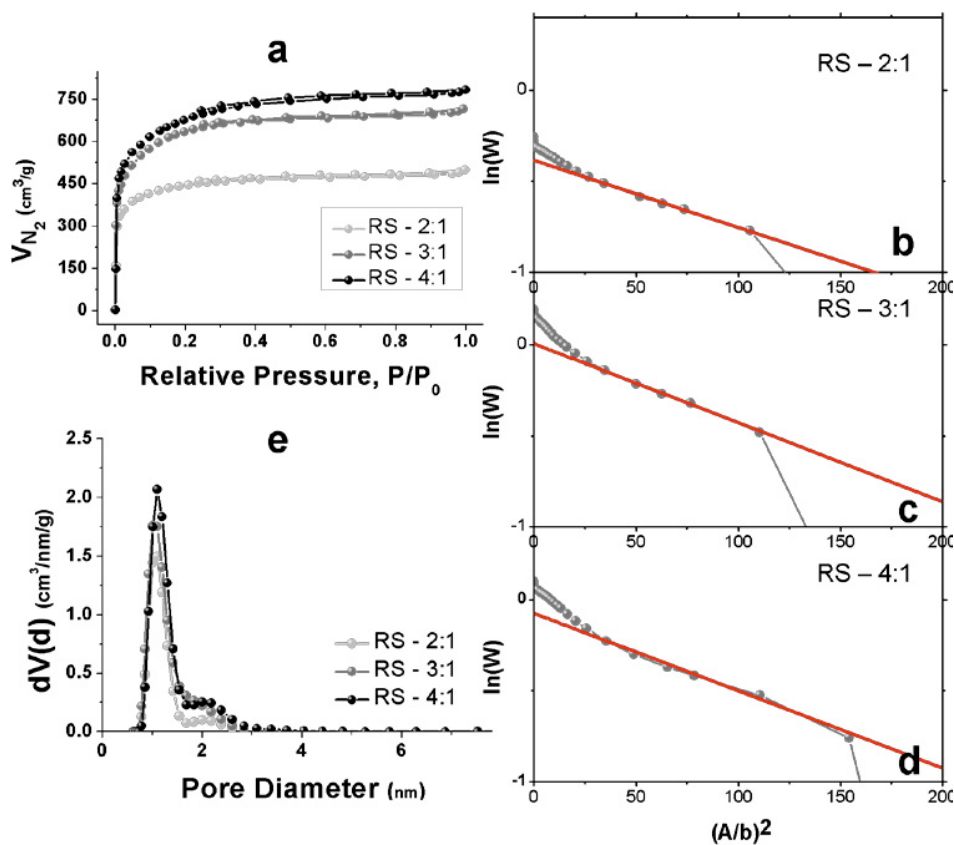

Figure 3-35: a) N$_2$ adsorption isotherms, b), c), d) application of DR equation to N$_2$ adsorption isotherms and e) N2 adsorption QSDFT PSD of ACs (RS-2:1, RS-3:1, RS-4:1).

The characterisation of the synthesised ACs (i.e. RS-2:1, RS-3:1, RS-4:1) follows the same structure employed in the previous section. Firstly N_2 adsorption was used to characterise the upper micropore and mesopore range (Figure 3-35). A Type I profile describes all the measured N2 isotherms (Figure 3-35a). Increasing KOH ratio leads to higher gas uptakes and to a broader PSD, as indicated by the progressive enlargement of the isotherms knee at low relative pressures. This last finding is also confirmed by applying the DR and QSDFT models to the N_2 isotherms. In the former case, larger deviations of the experimental results from the linear fit are observed for RS-3:1 and RS-4:1(Figure 3-35 b-c-d), indicating a greater fraction of pore volume out of the micropore region. In the latter case, the PSDs highlight how the fraction of mesopore becomes more prominent for high KOH ratio values. From this analysis, it is also evident that increasing the KOH ratio value from 2:1 to 3:1 affects the ACs porosity to a larger extent than a further increase from 3:1 to 4:1, whose effect on the PSD is relatively negligible (Table 3-4).

Table 3-4. Calculated surface area (S) and pore volume (V) using different models (subscript) on either N_2 or CO_2 isotherms for RS-2:1, RS-3:1, RS-4:1

Sample	$S_{N2\text{-}BET}$ (m²/g)	$V_{N2\text{-}Ex}$ (cm³/g) [a]	$V_{N2\text{-}DR}$ (cm³/g)	$V_{CO2\text{-}NLDFT}$ (cm³/g)	$V_{CO2\text{-}DR}$ (cm³/g)
RS-2:1	1665	0.77	0.68	0.40	0.39
RS-3:1	2361	1.11	0.93	0.44	0.45
RS-4:1	2481	1.21	1.01	0.50	0.49

CO_2 gas adsorption was used to probe the narrow microporosity of the synthesised ACs (Figure 3-36). RS-4:1 shows the largest gas uptake, while RS-2:1 and RS-3:1 approximately achieve the same value (Figure 3-36a). However, the isotherms overlap in the lower relative pressure region (< 0.010) is a clear evidence of a different PSD also in the narrow micropore range. RS-2:1 has a higher uptake at lower relative pressure, suggesting a higher fraction of very small narrow micropores (< 0.5 nm). RS-3:1 and RS-4:1 isotherms, instead, have broader profiles indicating a shift of the PSD towards larger pore widths. These observations are also confirmed by the obtained NLDFT PSDs (Figure 3-36 b). RS-3:1 and RS-4:1 have very similar PSD with a higher pore fraction in the range 0.5-0.9 nm. On the other hand, RS-2:1 PSD has a major shoulder at pore width values < 0.5 nm.
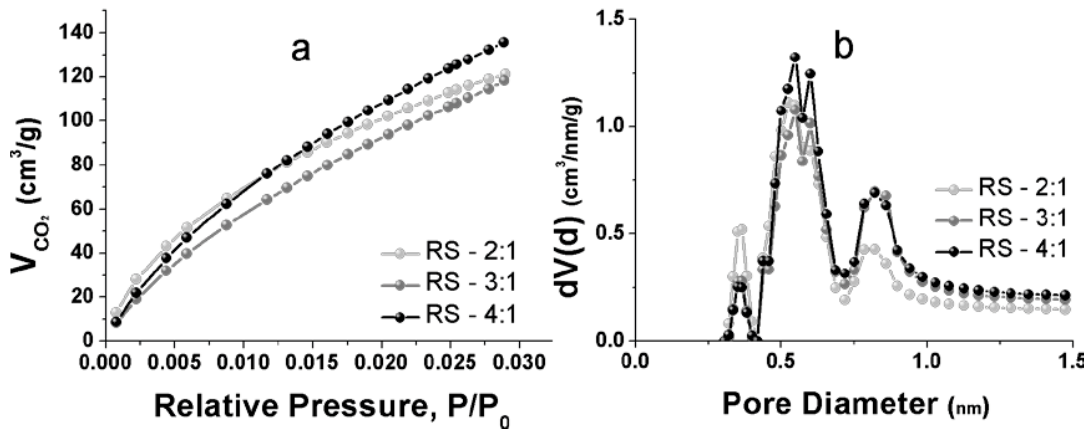
Figure 3-36: a) CO$_2$ (273 K) isotherms and b) NLDFT PSD of ACs (RS-2:1, RS-3:1, RS-4:1)

As shown in the previous section, the calculated surface area and pore volume values can be used to effectively summarise the main results, obtained from the porosity characterisation of RS-2:1, RS-3:1 and RS-4:1 (Table 3-4). The existence of a general trend characterising the porosity development of the three ACs is glaring. Low KOH ratio values (2:1) produce a lower extent of activation and favour the formation of microporous ACs with a narrow PSD, as suggested by the reduced difference between its total pore volume (i.e. V_{N2-EX}) and narrow micropore volume (i.e V_{CO2-DR}) values. Using higher amounts of KOH leads to higher porosity development, as indicated by larger surface area and total pore volume values. However, their increase is partially the result of pore widening, since the PSD for RS-3:1 and RS-4:1 is clearly more shifted towards the supermicropore and mesopore ranges. These observations are in agreement with the trends generally observed during KOH activation of fossil fuels-derived carbonaceous substrates (e.g. pitch),[94a, 113] confirming the similar reactivity of HTC carbons during chemical activation and their resultant high suitability as ACs precursors.
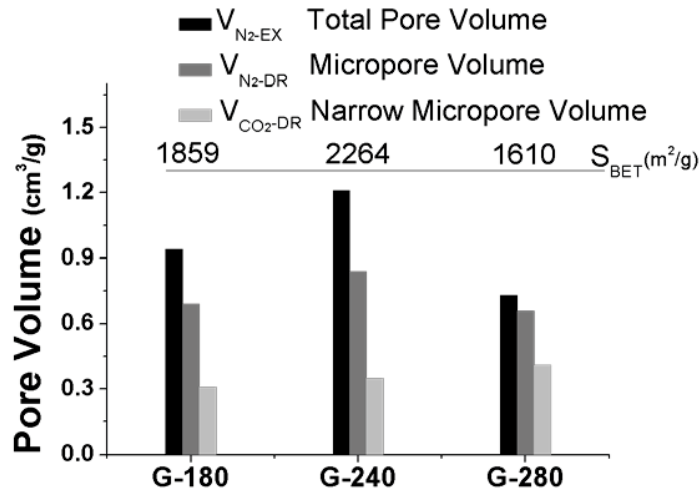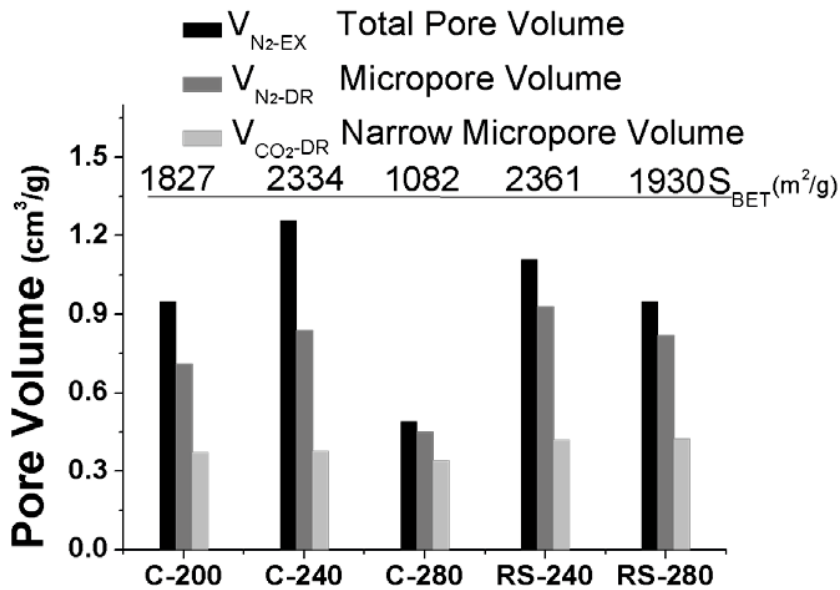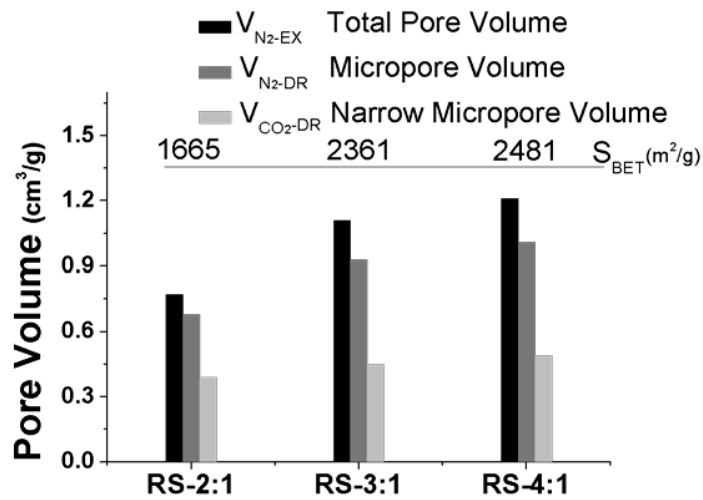
Figure 3-37: Calculated surface area (S) and pore volume (V) using different models (subscript) on either N$_2$ or CO$_2$ isotherms for RS-2:1, RS-3:1, RS-4:1

The most interesting outcome of this analysis is provided by the comparison between the results obtained from this section and the previous one (Figure 3-37). The effects of HTC temperature on the key parameters, defining the ACs porosity (i.e. surface area, pore volume and PSD), are comparable in magnitude to the ones observed for samples obtained at different KOH ratios. As a consequence, varying the temperature the HTC carbons are synthesised at, allows a degree of control on the ACs' porosity comparable to one of the main variables of the KOH activation process. It is thus obvious that HTC temperature is a key parameter, whose importance should not be underestimated when it comes to tuning the porous structure of HTC carbons derived ACs for specific applications.

3.5 Summary and Outlook

In this chapter, I have evaluated the recent main research directions related to the introduction of porosity to the HTC-based carbons.

The combined HTC – templating technique has been revealed to be a useful technique for our group to get an access to functional nanostructured carbon materials. From these presented examples, we have learned that this combined HTC –templating strategy allows simultaneous control of materials morphology, surface character and pore properties, widening, thus, the possible applications fields of promising porous HTC materials. Furthermore, the flexibility of

the presented approach allows access to a wide range of functional materials with surface functionality / chemistry tuneable *via* selection of post carbonisation treatment temperature.

Carbon beads and ordered mesoporous carbons were produced through the combined HTC – hard templating technique using the corresponding silica sacrificial templates. In a very similar manner, tubular carbons could be synthesised using the macroporous anodic alumina membrane template. The presented materials are suitable for various applications such as heterogeneous catalysis, separation/adsorption, or electrochemistry (more details in Chapter 5). Here, the possibility of controlling the surface chemistry from oxygenated functionality rich character towards increased aromatic / pseudo graphitic character *via* post carbonisation step provided the added advantage. As such these highly flexible materials can be very interesting candidates as separation media allowing the separation of non-polar analytes but also polar analytes (e.g. neutral sugars, sugar alcohols). Furthermore, introduction of other important chemical moieties using the existing oxygenated surface functional groups will be of great interest.

When HTC is combined with the soft templating technique, a direct access to functional ordered micro / meso porous materials was possible *via* a direct "templating" of block copolymer micellar templates. The cooperative self-assembly of block copolymer species and D-fructose (e.g., biomass-derived carbon source) occurring in an aqueous phase at 130°C is considered responsible for the stable formation of the ordered block copolymer – carbon composite. Importantly, pore size could be shifted into mesopore region simply through the addition of organic pore swelling agent. Further studies on the formation mechanism (e.g. *via* in-situ SAXS/SANS studies or ^{13}C-NMR study of the reaction solution) and the corresponding synthesis optimisation are desirable for this highly interesting soft templating system. Such information would then allow us to ultimately manipulate the formed ordered phases opening access to materials with enhanced porous features (e.g. increased pore size and pore volume), necessary for successful real world application. Regularly ordered pore structuring confers particular properties such as controlled linear electronic conduction pathways and fast charge-discharge properties or could facilitate fast encapsulation and release of drug molecules.

The use of bioresources (e.g. crustacean shells) were also introduced as potentially HTC material sources, whereby the naturally occurring bioinorganic/organic composites were converted to extremely promising, highly textured, hierarchically porous nitrogen doped carbon networks.

Furthermore we have eluded to the first step towards the true transfer of traditional sol-gel principles typically used in inorganic materials preparation to this new rapidly developing area of HTC allow in principle access to a whole new range of nanostructured functional carbonaceous material platforms. In this sense the previous limitations in many applications (i.e. a lack of developed porosity in HTC material) has been overcome and it is expected that associated improvements in catalytic efficient and adsorption capacity will be markedly improved as a result.

Furthermore, in the last section we have also discussed four different pathways for the successful preparation of HTC monoliths with tuneable morphologies, pore properties and chemistries which seem to lend themselves directly to applications in flash and analytical chromatography and the immerging catalytic and separation challenges associated with the 21st century Biorefinery concept.

Finally, we could also show that that HTC carbons are excellent precursors for the synthesis of ACs *via* KOH chemical activation. Regardless of the parent biomass (i.e. glucose, cellulose or rye straw), highly microporous ACs could be generated. The HTC temperature was found to be an extremely influential parameter affecting the porosity development and PSDs of the ACs to the same extent as the KOH ratio (i.e. one of the main KOH activation process variables). The use of higher HTC temperatures (i.e. 280 ^{o}C) led to lower porosity development, but to a narrower PSD mostly composed of micropores. On the other hand, KOH chemical activation of HTC carbons, synthesised at lower temperatures (i.e. 180 - 240°C), produced ACs with higher total pore volume and broader PSDs, characterised by a significant mesopores fraction.

Further improvements of the synthesised ACs performance could certainly be achieved by optimising the activation and HTC synthesis parameters, in such a way as to tailor their PSDs to the adsorbate. Furthermore, additional testing of the synthesised ACs would also be required, in such a way as to assess their performance under a larger range of operating conditions and to quantify other crucial parameters for their effective application (e.g. packing density).

If porous sustainable HTC materials can be utilised successfully as separation or catalytic devices in this new chemical production concept then this would represent a step forward towards a complete, holistic, synergistic Biorefinery and in principle a near closed CO_2 loop in chemical manufacture.

3.6 References:

[1] S. Kondo, T. Ishikawa, I. Abe, *Science of Adsorption*, Maruzen, Tokyo, 2001.

[2] N. A. Eltekova, D. Berek, I. Novák, F. Belliardo, *Carbon* 2000, *38*, 373-377.

[3] K. M. Steel, W. J. Koros, *Carbon* 2003, *41*, 253-266.

[4] P. Makowski, R. Demir Cakan, M. Antonietti, F. Goettmann, M.-M. Titirici, *Chem. Commun.* 2008, 999-1001.

[5] P. Serp, J. L. Figueiredo., *Carbon Materials for Catalysis*, A John Wiley & Sons, Inc, USA, 2009.

[6] D. S. Su , R. Schlögl, *ChemSusChem* 2010, *3*, 136-168.

[7] E. Antolini, *Energy & Environmental Science* 2009, *2*, 915-931.

[8] S. H. Joo, K. Kwon, D. J. You, C. Pak, H. Chang, J. M. Kim, *Electrochimica Acta* 2009, *54*, 5746-5753.

[9] R. Othman, A. L. Dicks, Z. Zhu, *International Journal of Hydrogen Energy* 2012, *37*, 357-372.

[10] J. H. Knox, B. Kaur, G. R. Millward, *Journal of Chromatography A* 1986, *352*, 3-25.

[11] T. Hanai, *Journal of Chromatography A* 2003, *989*, 183-196.

[12] R. J. White, C. Antonio, V. L. Budarin, E. Bergström, J. Thomas-Oates, J. H. Clark, *Advanced Functional Materials* 2010, *20*, 1834-1841.

[13] G.Q. Lu, X. S. Zhao, *Nanoporous Materials: Science and Engineering,*, Imperial College Press,, London, 2005.

[14] A. G. Pandolfo, A. F. Hollenkamp, *Journal of Power Sources* 2006, *157*, 11-27.

[15] M.-M. Titirici, R. J. White, C. Falco, M. Sevilla, *Energy & Environmental Science* 2012, *5*, 6796-6822.

[16] M.-M. Titirici, M. Antonietti, *Chemical Society Reviews* 2010, *39*, 103-116.

[17] F. Schüth, *Angewandte Chemie International Edition* 2003, *42*, 3604-3622.

[18] R. Ryoo, S. H. Joo, M. Kruk, M. Jaroniec, *Advanced Materials* 2001, *13*, 677-681.

[19] C. Liang, K. Hong, G. A. Guiochon, J. W. Mays, S. Dai, *Angewandte Chemie International Edition* 2004, *43*, 5785-5789.

[20] C. Liang, S. Dai, *J. Am. Chem. Soc.* 2006, *128*, 5316-5317.

[21] F. Zhang, Y. Meng, D. Gu, Yan, C. Yu, B. Tu, D. Zhao, *J. Am. Chem. Soc.* 2005, *127*, 13508-13509.

[22] Y. Huang, H. Cai, T. Yu, F. Zhang, F. Zhang, Y. Meng, D. Gu, Y. Wan, X. Sun, B. Tu, D. Zhao, *Angewandte Chemie International Edition* 2007, *46*, 1089-1093.

[23] Y. Meng, D. Gu, F. Zhang, Y. Shi, H. Yang, Z. Li, C. Yu, B. Tu, D. Zhao, *Angewandte Chemie International Edition* 2005, *44*, 7053-7059.

[24] Y. Meng, D. Gu, F. Zhang, Y. Shi, L. Cheng, D. Feng, Z. Wu, Z. Chen, Y. Wan, A. Stein, D. Zhao, *Chem. Mat.* 2006, *18*, 4447-4464.

[25] M. M. Titirici, A. Thomas, M. Antonietti, *Advanced Functional Materials* 2007, *17*, 1010-1018.

[26] S. Kubo, University of Potsdam (Potsdam, Germany), 2011.

[27] M.-M. Titirici, A. Thomas, M. Antonietti, *Journal of Materials Chemistry* 2007, *17*, 3412-3418.

[28] S. Kubo, I. Tan, R. J. White, M. Antonietti, M.-M. Titirici, *Chem. Mat.* 2010, *22*, 6590-6597.

[29] R. J. White, K. Tauer, M. Antonietti, M.-M. Titirici, *J. Am. Chem. Soc.* 2010, *132*, 17360-17363.

[30]   K. Tang, R. J. White, X. Mu, M.-M. Titirici, P. A. van Aken, J. Maier, *ChemSusChem* 2012, *5*, 400-403.

[31]   K. Tang, L. Fu, R. J. White, L. Yu, M.-M. Titirici, M. Antonietti, J. Maier, *Adv. Energy Mater.* 2012, *2*, 873-877.

[32]   Nicolas Brun, Ken Sakaushi, Linghui Yu, Lars Giebeler, Jürgen Eckert, M. M. Titirici, *Energy & Environmental Science* 2012, submitted.

[33]   S. Kubo, R. J. White, N. Yoshizawa, M. Antonietti, M.-M. Titirici, *Chem. Mat.* 2011, *23*, 4882-4885.

[34]   P. Bloss, W. D. Hergeth, E. Döring, K. Witkowski, S. Wartewig, *Acta Polymerica* 1989, *40*, 260-265.

[35]   K. S. W. Sing, *Pure & Appl. Chem.* 1985, *57*, 603.

[36]   N. Baccile, G. Laurent, F. Babonneau, F. Fayon, M.-M. Titirici, M. Antonietti, *The Journal of Physical Chemistry C* 2009, *113*, 9644-9654.

[37]   J. L. Blin, B. L. Su, *Langmuir* 2002, *18*, 5303-5308.

[38]   Q. Huo, D. I. Margolese, G. D. Stucky, *Chem. Mat.* 1996, *8*, 1147-1160.

[39]   R. J. White, V. Budarin, R. Luque, J. H. Clark, D. J. Macquarrie, *Chemical Society Reviews* 2009, *38*, 3401-3418.

[40]   L. Addadi, S. Weiner, *Angewandte Chemie International Edition in English* 1992, *31*, 153-169.

[41]   A. Sugawara, T. Nishimura, Y. Yamamoto, H. Inoue, H. Nagasawa, T. Kato, *Angewandte Chemie International Edition* 2006, *45*, 2876-2879.

[42]   R. J. White, M. Antonietti, M.-M. Titirici, *Journal of Materials Chemistry* 2009, *19*, 8645-8650.

[43]   R. Ryoo, S. H. Joo, S. Jun, *The Journal of Physical Chemistry B* 1999, *103*, 7743-7746.

[44]   F. Su, C. K. Poh, J. S. Chen, G. Xu, D. Wang, Q. Li, J. Lin, X. W. Lou, *Energy & Environmental Science* 2011, *4*, 717-724.

[45]   K. Gong, F. Du, Z. Xia, M. Durstock, L. Dai, *Science* 2009, *323*, 760-764.

[46]   Mario Soorholtz, Robin J. White, Tobias Zimmermann, Maria-Magdalena Titirici, Markus Antonietti, R. Palkovits, F. Schüth, *Chem. Commun.* 2012, submitted.

[47]   R. Czerw, M. Terrones, J. C. Charlier, X. Blase, B. Foley, R. Kamalakaran, N. Grobert, H. Terrones, D. Tekleab, P. M. Ajayan, W. Blau, M. Ruhle, D. L. Carroll, *Nano Letters* 2001, *1*, 457-460.

[48]   H. Kabbour, T. F. Baumann, J. H. Satcher, A. Saulnier, C. C. Ahn, *Chem. Mat.* 2006, *18*, 6085-6087.

[49]   X. Lu, M. C. Arduini-Schuster, J. Kuhn, O. Nilsson, J. Fricke, R. W. Pekala, *Science* 1992, *255*, 971-972.

[50]   K. Nakanishi, H. Minakuchi, N. Soga, N. Tanaka, *Journal of Sol-Gel Science and Technology* 1997, *8*, 547-552.

[51]   R. W. Pekala, *Journal of Materials Science* 1989, *24*, 3221-3227.

[52]   H. Tamon, H. Ishizaka, *Journal of Colloid and Interface Science* 2000, *223*, 305-307.

[53]   M. C. Gutierrez, F. Pico, F. Rubio, J. Manuel Amarilla, F. Javier Palomares, M. L. Ferrer, F. del Monte, J. M. Rojo, *Journal of Materials Chemistry* 2009, *19*, 1236-1240.

[54]   N. Job, A. Théry, R. Pirard, J. Marien, L. Kocon, J.-N. Rouzaud, F. Béguin, J.-P. Pirard, *Carbon* 2005, *43*, 2481-2494.

[55]   G. Dayong, S. Jun, L. Nianping, W. Guangming, Z. Bin, Z. Zhihua, N. Xingyuan, *Journal of Reinforced Plastics and Composites* 2011, *30*, 827-832.

[56]   R. Saliger, U. Fischer, C. Herta, J. Fricke, *Journal of Non-Crystalline Solids* 1998, *225*,

81-85.

[57]   J. Marie, R. Chenitz, M. Chatenet, S. Berthon-Fabry, N. Cornet, P. Achard, *Journal of Power Sources* 2009, *190*, 423-434.

[58]   S. A. Al-Muhtaseb, J. A. Ritter, *Advanced Materials* 2003, *15*, 101-114.

[59]   N. Baccile, M. Antonietti, M.-M. Titirici, *ChemSusChem* 2010, *3*, 246-253.

[60]   R. J. White, N. Yoshizawa, M. Antonietti, M.-M. Titirici, *Green Chemistry* 2011, *13*, 2428-2434.

[61]   P. F. Barron, M. A. Wilson, *Nature* 1981, *289*, 275-276.

[62]   Y. F. Jia, B. Xiao, K. M. Thomas, *Langmuir* 2001, *18*, 470-478.

[63]   A. C. Lua, T. Yang, *Journal of Colloid and Interface Science* 2004, *274*, 594-601.

[64]   M. a. Pérez-Cadenas, C. Moreno-Castilla, F. Carrasco-Marín, A. n. F. Pérez-Cadenas, *Langmuir* 2008, *25*, 466-470.

[65]   J. M. Conner, V. C. Bulgrin, *Journal of Inorganic and Nuclear Chemistry* 1967, *29*, 1953-1961.

[66]   M. Levy, E. A. Doisy, *Journal of Biological Chemistry* 1929, *84*, 749-762.

[67]   T.-P. Fellinger, R. J. White, M.-M. Titirici, M. Antonietti, *Advanced Functional Materials* 2012, *22*, 3254-3260.

[68]   T. Ståhlberg, S. Rodriguez-Rodriguez, P. Fristrup, A. Riisager, *Chemistry – A European Journal* 2011, *17*, 1456-1464.

[69]   O. Bobleter, *Progress in Polymer Science* 1994, *19*, 797-841.

[70]   T. S. Hansen, J. Mielby, A. Riisager, *Green Chemistry* 2011, *13*, 109-114.

[71]   T. A. Houston, B. L. Wilkinson, J. T. Blanchfield, *Organic Letters* 2004, *6*, 679-681.

[72]   P. A. Wehrli, V. Chu, *The Journal of Organic Chemistry* 1973, *38*, 3436-3436.

[73]   A. Thomas, F. Goettmann, M. Antonietti, *Chem. Mat.* 2008, *20*, 738-755.

[74]   J. Ryu, Y. W. Suh, D. J. Suh, D. J. Ahn, *Carbon* 2010, *48*, 1990-1998.

[75]   W. L. Zhang, H. X. Tao, B. H. Zhang, J. W. Ren, G. Z. Lu, Y. Q. Wang, *Carbon* 2011, *49*, 1811-1820.

[76]   A. P. Katsoulidis, M. G. Kanatzidis, *Chem. Mat.* 2011, *23*, 1818-1824.

[77]   N. Brun, C. A. Garcia-Gonzalez, I. Smirnova, M. M. Titirici, *in preparation* 2012.

[78]   aN. Brun, A. Babeau-Garcia, M. F. Achard, C. Sanchez, F. Durand, G. Laurent, M. Birot, H. Deleuze, R. Backov, *Energy & Environmental Science* 2011, *4*, 2840-2844; bN. Brun, A. B. Garcia, H. Deleuze, M. F. Achard, C. Sanchez, F. Durand, V. Oestreicher, R. Backov, *Chem. Mat.* 2010, *22*, 4555-4562; cV. Flexer, N. Brun, R. Backov, N. Mano, *Energy & Environmental Science* 2010, *3*, 1302-1306; dV. Flexer, N. Brun, O. Courjean, R. Backov, N. Mano, *Energy & Environmental Science* 2011, *4*, 2097-2106.

[79]   aT. Fujiu, G. L. Messing, W. Huebner, *Journal of the American Ceramic Society* 1990, *73*, 85-90; bM. X. Wu, T. Fujiu, G. L. Messing, *Journal of Non-Crystalline Solids* 1990, *121*, 407-412; cG. T. Chandrappa, N. Steunou, J. Livage, *Nature* 2002, *416*, 702-702.

[80]   aN. Brun, S. Ungureanu, H. Deleuze, R. Backov, *Chemical Society Reviews* 2011, *40*, 771-788; bN. R. Cameron, D. C. Sherrington, *Biopolymers Liquid Crystalline Polymers Phase Emulsion* 1996, *126*, 163-214; cH. F. Zhang, A. I. Cooper, *Soft Matter* 2005, *1*, 107-113; dF. Carn, A. Colin, R. Backov, *Organic/Inorganic Hybrid Materials-2004* 2005, *847*, 159-164.

[81]   D. Barby, Z. Haq, European Patent 0060138, 1982.

[82]   N. Brun, L. Edembe, S. Gounel, N. Mano, M. M. Titirici, *Energy & Environmental Science* 2012, *submitted*.

[83]   aA. F. Gross, A. P. Nowak, *Langmuir* 2010, *26*, 11378-11383; bN. Thongprachan, T.

Yamamoto, J. Chaichanawong, T. Ohmori, A. Endo, *Adsorption-Journal of the International Adsorption Society* 2011, *17*, 205-210.

[84] aD. Wang, N. L. Smith, P. M. Budd, *Polymer International* 2005, *54*, 297-303; bN. Cohen, M. S. Silverstein, *Polymer* 2011, *52*, 282-287.

[85] aW. Kicinski, M. Szala, M. Nita, *Journal of Sol-Gel Science and Technology* 2011, *58*, 102-113; bF. J. Maldonado-Hodar, C. Moreno-Castilla, J. Rivera-Utrilla, Y. Hanzawa, Y. Yamada, *Langmuir* 2000, *16*, 4367-4373.

[86] aO. Lepine, M. Birot, H. Deleuze, *Colloid and Polymer Science* 2008, *286*, 1273-1280; bC. Youssef, R. Backov, M. Treguer, M. Birot, H. Deleuze, *Journal of Polymer Science Part a-Polymer Chemistry* 2010, *48*, 2942-2947.

[87] A. El Kadib, R. Chimenton, A. Sachse, F. Fajula, A. Galarneau, B. Coq, *Angewandte Chemie-International Edition* 2009, *48*, 4969-4972.

[88] aS. Kubo, I. Tan, R. J. White, M. Antonietti, M. M. Titirici, *Chemistry of Materials* 2010, *22*, 6590-6597; bS. Kubo, R. Demir-Cakan, L. Zhao, R. J. White, M. M. Titirici, *ChemSusChem* 2010, *3*, 188-194; cR. J. White, K. Tauer, M. Antonietti, M. M. Titirici, *J. Am. Chem. Soc.* 2010, *132*, 17360-17363.

[89] R.C. Bansal, J.B. Donnet, F. Stoeckli, *Active Carbon*, Marcel Dekke, New York, 1988.

[90] H. Jankowska, A. Swiatkowski, J. Choma, *Active Carbon*, Ellis Horwood, New York, 1991.

[91] T. Kyotani., *Porous Carbon, in Carbon Alloys. Novel Concepts to Develop Carbon Science and Technology*, Elsevier Science, Oxford, 2003.

[92] F. Derbyshire, M. Jagtoyen, R. Andrews, A. Rao, I. Martin-Gullon, E. A. Grulke, *Activated Carbon in Environmental Applications, in Chemistry and Physics of Carbon 27*, New York, 2001.

[93] L.R. Radovic, C. Moreno-Castilla, J. Rivera-Utrilla, *Carbon materials as adsorbents in aqueous solutions*, Marcel Dekker, New York, 2001.

[94] aD. Lozano-Castello, M. A. Lillo-Rodenas, D. Cazorla-Amoros, A. Linares-Solano, *Carbon* 2001, *39*, 741-749; bM. A. Lillo-Rodenas, D. Lozano-Castello, D. Cazorla-Amoros, A. Linares-Solano, *Carbon* 2001, *39*, 751-759; cD. Lozano-Castello, J. M. Calo, D. Cazorla-Amoros, A. Linares-Solano, *Carbon* 2007, *45*, 2529-2536.

[95] aL. Khezami, A. Chetouani, B. Taouk, R. Capart, *Powder Technol.* 2005, *157*, 48-56; bA. H. Basta, V. Fierro, H. El-Saied, A. Celzard, *Bioresource Technology* 2009, *100*, 3941-3947.

[96] L. Wei, M. Sevilla, A. B. Fuertes, R. Mokaya, G. Yushin, *Adv. Energy Mater.* 2011, *1*, 356-361.

[97] M. Sevilla, A. B. Fuertes, R. Mokaya, *Energy & Environmental Science* 2011, *4*, 1400-1410.

[98] M. Sevilla, A. B. Fuertes, *Energy & Environmental Science* 2011, *4*, 1765-1771.

[99] L. Zhao, N. Baccile, S. Gross, Y. Zhang, W. Wei, Y. Sun, M. Antonietti, M.-M. Titirici, *Carbon* 2010, *48*, 3778-3787.

[100] L. Zhao, L.-Z. Fan, M.-Q. Zhou, H. Guan, S. Qiao, M. Antonietti, M.-M. Titirici, *Advanced Materials* 2010, *22*, 5202-5206.

[101] S. Román, J. M. Valente Nabais, B. Ledesma, J. F. González, C. Laginhas, M. M. Titirici, *Microporous and Mesoporous Materials* 2013, *165*, 127-133.

[102] F. Carrasco-Marin, M. V. Lopez-Ramon, C. Moreno-Castilla, *Langmuir* 1993, *9*, 2758-2760.

[103] A. V. Neimark, Y. Z. Lin, P. I. Ravikovitch, M. Thommes, *Carbon* 2009, *47*, 1617-1628.

[104] J. Weber, J. Schmidt, A. Thomas, W. Bohlmann, *Langmuir* 2010, *26*, 15650-15656.

[105] J. Silvestre-Albero, A. Silvestre-Albero, F. Rodríguez-Reinoso, M. Thommes, *Carbon* 2012, *50*, 3128-3133.

[106] K. S. Walton, R. Q. Snurr, *Journal of the American Chemical Society* 2007, *129*, 8552-8556.

[107] M. Kruk, M. Jaroniec, J. Choma, *Carbon* 1998, *36*, 1447-1458.

[108] A. V. Neimark, Y. Lin, P. I. Ravikovitch, M. Thommes, *Carbon* 2009, *47*, 1617-1628.

[109] G. Y. Gor, M. Thommes, K. A. Cychosz, A. V. Neimark, *Carbon* 2012, *50*, 1583-1590.

[110] J. L. Figueiredo, M. F. R. Pereira, M. M. A. Freitas, J. J. M. Orfao, *Carbon* 1999, *37*, 1379-1389.

[111] C. Falco, N. Baccile, M.-M. Titirici, *Green Chemistry* 2011, *13*, 3273-3281.

[112] M. A. Lillo-Rodenas, J. Juan-Juan, D. Cazorla-Amoros, A. Linares-Solano, *Carbon* 2004, *42*, 1371-1375.

[113] A. Wahby, J. M. Ramos-Fernandez, M. Martinez-Escandell, A. Sepulveda-Escribano, J. Silvestre-Albero, F. Rodriguez-Reinoso, *ChemSusChem* 2010, *3*, 974-981.

4 Functionalisation of Hydrothermal Carbons

4.1 Introduction

In the previous chapter I have disclosed several possibilities to introduce porosity into HTC materials as a prerequisite to almost all applications that will be described in the next chapter. Besides high surface area and a well-defined porous structure, another requirement carbon materials must fulfil is functionality.

This is perhaps one of the biggest advantage of HTC materials compared with other nanostructured forms of carbon: **straightforward functionalisation**. The low carbonisation temperatures allow on one hand "*in situ*" parallel processes to occur (i.e. chemical reactions, nanoparticles formation) and, one the other hand, the production of carbon materials rich in polar functional groups. Such oxygenated groups can be further transformed into other chemical functionalities or facilitate hybridisation with various inorganic moieties.

In this chapter I will first discuss various possibilities for functionalising HTC materials with heteroatoms or other chemical groups using either "*in situ*" or "*post functionalisation*" processes. In the second part, I will give an overview on the production of various HTC-inorganic nanocomposites from my own research groups as well as the available literature. Coating technologies, one step processes or post-synthetic treatments will be described.

Finally I will also discuss the use of HTC materials themselves as sacrificial templates for the production of various inorganic porous structures.

4.2 *"In situ"* Chemical Functionalisation of HTC Materials

For the development of nanostructured materials for high end applications, some of the most important factors concerning material properties are:

- **Conductivity** (*e.g.* electronic applications)

- **Surface functionality** (*e.g.* adsorption, acid/base catalysis)

- **Surface area** (virtually all applications)

4.2.1 Heteroatom Doping

Pure carbon materials can fulfil the above mentinoned criteria to a certain extent, but to broaden the range of possible applications, heteroatom modification (*i.e.* "doping") is a useful tool to tune material´s properties. The introduction of, *e.g.* sulfur, boron or nitrogen into a carbon material can result in improved electrical conductivity, material stability and catalytic performance due to an increased number of active sites.[1] Remarkable progress has been made in recent years regarding the use of such carbon-based materials, and it can be expected that this trend will continue in the future.[2] Current synthetic procedures for carbon materials most commonly involve high temperature heat treatment under inert conditions (pyrolysis),[3] chemical vapor deposition[2c, 4] or arc discharge techniques.[5]

Besides being very energy consuming, these techniques also often require the use of harmful precursors which are in turn produced from fossil fuels. It is therefore a point of great interest to not only focus on the sustainability of the final application (*e.g.* electric vehicles, hydrogen fuel cells, solar cells, *etc.*) but equally on the sustainability of the entire process, *i.e.* from choosing the precursor, the synthesis conditions through to the final application. Hydrothermal carbonisation can offer the basis for such technologies. The advantages of HTC are the possibility of using cheap, readily available starting materials in a simple, low cost synthesis which requires only water as solvent.[6] Also, the abundance of heteroatoms in natural molecules such as amino acids and proteins allows for the synthesis of doped carbon materials in one step directly from biowaste, *e.g.* HTC of prawn shells.[7]

4.2.1.1 Nitrogen

As it will be described in detail in the next chapter nitrogen doped carbon materials are currently applied in several timely technological fields, especially renewable energy. Thus, the electrochemical performance of carbons can be further enhanced by nitrogen doping providing supercapacitance (in supercapacitors), inherent catalytic activity in fuel cells as well as extra Li-storage sites. Lithium ion batteries anodes employing N doped graphene demonstrate capacities as high as 1043 and 1549 mAh/g respectively. [8.9] It was proposed that the nitrogen atom could drastically alter the electronic performance, offer more active sites and enhance the interaction between the carbon structure formed and lithium, thus it is expected to improve the kinetics of lithium diffusion and transfer, benefic for electrochemical performance. [10,11]

The N-functionalities of (micro) porous carbons are valuable for supercapacitors applications as they are able to undergo redox reactions with the electrolyte and thus increase their capacity. [3a, 12] In addition N-doped carbons showed intrinsic properties as metal free catalysts in oxygen reduction reaction at the cathodic site of a fuel cell. [13] DFT calculations suggest that a possible explanation would be the high electronegativity of the nitrogen atom which then can polarise the C–N bond resulting in a reduced energy barrier of the adjacent carbon atom towards ORR. [14]

The synthesis of nitrogen doped carbons has been achieved *via* a variety of pathways, such as post treatment of carbon with ammonia, [15] amines or urea [16] and also more direct approaches using acetonitrile, [17] pyrrole, [18] polyacetonitrile, [19] or polyaniline [20] as starting products. In the context of availability and sustainability, nature offers various nitrogen containing precursors such as amino acids, peptides/glycopeptides, proteins, and aminated/amidated saccharides and polysaccharides. (*e.g.* glucosamine, N-Acetyl glucosamine). It has been repeatedly reported that these bio-monomers and –polymers can give rise to sustainable, nitrogen doped carbon materials.

The first report on nitrogen doped hydrothermal carbon was published in 2009 by our group (Titirici, White *et al.*). We used prawn shell waste as precursor in hydrothermal carbonisation.[21] Prawn shells are natural hybrid composite materials formed from chitin (a polysaccharide containing N-acetyl glucosamine units) and calcium carbonate. Hydrothermal carbonisation of chitin results in a formation of nitrogen containing carbonaceous material around the inorganic scaffold (see Figure 3-11 and 3-12 Chapter 3). Following HTC treatment, the scaffold was removed by washing with acid, leaving behind a porous, nitrogen doped material (as discussed in chapter 3). The nitrogen content of their material was 5.8 wt % according to elemental analysis and XPS revealed the presence of various nitrogen species (pyridinic, pyrrolic, and quartenary as seen in Figure 4-1).

Peak Assignment:
1. 398.2 eV (Pyridinic (**N-6**))
2. 400.1 eV (Pyrrolic (**N-5**))
3. 401.7 eV (Quartenary N (**N-Q**))
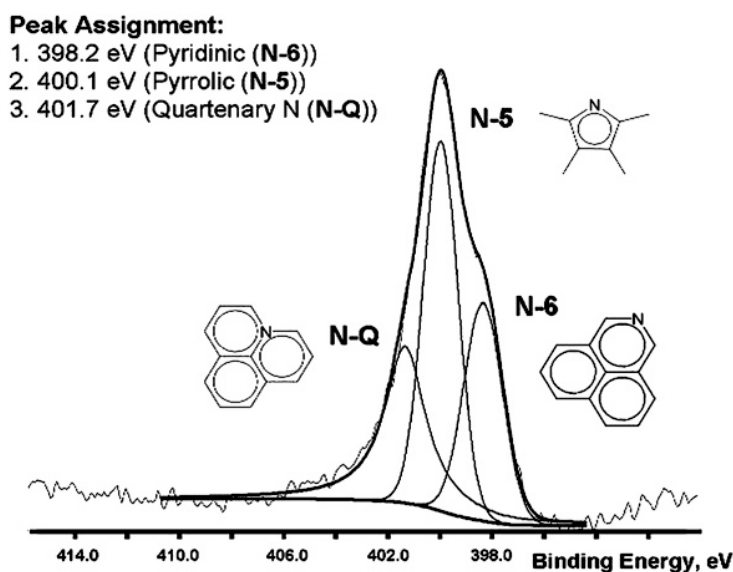
Figure 4-1: High resolution XPS spectra of the N 1(s) photoelectron region for acid washed N-doped carbon material (NB: peaks assigned using charge correction;taken with permission from [21])

In 2010, we (Baccile, Titirici *et al.*) reported on the hydrothermal treatment of glucose in the presence of the glycoprotein ovalbumin.[22] We showed that the nitrogen contained in the protein was incorporated into the final hydrothermal carbon framework while the presence of the protein also had an effect on the material morphology. Nitrogen contents of up to 8.2 wt % could be obtained. The carbon material consisted of smaller particles than when pure glucose was used as a precursor, presumably due to a surface stabilising effect of the protein in the hydrothermal reaction mixture. Through further investigations, we published later the formation of nitrogen doped organic aerogels (*i.e.* interconnected small particles arranged in a 3-dimensional porous structure) obtained by addition of ovalbumin to glucose (see Figure 3.14 Chapter 3).[23]

Other examples from our research group include the use of glucosamine or chitosan directly as carbon and nitrogen precursors,[24] as well as the addition of glycine to the hydrothermal treatment of glucose.[25] Interestingly, the nitrogen content from pure N-containing precursors (*i.e.* using only glucosamine or chitosan) ranged from 6.5 wt % to 9.4 wt % (depending on the temperature used) which is similar to the approximately 8.5 wt % obtained my mixing 0.4 g of glycine with 1 g of glucose.

Zhang et al prepared nitrogen doped carbons from sucurose in the presence of amonia [26] while Liu et al produced nitrogen doped fluorescent nanoparticles upon the hydrothermal carbonisation of grass.[27]

Overall it seems to be the case that the level of nitrogen doping *via* the aforementioned methods is limited but at the same time it is possible to achieve relatively high doping levels by using only small amounts of nitrogen source together with a readily available carbon source such as glucose. This is an advantage of HTC over other methods such as simple pyrolysis because it allows for more efficient use of heteroatom-containing precursors. During hydrothermal treatment at mild temperatures stable (aromatic) nitrogen species are formed which then remain in the carbonaceous scaffold during further pyrolysis at higher temperatures. How does the nitrogen incorporation during HTC take place? This question is under debate, however, it is generally accepted that Maillard chemistry plays a crucial role in the process.[22, 25, 28]
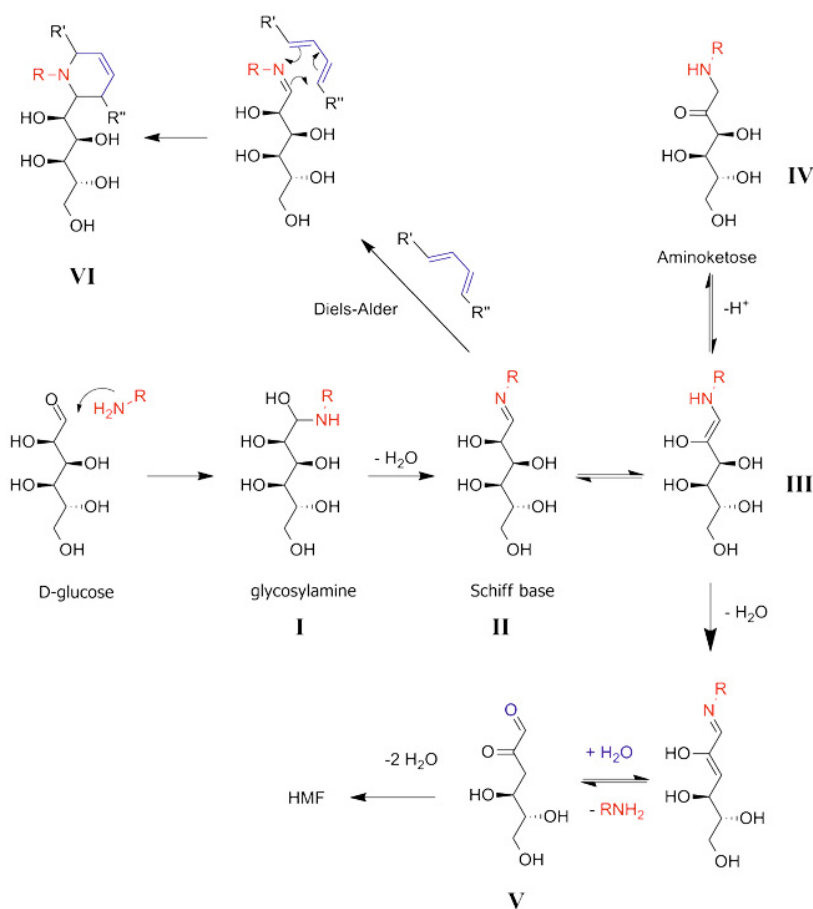
Figure 4-2: Some examples in the Maillard reaction (taken from [29]).

199

The Maillard reaction is not one specific reaction but rather refers to a group of reactions occurring between reducing sugars and amino acids. In the process, hundreds of different compounds can be created which can themselves react further in various ways. It is therefore impossible to provide a definite mechanistic pathway for the formation of N-doped HTC materials derived from saccharides and various nitrogen containing dopant molecules.[30] Some of the relevant steps in the Maillard reaction cascades are briefly presented here in order to demonstrate some of the ways in which heteroatoms can be incorporated into hydrothermal carbon from glucose or other reducing sugars.

The process starts with the nucleophilic attack of an amine (*e.g.* in amino acids) on the aldehyde of the sugar to produce glycosylamines (Figure 4-2 I), which subsequently loses water to give a Schiff base (Figure 4-2 II). The α-hydroxy aldehyde motif allows for the rearrangement of the Schiff bases to aminoketoses or so-called Amadori compounds (Figure 4-2 III and IV). [31] Compound III can form α-dicarbonyl species (Figure 4-2V) which could go through successive dehydration to form hydroxymethylfurfural (HMF, the main reactive intermediate in HTC as was explained in the previous chapter).

We conducted ^{13}C and ^{15}N solid state NMR studies of hydrothermal carbon obtained from glucose and glycine and showed that the free amine groups in glycine are mostly converted into aromatic (modified pyrazines, pyranones and pyrroles) binding motifs. We pointed out that these aromatic structures are most likely formed as a consequence of degradation reactions such as the Strecker degradation.[25, 32] Network-forming Maillard reactions on the other hand are responsible for the formation of cyclic amines and other non-aromatic nitrogen species.(Figure 4-3).[33]
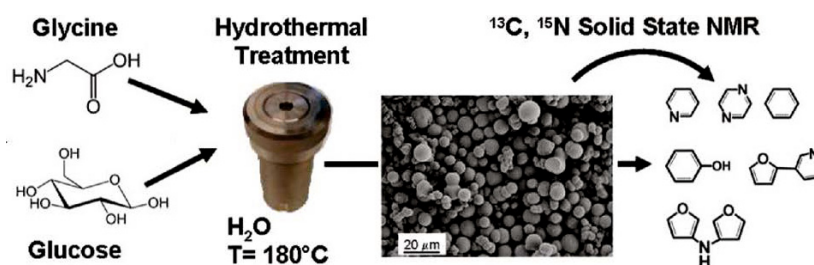
Figure 4-3 ssNMR studies carried out on nitrogen doped carbons from glucose and glycine revealed the presence of various aromatic nitrogen species in the hydrothermal carbon (taken from ref [25]).

In the majority of cases, the introduction of a dopant into hydrothermal carbon has a large effect on the product morphology. If pure glucose is treated hydrothermally at 180 °C, the resulting material morphology comprises spherical particles with a diameter of about 200 nm.[34] When a co-monomer such as an amino acid is added to this recipe, the particle size as well as size distribution usually increases.[35] This change in particle size can be understood by considering how nucleation takes place in HTC and how the presence of additional reactants can affect the nucleation process. The LaMer model is widely cited in colloid chemistry to explain the formation of monodisperse particles from supersaturated solutions.[36] Briefly, it involves the increase in concentration of a dissolved species until a critical point is reached; at which rapid nucleation ("burst nucleation") occurs. A growth phase follows, during which the remaining monomer in solution diffuses to the nuclei formed in the seeding stage. The first nucleation stage can be described as homogeneous nucleation whereas the growth phase is basically heterogeneous nucleation, because monomers add onto pre-existing nuclei.[37] Once the first species has formed nuclei *via* homogeneous nucleation, the next species may preferentially nucleate heterogeneously and therefore determine the final number of particles and their size. The difference in solubility of formed intermediates in water and the changing solvent properties of water itself as it is heated to 180 °C results in variations in the critical concentrations needed to drive nucleation. The more complex the reaction mixture, the more different products are formed at different points in time.[38] Having additional co-monomers such as amino acids in the hydrothermal reaction mixture is therefore expected to result in an increased particle size and overall size distribution. However, when HTC is carried out with pure nitrogen containing precursors such as glucosamine or chitosan, smaller particle sizes than those from pure glucose have been observed (Figure 4-4).[24a] This may be due to the fast rates at which Maillard reactions occur, resulting in early nucleation and hence smaller final particle size.
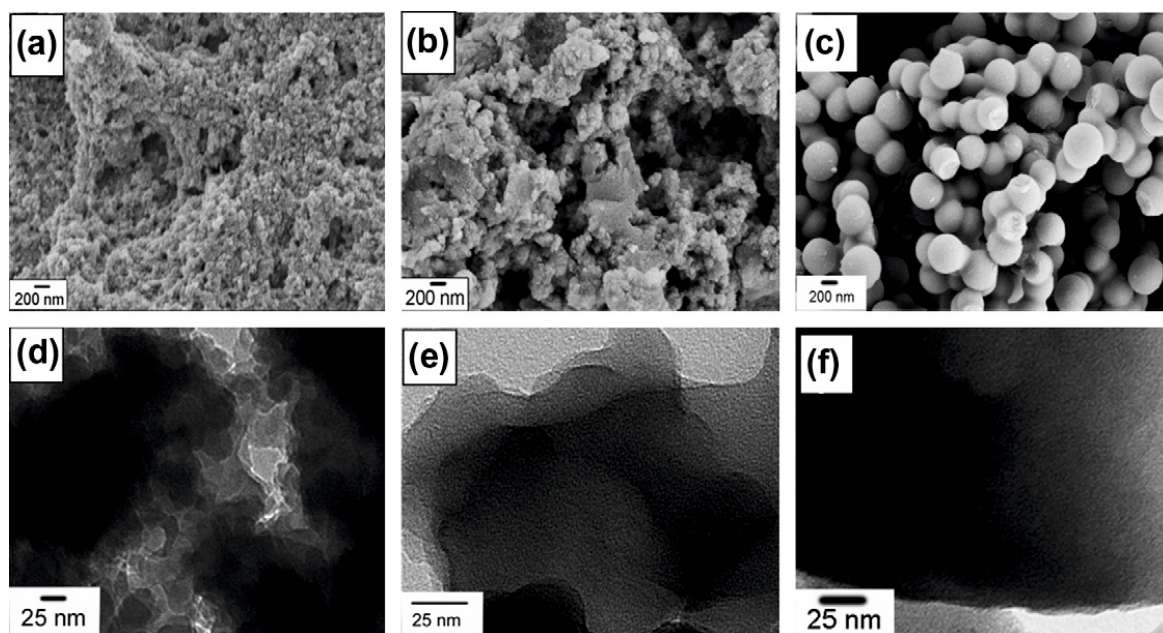
Figure 4-4 – Scanning (a)–(c) and transmission (d)–(f) electron micrographs of the nitrogen-doped carbons obtained upon hydrothermal carbonisation of (a) and (d) chitosan (HC-CH); (b) and (e) glucosamine (HC-GA) (c) and (f) glucose (HC-G).[24a]

In some cases the addition of a co-monomer may give rise to smaller particles than obtained from pure glucose *via* some surface stabilizing effect. One example is the previously mentioned HTC of glucose in the presence of albumin, but also HTC of glucose in the presence of ethylene diamine (EDA) which dramatically alters the product morphology as shown in Figure 4-5.[22, 28, 39] To study the formation mechanism of the unique net-cross structure of N-doped carbons, Sun and co-workers performed a series of control experiments. Firstly, to determine the effect of reactant concentration on structure, EDA amounts were tuned from 0.2 mL, 0.5 mL, 1.0 mL up to 2.0 mL with a fixed glucose concentration of 1M at 180° C for 8 h (Figure 4-5). The morphologies of the carbon materials changed significantly with increasing EDA amount. Only spherical materials particles were obtained when the EDA amount was less than 0.2 mL (Figure 4-5a). The product after addition of 0.5 mL EDA seemed to be composed of many aggregated spheres with an average diameter of 80 nm (b), obviously smaller than the previous sample. When the EDA amounts were more than 1 mL (Figure 4-5 c and d), the carbonaceous materials were completely converted into a similar mesoporous structure, in

which the links between carbon spheres became clearer. The results confirmed that under mild conditions, the addition of EDA depressed the size of these spherical units and promoted their links to form a net-cross structure.
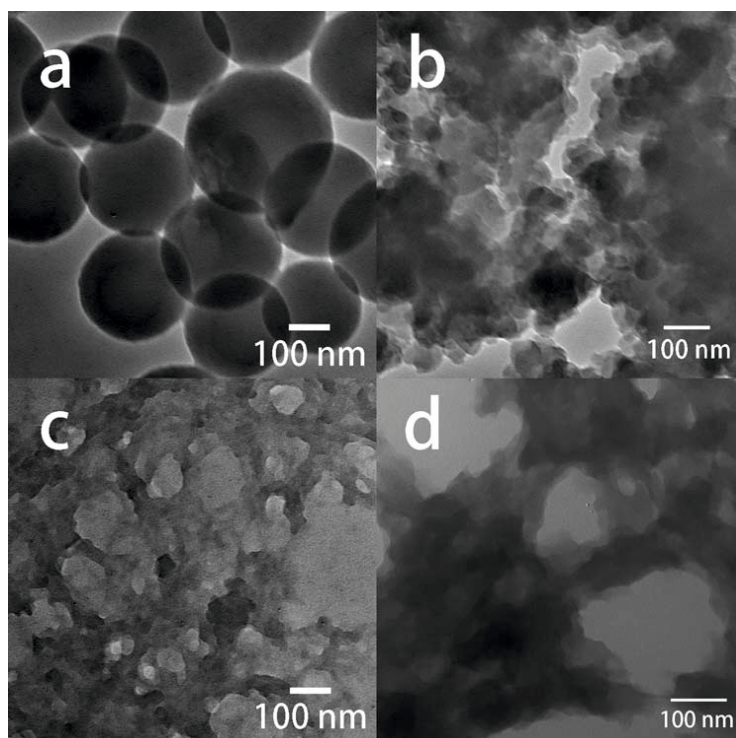
Figure 4-5 TEM images of NC prepared in different ratios of glucose/EDA: (a) 1 M/0.2 mL, (b) 1 M/0.5 mL, (c) 1 M/1 mL, (d) 1 M/2 mL (taken from [39]).

The as-synthesised hydrothermal carbons are generally non-conductive because of their low temperature synthesis. In order to render these materials electrically conducting, they may be further treated in a pyrolysis step at sufficiently high temperatures (usually 750 °C and above). This heat treatment results in further dehydration, decarboxylation of the carbonaceous material as well as further condensation and aromatisation (see chapter 2, section 2.2.4 and 2.3.7). The presence of *in situ* dopants can significantly influence the electrical conductivity of the material. The applications of N doped carbon will be largely discussed in chapter 5. Here I will only give a few examples of how N doped materials can be used for some very specific application.

In 2010 our group showed that nitrogen doped carbons obtained *via* HTC (using glucosamine or chitosan as carbon precursor) have a higher electrical conductivity than undoped hydrothermal materials.[24a] In order to achieve electrical conductivity we used a pyrolysis step at 750 °C after the HTC at 180 °C. A sample obtained from pure glucose exhibit a specific electrical conductivity

of around 80 Sm^{-1} while both N-doped carbon materials from chitosan or glucosamine exhibited higher values of over 100 Sm^{-1}.

The first report on a specific application, namely as supercapacitor materials, appeared later that same year.[12d] Details are given in Chapter 5. Another example of specific applications is the formation of a nanolatex system consisting of nitrogen doped (glucosamine-derived) hydrothermal carbon spheres dispersed in an ionic liquid polymer.[24b] Film formation of the nanolatex gave rise to cohesive films with high electrical conductivity (when pyrolised carbons were used) and promising thermal insulation properties.

Another example where N doped carbons proved their superior properties is provided by Liu *et al.* They loaded Pt nanoparticles onto nitrogen doped mesoporous carbon materials obtained from glucose and ethylenediamine as described previously (see Figure 4-5 however annealed at a comparatively low temperature of 400 °C). Their material was used to catalyse *p*-nitrophenol reduction by $NaBH_4$ and compared to supports without nitrogen doping as well as doped and undoped supports without Pt nanoparticles (Figure 4-6).[39] The material doped with nitrogen showed significantly higher conversion than the undoped material or the supports without platinum nanoparticles.
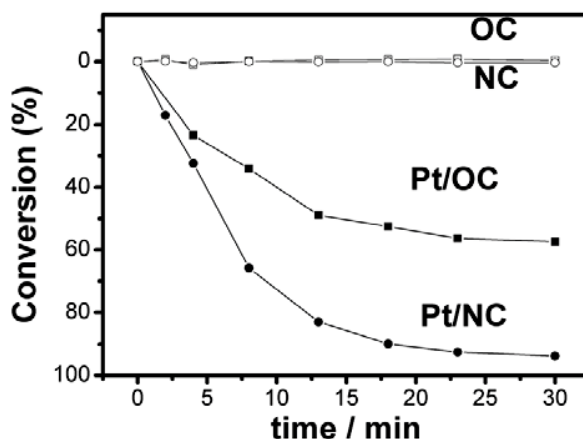
Figure 4-6 Conversions of p-nitrophenol obtained with HTC, Pt/HTC, N-doped HTC (B) and Pt/N-foed HTC catalysts (catalyst: 5 mg, p-nitrophenol: 0.15 mM, NaBH4: 47 mM, room temperature and atmospheric pressure taken from [39])

The better catalytic performance of Pt@N-doped HTC was mainly attributed to a uniform dispersion of active sites of Pt NPs on the surface of the mesoporous carbons, as revealed by the

TEM analysis. It was clearly observed that Pt NPs loaded on N-doped carbon were smaller and exhibited a quite discrete dispersion while the ones on non-doped HTC tended to agglomerate. From the size distributions of Pt N-doped HTC it was confirmed that they were more uniform, with a smaller average diameter of 4.6 nm compared with those deposited on non-doped HTC (6.7 nm). The reason why N-doping could help Pt NPs assemble uniformly on the carbon surface seemed to be explained by the interactions between the empty orbital of a Pt atom and the free electron pair of an N atom,which could limit the mobility of the Pt NPs and prevent them from agglomerating.

4.2.1.2 Sulfur

Complementing nitrogen as a dopant, sulfur is receiving increasing attention in current carbon materials research. In contrast to nitrogen which is often used to alter electronic properties of the carbon material, sulfur has been used more for the alteration of physical properties (*i.e.* to induce structural defects or increase interlayer spacing of graphitic lattices) and for applications where its easily polarisable lone pairs (and thus chemical reactivity) are of importance. Sulfur doped carbon materials have, for example, shown beneficial effects on the selective adsorption of waste metals[40] and the desulfurylation of crude oil.[41] The synthesis of these sulfur doped materials generally involves the pyrolysis of sulfur containing, polymer based carbons,[40-42] but also arc vaporization in the presence of sulfur containing compounds such as thiophenes.[5a] Yang *et al.* reported on the synthesis of sulfur doped graphene with enhanced electrocatalytic properties in the ORR, prepared by annealing graphene oxide and benzyl disulfide under argon at high temperatures (600 to 1050 °C).[43] Choi *et al.* synthesised heteroatom doped carbon materials by the pyrolysis of amino acid/metal chloride composites. They were able to show that materials containing both nitrogen and sulfur increased the material's ORR activity in acidic media, relative to undoped or purely nitrogen doped carbons.[3a] Tsubota *et al.* prepared sulfur and nitrogen dual doped carbons *via* the pyrolysis of thiourea and formaldehyde.[3b] Their material exhibited superior performance as supercapacitor electrodes than commercial activated carbons. The combined incorporation of nitrogen and sulfur may therefore also yield interesting properties.

In the context of HTC, analogous experiments to the aforementioned N-doped systems have been carried out by our group (Wohlgemuth *et al.*). We used small molecules (cysteine, thienyl-cysteine) as co-monomers in the HTC of glucose.[35] Considering that both cysteine (Cys) and

thienyl-cysteine (TCys are amino acids, incorporation of Cys and TCys is thought to involve the Maillard reaction pathway). However, both molecules contain an additional nucleophile (thiol or thienyl moiety to the free amine). Because sulfur nucleophiles cannot undergo classical Maillard reaction cascades (they cannot form Schiff bases), alternative reactions must take place. We could show that in the case of sulfur, the heteroatom binding state in the final hydrothermal carbon may be controlled during HTC. If an aliphatic sulfur source like Cys is used as an additive, nitrogen and sulfur dual doped carbon materials with aliphatic (thio-ether or thiol) sulfur binding motifs are obtained (after HTC at 180 °C). Note that HMF also contains an α,β-unsaturated aldehyde motif, allowing Michael addition to take place, representing one way of forming thio-ethers.[44] In contrast, the use of aromatic sulfur precursors such as TCys results in nitrogen and sulfur dual doped materials with aromatic (thiophene) binding motifs. This was confirmed by XPS analysis (Figure 4-7).[35]

In another example, we synthesised sulfur (and nitrogen) doped carbon aerogels using thiophene carboxaldehyde as sulfur source.[1e] Again, the thiophene motif was retained in the as-synthesised hydrothermal carbons, implying that these types of monomers are incorporated either *via* an electrophilic aromatic substitution or chemistry involving the aldehyde. However, detailed mechanistic investigations are still required.
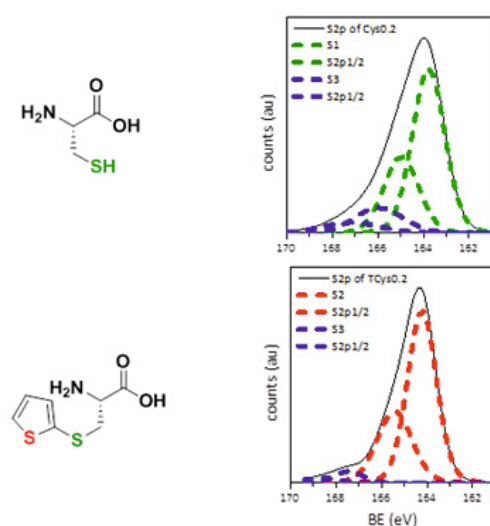
Figure 4-7 Deconvoluted S2p photoelectron envelopes for hydrothermal carbon obtained from glucose and Cys or glucose and TCys after HTC at 180 °C. The green, red and blue dashed lines correspond to aliphatic (thiol, thio ether), aromatic (thiophene) and oxidized (sulfone, sulfonic acid, sulfoxide) sulfur species, respectively.

We have shown that sulfur and nitrogen dual doped carbon spheres exhibited higher electrical conductivity than undoped carbon materials after pyrolysis at 900 °C.[35] It is however unclear whether this effect comes from the sulfur or the nitrogen dopant. The presence of sulfur atoms in the carbon scaffold was shown to increase the graphitic interlayer spacing due to the large size of the sulfur atom. However, we were unable to test the materials for specific applications due to the low surface area of the carbon microspheres.

In one later report on sulfur/nitrogen dual doped carbon aerogels we could show that the presence of sulfur in addition to nitrogen greatly improves the electrocatalytic performance towards oxygen reduction of the pyrolised (900 °C) materials in both acidic and alkaline media (see Chapter 5/electrocatalysis).[1e] This was postulated to be due to a synergistic effect between nitrogen (which activated oxygen dissociation) and sulfur (which aids proton transport), although detailed mechanistic investigations are still required.

4.2.1.3   Boron

Boron is another important highly desired dopant in carbon materials and B doped materials proved to have also very important applications in H_2 storage due to the modification of energy landscape of adsorbing surfaces and strong surface heterogeneity. [45] Boron doping is also considered to be one of the very few promising candidates for chemical protection of C/C composite materials against oxidation. [46] This was thoroughly studied by Radovic, Thrower at al in ref [47]. In addition recently boron doped carbons also proved to have superior electrochemical properties. [48] As in the case of other heteroatom doped carbons born doping was mainly achieved in carbon nanotubes and recently graphene, using high temperatures procedures. [49]

Up to now there is no hydrothermal process to produce boron doped carbon materials from biomass precursors. However, there are a few manuscripts on the fabrication of 2D ordered mesoporous carbons (OMCs) *via* a one-pot organic-organic aqueous self-assembly approach, using resorcinol (R) and formaldehyde (F) as the carbon precursor and triblock copolymer Pluronic F127 as the mesoporous structural template.

Zhang et al used boric acid and/or phosphoric acid, where the F127 soft-template underwent a self-assembly process under a strong acidic condition to form a polymer with ordered mesostructure, which was then carbonised at 800°C in a nitrogen atmosphere to form B-incorporated, P-incorporated, or B, P-coincorporated OMCs. Such resulting heteroatom-

incorporated OMCs exhibited superior electrochemical performances to non-incorporated counterparts when used as electrodes of supercapacitors. [50]

In a very recent work Su together with the previous authors showed that the capacitance of such materials can be increased up to 177 F/g. This is assumed to be due to the fact that B and P elements were introduced in the form of oxygen-containing groups and may interact mutually as the hydrothermal temperature is increased.

4.2.2 *"In situ"* Functionalisation with Organic Monomers

Along with the Maillard chemistry, non-Maillard reactions are also thought to simultaneously take place in hydrothermal environment. Hydroxymethyl furfural (HMF) and other furanic intermediates produced during HTC process (see chapter 2 for more details) are considered to play a major role in non-Maillard pathway to form nitrogen doped HTC carbons. One of the possible pathways for nitrogen incorporation is *via* Diels Alder (DA) cycloaddition. Imines (Figure 4-2 II) formed through Maillard chemistry could most likely go through imino-DA reactions with reactive dienes found in furans resulting in a formation of heterocycles (Figure 4-2 VI).[51] The reactivity of furans towards dienophiles were confirmed upon addition of vinyl monomers such as acrylic acid (AA) and vinyl imidazole (VI).[52]

Our group determined that the addition of AA and VI resulted in hydrothermal carbons rich in carboxylate groups or doped with up to 8.2 wt% nitrogen (in the form of imidazoles), respectively. Solid state carbon NMR studies of acrylic acid functionalised hydrothermal carbons revealed the decreased content in sp^2 carbons (and increased signal from sp^3 region) from modified carbons compared to the standard un-functionalised HTC carbon. Furthermore, the signals from the furanic become smaller whereas increases in aromatic peaks are observed as more acrylic acid is added to the reaction mixture (Figure 4-8).
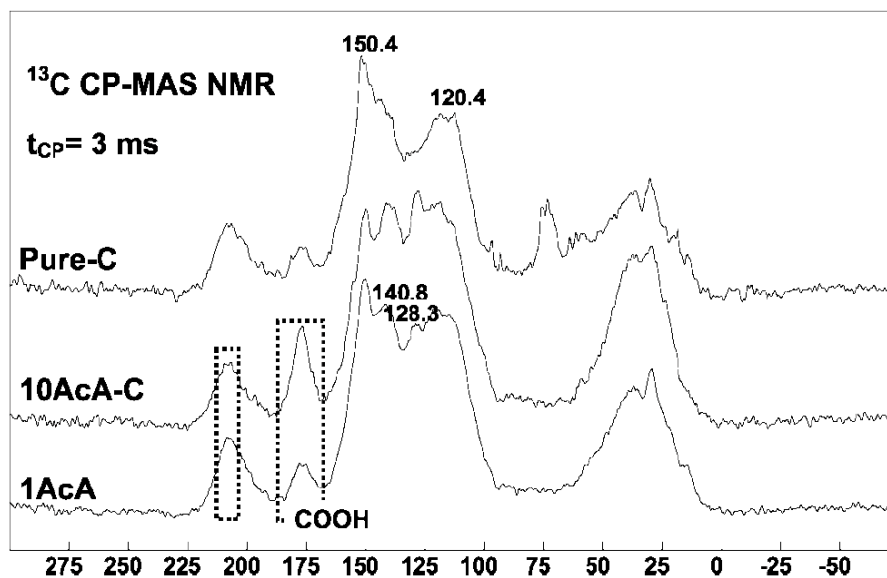
Figure 4-8: ^{13}C **solid-state NMR of acrylic acid functionalised carbonaceous materials. Top: no acrylic acid added, middle: 10 wt% acrylic acid added as a dopant, bottom: 1 wt% acrylic acid added as a dopant (taken from** [52a]**)**

In this case, the function of the added small molecules can be transferred over to the final *in situ* functionalised HTC material. In another words, HTC material becomes the solid support for the added molecule, where its functionalities are presented on its surface.

As seen with free carboxylates, the carboxylate rich HTC materials exhibited metal chelating characteristic with high capacities of 351.4 mg/g for Pb(II) and 88.8mg/g for Cd(II) which is demonstrates the material's high potential for water purification applications [52a] (see more details in Chapter 5/ adsorption 5.7.1)

Zeta potential and FTIR experiments of the resulting imidazole-functionalised carbonaceous materials demonstrated the presence of unaltered imidazole groups. To further prove their existence on the HTC carbon surface, these materials were successfully used as catalysts for various transesterification, Knoevenagel and Aldol reactions. To improve performance, the imidazole surface groups were converted to imidazolium groups by alkylation using butyl bromide (sample name HC-10Bu2ImBr, Figure 4-9).
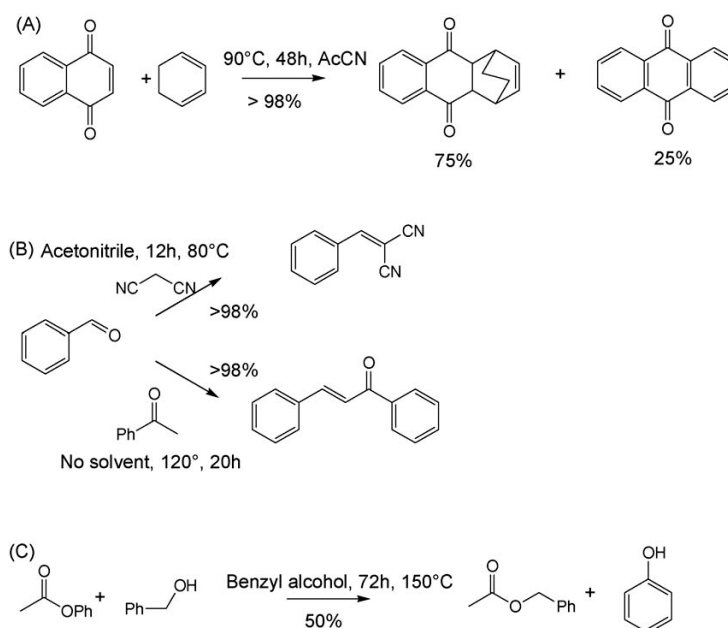
Figure 4-9: Reactions catalysed by imidazole-functionalised hydrothermal carbon (HC-10Bu2ImBr): (A) Diels–Alder, (B) Knoevenagel and Aldol condensation, (C) transesterification.[52b]

Overall, it is clear that *in situ* functionalization of carbon materials *via* HTC can greatly influence the final material's physicochemical properties. *In situ* doping has the great advantage of being simple to carry out, usually requiring only a one pot reaction and if needed a post pyrolysis step. This approach will alter the bulk material properties, although certain variations (e.g. in the type of heteroatom species present) between batches are to be expected since the method allows for very little chemical control.

For a more controlled modification of hydrothermal carbons, post-modification for the introduction of heteroatoms may be a more appropriate approach. These post-modified carbons will be discussed in the next section.

4.3   Chemical Post-Modification of Carbonaceous Materials

The potential downside with the *in situ* functionalisation method is the HTC condition itself (>180 °C, water as a solvent, pressure), where structures of many conventional small molecules could be altered. In this regard, post-modification of the pre-formed HTC material compared to *in situ* functionalisation could offer a milder and controlled functionalisation process. Another difference between the *in situ*-, and the post-modification approach is that while *in situ* approach

results in the introduction of additives throughout the bulk material, post-modification allows only for the surface to be modified. Regardless, along with the *in situ* functionalisation, post-modification of HTC materials has potentials to allow for further control over the synthesis of HTC carbons with desired properties.

Typical materials produced from HTC present polar oxygenated surface groups such as hydroxyl groups, ketones, and carboxylic acids, which can also act as a handle for the surface modification of HTC carbons. Another major characteristic of a HTC carbon (discussed in detail in chapter 2), lies in the abundance of furans.[52a] Post-pyrolysis of the HTC carbon leads to decreased content in the polar functional groups as well as the furanic structure, rearranging to more condensed arene structure (see chapter 2, section 2.3.7). The presence/absence of the polar functional groups as well as the furanic/arene core depends on the pyrolysis temperature. In this regard, the functionalisation strategy may alter, based on the preparation condition of the HTC carbon. Herein, a short list of post-modification of HTC carbons as well as alternative potential post-modification strategies will be introduced and discussed.

4.3.1 Nucleophilic Substitutions

Our group achieved the etherification of HTC by addition of 3-chloropropyl amine to ordered hydrothermal carbons (OHC) prepared at 180°C Figure 4-10a.[53] The modification was confirmed from elemental analysis (~ 4.5 N%), FT-IR, and TGA. Furthermore, while amino-modified OHC exhibited positive zeta potential in acidic media, the unmodified OHC was found to have a negative zeta potential even in the acidic media, further supporting the success of the substitution. Chemical modification was found to have little influence of the structure of the OHC, as observed from SAXS patterns and N_2 adsorption isotherms.

As an alternative strategy to modify the surface hydroxyl groups, our group had also silylated the hydroxyl groups of the carbon hollow sphere prepared at 550°C using (3-aminopropyl) triethoxysilane (APTES) Figure 4-10 b).[54] FT-IR of the APTES functionalised carbon hollow sphere showed the appearance of symmetric N-H and C-H stretching vibration bands in the 3000-2800 cm^{-1} region confirming the successful introduction of surface amino groups. The introduction of the amine was also confirmed by elemental analysis (4.1 N%) as well as the pH sensitive water dispersion behaviour.
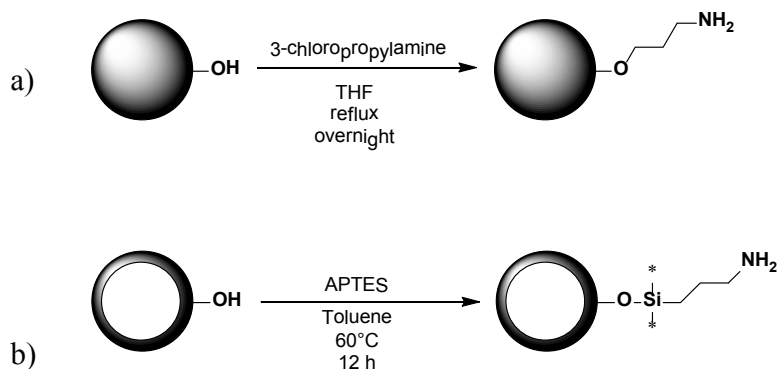
Figure 4-10:a) Amination of carbonaceous sphere using 3-chloropropylamine; b) Modification of hollow spheres with APTES (taken from[53]).

Surface amino groups of APTES modified HTC carbons have been further used as a handle for subsequent surface functionalisation. Amidation of N-hydroxysuccinimide-activated poly(N-isopropylacrylamide)(pNIPAM, ~30 kDa) has been carried out to prepare polymer grafted carbons.[55] Based on the results found from elemental analysis, surface grafting density of pNIPAM on the HTC carbon surface was determined to be 1.9 mg/m^2. The thermoresponsive behavior of pNIPAM grafted carbons was tested by cycling the temperature of the carbon-aqueous dispersion between 15 – 40°C. Clear differences in dispersion behavior were observed temperatures below and above the LCST of pNIPAM as shown in Figure 4-11. Such stimuli-responsive carbon capsules with porous walls have a great potential to be used as drug delivery platforms where the release could be triggered by temperature change. In this respect we need to mention that the lowest critical solution temperature where the polymer is changing its properties from hydrophilic to hydrophobic (from expanded to coiled structure respectively) could be modulated to body temperature. In the future other stimuli responses could be added to such carbon structures such as for example light and pH.
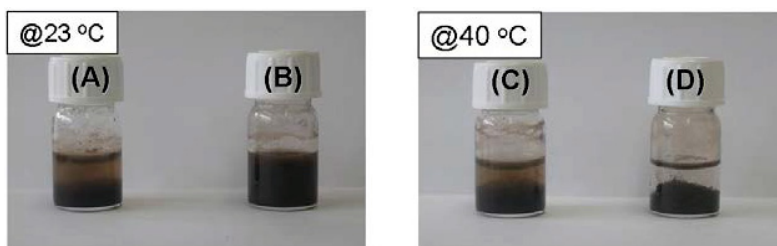
Figure 4-11. (A) HCT and (B) HCT-PNiPAAm (0.3 wt%) in water at 23 °C and (C) HCT and (D) HCT-PNiPAAm (0.3 wt%) in water at 40 °C.

212

4.3.2 Cycloadditions

Despite the popularity of Diels-Alder (DA) cycloaddition mediated functionalisation of carbon materials such as CNT,[56] graphene,[57] and fullerene,[58] the application of DA for the preparation of surface modified carbonaceous material has yet to be fully explored. To our knowledge, the first example for the DA addition mediated surface modification of preformed carbonaceous materials was carried out by Kaper *et al.*[59] In this study, five types of carbon/carbonaceous materials were modified using potential dienophiles as shown in Figure 4-12. The addition was confirmed along with the decreased surface area, pore volume, and pore size of the carbon material.
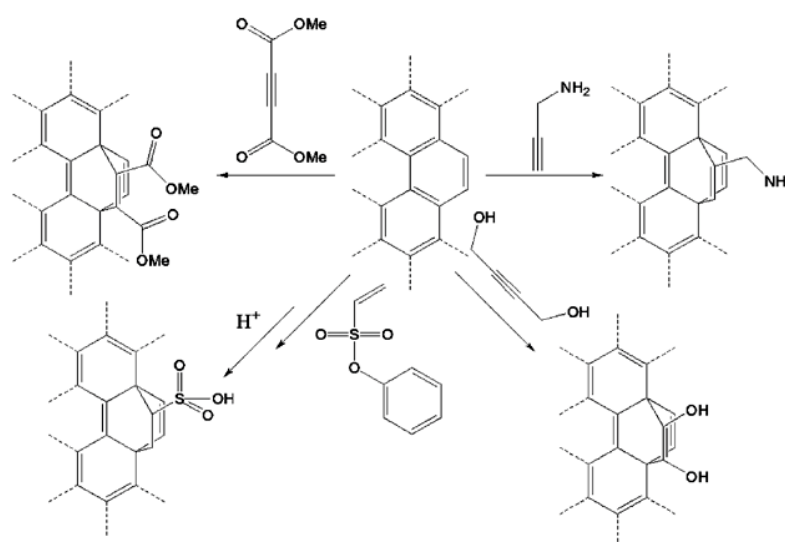
Figure 4-12: Suggested reaction scheme for the functionalisation of carbonaceous materials by a Diels–Alder reaction.

Urakami *et al.* has also attempted to surface functionalise HTC carbon spheres using dieophiles.[60] HTC material prepared at 180°C and carbon spheres post-pyrolyzed at 550°C were modified using maleimide (MI), tetracyanoethylene (TCNE), and 4,5-dicyano-1,3-dithiol-2-one (DCDTO). DCDTO-functionalised HTC samples were then hydrolysed in an attempt to obtain thiol-functionalised HTC@180 and @550 (Figure 4-13a). As shown in Figure 4-13b, FTIR showed the disappearance of the dithiocarbonyl band at 1730 cm^{-1} upon acid-catalysed alcoholysis. SEM images showed no apparent morphological differences between the unfunctionalised-, DCDTO functionalised-, and the hydrolysed-HTC samples. To prove the

213

accessibility of surface bound thiols, polyethylene glycol (PEG480) acrylate and anthracene acrylate were successfully attached onto carbon surface *via* conjugate addition.
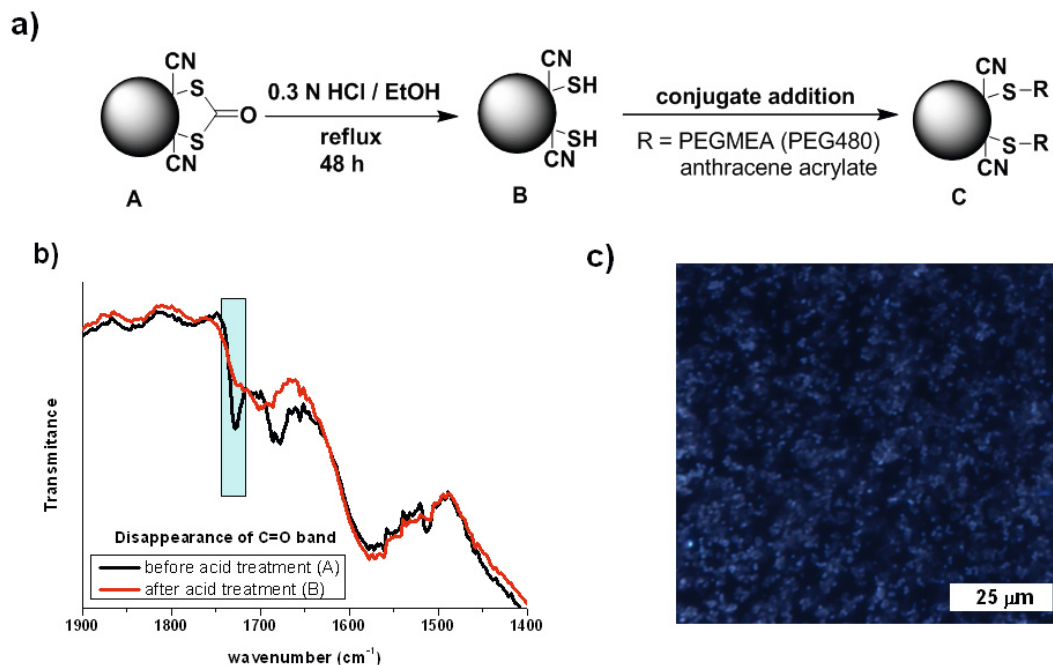
Figure 4-13: a) Proposed reaction scheme of the alcoholysis and the subsequent conjugate addition b) FTIR if before (A) and after (B) the acid catalysed alcoholysis c) Fluorescent image of anthracene-functionalised HTC@180 (taken from [60]).

4.3.3 Other approaches

Macia-Agullo *et al.* has prepared sulfonated HTC microspheres by treating the HTC material prepared from glucose/225°C with concentrated H_2SO_4 for 15 hours at 150°C.[61] Despite the harsh reaction condition, sulfonation process did not alter the spherical morphology, particle size, no the surface area of the HTC material. The sulfur content was determined by elemental analysis (< 2%) and S2p peak from XPS spectrum corresponded to that of an oxidized sulfur. The sulfonated HTC material was applied as a solid acid catalyst for esterification of oleic acid for the production of biofuels and exhibited higher catalytic activity than commercial solid acids, such as Amberlyst-15 (See Chapter 5/ heterogenous catalysis).

Shoujian Li and coworkers reported that a large number of oxygen-containing functional groups (OFGs) could be additionally created on the surface of HTC material by simple thermal treatment

at low temperature (i.e. 300°C) under air.[62] Furthermore, surface character (e.g. polarity) and functional group type can be tuned by employing simple post-carbonisation under an inert atmosphere. By heat treatment at T = 350°C, –OH groups disappear and the surface groups such as "–C=O" and –C(O)OH become more dominant. Additional treatment at T = 500°C eliminates some "carbonyl" features, while most of the carboxylic groups remain. Further treatment at higher temperatures (i.e. T > 550°C) eliminates the majority of the residual oxygenated groups and converts the carbon structure into a turbostratic-like disordered carbon structure with an increasingly more classical aromatic character and hydrophobic properties.

4.3.4 Perspectives for HTC Chemical Post-Modification

Compared to other carbon materials such as carbon nanotubes, fullerene, graphene/graphene oxides, and porous carbon materials (i.e. CMK-series), the post-modification strategy of HTC materials are still under developed. One of the unique characters of the HTC material is that the surface presented functional groups can be greatly influence depending on the preparation approaches from more hydrophilic (-OH, -COOH)/furanic character to hydrophobic/condensed arene-like characters. The change in the surface chemistry of the HTC materials also implies that the post-modification strategies must be adjusted to the HTC material of interest.

As indicated in previous sections, the abundance of furans within the HTC structure makes an attractive target for further modifications. Traditionally speaking, furans and furan-related molecules have been heavily investigated due to their significance as an important intermediate in the conversion from biomass to various chemicals as well as their presence in numerous bioactive natural products. The importance of furans has caused chemists to investigate the synthesis and various functionalisation methods of furans. In this regard, the accumulated knowledge of classical furan chemistry should be exploited towards new functionalisation strategy of the HTC material. As an example, furans are known to be functionalised using electrophiles and go through transformations such as acylation, alkylation, halogenation, nitration, and condensations. Furthermore, furans can go through metallations and further cross-coupling reactions. [63] [64]

In addition to furan chemistry, other chemical modification strategies incorporating oxygenated polar functional group should be further investigated as well. Other than etherification and silylation, surface present hydroxyl groups may also be used to react with electrophilic carbonyls (activated esters, isocyanates). Carbonyl groups on the HTC surface may also be utilised as a

handle to introduce heteroatoms through imine formation, conjugate addition, as well as introduction of sulfur atoms *via* the use of Lawesson's reagent.

For the modification of the HTC material with more condensed arene structure, functionalisation knowledge from other established carbon materials (fullerene, CNT, graphene, graphene oxide, and various porous carbon materials) could be used as an example.[65] Other than the [4+2], other cycloadditions such as 1,3-dipolar cycloaddition or [2+1] carbene, nitrene chemistry may be adopted.[65c, 66] Swager and co-workers have recently showed that other pericyclic reactions such as claisen rearrangements could be applied for the functionalisation of graphene oxides.[67] Electrophilic aromatic substitution such as Friedel-Crafts arylation or aryl diazonium chemistry has also been a utilized as a modification strategy.[68] Other oft used modification approaches include, halogenation and addition of carbon radicals.[69]

One of the platform modification strategies has been the oxidation of carbon materials. Classically, carboxylic acid has been introduced to these materials *via* the use of strong acids such as HNO_3/H_2SO_4 or in basic condition such as ammonium peroxide/hydrogen peroxide.[70] More recently, milder alternative oxidation conditions have been investigated.[71] The carboxylic groups are often activated the further modified to esters and amides. Carbon materials can also be altered through ozonolysis, where reductive or oxidative work-up could be applied to the molozonide intermediate to form various oxygenated functional groups.[72] Epoxidation is another attractive modification approach for carbon materials,[73] due to its facile installation and the possibility for the subsequent nucleophilic ring-opening for further modification.[74]

4.4 Coating HTC onto Preformed Nanostructures

For the HTC process, another important and convenient advantage is that it can be used to rationally form the carbonaceous shell on the surface of pre-formed nanostructures. The coating process can be easily controlled and the HTC carbonaceous shell can form on the surface of most nanostructures, such as inorganic, organic, and polymeric nanostructures. However, this strongly depends on the surface properties of these nanostructures.

Such carbonaceous shells not only protect the respective nanostructures, but also bring new chemical or physical properties. Such resulting nanocomposites showed important applications in many fields, such as catalysis, fuel cells, drug delivery, and bio-imaging. (see next chapter for more details).

A particularly interesting example is the synthesis of uniform Te@carbonaceous composite nanocables using the HTC process in combination with ultralong Te nanowires with diameters of several nanometers described by Shu-Hong Yu and co-workers. Te nanowires can subsequently act as sacrificial templates and glucose as the starting reagent (Figure 4-14a-b).[75] Te nanowires could not only restrain the usual homogeneous nucleation of carbonaceous spheres (see Chapter 2, section 2.2.1) but also promote the heterogeneous deposition of carbonaceous shell on the backbone of Te nanowires. The diameter of the final nanocables could be easily adjusted by changing the hydrothermal carbonisation time, or the ratio of the tellurium and glucose. The same authors also synthesised silica/carbon-encapsulated core shell spheres using the HTC process with silica spheres as the template and glucose as carbon precursor.[76] The carbonaceous shell could protect the nanostructures, after some additional heat treatment and graphitisation process, improving thus the physical properties of the newly resulting nanocomposites.

Carbon-coated Fe_3O_4 nanospindles could be synthesised by the HTC process and the subsequent heat treatment by the same researchers (Figure 4-14-5c).[77] These composites could be used as a superior anode material for lithium-ion batteries with high coulombic efficiency in the first cycle, high reversible capacity, enhanced cycling performance, and high rate capability compared with bare hematite spindles and commercial magnetite particles. The improved performance was mainly attributed to the uniform and continuous carbon coating layers, which increased the electronic conductivity, forming and stabilising uniform and thin solid electrolyte interphase film on the surface.

Similarly, our group produced carbon-coated Si nanocomposites, coating a thin HTC layer on the surface of commercially available Si nanoparticles followed by additional heat treatment. Such composites displayed a significant improved lithium-storage performance because of the generation of a passivated layer of SiO_x and carbon (Figure 4-14 e-f)-details in chapter 5, section 5.2.1.1.2.[78]

Carbonaceous shell has been used as a powerful tool for the smart design of complex nanocomposites. One example is the synthesis of the coaxial SnO_2@carbon hollow nanospheres produced by removing silica from the original SiO_2@SnO_2@carbon structures.[79] The as-synthesised nanocomposites performed as high-energy anode materials for the lithium-ion battery with exceptionally good life cycles (100) and good rate capability.

Similarly, complex nanostructures of tin-nanoparticles encapsulated in elastic hollow carbon spheres (TNHCs) have been successfully synthesised by Zhang et al (Figure 4-14 g-h).[80] SiO_2 spheres were used as the core for the deposition of SnO_2 shell *via* the hydrolysis of Na_2SnO_3. After etching the core of SiO_2 by sodium hydroxide solution, SnO_2 hollow spheres were coated with a carbonaceous shell *via* the HTC process. After additional heat treatment at 700°C for 4 h under N_2 atmosphere, complex TNHCs hybrid materials were synthesised. Such hybrid materials were promising anodes for high-performance lithium-ion batteries with high specific capacity, high volume capacity and good cycle performance.
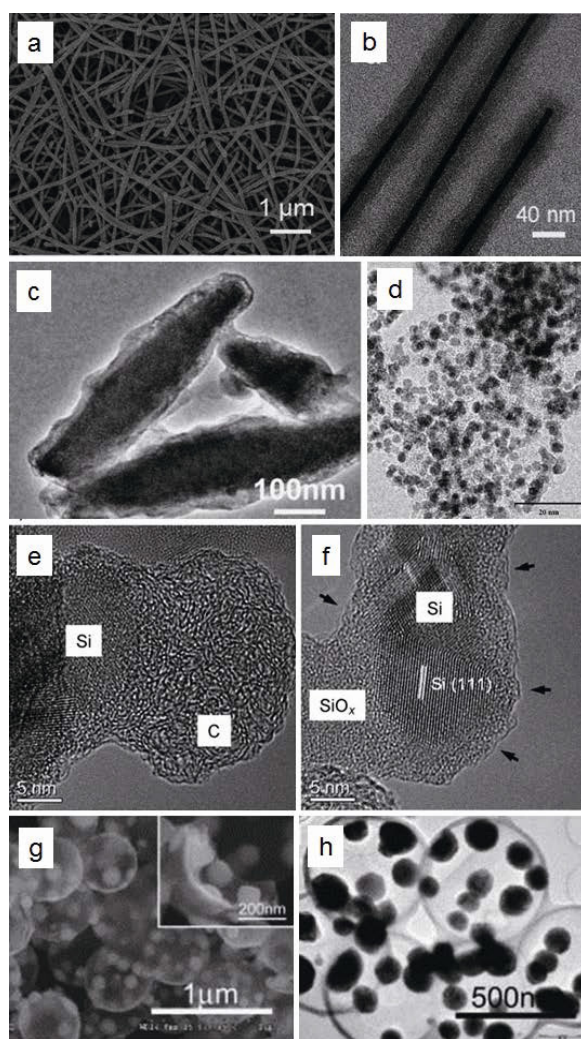
Figure 4-14: (a-b) SEM and TEM images of Te@carbonaceous composite nanocables. [75] (c) TEM images of carbon-coated Fe_3O_4 nanospindles. [77] (d) TEM images of carbon-decorated FePt nanoparticles.[81] (e-f) TEM images of carbon-coated Si nanocomposites. [78a] (g-h) SEM and TEM images of tin-nanoparticles encapsulated in elastic hollow carbon spheres. [80]

4.5 Post-Synthetic Decoration of HTC with Inorganic Nanostructures

As mentioned in the introduction, the important advantage of the HTC carbonaceous materials is their rich surface functional groups, such as hydroxyl and carboxyl groups. These surface functional groups have shown remarkable reactivity and the capability of decorating the pre-formed materials with various functions. Based on the redox reaction, they could *in situ* reduce and stabilize noble-metal ions forming very fine noble metal nanostructures, such as Ag, Au, Pt, and Pd.[82] The whole process is "green" without using other reducing agents or stabilising surfactants or polymers. The obtained noble metal nanostructures not only have uniform sizes, but also clean surfaces, which is beneficial for the further modification with biomolecules or drugs.[83]
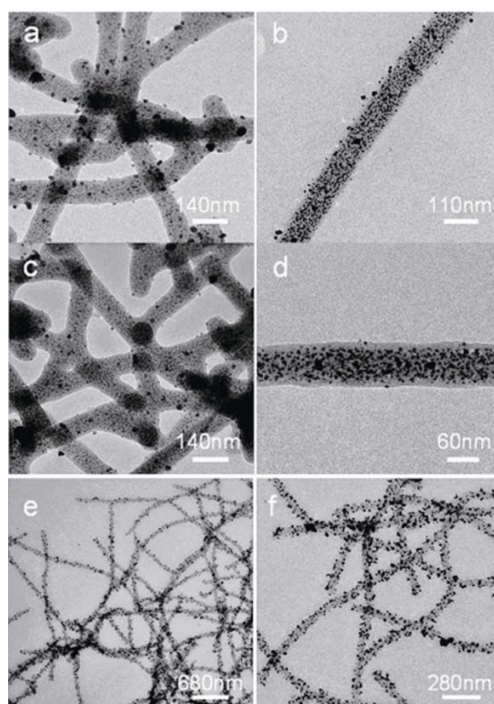
Figure 4-15 TEM images of noble metal nanoparticles loaded on the surfaces of carbonaceous nanofibers. (a-b) Pd nanoparticles with an average diameter of 6 nm; (c-d) Pt nanoparticles with an average diameter of 7 nm; and (e-f) Au nanoparticles ranging from 7 to 15 nm in diameter. [82b]

Another example is the so-called "golden fleece" nanocomposites from Shu Hong Yu´s group. They are uniform carbonaceous nanofibers loaded with noble-metal nanoparticles. A different diameter and distribution was noticed for different noble metals (Figure 4-15).[82b] The carbonaceous nanofibers produced using the HTC process have rich surface functional groups

that can *"in situ"* reduce the noble-metal ions into noble-metal nanoparticles, such as Pd, Pt, and Au. These nanocomposites have shown high permeation and stability, high surface areas, and enhanced chemical reactivity, which makes them ideal candidates for use in heterogeneous catalysis.

Carbonaceous nanospheres, synthesised by the HTC process, have successfully demonstrated their surface reactivity by loading silver and palladium nanoparticles on their surfaces without using other reducing and stabilising agents.[82a]

Another concept making use of the reactivity of the HTC materials is the self-assembly process, based on the electrostatic attraction of surface charge. Nanoparticles with different surface charge can be easily self-assembled on the surface of the carbonaceous materials. For example, citrate-stabilized gold nanoparticles have been assembled on the surface of carbonaceous spheres to fabricate a core-shell hybrid material.[83b] The resulting nanocomposites have shown satisfactory chemical stability and good biocompatibility, and are expected to be promising templates for bimolecular immobilisation and biosensor fabrication.

4.6   One-Step HTC Synthetic Method

When noble metal ions were first added into the HTC process of carbohydrates or organic monomers, novel carbonaceous-encapsulated core-shell nanocomposties could be successfully produced by one-step HTC process.[84] The diameter, the length and the thickness of the carbonaceous shell could be nicely controlled. The advantages of this one step HTC process include: (I) the carbonisation process, the reduction and nucleation-growth of noble metal ions could proceed simultaneously; (II) the noble metal ions could catalyse the carbonisation process while carbon reagents or intermediates could effectively reduce the noble metal ions; (III) this one-step HTC process could produce novel and valuable nanocomposites in a large scale batch and high quality.

One example is represented by the one-step HTC synthesis of silver-carbonaceous nanocables (Figure 4-16).[85] These nanocables, with lengths up to 10 μm and diameters of 200-500 nm, have pentagonal-shaped silver nanowires as cores and tend to branch or fuse with each other. A possible mechanism for their formation has been proposed as following: Firstly, the silver ions are reduced by starch, forming silver nanostructures entrapped in a starch-gel matrix.

Aggregation of these matrixes could enhance the carbonisation process of starch. A partially hollow structure will be formed and the silver nanoparticles will move to this hollow interior and fuse with the already existing ones *via* an oriented attachment mechanism. Continuation of these steps could lead to the growth of the elongated silver nanostructures and carbonaceous shells forming the final complex structures. The as-synthesised individual silver-carbonaceous nanocables have shown excellent conductivity, which makes them ideal materials for constructive interconnects in nanodevices.
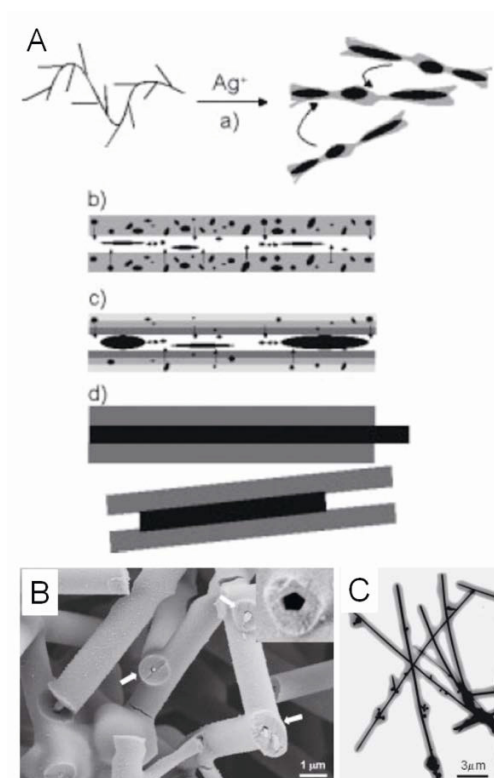
Figure 4-16 (A) Schematic formation mechanism of the silver-carbonaceous nanocables. (B-C) SEM and TEM images of silver-carbonaceous nanocables. [85]

A series of interesting publication regarding the poly(vinyl alcohol) (PVA) assisted synthesis of coaxial nanocables has gained much attention in the HTC technology.[86] First, flexible silver@cross-linked PVA coaxial nanocables have been produced. (Figure 4-17-8a-c).[86a] These nanocables, normally with a diameter of 0.7-4 μm and length up to 100 μm, are comprised of a smooth core about 150-200 nm in diameter and the surrounding sheath about 0.5-1 μm in thickness. These nanocables can pack in a parallel fashion forming bundle structure. A synergistic

soft-hard template mechanism has been proposed. The synergistic effects of both the stabilization of PVA and the binding interaction of cross-linked PVA with the silver nanowires are responsible for the formation of cables and bundles. Further, some glucose-based saccharide, including glucose, β-cyclodextrin, starch, and maltose, can take part in this PVA-assisted synthesis process, forming flexible silver@carbon-rich composite submicrocables (Figure 4-17 d-f).[86b]

This PVA-assisted synthesis process can be extended to the synthesis of Cu@cross-linked PVA coaxial microcables.[86c, 86d] Unique necklace-like Cu@cross-linked PVA coaxial microcables with strict wire-bead forms have been successfully synthesised (Figure 4-17 g-i).[86c] The necklace-like microcables have the length of several hundreds of micrometers to millimeters and diameter in the range from several to twenty micrometers. The synergistic soft-hard template mechanism could explain the formation process of these cable-like structures. Further, Cu@carbonaceous submicrocables can be synthesised in the presence of some glucose-based saccharide, including glucose, β-cyclodextrin, starch, and maltose.[86e]
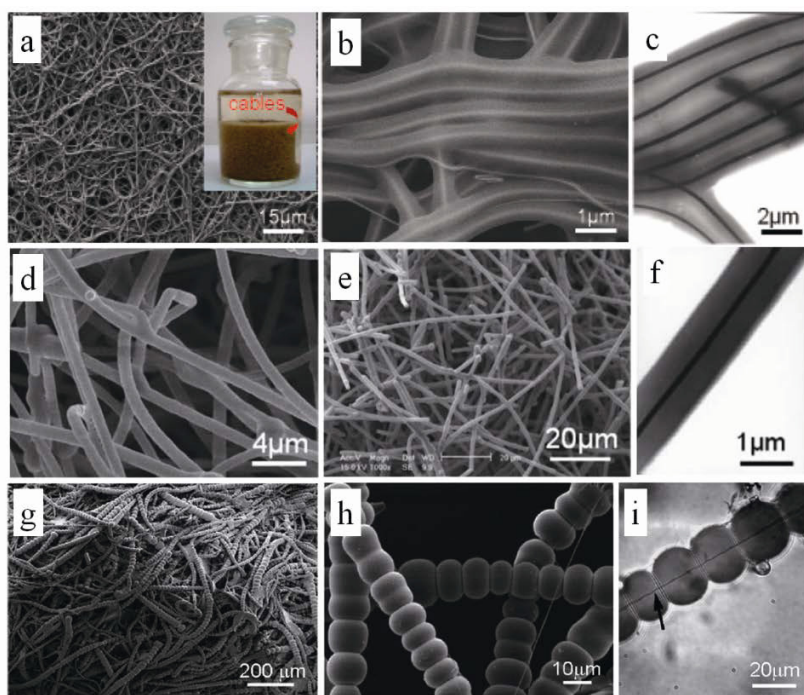
Figure 4-17 (a-c) SEM and TEM images of flexible silver@cross-linked PVA coaxial nanocables.[86a] (d-f) SEM and TEM images of flexible silver@carbon-rich composite submicrocables.[86b] (g-i) SEM and TEM images of unique necklace-like Cu@cross-linked PVA coaxial microcables with strict wire-bead. [86c]
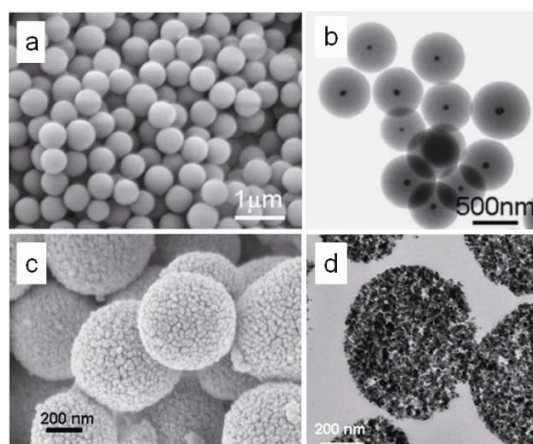
Figure 4-18 (a-b) SEM and TEM iamges of monodisperse silver/phenol formaldehyde resin core-shell nanospheres. Reproduced with permission from [87]. (c-d) SEM and TEM images of mesoporous SnO$_2$ microspheres with nanoparticles assembly. [88]

Core-shell nanoparticles can be synthesised directly by the one-step HTC process.[87, 89] For example, biocompatible and green luminescent monodisperse silver/phenol formaldehyde resin core-shell nanospheres have been successfully produced by the one-step HTC process (Figure 4-18 a-b).[87] These nanospheres have some interesting architectures including centric, eccentric, and coenocyte core-shell spheres with the diameter of 180-1000 nm, which can be used potentially as *in vivo* bioimaging agents.

Pd@C core-shell nanoparticles has also been successfully synthesised in our group by the one-step HTC process. [89] They have shown selectively catalytic capability for the batch partial hydrogenation of hydroxyl aromatic derivatives (see chapter 5-section 5.3.1).

One-step HTC process can synthesise carbonaceous nanocomposites with more complex structures and specific properties.[88, 90] For instance, core-shell Pt@C nanoparticles can embed in the porous channels of mesoporous silica (SBA-15) by the one-step HTC process.[90a] After high temperature carbonisation and removal of SBA-15, the final complex nanocomposites have shown high catalytic capability for methanol-tolerant oxygen electroreduction in direct methanol fuel cell. Furthermore using the one-step HTC process hollow core-shell mesospheres with aggregated crystalline SnO$_2$ nanoparticles [90b] and mesoporous SnO$_2$ microspheres with nanoparticles assembly have been synthesised (Figure 4-18 c-d). [88] Both of these SnO$_2$ nanocomposites have showed high capability of lithium ion storage.

As an alternative to the post-coating technologies reported in section 4.4, an one-step synthesis for the production of a LiFePO$_4$ mesocrystal coated with a thin layer of carbon or N-doped carbon has been directly produce by simply adding glucose/glucoseamine as a carbon to the solvothermal synthetic procedure [91]. There was no difference in the morphology or crystalline structure with or without the addition of the carbon precursor. However the composite made in the presence of the carbon precursor showed an increased conductivity and an enhanced performance when utilised as a cathode in Li ion batteries (details in section 5.2.1.1.4).

4.7 HTC as Sacrificial Templates for Inorganic Porous Materials

The as-synthesised carbonaceous nano- or micromaterials have been used as sacrificed templates for the synthesis of hollow and complex nanostructures, which have shown important potential applications in catalysis, sensing, chemical biological separation, and lithium ion batteries.[82a, 92]

This methodology was firstly developed our group and is schematically represented in Figure 4-19. [93] The advantages of this carbonaceous sacrificed template method include: (I) well-controlled heat treatment method could easily remove/graphitise the carbonaceous materials depending on the atmosphere under which is conducted (O$_2$ / N$_2$) (II) a series of metal or bimetal oxide hollow structures have been produced, (III) this sacrificed template method is an economic and facile technique and can produce complex metal oxide hollow structures in large scale and high quality. The general synthetic process was based on the negative charge of carbonaceous materials (Figure 4-19 a-c).[93-94] First, metal ions were adsorbed from solution to the surface layer of carbonaceous materials. Then heat treatment process followed by the controlled removal of the carbonaceous core or shell was accomplished *via* calcination.

This carbonaceous sacrificed template method has been since its discovery widely used to synthesize metal or dimetal oxide hollow spheres, such as Ga$_2$O$_3$,[94a, 95] GaN,[95] WO$_3$,[96] SiC,[97] ZnO,[98] Mn-doped ZnO,[99] SnO$_2$,[100] NiO,[101] CoO,[94a] In$_2$O$_3$,[102] TiO$_2$,[103] SiO$_2$,[76] CuO,[94b] MgO,[93] CeO$_2$,[93] MnO$_2$,[104] Mn$_3$O$_4$,[94a] Al$_2$O$_3$,[94a] ZrO$_2$,[105] Cr$_2$O$_3$,[94a] layered double hydroxide (LDH),[106] Y$_2$O$_3$:Eu,[107] La$_2$O$_3$,[94a] Y$_2$O$_3$,[94a] Lu$_2$O$_3$,[94a] MFe$_2$O4 (M = Zn, Co, Ni, and Cd),[65a] Fe$_2$O$_3$,[108] and Bi$_2$WO$_6$.[109].

Size and structures of these hollow spheres can be well controlled by the templates. These metal oxide hollow spheres have shown high potential applications in gas sensitivity or catalysis.

Further, metal oxide hollow nanofibres or nanotubes have been successfully synthesised using carbonaceous nanofibres as sacrificed templates (Figure 4-19 d-e). [65a, 110]
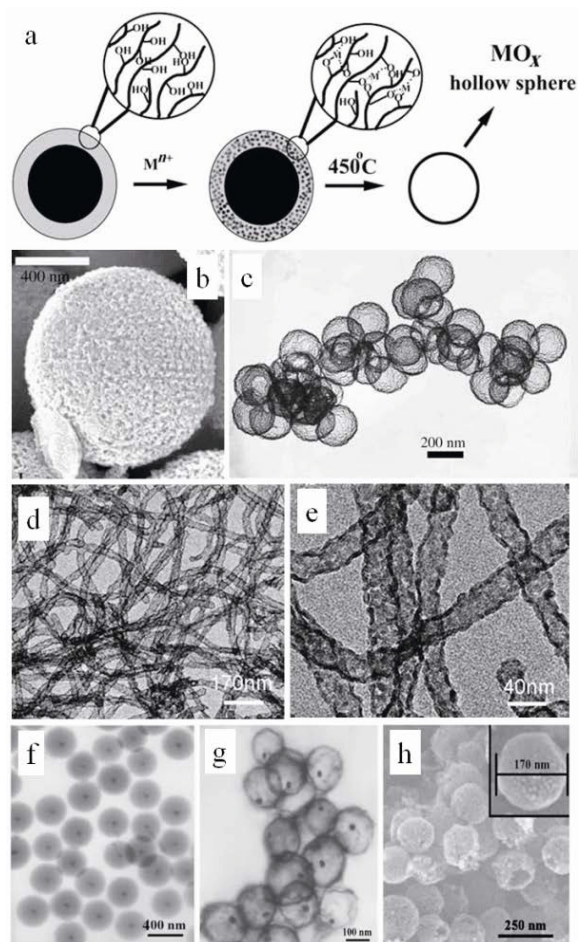
Figure 4-19 (a) Schematic formation mechanism of the metal oxide hollow spheres by using carbonaceous spheres as templates. (b-c) SEM and TEM images of the SnO$_2$ hollow nanospheres.[94a] (d-e) SEM and TEM images of TiO$_2$ nanotubes. [110b](f) TEM image of Ag@C core–shell microspheres. (g-h) TEM and SEM images of jingle-bell-shaped hollow structured nanomaterials. [111]

More complex nanocomposites can be synthesised by this carbonaceous sacrificed template route.[111-112] For example, a series of jingle-bell-shaped hollow structured nanomaterials marked as Ag@MFe$_2$O$_4$ (M = Ni, Co, Mg, Zn), consisting of ferrite hollow shells and silver nanoparticle cores, has been successfully produced by this sacrificed templating method (Figure 4-19 f-h).[111] The synthesis process included firstly coating the Ag nanoparticle core with a glucose-derived carbonaceous layer *via* the HTC process, directly adsorbing metal cations Fe^{3+} and M^{2+} on the surface of the carbonaceous layers, and finally calcinating the sample to remove the middle

225

carbonaceous shell and transform the metal ions into pure phase ferrites. These nanocomposites have shown multifunctional properties, including magnetic, optical, and antibacterial properties.
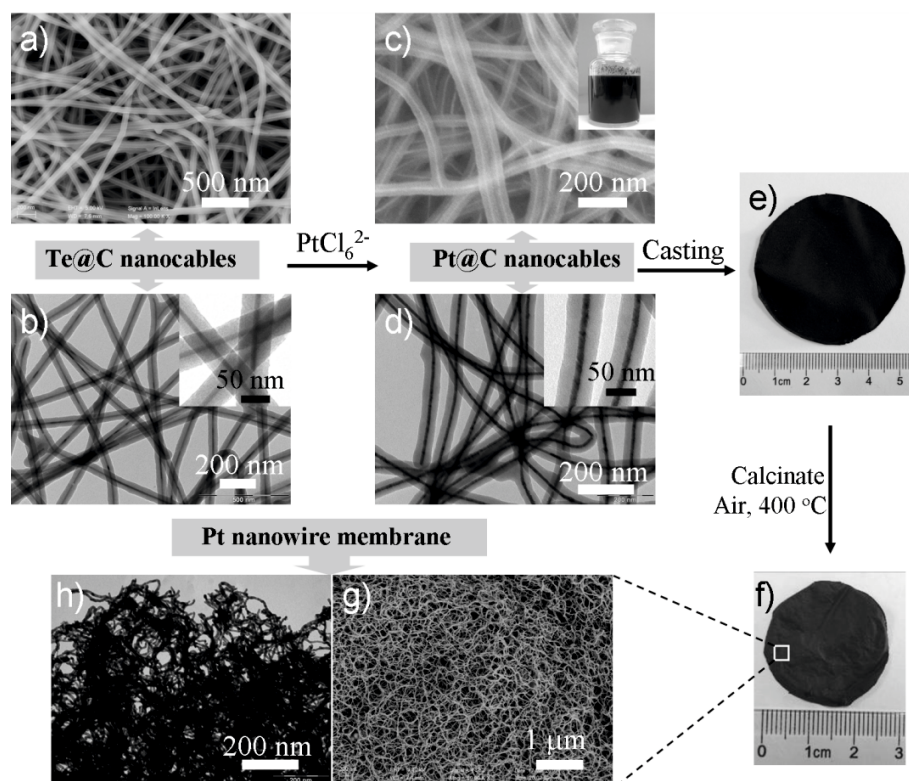
Figure 4-20: Schematic formation process of the free-standing Pt nanowire membrane by using carbonaceous sacrificed template method. Reproduced with permission from [113].

These nanocomposites have shown multifunctional properties, including magnetic, optical, and antibacterial properties. Further, using a quite similar procedure, $Fe_3O_4@TiO_2$ core-shell microspheres were synthesised, which has shown the highly specific capture ability of phosphopeptides for the application of direct matrix-assisted laser desorption ionisation time-of-flight (MALDI-TOF) mass spectrometry analysis.[112]

Interestingly, this carbonaceous sacrificed template method can be applied for the synthesis of two-dimensional free-standing macroscopic membranes with high porosity, good flexibility, large area per unit volume, and an interconnected open pore structure. For instance, a free-standing Pt nanowire membrane has been prepared *via* this multistep sacrificed template method (Figure 4-20).[113] First, Te nanowires were used as template for the synthesis of well-defined

Te@carbonaceous nanocables *via* the hydrothermal carbonisation process. Second, These Te@C nanocables were transformed into Pt@C nanocables with the galvanic replacement reaction. Third, These Pt@C nanocables could be assembled into a two-dimensional free-standing membrane by a simple casting process. Finally, after calcination of the Pt@C membrane at high temperature, the free-standing Pt nanowire membrane was formed. SEM and TEM images have shown that the Pt nanowire membrane was composed of very fine wire-like nanostructures with lengths of several tens of micrometers and these Pt nanowires interconnected with each other to form a highly porous nanowire network structure. This unique porous network structures could greatly facilitate electron transport and gas diffusion. The Pt nanowire membrane was a good electrocatalyst for the oxygen reduction reaction and has higher catalytic activity and stability than commercial Pt/C and Pt black catalysts.

4.8 Conclusion and Outlook

In this chapter I have discussed different strategies for the functionalisation of HTC materials. The first part dealt with chemical functionalisation using either "*in situ*" or "post modification treatments". For the "*in situ*" functionalisation, an important role is played by the heteroatom doped materials. The advantage of the HTC process is the mild carbonisation temperatures which allow chemical reactions between the precursor and the dopant species. Thus, a high amount of dopants can be introduced and maintained even at high post-processing temperatures. Mainly nitrogen has been used as a dopant in HTC *via* Maillard reactions conferring interesting new properties such as increased electronic conductivity or intrinsic catalytic activity. Sulfur and boron are expected to complement nitrogen in HTC materials in the near future.

In addition to heteroatom doping, other chemical functions can be also introduced by various co-reagents such as for example organic monomers. Here cycloaddition reactions between the furanic ring of HTC and the organic monomer are thought to play the most important role.

Besides the "*in situ*" chemical functionalisation, post modification is another elegant strategy to introduce various functions into HTC materials making use of either oxigentated surface or the furanic-arene aromatic character.

In the second part of this chapter I presented a palette of HTC nanocomposites derived from biomass, carbohydrates, and organic molecules. We have learned that some promising strategies have been designed for the synthesis of these materials, which I have briefly presented here while

leading the interested reader to the corresponding reference. Carbonaceous nanocomposites with combined and improved properties have been synthesised by the three main methods, which include coating of preformed nanostructures, decorating the pre-formed HTC materials with inorganic nanostructures and direct synthesis by one-step method. Furthermore, carbonaceous materials can act as good sacrificed templates or support shells for the production of hollow and complex nanostructures, as well as the free-standing membranes.

Importantly, the as-synthesised carbonaceous nanomaterials and nanocomposites *via* the HTC process, have already demonstrated their significant values in many practical application fields, such as environment, catalytic, energy, and biological applications which we have pointed out while describing various synthetic approaches. However, more emphasis on the multitude of applications of the HTC material will be presented in detail in Chapter 5.

Although carbonaceous nanomaterials and nanocomposites *via* the HTC process has achieved so far excellent success in both synthesis and applications, there are still many challenges and questions that should be faced and solved. Further exploration will facilitate the rational design of a variety of carbonaceous nanomaterials and nanocomposites with hierarchical porosity, interesting functionalities, and significant practical values.

4.9   References

[1]   aH. J. Dai, *Accounts of Chemical Research* **2002**, *35*, 1035-1044; bK. P. Gong, F. Du, Z. H. Xia, M. Durstock, L. M. Dai, *Science* **2009**, *323*, 760-764; cM. Terrones, P. M. Ajayan, F. Banhart, X. Blase, D. L. Carroll, J. C. Charlier, R. Czerw, B. Foley, N. Grobert, R. Kamalakaran, P. Kohler-Redlich, M. Ruhle, T. Seeger, H. Terrones, *Appl. Phys. A-Mater. Sci. Process.* **2002**, *74*, 355-361; dA. Marchand, J. V. Zanchetta, *Carbon* **1966**, *3*, 483-491491; eS.-A. Wohlgemuth, R. J. White, M.-G. Willinger, M.-M. Titirici, M. Antonietti, *Green Chemistry* **2012**, *14*, 1515-1523.

[2]   aE. T. Thostenson, Z. F. Ren, T. W. Chou, *Compos. Sci. Technol.* **2001**, *61*, 1899-1912; bP. Avouris, Z. H. Chen, V. Perebeinos, *Nat. Nanotechnol.* **2007**, *2*, 605-615; cH. J. Dai, *Surf. Sci.* **2002**, *500*, 218-241.

[3]   aH. M. Jeong, J. W. Lee, W. H. Shin, Y. J. Choi, H. J. Shin, J. K. Kang, J. W. Choi, *Nano Letters* **2011**, *11*, 2472-2477; bT. Tsubota, K. Takenaka, N. Murakami, T. Ohno, *Journal of Power Sources* **2011**, *196*, 10455-10460.

[4]   Y. Xia, R. Mokaya, *Advanced Materials* **2004**, *16*, 1553-1558.

[5]   aS. Glenis, A. J. Nelson, M. M. Labes, *J. Appl. Phys.* **1999**, *86*, 4464-4466; bT. W. Ebbesen, P. M. Ajayan, *Nature* **1992**, *358*, 220-222.

[6]   aB. Hu, K. Wang, L. Wu, S.-H. Yu, M. Antonietti, M.-M. Titirici, *Advanced Materials* **2010**, *22*, 813-828; bA. Funke, F. Ziegler, *Biofuels Bioprod. Biorefining* **2010**, *4*, 160-177.

[7]   R. J. White, M. Antonietti, M. M. Titirici, *J. Mater. Chem.* **2009**, *19*, 8645-8650.

[8]   H. Wang, C. Zhang, Z. Liu, L. Wang, P. Han, H. Xu, K. Zhang, S. Dong, J. Yao, G. Cui, *J. Mater. Chem.* **2011**, *21*, 5430-5434.

[9]   Z.-S. Wu, W. Ren, L. Xu, F. Li, H.-M. Cheng, *Acs Nano* **2011**, *5*, 5463-5471.

[10]   X. Ma, E. G. Wang, *Applied Physics Letters* **2001**, *78*, 978-980.

[11]   X. Ma, E. G. Wang, R. D. Tilley, D. A. Jefferson, W. Zhou, *Applied Physics Letters* **2000**, *77*, 4136-4138.

[12]   aC. O. Ania, V. Khomenko, E. Raymundo-Pinero, J. B. Parra, F. Beguin, *Advanced Functional Materials* **2007**, *17*, 1828-1836; bN. D. Kim, W. Kim, J. B. Joo, S. Oh, P. Kim, Y. Kim, J. Yi, *Journal of Power Sources* **2008**, *180*, 671-675; cL. Li, E. Liu, J. Li, Y. Yang, H. Shen, Z. Huang, X. Xiang, W. Li, *Journal of Power Sources* **2010**, *195*, 1516-1521; dL. Zhao, L.-Z. Fan, M.-Q. Zhou, H. Guan, S. Qiao, M. Antonietti, M.-M. Titirici, *Advanced Materials* **2010**, *22*, 5202-5206.

[13]   aK. Gong, F. Du, Z. Xia, M. Durstock, L. Dai, *Science* **2009**, *323*, 760-764; bS. Kundu, T. C. Nagaiah, W. Xia, Y. Wang, S. Van Dommele, J. H. Bitter, M. Santa, G. Grundmeier, M. Bron, W. Schuhmann, M. Muhler, *Journal of Physical Chemistry C* **2009**, *113*, 14302-14310; cS. Maldonado, K. J. Stevenson, *Journal of Physical Chemistry B* **2005**, *109*, 4707-4716; dH. Niwa, K. Horiba, Y. Harada, M. Oshima, T. Ikeda, K. Terakura, J.-i. Ozaki, S. Miyata, *Journal of Power Sources* **2009**, *187*, 93-97; eL. Qu, Y. Liu, J.-B. Baek, L. Dai, *Acs Nano* **2010**, *4*, 1321-1326.

[14]   R. A. Sidik, A. B. Anderson, N. P. Subramanian, S. P. Kumaraguru, B. N. Popov, *The Journal of Physical Chemistry B* **2006**, *110*, 1787-1793.

[15]   F. Jaouen, M. Lefèvre, J.-P. Dodelet, M. Cai, *The Journal of Physical Chemistry B* **2006**, *110*, 5553-5558.

[16]   R. Pietrzak, H. Wachowska, P. Nowicki, *Energy & Fuels* **2006**, *20*, 1275-1280.

[17]   P. H. Matter, E. Wang, M. Arias, E. J. Biddinger, U. S. Ozkan, *The Journal of Physical Chemistry B* **2006**, *110*, 18374-18384.

[18]   S. Glenis, A. J. Nelson, M. M. Labes, *J. Appl. Phys.* **1996**, *80*, 5404-5407.

[19]   T. Iijima, K. Suzuki, Y. Matsuda, *Synthetic Metals* **1995**, *73*, 9-20.

[20]   L. Li, E. Liu, Y. Yang, H. Shen, Z. Huang, X. Xiang, *Materials Letters* **2010**, *64*, 2115-2117.

[21]   R. J. White, M. Antonietti, M.-M. Titirici, *J. Mater. Chem.* **2009**, *19*, 8645-8650.

[22]   N. Baccile, M. Antonietti, M.-M. Titirici, *ChemSusChem* **2010**, *3*, 246-253.

[23]   R. J. White, N. Yoshizawa, M. Antonietti, M.-M. Titirici, *Green Chemistry* **2011**.

[24]   aZ. Li, N. Baccile, S. Gross, Z. Yuanjian, W. Wei, S. Yuhan, M. Antonietti, M. M. Titirici, *Carbon* **2010**, *48*, 3778-37873787; bL. Zhao, R. Crombez, F. P. Caballero, M. Antonietti, J. Texter, M.-M. Titirici, *Polymer* **2010**, *51*, 4540-4546.

[25]   N. Baccile, G. Laurent, C. Coelho, F. Babonneau, L. Zhao, M.-M. Titirici, *The Journal of Physical Chemistry C* **2011**, *115*, 8976-8982.

[26]   D. Y. Zhang, Y. Hao, Y. Ma, H. X. Feng, *Appl. Surf. Sci.* **2012**, *258*, 2510-2514.

[27]   S. Liu, J. Tian, L. Wang, Y. Zhang, X. Qin, Y. Luo, A. M. Asiri, A. O. Al-Youbi, X. Sun, *Advanced Materials* **2012**, *24*, 2037-2041.

[28]   R. J. White, N. Yoshizawa, M. Antonietti, M.-M. Titirici, *Green Chemistry* **2011**, *13*, 2428-2434.

[29]   S.-A. Wohlgemuth, PhD Thesis thesis, (University of Potsdam), **2012**.

[30]   H. Steinhart, *Angewandte Chemie International Edition* **2005**, *44*, 7503-7504.

[31]   F. Ledl, E. Schleicher, *Angewandte Chemie International Edition in English* **1990**, *29*, 565-594.

[32]   aE. Capuano, V. Fogliano, *LWT - Food Science and Technology* **2011**, *44*, 793-810; bJ. Koch, M. Pischetsrieder, K. Polborn, T. Severin, *Carbohydrate Research* **1998**, *313*, 117-123.

[33]   X. Fang, K. Schmidt-Rohr, *Journal of Agricultural and Food Chemistry* **2009**, *57*, 10701-10711.

[34]   M. M. Titirici, M. Antonietti, *Chem. Soc. Rev.* **2010**, *39*, 103-116.

[35]   S.-A. Wohlgemuth, F. Vilela, M.-M. Titirici, M. Antonietti, *Green Chemistry* **2012**, *14*, 741-749.

[36]   V. K. Lamer, R. H. Dinegar, *J. Am. Chem. Soc.* **1950**, *72*, 4847-4854.

[37]   A. Laaksonen, V. Talanquer, D. W. Oxtoby, *Annu. Rev. Phys. Chem.* **1995**, *46*, 489-524.

[38]   aC. Billaud, C. Maraschin, M. N. Peyrat-Maillard, J. Nicolas, in *Maillard Reaction: Chemistry at the Interface of Nutrition, Aging, and Disease, Vol. 1043* (Eds.: J. W. Baynes, V. M. Monnier, J. M. Ames, S. R. Thorpe), New York Acad Sciences, New York, **2005**, pp. 876-885; bC. Billaud, C. Maraschin, Y. N. Chow, S. Cheriot, M. N. Peyrat-Maillard, J. Nicolas, *Mol. Nutr. Food Res.* **2005**, *49*, 656-662.

[39]   Z. Liu, C. Zhang, L. Luo, Z. Chang, X. Sun, *J. Mater. Chem.* **2012**, *22*, 12149-12154.

[40]   C. Petit, G. W. Peterson, J. Mahle, T. J. Bandosz, *Carbon* **2010**, *48*, 1779-1787.

[41]   M. Seredych, M. Khine, T. J. Bandosz, *ChemSusChem* **2011**, *4*, 139-147.

[42]   J. P. Paraknowitsch, A. Thomas, J. Schmidt, *Chemical Communications* **2011**, *47*, 8283-8285.

[43]   Z. Yang, Z. Yao, G. Li, G. Fang, H. Nie, Z. Liu, X. Zhou, X. a. Chen, S. Huang, *Acs Nano* **2011**.

[44]   aV. A. Yaylayan, C. P. Locas, *Mol. Nutr. Food Res.* **2007**, *51*, 437-444; bG. T. Wondrak, R. Tressl, D. Rewicki, *Journal of Agricultural and Food Chemistry* **1997**, *45*, 321-327.

[45]   B. Kuchta, L. Firlej, S. Roszak, P. Pfeifer, *Adsorpt.-J. Int. Adsorpt. Soc.* **2010**, *16*, 413-421.

[46]   D. W. McKee, *Chemistry and Physics of Carbon*, New York, **1991**.

[47]   L. R. Radovic, M. Karra, K. Skokova, P. A. Thrower, *Carbon* **1998**, *36*, 1841-1854.

[48]   aE. Frackowiak, K. Kierzek, G. Lota, J. Machnikowski, *Journal of Physics and Chemistry of Solids* **2008**, *69*, 1179-1181; bZ. Jin, X. Wei, Z. Shuping, Z. Yi, *Solid State Sciences* **2011**, *13*, 2000-2006; cU. Tanaka, T. Sogabe, H. Sakagoshi, M. Ito, T. Tojo, *Carbon* **2001**, *39*, 931-936; dX.-l. Zhai, Y. Song, L.-j. Zhi, J.-l. Shi, Q.-g. Guo, *New Carbon Materials* **2011**, *26*, 211-216.

[49]   L. S. Panchakarla, A. Govindaraj, C. N. R. Rao, *Inorganica Chimica Acta* **2010**, *363*, 4163-4174.

[50]   X. Zhao, A. Wang, J. Yan, G. Sun, L. Sun, T. Zhang, *Chemistry of Materials* **2010**, *22*, 5463-5473.

[51]   P. Buonora, J.-C. Olsen, T. Oh, *Tetrahedron* **2001**, *57*, 6099-6138.

[52]   aR. Demir-Cakan, N. Baccile, M. Antonietti, M.-M. Titirici, *Chemistry of Materials* **2009**, *21*, 484-490; bR. Demir-Cakan, P. Makowski, M. Antonietti, F. Goettmann, M. M. Titirici, *Catal. Today* **2010**, *150*, 115-118.

[53]   M.-M. Titirici, A. Thomas, M. Antonietti, *J. Mater. Chem.* **2007**, *17*, 3412-3418.

[54]   R. J. White, K. Tauer, M. Antonietti, M.-M. Titirici, *J. Am. Chem. Soc.* **2010**, *132*, 17360-17363.

[55]   S. Kubo, I. Tan, R. J. White, M. Antonietti, M. M. Titirici, *Chemistry of Materials* **2010**, *22*, 6590-6597.

[56] aS. Munirasu, J. Albuerne, A. Boschetti-de-Fierro, V. Abetz, *Macromolecular Rapid Communications* **2010**, *31*, 574-579; bJ. L. Delgado, P. de la Cruz, F. Langa, A. Urbina, J. Casado, J. T. L. Navarrete, *Chemical Communications* **2004**, 1734-1735; cC.-M. Chang, Y.-L. Liu, *Carbon* **2009**, *47*, 3041-3049.

[57] aE. Bekyarova, S. Sarkar, S. Niyogi, M. E. Itkis, R. C. Haddon, *Journal of Physics D-Applied Physics* **2012**, *45*; bS. Sarkar, E. Bekyarova, S. Niyogi, R. C. Haddon, *J. Am. Chem. Soc.* **2011**, *133*, 3324-3327.

[58] aF. Diederich, C. Thilgen, *Science* **1996**, *271*, 317-323; bB. Krautler, M. Puchberger, *Helv. Chim. Acta* **1993**, *76*, 1626-1631.

[59] H. Kaper, A. Grandjean, C. Weidenthaler, F. Schueth, F. Goettmann, *Chemistry-a European Journal* **2012**, *18*, 4099-4106.

[60] H. Urakami, F. Vilela, M. Antonietti, *Chemical Communications* **2012**.

[61] J. A. Macia-Agullo, M. Sevilla, M. A. Diez, A. B. Fuertes, *Chemsuschem* **2010**, *3*, 1352-1354.

[62] Z. Chen, L. Ma, S. Li, J. Geng, Q. Song, J. Liu, C. Wang, H. Wang, J. Li, Z. Qin, S. Li, *Appl. Surf. Sci.* **2011**, *257*, 8686-8691.

[63] F. M. Dean, *Advances in Heterocyclic Chemistry* **1982**, *30*, 167-238.

[64] F. M. Dean, *Advances in Heterocyclic Chemistry* **1982**, *31*, 237.

[65] aA. Stein, Z. Wang, M. A. Fierke, *Advanced Materials* **2009**, *21*, 265-293; bC. Liang, Z. Li, S. Dai, *Angewandte Chemie-International Edition* **2008**, *47*, 3696-3717; cK. Balasubramanian, M. Burghard, *Small* **2005**, *1*, 180-192; dX. Huang, Z. Y. Yin, S. X. Wu, X. Y. Qi, Q. Y. He, Q. C. Zhang, Q. Y. Yan, F. Boey, H. Zhang, *Small* **2011**, *7*, 1876-1902; eT. Kuila, S. Bose, A. K. Mishra, P. Khanra, N. H. Kim, J. H. Lee, *Prog. Mater. Sci.* **2012**, *57*, 1061-1105.

[66] aZ. L. Yao, N. Braidy, G. A. Botton, A. Adronov, *J. Am. Chem. Soc.* **2003**, *125*, 16015-16024; bM. Holzinger, O. Vostrowsky, A. Hirsch, F. Hennrich, M. Kappes, R. Weiss, F. Jellen, *Angewandte Chemie-International Edition* **2001**, *40*, 4002-+.

[67] W. R. Collins, W. Lewandowski, E. Schmois, J. Walish, T. M. Swager, *Angewandte Chemie-International Edition* **2011**, *50*, 8848-8852.

[68] aJ. L. Bahr, J. M. Tour, *Chemistry of Materials* **2001**, *13*, 3823-+; bM. S. Strano, C. A. Dyke, M. L. Usrey, P. W. Barone, M. J. Allen, H. W. Shan, C. Kittrell, R. H. Hauge, J. M. Tour, R. E. Smalley, *Science* **2003**, *301*, 1519-1522; cT. S. Balaban, M. C. Balaban, S. Malik, F. Hennrich, R. Fischer, H. Rosner, M. M. Kappes, *Advanced Materials* **2006**, *18*, 2763-+; dB. Liu, C. E. Bunker, Y. P. Sun, *Chemical Communications* **1996**, 1241-1242.

[69] aG. A. Olah, I. Bucsi, C. Lambert, R. Aniszfeld, N. J. Trivedi, D. K. Sensharma, G. K. S. Prakash, *J. Am. Chem. Soc.* **1991**, *113*, 9385-9387; bC. E. Hamilton, J. R. Lomeda, Z. Sun, J. M. Tour, A. R. Barron, *Nano Research* **2010**, *3*, 138-145; cP. Umek, J. W. Seo, K. Hernadi, A. Mrzel, P. Pechy, D. D. Mihailovic, L. Forro, *Chemistry of Materials* **2003**, *15*, 4751-4755; dY. M. Ying, R. K. Saini, F. Liang, A. K. Sadana, W. E. Billups, *Organic Letters* **2003**, *5*, 1471-1473.

[70] aI. D. Rosca, F. Watari, M. Uo, T. Akaska, *Carbon* **2005**, *43*, 3124-3131; bV. Datsyuk, M. Kalyva, K. Papagelis, J. Parthenios, D. Tasis, A. Siokou, I. Kallitsis, C. Galiotis, *Carbon* **2008**, *46*, 833-840; cJ. Zhang, H. L. Zou, Q. Qing, Y. L. Yang, Q. W. Li, Z. F. Liu, X. Y. Guo, Z. L. Du, *Journal of Physical Chemistry B* **2003**, *107*, 3712-3718.

[71] aL. Zhang, Q. Q. Ni, Y. Q. Fu, T. Natsuki, *Appl. Surf. Sci.* **2009**, *255*, 7095-7099; bL. Zhang, Y. Hashimoto, T. Taishi, Q. Q. Ni, *Appl. Surf. Sci.* **2011**, *257*, 1845-1849.

[72]   aS. Banerjee, S. S. Wong, *Journal of Physical Chemistry B* **2002**, *106*, 12144-12151; bB. Kakade, R. Mehta, A. Durge, S. Kulkarni, V. Pillai, *Nano Letters* **2008**, *8*, 2693-2696.

[73]   D. Ogrin, J. Chattopadhyay, A. K. Sadana, W. E. Billups, A. R. Barron, *J. Am. Chem. Soc.* **2006**, *128*, 11322-11323.

[74]   W. R. Collins, E. Schmois, T. M. Swager, *Chemical Communications* **2011**, *47*, 8790-8792.

[75]   H. S. Qian, S. H. Yu, L. B. Luo, J. Y. Gong, L. F. Fei, X. M. Liu, *Chem. Mater.* **2006**, *18*, 2102-2108.

[76]   Y. Wan, Y. L. Min, S. H. Yu, *Langmuir* **2008**, *24*, 5024-5028.

[77]   W. M. Zhang, X. L. Wu, J. S. Hu, Y. G. Guo, L. J. Wan, *Adv. Funct. Mater.* **2008**, *18*, 3941-3946.

[78]   aY. S. Hu, R. Demir-Cakan, M. M. Titirici, J. O. Muller, R. Schlogl, M. Antonietti, J. Maier, *Angew. Chem. Int. Ed.* **2008**, *47*, 1645-1649; bR. D. Cakan, M. M. Titirici, M. Antonietti, G. L. Cui, J. Maier, Y. S. Hu, *Chem. Commun.* **2008**, 3759-3761.

[79]   X. W. Lou, C. M. Li, L. A. Archer, *Adv Mater* **2009**, *21*, 2536-2541.

[80]   W. M. Zhang, J. S. Hu, Y. G. Guo, S. F. Zheng, L. S. Zhong, W. G. Song, L. J. Wan, *Adv Mater* **2008**, *20*, 1160-1165.

[81]   N. Caiulo, C. H. Yu, K. M. K. Yu, C. C. H. Lo, W. Oduro, B. Thiebaut, P. Bishop, S. C. Tsang, *Adv. Funct. Mater.* **2007**, *17*, 1392-1396.

[82]   aX. M. Sun, Y. D. Li, *Angew. Chem. Int. Ed.* **2004**, *43*, 597-601; bH. S. Qian, M. Antonietti, S. H. Yu, *Adv. Funct. Mater.* **2007**, *17*, 637-643; cS. C. Tang, S. Vongehr, X. K. Meng, *J Phys Chem C* **2010**, *114*, 977-982; dB. Hu, Y. Zhao, H. Z. Zhu, S. H. Yu, *Acs Nano* **2011**, *5*, 3166-3171; eB. Hu, H. Z. Zhu, J. P. Li, W. P. Xu, S. H. Yu, **2011**, Submitted.

[83]   aB. R. Selvi, D. Jagadeesan, B. S. Suma, G. Nagashankar, M. Arif, K. Balasubramanyam, M. Eswaramoorthy, T. K. Kundu, *Nano Lett.* **2008**, *8*, 3182-3188; bR. J. Cui, C. Liu, J. M. Shen, D. Gao, J. J. Zhu, H. Y. Chen, *Adv. Funct. Mater.* **2008**, *18*, 2197-2204.

[84]   aX. M. Sun, Y. D. Li, *Adv Mater* **2005**, *17*, 2626-2630; bX. C. Song, Y. Zhao, Y. F. Zheng, E. Yang, J. Fu, Y. He, *Cryst Growth Des* **2008**, *8*, 1823-1826; cW. Z. Wang, S. L. Xiong, L. Y. Chen, B. J. Xi, H. Y. Zhou, Z. D. Zhang, *Cryst Growth Des* **2006**, *6*, 2422-2426; dZ. Fang, K. B. Tang, S. J. Lei, T. W. Li, *Nanotechnology* **2006**, *17*, 3008-3011; eJ. C. Yu, X. L. Hu, Q. Li, L. Z. Zhang, *Chem. Commun.* **2005**, 2704-2706; fW. Z. Wang, S. Qiu, B. J. Xi, L. Y. Chen, S. L. Xiong, Z. D. Zhang, *Chem.-Asian J.* **2008**, *3*, 834-840; gX. L. Hu, J. C. Yu, J. M. Gong, *J Phys Chem C* **2007**, *111*, 5830-5834; hG. Y. Chen, B. Deng, G. B. Cai, W. F. Dong, W. X. Zhang, A. W. Xu, *Cryst Growth Des* **2008**, *8*, 2137-2143; iW. Z. Wang, L. Sun, Z. Fang, L. Y. Chen, Z. D. Zhang, *Cryst Growth Des* **2009**, *9*, 2117-2123; jB. Deng, A. W. Xu, G. Y. Chen, R. Q. Song, L. P. Chen, *J Phys Chem B* **2006**, *110*, 11711-11716.

[85]   S. H. Yu, X. J. Cui, L. L. Li, K. Li, B. Yu, M. Antonietti, H. Colfen, *Adv Mater* **2004**, *16*, 1636-1640.

[86]   aL. B. Luo, S. H. Yu, H. S. Qian, T. Zhou, *J. Am. Chem. Soc.* **2005**, *127*, 2822-2823; bL. B. Luo, S. H. Yu, H. S. Qian, J. Y. Gong, *Chem. Commun.* **2006**, 793-795; cY. J. Zhan, S. H. Yu, *J. Am. Chem. Soc.* **2008**, *130*, 5650-5651; dJ. Y. Gong, L. B. Luo, S. H. Yu, H. S. Qian, L. F. Fei, *J. Mater. Chem.* **2006**, *16*, 101-105; eJ. Y. Gong, S. H. Yu, H. S. Qian, L. B. Luo, T. W. Li, *J Phys Chem C* **2007**, *111*, 2490-2496.

[87]   S. R. Guo, J. Y. Gong, P. Jiang, M. Wu, Y. Lu, S. H. Yu, *Adv. Funct. Mater.* **2008**, *18*, 872-879.

[88] R. Demir-Cakan, Y. S. Hu, M. Antonietti, J. Maier, M. M. Titirici, *Chem. Mater.* **2008**, *20*, 1227-1229.

[89] P. Makowski, R. D. Cakan, M. Antonietti, F. Goettmann, M. M. Titirici, *Chem. Commun.* **2008**, 999-1001.

[90] aZ. H. Wen, J. Liu, J. H. Li, *Adv Mater* **2008**, *20*, 743-747; bD. Deng, J. Y. Lee, *Chem. Mater.* **2008**, *20*, 1841-1846.

[91] J. Popovic, R. Demir-Cakan, J. Tornow, M. Morcrette, D. S. Su, R. Schlogl, M. Antonietti, M. M. Titirici, *Small* **2011**, *7*, 1127-1135.

[92] aQ. Wang, H. Li, L. Q. Chen, X. J. Huang, *Carbon* **2001**, *39*, 2211-2214; bM. M. Titirici, M. Antonietti, N. Baccile, *Green Chem* **2008**, *10*, 1204-1212.

[93] M. M. Titirici, M. Antonietti, A. Thomas, *Chem. Mater.* **2006**, *18*, 3808-3812.

[94] aX. M. Sun, J. F. Liu, Y. D. Li, *Chem. Eur. J.* **2006**, *12*, 2039-2047; bH. S. Qian, G. F. Lin, Y. X. Zhang, P. Gunawan, R. Xu, *Nanotechnology* **2007**, *18*, 355602.

[95] X. M. Sun, Y. D. Li, *Angew. Chem. Int. Ed.* **2004**, *43*, 3827-3831.

[96] X. L. Li, T. J. Lou, X. M. Sun, Y. D. Li, *Inorganic Chemistry* **2004**, *43*, 5442-5449.

[97] Y. Zhang, E. W. Shi, Z. Z. Chen, X. B. Li, B. Xiao, *J. Mater. Chem.* **2006**, *16*, 4141-4145.

[98] aX. Wang, P. Hu, F. L. Yuan, L. J. Yu, *J Phys Chem C* **2007**, *111*, 6706-6712; bY. Zhang, E. W. Shi, Z. Z. Chen, B. Xiao, *Mater. Lett.* **2008**, *62*, 1435-1437.

[99] Y. Zhang, E. W. Shi, Z. Z. Chen, *J. Cryst. Growth* **2008**, *310*, 2928-2933.

[100] C. H. Wang, X. F. Chu, M. M. Wu, *Sensors Actuat. B-Chem.* **2007**, *120*, 508-513.

[101] aX. Wang, L. J. Yu, P. Hu, F. L. Yuan, *Cryst Growth Des* **2007**, *7*, 2415-2418; bC. C. Li, Y. L. Liu, L. M. Li, Z. F. Du, S. J. Xu, M. Zhang, X. M. Yin, T. H. Wang, *Talanta* **2008**, *77*, 455-459.

[102] Z. Guo, J. Y. Liu, Y. Jia, X. Chen, F. L. Meng, M. Q. Li, J. H. Liu, *Nanotechnology* **2008**, *19*, 345704

[103] aY. H. Ao, J. J. Xu, D. G. Fu, C. W. Yuan, *Electrochem. Commun.* **2008**, *10*, 1812-1814; bY. H. Ao, J. J. Xu, D. G. Fu, C. W. Yuan, *Catal. Commun.* **2008**, *9*, 2574-2577.

[104] N. Wang, Y. Gao, J. Gong, X. Y. Ma, X. L. Zhang, Y. H. Guo, L. Y. Qu, *Eur. J. Ino. Chem.* **2008**, 3827-3832.

[105] C. Y. Guo, P. Hu, L. J. Yu, F. L. Yuan, *Mater. Lett.* **2009**, *63*, 1013-1015.

[106] P. Gunawan, R. Xu, *Chem. Mater.* **2009**, *21*, 781-783.

[107] G. Jia, M. Yang, Y. H. Song, H. P. You, H. J. Zhang, *Cryst Growth Des* **2009**, *9*, 301-307.

[108] J. G. Yu, X. X. Yu, B. B. Huang, X. Y. Zhang, Y. Dai, *Cryst Growth Des* **2009**, *9*, 1474-1480.

[109] M. Shang, W. Z. Wang, H. L. Xu, *Cryst Growth Des* **2009**, *9*, 991-996.

[110] aR. S. Yuan, X. Z. Fu, X. C. Wang, P. Liu, L. Wu, Y. M. Xu, X. X. Wang, Z. Y. Wang, *Chem. Mater.* **2006**, *18*, 4700-4705; bJ. Y. Gong, S. R. Guo, H. S. Qian, W. H. Xu, S. H. Yu, *J. Mater. Chem.* **2009**, *19*, 1037-1042.

[111] S. H. Li, E. B. Wang, C. G. Tian, B. D. Mao, Z. H. Kang, Q. Y. Li, G. Y. Sun, *J. Solid State Chem.* **2008**, *181*, 1650-1658.

[112] Y. Li, J. S. Wu, D. W. Qi, X. Q. Xu, C. H. Deng, P. Y. Yang, X. M. Zhang, *Chem. Commun.* **2008**, 564-566.

[113] H. W. Liang, X. Cao, F. Zhou, C. H. Cui, W. J. Zhang, S. H. Yu, *Adv Mater* **2011**, *23*, 1467-1471.

5 Applications of Hydrothermal Carbons

5.1 Introduction

Starting with the discovery of fullerenes [1] and carbon nanotubes [2] the material science related to valuable carbon materials has become a hot area, motivated by its potential applications. [3] Many synthetic methods, such as high-voltage-arc electricity, laser ablation or hydrothermal carbonisation have been reported for the preparation of amorphous, porous or crystalline carbons with different size, shape and chemical compositions.

During the last years, carbon materials retain great development because of their numerous applications in energy storage and conversion, adsorption, catalysis and many other fields of current interest. There is no wonder that a number of novel nanostructured carbon materials have been processed later, many of them from molecular level using bottom-up strategies. To date, it has been possible to create materials with well-defined nanostructures, morphologies and tuneable surfaces. [4]

We already know from the previous chapters that the HTC technique is a sustainable and flexible alternative to synthesise carbon materials. It uses low cost precursors, water as a carbonisation media and lower temperatures in comparison with other carbonisation methods enabling thus the presence of polar surface groups which can be modulated by additional heat treatment.

Chapter 3 showed how it is possible to introduce tailored porosities into these types of materials and change their morphologies while Chapter 4 how HTC materials can be combined with inorganics resulting in hybrid materials with novel properties as well be modified with various functionalities and heteroatoms.

It can thus be foreseen that HTC materials are suitable for a wide range of important applications from adsorption and catalysis to energy storage and generation. Indeed, the most appealing feature of HTC is the fact that it represents an easy, green and kg-scalable process, allowing the production of various carbon and hybrid nanostructures with practical applications on a price base which is comparatively lower then corresponding petrochemical processes. Even though relatively in their infancy, HTC materials have already found numerous applications including soil enrichment (not discussed in this thesis but see references [5]), catalysis, water purification, energy and gas storage, sensors and bio-

applications. In this chapter, examples where HTC materials have proved to be not only sustainable, but to possess extraordinary properties which in some cases surpass those of current " golden standards" will be introduced and discussed. I will give some examples describing the application of carbonaceous materials made using the HTC process in the previously mentioned fields such as catalysis, energy storage, adsorption, medicine and sensors.

5.2 Energy Storage

Climate change and the decreasing availability of fossil fuels require society to move towards sustainable and renewable resources. As a result, we are observing an increase in renewable energy production from sun and wind, as well as the development of electric vehicles with low CO_2 emissions. As the sun does not shine during the night, wind does not blow on demand and we all expect to drive our car with a few hours of autonomy, energy storage systems are starting to play a larger role in our lives.

Therefore, in response to the needs of modern society and emerging ecological concerns, it is now essential that new, low-cost and environmentally friendly energy conversion and storage systems are found. This is why over the past few years, the number of publications and research groups working in the field of "sustainable materials for energy storage" applications was "exploding". The performance of these energy storage devices depends initially on the properties of the materials they are made off. Innovative materials chemistry lies at the heart of the advances that have already been made in energy conversion and storage, for example the introduction of the rechargeable lithium battery, development of supercapacitors and the emerging new and high energy density technologies such as Li-S and Li-air batteries.

Further breakthroughs in materials, not incremental changes, hold the key to new generations of energy storage and conversion devices. Additionally, it is strongly desired that these materials should be easy to make, cheap and if possible base on renewable resources.

Figure 5-1 shows a schematic representation on how such high-performance green materials such as for example hydrothermal carbons should have specific characteristics and be designed for performing specific tasks, either as electrode materials for lithium-ion batteries and supercapacitors, catalysts for oxygen reduction reaction in fuel cells or host materials for hydrogen storage.
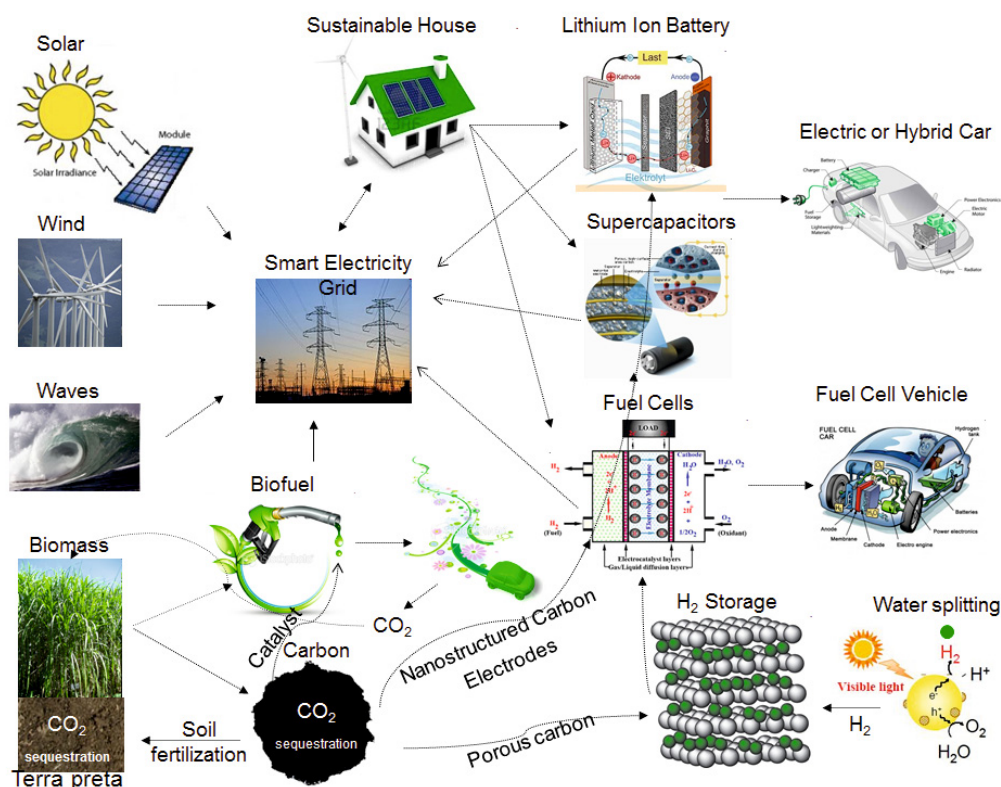
Figure 5-1: Schematic representation of renewable energy generation, storage and utilisation using modern electrochemical devices based on "green" carbon materials

Within this section I will provide a brief overview on the use of HTC materials for such energy storage related applications when used as electrodes in rechargeable batteries or supercpacitors.

5.2.1 Electrodes in Rechargeable Batteries

Rechargeable batteries are made up of one or more electrochemical cells and are also known as secondary cells because the electrochemical reactions are electrically reversible. Several different combinations are currently commercially used including: lead-acid, nikel cadmium (NiCd), [6] nikel metal hydride (NiMH), [7] lithium ion (Li-ion) [8] and lithium ion polymer. [9] Many other are under development: thin film lithium, [8f] [10] Li-S, [11] Na-S, [12] Mg-ion, [13] Li-air [14] and others. Although such rechargeable batteries have a higher initial cost, their main advantage is that they can be recharged cheaply and used many times.

Rechargeable batteries are used today for automobile starters, portable consumer devices, light vehicles (electric bicycles, golf carts, motorised wheelchairs) and uninterruptable power supplies. The emerging applications are in hybrid electrical vehicles and electrical vehicles.

Grid energy storage applications use rechargeable batteries for load levelling, where they store electric energy for use during peak load periods, and for renewable energy uses such as storing power generated from photovoltaic arrays during the day, to be used at night.

Due to all these very important current and foreseen applications there is a lot of research dedicated to the improvement of these devices. The main driving forces are the reduction of the cost and weight while increasing their lifetime and power. As previously mentioned there are many types of rechargeable batteries under development, a number of them holding progress in electrode materials, electrolytes and engineering. Describing all of them in detail is out of the scope of this chapter and details can be found in the literature. [15] [8e]

I will focus here on three main technologies, one already commercially available (Li-ion batteries LIBs) and two under development (Na-ion batteries NIBs) and Li-S batteries while describing the progress made in the use of HTC materials and composites as electrodes for these very important devices.

5.2.1.1 HTC as Electrodes in Li –Ion Batteries (LIBs)

Rechargeable lithium batteries have reformed the portable electronic industry. This is due to their superior energy density (they can store 2-3 times more energy per unit weight and volume in comparison with conventional rechargeable batteries).

LIBs are lithium ion devices comprising a graphite negative electrode (anode), a non-aqueous liquid electrolyte and a positive electrode (cathode) of a spinel type oxide $LiMO_2$ (where M = Co and sometimes Mn and Ni). On charging, lithium ions are desintercalated from the layered $Li\,MO_2$ intercalation host, pass across the electrolyte and intercalated between the graphite layers in the anode. Discharge reverses the process (Figure 5-2). The electrons of course pass around the external circuit
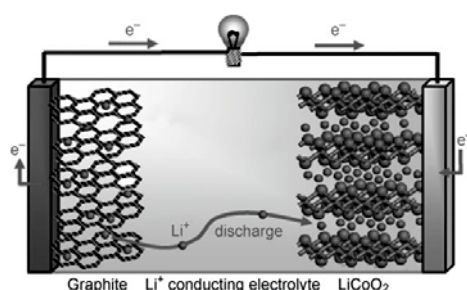
Figure 5-2: Schematic representation of a lithium-ion battery. Negative electrode (graphite), positive electrode ($LiCoO_2$), separated by a non-aqueous liquid electrolyte (taken with permission from [8b]).

5.2.1.1.1 Anodes based on Intercalation /Desintercalation

The storage of one Li atom between every six carbon atoms is only valid for graphite. This LiC_6 stoichiometry permits to graphite a storage capacity of 372 mAhg^{-1}, a value lower that it can be obtained with other materials as we will see later. However, this low storage capacity results in only a small volumetric change of about 10% and allows for a life of at least 500 cycles depending on the current rate used. The anode reaction based on intercalation and desintercalation is:

$$_yC + {}_xLi + e = Li_xC_y$$
(Equation 5-1)
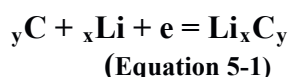
Disordered carbons (the so called hard carbons) can easily exceed this theoretical value reported for graphite. This phenomenon is still hard to explain by classical graphite intercalation science and new mechanisms are under development. A more detailed discussion about the possible Li storage in carbon nanostructures can be found in [16] The main problem associate with carbon materials is that the values for higher capacities are obtained when the potential is close to 0V vs Li/Li$^+$, which is not safe, especially for high power applications such as for example electrical vehicles.

There are a multitude of manuscripts on the use of pure carbon materials as negative electrodes in Li ion batteries as well as some very good reviews summarising all these findings. [8c, 17] [3a] I will only limit here to the use of hydrothermal carbons for such applications.

The first study using HTC as a negative electrode in Li-ion batteries was performed by Huang et al. [18] The authors demonstrated that the reversible lithium insertion/extraction capacity of this kind of material is much higher than the theoretical capacity of graphitised carbonaceous materials. However these materials had relatively high surface area and a high number of micropores which are known not to be beneficial for Li storage. [19]

Therefore our group (Titirici, White) in collaboration with Kun Tang from MPI Stuttgart limited the thickness of the carbon shell to only few nm, producing HTC hollow spheres. [20] The electrochemical behaviour of the hollow carbon nanospheres was characterised by cyclic voltammetry (CV) at a scan rate of 0.1 mVs^{-1} (Figure 5-3a). The voltamogram showed two cathodic peaks at 1.3 and 0.8 V that appear only in the first cycle. It is reasonable to assume

that the peak at higher potential is due to the reaction of Li with surface functional groups located at the carbon surface whereas the peak at 0.8V is related to the formation of solid electrolyte interface (SEI). This is a typical problem associated with carbon materials related to the decomposition of the electrolyte onto the electrode surface and trapping some Li inside. This contributes to the large irreversible capacity of the first discharge process. The phenomenon was further confirmed by the galvanostatic discharge charge results (Figure 5-3b).
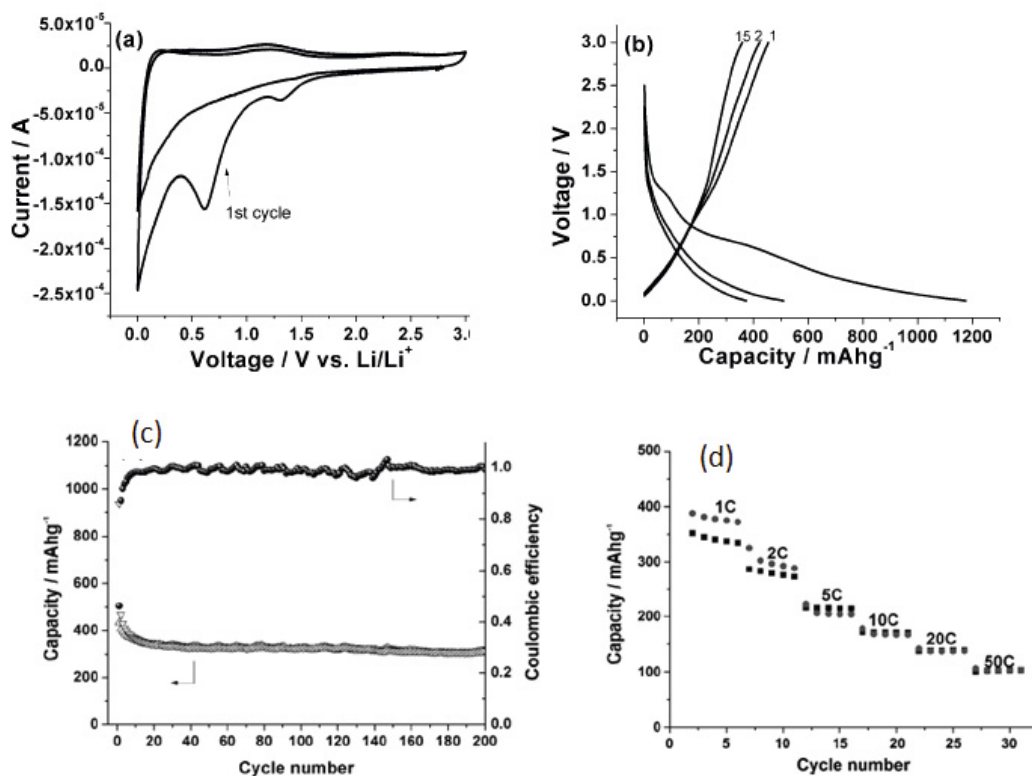
Figure 5-3: a) Cyclic voltametry of hollow carbon spheres. The graph shows the first two cycles between 3 and 0 V at a scan rate of 0.1 mVs^{-1}.b) Galvanostatic discharge/charge curves of hollow carbon nanospheres at a rate of 1C. c) Cycle performance of hollow carbon nanospheres cycled at a rate of 1C. d) Rate performance of hollow carbon nanospheres (taken with permission from [21]).

Two plateaus at 1.4 and 0.8 V are observed in the first discharge curve corresponding to the additional peaks in the CV curves. A large irreversible capacity of 700 mAh/g was found over the first cycle as expected. From the presented results, it is obvious that both electrolyte decomposition on the electrode/electrolyte surface and irreversible lithium insertion into potentially unique positions, such as cavities or sites in the vicinity of residual hydrogen atoms in the carbon material, cause the large irreversible capacity as reported earlier for such

kind of materials. [22] The reversible capacity at 1C rate for the hollow carbon nanospheres could reach up to 370 mAh/g, which is slightly higher than graphite (Figure 5-3c). While previous reports suggest that non-graphitic carbons show a continuous and progressive decay in capacity during cycling, here the investigated hollow spheres presented excellent cycling performance at 1C rate. After 200 discarge/charge cycles, a reversible capacity as high as 310 mAh/g was retained, while the coulombic efficiency approached almost 100%. However, the real advantage of such hollow carbon spheres besides the high cyclability is the outstanding rate capabilities (Figure 5-3d). A specific charge capacity of 200 mAh/g is reached at 5C and when the current density is increased from 1C to 20C the capacity retention can approach 50%. Even at a high rate of 50 C (18.6 A/g), a capacity of 100 mAh/g is still maintained. This value is much higher than traditional graphite electrodes (almost negligible at such a high rate). We should also mention that the rate performance is much higher than that of a similar carbon but as full sphere, indicating that indeed the hollow nanosphere morphology plays a vital role for the excellent electrochemical performance. [21]

A similar excellent performance was also confirmed by Xia et al who prepared one dimensional hierarchical porous hydrothermal carbon fibers from alginic acid fibers. [23] The carbon fibers consist of a 3D network of nano-sized carbon network with excellent rate capability and capacity retention compared with commercial graphite.

Another material in which Li can be inserted is TiO_2. [24, 25] Regardless of various polymorphs of TiO_2 (rutile, anatase, brookite) the insertion reaction of Li-ion into TiO_2 can be expressed as:

$$\textbf{TiO}_2 + \textbf{xLi}^+ + \textbf{xe}^- = \textbf{Li}_x\textbf{TiO}_2 \qquad\qquad \textbf{(Equation 5-2)}$$

In this redox reaction, the insertion of positively charged Li^+ is balanced with an uptake of electrons to compensate Ti^{iii} cations in the Ti^v sublatice, which usually results in a sequential phase transformation occurring in original TiO_2 as a function of Li^+ content. [24a]

The theoretically calculated capacity of TiO_2 is 330 mAh/g, which is a little lower than of graphite. [26] However the volume change of TiO_2 is less than 4% as Li ion inserted into TiO_2 electrodes This affords TiO_2 an outstanding structure stability after Li-ion insertion and thus extremely long cycling life as electrodes in LIBs.

Safety is another crucial concern in LIBs. However the working potential for most high-capacity materials including graphite in in the region of 0-0.5 V (versus Li/Li$^+$). In such a low operation voltage region, the electrolyte is prone to decompose and form the SEI on the anode surface, as we could observe in the example shown in Figure 5-3. Concurrently with the electrolyte decomposition, gases are released and build up pressure in the cell. This situation will endanger the safety of the battery system as gases accumulate with increasing cycling time. Another advantage of TiO$_2$ in this respect is that it operates at a higher voltage (1.5-1.8 V versus Li/Li$^+$) and generates less energy than other anode materials. The formation of SEI on its surface is thus avoided at such a high potential which greatly improves the overall safety of the battery. In addition another great advantage is that TiO$_2$ is cheap. The disadvantage is that like for any inorganic material, TiO$_2$ is not electrically conductive ($\sim 1 \times 10^{-12}$ S m^{-1}) resulting in low energy/power densities. Its conductivity can be improved by combining it with carbon in small amounts.

Thus, carbon coated TiO$_2$ nanotubes were prepared by a simple one-step hydrothermal method with the addition of glucose in the starting powder. A thin carbon coating was obtained on the nanotube surface which effectively suppressed the aggregation of TiO$_2$ nanotubes during post calcination. This action resulted in better ionic and electronic kinetics when applied to Li ion batteries. Consequently carbon-coated TiO$_2$ nanotubes delivered a remarkable lithium-ion intercalation/desintercalation performance with reversible capacities of 286 and 150 mAh/g at 250 and 750 mAh/g respectively. [27]

In the TiO$_2$ family, spinel-type lithium titanates have also attracted great interest as anode materials in LIBs. This is due to their unique characteristics such as: (1) zero strain during charging and discharging; (2) excellent cycle reversibility; (3) fast Li$^+$ insertion-desinsertion and (4) high litigation voltage plateau at 1.55 V vs Li/Li$^+$ which avoids the formation of metallic lithium and therefore improved the safety of the battery.

Carbon coating of fine Li$_4$Ti$_5$O$_{12}$ was carried out by HTC followed by carbonisation at 800°C. The materials behave excellent when applied as anodes in LIBs with excellent rate performance. [28]

5.2.1.1.2 Anodes based on Alloying Reactions

Some metals and semiconductors can react with Li forming alloys according to Li$_x$M$_y$ through electrochemical processes. [8a, 29] The reaction is partially reversible and involves a

large number of atoms per formula unit. The specific volumetric and gravimetric capacities exceed those of graphite. For example Li $_{4.4}$Sn has a gravimetric capacity of 993 mAh/g versus 372 mAh/g for graphite. The corresponding values for Li$_{4.4}$ Si are 4200 mAh/g. Because of their high theoretical capacities many efforts have been made to apply such materials as anodes in LIBs. [29b] However, such alloying reactions are normally associated with severe volume changes during Li insertion/ desinsertion leading to a very fast decay in capacity with cycling. Another associated problem, as for the TiO$_2$, is the low conductivity of such materials.

In order to overcome such problems our group successfully coated *"in situ"* commercially available silicon nanoparticles with a thin layer (25%wt-10 nm) of HTC material *via* the conversion of D-glucose (Figure 5-4a). [30]
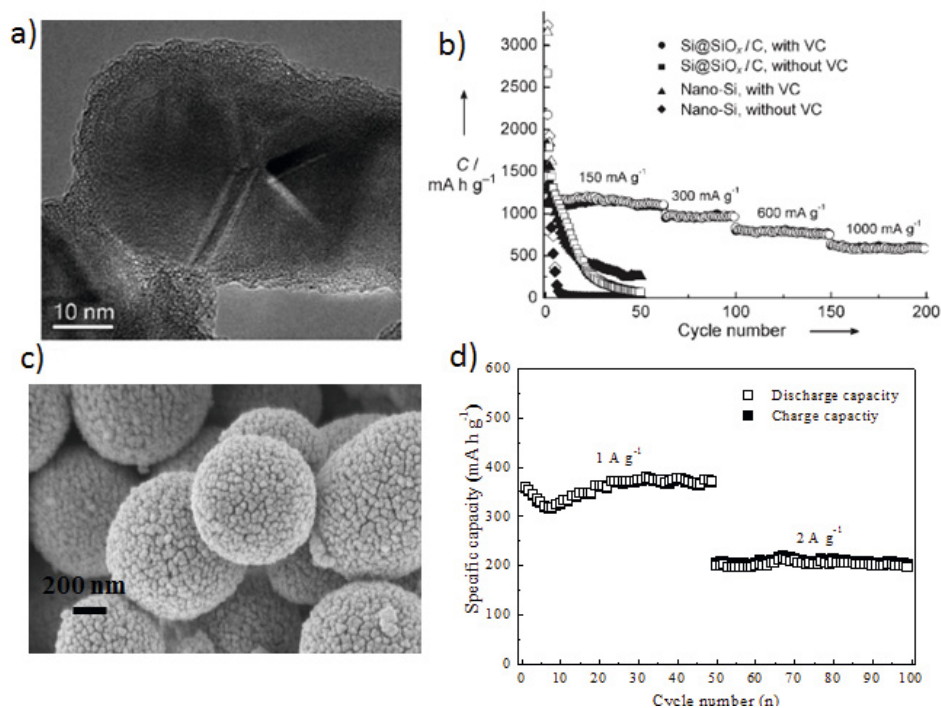
Figure 5-4: a) HRTEM of the Si@SiOx/C composite showing the crystalline silicon in the middle coated with a thin amorphous layer of SiOx and carbon; b) Cycling and rate performance of pure Si nanoparticles and Si@SiOx/C nanocomposite electrodes cycled in VC-free and VC containing electrolytes (LiPF$_6$ in EC/DMC solutions (solid symbols: charge; empty symbols: discharge). c) SEM micrograph of SnO$_2$ microspheres made out of aggregated nanoparticles. d) variation in discharge/charge capacity versus cycle number for the mesoporous SnO$_2$ sample cycled at current densities of 1 and 2 A/g (taken with permission from [30-31])

During the hydrothermal treatment a thin layer of SiO_x was also formed on the particles surface. The resulting $Si@SiO_x/C$ composite was further carbonised to increase its conductivity. The resulting material showed a markedly improved cyclability compared with the pure Si (Figure 5-4b). Especially when working in the presence of vinylene carbonate additive (VC) in the electrolyte, an excellent cycling performance was achieved. The reversible capacity was as high as 1100 mAh/g at a current density of 150 mA/g, with no further decay in capacity, even after 60 cycles.

Pre-formed SnO_2 nanoparticles were incorporated inside HTC spheres derived from the conversion of D-glucose also by our research group. The resulting composites were carbonised and utilised as electrodes in Li ion batteries. The carbon could be subsequently removed resulting in mesoporous SnO_2 microparticles (Figure 5-4 c). Here, HTC acts as an assembly medium of the initial nanoparticles into mesoporous SnO_2 nanosphers leading to a better packing density and superior Li insertion properties (Figure 5-4d). [31]

The reaction of SnO_2 with Li takes place according to the following reaction [32]:
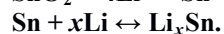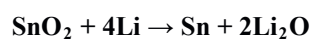
$$SnO_2 + 4Li \rightarrow Sn + 2Li_2O \qquad \text{(Equation 5-3)}$$
$$Sn + xLi \leftrightarrow Li_xSn. \qquad \text{(Equation 5-4)}$$

The maximum theoretical capacity of the SnO_2 anode is 781 mAh/g by this mechanism. The irreversible initial capacity loss is due to the formation of amorphous Li_2O matrix.

Cao et al have also reported on the preparation of multilayered nanocrystalline SnO_2 hollow spheres *via* a chemically induced self-assembly approach performed under hydrothermal conditions. [33] First, a multilayered, spherical SnO_2-HTC composite is produced through a condensation-polymerisation and carbonisation of sucurose accompanied by hydrolysis of $SnCl_4$ during the hydrothermal reaction. After the removal of the carbon hollow SnO_2 spheres were obtained with good electrochemical performance when applied as anode materials in LIBs.

Wu et al reported on the synthesis of carbon-coated SnO_2 nanotubes through a simple glucose hydrothermal and subsequent carbonisation approach using Sn nanorods as sacrificial templates. The as-synthesised SnO_2-C nanotubes have been applied as anodes in LIBs and exhibited improved cyclic performance compared to pure SnO_2 nanotubes. The hollow

nanostructure, together with the carbon matrix which has good buffering effect and high electronic conductivity, can be responsible for the improved cyclic performance. [34]

In a similar fashion with coating the silicon nanoparticles, Li et al synthesised SnO_2@carbon core-shell nanochains (SCNCs) by carbonisation of a SnO_2@ carbonaceous polysaccharide (CPS) precursor at a relatively low temperature. The strategy results in the carbonisation of CPS whilst avoiding the carboreduction of SnO_2 at 700°C. It has been shown that moderate carbon content contributed to the 1D growth of SCNCs. The thickness of the carbon shell could be easily manipulated by varying the hydrothermal treatment time. Such unique nanochain architecture could afford a very high lithium storage capacity as well as a desirable cycling performance. More than 760 mAh/g of reversible capacity was achieved at a current density of 300 mA/g and above 85% retention could be obtained after 100 charge-discharge cycles. TEM analysis of electrochemically-cycled electrodes indicated that the structural integrity of the SnO_2@carbon core-shell nanostructure was retained during the electrochemical cycling, contributing to the good cycling performance demonstrated by the robust carbon shell. [35]

Following a procedure initially described by our group [36], Archer and co-workers used the glucose mediated hydrothermal method for a gram-scale synthesis of nearly monodisperse hybrid SnO_2 nanoparticles. [37] Glucose was playing here a dual role: 1. the facilitation of rapid precipitation of polycrystalline SnO_2 nanocolloids and 2. the creation of a uniform carbon coating on the SnO_2 cores. The thickness of the coated layer could be easily manipulated by the variation of the glucose concentration in the synthesis medium. The resulting SnO_2 colloids coated with carbon exhibited significantly enhanced cycling performance for lithium storage. By reduction with H_2 the authors demonstrated a simple route to carbon-coated Sn nanospheres. Li storage properties of the later materials are also reported in the manuscript suggesting that the large irreversible losses in these materials are caused not only by the initial irreversible reduction of SnO_2 as generally perceived in the field, but also by the formation of SEI. [37]

5.2.1.1.3 Anodes based on Conversion Reactions

Another possibility to increase the capacity of an anode in LIBs are the so called "conversion reactions" as firstly reported by Poizot in 2000. [38] Li can thus be stored reversibly in a transition metal oxide through a heterogenous conversion reaction according to:

$$M_aX_b + (b \cdot n) \, Li \leftrightarrow aM + bLi_nX \qquad\qquad \textbf{(Equation 5-5)}$$

Where: M = transition metal, X = anion, and n = formal oxidation state of X.

Later, reversible Li storage was also observed in transition metal fluorides, sulfides, phosphides and nitrides [39] [40] It has been also shown that a small nanoparticle size it is beneficial for such conversion reactions. [8b]

Taking in consideration these arguments and with additional benefits from the conductive carbon phase, many carbon-metal oxides and nitrides have been prepared as successful electrodes in Li ion batteries. We will again only mention here the ones prepared using the hydrothermal carbonisation of inorganic precursors and carbohydrates.

Tu et al prepared a spherical NiO-C composite by dispersing NiO in glucose solution and subsequent carbonisation under hydrothermal conditions at 180°C. Electrochemical tests showed that the NiO-C composite exhibited higher initial coulombic efficiency (66.6%) then the pure NiO (56.4%) and better cycling performance. The improvement of these properties was attributed to the carbon as it can reduce the specific surface area and enhance the conductivity. [41]

Co-Fe layered double hydroxide nanowall arrays have been grown directly from a flexible alloy substrate by a facile hydrothermal method in the presence of glucose. After annealing treatment in argon atmosphere, carbon coated Co-Fe mixed oxide nanowalls arrays were further investigated as anode materials for LIBs. They exhibited improved electrical conductivity and superior electrochemical performance in terms of specific capacity and cyclability as compared to a carbon-free sample and a sample made by a previous carbon-coating method. [42]

Co_2SnO_4@C core-shell nanostructures were prepared through a simple glucose hydrothermal and subsequent carbonisation approach. The as-synthesised Co_2SnO_4@C core-shell nanostructures have been applied as anodes for Li-ion batteries with improved cycling performance compared to the pure materials. [43]

5.2.1.1.4 Positive Electrodes (Cathodes)

Besides negative electrodes in Li-ion batteries, the development of improved cathode materials is recognised as even more challenging. [44] Although transition metal oxides (with

245

the golden standard being $LiCoO_2$-see Figure 5-2) are commonly used as energy storage materials in today´s modern portable devices, concerns over safety and cost have prompted research into other new positive electrode materials for lithium ion batteries. Several new compounds have been explored as possible alternatives, including those obtained by introducing large polyanions of the form $(XO_4)^{y-}$ (X= S, P, Si, As, Mo, W) into the lattice. An inductive effect from $(PO_4)^{3-}$ and $(SO_4)^{2-}$ ions raises redox energies compared to those in oxides and stabilises the structure. [45] The presence of polyanion $(XO_4)^{y-}$ with strong X-O covalent bonds increases the potential as a result of the strong polarization of oxygen ion toward the X cation, which lowers the covalency of the M-O bond. Research shows that most of the lithium metal phosphate and sulphate compounds containing FeO_6 octahedra as the redox center, have potentials in the range of 2.8-3.5 V versus Li/Li^+. [46] Another advantage of using Fe based compounds is that, in addition to being naturally abundant and inexpensive, they are less toxic then other transitional metal compounds.

The focus of the LIBs community further intensified on this class of compounds with Pahadi´s report on the electrochemical properties of $LiFePO_4$ (LFP). [47] LFP satisfies many of the criteria for an electrode material in a Li-ion battery: it can reversibly intercalate Li at a high voltage (3.5V) and has a gravimetric capacity of 170 mAh/g, which gives a cell a high energy density. LFP is stable against overcharge or discharge and is compatible with most electrolyte systems. [48] LFP is also environmentally friendly, for it is found in nature as the mineral triphylite and is made from abundant elements, reducing its production costs.

Some drawbacks associated with LFP are its low electronic conductivity (1x 10^{-9} S/cm at room temperature) which limits its electrochemical performance as the electrons cannot easily transport through the material. LFP becomes conductive in the presence of small amounts of carbon [49] as well as when doped with various cathions forming compounds of the type $Li_{1-x}M^{z+}_xFePO_4$ ($z \geq 2$) with exceptional conductivities when sintered at 800°C-due to charge compensation (10 times higher than pure LFP). [50]
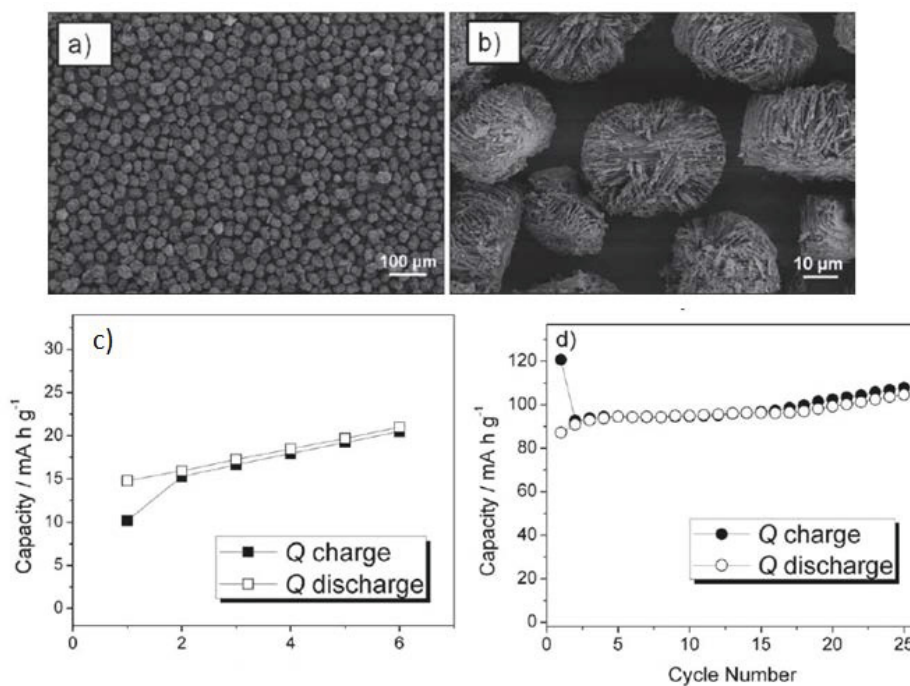
Figure 5-5: a) and b) SEM microgrpahs of the LFP@C mesocrystals; c) charge-discharge capacity versus cycle number plot for the pristine LFP. d) charge-discharge capacity versus cycle number plot for the LFP@C showing superior performance (adapted with permission from [51]).

Our group synthesised in one step a hierarchical mesocrystal of LFP coated with a thin layer of nitrogen doped carbon (Figure 5-5a, b). Due to an increased conductivity of the nitrogen doped carbon the coated material exhibited a superior performance compared with the pure LFP (Figure 5-5 c, d). [51]

Paranthaman et al modified the surface of rod-like $LiFePO_4$ with a conductive nitrogen-doped carbon layer using hydrothermal processing followed by post-annealing in the presence of an ionic liquid. The conductive surface modified rod-like LiFePO4 exhibited good capacity retention and high rate capability as the nitrogen-doped carbon layer improved conductivity and prevented aggregation of the rods during cycling. [52]

Similar to phospholivines, the ortosilicates (Li_2MSiO_4, where M= Fe but also Mn and Co) have been employed recently as alternative cathodes in LIBs. Their main advantages are cell safety, the possibility of extraction of more than one Li^+ ion per unit formula, high theoretical capacity (333 mAh/g). [53] Moreover, the orthosilicate group material render excellent thermal stability offered through strong Si-O bonding. However, they have the same disadvantage suffered similarly by their related olivine phosphates, very poor electronic conductivity.

Exploiting the advantages of hydrothermal synthesis, Aravindan et al prepared in one step carbon coated Li_2MnSiO_4 with a flower-like morphology similar the one of LFP in Figure 5-5 a, b and good electrochemical performance (100 mAh/g). [54] The improvement of the electronic conductivity due to the carbon coating was validated through electrochemical impedance spectroscopy.

Since Sony announced the first version of commercialized LIB in 1991, LIB has rapidly penetrated into everyday life. In this subchapter I have tried to show the main research directions taken for improving the performance of the electrode materials in LIBs with focus on the HTC technology. Li-ion technology relies on a rich and versatile chemistry leading to wide range of attractive electrode materials for both positive ($LiCoO_2$, $LiMn_2O_4$, $LiFePO_4$) and negative electrodes (C, Sn, Si, etc.). Much progress has been achieved in this filed and the HTC materials proved to be successful candidates for this task.

5.2.1.2 HTC as Electrodes in Na-Ion Batteries (NIBs)

There has been recent concern that the amount of the Li resources that are buried in the earth would not be sufficient to satisfy the increased demands on LIB. [55] While there is ample evidence that this is no cause for immediate worry, the very large market share of electric vehicles can put a strain on Li production capability. [56]

Sodium (Na) is located below Li in the periodic table and they share similar chemical properties in many aspects. The fundamental principles of the NIB and LIB are identical; the chemical potential difference of the alkali-ion (Li or Na) between two electrodes (anode and cathode) creates a voltage on the cell. In charge and discharge the alkali ions shuttle back and forth between the two electrodes. There are several reasons to investigate Na-ion batteries. Recent computational studies by Ceder et al. [57] on voltage, stability and diffusion barrier of Na-ion and Li-ion materials indicate that Na-ion systems can be competitive with Li-ion systems. In any case, Na-ion batteries would be interesting for very low cost systems for grid storage, which could make renewable energy a primary source of energy rather than just a supplemental one.

As battery applications extend to large-scale storage such as electric buses or stationary storage connected to renewable energy production, high energy density becomes less critical. Moreover, the abundance and low cost of Na in the earth can become an advantage when a large amount of alkali is demanded for large-scale applications, though at this point, the cost

248

of Li is not a large contribution to the cost of LIBs. But most importantly, there may be significant unexplored opportunity in Na-based systems. Na-intercalation chemistry has been explored considerably less than Li-intercalation, and early evidence seems to indicate that structures that do not function well as Li-intercalation compounds may work well with Na. Hence, there may be opportunity to find novel electrode materials for NIB. [58]

Many materials have been proposed in the literature as possible cathodes for Na-ion batteries, whereas only some carbon-based anodes have been pointed out for this storage technology. The best candidates to be cathodic materials in a Na-ion battery are phosphate based materials, because of their thermal stability and higher voltage due to the inductive effect. [59] We can mention olivine NaFePO4, with the highest theoretical specific capacity, NaVPO4F, $Na_3V_2(PO_4)_2F_3$, Na_2FePO_4F and $Na_3V_2(PO4)_3$. These phosphates require conductive coating and nanostructured morphology in order to improve their electrochemical performance. [60]

The development of negative electrodes is however more challenging. Graphite, the standard anode material in current lithium-ion batteries, seems not suited for a sodium based system, as Na hardly forms staged intercalation compounds with graphite. [61] The situation is different when amorphous carbons are used as intercalation media and it is suggested that the storage mechanisms for Na and Li are similar, although the capacity is smaller in the case of sodium. [62] Thus, several types of non-graphitic carbon materials have been tested and capacities between 100 and 300 mAh g^{-1} under differing conditions were found. [63] [64] Although these capacities are promising, the cells were only cycled for a few times and, more importantly, could be only obtained at extremely low currents (typically C-rates between C/70 and C/80) or at elevated temperatures(> 60 ° C), which indicates very slow kinetics for the sodium storage process Thus alternative carbon materials are needed in order to achieve satisfying performance at room temperature and at higher currents.

A recent and very important manuscript in the field, describes clear improvements with faster kinetics and higher capacity by introducing nanoporosity and a hierarchical pore system into the carbon anode. High capacities can be achieved at room temperature at high currents (e.g. C-rate of C/5, i.e. 15 times faster than C/75), while also exhibiting long cycling stability. The outstanding performance of the templated carbon is illustrated by comparing with several commercially available porous carbon materials and non-porous graphite as reference. [65]

This is a great progress in the field , however still a great deal of research needs to be dedicated to the production and improvement of carbon materials and carbon composites for Na ion batteries and more and more reports are being published in the literature on this topic. [66] [67] [68]

As Na$^+$ can be inserted in disordered amorphous carbons, HTC materials should also be considered as a class of suitable candidates as anodes for NIBs. In this respect, our group have applied HTC hollow spheres as a negative electrode in NIB. [69]
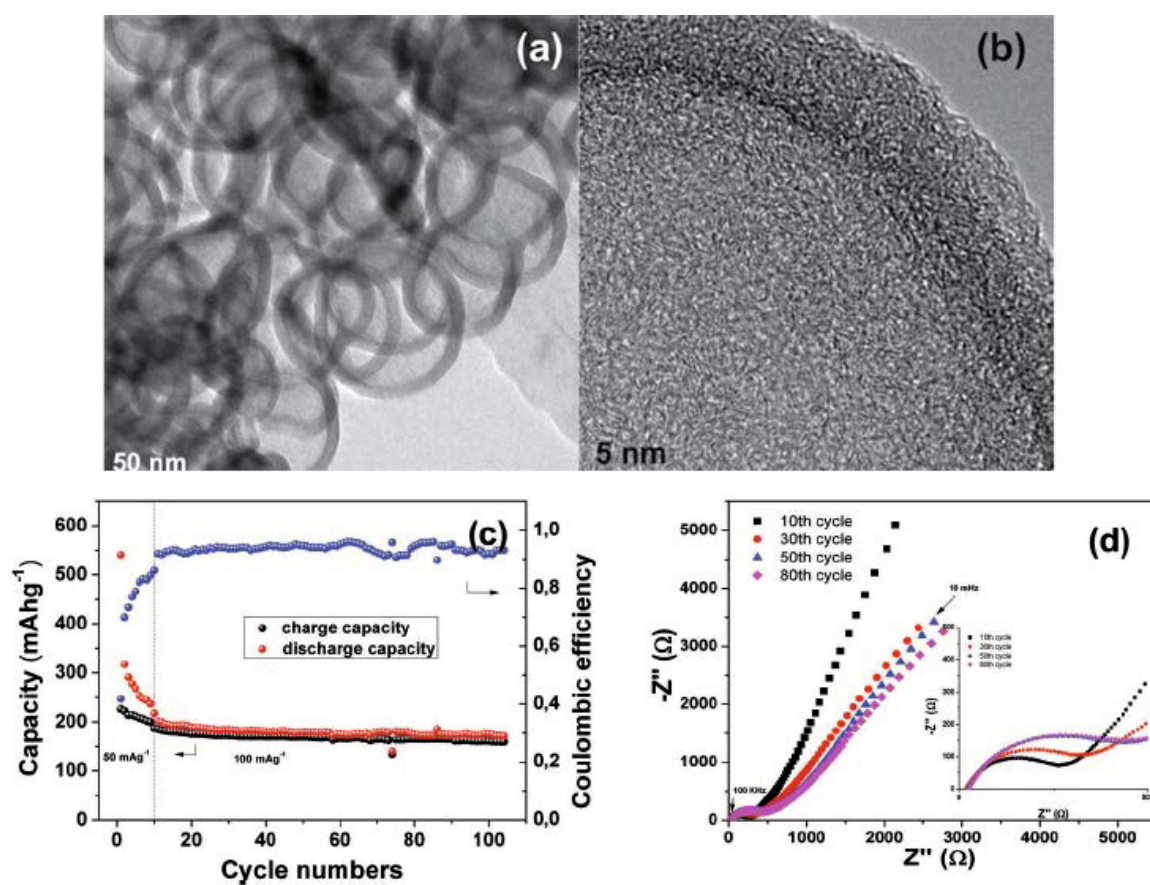
Figure 5-6: a) TEM image and (b) HR-TEM image of hollow carbon nanospheres, (c) Cycle performance of hollow carbon nanospheres, (d) Impedance spectra of hollow carbon nanospheres electrode after 10 th , 30 th , 50 th , and 80 th cycle. The inset is the enlarged spectra (taken with permission from[69]).

The materials have been prepared as previously described for LIBs by coating latex nanoparticles with glucose followed by hydrothermal carbonisation and further calcination to remove the latex and increase the conductivity of carbon (Figure 5-6a,b). [20] The cycling stability during sodium insertion/extraction in the hollow carbon nanospheres was investigated at a current density of 50 mAg^{-1} for the first ten cycles and then 100 mAg^{-1} for

subsequent cycles (Figure 5-6c). It is thought that the observed capacity loss over the initial cycling steps stems from SEI film stabilisation and irreversible sodium ion insertion. After 100 cycles, a reversible capacity of $\sim$ 160 mAhg^{-1} is stably maintained. The coulombic efficiency approaches $\sim$ 94% after several cycles, whilst the observed irreversible capacity during each cycle is attributed to the incomplete stabilisation of SEI for the presented sodium battery system. The electrochemical impedance spectra of the hollow carbon nanospheres electrode was measured (Figure 5-6 d). The Nyquist plots consist of a depressed semicircle in the high- and middle-frequency regions and a straight line in the low-frequency region. The semicircle can be attributed to the SEI film and contact resistance at high frequencies and a charge-transfer process in the middle-frequency, while the linear increase in the low-frequency range may reflect Warburg impedance associated with sodium ion diffusion in the carbon electrode. [70] The rate performance of these materials was also excellent and clearly superior to non-porous hydrothermal carbon spheres obtained from glucose without the latex templates proving the important role played by the hollow sphere morphology. [69]

5.2.1.3 HTC Cathodes for Li-S Batteries

LIBs have transformed portable electronics and will play a key role in the electrification of transport. However, the highest energy storage possible for Li-ion batteries is insufficient for the long-term needs of society, for example, extended-range electric vehicles. To go beyond the horizon of Li-ion batteries is a formidable challenge; there are few options and one of them is Li-S batteries. [71] [11c]

Under intense examination for well over two decades, the cell in its simplest configuration consists of sulphur as the positive electrode and lithium as the negative electrode [72] Li-S cells operates on a principle very different from the Li ion battery described above. The redox couple, described by the reversible reaction lies near 2.2 V with respect to Li^+/Li^0, a potential about 2/3 of that exhibited by conventional positive electrodes. [73]

$S_8 + 16Li = 8Li_2S$ **(Equation 5-6)**
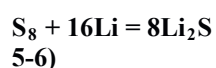
However, this is compensated by the very high theoretical capacity afforded by the non-topotactic "assimilation" process, of 1675mAh g^{-1}. Thus, compared with intercalation batteries, Li-S cells have the opportunity to provide a significantly higher energy density (a

product of capacity and voltage). Values can approach 2500Wh kg^{-1} or 2800Wh l^{-1} on a weight or volume basis respectively, assuming complete reaction to Li$_2$S. Despite its considerable advantages, the Li-S cell is plagued with problems that have slowed down its widespread practical realisation.

One of the problems in Li-S batteries is sulfur´s low electrical conductivity. Another problem is the fact that the polysulfides, which are generated at the cathode during charging, are soluble into most of the utilised electrolytes and thus migrate to the anode where they react with the lithium electrode to form lower-order polysulfides which are then transported back to the sulfur cathode and regenerate the higher form of polysulfides. [11f] Such a polysulfide "shuttle" process decrease the utilisation of the overall active material mass during discharge, triggers current leakage, poor cycleability and reduced columbic efficiency of the battery. [11e]

Some significant progress in overcoming these two very important challenges associated with Li-S batteries commence after the pioneer work of Nazar at al. [74] They have demonstrated for the first time that those cathodes based on nanostructured sulphur/mesoporous carbon materials can overcome these challenges to a large degree, and the Li-S cell can exhibit stable, high, reversible capacities (up to 1320mAh g^{-1}) with good rate properties and cycling efficiency. The proof-of-concept studies are based on CMK-3, the most well-known member of the mesoporous carbon family obtained from replication of SBA 15 silica. [75]

The melt is imbibed into the channels by capillary forces, whereupon it solidifies and shrinks to form sulphur nanofibres that are in intimate contact with the conductive carbon walls. Such an intimate contact of the insulating sulphur and discharge-product sulphides with the retaining conductive carbon framework at nanoscale dimensions affords excellent accessibility of the active material. The carbon framework not only acts as an electronic conduit to the active mass encapsulated within, but also serves as a mini electrochemical reaction chamber. The entrapment ensures that a more complete redox process takes place, and results in enhanced utilisation of the active sulphur material. This is vital to the success of all conversion reactions to ensure full reversibility of the back-reaction. Following this report, the topic related to the development of novel cathodes for Li-S cells based on nanostructured carbon/sulfur composites flourished and more and more research interest is dedicated to improving the performance of Li-S cells. [11a] [76]

Among these carbon materials, hydrothermal carbons just started to find their role. The first HTC materials tested as cathodes in Li-S batteries following sulfur infiltration were the carbon hollow spheres previously applied by our group as electrodes in Li [21] and Na [69] storage. This time they were prepared using silica templates instead of latex (Figure 5-7a, b). Three different HTC-S composites were compared. [77] The first two were hollow spheres (HS) however prepared using two different infiltration techniques for sulfur: melt diffusion and simple physical mix. The third tested material was a non-porous HTC infiltrated with sulfur by simple physical mixing. As shown in Figure 5-7c, stable cycling properties could be obtained when using the nanostructured HS. This indicates that the highly porous shells of HS acts as an absorbent for soluble polysulfides, especially since a very small amount of silica remains from the template. Small amounts of silica within the carbon matrix proved beneficial for polysulfide adsorption. [78]
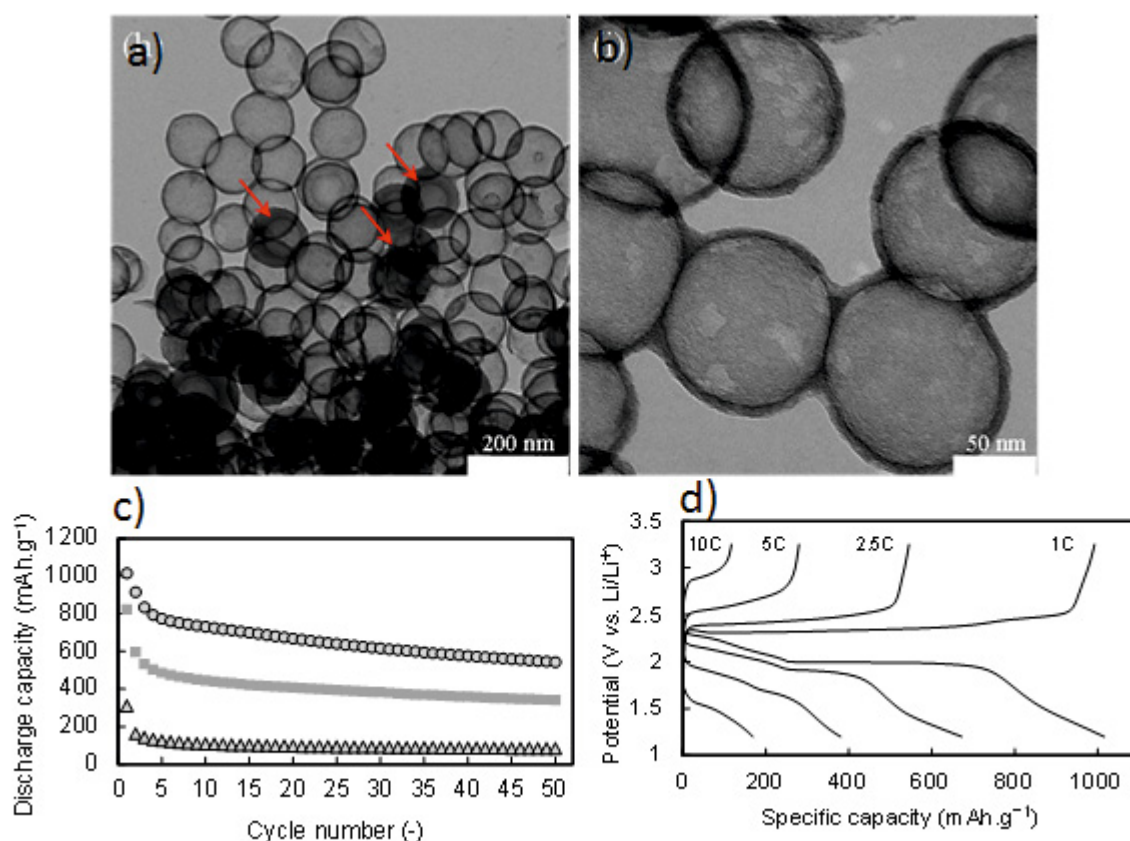
Figure 5-7: Micrographs obtained by transmission electron microscopy of (a-b) Carbon-based hollow spheres obtained after hydrothermal treatment at 180 °C in presence of glucose, pyrolysis at 950 °C and silica removal, 950-CarbHS-G. Red arrows highlight the presence of residual silica within the carbon hollow spheres. c) Cycling performances at 1C for various electrodes using hydrothermal carbons. The cycling stability of the HS HTC-S composite made by melt diffusion method is indicated by circles. The

cycling performance of the simple mixture of HS HTC-S is indicated by squares, while the one associated with the mixture of HTC non-hollow microspheres and S is indicated by triangles. d) Rate performance for HS-HTC –S composite prepared by melt diffusion. The specific capacity was calculated based on the mass of sulphur.

The higher specific capacity obtained *via* the melt diffusion method reveals the formation of a better conductive contact in the HS/S composite compared to the physical mixture of HS and S. The results obtained for non-hollow microspheres underlined two benefits related to the use of HS in Li-S cells : (i) the nanosized spheres improve the specific capacity by ensuring the formation of a conductive network in the cathode made by a composite consisting of carbon spheres, sulfur and binders. If we compare the specific capacity at the 1st cycle of the mixtures made by HS and non-hollow microspheres, the hollow spheres showed a capacity of more than 800 $mAh.g^{-1}$ while it remained at only 300 $mAh.g^{-1}$ for non-hollow HTC microspheres; (ii) while the capacity decreased rapidly for the non-hollow microspheres, the HS/S composite, which displayed a discharge capacity of 1000 $mAh.g^{-1}$ at the 1st cycle, maintained a discharge capacity of 600 $mAhg^{-1}$ at the 50th cycle. The drop in specific capacity during the first few cycles can be explained by the formation of S layers on the surface of HS due to the strong affinity of sulfur for carbon. This result reveals that the unique nanostructure of the hollow nanospheres is the essence of the high-performance electrochemical properties.

Finally, the rate capability of the HS/S composite cathode was investigated and a remarkably high specific power was observed. The HS/S composite cathode showed an initial discharge capacity of 1000 $mAh.g^{-1}$, 700 $mAh.g^{-1}$, and 400 $mAh.g^{-1}$ at 1C, 2.5C, and 5C, respectively. Even at a very high current density of 10C (=16.75 $A.g^{-1}$), our cathode showed a discharge capacity of 170 $mAh.g^{-1}$. If we assume that a full Li-S cell using HS contains 25 wt% of Li_2S, this full cell will provide a specific energy of 460 $Wh.kg^{-1}$ and a specific power of 5000 Wkg^{-1}.

5.2.2 Electrodes in Supercapacitors

Electrochemical capacitors, usually called also supercapacitors, are of great interest as high power electrochemical energy storage devices as they combine high power density with long cycle life and wide operational temperature range, properties that are currently unattainable in Li-ion batteries. However, the energy density achieved by commercial products (about 5 Wh/kg) limits their use to few seconds of charge/discharge, hampering their utilisation in

energy harvesting applications. Therefore, efforts are focused now on increasing the energy density of supercapacitors.

Based on the charge storage mechanism, electrochemical capacitors can be divided in: i) electrochemical double layer capacitors, where the energy storage is based on the electrostatic adsorption of electrolyte ions on the surface area of electrically conductive porous electrodes and ii) pseudo-capacitors, where the energy is stored through redox reactions at the electrode/electrolyte interface. [79] Porous carbon materials are the main candidate for supercapacitors in terms of cost, availability, large surface area, versatility with regards to porosity development and surface chemistry, good conductivity and a lack of negative environmental impact. They behave mainly as electrochemical double layer capacitors, with their large surface area providing high capacitance values. Nevertheless, many carbons possess surface functional groups (i.e. activated carbons). This gives rise to an additional pseudo-capacitance contribution. Thus, nitrogen and oxygen functionalities are known to take part in faradaic redox reactions, increasing the capacitance values and thus the energy density of the supercapacitors. [80] [81] [82] [83] An additional advantage of oxygen and/or nitrogen functionalities is better wettability of the electrodes and in the case of nitrogen, also improved electronic conductivity.Taking into account these considerations, the common methods for increasing the capacitance of carbon electrodes focus on the preparation of high-surface-area carbons with appropriate pore size and surface functionalities.

As described before in the thesis, HTC carbons are oxygen-rich by nature, with the oxygen content being tuned through the operating conditions (temperature, time, precursor and concentration). [84] [85] [86] In addition, by selecting appropriately the initial carbon precursor, operating conditions or additional additives, other functionalities can be introduced in the final carbonaceous materials.

As described in Chapter 4, our group produced nitrogen-rich carbon materials by carrying the HTC process in the presence of ovalbumin [87] or by using nitrogen containing carbohydrates as carbon precursors. [88] Unfortunately, as mentioned in Chapters 2 section 2.3.8 HTC materials generally possess almost no open porosity and their heat-treatment at elevated temperatures can only lead to moderate increase in surface area, which hampers their application in surface area sensitive applications, such as supercapacitors. However, this

limitation has been circumvented recently by the chemical activation of HTC carbons, as described in Chapter 3 section 3.4.

Wei, Sevilla et al. were the first to analyse the supercapacitor performance in organic electrolyte (1 M TEABF$_4$ in acetonitrile) of HTC cellulose (C), starch (S) and sawdust (W) activated at 700 and 800ºC with a KOH/sample weight ratio = 4 [89] Those carbon materials possessed BET surface areas in the ~2100-3000 m^2/g and pore volumes up to ~ 1.4 cm^3/g, with a relatively narrow pore size distribution in the supermicropore range with virtually no pores > 3 nm. The performance of those materials was spectacular, recording the highest capacitance ever reported for porous carbons in a symmetric two-electrode configuration using such electrolyte, i.e. 236 F/g (100 F/cm^3) at 1 mV/s (Figure 5-8 a). It exceeded the specific capacitance of commercial activated carbons optimized for EDLC applications, such as YP-17D, by 100 %. The samples were capable of retaining 64 to 85% of the capacitance when the current density was increased from 0.6 to 20 A/g (Figure 5-8 b). The samples activated at the highest temperature (800ºC), which were the ones with the largest volume of small mesopores in the range 2 - 3 nm, showed better capacitance retention at high sweep rates in the CV measurements or higher current densities in the charging/discharging tests (Figure 5-8 b). The small reduction-oxidation (redox) peaks visible in the CV at ~0 and 2 V at the slowest sweep rate (Figure 5-8 a) are believed to originate from oxygen-containing functional groups remaining in the carbon samples. Such peaks completely disappear at the rate of 10 mV/s, suggesting relatively slow redox reaction kinetics. This may further suggest that the pure EDLC capacitance (without pseudocapacitance contribution) in these materials exceeds 193 F/g. This combination of very high specific and volumetric capacitance and good rate capability of the hydrothermally synthesised porous carbons is unmatched by state-of-the art activated carbons, carbon nanotubes, carbon onions and graphene. Taking into account these results, the study of their capacitance behaviour in aqueous and/or ionic liquids, where pseudocapacitance effects due to oxygen functionalities are larger, is highly desirable.
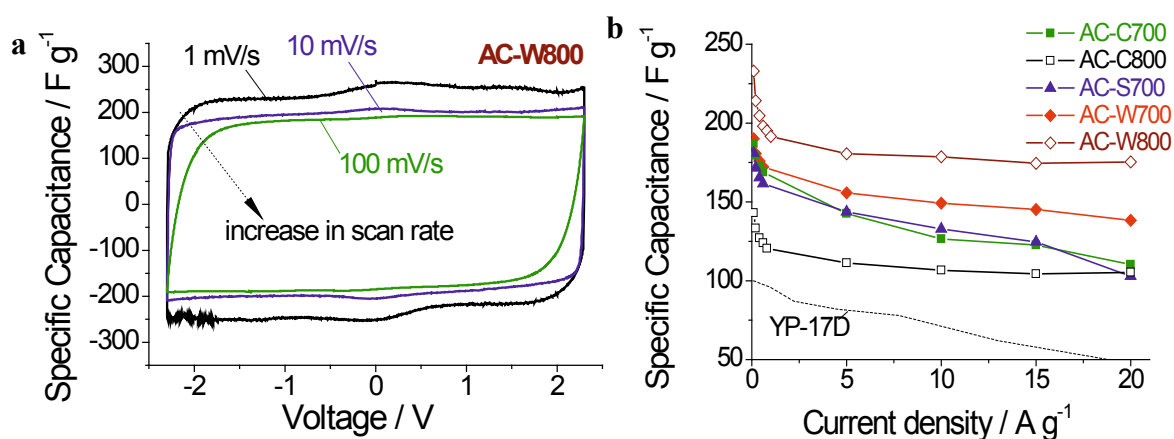
Figure 5-8: Electrochemical characterization of activated carbons derived from hydrothermally synthesised carbon materials in 1 M TEABF4 solution in acetonitrile at room temperature: a) cyclic voltammograms (CV) of the activated carbon obtained from sawdust at 800ºC with KOH/sample = 4 (AC-W800) and b) capacitance retention with current density in comparison with that of commercially available YP-17D activated carbon (extracted from ref. [89] with permission).

Wang et al. have also applied chemical activation to hydrothermal carbons, in this case using phosphoric acid as activating agent and rice husk as carbon precursor. [90] The authors varied the activation temperature between 300 and 700ºC and the weight ratio of phosphoric acid to hydrothermal carbons between 1 and 6. In this way, the obtained porous materials ranged from supermicroporous to mesoporous, with BET surface areas in the ~700 – 2700 m^2/g range and pore volumes up to ~ 2 cm^3/g. Though no PSDs are shown, from the shape of the isotherms, it can be envisaged that they are broader than those of the activated carbons obtained by Sevilla et al. It should be noted that several authors have pointed out that KOH produces narrower PSDs in comparison with other activating agents. [91] [92] [80] The specific capacitance of these activated carbons reached 130 F/g (measured at 2 mV/s) in an aqueous solution of KOH 6 M, value quite below that measured for activated carbons with similar BET surface area but with narrower PSD in the micro-supermicropore range (235 - 286 F/g). [93] This is due to the fact that, as shown by Chmiola et al. [94] a good matching between the electrode pore size and the dimensions of the electrolyte ions is critical for an optimal performance of supercapacitors. They observed an anomalous increase of the specific capacitance for subnanometer pores, which defeated the traditional belief that pores smaller than the size of solvated electrolyte ions do not contribute to energy storage.

Our research group analysed the capacitance behaviour of nitrogen-containing hydrothermal carbons activated with KOH (weight ratio of KOH to hydrothermal carbons = 1 to 4, and T = 600ºC). [95] Although KOH activated, the carbons did not achieve a high degree of activation (surface area < 600 m^2/g). This was due to the low temperature used for the activation (600ºC) chosen in order not to remove all the nitrogen heteroatoms contained in the initial N doped HTC precursor. Despite their low surface area, those materials exhibited excellent electrochemical performance in KOH 6 M and H$_2$SO$_4$ 1 M, achieving specific capacitances up to 220 and 300 F/g at a current density of 0.1 A/g in basic and acidic electrolyte respectively. This superior capacitance is due to the combination of EDLC capacitance and pseudocapacitance arising from redox reactions of the nitrogen functionalities. Humps can be detected at around 0.5 V (Figure 5-9 a), being more obvious in acidic than in basic medium, probably because of the basic character of the functionality in these carbon materials. [81] When compared with the non-activated hydrothermal carbon, the dependence of the electrosorption process on surface area is obvious. Thus, in spite of having higher nitrogen content than the activated samples, i.e 6.7 % vs. 2.3 - 5.2%, the hydrothermal carbon exhibits very low specific capacitance (< 5 F/g), which is a clear reflection of its low specific surface area, i.e. 18 m^2/g. It is worth noting that the chemical activation process leads to a reduction of the nitrogen content of the materials, this reduction being larger with the hardening of the activation conditions (i.e. increase of the amount of KOH used). Thus, it decreases from 6.7 % in the hydrothermal carbon to 2.3 - 5.2 % for the activated carbons obtained with a ratio varying from 1 to 4 respectively as a consequence of preferential oxidation of nitrogen functionalities during the activation process. [96] [97] This indicates that the activation parameters must be carefully chosen in order to get a good compromise between surface area and nitrogen content. Nevertheless, the values of capacitance achieved with these materials are comparable to activated carbons reported in the literature with a much higher surface area (> 3000 m^2/g) [93] and higher than that of a high surface area and high nitrogen-content carbon derived from polyacrylonitrile (160 F/g). [98] Additionally, good capacitance retention at high current density (4 A/g) is observed (Figure 5-9 b), which proves good conductivity and quick charge propagation in both acid and base electrolytes.
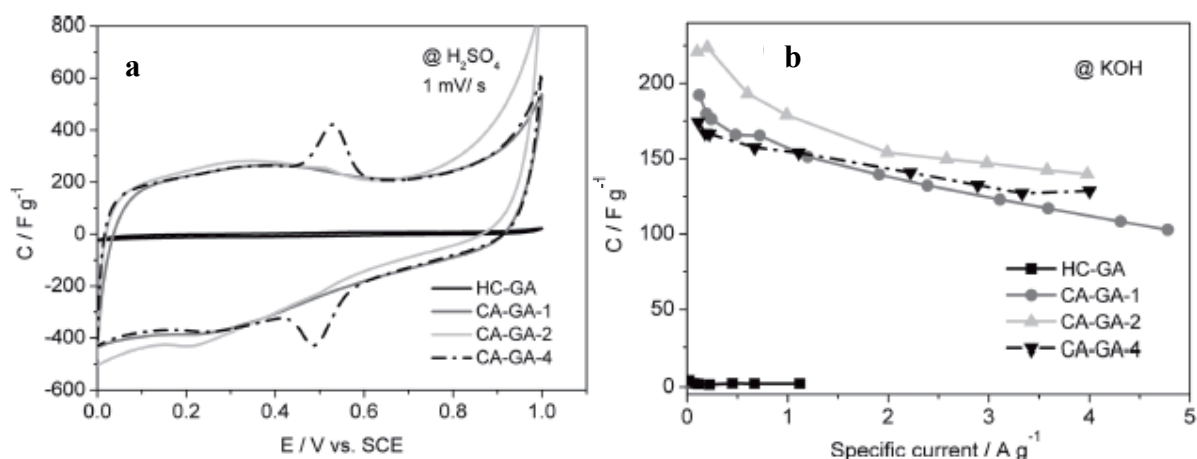
Figure 5-9. **Electrochemical performance of different carbons using a three-electrode cell: a) cyclic voltammograms at a scan rate of 1 mV/s in H_2SO_4 1 M and b) capacitance retention with current density in KOH 6M (adapted from ref. [95] with permission).**

Recently Zhu et al. prepared electrodes for supercapacitors from hydrothermally carbonised fungi (HTC at 120ºC for 6h). [99] The product resulting from the HTC process was characterised by small particles (50-200 nm) fused together to give rise to sheets or tubular networks. The oxygen content was 13.4 % (a 50 % decrease from raw fungi). The value of the BET surface area was typical for hydrothermal carbons, $\sim$ 14 m^2/g. With the aim of creating porosity, as well as improving the electronic conductivity, the authors pyrolysed the hydrothermal carbon at 700ºC for 3 h. As a result, the oxygen content decreased to 5 %, but the surface area increased to 80 m^2/g. Surprisingly, even though the oxygen content is not high and the surface area is really low, the material stored up to 196 F/g at a scan rate of 1 mV/s, value comparable to high surface area carbons like Maxsorb, or highly doped carbons obtained from seaweed. [100] However, with the increase of the scan rate, the decrease of the capacitance was quite high ($\sim$ 40 % decrease at 50 mV/s). The authors explain the large specific capacitance of the material on the basis of its small particle size, which reduces the ion and electron transport path and increases the material usage, as pseudocapacitors store charges in the first few nanometers below the surface. Furthermore, it showed a high electrochemical stability (after repeated galvanostatic cycling, the specific discharge capacitance decreased slowly and stabilised at 180 F/g after 1000 cycles) and the maximum cell voltage reached 1 V for reversible charging as a consequence of the existence of oxygen.[100] This material exhibits therefore a promising behaviour (stability, energy density,

power density, surface capacitance, and volumetric capacitance) as electrode in supercapacitors.

Besides heteroatom doping, another possibility of inducing pseudocapacitance in carbon materials when used as electrodes in supercapacitors is their modification with certain metal oxide nanoparticles such as manganese or ruthenium oxide. The pioneering work on the pseudocapacitive behaviour of manganese oxide in an aqueous solution was published in 1999 by Lee and Goodenough. [101] Both charge storage mechanisms involve a redox reaction between the III and IV oxidation states of Mn ions. In general, hydrated manganese oxides exhibit specific capacitances within the $100–200$ F g^{-1} range in alkali salt solutions, which are much lower than those for RuO_2 ECs. As MnO_2 has no electrochemical conductivity, very often MnO_2/C structures are utilised. [102] Furthermore it is possible to combine the supercapacitive properties of MnO_2 with the double layer storage mechanism of microporous carbons for increasing the capacity value in the so called "asymmetric capacitors". [102]

Applied to HTC, Zhang et al used carbonaceous MnO_2 rattle-type hollow spheres synthesised under mild hydrothermal conditions. [103] The as-prepared materials showed mesoporous MnO_2 shell and a carbonaceous sphere core. The composition and shell thickness of the hollow spheres can be controlled experimentally. The capacitive performance of the hollow structures was evaluated using both cycle voltammetry and charge discharge methods. The results demonstrated a specific capacitance as high as 184 F/g at a current density of 125 mA/g.

To sum up this subsection, the results described above clearly indicate that the post-synthesis activation of hydrothermal carbons is a powerful tool to increase their porosity, enabling thus their use in an application in which otherwise they could not be used. The oxygen functionalities present in those materials represent a clear advantage providing an additional pseudocapacitance contribution to the EDLC capacitance, which can enhance their performance. Furthermore, the use of nitrogen-containing substances as precursors in the hydrothermal carbonisation process allows the introduction of nitrogen functionalities in the activated carbons, providing thus additional pseudocapacitance effects. However, optimisation of the activation conditions (temperature and amount of KOH) is necessary to achieve a good compromise between surface area, pore volume and pore size and oxygen and

nitrogen contents. Finally another possibility to increase the capacitance of HTC materials is their decoration with redox active nanoparticles such as MnO_2 or RuO_2.

In the future, the discovery of novel methodologies for synthesising HTC materials in which chemical activation will no longer be necessary will be desired. This could be accomplished for example utilising molten slats[104] or deep eutectic mixtures[105] to induce microporosity in such materials while maintaining a high level of functional groups for pseudocapacitance.

5.3 Heterogeneous Catalysis

Heterogeneous catalysis has always been an inherently nanoscopic phenomenon with important technological and societal consequences for energy conversion and the production of chemicals. Architectures with all of the appropriate electrochemical and catalytic requirements, including large surface areas readily accessible to molecules, may now be assembled on the benchtop. [106] Designing catalytic nanoarchitectures inspired by Nature using renewable resources with control over porosity and functionalities offers the promise of even higher activity and low cost.

Carbon materials play a very important role in various heterogenous catalytic reactions either as catalyst supports or exhibiting catalytic properties themselves following various functionalisation. There are many reports, reviews [107] [108] and books [3b] dedicated to this subject.

In this chapter I will describe some examples where the carbon materials prepared using hydrothermal carbonisation found important applications in heterogenous catalysis. One of the main advantages of HTC materials compared to other "standard" catalytic carbons is the low temperature synthesis enabling them with polar surface functionalities. These polar groups make them hydrophilic, factor that can alter their selectivity when utilised as catalyst supports during various reactions. [109] In addition, the presence of such surface groups allows their further functionalisation with various catalytically active sites.

I will first describe the utilisation of HTC materials as supports for various nanoparticles in heterogenous catalysis followed by few examples where I will show that various functional groups on the HTC surface can catalyse important chemical reactions.

5.3.1 HTC as a Catalyst Support

The fusion between nanoparticle and nanoporous materials technology represents one of the most interesting and rapidly expanding areas in nanotechnology. [110] The harnessing of nanoscale activity and selectivity, provides extremely efficient catalytic materials. Nanoparticles typically provide highly active catalytic centers but are very small and thermodynamic unstable state due to their high surface energies.

In the literature there are several methods to stabilise nanoparticles such as capping with other ligands, or the production of core-shell particles. [111] [35] However, when the main application targets catalysis, the application of such materials is limited due to undesired aggregation and poisoning of the catalyst. An elegant possibility to overcome all these problems is the uniform dispersion of such active monodisperse nanoparticles onto porous materials. [112] Depending on the functional groups present on the carbon support and its porosity it should be possible to control the size and shape of the resulting nanoparticles.

HTC materials given their functional groups and the core/shell structure with more hydrophobic polyfuran compounds at the core and polar functional groups at the rim of the particle are particularly interesting catalyst for the dispersion of various nanoparticles. Thus, our group proved how important is the fact that the HTC carbon material is hydrophilic. We prepared a core/shell material containing Pd nanoparticles dispersed on the more hydrophobic carbon core surrounded by oxygenated functional group by simply hydrothermally treating furfural in the presence of Pd acetylacetonate (Figure 5-10a). [109] The furfural precursor played here a double role. On one hand it formed the hydrophilic HTC material and on the other hand was able to reduce the Pd (acac)$_2$ to elemental metallic Pd nanoparticles during the HTC process.

Such a metal–carbon nanocomposite catalyst prepared in one–step reaction, was highly selective for the hydrogenation of phenol to cyclohexanone a reaction otherwise very difficult to achieve when using "classical" hydrophobic carbon supports (Figure 5-10b). We need to mention here that cyclohexanone is one of the main intermediates in the preparation of caprolactam and adipic acid which are for instance used in the manufacturing of nylon-6, nylon-6,6 and polyamide resins. A complete conversion of the phenol into cyclohexanol was observed using commercial charcoal- and alumina-supported palladium.
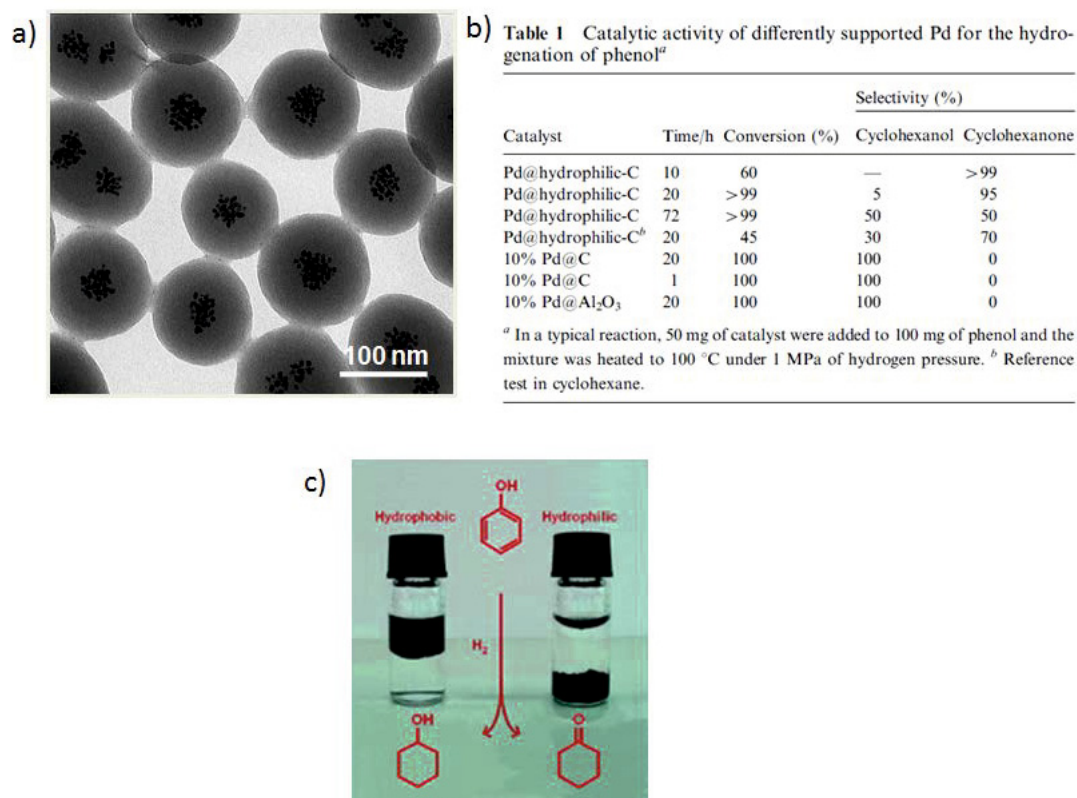
Figure 5-10: a) TEM microgrpah of the HTC/Pd core/shell morphology; b)Table describing the catalytic activity of our HTC/Pd material in comparison with other commercially available materials; c) picture illustrating the mechanism of conversion of phenol to cyclohexanone oh hydrophilic carbon and to cyclohexanol on hydrophobic carbon (taken with permission from[109]).

Even with shorter reaction times (down to 1 h) partial hydrogenation products could not be detected. Moreover, no differences in the reactivity were observed between charcoal and alumina. Both supports loaded with a similar amount of Pd led directly to cyclohexanol （Figure 5-10b）. In contrast, in the case of palladium supported on hydrophilic hydrothermal carbon, the hydrogenation was selective to cyclohexanone. After 20 h of reaction, we obtained 95% of cyclohexanone with a conversion rate close to 99% (Figure 5-10b)

The lower hydrogenation speed of the ketone compared with the aromatic ring is not likely to rely on the intrinsic properties of the palladium nanoparticles as no such effect was observed with the commercial catalysts. The active particles are placed in a confined microenvironment with special chemical functionalities. The reactive pocket around our nanoparticles is very hydrophilic and decorated with –OH, C=O and –COOH species. A possible mechanism accounting for the observed reactivity could then rely on the fact that phenol, being a strongly H-bridge interacting system, was enriched in the pores, while cyclohexanone, being more

263

hydrophobic, was displaced from the reactive pocket and thus cannot easily further react (Figure 5-10c). Such mechanisms, involving specific interactions between the substrate and the reactive pocket, are known to control the reactivity of enzymes and are a major goal for biomimetic catalysis. This could explain why our hydrophilic support provided a more selective catalyst than the commercial hydrophobic charcoal-supported system.

Using a similar "*in situ*" procedure, Wu et al preapred Ag/carbon hybrids using the redox properties of glucose and silver nitrate in the presence of imidazolium ionic liquid under hydrothermal conditions. [113] Monodisperse carbon hollow sub-microspheres encapsulating Ag nanoparticles and Ag/carbon cables were selectively prepared by varying the concentration of ionic liquid. Other reaction parameters, such as reaction temperature, reaction time and the mole ratio of silver nitrate to glucose, played an important role in controlling the structures of the products. The catalytic property of the hybrid in the oxidation of 1-butanol by H_2O_2 was investigated.

Utilising a similar procedure to the one initially described our group for the one strep synthesis of carbon / inorganic nanoparticles, [36] Yu at al prepared an Fe_xO_y@C spheres as an excellent catalyst for Fischer-Tropsch synthesis. [114] Glucose and iron nitrate were hydrothermally treated together for the fabrication of carbonaceous spheres embedded with iron oxide nanoparticles. This route is also applicable to a range of other naturally occurring saccharides and metal nitrates. A catalytic study revealed the remarkable stability and selectivity of the reduced FexOy@C spheres in the Fischer-Tropsch synthesis, which clearly exemplifies the promising application of such materials.

Besides this one step *"in situ"* functionalisation of HTC, nanoparticles can be incorporated in a post-functionalisation step, following the preparation of HTC. His has been largely described in Chapter 4.

Our group described the preparation of porous nitrogen doped carbon materials naturally inspired from lobster shells [115] followed by their decoration with Pt [+2] using a post-impregnation method with $PtCl_2$ (Figure 5-11a). [116] Thermal stability and robustness towards acidic solvents make such materials very interesting as possible solid catalysts in the Periana system for the oxidation of methane to methanol. [117] The direct utilisation of methane *via* C-H activation remains a challenge as the development of efficient catalysts with sufficient activity and selectivity is hindered by the high binding energy of the

methane C-H bond.[118] Thus, a viable methane-to-liquid process still suffers from ineffective catalytic systems. The C-H activation of hydrocarbons by transition metal complexes presents a promising pathway.[119] One of the most active (homogeneous) catalytic systems is that reported by Periana and co-workers.[117, 120]. Thus, the catalytic activity of the N-doped carbons subsequently coordinated with Pt^{2+} ($Pt@ExLob900$) for methane oxidation was compared here to the standard periana system ($Pt@bpymCl_2$) as well as with a nitrogen-rich Covalent Triazine Framework ($Pt@CTF$), acting as solid ligand (Figure 5-11 b).[121] The initial catalytic activity of our material is superior to the molecular benchmark originally described by Periana and significantly better than that of the previously reported solid catalysts. Recycling experiments revealed that this novel solid looses activity to some extent (Figure 5-11 c). This deactiviation, however, is not associated with loss of platinum, since the platinum leaching is negligible. The reason for the loss of activity is still under investigation. However, the remarkable catalytic performance may provide new insights for further targeted material development that in turn could bring catalytic methane utilisation closer to technical feasibility.
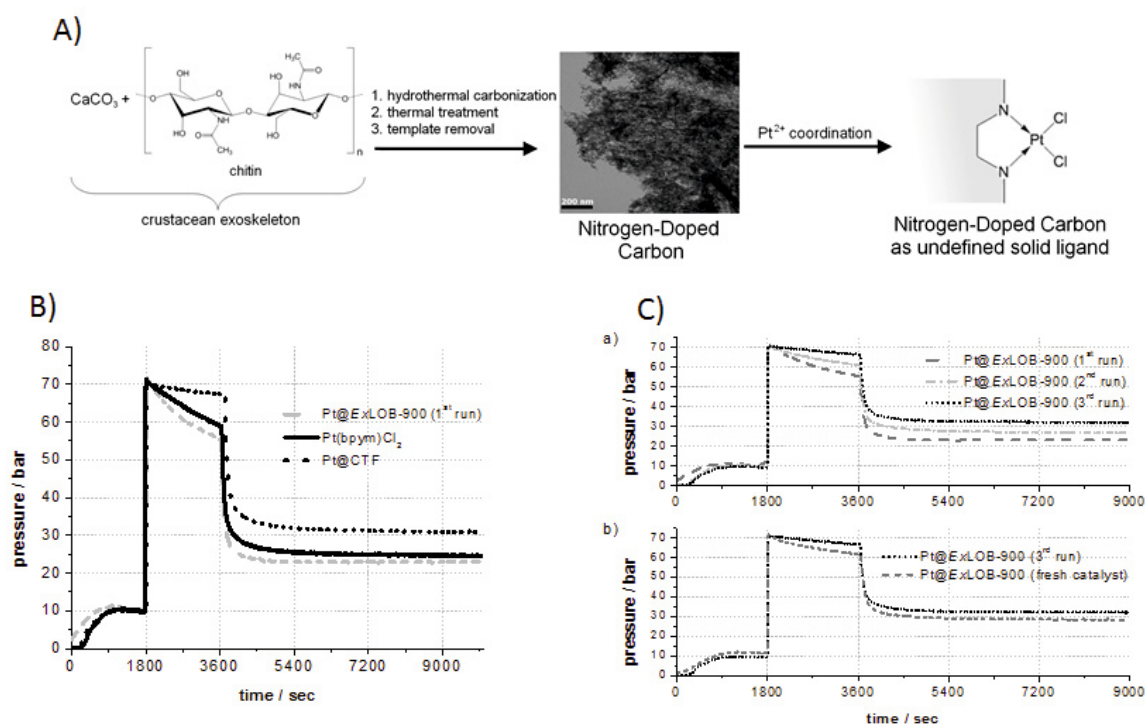
Figure 5-11: A) Preparation of coordinatively modified Pt@NDC materials derived from crustacean exoskeleton of lobsters (*Ex*LOB). B) Pressure-time plots for catalyst comparison (reaction conditions: 10 µmol Pt equivalents catalyst, 215°C, 1000 rpm, 30.4 mL Hastelloy autoclave); C)) Pressure-time plots for Pt@*Ex*LOB-900 recycling experiments. b) Pressure-time plots for fresh and recycled catalyst (Pt@*Ex*LOB-900 (3rd run; Taken from [116]).

Carbon nanofibers produced by hydrothermal carbonisation display remarkable reactivity and the capability for *in situ* loading with very fine noble-metal nanoparticles such as Pd, Pt, and Au. Large quantities of uniform carbon nanofibers embedded/confined with various kinds of noble-metal nanoparticles can be easily prepared, resulting in the formation of the so-called uniform and well-defined "hybrid fleece" structures as already described in Chapter 4. These hybrid carbon structures embedded with noble-metal nanoparticles in a heterogeneous "fleece" geometry serve as excellent catalysts for a model reaction involving the conversion of CO to CO_2 at low temperatures. [122]

NiAl-layered double hydroxide/carbon (LDH/C) composites with adjustable compositions were successfully assembled by crystallization of LDH in combination with carbonisation of glucose under hydrothermal conditions, and further utilised as an integrated catalyst for the growth of carbon nanotubes (CNTs) in catalytic chemical vapor deposition (CVD) of acetylene. The results revealed that the supported Ni nanoparticles with the small crystallite size of about 10 nm could be obtained by *in situ* self-reduction of the as-assembled hybrid LDH/C composites in the course of CVD. The Ni nanoparticles obtained here exhibited excellent activity for catalytic growth of CNTs, which could be delicately tuned by varying the compositions of hybrid composites. [123]

Ming at al showed a new procedure for the functionalisation of carbon nanotubes (CNTs) with the use of biomass as starting materials. A mixture of aromatic compounds obtained from the hydrothermal treatment of biomass, rather than the traditional polymer monomers, was used as the nanoscale building blocks to knit an oxygenated network-coat on the CNTs layer-by-layer. The obtained f-CNTs were proved to be a promising catalyst support for metal catalysts, such as Ru/f-CNTs and showed high activity and selectivity for the hydrogenation of citral to unsaturated alcohol. [124]

5.3.2 HTC with Various Chemical Functionalities and Intrinsic Catalytic Properties

From the previous subsection we could learn that the surface functional groups on HTC can actively participate in directing the type of nanoparticles which will be loaded on its surface (reduced metals, metal oxides), create metal complexes with metals or control the selectivity in certain chemical reactions. In addition, the presence of the polar surface groups on HTC

surface offers yet another great advantage: easy chemical functionalization as described in the previous chapter.

Silica is an ideal example of a material that can be easily textured at both the macroscopic and mesoscopic scales and functionalised with various organic groups under mild conditions. [125] [126] However, easy post-synthesis surface functionalisation of carbonaceous material, equivalent to what is achieved on silica, is still challenging. [127] This is not the case for HTC as the presence of surface oxygenated groups enables its straight-forward functionalisation in a very similar manner with silica (see Chapter 4). I will focus in this subchapter on a few examples of functional HTC carbons with intrinsic catalytic properties.

We established a methodlogy to produce functional HTC by hydrothermal carbonisation of carbohydrates in the presence of small amounts of functional monomers. [128] For example, the hydrothermal carbonisation of glucose in the presence of small amounts of functional organic monomer (vinyl imidazole), inside a porous network of a silica template, followed by subsequent removal of the sacrificial template leads to a mesoprous HTC with vinylimidazole surface groups on its surface. The resulting grafted imidazole moieties were, in a second step, converted into the corresponding alkyl imidazoliums and successfully employed as catalysts for various reactions including transesterification, Diels–Alder or Knoevenagel condensations (see Chapter 4 and [129]).

Given the depletion of fossil-fuels and the alarming facts associated with global warming there is an increasing interest in discovering new and efficient catalysts for the chemical conversion of biomass into biofules. [130] Homogeneous-acid catalysts, such as sulfuric acid, are commonly employed. However these catalysts have several drawbacks, such as corrosion and toxicity problems, cost, inefficient separation procedures and the need to neutralise the waste streams. These problems could be solved by developing heterogeneous solid-acid catalysts, which can be more easily and efficiently separated from the products, enabling their reuse. However, most solid-acid catalysts reported so far are expensive or involve complex synthetic procedures, which impede their commercialisation. These include acid zeolites, mesostructured silica functionalised with sulfonic groups, tungstated zirconia, sulfated zirconia, sulfonated polymers (Amberlyst- 15), and Nafion-based composites. [131] In this respect, HTC presents again multiple advantages. It is low-cost, based on biomass precursors itself, stable, its porosity can be tuned and it is already acidic. In addition, its surface

functionality can help its further modification with stronger acidic groups such as for example -SO$_3$H groups.

Thus, Sevilla, Fuertes et al, used the sulfonation of carbonaceous microspheres obtained by the hydrothermal carbonisation of glucose (Figure 5-12 a). This synthetic strategy circumvents gas-phase pyrolysis, thereby avoiding the emission of harmful gases, and yields a solid acid comprising of spherical particles of uniform, micrometer-regime size (Figure 5-12-b). The activity of this sulfonated carbon catalyst towards the esterification of oleic acid with ethanol, a typical reaction in the synthesis of biodiesel, was investigated. Figure 5-12c shows the formation of ethyl oleate during reaction at 55 °C. For comparison, results for equivalent amounts of sulfuric acid, p-toluenesulfonic acid, and Amberlyst-15 are also shown. In the absence of catalyst (blank experiment) the ethyl oleate yield was only 3.5% after 24 h. As expected, the homogeneous catalysts (sulfuric acid and p-toluenesulfonic acid) showed the highest activities, but they lack the advantages of solid acids pointed out before. The HTC with sulphonic groups sample exhibited a higher activity than Amberlyst-15 despite the fact that the latter has a higher density of sulfonic groups. This may due to the fact that the sulfonated carbon microspheres are highly hydrophylic, as pointed out before for the case of phenol hydrogenation to cyclohexanone (section 5.3.1. [109]). This facilitates the adsorption of a large amount of hydrophylic molecules such as ethanol and favours the access of the reactants to the -SO$_3$H sites.
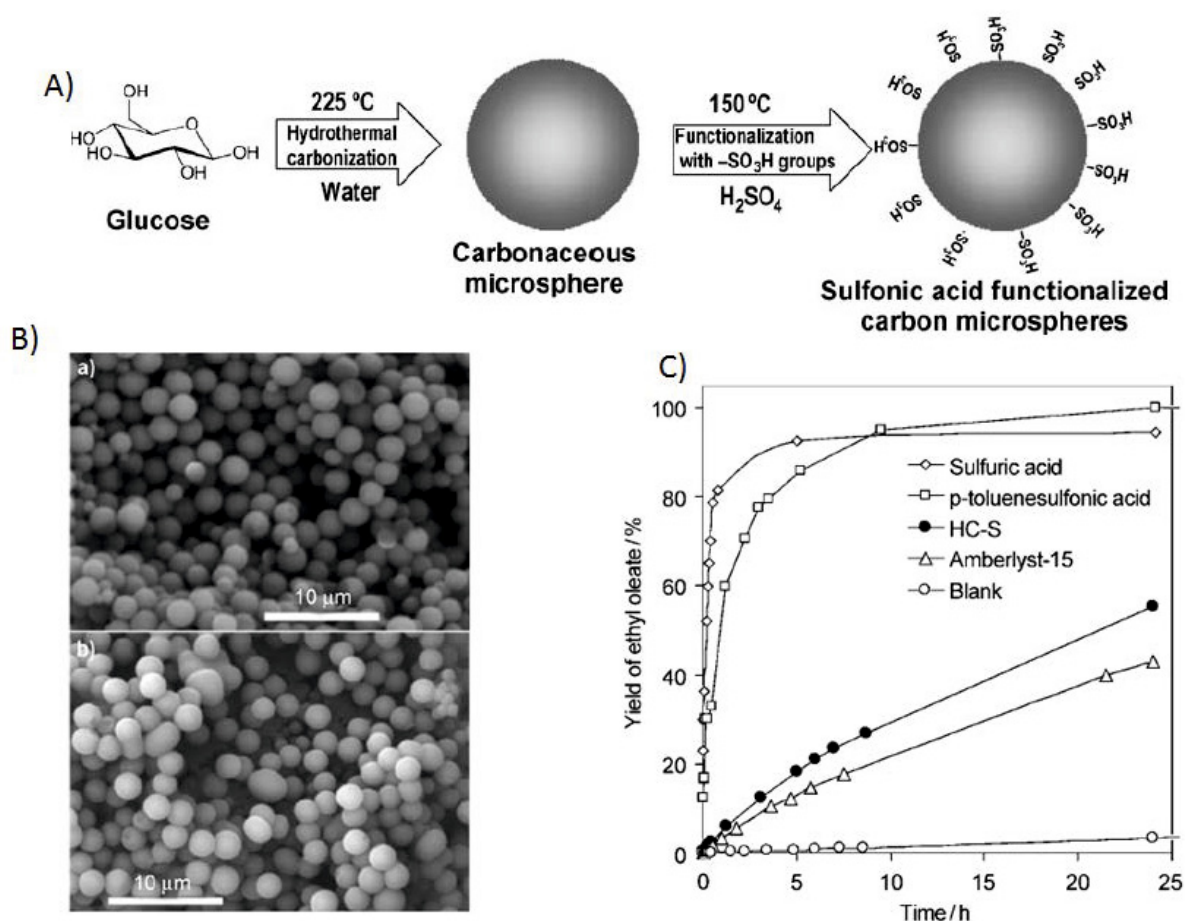
Figure 5-12 A) Schematic illustration of the synthetic procedure for obtaining carbon microspheres functionalised with -SO$_3$H groups; B) SEM images of a) the hydrothermally carbonised glucose, and b) the sulfonated sample; Time courses of the esterification of oleic acid with ethanol. The yield of ethyl oleate is based on oleic acid. Reaction temperature: 55°C (taken with permission from [132]).

In a similar approach, Xiao et al produced novel biacidic carbon *via* one-step hydrothermal carbonisation of glucose, citric acid, and hydroxyethylsulfonic acid at 180°C for only 4 h. The novel carbon had an acidity of 1.7 mmol/g with the carbonyl to sulfonic acid groups molar ratio of 1:3. The catalytic activities of the carbon were investigated through esterification and oxathioketalization. The results showed that the carbon owned comparable activities to sulfuric acid, which indicated that the carbon holds great potential for the green processes related to biomass conversion. [133]

It is my personal believe that the HTC materials produced from biomass could play in the future an important role in the conversion of lignocellulosic biomass into useful products and biofules. Firstly, about 30-40 % of the products resulting from HTC of biomass are left in the liquid phase. [134] Thus, if part of the HTC solid materials making the other 60-70% fraction

could be used to competently convert the liquid phase into useful products, the efficiency of this process will be greatly improved. Furthermore, the ratio of liquid to solid fraction as well as their composition could be controlled throughout appropriate synthesis conditions (i.e. temperature, pressure, catalyst, additives). In this respect, it has been previously showed that various *"Starbon"* materials, a process with many similarities to HTC regarding the flexibility of the resulting carbons [135] can act as efficient catalysts with tuned selectivity depending on the preparation method and the reaction conditions. [136]

5.4 Electrocatalysis in Fuel Cells

Fuel cells are electrochemical devices that convert chemical energy from a fuel intro electric energy continuously, as chemicals constantly flow into the cell. They consist of an anode, a cathode and an electrolyte as schematically shown in Figure 5-13. In the anode, the fuel is oxidised to produce electrons, which travel along an external circuit to the cathode creating an electrical current, and protons, which pass through the electrolyte to the cathode, where the oxidant combines with the protons and electrons to produce water as only byproduct.

As fuels, hydrogen, alcohols or hydrocarbons can be used, and as oxidant, normally oxygen is used. In both cathode and anode, catalysts are necessary for the outcome of the electrochemical reactions at low temperature. Present fuel-cell prototypes often use catalysts selected more than 25 years ago. Commercialisation aspects, including cost and durability, have revealed inadequacies in some of these materials. Therefore, the development of novel and alternative catalysts with a lower production cost and better efficiency then the traditional ones is the main driving force in the research dedicated to fuel cells.

Catalysts in fuel cells are composed in most of the cases of noble metal nanoparticles (Pt, Pd) dispersed over a support, which normally consists of carbon. Carbon is a typical electrocatalyst support for fuel cell applications due to good electrical and mechanical properties and versatility in pore size and distribution. However some carbon materials, especially heteroatom doped ones showed intrinsic catalytic properties themselves.

For hydrogen gas fed fuel cells at their current technological stage, hydrogen production, storage, and transportation are the major challenges in addition to cost, reliability and durability issues. Direct methanol fuel cells (DMFCs), using liquid and renewable methanol fuel, have been considered to be a favorable option in terms of fuel usage and feed strategies

Compared to hydrogen-fed fuel cells, which have a reforming unit, or low capacity in the hydrogen storage tank, DMFC uses a liquid methanol fuel, which is easily stored and transported and simplifies the fuel cell system. [138]
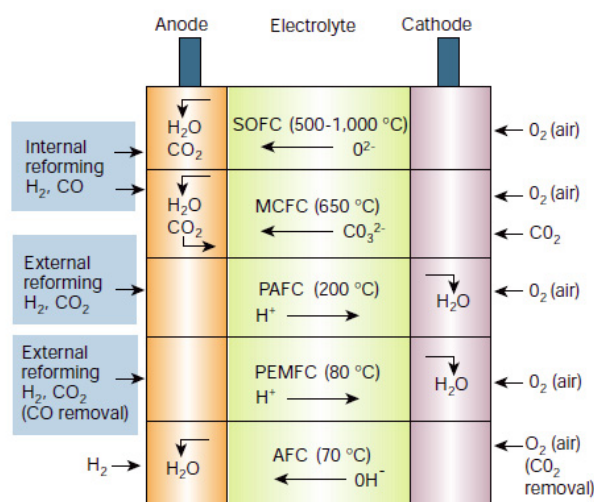
Figure 5-13: Summary of fuel-cell types. The oxidation reaction takes place at the anode and involves the liberation of electrons (for example, $O^{2-} + H_2 = H_2O + 2e^-$ or $H_2 = 2H^+ + 2e^-$). These electrons travel round the external circuit producing electrical energy by means of the external load, and arrive at the cathode to participate in the reduction reaction (for example, $1/2O_2 + 2e^- = O^{2-}$ or $1/2O_2 + 2H^+ + 2e^- = H_2O$; taken with permission from [137])

In this subsection I will discuss both, direct methanol fuel cells as well as hydrogen fuel cells, focusing on the development of sustainable HTC based carbon catalysts either as supports or as catalysts with intrinsic properties for both methanol electroxidation at the anode as well as well as on the oxygen reduction reaction at the cathode.

5.4.1 Catalyst Supports in Direct Methanol Fuel Cells

Catalysis in electrochemical systems such as fuel cells takes place in the interface between the reactant, the catalyst and the electrolyte, which is known as triple-phase boundary. Therefore, the support should possess a highly accessible porosity, which facilitates the contact between those three phases and also good conductivity because it has to conduct the electrons generated in the reaction. The key properties of a carbon electrocatalyst support are therefore: i) high crystallinity (good electric conductivity), ii) relatively high surface area for a good dispersion of the catalyst nanoparticles, iii) open and accessible porosity and iv) resistance against corrosion. As shown in Chapter 2 the crystallinity of HTC carbon can be increased by heat-treatment at high temperature or *via* catalytic graphitisation. [139] These processes

271

generate also certain porosity which can be useful for the deposition of catalyst nanoparticles. Additionally, the high concentration of oxygen groups may be useful as they can act as anchoring sites for the deposition of catalyst nanoparticles, avoiding as well their agglomeration. These considerations have driven several authors to study the performance of HTC carbon as electrocatalyst support as described below.

Currently, most research in this area is focused on exploring new anode catalysts that can effectively enhance the methanol electro-oxidation kinetics while some activities on methanol tolerant cathode catalysts are also carried out.

The first to explore the use of a HTC-based carbon as an electrocatalyst support for the electrooxidation of methanol was Yang et al. [140] They deposited 10 wt % Pt nanoparticles over carbon spherules obtained by HTC of sucrose at 190ºC and post-treatment at 1000ºC using two different methods, i.e. a polyol method and chemical reduction with $Na_2S_2O_4$. The carbon spherules heat-treated at 1000ºC had a BET surface area of 400 m^2/g, which arised from the presence of micropores of 0.6-1.6 nm. The materials were amorphous although some improvement in the structural ordering was observed. The authors found that the medium used for the preparation of the catalyst had a strong influence on the dispersion of the Pt nanoparticles on the spherules. Thus, whereas the nanoparticles deposited through the polyol method exhibited a size of ~ 5 nm, those deposited in aqueous solution tended to agglomerate and exhibited a broader particle size distribution, from 6 to 40 nm. As shown in Figure 5-14 a, the nanoparticles are deposited on the surface of the carbon spherules and crystallised with a face centered cubic (fcc) structure. This agrees with the fact that the nanoparticles are bigger than the pore size of the spherules.

The prepared catalysts exhibited lower electrochemically active surface areas of Pt (18.2 and 54 m^2/g for the polyol and chemical reduction methods, respectively) than commercial Pt/Vulcan XC-72 (61.4 m^2/g) due to the larger particle size (3.7 nm for Pt/Vulcan XC-72). However, the Pt utilisation in the catalyst prepared through a polyol method (90.5 %) was higher than that of Pt/Vulcan XC-72 (81 %). The authors attributed this to the better contact of the electrolyte with the Pt particles on the monodispersed spherules. On the other hand, the low Pt utilisation in the catalyst prepared *via* chemical reduction in aqueous solution (34.4 %) is attributed to the agglomeration of the Pt nanoparticles. With regards to the electrooxidation of methanol (see Figure 5-1 b), the catalyst prepared through the polyol method is the one

exhibiting the highest current. Although this sample a had lower electrochemically active surface area than Pt/Vulcan, it showed a better performance in methanol electrooxidation probably due to the higher utilisation of the Pt nanoparticles as a result of a higher accessibility.
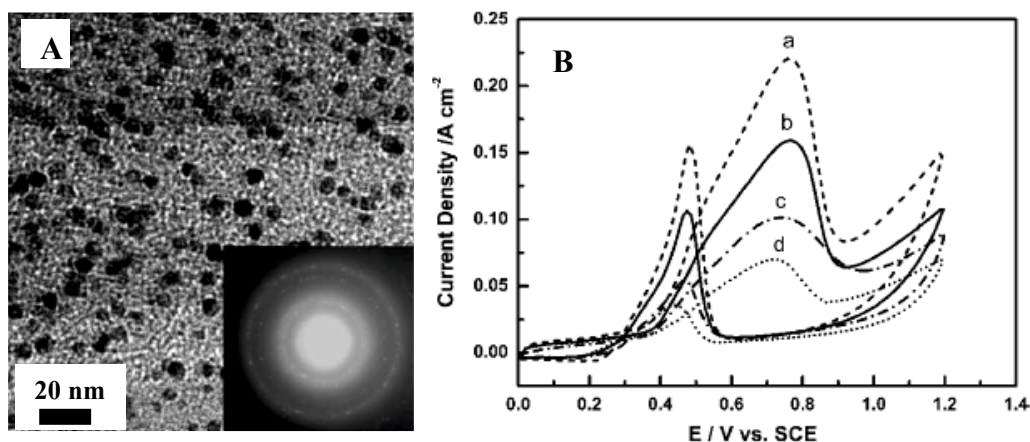
Figure 5-14. A) Low-magnification HRTEM image of Pt nanoparticles (inset: selected area electron diffraction pattern of Pt nanoparticles) and B) Cyclic voltammogram curves of the different electrodes in 1.0M H_2SO_4 + 1.0M CH_3OH solution at 40°C at scan rate of 50mV/s: (a) Pt catalyst prepared _via_ polyol method, (b) commercial Pt/Vulcan XC-72, (c) Pt catalyst prepared with commercial graphitised mesocarbon microbeads (MCMB) and (d) Pt catalyst prepared _via_ chemical reduction in aqueous solution (extracted from ref [140] with permission).

Kim et al. analysed the performance of a HTC graphitic carbon made in the presence of iron and post-treated at 900° as support for Pt/Ru particles. [141] A BET surface area of 252 m^2/g was measured for that material (SC-g). The authors also performed the HTC process in the absence of Fe and under static or dynamic conditions (SC-1 and SC-2, respectively). Amorphous carbon materials with BET surface areas of 112 and 383 m^2/g, respectively were produced. The Pt/Ru nanoparticles (60 wt%) were deposited by a $NaBH_4$-reduction method. The size of the particles, determined by XRD analysis, was 3.5, 2.6 and 2.7 nm for SC-1, SC-2 and SC-g. The larger particle size in the former, SC-1, is due to its smaller surface area, as demonstrated by TEM images, which showed the formation of more agglomerates than in the other two materials. The performance of these catalysts towards methanol electrooxidation was analysed by cyclic voltammetry at room temperature in 0.5 M H_2SO_4 solution containing 2 M CH_3OH with a scan rate of 10 mV/s and compared to that of PtRu/Vulcan. All the supported PtRu catalysts showed an anodic peak current at 0.45-0.5 V, which is attributed to the methanol electrooxidation. Comparing their anodic peak current densities, only PtRu/SC-g possessed a higher value (21.3 mA/cm^2) than PtRu/Vulcan (16.4 mA/cm^2). This is due to its

graphitic structure, which enhances its electrical conductivity. On the other hand, PtRu/SC-2 exhibited a higher catalytic activity (12.8 mA/cm^2) than PtRu/SC-1 (9.9 mA/cm^2) due to the higher metal dispersion in SC-2. However, both exhibited lower catalytic activity than PtRu/Vulcan owing to the higher graphitic ordering in Vulcan.

Sevilla et al. followed a different approach for the generation of graphitic structures from hydrothermal carbon. [142] [143] They used a two-step process in which the synthesised hydrothermal carbon was impregnated with nickel nitrate and subjected to a heat-treatment at 900ºC. As a result, carbon nanocoils were formed, as shown in Figure 5-15a. They were highly crystalline as revealed by the well-defined (002) lattice fringes in the HRTEM image in Figure 5-15b. These carbon nanocoils exhibited as well relatively high BET surface areas, of 114- 134 m^2/g, which can be exclusively ascribed to the external surface of the nanoparticles, i.e. they do not contain framework confined porosity. This result implies that mass transfer resistances of reactant/products involved in the electrooxidation of methanol will be minimised. These nanocoils gather thus the key properties of electrocatalyst supports. i.e. relatively high and easily accessible surface area, and high crystallinity. This was confirmed by their used as electrocatalyst supports towards the oxidation of methanol. Thus, Sevilla et al. deposited Pt/Ru nanoparticles [142] or Pt nanoparticles [143] over the graphitic carbon nanocoils and analysed their behaviour for methanol electrooxidation, comparing it with that of a carbon support widely used as electrocatalyst support, i.e. Vulcan XC-72R. It is remarkable that a high dispersion of nanoparticles (black dots in Figure 5-15b, size =3-3.3 nm) is obtained although their surface area is half that of Vulcan (Pt particle size = 2.6 nm). For both Pt/Ru and Pt nanoparticles, the electrocatalysts prepared with the carbon nanocoils exhibited a higher activity than that of Vulcan, which is consequence of the fact that nanocoils combine good electrical conductivity and accessible surface. Additionally, the crystalline structure confers those materials a high resistance against oxidation, which suggests that these electrocatalytic systems will have, under an oxidative environment (typical of fuel cell electrodes), a longer durability.
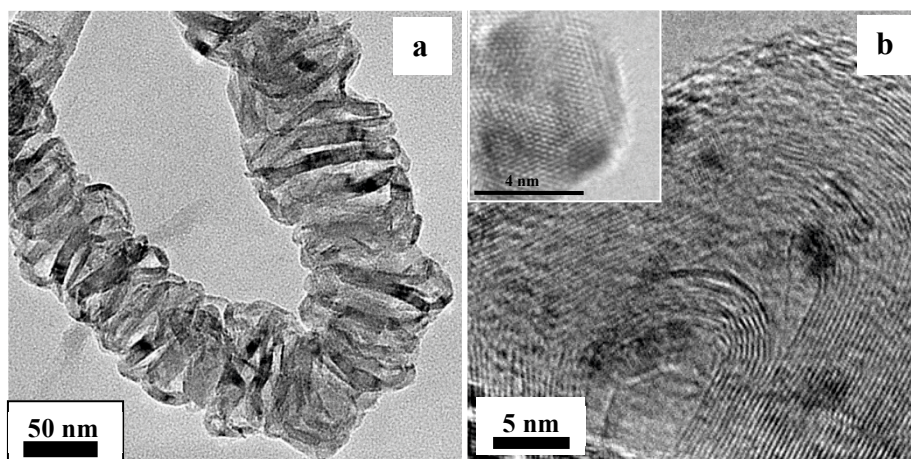
Figure 5-15. a) TEM image of a carbon nanocoil obtained from hydrothermally carbonised sucrose and b) HRTEM image of a carbon nanocoil obtained from hydrothermally carbonised sucrose with deposited catalyst nanoparticles as dark points (inset, detail of a PtRu nanoparticle showing the cubic structure;extracted from ref. [142-143] with permission).

Joo et al., on the other hand, integrated the templating route and the catalytic graphitisation technique in the hydrothermal carbonisation process with the aim of synthesising graphitic porous carbons. [144] The authors used uniform silica particles (100 nm) as sacrificial template, sucrose as carbon precursor and iron as graphitisation catalyst. The HTC process (190°C for 10 hours under vigorous stirring) was followed by heat-treatment at 900°C. In this way, the authors synthesised a carbon material composed of large spherical pores of 100 nm, which are a faithful replica of the silica particles, exhibiting a high surface area (425 m^2/g) and a large pore volume (0.42 cm^3/g). Additionally, this material possesses a graphitic nature, as probed by HRTEM, XRD and Raman spectroscopy. Thus, well-defined (002) lattice fringes are observed in HRTEM images, a sharp (002) diffraction peak in the XRD patterns (d$_{002}$ = 0.335 nm and L$_c$ = 9.8 nm) and the G'-band at ca. 2720 cm^{-1} in the Raman spectra, besides the D- and G-bands at 1350 and 1580 cm^{-1} respectively. The preparation of the Pt catalyst, on the other hand, was carried out by formaldehyde reduction method. This catalyst exhibited higher methanol electro-oxidation current density than a commercial Pt catalyst (ETEK) and a catalyst supported over porous amorphous carbon synthesised by polymerisation of sucrose without hydrothermal treatment. This high activity is closely related to the unique properties of graphitic carbon together with the porous characteristics of the material, which favor the mass transfer.

Wen et al. also combined the templating technique with the hydrothermal carbonisation process, without the addition of any graphitisation catalyst, and prepared Pt-supported

catalysts. [145] [146] In one of the works, these authors used an anodic aluminum oxide (AAO) as template and glucose as hydrothermal carbon precursor, and the HTC process was followed by heat-treatment at 900ºC. [145] The authors obtained carbon nanotubes with an open-end structure and a diameter around 200 nm (wall thickness ~ 10 nm), which is close to the pore size of the AAO template. For the deposition of Pt nanoparticles (20 wt%), the AAO/CNT composites were immersed in a H_2PtCl_6 and $NaBH_4$ solution several times after pyrolysis. The Pt–CNT–Pt hybrid composites were then liberated by dissolving the AAO template with HF. The authors found that Pt nanoparticles (fcc structure and size ~ 3.5 nm) can be decorated on both the inner and outer surfaces of the CNTs. To study the electrocatalytic performance of these materials for methanol oxidation, a commercial carbon material (Vulcan-XC 72) was also utilised as Pt catalyst support (containing about 16.7 wt% Pt). In this case, the size of the nanoparticles was about 3.7 nm, and they were uniformly dispersed on the surface of the material. The electrochemically active surface area, measured in 0.5 M H_2SO_4, was ~ 39 m^2/g for the catalyst Pt-CNTs-Pt and ~ 25 m^2/g for Pt/Vulcan XC-72. The larger electrochemically active surface area may be attributed to the good dispersion of Pt nanoparticles on the CNTs. When subjected to cyclic voltammetry in 0.5 M H_2SO_4 solution containing 0.5 M CH_3OH, the Pt-CNT-Pt catalyst exhibits a higher mass peak current density (25.3 mA/g) than Pt/Vulcan (14.7 mA/g), which indicates a higher catalytic activity for the CNTs-supported catalyst. Additionally, Pt-CNTs-Pt had a higher tolerance to incompletely oxidised species accumulated on the surface of the electrode compared with Pt/Vulcan. This superior catalytic performance of Pt-CNTs-Pt in the electrochemical oxidation of methanol may be due to the fact that the aligned nanochannels within the catalyst facilitate diffusion of the electrolyte and methanol.

In another publication, the authors used a different template, SBA-15, and introduced directly the Pt precursor into the autoclave, so that hydrothermal carbonisation and deposition of the Pt nanoparticles on the HTC carbon took place simultaneously [146] The samples were then carbonised at 750ºC and, finally, the template removed to obtain the Pt@C/MC catalyst. For comparison reasons, these authors also prepared Pt/CMK-3 and Pt/Vulcan XC-72 catalysts. A TEM inspection of Pt@C/MC shows a good morphology replication from SBA-15 and a uniform dispersion of Pt nanoparticles on the porous carbon. Furthermore, HRTEM evidences that the small Pt nanoparticles (~ 3-5 nm and fcc structure) are well detached from each other, which suggests that this synthetic method could effectively prevent agglomeration of Pt

nanoparticles. However, replication of the porous structure of SBA-15 was not achieved, as confirmed by XRD. This could be ascribed to the fragility of the thin film of carbon, which would partially collapse during template removal. On the other hand, Pt nanoparticles were covered by a thin layer of carbon film. The BET surface area of the catalyst Pt@C/MC was 633 m^2/g and the pore volume 0.55 cm^3/g, the PSD exhibiting one sharp maximum at 3.5 nm and a weak broad peak at 14.5 nm. Additionally, textural mesoporosity was also observed, as well as the presence of microporosity. This catalyst exhibited no catalytic activity towards methanol oxidation and in fact a capacity to tolerate high concentrations of methanol. However, it had an admirable activity for oxygen reduction reaction (ORR) due to the large surface are of the support (mesoporous carbon) as well as the well-distributed Pt nanoparticles. On the contrary, the activity for ORR was greatly impaired on the electrodes prepared with Pt/CMK-3 and Pt/Vulcan XC-72 because of methanol oxidation. The authors believe that it is the unique nanostructure of the Pt@C/MC composites obtained that endowed the nanoscale hybrid material with high catalytic activity for methanol tolerant ORR which is also a very importat issue in methanol fuel cells. Since the Pt nanoparticles were overlaid by a film of carbon that contained micropores formed during the thermal treatment, this made possible for oxygen to access the nanoparticles while methanol was hindered. Finally, the authors also evaluated the electrocatalyst durability through repeated CV cycles in an O_2-saturated electrolyte consisting of 0.5 M methanol. The variation in the current density was only ~ 4% after 40 cycles, suggesting that the Pt@C/MC electrode has a considerable stable electrocatalytic activity for ORR despite the existence of the well-known "poisonous" methanol in the electrolyte. Furthermore, the loss of electrochemically active surface area of Pt would be greatly alleviated as a result of the carbon film on the surface of the nanoparticles.

In an earlier work, Wen et al. deposited Pt nanoparticles through chemical reduction with $NaBH_4$ over hollow carbon spheres and semispheres (HCSs). [147] These HCSs were synthesised by hydrothermal carbonisation of glucose with the aid of sodium dodecyl sulfate (SDS) at 170ºC (10h) followed by heat-treatment at 900ºC. A good dispersion of Pt nanoparticles (fcc structure and particle size = 5.7 nm) on the inner and outer surface of the hollow hemispheres was observed. This catalyst exhibited a higher activity towards methanol oxidation than those prepared with Vulcan XC-72 and microspheres prepared by HTC of

glucose in the absence of SDS. This can be attributed to the higher BET surface area, well-dispersed Pt nanoparticles, high conductivity and the reduction of the liquid sealing effect.

Another work where the deposition of Pt/Ru nanoparticles was as well performed during the HTC process has been recently published by Marques Tusi et al. [148] Thus, Pt and Ru salts were added to an aqueous solution of starch, the pH adjusted at ~ 11, then the mixture was subjected to HTC at 200ºC for 6 h and finally to a heat-treatment at 900ºC. Without this high temperature heat-treatment, the samples were not active for methanol electro-oxidation, which is probably due to their low electrical conductivity. The XRD analysis of the catalysts showed the coexistence of Pt-Ru alloy with fcc structure and metallic Ru phase with hexagonal close-packed structure (hcp). The average crystallite sizes determined by XRD agreed well with the values determined by TEM observation and were in the 8-13 nm range depending on the Pt:Ru atomic ratio. However, the particle size distributions were quite broad. The electrochemical oxidation of methanol was evaluated in a solution 1 M methanol in 0.5 M H_2SO_4 at a sweep rate of 10 mV/s at room temperature. Electro-oxidation of methanol started at 0.45-0.55 V *vs.* RHE, value typical for Pt/Ru carbon supported catalysts (vs. 0.7-0.8 V for Pt carbon supported catalysts) and an increase of current values was observed with the increase of Ru content in the catalysts.

In all the works described so far, the HTC process was carried out at a low temperature, i.e. 180-200ºC, so that an additional step was necessary for increasing the conductivity of the materials (graphitisation process or heat-treatment at a higher temperature, up to 1000ºC). That additional step was avoided by Xu et al. by performing the HTC process at a much higher temperature, i.e. 600ºC. [149] As a result, they obtained carbon microspheres of about 1500-2000 nm which, despite the high temperature used, exhibited abundant hydroxyl groups, as probed by FTIR. The authors used those carbon microspheres as support for Pd and Pt nanoparticles, deposited through chemical reduction using $NaBH_4$. The obtained results showed well-dispersed Pt and Pd nanoparticles on the outer surface of the carbon microspheres. The size of the nanoparticles was smaller than for the carbon black used as reference. This seems a bit striking as hydrothermal carbons normally exhibit very low surface areas, which would lead to coalescence of the metal nanoparticles. As the authors have pointed out, this is probably due to the stabilisation of the nanoparticles by strong bonding interactions with the oxygen groups still present on the surface of the microspheres. As a result, the catalysts prepared with the carbon microspheres exhibited larger electroactive

278

surface areas (doubled that of the catalyst with carbon black) and higher activity towards methanol/ethanol oxidation in alkaline media than the catalyst prepared with carbon black. This higher activity is probably also due to the fact that the nanoparticles are more accessible in the carbon microspheres as they are deposited over their external surface. Additionally, the micrometer sized carbon spheres act as structure units to form pores and channels that significantly reduce liquid sealing effect.

In the future, the diminution or even complete elimination of such scarce and expensive metals able to catalyse the electro oxidation reaction is highly desired. At the same time, CO is a very stable intermediate resulting from methanol decomposition and at the same time a strong poison for the Pt electrode thus seriously reducing its activity. In the desire of finding alternative active catalysts, Mavrikakis et al has recently applied the density function theory (DFT) to investigate the structure sensitivity of methanol electrooxidation on eight transition metals. [150] In this respect Yang at al reported ruthenium free, carbon-supported cobal and tungsten containing binary and ternary Pt catalysts for the anodes of DMFC. [151] Maier et al described the results of a high throughput screening study for direct methanol fuel cell (DMFC) anode catalysts consisting of new elemental combinations with an optical high-throughput screening method, which allowed the quantitative evaluation of the electrochemical activity of catalysts. [152] It is predictable that novel catalyst supports will need to be developed for these new emerging active centers for methanol electrooxidation where HTC will also play an important role.

5.4.2 Heteroatom Doped Carbons with Intrinsic Catalytic Activity for ORR

Fuel cell reactions invariably involve an oxygen reduction reaction (ORR) at the cathode, which is one of the main rate-decreasing steps on platinum (Pt)-catalysts in the water formation reaction and energy conversion efficiency in polymer electrolyte membrane fuel cells (PEMFCs). The Pt scarcity and cost have led to the development of alternative catalyst materials for fuel cell applications.

As a solution to increase activity towards oxygen reduction and provide a long-term solution to Pt cost and scarcity, a variety of non-noble metal-based catalysts has been investigated as promising cathode catalysts for fuel cells. The choice of suitable materials for this purpose is obviously restricted by all the conditions required to obtain a long lifetime under the working conditions of a fuel cell. Since Jasinski's first report on the ORR catalytic activity of metal–

N4 (M–N4) chelates as cobalt phthalocyanines [153] transition metal porphyrins have been thoroughly studied as attractive candidates for active and reliable catalysts for fuel cell cathodes. [154] [155]

Recently for the ORR reaction in fuel cells such nitrogen doped carbons play one of the most important roles. [156] They can either enhance the ORR reaction for non-precious metal catalysts, [157] or show methanol tolerant oxygen reduction. [158] Some of the carbon supports used for the ORR reaction in fuel cells showed catalytic properties themselves, in the absence of any metal. Hence, it was showed that nitrogenated carbon nanotube (NCNT) arrays might have unusually higher electrocatalytic activity for oxygen reduction than nitrogen-free carbon nanotubes (CCNTs). [159] [160] Vertically aligned nitrogen containing carbon nanotubes (VA-NCNTs) are an effective ORR electrocatalyst, even after a complete removal of residual Fe. These metal-free VA-NCNTs catalyse ORR through a 4e- process with an enhanced electrocatalytic activity, long operation stability, and lower overpotential and tolerance to crossover effects than Pt in alkaline electrolytes. [159] The integration of electron-accepting nitrogen atoms in the conjugated CNT plane appears to impart a relatively high positive charge density on adjacent carbon atoms. The charge density distribution, coupled with aligning the NCNTs, provides a 4e- reduction and excellent performances (a steady-state output potential of -80 mV and a current density of 4.1 mA cm^{-2} at -0.22 V, compared with -85 mV and 1.1 mA cm^{-2} at -0.20 V for a Pt–carbon electrode). [161] Doping CNTs with nitrogen heteroatoms leads to active sites which promote parallel diatomic adsorption of O_2 which could effectively weaken the O–O bond. Simultaneous doping of CNTs with boron and nitrogen also proved efficient possibly due to active centers as B–N–C moieties. [162]

Concerning sustainability, most of the synthesis methods used to produce the aforementioned nitrogen doped carbon materials show drawbacks in the, often harsh, reaction conditions used. In order to avoid these aspects nitrogen doped materials have been prepared using the HTC process either directly using N-containing precursors [88] or by incorporation of aminoacids[163] or proteins[86] into the HTC process. These procedures have been described in detail in Chapter 4.

While the HTC materials have been intensively used as catalyst supports for the anode electrooxidation reaction, the reports involving the use of HTC for the ORR reaction at the cathode are by far less numerous.

To the best of our knowledge, there is no report yet in the literature concerning the ORR behaviour of nitrogen doped hydrothermal carbons, except our own which will be presented below. [164]

As described in detail in Chapter 4, complementing nitrogen as a dopant, sulfur is receiving increasing attention in current carbon materials research. The synthesis of these sulfur doped materials generally involves the pyrolysis of sulfur containing polymer based carbons, [165] [166] [167] [168] but also arc vaporization in the presence of sulfur containing compounds such as thiophenes. [169]

Concerning the combined incorporation of sulfur and nitrogen within the same material, only a few reports exist in the literature. Sulfur-assisted growth of carbon nanotubes by chemical vapor deposition of acetonitrile was shown to increase the nitrogen doping levels as well as the magnetic properties of the nanotubes. [170]

Regarding S-doped materials for ORR, Choi et al. synthesised heteroatom doped carbon materials by the pyrolysis of amino acid/metal chloride composites. They obtained sulfur doping levels of 2.74 wt% using cysteine and were able to show that materials containing both nitrogen and sulfur increased the material's ORR activity in acidic media, relative to undoped or purely nitrogen doped carbons. [171]

Regarding hydrothermal carbons doped with sulfur or dually doped with sulfur and nitrogen, our group was the first to report on the one-pot hydrothermal synthesis of tunable dual heteroatom-doped carbon microspheres using carbohydrates and cysteine or cysteine derivatives (see chapter 4 and ref [172]). The addition of cysteine gives rise to pending sulfur functionalities, while addition of thienyl-cysteine results in structurally bound sulfur within the carbonaceous framework. Post pyrolysis offers an additional tool for controlling the material stability and results in microporosity as well as superior conductivity relative to undoped carbon microspheres from glucose. Nitrogen doping levels of about 4 wt% and sulfur doping levels of 3 wt% to12 wt% could be achieved.

We have introduced porosity in such N, S or dual N and S doped materials using protein gelation as described in Chapter 3, section 3.3.1. [87] The morphology of the solely nitrogen doped and the dual N and S doped materials is shown in Figure 5-16 A-C. The simultaneous incorporation of nitrogen and sulfur into the HTC-derived carbons was confirmed by

elemental analysis and X-ray photoelectron spectroscopy. Overall, all three materials exhibited promising structures and compositions for catalytic applications, such as high surface areas, large diameters, continuous 3-dimensionally arranged porous morphologies (and hence good mass transfer properties) leading to accessible dopant sites. However, the amorphous nature of hydrothermal carbon directly after HTC at 180 °C has the drawback of a rather low electrical conductivity. In order to convert the "organic aerogels" into "carbon aerogels" which are suitable for electrocatalytic applications, a pyrolysis step at 900 °C was added to the synthesis process. During this step, the N and S groups were converted into functionalities incorporated into aromatic carbon domains while the conductivity increased up to 2657 S m^{-1}.

The effect of sulfur-doping in addition to nitrogen-doping, i.e., the catalytic activity of CA-TC-900 (materials prepared from glucose and thienyl cysteine in the presence of ovalbumin) and CA-TCA 900 (materials prepared from glucose and 2-thiophene carboxaldehyde in the presence of ovalbumin) was compared to solely nitrogen doped CA-900 (material from glucose and albumin).

Cyclic voltammetry at a scan rate of 100 mV s^{-1} and rotating disk electrode (RDE) voltammetry at a scan rate of 10 mV s^{-1} were conducted in 0.1 M KOH and 0.1 M HClO4 (Figure 5-16 D, E). In both cases, featureless voltammetric curves were observed for all doped carbon aerogels in the N$_2$-saturated solution. The area of the voltammograms arises from capacitive currents of the electrodes. In contrast, a well-defined cathodic peak appeared in the O$_2$-saturated 0.1 M KOH solution (Figure 5-16 E), clearly demonstrating the electrocatalytic activity of the doped carbon aerogels towards oxygen reduction. The areas of the voltammograms are larger in O$_2$-saturated solution due to Faradaic currents (i.e., current generated by charge transfer between reacting species).

In 0.1 M HClO$_4$, faradaic currents are similarly observed for the doped aerogels O$_2$-saturated solution (Figure 5-16D). Because the aerogels are less active in acidic than in alkaline media, the pronounced cathodic peaks found in 0.1 M KOH are not visible in 0.1 M HClO$_4$ at the same scan rate of 10 mV s^{-1}. The small redox peaks observed for CA-900 and CA-TC-900 in N$_2$-saturated solution may be a result of heteroatom protonation on the carbon surface. The polarisation curves obtained from RDE (1600 rpm) voltammetry in O$_2$-saturated 0.1 M HClO$_4$ and 0.1 M KOH are shown in Figure 5-16 F and E respectively. Compared to Pt@C

however, the aerogels are still not competitive. In 0.1 M KOH, the performance of the doped aerogels is far more comparable with that of Pt@C. Compared to Vulcan, CA-900 shows an improved onset potential of −185 mV as well as slightly improved current densities within the scanned potential range. The onset potential of the sulfur and nitrogen containing aerogels is more positive (both at around −130 mV) and the maximum current density is considerably higher than for Vulcan.
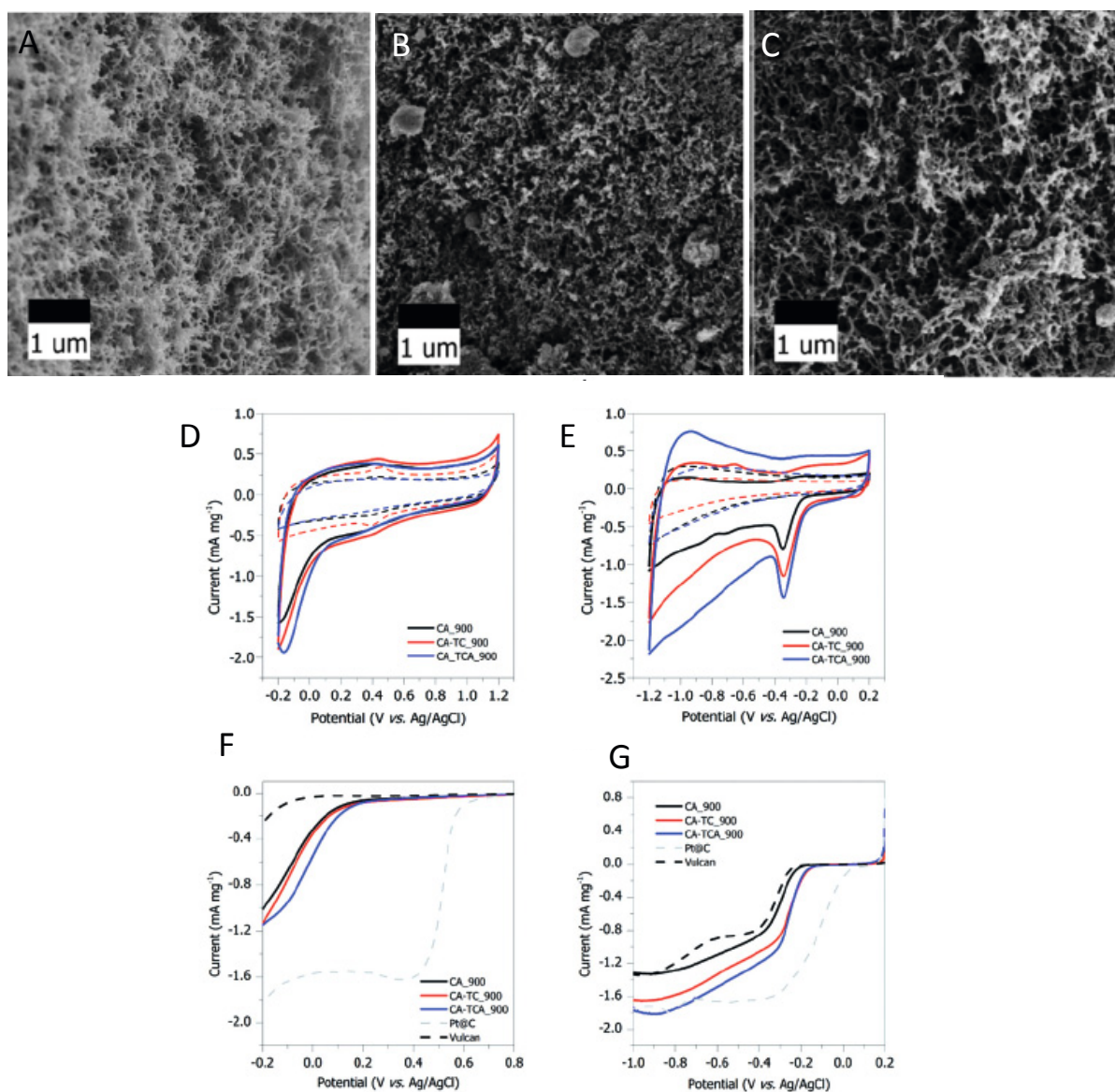
Figure 5-16: SEM micrographs of A) N-doped carbon aerogel (CA); B) N and S doped carbon aerogel obtained using thieny cysteine (CA-TC); C) N and S doped aerogel obtained using 2-thiophene carboxaldehyde (CA-TCA); Cyclic voltammograms of doped carbon aerogels compared to Pt@C and Vulcan in (D) 0.1 M HClO4 and (E) 0.1 M KOH. RDE polarization curves at C a 1600 rpm of doped carbon aerogels compared to 20 wt% Pt@C and Vulcan in (F) 0.1 M HClO4 and (G) 0.1 M KOH (from [164])

The current knowledge in the scientific literature regarding sulfur and ORR is limited, and sulfur is usually thought to improve Pt particle adsorption onto carbon supports and thereby the lifetime of the electrode. [173] But what is the role of sulfur in metal-free catalysts, and how does sulfur compare to nitrogen as a dopant remains an open question.

In nitrogen-doped carbons, factors such as enhanced π-bonding, electrical conductivity and Lewis basicity may facilitate reductive O_2 adsorption at the carbon surface. [174] Structural defects in the carbon crystal lattice, which are caused by the introduction of dopants, also result in more edge-active sites. [175] It has, however, been shown that undoped carbon materials with more edge sites did not have an improved catalytic performance, [176] indicating that edge-bound heteroatoms, (e.g., pyridinic nitrogen), are catalytically important. It is generally accepted that the binding state is relevant with respect to the catalytic activity of nitrogen, though there are different opinions as to which exact binding states are responsible for the good activity and 2 or 4 electron process selectivity. Pyridinic edge sites have been proposed as a likely candidate because edge planes facilitate oxygen chemisorption. [177] On the other hand, some reports also suggest that pyridinic nitrogen may not be an effective promoter of the 4 electron ORR process. Luo et al. synthesised purely pyridinic nitrogen doped carbons and found them to be selective for a 2 electron reduction pathway. [178] Lui et al. recently proposed that graphitic nitrogen accounts for good catalytic activity. They also showed that the nitrogen content does not directly correlate with the catalyst performance – materials (nitrogen-doped mesoporous graphitic arrays) with higher nitrogen content showed lower selectivity and activity. [179]

A report by Strelko et al. suggested that there is a critical concentration of heteroatoms in a carbon matrix which will exhibit maximum catalytic activity and that this can be explained by the collective electronic properties and a minimal bandgap. They identified pyrrolic nitrogen as the binding state that gives rise to the smallest bandgap, and thus the best electron transfer capabilities. [180] DFT calculations suggest that nitrogen is not itself the catalytically active site, but that the high electronegativity of nitrogen polarizes the C–N bond, and the adjacent carbon atom therefore has a reduced energy barrier towards ORR. [175] [181]

As if for nitrogen the opinions are much divided and there is no clear path and seems to be dependent on electronic, morphological and pore properties, for sulfur doping the situation is even more complicated.

Sulfur and carbon have electronegativities of 2.58 and 2.55, respectively (on the Pauling scale). Nitrogen on the other hand has an electronegativity of 3.04. This means that the C–S bond is not as polarized as the C–N bond, so a catalytic pathway based on a $\delta +$ adjacent carbon atom is unlikely to occur for sulfur.

Sulfur is a large atom with an atomic radius of 100 pm compared to nitrogen (65 pm) and carbon (70 pm). [182] The disruption of the carbon connection pattern is therefore more pronounced than for nitrogen. It is therefore likely that sulfur-doping will induce more strain and defect sites in the carbon material, which may facilitate charge localisation and the coupled chemisorption of oxygen.

Sulfur has large, polarizable d-orbitals (sulfur groups are usually soft nucleophiles). The lone pairs of sulfur can therefore easily interact with molecules in the surrounding electrolyte. This effect is expected to be much more pronounced than that for nitrogen.

Sulfur is, however, known to take part in proton transfer reactions. DFT calculations carried out by Chamorro et al. suggested that proton transfer in thiooxalic acid derivatives is facilitated by the high polarisability of the sulfur atom, which mediates ionpair like transition states during the transfer process. [183] Scheiner et al. carried out ab initio calculations and showed that the greater polarizability of SH_2 as compared to OH_2 leads to greater charge transfer between $(H_2S–H–SH_2)^+$ units than between $(H_2O–H–OH_2)^+$ units and to a larger extent of spatial regions of density charge. [184]

In their publication on sulfur-doped graphene as ORR catalysts, Yang et al. propose that the increased spin density of sulfur compared to nitrogen or other dopants may be responsible for the increased catalytic activity. [185] This would mean that sulfur is favourable to interact with the triplet state of oxygen, as preservation of spin is a serious catalytic problem.

Given all these hypotheses existing in the literature for the solely N and S doped carbons, in the case sulfur and nitrogen dual doped carbon aerogels, a synergistic mechanism between sulfur and nitrogen, whereby nitrogen activates the oxygen molecule (either directly or indirectly *via* the adjacent carbon atom), while sulfur facilitates the proton transfer during the reduction process could be likely to happen. However, careful theoretical studies are necessary in order to understand the electron transfer process and the role of each individual dopant as well as the synergetic effect.

What is clear is the fact that sulfur has a clear positive effect when added to nitrogen-doping on the electrocatalytic performance in the oxygen reduction reaction in both acidic and basic media. More studies need to follow in the very future.

To summarise this subsection, very little research has been done regarding the use of heteroatom doped hydrothermal carbons as electrocatalysts for the ORR reaction. This is surprising given all the advantages offered by HTC in terms of low cost, easy production and especially easy functionalisation with any heteroatom of choice using organic chemistry (see Chapter 4 on Maillard reaction for example). Given the huge amount of literature already available on the performance of heteroatom doped HTCs in supercpacitors, we are expecting a rapid and significant growth of research interest in this exciting and important field of research.

5.5 Photocatalysis

Efficient photocatalytic processes have the potential to yield major steps forward in tackling some of society's greatest challenges; clean energy demand (water splitting for hydrogen generation) and environmental pollution (degradation of environmental pollutants in aqueous contamination and waste water treatment , carbon dioxide remediation , self-cleaning activity and air purification).

The development of effective semiconductor photocatalysts has therefore emerged into one of the most important goals in materials science. Indeed, since the first demonstration of photocatalytic water splitting on a titanium dioxide (TiO_2) electrode by Fujishima and Honda [186] the level of research in the field has grown at an exponential rate.

Energy provided by the Sun (around $1.5 \cdot 10^5$ terawatts [187]) greatly exceeds the one consumed by human civilization (around 13 terawatts [187]). However, only a fraction of this energy is harvested by current photocatalytic materials, which typically have solar photoconversion efficiencies of <5%.

Titanium dioxide (TiO_2) has been widely used as a photocatalyst for solar energy conversion and environmental applications because of its low toxicity, abundance, high photostability, and high efficiency. [188] [189] [190] However, the application of pure TiO_2 is limited, because it requires ultraviolet (UV) light, which makes up only a small fraction (< 5 %) of the total solar spectrum reaching the surface of the earth.

Therefore, over the past few years, considerable efforts have been directed towards the improvement of the photocatalytic efficiency of TiO_2 in the visible (vis)-light region. [191] [192] This has been mainly achieved by introducing various dopants into the TiO_2 structure which can narrow its bandgap. In this respect, non-metal doping with atoms such as with B, F, N, C, S, have demonstrated a significant improvement of the visible-light photocatalytic efficiency. [190] [193] [194] Among these, carbon doping received particular attention. [190] An active debate regarding the fundamental nature of the non-metal species causing the visible-light absorption in such modified-TiO_2 materials has continued in the community, and two hypotheses have coexisted for several years: i) the non-metal substitutes a lattice atom (i.e., doping), and ii) the non-metal forms chromophoric complexes at the surface (i.e., sensitisation).

TiO_2 was firstly doped both hydrothermally and solvothermally with carbon by our research group. [195] We showed that the surface of nanometer-sized carbon materials can also show collective polarisation modes and therefore, these optical absorption transitions are feasible to sensitize TiO_2 showing an improved TiO_2 hole reactivity, while the electron is taken up by the carbon component. This resulted in an improved photocatalytic activity over the complete spectral range. In order to avoid carbon from doping directly into bulk TiO_2 lattice our hybrid TiO_2 /C was synthesised at low temperature under solvothermal conditions by a one-step carbonisation of furfural in the presence of Ti-isopropoxide, allowing for the formation and co-assembly of carbon and TiO_2 into an interpenetrating C/TiO_2 nanoarchitecture (Figure 5-17 a-c). Figure 5-17d shows the comparison between C@TiO2 and some control samples towards the degradation of methyl orange (MO) in aqueous solution under visible light. The C@TiO_2 showed the highest photocatalytic activity of all compared materials in visible light ($\lambda > 420$ nm). Both the commercial P25 and N-doped P25 showed only an activity level comparable with the self-degradation of MO under the same irradiation conditions. Complementing the chemical reactivity experiments, the photocurrent generation of C@TiO_2 was also investigated (Figure 5-17 e). Promisingly, the C@TiO_2 material was indeed able to generate significant photocurrents under both UV and visible-light irradiation. A typical n-type photocurrent was generated with UV ($\lambda > 320$ nm), while under visible-light irradiation the material exhibits both n-type and p-type currents. This was explained by the fact that UV-absorption also activates pure TiO_2 bands, while the ambipolar, biphasic nature of C@TiO_2 is

activated under visible light. This allows both electrons and holes to contribute to the charge transport, which is crucial for photo-electrochemical applications.
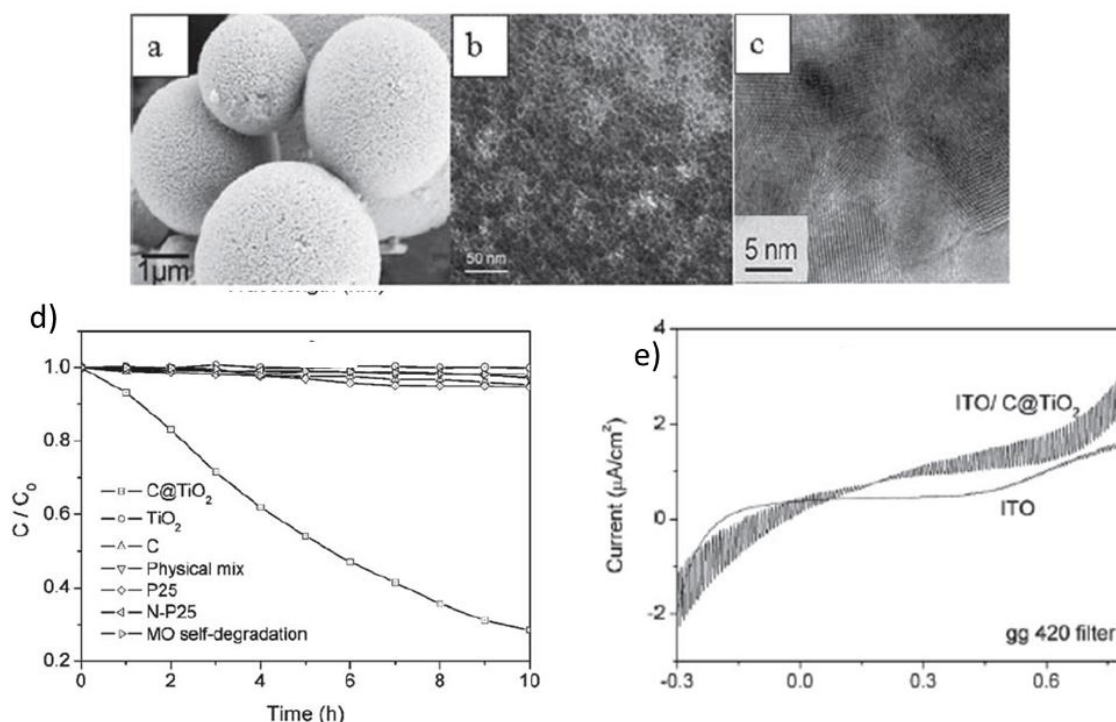
Figure 5-17: a) SEM; b) TEM; c) HR-TEM of the C@TiO$_2$ composite; d) Photocatalytic degradation of MO in the presence of C@TiO2 and other samples under visible light irradiation (λ > 420 nm); e) Photocurrent of ITO/C@TiO$_2$ as a function of potential under chopped visible light (taken with permission from [195]).

Following our report, Chen at al has also prepared a carbon-deposited TiO$_2$ using a very similar one-pot hydrothermal process and glucose as a carbon source. [196] This TiO$_2$@C composite had also remarkable light absorption in the visible region. It was found that the photocatalytic activity of TiO2@C was greatly enhanced compared to noncarbon-TiO$_2$ under visible irradiation for the degradation of Acid Orange 7 (AO7) and 2,4-dichlorophenol (2,4-DCP). The authors claimed that two kinds of sensitisation processes, carbon sensitisation and dye sensitisation, were responsible for the visible light induced photocatalysis of TiO$_2$@C.

Zhang at al reported the fabrication of a novel mesoporous C-TiO$_2$ photocatalyst *via* an ethanol supercritical solvothermal method involving tetrabutyl titanate and raw rice. [197] The as-prepared C-TiO$_2$ possessed a bimodal carbon-modification effect, including carbon doping in the lattice of TiO$_2$ and carbon sensitising the surface of TiO$_2$. The ethanol supercritical treatment also contributed to the development of a mesoporous structure with large surface

area (160 m^2/g) and high crystallinity of anatase. These materials exhibited an excellent photocatalytic performance and recyclability for phenol oxidation under visible light irradiation (> 420 nm).

Hierarchical porous TiO$_2$-carbon hybrid composites with a hollow structure were successfully fabricated by Zhuang et al, using one-pot low-temperature solvothermal approach in the presence of dodecylamine. [198] The growth mechanism of the hierarchical hollow spheres was demonstrated to include the condensation of a carbon source, the co-instantaneous *in situ* hydrolysis of Ti-alkoxide, and the consequent assembly of TiO$_2$@C hybrid nanoparticles on a self-conglobated template. As compared with the TiO$_2$@C solid spheres (86%), the hierarchical TiO$_2$@C hybrid hollow spheres exhibited enhanced photocatalytic efficiency (97%) for the visible-light photooxidation of rhodamine B. Investigations demonstrated that the enhancement can be attributed to the hierarchical porous hollow structure. Moreover, the superoxide radical was detected as the main active species generated in the oxidation reaction of RhB over TiO$_2$@C photocatalysts. A corresponding mechanism was also proposed for the photocatalysis process.

Zhang at al prepared core/shell nanofibers of TiO$_2$@carbon embedded by Ag nanoparticles (TiO$_2$@C/Ag NFs) combining the electrospinning technique, the hydrothermal method and an *in situ* reduction approach. [199] The results showed that an uniform carbon layer of approximately 8 nm in thickness was formed around the electrospun TiO$_2$ nanofibers and small Ag nanoparticles (Ag NPs) were dispersed well inside the carbon layer. The TiO$_2$@C/Ag NFs had remarkable light absorption in the visible region. The photocatalytic studies revealed that the TiO$_2$@C/Ag NFs exhibited enhanced photocatalytic efficiency of photodegradation of Rhodamine B (RB) and Methyl Orange (MO) compared with the pure TiO$_2$ nanofibers, TiO$_2$@carbon core/shell nanofibers and TiO$_2$/Ag nanofibers under visible light irradiation, which might be attributed to the good light absorption capability and high separation efficiency of photogenerated electron–hole pairs based on the photosynergistic effect among the three components of TiO$_2$, carbon and Ag.

Wang et al used an approach to prepare carbon-doped TiO$_2$ hollow spheres (THS) with hierarchical pore structure using HTC carbon spheres according to the initial procedure described by our group. [36] The HTC carbon spheres played a dual role as both single hard template and the source of carbon doping. It is important to note that the resultant THS

interconnected with each other *via* smaller pores to form hierarchical macroporous channesl and a plentiful of mesopores located at the macropore walls. Furthermore, the size of macroporous channels and the thickness of macropore walls can be systematically tuned by adjusting synthesis parameters. The unique hierarchical macroporous channel structure was confirmed to dramatically enhance the photocatalytic performance of THS. [200]

Shao et al synthesised Zn_2TiO_4@carbon core/shell nanofibers (Zn_2TiO_4@CNFs) with different thickness of carbon layers (from 2 to 8 nm) combining the electrospinning technique and hydrothermal carbonisation method. [201] The results showed that an uniform carbon layer was formed around the electrospun Zn_2TiO_4 nanofiber (Zn_2TiO_4 NFs). By adjusting the hydrothermal fabrication parameters, the thickness of the carbon layer varied linearly with the concentration of glucose. Furthermore, the core/shell structure formed between Zn_2TiO_4 and carbon enhanced the charge separation of pure Zn_2TiO_4 under ultraviolet excitation, as evidenced by the photoluminescence spectra. The photocatalytic studies revealed that the Zn_2TiO_4@C NFs exhibited enhanced photocatalytic efficiency for the photodegradation of Rhodamine B (RB) compared with the pure Zn_2TiO_4 NFs under ultraviolet excitation, which might be attributed to the high separation efficiency of photogenerated electrons and holes based on the synergistic effect between carbon and Zn_2TiO_4. Notably, the Zn_2TiO_4@C NFs could be recycled easily by sedimentation without a decrease in the photocatalytic activity.

Another very interesting approach recently published by Ozin et al is based on using carbon quantum dots as sensitizers for photovoltaic applications in nanocrystalline TiO_2 based solar cells. [202]

Carbon quantum dots (CQD) are intriguing recently discovered members of the carbon nanomaterials family alongside carbon nanotubes, fullerenes, and graphene. The general description of CQDs is nanometer sized particles consisting of a sp^2 hybridized graphitic core functionalised with polar carboxyl or hydroxyl groups on the surface. Initial CQD synthesis efforts focused on top-down methods such as laser ablation or electrochemical oxidation. Less expensive and more scalable solution phase methods involve (hydro) thermal decomposition of carbon precursors and microwave assisted pyrolysis of carbohydrates. In this particular paper, the authors used the dehydration of γ-butyrolactone using concentrated sulphuric acid resulting in a carbonaceous material dispersed in residual acidic butyrolactone. Due to the low electron contrast between CQDs and carbon coated TEM grids, acquiring high quality TEM

images was a challenge, and therefore AFM imaging was performed to obtain a more reliable nanoparticle size distribution, (Figure 5-18 a, b). The average height of CQD nanoparticles was found to be 9 - 6 nm by AFM with significant numbers of larger particles in the range of 20–30 nm, some of which were also visible by TEM. Photoluminoscence spectra (PL) of aqueous CQDs showing the excitation dependent nature of the photoluminescence is shown in Figure 5-18c. A large red-shift in the PL maximum from approximately 470 to 580 nm was observed upon increase of the excitation wavelength from 350 to 500 nm, most likely attributed to optical selection of differently sized CQDs in the colloidal dispersion. The absolute PL quantum yield of these CQD dispersions was determined to be 0.5%. This value is likely related to efficient non-radiative competing pathways involving vibrational relaxation enabled by high frequency core and surface modes.

The broad absorption spectra, ease of synthesis from a single molecule precursor and solution processable nature of CQDs makes them potentially valuable as sensitizers for nanocrystalline TiO_2 based solar cell applications. DSSC's have the capacity to be a useful solution to the impending energy challenge facing our planet due to their low cost, environmental friendliness, and nearly angle-independent performance under diffuse light. The current state of the art Ru-complex sensitizers offer good performance but rely on expensive, scarce ruthenium, and are often time-consuming to synthesise. To explore whether these issues can be surmounted the CQD synthesised here were checked as alternative sensitizers for TiO_2 solar cells.

The absorption spectrum of a thin film of CQDs is shown in Figure 5-18 d, displaying the broad absorption throughout the visible region. An electronic band gap of approximately 1.1 eV for an indirect transition and 3.1 eV for a direct transition was calculated using Tauc relations [203] with the experimental absorption onset at approximately 800 nm (Figure 5-18d). The current–voltage characteristics of a CQD sensitized solar cell prepared from an aqueous CQD solution under simulated AM 1.5 irradiation are shown in Figure 5-18 d. A short-circuit current density (J_{sc}) of 0.53 mA cm^{-2} and an open-circuit voltage (V_{oc}) of 0.38 V were produced with a fill factor (FF) of 0.64, for a power conversion efficiency of 0.13%. Cells fabricated from MeOH CQD solutions and aqueous CQDs refluxed in HNO_3 to ensure complete surface oxidation showed similar performance, whereas a non-sensitized nanocrystalline TiO_2 gave an efficiency of 0.03% (data not shown). It is hoped that

refinements in the surface chemistry, corrosion stability, charge transport and charge injection properties of CQDs will lead to improved performance.
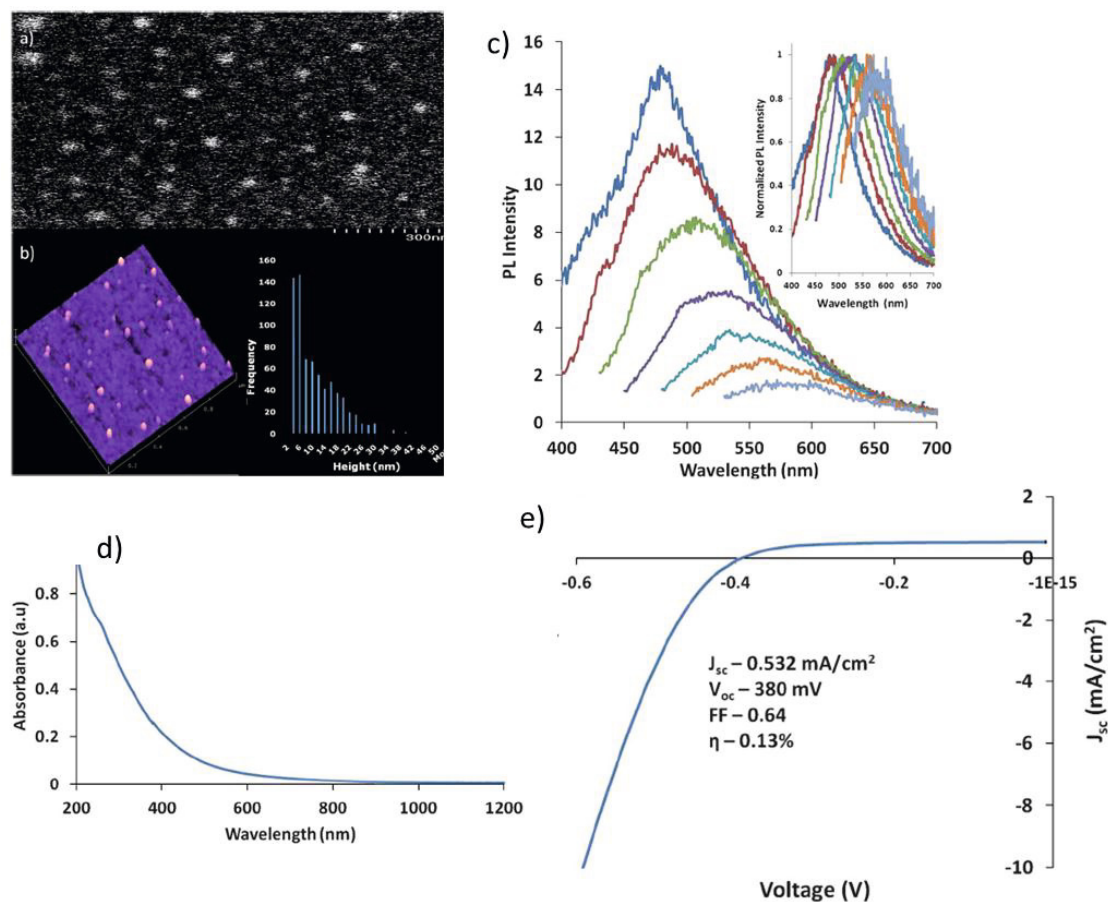
Figure 5-18: a) a) TEM image of CQDs drop cast on a carbon-coated TEM grid (b) AFM image and particle height distribution of a CQD thin film spincoated onto a Si wafer.c) PL spectra of purified CQDs at different excitation wavelengths from 350 nm to 500 nm increasing at 25nm intervals. (Inset) Normalized PL spectra at the corresponding excitation wavelengths. d) UV-Vis-NIR absorption spectrum of CQD thin film on quartz substrate; e) Current–voltage characteristics of aqueous CQD-sensitized solar cell (taken with permission from [202])

Kang et al also prepared ZnO/carbon quantum dots (ZnO/CQDs) nanocomposites by a one-step hydrothermal reaction and used the resulting composite as superior photocatalysts for the degradation of toxic gas (benzene and methanol) under visible light at room temperature. The presented results showed that these nanocomposites exhibited higher photocatalytic activity (degradation efficiency over 80%, 24 h) compared to N doped TiO_2 and pure ZnO nanoparticles under visible light irradiation. In the present catalyst system, the crucial roles of CQDs in the enhancement of photocatalytic activity of the ZnO/CQDs nanocomposites are illustrated. [204]

Various nanocarbon-TiO_2 (and other semiconductor) systems have been widely investigated and are promising materials for future high activity photocatalysts. Besides providing a high-surface area support and immobilisation for TiO_2 photocatalyst particles, the presence of the carbonaceous material and nanostructuring may facilitate enhanced photocatalytic activity through one or all of the three primary mechanisms: minimisation of electron/ hole recombination, band-gap tuning/photosensitization and provision of high quality highly adsorptive active sites. Novel nanocarbon-TiO_2 combinations have been developed in the past few years, some of which also based on HTC and they offer opportunities for the design of new photocatalytic systems. The primary challenge to further exploitation of synergistic effects lies in better understanding the mechanisms of enhancement, in parallel with control and understanding of synthesis.

5.6 Gas Storage

5.6.1 CO_2 Capture using HTC

The mitigation of carbon dioxide emissions is a crucial issue as this gas is the main anthropogenic contributor to climate change. Among the possible strategies for CO_2 abatement, capture and storage have attracted keen interest. In this regard, the use of solid sorbents to capture CO_2 by means of pressure, temperature or vacuum swing adsorption systems constitutes a promising alternative. [205] To accomplish this objective, the sorbents need to satisfy important conditions: i) low-cost and high availability, ii) large CO_2 uptake, iii) high sorption rate, iv) good selectivity between CO_2 and other competing gases (i. e. N_2) and v) easy regeneration. However, the development of a solid sorbent that satisfies all these conditions has proved so far to be complex. Taking into account the potential scale involved in the production of porous carbons for CO_2 capture, the use of renewable sources for fabricating these materials would seem highly desirable. A good option is the use of biomass or biomass-derived products as precursors for the production of carbon sorbents for CO_2 capture. In this respect, low-cost sustainable porous carbons such as those derived from HTC materials would constitute a good alternative.

The CO_2 capture performance of HTC-based activated carbons was recently investigated by Sevilla and Fuertes. [206] These authors analysed the use as CO_2 adsorbents of porous carbons obtained by chemical activation of several HTC materials prepared from starch, cellulose and eucalyptus sawdust. The hydrothermal carbonisation of these materials was carried out at

temperatures in the 230-250 ºC range for 2 hours. The chemical activation was performed with KOH at temperatures in the 600-850ºC range. They observed that the textural properties of the activated carbons derived from sawdust are similar to those obtained from starch or cellulose. This result demonstrates that an inexpensive and widely available biomass sub-product such as sawdust constitutes excellent precursors for the preparation of chemically activated carbons *via* HTC materials. In Table 5-1 are listed the textural properties (i. e. surface area and pore volume) of the sawdust-based HTC activated carbons produced at several reaction temperatures by using two KOH/HTC mass ratios. They exhibit BET surface areas between 1260 m^2 g^{-1} and 1940 m^2 g^{-1}. As indicated, both the surface area and the pore volumes are mostly associated to micropores (< 2 nm).

Table 5-1. Textural properties of HTC-based activated carbons derived from eucalyptus sawdust (adapted from [206] with permission)

Activation temperature	(KOH/HTC)=2		(KOH/HTC)=4	
	S_{BET} [m^2 g^{-1}] [a]	V_p [cm^3 g^{-1}] [a]	S_{BET} [m^2 g^{-1}] [a]	V_p [cm^3 g^{-1}] [a]
600 ºC	1260 (98)	0.62 (89)	2370(86)	1.15 (79)
650 ºC	1380 (98)	0.67 (91)	-	-
700 ºC	1390 (98)	0.69 (90)	2250 (93)	1.03 (88)
800 ºC	1940 (95)	0.97 (85)	2850 (95)	1.35 (91)

[a] The percentage of surface area and pore volume corresponding to micropores is indicated in parentheses.

The CO_2 adsorption uptake for several HTC activated carbons is listed in Table 5-2 for a pressure of 1 bar and three adsorption temperatures (0 ºC, 25 ºC and 50 ºC). It can be seen that the CO_2 capture capacities of the HTC-based porous carbons prepared from starch, cellulose or eucalyptus sawdust are quite substantial and similar (about 5.5–5.8 mmol $CO_2 \cdot g^{-1}$, 243–256 mg $CO_2 \cdot g^{-1}$). This result is coherent with the fact that the pore characteristics of these materials are analogous. The HTC-sawdust activated carbons prepared by using KOH/HTC=4 exhibit similar CO_2 uptakes irrespective of the activation temperature. Indeed, the capture capacities at adsorption temperatures of 0 ºC and 25 ºC are in the 5.2–5.8 mmol CO_2 g^{-1} and

2.9–3.5 mmol $CO_2 \cdot g^{-1}$ ranges respectively. Interestingly, the HTC-sawdust-based porous carbons prepared under mild activation conditions (KOH/HTC=2) exhibit better CO_2 capture capacities than under KOH/HTC=4. Thus, at room temperature (25 °C), CO_2 adsorption capacities up to 6.6 mmol CO_2 g^{-1} and 4.8 mmol CO_2 g^{-1} were obtained for the samples prepared with KOH/HTC mass ratio of 2 and reaction temperatures of 700ºC and 600ºC respectively. These outstanding CO_2 adsorption uptakes are ascribed to the fact that a large fraction of the porosity of the mildly activated HTC samples corresponds to narrow micropores, which have strong adsorption potentials that enhance their filling by the CO_2 molecules.

Table 5-2 CO_2 capture capacities of the porous carbons at different adsorption temperatures and 1 atm (adapted from ref. [206] with permission).

HTC precursor	Chemical activation		CO_2 uptake, mmol·g^{-1} (mg·g^{-1})		
	T (ºC)	KOH/HTC	0 °C	25 °C	50 °C
Starch	700	4	5.6 (247)	3.5 (152)	2.2 (196)
Cellulose	700	4	5.8 (256)	3.5 (155)	1.8 (79)
Eucalyptus sawdust	600	4	5.2 (230)	2.9 (128)	-
	700	4	5.5 (243)	2.9 (128)	1.8 (79)
	800	4	5.2 (227)	3.0 (130)	-
	600	2	6.1 (270)	4.8 (212)	3.6 (158)
	650	2	6.0 (262)	4.7 (206)	3.3 (145)
	700	2	6.6 (288)	4.3 (190)	2.6 (116)
	800	2	5.8 (255)	3.9 (170)	3.1 (136)

For practical applications, in addition to a high CO_2 adsorption capacity, sorbents need to show fast adsorption kinetics, a high selectivity towards CO_2 and they must also be easy to regenerate. Sevilla and Fuertes [206] examined the performance of HTC-sawdust activated carbons in relation to these prerequisites. As shown in Figure 5-19(a), the CO_2 adsorption is very fast, around 95 % of CO_2 uptake occurring in a span of 2 min. By contrast, N_2

295

adsorption is slower, around 60 min being needed for the maximum adsorption uptake to take place. Then, the $[CO_2/N_2]$ selectivity measured under equilibrium conditions is 5.4. Easy regeneration is another critical property that must be considered when designing CO_2 sorbents. In this respect, for the HTC-based carbons > 95 % of CO_2 is desorbed within 3 min under these conditions. This is illustrated in Figure 5-19(b), where the adsorption–desorption cycles are represented. They were repeated seven times and no noticeable changes were observed in the desorption kinetics or CO_2 uptake.
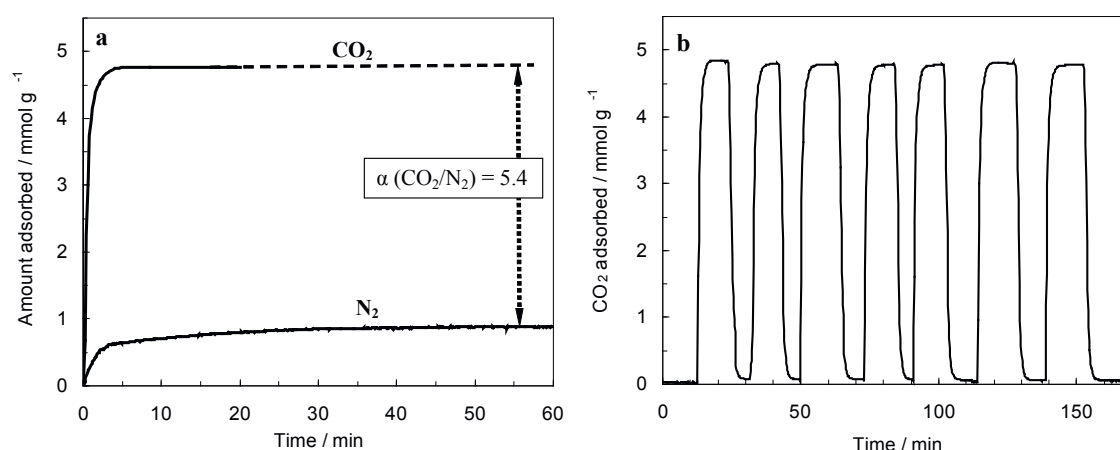
Figure 5-19. (a) Adsorption kinetics of CO_2 and N_2 at 25ºC and (b) CO_2 adsorption-desorption cycles obtained at 25ºC (CO_2 concentration: 100 %). The carbon sample used in this experiment was prepared from a HTC-sawdust carbon activated at 600ºC with KOH/HTC=2 (adapted from ref. [206] with permission).

Another interesting approach in relation to the use of the HTC materials for the CO_2 capture is based on their functionalisation with amine groups which exhibit a high affinity to CO_2. In this respect we [207] reported the CO_2 capture by means of an amine-rich HTC product. This material was prepared by a two-step process: a) hydrothermal carbonisation of glucose in presence of small amounts of acrylic acid and b) functionalisation of carboxylic-rich HTC products with triethylamine. This aminated HTC material shows high CO_2 capture capacities (up to 4.3 mmol $CO_2 \cdot g^{-1}$ at -20ºC). More important, these materials exhibit a very high $[CO_2/N_2]$ selectivity at low (-20 ºC) and high (70 ºC) temperatures, up to 110 at 70 ºC.

Zhang et al prepared nitrogen-containing porous carbons from an ocean pollutant Enteromorpha prolifera, *via* hydrothermal carbonisation followed by potassium hydroxide activation. Carbons contained as much as 2.6% nitrogen in their as-prepared state. The inorganic minerals contained in the carbon matrix contributed to the development of

mesoporosity and macroporosity, functioning as an *in situ* hard template. The carbon manifested high CO_2 capacity and facile regeneration at room temperature. The CO_2 sorption performance was investigated in the range of 0-75 degrees C. The dynamic uptake of CO_2 was 61.4 mg/g and 105 mg/g at 25 degrees C and 0 degrees C, respectively, using 15% CO_2 (v/v) in N_2. Meanwhile, regeneration under Ar at 25 degrees C recovered 89% of the carbon's initial uptake after eight cycles.

Our group has recently prepared highly porous N-doped carbon materials with apparent surface areas in the 1300 - 2400 m^2/g range and pore volumes up to 1.2 cm^3/g from mixtures of algae and glucose. [208] The porosity of these materials was made up of uniform micropores, most of them having sizes < 1 nm. Moreover, they had N contents in the 1.1 - 4.7 wt% range, this heteroatom being mainly in pyridone-type structures. These microporous carbons present unprecedented large CO_2 capture capacities, up to 7.4 mmol/g (1 bar, 0 ºC). The importance of the pore size on the CO_2 capture capacity of microporous carbon materials was clearly demonstrated. Indeed, a good correlation between the CO_2 capture capacity at sub-atmospheric pressure and the volume of narrow micropores was observed pointing out the unimportance of the pyridone-type structures present in the structure of these materials. [208] Recently, a variety of microporous polymers have been reported to have high CO_2 over N_2 selectivity, which is a very interesting feature in the field of CO_2 capture. [209] [210] [211] [212] [213] As the as-prepared HTC carbons are microporous and possess polymer-like behaviour, it was interesting to investigate their ability as selective CO_2 sorption materials. To compare the adsorption ability for CO_2 and N_2, the N_2 uptake of xylose-derived HTC material (HTC-X) at 273 K was measured Figure 5-20.
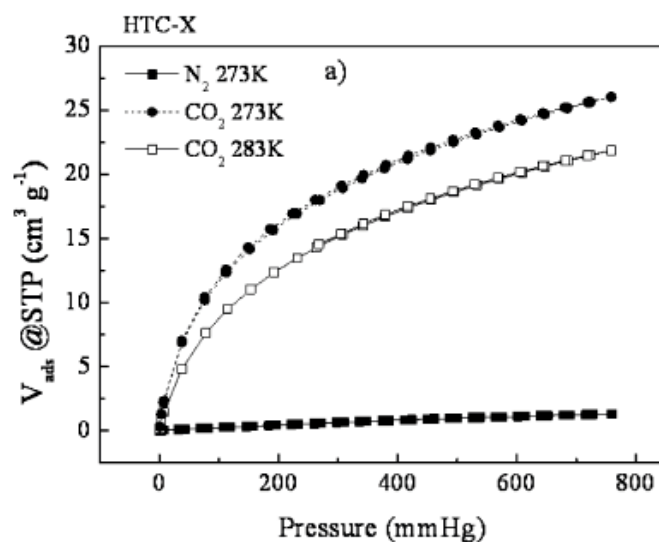
Figure 5-20: N_2 and CO_2 sorption isotherms of HTC-X, measured at 273 K and CO_2 sorption isotherm measured at 283 K. Taken with permission from [214]

The uptake of ~ 1.3 cm^3 g^{-1} at standard temperature and pressure (STP) is small as compared to the CO_2 uptake of 26.0 cm^3 g^{-1} at STP. This can be calculated to an apparent CO_2/N2 selectivity of 20 at 273 K, 1 bar, and 1:1 gas composition. This selectivity is not extraordinarily high, but it definitely presents a competitive result. The selectivity range is comparable to that of some microporous polymers, which show comparable CO_2 uptakes. [209] [212] Given the fact that HTC materials are simply made out of biomass by simple autoclave treatment below 200°C, this represents an extra advantage compared with the complicated and more expensive synthesis of porous polymers.

5.6.2 Hydrogen Storage using HTC

Hydrogen storage is currently one of the main obstacles towards the commercial use of hydrogen in fuel cell systems. Among the large variety of materials investigated as carriers for hydrogen storage, porous carbons have generated a great attention. The interest in porous carbons lies in the fact that they are relatively cheap and accessible on a commercial scale and, in addition, their pore structure can be easily designed, which is important to optimize the hydrogen storage capacity. In this sense, porous carbons with very large BET surface areas (> 2000 m^2·g^{-1}) and a porosity made up by micropores of around 1 nm have demonstrated to exhibit a large capacity to adsorb hydrogen. [215]

Carbons with these characteristics have been prepared by chemical activation of a variety of precursors (i. e. coal, petroleum pitch, polymers, biomass products, etc). Recently, Sevilla et al. reported the use as H_2 adsorbents of porous carbons produced by chemical activation (KOH) of HTC materials obtained by hydrothermal carbonisation of glucose, starch, furfural, cellulose and sawdust. [216] The main textural parameters for the HTC-based activated carbons, as well as their hydrogen storage capacity at 1 and 20 and at -196ºC, are given in Table 5-3. Independently on the type of precursor selected to produce the HTC material, all the activated samples exhibited similar textural properties: i) large BET surface areas, around 2200 $m^2 \cdot g^{-1}$, ii) pore volume of ~ 1 $cm^3 \cdot g^{-1}$ and iii) a porosity made up mainly by micropores (< 2 nm). Their hydrogen storage capacity is ~ 2.5 wt % at 1 bar and in the 5.3–5.6 wt % range at 20 bar. These hydrogen uptakes are in most cases superior to those obtained for other activated carbons with large surface area under similar conditions.

Table 5-3. Hydrogen uptake capacity and textural properties of chemically activated carbons produced from HTC materials (adapted from ref. [216] with permission).

Precursor	BET surface area (m²·g⁻¹)	Pore volume (cm³·g⁻¹)	Micropore volume (cm³·g⁻¹)	H₂ uptake (wt %) [b]
Furfural	2180	1.03	0.94	5.4 (2.5)
Glucose	2120	1.00	0.91	5.3 (2.4)
Starch	2190	1.01	0.92	5.4 (2.4)
Cellulose	2370	1.08	0.96	5.6 (2.5)
Wood	2250	1.03	0.91	5.6 (2.5)

5.7 Adsorption of Pollutants from Water

The removal of heavy metals or organic pollutants from water is of special concern due to their recalcitrance and persistence in the environment. Various methods for treatment of water have been extensively studied. These technologies include chemical precipitation, ion-exchange, membrane filtration, coagulation-flocculation, flotation, electrochemical methods

and adsorption. In general, most of the technologies are often expensive and mostly effective in removing one single metal or organic contaminant. However, in practice, wastewater contains both heavy metal and organic pollutants, in this respect, adsorption is a viable and a cost-effective option since it can efficiently remove both metals and organics.

Among other possible applications indicated above, hydrothermal carbonaceous materials rich in functional groups are promising candidates for use as cheap, sustainable, and effective sorption materials for removal of heavy metals or organic pollutants. The possibility of water purification achieved with HTC materials with an overall low cost base is definitely an attractive alternative, especially for the developing world.

5.7.1   Removal of Heavy Metals

Water pollution by heavy metals is known to be a serious worldwide environmental problem with significant impact on living organisms and the environment due to their high toxicity and non-biodegradability, tending to bioaccumulate through the food chain. Chromium, nickel, cadmium, zinc and lead are some of the heavy metals commonly associated with water pollution. The concentration in drinking water of any of them must be in the ppm range. Adsorption is the most widely used method to remove heavy metals owing to its simplicity and low cost, activated carbons being normally used due to their large surface area and pore volume, as well as high chemical and thermal stability.

However, more economical sorbents as well as "greener" and easier synthesis routes are desirable, and in that sense, hydrothermal carbons are great candidates. Even though they do not exhibit porosity, they possess abundant oxygen functionalities that can bind the metal ions through an ion-exchange mechanism.

 Our group described the first use of hydrothermal carbon as sorption materials in which they concurrently demonstrate the possibility of tuning the surface functionally of carbon spheres. [128] In their strategy, the main precursor was a cheap water-soluble carbohydrate (glucose), while an organic monomer (i.e. acrylic acid) was required in very small amounts in order to provide the functionality. This method offers a facile, cheap and general route towards the production of carbonaceous materials with a variety of functionalities. A small amount of vinyl organic monomers addition into the HTC of D-glucose gave rise to a new type of hybrid between carbon and polymer latex. The vinyl organic monomers are here partially replaced by the controlled dehydration products of carbohydrates, which are then

copolymerized or undergo cycloaddition reaction with functional co-monomers (see Chapter 4).

Depending on the monomer used, this present synthetic strategy can be extended to various compositions yielding materials that combine the surface properties of the polymers with the structural, mechanical, thermal, and electric properties of the carbon framework.

In the adsorption study, acrylic acid was employed, resulting in carbon spheres rich in carboxylic groups. Acrylic acid plays a double role in this process: on one hand, it donates the functionality and, on the other hand, it reacts with the compounds formed in the previous step of HTC *via* cycloaddition reactions stabilising the small droplets and leading to assembly into macroporous materials. (Figure 5-21a)

The synthesised materials were investigated in adsorption experiments for the removal of heavy metals from aqueous solutions. The adsorption capacity was as high as 351.4 mg per g for Pb(II) and 88.8 mg per g for Cd(II), which is well beyond ordinary sorption capacities, proving the efficiency of the materials to bind and buffer ions, or more specifically to remove heavy metal pollutants.(Figure 5-21b,c).
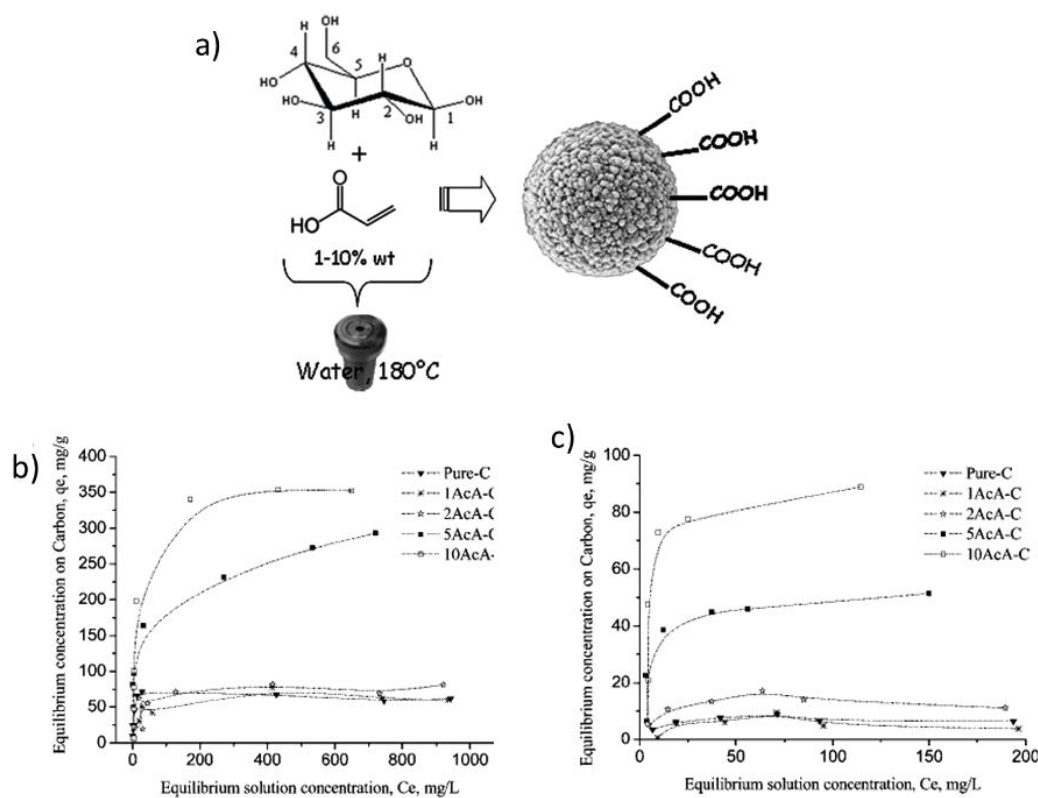
Figure 5-21: a) Schematic representation of carboxylic acid functionalisation techniques using glucose and small ammounts of acrylic acid; b) Pb(II) and c) Cd(II) adsorption isotherms on the obtained carbonaceous material. 1-10 repesent the wt% of acrylic acid added in respect to the total glucose concentration (taken with permission from 128)

In a similar manner, our group studied the impact of vinyl imidazole monomer into the hydrothermal carbonisation. [129] The successful incorporation of imidazole group into the resulting materials was confirmed by elemental analysis, FT-IR, zeta potential measurement and ^{13}C solid state NMR. Zeta potential measurements also confirmed the presence of the imidazole ring anchored to the carbon materials. While the pure HTC materials had a negative zeta potential over all the pH range, the imidazole containing materials showed positive values at an acidic pH due to the protonation of the nitrogen atom linked to the carbon. The isoelectric point (IEP) increased from pH=2 up to pH=6 depending on the amounts of monomer used clearly demonstrating the basic character of the materials.

The synthesised carbonaceous materials containing imidazole groups were used as an adsorbent for removal of hexavalent chromium from the water at pH 4. A colorimetric method was used to measure the concentrations of the Cr(VI). The pink colored complex, formed from 1,5-diphenylcarbazide and Cr(VI) in acidic solution, was spectrophotometrically analysed at 540 nm. Adsorption isotherms and sorption capacities of the bare hydrothermal carbon spheres without having imidazole groups showed the lowest binding capacity around 30mg/g. However the capacity increased upon increasing the functionality and reached 70mg/g Cr(VI) binding capacity. It has been proved that, when Cr(VI) comes in contact with organic substances or reducing agents, especially in an acidic medium, Cr(VI), it is spontaneously reduced to Cr(III). [217] The total Cr species in the equilibrium solution was also analysed by ICP and it was observed that there is no difference in the concentration of the final liquids detected by colorimetric method. In this respect, it was concluded that the removal of Cr(VI) by imidazole functionalised materials from water took place *via* anionic adsorption and not *via* reduction of hexavalent chromium to trivalent chromium. [218]

Chen et al. also studied the adsorption of Pd and Cd metals with a material prepared by HTC of glucose post-treated at 300ºC in air. [219] The authors found that, whereas the temperature of the post-treatment in air had a great influence on the amount of carboxylic groups introduced in the HTC materials, the time had little. For example, the content of carboxylic groups at

350ºC was five times higher than at 100ºC, while at 300ºC the content increased from 3.42 mmol/g for 1 h of heating to 3.70 mmol/g for 5 h. In this way, the adsorption capacity of the sample treated in air at 300ºC was 326.1 ± 3.0 mg/g for Pb^{2+} and 150.7 ± 2.7 mg/g for Cd^{2+} (Table 5-4), values 3 and 30 times higher than that of as synthesised HTC.

Removal of radioactive element, i.e. uranium, was also subjected using the HTC technology from lignocellulosic biomass. [220] Most precisely, biochar was produced here from switchgrass at 300 ºC in subcritical water and characterised using XRD, FT-IR spectroscopy, SEM, and thermogravimetric analysis. The physiochemical properties indicated that the biochar could serve as an excellent adsorbent to remove uranium from groundwater. A batch adsorption experiment at the natural pH of biochar indicated an H-type isotherm. The adsorption data were fitted using a Langmuir isotherm model and the sorption capacity was estimated to be ca. 2.12 mg of U g^{-1} of biochar. The adsorption process was highly dependent on the pH of the system. An increase towards neutral pH resulted in the maximum adsorption of ca. 4 mg U g^{-1}. These results indicated that biochar could be used as an effective adsorbent for U(VI), as a reactive barrier medium.

The purpose of removal of uranium was also studied by a salicylideneimine-functionalised hydrothermal carbon. [221] The resulting adsorption material was obtained *via* hydrothermal carbonisation at mild temperature (573.15 K), amination, and grafting with salicylaldehyde in sequence. Adsorption behaviours of the extractant on uranium(VI) were investigated by varying the pH values of the solution, adsorbent amounts, contact times, initial metal concentrations, temperatures, and ionic strengths. An optimum adsorption capacity of 1.10 mmol g^{-1} (261 mg g^{-1}) for uranium (VI) was obtained at pH 4.3. The adsorption process fitted pseudo-second-order model and Langmuir isotherm. Thermodynamic parameters (H = +8.81 kJ mol^{-1}, S = +110 J K^{-1} mol^{-1}, G = −23.0 kJ mol^{-1}) indicated the adsorption process was endothermic and spontaneous. Results from batch adsorption test in simulated nuclear industrial effluents, containing Cs^+, Sr^{2+}, Ba^{2+}, Mn^{2+}, Co^{2+}, Ni^{2+}, Zn^{2+}, La^{3+}, Ce^{3+}, Nd^{3+}, Sm^{3+}, and Gd^{3+}, showed the adsorbent could separate uranium(VI) from those competitive ions with high selectivity.

Another study compared two types of biochars prepared from hydrothermal liquefaction of pinewood and rice husk for lead removal from aqueous solution. [222] The results indicated that the investigated biochars were effective for lead removal with capacities of 4.25 and 2.40

mg per g for HTC pine wood and HTC rice husk, respectively. The adsorption equilibrium was achieved in ca. 5 h, whilst higher temperatures favored the removal capacity implying that the adsorption was an endothermic process.

Liu et al. used also a hydrothermal carbon for the removal of heavy metals (i.e. Cu). [223] In this case, the hydrothermal carbon was prepared from pinewood hydrothermally treated at 300ºC for 20 min (denoted H300). For comparison purposes, a pyrolytic char was also prepared by pyrolysis of pinewood at 700ºC for 2h (denoted P700). The elemental analysis clearly evidences the higher oxygen content of the hydrothermal carbon (34.8 %) in comparison with the pyrolytic char (3.8 %). This was further confirmed by Boehm titration and FTIR analysis. From a textural point of view, both materials exhibited a low porosity development, with BET surface areas of 21 and 29 m^2/g for the hydrothermal carbon and the pyrolytic char, respectively. The hydrothermal carbon had an estimated maximum adsorption capacity of Cu^{2+} of 4.46 mg/g *vs.* 2.75 mg/g for the pyrolytic carbon (Table 6.4). The adsorption of Cu^{2+} took place through an ion-exchange mechanism with the H^+ of the oxygen-containing groups, which was manifested in a decrease of the pH of the solution.

Xu et al. functionalised the surface of an activated carbon (obtained by calcining bulk activated carbon at 400ºC for 4h) with glucose-derived carbon nanospheres (obtained at 180-190ºC and 3-6 h). [224] The analysis of the as-synthesised carbon-carbon composite by SEM and TEM evidenced that the carbon nanospheres (~ 100 nm) were well-dispersed on the surface and pores of the activated carbon host and they were anchored onto or embedded in the host. This was translated into a large decrease of the BET surface area and pore volume, which reached values of 222 m^2/g and 0.147 cm^3/g respectively. However, it also translated into the increase of the amount of oxygen-containing functional groups with respect to the activated carbon, as evidenced by temperature programmed desorption (TPD), FTIR and XPS analysis. As a result, the composite material showed much better adsorption capability of CrO_4^{2-} and Fe^{3+} than the initial activated carbon. Thus, the estimated maximum adsorption capacity of CrO_4^{2-} and Fe^{3+} for this composite was 180 µmol/g (0.81 µmol/m^2) and 1501 µmol/g (6.76 µmol/m^2) respectively, whereas for the activated carbon was 32 mmol/g (0.030 µmol/m^2) and 912 µmol/g (0.84 µmol/m^2) respectively.

An attapulgite clay@carbon (ATP@C) nanocomposite adsorbent was used for removal of Cr(VI) and Pb(II) ions. [225] The composite was synthesised by a one-pot hydrothermal

carbonisation process under mild conditions using two materials; attapulgite clay (ATP), which is a magnesium aluminum silicate that is abundant in nature, and glucose. Compared to carbon-based materials, this ATP@C nanocomposite exhibits a high adsorption ability for Cr(VI) and Pb(II) ions with maximum adsorption capacities of 177.74 and 263.83 mg g^{-1}, respectively.

Based on all these reports, a comparison of different sorption capacities for various heavy metals using different HTC adsorbents is given in Table 5-4

Table 5-4. Comparison of the adsorption capacity of heavy metals of different adsorbents

Adsorbent [ref]	Heavy metal	Adsorption capacity (mg/g)	Conditions
10AcA-C [45]	Pb^{2+}	351.4	pH 6; room T
	Cd^{2+}	88.8	
Leonardite (low-rank coal) [45]	Pb^{2+}	250.7	pH 5.4-5.6; room T
	Cd^{2+}	50.6	
HNO$_3$ oxidised CNT [45]	Pb^{2+}	97.08	pH 5; room T
	Cd^{2+}	10.86	
Carbon aerogel [45]	Pb^{2+}	~ 35	pH 4.5; 37ºC
	Cd^{2+}	~ 15	
Amberlite IR-120 synthetic sulfonated resin [45]	Pb^{2+}	19.6	pH 4-8; room T
	Cd^{2+}	201.1	
HTC treated in air at	Pb^{2+}	326.1	pH 4; room T

300ºC [46]	Cd^{2+}	150.7	
H300 [47]	Cu^{2+}	4.46	Room T
P700 [47]		2.75	
Sawdust carbon [47]	Cu^{2+}	5.73	30ºC
Nanoarchitectured activated carbon [48]	CrO_4^{2-}	20.9	pH 8; room T
	Fe^{3+}	83.8	pH 1.8; room T
Activated carbon [48]	CrO_4^{2-}	3.71	pH 8; room T
	Fe^{3+}	50.9	pH 1.8; room T

Ni *et al.* was prepared honeycomb-like Ni@C composite nanostructures *via* a two-step solution route. [226] Homogeneous Ni nanospheres with an average diameter of 100 nm were first obtained *via* a DMF–water mixed solvothermal route; then honeycomb-like Ni@C composite nanostructures were prepared through the hydrothermal carbonisation of glucose solutions with suitable amounts of Ni nanospheres. The products were characterised by XRD, SEM, TEM, ED, EDS and Raman spectroscopy. Furthermore, the honeycomb-like Ni@C composite nanostructures presented good capacities for selective adsorption of Pb^{2+}, Cd^{2+} and Cu^{2+} ions in water. The order of adsorbing capacities for the three ions is $Pb^{2+} > Cu^{2+} > Cd^{2+}$ and the removal capacities were calculated to be 21.45, 14.3 and 6.43 mg g^{-1}, respectively. Because of the presence of magnetic cores, the present adsorbents can be easily separated from solutions under an external magnetic field and can be reused *via* washing with deionized water.

Magnetic carbonaceous nanoparticles also were subjected by Lee *et al.* through a two-step solution phase thermal synthesis. [227] Fe_3O_4 magnetic nanoparticles (MNPs) with size less than 100 nm were first generated from $FeCl_3$ in a solvothermal reaction. The size could be significantly reduced to approximately 30 nm when 1,6- hexanediamine was employed in the reaction solution to functionalise the surface of MNPs with amine. Both the plain and amine-functionalised MNPs (MH) were encapsulated in the carbonaceous shell by hydrothermal

treatment in 0.5M glucose solution. The saturation magnetisation of MH decreased significantly from 70 to 25 emu/g after carbonaceous shell was formed. The surface charge of MNPs and MNPs@C particles were studied by measuring their zeta potentials at pH ranging from 2 to 12. All the particles had their zeta potential decrease with pH. MH particle possesses the highest point of zero charge (PZC) at pH about 6.5 and decreases to 2 after hydrothermal carbonisation treatment. The plain particle has a slightly lower PZC of pH 6.0 and reduces to 3.5 after carbonisation treatment. The reduced PZC of MNPs@C particles is due to the presence of carbonaceous shell since the carbonaceous surface is known to be hydrophilic and mainly consisted of acidic carboxyl and carbonyl groups. The carbonaceous shell not only can protect the magnetic nanoparticles from the corrosive environment but also possesses a high adsorption capacity towards Pb(II). The adsorption isotherm at room temperature was well-fitted by Langmuir model with a maximum adsorption capacity of 123 mg/g.

Xu *et al.* reported the synthesis and activation of colloidal carbon nanospheres (CNS, 400–500 nm in diameter) *via* hydrothermal treatment of glucose solution and used as adsorbents for Ag(I) ions from aqueous solutions. [227] The surface of nonporous CNS after being activated by NaOH was enriched with –OH and –COO⁻ functional groups. Despite the low surface area (<15 m^2/g), the activated CNS exhibited a high adsorption capacity of 152 mg silver/g. Under batch conditions, all Ag(I) ions can be completely absorbed in less than 6 min with the initial Ag(I) concentrations lower than 2 ppm. This was attributed to the minimum mass transfer resistance as Ag(I) ions were all deposited and reduced as Ag^o nanoparticles on the external surface of CNS. The kinetic data was fitted to the pseudo-second order kinetics model. The NaOH activated CNS reported could represent a low-cost adsorbent nanomaterials for removal of trace Ag(I) ions for drinking water production.

Hydrothermal carbon materials can also be employed as a membrane structure and was first reported by Yu *et al.* performing the filtration and separation of nanoparticles with different sizes from solution. [228] For this study, initially hydrothermal carbon fiber (CNF) systhesized [229] by dispersion of Te nanowires into of glucose solution followed by hdrothermal treatment of the mixed solution at 160 °C resulting Te@C nanocables and after removal of the Te cores by chemical etching, pure CNFs was obtained. Then those free-standing CNF membranes were fabricated through a solvent-evaporation–induced self-assembly process. A woollike homogeneous suspension was obtained by vigorous magnetic

stirring of the CNF in ethanol for several hours. After casting the suspension onto a Teflon substrate and drying at ambient temperature, a brown paper-like material was formed, which could be easily detached from the substrate without cracking. The fabricated CNF membranes are very flexible and mechanically robust enough for filtration under a high applied pressure without any damage. These CNF membranes have very narrow pore size distributions and show size-selective rejection properties. The cut-off sizes of these free-standing membranes could be controlled precisely by carefully regulating the diameters of the CNFs. The performance of the CNF membrane was tested by filtering different size particles from solution. The separation of Au nanoparticles with two different sizes has been successfully achieved. It is believed that the size-dependent separation ability of these membranes also makes them suitable for separation of a wide range of other materials on the nanometer or micrometer-scale, such as polymers, viruses, bacteria, microorganisms, and so on. The results suggest two unique advantages of the CNF membranes, i.e., high flux and high selectivity. Although there are commercially available membranes with a range of pore sizes, the filtration rate of them is usually low when the cut-off size is below 100nm because of their intrinsic structures.

5.7.2 Removal of Organic Pollutants

Hydrothermal carbon materials were also studied for organic pollutants removals. The fabrication of hydrothermal carbon based nanofiber (CNF) functionalised by beta-cyclodexrins (β-CD) as a membrane was subjected for molecular filtration. [230] CDs are important for removal of the organic pollutants to form inclusion complexes in aqueous media with a wide variety of organic substrates, including many organic pollutants. First CNF was synthesizsed thorough a method described at reference [229] Then those CNF was functionized by β-CD, and the free-standing CNF-β-CD membrane was prepared by a simple filtration process. The membrane shows a capability to function as an ideal molecular filter through complexation of phenolphthalein molecules with the cyclodextrin molecules grafted on the CNFs. It was considered that as a typical dye pollutant, fuchsin acid can also be effectively removed from the solution through such a membrane.

Xing *et al.* compared pyrolysis and HTC biochars for the adsorption of bisphenol A, 17α-ethinyl estradiol, and phenanthrene from water. [231] The thermal biochars were produced from feedstocks of poultry litter and wheat straw, respectively, through pyrolysis at T= 400 °C. The

HTC biochars were prepared from poultry litter and swine solids at T=300 $^{\circ}$C. XRD and solid state NMR spectroscopy results suggested that HTC biochars consisted of more amorphous aliphatic-C, possibly being responsible for their high sorption capacity of phenol. This study demonstrated that hydrothermal biochars could absorb a wider spectrum of both polar and non-polar organic contaminants than thermally produced biochars, suggesting that the investigated HTC biochar is a potential sorbent for agricultural and environmental applications.

Another interesting example of use of hyrdrothermal carbon materials is to remove dye pollutants from water. [232] In their study, Orange-II ($C_{16}H_{11}N_2NaO_4S$), an anionic dye, was chosen as the model pollutant in water. The fabrication of rattle type carbon$-$ γ Al_2O_3 particles were prepared by using glucose and aluminum nitrate *via* a one-pot hydrothermal synthesis at 180°C for 24h followed by calcinations at 450 $^{\circ}$C for 2h. The microstructure, morphology, and chemical composition of the resulting materials were characterised by X-ray diffraction, energy dispersive X-ray spectroscopy, scanning electron microscopy, transmission electron microscopy, and N_2 adsorption$-$desorption techniques. These rattle-type spheres were composed of a porous Al_2O_3 shell (thickness $\approx$ 80 nm) and a solid carbon core (diameter $\approx$ 200 nm) with variable space between the core and shell. Furthermore, adsorption experiments indicate that the resulting carbon$-$alumina particles are powerful adsorbents for the removal of Orange-II dye from water with maximum adsorption capacity of 210 mg/g. At the pH studied, Orange-II is expected to be adsorbed on the surface of aluminum oxide due to electrostatic attraction between the aluminum oxide shell and sulfonic acid groups of the Orange-II molecules. The fast Orange-II uptake is attributed to the combination of several factors, such as high specific surface area, large pore volume, unique rattle-type structure, and high adsorption affinity of the carbon core. Moreover, keeping pH in the range between 5 and 6 facilitated electrostatic interactions because the aluminum oxide surface was positively charged (isoelectric point of Al_2O_3 $\approx$ 9.0). The adsorption kinetics of Orange-II on the carbon$-$alumina samples studied followd the pseudosecond-order kinetic model. The equilibrium adsorption data are well represented by Langmuir isotherm equation.

The results described above clearly indicate that for adsorption of both heavy metals as well as organic polutants, the low surface area of HTC products does not constitute a problem, as it is the case for supercapacitors, but it is their functional groups which are the main driving force for the adsorption.

5.8 HTC Materials in Sensor Applications

The emerging applications of carbon nanomaterials in electrochemical sensors have led to production of CNT, Cyrstalline Diamond (CD) and diamond like carbons (DLC) in a large scale. It will soon be possible to take advantage of demanding properties of novel carbon-derived materials to develop a myriad of new applications for chemical sensing. Among these novel-carbon materials HTC material will play also an important role as they are cheap, have chemical functionalities and they can be easily hybridized with inorganic nanoparticles.

5.8.1 Chemical Sensors

Marken et al [233] recently reported the use of electrochemical properties of HTC materials with positive surface charge obtained in the form of a nanoaggregate *via* mild hydrothermal treatment of chitosan following the procedure initially reported by our group. [88] The hydrothermal carbon was deposited on ITO as a film and employed to bind redox active anions. The extremely low electrical conductivity of the hydrothermal nanocarbon limited the accuracy of specific binding capacity measurements and therefore a nanocomposite approach was investigated next. Negatively charged Emperor 2000 carbon nanoparticles were mixed in equal weight amounts with hydrothermal nanocarbon (180°C) and due to the strong interaction of positive and negative carbon robust composite films are formed on ITO electrodes upon solvent evaporation. The redox system chosen here for a survey of anion binding ability was the reduction of indigo carmine a hydrophobic double negatively charged dye molecule. When dipped into 1 mM indigo carmine in 0.1 M phosphate buffer pH 2, rinsed, and transferred into 0.1 M phosphate buffer pH 2 solution, a well-defined reversible reduction response was observed. With the negatively charged carbon nanoparticle additive, the hydrothermal nanocarbon deposit become electrically conducting and the peak currents for indigo carmine were enhanced. A comparison of indigo carmine binding for hydrothermal nanocarbons produced at 180°C, 200°C, and 230°C resulted in specific anion binding capacities of ca. 14 Cg^{-1}, 70 Cg^{-1}, and 20 Cg^{-1}, suggesting highest efficiency for materials produced at 200°C. Given a typical nitrogen content of 6.6% the availability of nitrogen as surface ammonium appears to be ca. 15%.

The honeycomb-like Ni@C composite nanostructures described in the adsorption section for the removal of Pb^{+2}, Cd^{+2} and Cu^{+2} showed also good electrochemical response in

0.1MNaOH, and could promote the oxidation of glucose. [226] This property was used in sensors for the detection of glucose (the detection limit is 0.9×10^{-6} M).

Sun et al, reported a simple, economical and green preparative strategy towards water-soluble, fluorescent carbon nanoparticles with a quantum yield of ~6.9% using the hydrothermal carbonisation of pomelo peel wastes as precursor. [234] The resulting nanoparticles were used as probes for a fluorescent Hg^{2+} detection, based on Hg^{2+} induced fluorescence quenching of carbon nanoparticles. This sensing system exhibited excellent sensitivity and selectivity toward Hg^{2+} and detection limit as low as 0.23 nM. The practical use of this newly designed system for the Hg^{2+} determination in lake water samples was successfully demonstrated.

The same authors prepared also fluorescent nitrogen-doped carbon nanoparticles using the hydrothermal carbonisation of grass as effective fluorescent sensing platform for label-free detection of Cu(II) Ions. The application of this method to detect Cu^{2+} ions in real water samples was also demonstrated successfully. [235]

Li et al reported on the production of a C@Ag nanocomposite using the hydrothermal carbonisation of glucose in the presence of $AgNO_3$ according to the publication of Sun et al. [236] The C@Ag composite were used for the modification of glassy carbon electrodes and used for the detection of tryptophan (Trp). [237] Trp is a vital constituent of proteins and indispensable in human nutrition for establishing and maintaining a positive nitrogen balance. Especially, the improper metabolization of Trp can create a waste product in the brain and cause hallucinations and delusions. Therefore, it is of great significance to develop a simple, accurate, rapid and inexpensive method for the determination of Trp. In the last decades, electrochemical techniques have been the most attractive methods for the determination of amino acids due to their favorable properties, such as high sensitivity, accuracy, easy operation and low cost. Silver has the highest electrical conductivity among all metals and is probably the most important material in plasmonics. However, Ag nanostructures are considered to be toxic and instable. It is well established that applying a coating of different material can eliminate the reactivity and toxicity of nano-Ag. The carbon shell cannot only protect Ag core but also contribute to the enhanced substrate accessibility and Trp-substrate interactions, while nano-Ag core can display good electrocatalytic activity to Trp at the same time. Under the optimum experimental conditions the oxidation peak current was linearly dependent on the Trp concentration in the range of 1.0×10^{-7} to 1.0×10^{-4} M with a detection

limit of 4.0 x 10^{-8} M (S/N = 3). In addition, the proposed electrode was applied for the determination of Trp concentration in real samples and satisfactory results were obtained. The technique offers enhanced sensitivity and may trigger the possibilities of the Ag@C nanocomposite towards diverse applications in biosensor and electroanalysis.

Using a similar methodology, Zhu et al fabricated monodisperse colloidal carbon nanospheres from glucose solution, and gold nanoparticles (AuNPs) using a rapid microwave-hydrothermal approach. The resulting AuNP/colloidal carbon nanosphere hybrid material (AuNP/C) have been characterised and used as a promising template for biomolecule immobilisation and biosensor fabrication because of their satisfactory chemical stability and good biocompatibility of AuNPs. In a particular publication, as an example, it was demonstrated that the as-prepared AuNP/C hybrid material can be conjugated with horseradish peroxidase-labeled antibody (HRP-Ab2) to fabricate HRP-Ab2-AuNP/C bioconjugates, which can then be used as a label for the sensitive detection of protein. [238] The amperometric immunosensor fabricated on a carbon nanotube-modified glass carbon electrode was very effective for antibody immobilisation. The approach provided a linear response range between 0.01 and 250 ng mL^{-1} with a detection limit of 5.6 pg mL^{-1}. The developed assay method was versatile, offered enhanced performances, and could be easily extended to other protein detection as well as DNA analysis.

5.8.2 Gas Sensors

As previously mentioned hydrothermal carbon spheres produced in the presence of various metal precursors can act as sacrificial templates from the production of a large variety of metal oxide hollow spheres. [36] Such porous inorganic metal oxides can also be used as gas sensors. When the ionic oxygen species (O^{2-}, O^-) fixed on the surface of the metal oxide react with reducing gas molecules, the trapped electrons release back the crystal grains, the potential barriers at the crystal grain boundary decrease and the resistance is dramatically increased. [239] For the porous hollow structures, the ionic oxygen can absorb onto both inner and outer surfaces and the detected gas molecules can penetrate through and react with them freely, thus increasing the sensitivity.

Using the HTC templating approach, Li et al. reported the synthesis of a WO_3 hollow spheres that showed certain selective response to organic gases. [240] They found that only with porous morphologies and small nanocrystals in the shell wall made the WO_3 hollow spheres exhibit

high sensitivity to organic gases at intermediate temperatures. The sensors were fabricated using thin films prepared from a powder suspension of as-synthesised WO_3 hollow spheres. They investigated the response of various gases, including alcohol, acetone, CS_2, NH_3, H_2S, benzene, petroleumether, acetonitrile, and so forth, using the commercial gas-sensing measurement system of HW-30. Table 5-5 summarises all of the response results. With increasing concentration of the gases, the sensitivity of the sensors sharply increased. The sensors were more sensitive to alcohol and acetone than to other organics. They showed much higher responses to H_2S and acetone than to alcohol, CS_2, and NH_3. At low concentrations, the sensor sensitivities to H_2S, acetone, alcohol, CS_2, and NH_3 were in descending sequence. The sensors had no response to benzene, petroleum ether, and acetonitrile when the gas species were at low concentrations. Only when the concentration of those gases was quite high (up to 500 ppm) did the sensors give a small response. The sensing mechanism of semiconducting oxide sensors usually is believed to be the surface conduction modulation by the absorbed gas molecules.

Table 5-5: Response Results (ppm) to Various Gases (taken with permission from [240])

Sensor	10	50	100	200	500	1000	2000	5000
H_2S	21.8	52.9	67.2					
NH3		1.5	1.7	2.14	2.89	3.15	3.57	4.38
alcohol		2.09	2.46	3.16	6.14	7.79	9.35	12.4
acetone		3.53	4.56	6.04	13.5	16	18.06	23.1
CS_2		1.56	1.83	2.54	5.06	7.2	11.02	14.3
benzene					2.56	3.06	3.43	4.06
CH_3CN					3.18	4.07	4.85	5.73
petroleum ether					2.72	2.92	3.67	4.91

That is, (1) the electrical properties of the semiconducting oxides showed dramatic changes with or without the adsorption of gas molecules (mechanism of sensitivity). (2) With different kinds of adsorbing gas molecules, the electrical properties would show different changes (mechanism of selectivity).

Similarly, using glucose-derived carbon spheres as template, Liu and co-workers [241] synthesised porous In_2O_3 hollow nanospheres that had a satisfactory response for ethanol, methanol, and other organic gases even at a very low concentration. Besides, the sensors had good recovery ability. After every measurement, the response curves returned back to the baseline very quickly.

Wu and co-workers reported on a hollow SnO_2 sphere structure that was very sensitive to $(C_2H_5)_3N$ and ethanol (7.1 for 1 ppb $(C_2H_5)_3N$ at 150 °C and 2.7 ppb for ethanol at 250°C, respectively) with a short response time, while the sensor based on SnO_2 nanoparticles alone showed much less response. [239]

Here we only provided a few examples where again the HTC carbons proved to have excellent properties for the production of various sensing devices. There is a lot of progress in the literature for using CNT in sensing devices. [242] As HTC is much cheaper, biomass based and easy to make, cumulated with its easy chemical modification, it is strongly believed that it will play an important role is sensing in the future.

5.9 Bioapplications

Recent years have witnessed unprecedented growth of research and applications in the area of nanoscience and nanotechnology. There is increasing optimism that nanotechnology, as applied to medicine, will bring significant advances in the diagnosis and disease treatment more precisely in fields such as drug delivery, diagnostics and bioimaginig and the production of biocompatible materials. [243] However, many challenges must be overcome if the application of nanotechnology is to realise the anticipated improved understanding of the patho-physiological basis of disease, bring more sophisticated diagnostic opportunities, and yield improved therapies.

Among the nanomaterials utilised for the above mentioned applications, carbon nanotubes and fullerenes have been studied in detail, although recent studies show that they exert adverse effects and toxicity. [244] [245] Therefore, new and non-toxic alternatives are still necessary in this filed.

Recently, scientists started also exploring favorable applications of HTC-based materials in medical applications such as for example bioimaging and drug delivery.

5.9.1 Drug Delivery

An ideal carrier for target drug delivery system should have three pre-requisites for their functions: (1) have target effects; (2) have sufficiently strong adsorptive effects for drugs to ensure transport of the drugs to the effect-relevant sites; and (3) be able to release the drugs into the effect-relevant sites. However, the requirement for new drug delivery systems is to improve the pharmacological profiles while decreasing the toxicological effects of the delivered drugs.

The transporting capabilities of carbon nanotubes combined with appropriate surface modifications and their unique physicochemical properties showed great promise to meet the above pre-requisites. [246] As previously mentioned, there are a lot of issues related to the biosaferty of carbon nanotubes. [247] [248] In addition they are expensive, difficult to make and based on fossil-derived precursors. Their functionalisation plays the most important role in drug delivery; however the functionalisation of carbon nanotubes is not a trivial task. [244] As described in Chapter 4 the functionalisation of HTC materials is straightforward. The HTC materials should possess low toxicity as they are derived from biomass. In addition, they are water dispersible and easy to upscale. They can be shaped either as hollow spheres, [20] aerogels [87] or nanotubes.[249] All these characteristics makes them very promising for applications in drug delivery.

Before going into such drug delivery applications using HTC, it is crucial to study the toxicity of these carbon materials. Thus Stanisheysky et al studied the toxicity of hydrothermal carbons of various sizes (from 10-500 nm) in vitro with a variety of cultured cell lines and found them non-toxic. [250] A size-dependent effect of HTC sphere addition on cell function has been observed. For example, HTC spheres can, in some cases, substantially increase interleukin-12 (IL-12) production by bone marrow dendritic cells. It has been further demonstrated that HTC spheres can be modified with fluorescent dye molecules or loaded with anti-cancer drugs for bioimaging or therapeutic purposes, respectively. The results of these tests and the strategies for the particle preparation and functionalisation for biomedical applications have been discussed.

Kundu and Selvi demonstrated that glucose-derived HTC carbon nanospheres are an emerging class of intracellular carriers. The surfaces of these spheres are highly functionalised and do not need any further modification. Besides, the intrinsic fluorescence property of

carbon nanospheres helps in tracking their cellular localisation without any additional fluorescent tags. The spheres were found to target the nucleus of the mammalian cells, causing no toxicity. Interestingly, the in vivo experiments showed that these nanospheres have an important ability to cross the blood-brain barrier and localise in the brain besides getting localised in the liver and the spleen. There is also evidence showing that they are continuously being removed from these tissues over time. Furthermore, these nanospheres were used as a carrier for the membrane-impermeable molecule CTPB (N-(4-chloro-3-trifluoromethylphenyl)-2-ethoxybenzamide), the only known small-molecule activator of histone acetyltransferase (HAT). Biochemical analyses such as Western blotting, immunohistochemistry, and gene expression analysis showed the induction of the hyperacetylation of histone acetyltransferase (HAT) p300 (autoacetylation) as well as histones both in vitro and in vivo and the activation of HAT-dependent transcription upon CTPB delivery. These results establish an alternative path for the activation of gene expression mediated by the induction of HAT activity instead of histone deacetylase (HDAC) inhibition. [251]

Using a combination of hydrothermal carbonisation and templating of mesoprous silica spheres,Shi et al prepared mesoporous carbon nanoparticles (MCN) with size below 200 nm and good water dispersibility. [252] They used MCM-48 type mesoporous silica as a hard template previously functionalised with amino groups in order to provide effective electrostatic attraction between positively charged $-NH_3^+$ ions on the pore surface of the solid template and negatively charged carbonaceous polysaccharide. Considering their biomedical application potentials, the uptake of the synthesised MCNs labeled with Rhodamine B (RhB@MCNs) by MCF-7 (human breast adenocarcinoma) cell lines was examined *via* TEM and confocal microscopy. These results suggest that those rhodamine molecules were really transported into the MCF-7 cells by MCN carriers. This further confirms that MCNs could be effectively internalised into living cells. In addition the authors have also evaluated the biocompability of the synthesised MCNs by incubating the MCF-7 cells with different concentrations of MCN suspensions in growth media. The results showed that no growth inhibition was present when the MCN concentration was below 5μg/mL even after 72h of incubation. This and other experiments not only with cancer cells but also with bifroblast cells showed that the cells survived with a concentration of 160 μg/ mL^{-1} and incubation time as long as 72h indicating the biocompatibility of HTC materials in vitro. As a

preliminary application study, the authors employed these well dispersed and uniform MCNs as hydrophobic anti-cancer drug carriers and took the representative chemotherapeutic drug camptothecin (CPT) as an example. It was found that drug loading capacity was as high as 17%, which was considerably higher than the reported loading amount using MSNs as carriers. The drug release profile is of great importance in applying the synthesised systems to a practical drug delivery. MCN delivery systems demonstrate no initial burst release but a sustained release feature with ca 80% CPT being released for as long as 5 days, as compared with the 99.8% free CPT released from the dialysis bag in 18 h. The sustained release characteristics are probably attributed to the slow drug diffusion from the mesochannels into the media solution. It should be noted that in the current investigation, DMSO was emplyed as a release medium, while no CPT was released when PBS solution was firstly used as a release medium presumably because free CPT is poorly soluble in the aqueous solution. This means that CPT will remain inside the mesochannels of MCNs in aqueous environment but release in the hydrophobic regions of the cell compartments once internalised by the cancer cells. These properties are vitally important for DDS because it allows the delivery vehicles to reach the cancer cells without significant leakage of the drug from the delivery system on their way into the physiological environment. To test the therapeutic effect of the synthesised CPT@MCNs, the authors studied cytotoxicity of the synthesised samples against MCF-7 cell lines. Growth inhibition and killing of cancer cells were observed when the cells were treated with either the suspension of CPT@MCNs or a DMSO solution of free CPT. In addition, the synthesised CPT@MCNs demonstrated a dose-dependent cytotoxic effect against MCF-7 cells and cytotoxicity was almost equivalent to the free drugs. Thus, the current synthesised MCNs can serve as effective carriers for CPT delivery and subsequently release in the cancer cells and can efficiently inhibit the growth of the cancer cell lines with minimal leakage into hydrophilic dispersion media.

In a different publication, Cui et al used a hydrothermal method to synthesise in one step magnetic $Fe_3O_4@C$ nanotubes (50–100 nm in diameter and several micrometres in length) *via* a hydrothermal rolling of grapheme oxide sheets .Thus, the authors synthesised $Fe_3O_4@C$ nanotubes with a high saturation magnetization of 24.5 emu g^{-1} (emu: electromagnetic units), good dispersability in water and no significant toxicity on healthy human gastric cells, GES-1. Moreover, these magnetic nanotubes exhibited a strong affinity to adriamycin with a high adsorption capacity (101.3 µg mg^{-1}) at room temperature. [253]

317

Nanocapsules are very attractive morphologies for drug/gene delivery due to their hollow and porous structures and facile surface functionalisation. The inner void can take up a large amount of drug while the open end pores serve as gates that control their release. Furthermore, hollow structures can be differently functionalised between the inner and the outer surface providing thus multifunctionality throughout sequential surface modifications. Most important, unlike spherical nanoparticles, the hollow structures can isolate drug/gene payload from the environment, they can transport the payloads safely into the cell without hydrolytic degradation of biological payload or aggregation of nanomaterials caused by many hydrophobic drug molecules during delivery into the cell. [254]

There are many possibilities to produce HTC hollow structures either by using various sacrificial templates such as alumina membranes, [249] latex and silica nanoparticles [20] or selenium cores. [255] However, despite the promising potential, the drug delivery capabilities of such hollow carbon nanostructures remained yet unexplored.

As mentioned previously the HTC nanospheres can be used as sacrificial templates to produce a wide variety of hollow metal oxide nanostructures, [36] with many applications in drug delivery. [256] We will only mention here only a few of these examples where the HTC materials mediated the formation of such inorganic hollow structures.

Hanagata and Kaskel prepared rattle-type $Fe_3O_4@SiO_2$ hollow mesoporous spheres with different particle sizes, different mesoporous shell thicknesses, and different levels of Fe_3O_4 content using HTC carbon spheres as templates. The effects of particle size and concentration of $Fe_3O_4@SiO_2$ hollow mesoporous spheres on cell uptake and their in vitro cytotoxicity to HeLa cells was evaluated. The spheres exhibited relatively fast cell uptake. Concentrations of up to 150 mu g mL^{-1} show no cytotoxicity, whereas a concentration of 200 mu g mL^{-1} showed a small amount of cytotoxicity after 48 h of incubation. Doxorubicin hydrochloride (DOX), an anticancer drug, was loaded into the $Fe_3O_4@SiO_2$ hollow mesoporous spheres, and the DOX-loaded spheres exhibit a higher cytotoxicity than free DOX. These results indicate the potential of $Fe_3O_4@SiO2$ hollow spheres for drug loading and delivery into cancer cells to induce cell death. [257] The situation might have been different if the authors would have used directly the carbon spheres loaded with magnetic F_3O_4 which are also possible to be synthesised as a rattle type structure.

Using the same HTC directed template route, You et al prepared well-dispersed Lu_2O_3 hollow spheres. The as-obtained $Lu_2O_3:Eu^{3+}$ hollow spheres exhibited red emission under UV excitation, and the $Lu_2O_3:Er^{3+}$ and $Lu_2O_3:Yb^{3+},Er^{3+}$ samples showed green and red emissions under 980 nm light excitation, respectively. The experimental result and analysis revealed that the two-photon process should be responsible for the upconversion luminescence of Yb^{3+} and Er^{3+} doped samples. The potential of such materials for drug delivery is discussed as a potential future application. [258]

Rare-earth (RE)-doped gadolinium oxide (Gd_2O_3) hollow nanospheres have been successfully prepared on a large scale *via* a template-directed method using hydrothermal carbon spheres as sacrificed templates. [259] SEM and TEM images revealed that these hollow-structured nanosphere spheres have the mesoporous shells composed of a large amount of uniform nanoparticles. By doping the RE ions (Yb/Er) into the Gd_2O_3 host matrix, these NPs emitted bright multicolored upconversion emissions that could be fine-tuned from green to red by adjusting the co-doped Yb/Er ratio under 980 nm NIR laser excitation. The possibility of using these upconversion nanoparticles for optical imaging in vivo has been demonstrated. It was also shown that these Gd_2O3 nanospheres brightened the T-1-weighted images and enhanced the r(1) relaxivity of water protons, which suggested that they could act as T-1 contrast agents for magnetic resonance (MR) imaging. Moreover, these hollow spheres could be used as drug delivery host carriers, and their drug storage/release properties were investigated using ibuprofen as the model drug. As a result, the so-prepared nanoscaled Gd_2O_3 hollow spheres bearing upconversion luminescence, MR imaging, and drug delivery capabilities could be potentially employed for simultaneous MR/fluorescent imaging and therapeutic applications.

5.9.2 Bioimaging

The development of targeted contrast agents such as fluorescent probes has made it possible to selectively view specific biological events and processes in both living and nonviable systems with improved detection limits, imaging modalities and engineered biomarker functionality. These contrast agents have become a mainstay in modern medicinal and biological research. The fabrication of luminescent-engineered nanoparticles (with multifunctional features) is expected to be integral to the development of next generation therapeutic, diagnosis and imaging technologies. Below I will present a few examples where

the hydrothermal carbonisation technology proved a powerful technique to produce small luminescent carbon nanoparticles.

Semiconductor quantum dots are the most widely used fluorescent nanoparticles; they have strong fluorescence, high photostability, broad excitation spectra, long fluorescence lifetime and narrow and tunable emission spectra. However, the release of heavy metals results in cytotoxicity and their environmental concerns limits its application. [260] Therefore, it is an urgent challenge to search for environmentally friendly fluorescent nanomaterials.

Fluorescent carbon nanoparticles (CNPs) were first produced by Sun and co-workers, [261] and shown to exhibit bright photoluminescence in the visible spectrum with either one- or two-photoexcitations. CNPs have drawn increasing attention due to their high photostability, tunable excitation and emission wavelength, excellent biocompatibility and environmental friendliness. [262] [263] [264] [265]

Shu Hong Yu synthesised biocompatible and green luminescent monodisperse silver/phenol formaldehyde resin core/shell spheres with controllable sizes, in the range of 180 to 1000 nm, and interesting architectures (centric, eccentric, and coenocytic core/shell spheres) *via* a facile one-step hydrothermal approach. These spheres can be used as bioimaging labels for human lung cancer H1299 cells. The results demonstrate that the nanoparticles can be internalised into cells and exhibit no cytotoxic effects, showing that such novel biocompatible core/shell structures can potentially be used as in vivo bioimaging labels. This facile one-pot polymerisation and encapsulation technique may provide a useful tool to synthesise other core/shell particles that have potential application in biotechnology. [266]

Liu at al, inspired by one publication from group our, [88] explored the one-step synthetic method to produce highly amino-functionalised fluorescent CNPs by hydrothermal carbonisation of chitosan at a mild temperature (180 °C). [267] The carbonisation and functionalisation will occur through the dehydration of chitosan, which leads to the formation of the fluorescent carbon nanoparticles (See Figure 5-22 a). HRTEM images (Figure 5-22b) clearly revealed that the CNPs were monodisperse and had a narrow size distribution of 4–7 nm in diameter. The optical properties of the CNPs showed a strong UV-vis absorption feature centered at 288 nm. The inset photograph of the CNPs solution is yellowish, transparent and clear under daylight and exhibited strong blue luminescence under UV excitation (Figure 5-22c). The fluorescence spectra are given in Figure 5-22d. The

phenomenon λ_{ex}-dependent λ_{em} is similar to that reported by Sun et al. and other groups; they concluded that surface passivation could produce defect sites on the surface of CNPs and the fluorescence emission arises from the radiative recombination of the excitons trapped by the defects. In this publication, the formation of CNPs and their surface functionalisation takes place simultaneously during the hydrothermal carbonisation process. The abundant functional groups, such as carboxyl acids and amines, can introduce different defects on the surface, acting as the excitation energy traps and leading to the different PL properties. The CNPs showed excellent photostability as the fluorescence intensity did not change, even after continuous excitation under a 150 W Xe lamp for several hours. The PL quantum yield (QY) of the upper brown CNPs was as high as 43% when excited at 360 nm which is much higher than most of the CNPs reported so far. To assess the prospects of the CNPs as a bioimaging material, A549 human lung adenocarcinoma cells were used to evaluate the cytocompatibility of the CNPs. The cell viability of the CNPs was determined by a methylthiazoleterazolium (MTT) assay. [268]

Assays of cell viability studies suggested that the CNPs demonstrate low cytotoxicity and were not found to pose any significant toxic effects. This result concluded that CNPs can be used in a high concentration for imaging or other biomedical applications. The CNPs were introduced into the A549 cells to show their bioimaging capabilities using a confocal microscopy test in vitro. The results showed that the photoluminescent spots were observed only in the cell membrane and cytoplasmic area of the cell but were very weak at the central region corresponding to the nucleus, which indicated that the CNPs easily penetrated into the cell but did not enter the nuclei (Figure 5-22e-g).
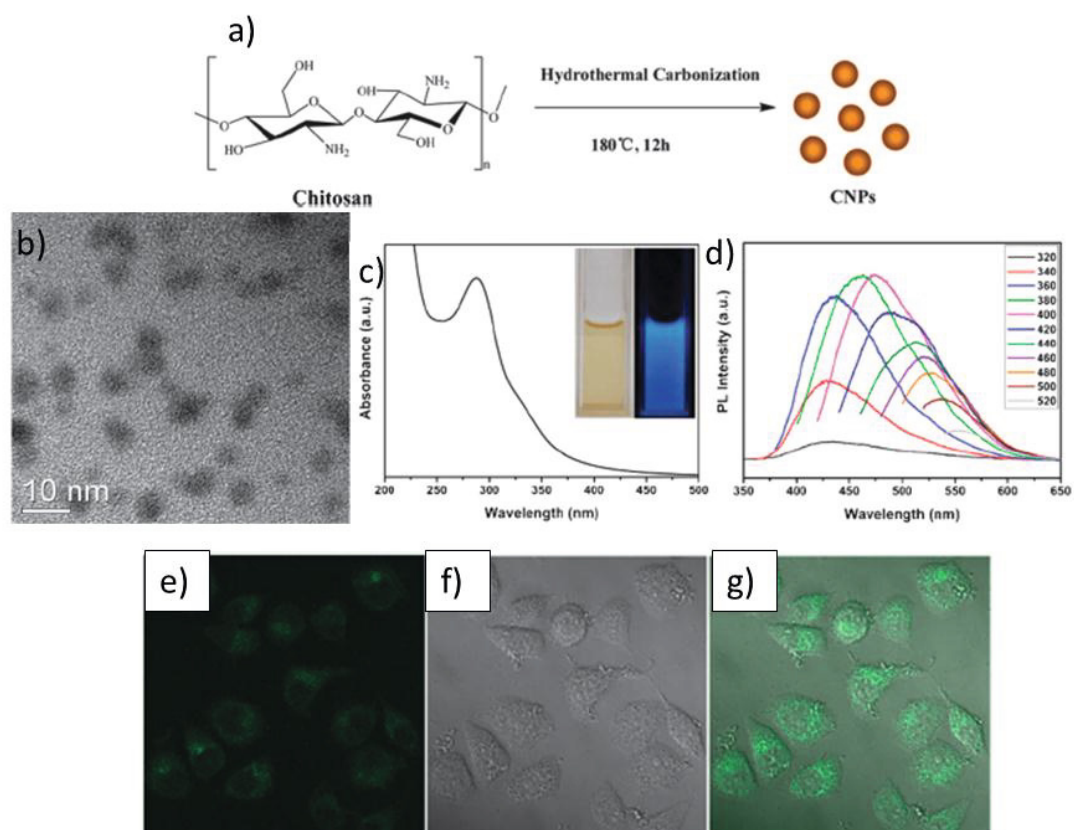
Figure 5-22: a) A schematic illustration of the prepration procedure of CNPs by hydrothermal carbonisation of chitosan; b) HRTEM image of CNPs; c) absorption spectra of the CNPs (inset: photograph of the samples excited by daylight and a 365 UV lamp); d) Emission spectra of the CNPs at different excitation wavelengths as indicated; e) confocal fluorescence microphotograph of A549 cells labeled with the CNPs at 37 1C for 24 h. (lex: 405 nm); f) A brightfield microphotograph of the cells; g) An overlay image of (e) and (f) (taken with permission from [267]).

It was thus demonstrated that it is possible to synthesise amino-functionalised fluorescent carbon nanoparticles as novel bioimaging agents by hydrothermal treatment of chitosan. No external surface passivation agent or further modification is necessary in their preparation. This green, cheap and convenient process represents a potential advance for large-scale production.

Highly fluorescent crystalline carbon nanoparticles (CNPs) can also be synthesised by one step microwave irradiation of carbohydrates with phosphoric acid at 100 W for 3 min 40 s. This method is also very simple, rapid and economical and hence can be used for large scale applications. The average particle sizes are 3 to 10 nm and they emit bright green fluorescence under the irradiation of UV-light. Therefore, the particles can be used as a unique material for bioimaging as well as drug delivery. To further increase the fluorescence

property of the synthetic carbon nanoparticles, they were simply functionalised using different organic dyes, such as fluorescein, rhodamine B and alpha-naphthylamine; the maximum fluorescence intensity was observed for the particles functionalised with fluorescein. It is very interesting to note that all of those compounds showed maximum fluorescence intensity at 225 nm excitation wavelength and for any excitation wavelength the peak positions were exactly at same the position as that of CNPs themselves, which was completely different from the individual precursors (dyes). All of the above compounds, including CNPs, have also been successfully introduced into the erythrocyte enriched fraction of healthy human blood cells with minimum cytotoxicity. [269]

Qu et al reported also a microwave method to convert carbohydrates into fluorescent carbon quantum dots without an additional passivation step. The secret was the presence of a tiny amount of an inorganic ion during the microwave treatment. Additionally, the photoluminescence intensity of the as-synthesised carbon dots did not change at the physiological and pathological pH range of 4.5–9.5 and showed no photobleaching. Furthermore, these carbon dots can enter into cells and can be used for photoluminescence-based cell-imaging applications. [270]

Although in their incipient phase, we do hope that throughout this subchapter dedicated to the bio-applications of HTC materials, researchers working in the field would become aware of the potential such materials hold for future drug delivery as well as bioimaging, either as carbon capsules, carbon nanostructures decorated with magnetic nanoparticles or fluorescent carbon quantum dots. They offer several advantages compared with the classical nanomaterials in terms of low cost precursors, easy synthesis and processing and plenty of functional groups.

5.10 Conclusions and Perspectives

The aim of this chapter was to show that despite their young age, HTC materials have already been used in a plethora of very important applications ranging from renewable energy to catalysis, photocatalysis, gas storage, water purification, sensing and medicine

The HTC materials have multiple advantages when compared with CNT, fullerenes and even graphene materials in terms of easy preparation, natural abundance of the precursors, CO_2 neutrality, up scaling, low temperature processes, water compatibility, functional surface

groups, to mention only a few. The wide range of applications speaks for themselves. The HTC materials can be applied with the same or even better performance in many important technological fields of the XXI century. Among these, CO_2 capture from plant material into carbon solids and soil enrichment were not discussed here. Information can be found in reference 5.

So far, mainly pure carbohydrates have been employed as precursors for the synthesis of such highly functional materials. Whilst still comparatively inexpensive and sustainable, the production of such high performance materials will be even more valuable if entirely based on (waste) biomass. Furthermore, we predict that heteroatom-doped carbon materials will continue to play an important role especially in fields such as adsorption, electrocatalysis or energy storage. HTC hybrid materials will continue to develop and expand into new and exciting nature-inspired self-assembled materials with future applications in catalysis, photocatalysis and sensors.

Especially in the field of biofuels production using the catalytic liquefaction of biomass, [130] the HTC carbons and hybrids with basic or acid character could play a particular role for various catalytic reactions when used as solid catalysts. It would of course be of great advantage to use biomass-derived carbons to catalyse the production of chemicals or biofuels out of biomass itself, providing a complete synergistic and holistic approach which could easily be integrated into future biorefinery schemes.

Another field where low cost porous HTC derived materials could be of great importance is chromatographic separations. Firstly the HTC materials can be shaped either as porous monoliths or porous spheres (see chapter 2). Secondly they possess surface functional groups just like silica based stationary phases. This offers them flexibility for various applications in either Hydrophilic Interactions Liquid Chromatography (HILIC), [271] or Reversed Phase Liquid Chromatography (RPLC). [272] Thirdly when post-carbonised at higher temperatures the carbons will become increasingly condensed, aromatised and hydrophobic, leading to stationary phase-like properties more commonly associated with porous graphitic carbon columns (PGCs). [273] The advantage of the HTC approach is the ability to moderate ''π'' stacking/delocalisation characteristics *via* carbonisation temperature selection—a material feature believed to determine the retention strength of such polar analytes. Such stationary phases are known for the efficient separations of polar analytes, including sugars and phenols

also derived from biomass. Obviously it will be extremely interesting to produce biomass derived stationary phases for separations of biomass components, filed of extreme importance for the production of biofueles.

We also need to mention that currently this technology is developed at a large production scale across Europe by a series of private companies (i.e. Carbon Solutions, AvaCO$_2$, Artec, Ingelia, Terranova-Energy and others). Their main interest in the commercialisation of such materials is biochar (CO$_2$ negative coal-like materials) for combustion, gasification and other thermal conversion processes for decentralised applications. The energy content of HTC chars has been measured to be between 25 and 35 MJ kg^{-1}, which is about 40% higher than that of the starting biomass precursor. [274] HTC material has also been evaluated in terms of energy densification and energy yield. The energy densification is the energy content of the char divided by the energy content of the feedstock, while the energy yield is defined as the char mass yield multiplied by the energy densification. Please see ref. [274] for more details. The energy densification was found to increase with the reaction temperature. Similarly (but to a lower extent), the energy densification increased with an increasing hold time at T = 255 °C. The total energy yield of the HTC char did not vary greatly over the sets of experiments conducted, ranging from 70 to 77%. Consistent with previous reports, the highest energy yield was observed at the lowest process temperature ratio, as confirmed also by our own experiments. [275]

Perhaps the most appealing large scale application of HTC process is, as suggested by Seifritz in a pioneering dissertation in 1993, [276] the fact that anthropogenic CO$_2$ emissions could be mitigated by converting biomass into charcoal. Thus, converting fast growing biomass (e.g. switch grass) into HTC, the CO$_2$ bound in the parent biomass will be no longer liberated *via* the photosynthesis process or atmospheric decomposition of the biomass residue, but bound to the final solid carbonaceous structure. This represents an efficient way of taking the CO$_2$ out of the carbon cycle and thus a solution for reducing the already alarming amounts of CO$_2$ present in the atmosphere, known to be responsible for the climate change. So ideally, low-tech biomass processing to hydrophilic porous carbon structures might therefore represent an efficient carbon sink that can be technologically accessed to handle significant parts of the CO$_2$ problem. The remaining question, however, is what can be done with such large amounts of HTC generated from a potential large scale process? The concept of biochar as an approach to carbon sequestration, as well as increasing soil fertility, raising agricultural productivity

and reducing pressure on forests, is receiving increasing attention over the past few years. [277] Several papers have been already published where the tremendous potential of HTC as a CO_2 negative solution for soil improvement is discussed.[5] However, before such a practical exercise of adding Mt of HTC to soil, the effects of HTC on earth cycles around the globe and especially on various crop productions need to be carefully investigated, particularly with regard to its toxicology. A complete understanding of the effect of HTC addition on soil and plant growth potentially expands on a hundred year's time frame and importantly needs to be performed in various ecosystem types around the world.

Besides being fast and simple, HTC also inherently requires wet starting products/biomass, as effective dehydration occurs only in the presence of water, thus removing the associated costs of precursor's drying and expanding the range of precursors to municipal wastes and sludge. In addition, the final carbon can be easily filtered off the reaction solution. This way, complicated drying schemes and costly isolation procedures can conceptually be avoided.

Whilst the (re)naissance of HTC technology is now effectively into its 10th year and many further developments and applications are to be still discovered, I hope to have provided a suitable introduction to the reader to the extremely broad scope and applicability of these exciting biomass-derived materials.

5.11 References

[1]   H. W. Kroto, J. R. Heath, S. C. O'Brien, R. F. Curl, R. E. Smalley, *Nature* **1985**, *318*, 162-163.
[2]   S. Iijima, *Nature* **1991**, *354*, 56-58.
[3]   aD. S. Su, R. Schloegl, *Chemsuschem*, *3*, 136-168; bL. R. Radovic, F. RodriguezReinoso, in *Chemistry and Physics of Carbon, Vol 25, Vol. 25* (Ed.: P. A. Thrower), **1997**, pp. 243-358.
[4]   A. H. Lu, G. P. Hao, Q. Sun, X. Q. Zhang, W. C. Li, *Macromol. Chem. Phys.* **2012**, *213*, 1107-1131.
[5]   aA. Gajic, H.-J. Koch, B. Maerlaender, *Zuckerindustrie* **2011**, *136*, 791-799; bC. George, M. Wagner, M. Kuecke, M. C. Rillig, *Applied Soil Ecology* **2012**, *59*, 68-72; cC. Kammann, S. Ratering, C. Eckhard, C. Mueller, *Journal of Environmental Quality* **2012**, *41*, 1052-1066; dM. C. Rillig, M. Wagner, M. Salem, P. M. Antunes, C. George, H.-G. Ramke, M.-M. Titirici, M. Antonietti, *Applied Soil Ecology* **2010**, *45*, 238-242; eF. Schuchardt, K.-D. Vorlop, *Landbauforschung* **2010**, *60*, 205-211; fS. Steinbeiss, G. Gleixner, M. Antonietti, *Soil Biology & Biochemistry* **2009**, *41*, 1301-1310.
[6]   aC. A. Nogueira, F. Delmas, *Hydrometallurgy* **1999**, *52*, 267-287; bA. K. Shukla, S. Venugopalan, B. Hariprakash, *Journal of Power Sources* **2001**, *100*, 125-148.
[7]   aN. Kuriyama, T. Sakai, H. Miyamura, I. Uehara, H. Ishikawa, T. Iwasaki, *Journal of Alloys and Compounds* **1993**, *202*, 183-197; bJ. J. Reilly, G. D. Adzic, J. R. Johnson,

T. Vogt, S. Mukerjee, J. McBreen, *Journal of Alloys and Compounds* **1999**, *293*, 569-582; cJ. Kleperis, G. Wojcik, A. Czerwinski, J. Skowronski, M. Kopczyk, M. Beltowska-Brzezinska, *Journal of Solid State Electrochemistry* **2001**, *5*, 229-249; dT. Sakai, A. Yuasa, H. Ishikawa, H. Miyamura, N. Kuriyama, *Journal of the Less-Common Metals* **1991**, *172*, 1194-1204.

[8]   aH. Li, Z. X. Wang, L. Q. Chen, X. J. Huang, *Adv. Mater.* **2009**, *21*, 4593-4607; bP. G. Bruce, B. Scrosati, J.-M. Tarascon, *Angewandte Chemie-International Edition* **2008**, *47*, 2930-2946; cM. Endo, C. Kim, K. Nishimura, T. Fujino, K. Miyashita, *Carbon* **2000**, *38*, 183-197; dB. Scrosati, J. Garche, *Journal of Power Sources* **2010**, *195*, 2419-2430; eJ. M. Tarascon, M. Armand, *Nature* **2001**, *414*, 359-367; fJ. B. Bates, N. J. Dudney, B. Neudecker, A. Ueda, C. D. Evans, *Solid State Ionics* **2000**, *135*, 33-45.

[9]   aC. K. Park, A. Kakirde, W. Ebner, V. Manivannan, C. Chai, D. J. Ihm, Y. J. Shim, *Journal of Power Sources* **2001**, *97-8*, 775-778; bK. Zaghib, M. Simoneau, M. Armand, M. Gauthier, *Journal of Power Sources* **1999**, *81–82*, 300-305.

[10]   aJ. Y. Song, Y. Y. Wang, C. C. Wan, *Journal of Power Sources* **1999**, *77*, 183-197; bF. Croce, G. B. Appetecchi, L. Persi, B. Scrosati, *Nature* **1998**, *394*, 456-458.

[11]   aN. Jayaprakash, J. Shen, S. S. Moganty, A. Corona, L. A. Archer, *Angewandte Chemie-International Edition* **2011**, *50*, 5904-5908; bY.-S. Su, A. Manthiram, *Electrochimica Acta* **2012**, *77*, 272-278; cX. Ji, L. F. Nazar, *Journal of Materials Chemistry* **2010**, *20*, 9821-9826; dM. Hagen, S. Doerfler, H. Althues, J. Tuebke, M. J. Hoffmann, S. Kaskel, K. Pinkwart, *Journal of Power Sources* **2012**, *213*, 239-248; eY. V. Mikhaylik, J. R. Akridge, *Journal of the Electrochemical Society* **2004**, *151*, A1969-A1976; fM. S. Song, S. C. Han, H. S. Kim, J. H. Kim, K. T. Kim, Y. M. Kang, H. J. Ahn, S. X. Dou, J. Y. Lee, *Journal of the Electrochemical Society* **2004**, *151*, A791-A795.

[12]   K. M. Abraham, R. D. Rauh, S. B. Brummer, *Electrochimica Acta* **1978**, *23*, 501-507.

[13]   aZ. L. Tao, L. N. Xu, X. L. Gou, J. Chen, H. T. Yuan, *Chemical Communications* **2004**, 2080-2081; bD. Aurbach, I. Weissman, Y. Gofer, E. Levi, *Chemical Record* **2003**, *3*, 61-73; cM. Morita, N. Yoshimoto, S. Yakushiji, M. Ishikawa, *Electrochemical and Solid State Letters* **2001**, *4*, A177-A179; dE. Levi, M. D. Levi, O. Chasid, D. Aurbach, *Journal of Electroceramics* **2009**, *22*, 13-19; eD. Aurbach, Y. Gofer, Z. Lu, A. Schechter, O. Chusid, H. Gizbar, Y. Cohen, V. Ashkenazi, M. Moshkovich, R. Turgeman, E. Levi, *Journal of Power Sources* **2001**, *97–98*, 28-32; fD. Aurbach, Z. Lu, A. Schechter, Y. Gofer, H. Gizbar, R. Turgeman, Y. Cohen, M. Moshkovich, E. Levi, *Nature* **2000**, *407*, 724-727.

[14]   aJ.-S. Lee, S. T. Kim, R. Cao, N.-S. Choi, M. Liu, K. T. Lee, J. Cho, *Advanced Energy Materials* **2011**, *1*, 34-50; bC. O. Laoire, S. Mukerjee, K. M. Abraham, E. J. Plichta, M. A. Hendrickson, *Journal of Physical Chemistry C* **2009**, *113*, 20127-20134; cG. Girishkumar, B. McCloskey, A. C. Luntz, S. Swanson, W. Wilcke, *Journal of Physical Chemistry Letters* **2010**, *1*, 2193-2203; dK. F. Blurton, A. F. Sammells, *Journal of Power Sources* **1979**, *4*, 263-279; eJ. Xiao, D. Wang, W. Xu, D. Wang, R. E. Williford, J. Liu, J.-G. Zhang, *Journal of the Electrochemical Society* **2010**, *157*, A487-A492; fI. Kowaluk, J. Read, M. Salomon, *Pure and Applied Chemistry* **2007**, *79*, 851-860.

[15]   M. Winter, J. O. Besenhard, *Lithium Ion Battery: Fundamentals and Performance*, Wiley-VCH, Weinheim, **1998**.

[16]   N. A. Kaskhedikar, J. Maier, *Adv. Mater.* **2009**, *21*, 2664-2680.

[17]   aH. Liu, L. J. Fu, H. P. Zhang, J. Gao, C. Li, Y. P. Wu, H. Q. Wu, *Electrochemical and Solid State Letters* **2006**, *9*, A529-A533; bC. Liu, H. M. Cheng, *Journal of Physics D-Applied Physics* **2005**, *38*, R231-R252.

[18]   Q. Wang, H. Li, L. Chen, X. Huang, *Carbon* **2001**, *39*, 2211-2214.

[19]   J. Hu, H. Li, X. J. Huang, *Solid State Ionics* **2005**, *176*, 1151-1159.

[20]   R. J. White, K. Tauer, M. Antonietti, M.-M. Titirici, *Journal of the American Chemical Society* **2010**, *132*, 17360-17363.

[21]   K. Tang, R. J. White, X. Mu, M.-M. Titirici, P. A. van Aken, J. Maier, *Chemsuschem* **2012**, *5*, 400-403.

[22]   V. Subramanian, H. Zhu, B. Wei, *The Journal of Physical Chemistry B* **2006**, *110*, 7178-7183.

[23]   X.-L. Wu , L.-L. Chen , S. Xin, Y.-X. Yin, Y.-G. Guo, Q.-S. Kong, Y.-Z. Xia, *Chemsuschem* **2010**, *3*, 703-707.

[24]   aC. L. Olson, J. Nelson, M. S. Islam, *The Journal of Physical Chemistry B* **2006**, *110*, 9995-10001; bS. Södergren, H. Siegbahn, H. Rensmo, H. Lindström, A. Hagfeldt, S.-E. Lindquist, *The Journal of Physical Chemistry B* **1997**, *101*, 3087-3090; cM. Wagemaker, G. J. Kearley, A. A. van Well, H. Mutka, F. M. Mulder, *Journal of the American Chemical Society* **2002**, *125*, 840-848.

[25]   G.-N. Zhu, Y.-G. Wang, Y.-Y. Xia, *Energy & Environmental Science* **2012**, *5*, 6652-6667.

[26]   Z. Yang, D. Choi, S. Kerisit, K. M. Rosso, D. Wang, J. Zhang, G. Graff, J. Liu, *Journal of Power Sources* **2009**, *192*, 588-598.

[27]   S. J. Park, Y. J. Kim, H. Lee, *Journal of Power Sources* **2011**, *196*, 5133-5137.

[28]   G. Xuefei, W. Chengyang, C. Mingming, W. Jiuzhou, Z. Jiaming, *Journal of Power Sources* **2012**, *214*, 107-112112.

[29]   aL. Y. Beaulieu, K. C. Hewitt, R. L. Turner, A. Bonakdarpour, A. A. Abdo, L. Christensen, K. W. Eberman, J. L. Krause, J. R. Dahn, *Journal of the Electrochemical Society* **2003**, *150*, A149-A156; bR. A. Huggins, *Journal of Power Sources* **1999**, *81*, 13-19.

[30]   Y.-S. Hu, R. Demir-Cakan, M.-M. Titirici, J.-O. Müller, R. Schlögl, M. Antonietti, J. Maier, *Angewandte Chemie International Edition* **2008**, *47*, 1645-1649.

[31]   R. Demir-Cakan, Y.-S. Hu, M. Antonietti, J. Maier, M.-M. Titirici, *Chemistry of Materials* **2008**, *20*, 1227-1229.

[32]   C. Kim, M. Noh, M. Choi, J. Cho, B. Park, *Chemistry of Materials* **2005**, *17*, 3297-3301.

[33]   H. X. Yang, J. F. Qian, Z. X. Chen, X. P. Ai, Y. L. Cao, *Journal of Physical Chemistry C* **2007**, *111*, 14067-14071.

[34]   W. Ping, D. Ning, Z. Hui, Y. Jingxue, Q. Yue, D. Yang, *Nanoscale* **2011**, *3*, 746-750750.

[35]   Y. Xiaoyuan, Y. Siyuan, Z. Baohua, S. Dan, D. Xianming, F. Yueping, L. Zesheng, W. Hongqiang, *Journal of Materials Chemistry* **2011**, *21*, 12295-1230212302.

[36]   M.-M. Titirici, M. Antonietti, A. Thomas, *Chemistry of Materials* **2006**, *18*, 3808-3812.

[37]   X. W. Lou, J. S. Chen, P. Chen, L. A. Archer, *Chemistry of Materials* **2009**, *21*, 2868-2874.

[38]   P. Poizot, S. Laruelle, S. Grugeon, L. Dupont, J. M. Tarascon, *Nature* **2000**, *407*, 496-499.

[39]   F. Badway, F. Cosandey, N. Pereira, G. G. Amatucci, *Journal of the Electrochemical Society* **2003**, *150*, A1318-A1327.

[40]   P. Poizot, S. Laruelle, S. Grugeon, J.-M. Tarascon, *Journal of the Electrochemical Society* **2002**, *149*, A1212-A1217.

[41]   X. H. Huang, J. P. Tu, C. Q. Zhang, X. T. Chen, Y. F. Yuan, H. M. Wu, *Electrochimica Acta* **2007**, *52*, 4177-4181.

[42]   J. Jiang, J. H. Zhu, R. M. Ding, Y. Y. Li, F. Wu, J. P. Liu, X. T. Huang, *Journal of Materials Chemistry* **2011**, *21*, 15969-15974.

[43]   Y. Qi, N. Du, H. Zhang, P. Wu, D. Yang, *Journal of Power Sources* **2011**, *196*, 10234-10239.

[44]   B. L. Ellis, K. T. Lee, L. F. Nazar, *Chemistry of Materials* **2010**, *22*, 691-714.

[45]   K. S. Nanjundaswamy, A. K. Padhi, J. B. Goodenough, S. Okada, H. Ohtsuka, H. Arai, J. Yamaki, *Solid State Ionics* **1996**, *92*, 1-10.

[46]   A. K. Padhi, K. S. Nanjundaswamy, C. Masquelier, S. Okada, J. B. Goodenough, *Journal of the Electrochemical Society* **1997**, *144*, 1609-1613.

[47]   A. K. Padhi, K. S. Nanjundaswamy, J. B. Goodenough, *Journal of the Electrochemical Society* **1997**, *144*, 1188-1194.

[48]   D. D. MacNeil, Z. Lu, Z. Chen, J. R. Dahn, *Journal of Power Sources* **2002**, *108*, 8-14.

[49]   C. Delacourt, C. Wurm, L. Laffont, J. B. Leriche, C. Masquelier, *Solid State Ionics* **2006**, *177*, 333-341.

[50]   S.-Y. Chung, J. T. Bloking, Y.-M. Chiang, *Nat Mater* **2002**, *1*, 123-128.

[51]   J. Popovic, R. Demir-Cakan, J. Tornow, M. Morcrette, D. S. Su, R. Schlögl, M. Antonietti, M.-M. Titirici, *Small* **2011**, *7*, 1127-1135.

[52]   S. Yoon, C. Liao, X.-G. Sun, C. A. Bridges, R. R. Unocic, J. Nanda, S. Dai, M. P. Paranthaman, *Journal of Materials Chemistry* **2012**, *22*, 4611-4614.

[53]   R. Dominko, *Journal of Power Sources* **2008**, *184*, 462-468.

[54]   V. Aravindan, K. Karthikeyan, J. W. Lee, S. Madhavi, Y. S. Lee, *Journal of Physics D-Applied Physics* **2011**, *44*.

[55]   B. L. Ellis, W. R. M. Makahnouk, Y. Makimura, K. T. and, L. F. Nazar, *Nat Mater* **2007**, *6*, 749-753.

[56]   S.-W. Kim, D.-H. Seo, X. Ma, G. Ceder, K. Kang, *Advanced Energy Materials* **2012**, *2*, 710-721.

[57]   V. L. Chevrier, G. Ceder, *Journal of the Electrochemical Society* **2011**, *158*, A1011-A1014.

[58]   V. Palomares, P. Serras, I. Villaluenga, K. B. Hueso, J. Carretero-Gonzalez, T. Rojo, *Energy & Environmental Science* **2012**, *5*, 5884-5901.

[59]   K. T. Lee, T. N. Ramesh, F. Nan, G. Botton, L. F. Nazar, *Chemistry of Materials* **2011**, *23*, 3593-3600.

[60]   Z. Jian, L. Zhao, H. Pan, Y.-S. Hu, H. Li, W. Chen, L. Chen, *Electrochemistry Communications* **2012**, *14*, 86-89.

[61]   J. Sangster, *Journal of Phase Equilibria and Diffusion* **2007**, *28*, 571-579.

[62]   X. Xin, M. N. Obrovac, J. R. Dahn, *Electrochemical and Solid-State Letters* **2011**, *14*, A130-133.

[63]   aD. A. Stevens, J. R. Dahn, *Journal of the Electrochemical Society* **2000**, *147*, 1271-1273; bD. A. Stevens, J. R. Dahn, *Journal of the Electrochemical Society* **2001**, *148*, A803-A811.

[64]   R. Alcantara, J. M. Jimenez-Mateos, P. Lavela, J. L. Tirado, *Electrochemistry Communications* **2001**, *3*, 639-642.

[65]   S. Wenzel, T. Hara, J. Janek, P. Adelhelm, *Energy & Environmental Science* **2011**, *4*, 3342-3345.

[66] S. Komaba, W. Murata, T. Ishikawa, N. Yabuuchi, T. Ozeki, T. Nakayama, A. Ogata, K. Gotoh, K. Fujiwara, *Advanced Functional Materials* **2011**, *21*, 3859-3867.

[67] J. Qian, Y. Chen, L. Wu, Y. Cao, X. Ai, H. Yang, *Chemical Communications* **2012**, *48*, 7070-7072.

[68] aB. L. Ellis, L. F. Nazar, *Current Opinion in Solid State & Materials Science* **2012**, *16*, 168-177; bY. Cao, L. Xiao, M. L. Sushko, W. Wang, B. Schwenzer, J. Xiao, Z. Nie, L. V. Saraf, Z. Yang, J. Liu, *Nano Letters* **2012**, *12*, 3783-3787.

[69] T. Kun, F. Lijun, R. J. White, Y. Linghui, M. M. Titirici, M. Antonietti, J. Maier, *Advanced Energy Materials* **2012**, *2*, 873-877.

[70] H. Yan , X. Huang , H. Li , L. Chen, *Solid State Ionics* **1998**, *11*, 113.

[71] P. G. Bruce, S. A. Freunberger, L. J. Hardwick, J. M. Tarascon, *Nat. Mater.* **2012**, *11*, 19-29.

[72] R. D. Rauh, K. M. Abraham, G. F. Pearson, J. K. Surprenant, S. B. Brummer, *Journal of the Electrochemical Society* **1979**, *126*, 523-527.

[73] H. Yamin, A. Gorenshtein, J. Penciner, Y. Sternberg, E. Peled, *Journal of the Electrochemical Society* **1988**, *135*, 1045-1048.

[74] X. Ji, K. T. Lee, L. F. Nazar, *Nat. Mater.* **2009**, *8*, 500-506.

[75] S. Jun, S. H. Joo, R. Ryoo, M. Kruk, M. Jaroniec, Z. Liu, T. Ohsuna, O. Terasaki, *Journal of the American Chemical Society* **2000**, *122*, 10712-10713.

[76] aY. S. H. L. J. Zhi, B. El Hamaoui, X. Wang, I. Lieberwirth, U. Kolb, J., K. M. Maier, *Adv. Mater.* **2008**, *20*, 1727; bC. Liang, N. J. Dudney, J. Y. Howe, *Chemistry of Materials* **2009**, *21*, 4724-4730.

[77] Nicolas Brun, Ken Sakaushi, Linghui Yu, Lars Giebeler, Jürgen Eckert, M. M. Titirici, *Energy & Environmental Science* **2012**, *submitted*.

[78] J. Xiulei, S. Evers, R. Black, L. F. Nazar, *Nat. Commun.* **2011**, *2*, 325 (327 pp.)-325 (327 pp.)325 (327 pp.).

[79] B. E. Conway, *Electrochemical supercapacitors: Scientific fundamentals and technological applications*, Kluwer Academic New York, **1999**.

[80] M. J. Bleda-Martínez, J. A. Maciá-Agulló, D. Lozano-Castelló, E. Morallón, D. Cazorla-Amorós, A. Linares-Solano, *Carbon* **2005**, *43*, 2677-2684.

[81] G. Lota, B. Grzyb, H. Machnikowska, J. Machnikowski, E. Frackowiak, *Chemical Physics Letters* **2005**, *404*, 53-58.

[82] W. Li, D. Chen, Z. Li, Y. Shi, Y. Wan, G. Wang, Z. Jiang, D. Zhao, *Carbon* **2007**, *45*, 1757-1763.

[83] M. Seredych, D. Hulicova-Jurcakova, G. Q. Lu, T. J. Bandosz, *Carbon* **2008**, *46*, 1475-1488.

[84] M. Sevilla, A. B. Fuertes, *Chemistry – A European Journal* **2009**, *15*, 4195-4203.

[85] M. Sevilla, A. B. Fuertes, *Carbon* **2009**, *47*, 2281-2289.

[86] N. Baccile, M. Antonietti, M.-M. Titirici, *ChemSusChem* **2010**, *3*, 246-253.

[87] R. J. White, N. Yoshizawa, M. Antonietti, M.-M. Titirici, *Green Chemistry* **2011**, *13*, 2428-2434.

[88] L. Zhao, N. Baccile, S. Gross, Y. Zhang, W. Wei, Y. Sun, M. Antonietti, M.-M. Titirici, *Carbon* **2010**, *48*, 3778-3787.

[89] L. Wei, M. Sevilla, A. B. Fuertes, R. Mokaya, G. Yushin, *Advanced Energy Materials* **2011**, n/a-n/a.

[90] L. Wang, Y. Guo, B. Zou, C. Rong, X. Ma, Y. Qu, Y. Li, Z. Wang, *Bioresource Technology* **2011**, *102*, 1947-1950.

[91] D. Lozano-Castelló, D. Cazorla-Amorós, A. Linares-Solano, *Fuel Processing Technology* **2002**, *77–78*, 325-330.

[92]   M. Molina-Sabio, F. Rodríguez-Reinoso, *Colloids and Surfaces A: Physicochemical and Engineering Aspects* **2004**, *241*, 15-25.

[93]   E. Raymundo-Piñero, K. Kierzek, J. Machnikowski, F. Béguin, *Carbon* **2006**, *44*, 2498-2507.

[94]   C. Largeot, C. Portet, J. Chmiola, P.-L. Taberna, Y. Gogotsi, P. Simon, *Journal of the American Chemical Society* **2008**, *130*, 2730-+.

[95]   L. Zhao, L.-Z. Fan, M.-Q. Zhou, H. Guan, S. Qiao, M. Antonietti, M.-M. Titirici, *Adv. Mater.* **2010**, *22*, 5202-+.

[96]   T. C. Drage, A. Arenillas, K. M. Smith, C. Pevida, S. Piippo, C. E. Snape, *Fuel* **2007**, *86*, 22-31.

[97]   M. Sevilla, R. Mokaya, A. B. Fuertes, *Energy & Environmental Science* **2011**, *4*, 2930-2936.

[98]   E. Frackowiak, G. Lota, J. Machnikowski, C. Vix-Guterl, F. Béguin, *Electrochimica Acta* **2006**, *51*, 2209-2214.

[99]   aH. Zhu, X. Wang, F. Yang, X. Yang, *Adv. Mater.* **2011**, *23*, 2745-2748; bS. M. Z. H. S. Zhou, M. Hibino, I. Honma, M. Ichihara, *Adv. Mater* **2002**, *15*, 2107.

[100] E. Raymundo-Piñero, F. Leroux, F. Béguin, *Adv. Mater.* **2006**, *18*, 1877-1882.

[101] H. Y. Lee, J. B. Goodenough, *Journal of Solid State Chemistry* **1999**, *144*, 220-223.

[102] S. Chen, J. Zhu, X. Wu, Q. Han, X. Wang, *ACS Nano* **2010**, *4*, 2822-2830.

[103] J. T. Zhang, J. Z. Ma, J. W. Jiang, X. S. Zhao, *J. Mater. Res.* **2010**, *25*, 1476-1484.

[104] J. Dupont, R. F. de Souza, P. A. Z. Suarez, *Chemical Reviews* **2002**, *102*, 3667-3691.

[105] A. P. Abbott, D. Boothby, G. Capper, D. L. Davies, R. K. Rasheed, *Journal of the American Chemical Society* **2004**, *126*, 9142-9147.

[106] D. R. Rolison, *Science* **2003**, *299*, 1698-1701.

[107] P. Serp, M. Corrias, P. Kalck, *Appl. Catal. A-Gen.* **2003**, *253*, 337-358.

[108] Y. Yang, K. Chiang, N. Burke, *Catalysis Today* **2011**, *178*, 197-205.

[109] P. Makowski, R. Demir Cakan, M. Antonietti, F. Goettmann, M.-M. Titirici, *Chemical Communications* **2008**, 999-1001.

[110] R. J. White, R. Luque, V. L. Budarin, J. H. Clark, D. J. Macquarrie, *Chemical Society Reviews* **2009**, *38*, 481-494.

[111] D. Astruc, F. Lu, J. R. Aranzaes, *Angewandte Chemie-International Edition* **2005**, *44*, 7852-7872.

[112] I. Fechete, Y. Wang, J. C. Vedrine, *Catalysis Today* **2012**, *189*, 2-27.

[113] S. Y. Wu, Y. S. Ding, X. M. Zhang, H. O. Tang, L. Chen, B. X. Li, *Journal of Solid State Chemistry* **2008**, *181*, 2171-2177.

[114] G. Yu, B. Sun, Y. Pei, S. Xie, S. Yan, M. Qiao, K. Fan, X. Zhang, B. Zong, *Journal of the American Chemical Society* **2010**, *132*, 935-+.

[115] R. J. White, M. Antonietti, M.-M. Titirici, *Journal of Materials Chemistry* **2009**, *19*, 8645-8650.

[116] Mario Soorholtz, Robin J. White, Tobias Zimmermann, Maria-Magdalena Titirici, Markus Antonietti, R. Palkovits, F. Schüth, *Chem Commun* **2012**, *ASAP*.

[117] R. A. Periana, D. J. Taube, S. Gamble, H. Taube, T. Satoh, H. Fujii, *Science* **1998**, *280*, 560-564.

[118] aH. Arakawa, M. Aresta, J. N. Armor, M. A. Barteau, E. J. Beckman, A. T. Bell, J. E. Bercaw, C. Creutz, E. Dinjus, D. A. Dixon, K. Domen, D. L. DuBois, J. Eckert, E. Fujita, D. H. Gibson, W. A. Goddard, D. W. Goodman, J. Keller, G. J. Kubas, H. H. Kung, J. E. Lyons, L. E. Manzer, T. J. Marks, K. Morokuma, K. M. Nicholas, R. Periana, L. Que, J. Rostrup-Nielson, W. M. H. Sachtler, L. D. Schmidt, A. Sen, G. A. Somorjai, P. C. Stair, B. R. Stults, W. Tumas, *Chemical Reviews* **2001**, *101*, 953-996;

bJ. H. Lunsford, *Catalysis Today* **2000**, *63*, 165-174; cR. H. Crabtree, *J. Chem. Soc.-Dalton Trans.* **2001**, 2437-2450; dM. C. Alvarez-Galvan, N. Mota, M. Ojeda, S. Rojas, R. M. Navarro, J. L. G. Fierro, *Catalysis Today* **2011**, *171*, 15-23.

[119]   aA. E. Shilov, G. B. Shul'pin, *Chemical Reviews* **1997**, *97*, 2879-2932; bA. E. Shilov, G. B. Shul'pin, *Activation and catalytic reactions of saturated hydrocarbons in the presence of metal complexes, Vol. 21*, Kluwer, Dordrecht, **2000**; cJ. A. Labinger, J. E. Bercaw, *Nature* **2002**, *417*, 507-514.

[120]   aD. Wolf, *Angewandte Chemie-International Edition* **1998**, *37*, 3351-3353; bB. L. Conley, W. J. Tenn, K. J. H. Young, S. Ganesh, S. Meier, V. Ziatdinov, O. Mironov, J. Oxgaard, J. Gonzales, W. A. Goddard, R. A. Periana, *Methane Functionalization*, Wiley-VCH Verlag GmbH & Co. KGaA, **2006**.

[121]   R. Palkovits, M. Antonietti, P. Kuhn, A. Thomas, F. Schüth, *Angew. Chem. Int. Ed.* **2009**, *48*, 6909-6912.

[122]   H. S. Qian, M. Antonietti, S. H. Yu, *Advanced Functional Materials* **2007**, *17*, 637-643.

[123]   X. Xiang, L. Bai, F. Li, *Aiche Journal* **2010**, *56*, 2934-2945.

[124]   J. Ming, R. X. Liu, G. F. Liang, H. Y. Cheng, Y. C. Yu, F. Y. Zhao, *Journal of Materials Chemistry* **2011**, *21*, 10929-10934.

[125]   C. Sanchez, B. Julian, P. Belleville, M. Popall, *Journal of Materials Chemistry* **2005**, *15*, 3559-3592.

[126]   C. Sanchez, C. Boissière, D. Grosso, C. Laberty, L. Nicole, *Chemistry of Materials* **2008**, *20*, 682-737.

[127]   H. Kaper, A. Grandjean, C. Weidenthaler, F. Schuth, F. Goettmann, *Chem.-Eur. J.* **2012**, *18*, 4099-4106.

[128]   R. Demir-Cakan, N. Baccile, M. Antonietti, M.-M. Titirici, *Chemistry of Materials* **2009**, *21*, 484-490.

[129]   R. Demir-Cakan, P. Makowski, M. Antonietti, F. Goettmann, M. M. Titirici, *Catalysis Today* **2010**, *150*, 115-118.

[130]   J. N. Chheda, G. W. Huber, J. A. Dumesic, *Angewandte Chemie-International Edition* **2007**, *46*, 7164-7183.

[131]   J. I. J. A. Melero, G. Morales, *Green Chemistry* **2009**, *11*, 1285-1308.

[132]   J. A. Macia-Agullo, M. Sevilla, M. A. Diez, A. B. Fuertes, *Chemsuschem* **2010**, *3*, 1352-1354.

[133]   X. Huiquan, G. Yingxue, L. Xuezheng, Q. Chenze, *Journal of Solid State Chemistry* **2010**, *183*, 1721-17251725.

[134]   N. D. Berge, K. S. Ro, J. Mao, J. R. V. Flora, M. A. Chappell, S. Bae, *Environmental Science & Technology* **2011**, *45*, 5696-5703.

[135]   R. J. White, V. Budarin, R. Luque, J. H. Clark, D. J. Macquarrie, *Chemical Society Reviews* **2009**, *38*, 3401-3418.

[136]   aV. L. Budarin, J. H. Clark, R. Luque, D. J. Macquarrie, *Chemical Communications* **2007**, 634-636; bR. Luque, L. Herrero-Davila, J. M. Campelo, J. H. Clark, J. M. Hidalgo, D. Luna, J. M. Marinas, A. A. Romero, *Energy & Environmental Science* **2008**, *1*, 542-564; cV. L. Budarin, J. H. Clark, R. Luque, D. J. Macquarrie, R. J. White, *Green Chemistry* **2008**, *10*, 382-387; dM. J. Gronnow, R. Luque, D. J. Macquarrie, J. H. Clark, *Green Chemistry* **2005**, *7*, 552-557.

[137]   B. C. H. Steele, A. Heinzel, *Nature* **2001**, *414*, 345-352.

[138]   H. S. Liu, C. J. Song, L. Zhang, J. J. Zhang, H. J. Wang, D. P. Wilkinson, *Journal of Power Sources* **2006**, *155*, 95-110.

[139]   M. Sevilla, A. B. Fuertes, *Chemical Physics Letters* **2010**, *490*, 63-68.

[140] R. Yang, X. Qiu, H. Zhang, J. Li, W. Zhu, Z. Wang, X. Huang, L. Chen, *Carbon* **2005**, *43*, 11-16.

[141] P. Kim, J. Joo, W. Kim, J. Kim, I. Song, J. Yi, *Catalysis Letters* **2006**, *112*, 213-218.

[142] M. Sevilla, G. Lota, A. B. Fuertes, *Journal of Power Sources* **2007**, *171*, 546-551.

[143] M. Sevilla, C. Sanchís, T. Valdés-Solís, E. Morallón, A. B. Fuertes, *Electrochimica Acta* **2009**, *54*, 2234-2238.

[144] J. B. Joo, Y. J. Kim, W. Kim, P. Kim, J. Yi, *Catalysis Communications* **2008**, *10*, 267-271.

[145] Z. Wen, Q. Wang, J. Li, *Advanced Functional Materials* **2008**, *18*, 959-964.

[146] Z. Wen, J. Liu, J. Li, *Adv. Mater.* **2008**, *20*, 743-747.

[147] Z. Wen, Q. Wang, Q. Zhang, J. Li, *Electrochemistry Communications* **2007**, *9*, 1867-1872.

[148] M. Marques Tusi, N. Soares de Oliveira Polanco, M. Brandalise, O. Vercino Correa, J. C. Villalba, F. Jacó Anaissi, A. Oliveira Neto, E. V. Spinacé, *Int. J. Electrochem. Sci.* **2011**, *6*, 484.

[149] C. Xu, L. Cheng, P. Shen, Y. Liu, *Electrochemistry Communications* **2007**, *9*, 997-1001.

[150] P. Ferrin, M. Mavrikakis, *Journal of the American Chemical Society* **2009**, *131*, 14381-14389.

[151] J. Zeng, J. Y. Lee, *International Journal of Hydrogen Energy* **2007**, *32*, 4389-4396.

[152] F. G. Welsch, K. Stowe, W. F. Maier, *ACS Comb. Sci.* **2011**, *13*, 518-529.

[153] R. Jasinski, *Nature* **1964**, *201*, 1212-1213.

[154] B. Wang, *Journal of Power Sources* **2005**, *152*, 1-15.

[155] U. I. Koslowski, I. Abs-Wurmbach, S. Fiechter, P. Bogdanoff, *The Journal of Physical Chemistry C* **2008**, *112*, 15356-15366.

[156] aH. Wang, T. Maiyalagan, X. Wang, *Acs Catalysis* **2012**, *2*, 781-794; bD. S. Su, J. Zhang, B. Frank, A. Thomas, X. Wang, J. Paraknowitsch, R. Schloegl, *Chemsuschem* **2010**, *3*, 169-180; cY. Zhou, K. Neyerlin, T. S. Olson, S. Pylypenko, J. Bult, H. N. Dinh, T. Gennett, Z. Shao, R. O'Hayre, *Energy & Environmental Science* **2010**, *3*, 1437-1446; dJ. P. Paraknowitsch, A. Thomas, *Macromol. Chem. Phys.* **2012**, *213*, 1132-1145.

[157] T. Onodera, S. Suzuki, T. Mizukami, H. Kanzaki, *Journal of Power Sources* **2011**, *196*, 7994-7999.

[158] S.-H. Liu, J.-R. Wu, *International Journal of Hydrogen Energy* **2011**, *36*, 87-93.

[159] K. Gong, F. Du, Z. Xia, M. Durstock, L. Dai, *Science* **2009**, *323*, 760-764.

[160] M. Bron, S. Fiechter, M. Hilgendorff, P. Bogdanoff, *Journal of Applied Electrochemistry* **2002**, *32*, 211-216.

[161] S. H. Joo, S. J. Choi, I. Oh, J. Kwak, Z. Liu, O. Terasaki, R. Ryoo, *Nature* **2001**, *412*, 169-172.

[162] J.-i. Ozaki, T. Anahara, N. Kimura, A. Oya, *Carbon* **2006**, *44*, 3358-3361.

[163] N. Baccile, G. Laurent, C. Coelho, F. Babonneau, L. Zhao, M.-M. Titirici, *The Journal of Physical Chemistry C* **2011**, *115*, 8976-8982.

[164] S.-A. Wohlgemuth, R. J. White, M.-G. Willinger, M.-M. Titirici, M. Antonietti, *Green Chemistry* **2012**, *14*, 1515-1523.

[165] M. Sevilla, A. B. Fuertes, *Microporous Mesoporous Mat.* **2012**, *158*, 318-323.

[166] C. Petit, G. W. Peterson, J. Mahle, T. J. Bandosz, *Carbon* **2010**, *48*, 1779-1787.

[167] M. Seredych, M. Khine, T. J. Bandosz, *Chemsuschem* **2011**, *4*, 139-147.

[168] J. P. Paraknowitsch, A. Thomas, J. Schmidt, *Chemical Communications* **2011**, *47*, 8283-8285.

[169] S. Glenis, A. J. Nelson, M. M. Labes, *J. Appl. Phys.* **1999**, *86*, 4464-4466.

[170] T. Cui, R. Lv, Z.-h. Huang, F. Kang, K. Wang, D. Wu, *Nanoscale Research Letters* **2011**, *6*, 77.

[171] C. H. Choi, S. H. Park, S. I. Woo, *Green Chemistry* **2011**, *13*, 406-412.

[172] S.-A. Wohlgemuth, F. Vilela, M.-M. Titirici, M. Antonietti, *Green Chemistry* **2012**, *14*, 741-749.

[173] W. S. Baker, J. W. Long, R. M. Stroud, D. R. Rolison, *Journal of Non-Crystalline Solids* **2004**, *350*, 80-87.

[174] Y. Shao, J. Sui, G. Yin, Y. Gao, *Applied Catalysis B: Environmental* **2008**, *79*, 89-99.

[175] H. Jin, H. Zhang, H. Zhong, J. Zhang, *Energy & Environmental Science* **2011**, *4*, 3389-3394.

[176] Yang, Xu, A. Tomita, T. Kyotani, *Chemistry of Materials* **2005**, *17*, 2940-2945.

[177] P. H. Matter, L. Zhang, U. S. Ozkan, *Journal of Catalysis* **2006**, *239*, 83-96.

[178] Z. Luo, S. Lim, Z. Tian, J. Shang, L. Lai, B. MacDonald, C. Fu, Z. Shen, T. Yu, J. Lin, *Journal of Materials Chemistry* **2011**, *21*, 8038-8044.

[179] R. Liu, D. Wu, X. Feng, K. Müllen, *Angewandte Chemie International Edition* **2010**, *49*, 2565-2569.

[180] V. V. Strelko, V. S. Kuts, P. A. Thrower, *Carbon* **2000**, *38*, 1499-1503.

[181] R. A. Sidik, A. B. Anderson, N. P. Subramanian, S. P. Kumaraguru, B. N. Popov, *The Journal of Physical Chemistry B* **2006**, *110*, 1787-1793.

[182] J. C. Slater, *The Journal of Chemical Physics* **1964**, *41*, 3199-3204.

[183] E. Chamorro, A. Toro-Labbe, P. Fuentealba, *The Journal of Physical Chemistry A* **2002**, *106*, 3891-3898.

[184] S. Scheiner, L. D. Bigham, *The Journal of Chemical Physics* **1985**, *82*, 3316-3321.

[185] Z. Yang, Z. Yao, G. Li, G. Fang, H. Nie, Z. Liu, X. Zhou, X. a. Chen, S. Huang, *ACS Nano* **2011**, *6*, 205-211.

[186] A. Fujishima, K. Honda, *Nature* **1972**, *238*, 37-38.

[187] G. W. Crabtree, N. S. Lewis, *Physics Today* **2007**, *60*, 37-42.

[188] R. Asahi, T. Morikawa, T. Ohwaki, K. Aoki, Y. Taga, *Science* **2001**, *293*, 269-271.

[189] M. A. Fox, M. T. Dulay, *Chemical Reviews* **1993**, *93*, 341-357.

[190] S. U. M. Khan, M. Al-Shahry, W. B. Ingler, *Science* **2002**, *297*, 2243-2245.

[191] K. Vinodgopal, D. E. Wynkoop, P. V. Kamat, *Environmental Science & Technology* **1996**, *30*, 1660-1666.

[192] S. Sakthivel, M. Janczarek, H. Kisch, *The Journal of Physical Chemistry B* **2004**, *108*, 19384-19387.

[193] S. In, A. Orlov, R. Berg, F. García, S. Pedrosa-Jimenez, M. S. Tikhov, D. S. Wright, R. M. Lambert, *Journal of the American Chemical Society* **2007**, *129*, 13790-13791.

[194] T. Ohno, T. Tsubota, K. Nishijima, Z. Miyamoto, *Chemistry Letters* **2004**, *33*, 750-751.

[195] L. Zhao, X. Chen, X. Wang, Y. Zhang, W. Wei, Y. Sun, M. Antonietti, M.-M. Titirici, *Adv. Mater.* **2010**, *22*, 3317-3321.

[196] J. Zhong, F. Chen, J. Zhang, *The Journal of Physical Chemistry C* **2009**, *114*, 933-939.

[197] Y. Zhang, P. Zhang, Y. Huo, D. Zhang, G. Li, H. Li, *Applied Catalysis B: Environmental* **2012**, *115–116*, 236-244.

[198] J. Zhuang, Q. Tian, H. Zhou, Q. Liu, P. Liu, H. Zhong, *Journal of Materials Chemistry* **2012**, *22*, 7036-7042.

[199] P. Zhang, C. Shao, Z. Zhang, M. Zhang, J. Mu, Z. Guo, Y. Sun, Y. Liu, *Journal of Materials Chemistry* **2011**, *21*, 17746-17753.

[200] J.-W. Shi, X. Zong, X. Wu, H.-J. Cui, B. Xu, L. Wang, M.-L. Fu, *ChemCatChem* **2012**, *4*, 488-491.

[201] P. Zhang, C. Shao, M. Zhang, Z. Guo, J. Mu, Z. Zhang, X. Zhang, P. Liang, Y. Liu, *Journal of Hazardous Materials* **2012**, *229–230*, 265-272.

[202] P. Mirtchev, E. J. Henderson, N. Soheilnia, C. M. Yip, G. A. Ozin, *Journal of Materials Chemistry* **2012**, *22*, 1265-1269.

[203] J. Tauc, R. Grigorovici, A. Vancu, *physica status solidi (b)* **1966**, *15*, 627-637.

[204] H. Yu, H. Zhang, H. Huang, Y. Liu, H. Li, H. Ming, Z. Kang, *New Journal of Chemistry* **2012**, *36*, 1031-1035.

[205] N. Hedin, L. Chen, A. Laaksonen, *Nanoscale* **2010**, *2*, 1819-1841.

[206] M. Sevilla, A. B. Fuertes, *Energy & Environmental Science* **2011**, *4*, 1765-1771.

[207] L. Zhao, Z. Bacsik, N. Hedin, W. Wei, Y. Sun, M. Antonietti, M.-M. Titirici, *Chemsuschem* **2010**, *3*, 840-845.

[208] M. Sevilla, C. Falco, M.-M. Titirici, A. B. Fuertes, *RSC Advances* **2012**.

[209] N. Ritter, I. Senkovska, S. Kaskel, J. Weber, *Macromolecules* **2011**, *44*, 2025-2033.

[210] N. Du, G. P. Robertson, I. Pinnau, M. D. Guiver, *Macromolecules* **2009**, *42*, 6023-6030.

[211] Q. Liu, A. Mace, Z. Bacsik, J. Sun, A. Laaksonen, N. Hedin, *Chemical Communications* **2010**, *46*, 4502-4504.

[212] J. Jeromenok, W. Böhlmann, M. Antonietti, J. Weber, *Macromolecular Rapid Communications* **2011**, *32*, 1846-1851.

[213] D. N. Dybtsev, H. Chun, S. H. Yoon, D. Kim, K. Kim, *Journal of the American Chemical Society* **2003**, *126*, 32-33.

[214] L. Yu, C. Falco, J. Weber, R. J. White, J. Y. Howe, M.-M. Titirici, *Langmuir* **2012**, *28*, 12373-12383.

[215] Y. Yürüm, A. Taralp, T. N. Veziroglu, *International Journal of Hydrogen Energy* **2009**, *34*, 3784-3798.

[216] M. Sevilla, A. B. Fuertes, R. Mokaya, *Energy & Environmental Science* **2011**, *4*, 1400-1410.

[217] aD. Park, Y.-S. Yun, J. M. Park, *Environmental Science & Technology* **2004**, *38*, 4860-4864; bD. Park, Y.-S. Yun, H. Y. Cho, J. M. Park, *Industrial & Engineering Chemistry Research* **2004**, *43*, 8226-8232.

[218] R. Demir-Cakan, University of Potsdam **2008**.

[219] Z. Chen, L. Ma, S. Li, J. Geng, Q. Song, J. Liu, C. Wang, H. Wang, J. Li, Z. Qin, S. Li, *Applied Surface Science* **2011**, *257*, 8686-8691.

[220] S. Kumar, V. A. Loganathan, R. B. Gupta, M. O. Barnett, *Journal of Environmental Management* **2011**, *92*, 2504-2512.

[221] H. Wang, L. Ma, K. Cao, J. Geng, J. Liu, Q. Song, X. Yang, S. Li, *Journal of Hazardous Materials* **2012**, *229–230*, 321-330.

[222] Z. Liu, F.-S. Zhang, *Journal of Hazardous Materials* **2009**, *167*, 933-939.

[223] Z. Liu, F.-S. Zhang, J. Wu, *Fuel* **2010**, *89*, 510-514.

[224] Y.-J. Xu, G. Weinberg, X. Liu, O. Timpe, R. Schlögl, D. S. Su, *Advanced Functional Materials* **2008**, *18*, 3613-3619.

[225] L.-F. Chen, H.-W. Liang, Y. Lu, C.-H. Cui, S.-H. Yu, *Langmuir* **2011**, *27*, 8998-9004.

[226] Y. Ni, L. Jin, L. Zhang, J. Hong, *Journal of Materials Chemistry* **2010**, *20*, 6430-6436.

[227] I. F. Nata, G. W. Salim, C.-K. Lee, *Journal of Hazardous Materials* **2010**, *183*, 853-858.

[228] H.-W. Liang, L. Wang, P.-Y. Chen, H.-T. Lin, L.-F. Chen, D. He, S.-H. Yu, *Adv. Mater.* **2010**, *22*, 4691-4695.

[229] H.-S. Qian, S.-H. Yu, L.-B. Luo, J.-Y. Gong, L.-F. Fei, X.-M. Liu, *Chemistry of Materials* **2006**, *18*, 2102-2108.

[230] P. Chen, H.-W. Liang, X.-H. Lv, H.-Z. Zhu, H.-B. Yao, S.-H. Yu, *ACS Nano* **2011**, *5*, 5928-5935.

[231] K. Sun, K. Ro, M. Guo, J. Novak, H. Mashayekhi, B. Xing, *Bioresource Technology* **2011**, *102*, 5757-5763.

[232] J. Zhou, C. Tang, B. Cheng, J. Yu, M. Jaroniec, *ACS Applied Materials & Interfaces* **2012**, *4*, 2174-2179.

[233] F. J. Xia, M. Pan, S. C. Mu, M. D. Jones, D. Wolverson, F. Marken, *Electroanalysis* **2012**, *24*, 1703-1708.

[234] W. B. Lu, X. Y. Qin, S. Liu, G. H. Chang, Y. W. Zhang, Y. L. Luo, A. M. Asiri, A. O. Al-Youbi, X. P. Sun, *Anal. Chem.* **2012**, *84*, 5351-5357.

[235] S. Liu, J. Tian, L. Wang, Y. Zhang, X. Qin, Y. Luo, A. M. Asiri, A. O. Al-Youbi, X. Sun, *Adv. Mater.* **2012**, *24*, 2037-2041.

[236] Sun, Li, *Langmuir* **2005**, *21*, 6019-6024.

[237] S. X. Mao, W. F. Li, Y. M. Long, Y. F. Tu, A. P. Deng, *Anal. Chim. Acta* **2012**, *738*, 35-40.

[238] R. Cui, C. Liu, J. Shen, D. Gao, J.-J. Zhu, H.-Y. Chen, *Advanced Functional Materials* **2008**, *18*, 2197-2204.

[239] W. Caihong, X. Chu, M. Wu, *Sensors and Actuators B: Chemical* **2007**, *120*, 508-513.

[240] X.-L. Li, T.-J. Lou, X.-M. Sun, Y.-D. Li, *Inorganic Chemistry* **2004**, *43*, 5442-5449.

[241] Z. Guo, J. Liu, Y. Jia, X. Chen, F. Meng, M. Li, J. Liu, *Nanotechnology* **2008**, *19*, 345704.

[242] N. Sinha, J. Z. Ma, J. T. W. Yeow, *J. Nanosci. Nanotechnol.* **2006**, *6*, 573-590.

[243] W. H. De Jong, P. J. A. Borm, *Int. J. Nanomed.* **2008**, *3*, 133-149.

[244] C. Menard-Moyon, E. Venturelli, C. Fabbro, C. Samori, T. Da Ros, K. Kostarelos, M. Prato, A. Bianco, *Expert. Opin. Drug Discov.* **2010**, *5*, 691-707.

[245] W. Zhang, Z. Zhang, Y. Zhang, *Nanoscale Research Letters* **2011**, *6*.

[246] S. K. Vashist, D. Zheng, G. Pastorin, K. Al-Rubeaan, J. H. T. Luong, F. S. Sheu, *Carbon* **2011**, *49*, 4077-4097.

[247] A. C. L. Tang, G.-L. Hwang, S.-J. Tsai, M.-Y. Chang, Z. C. W. Tang, M.-D. Tsai, C.-Y. Luo, A. S. Hoffman, P. C. H. Hsieh, *Plos One* **2012**, *7*.

[248] T. Yamashita, K. Yamashita, H. Nabeshi, T. Yoshikawa, Y. Yoshioka, S.-i. Tsunoda, Y. Tsutsumi, *Materials* **2012**, *5*, 350-363.

[249] S. Kubo, I. Tan, R. J. White, M. Antonietti, M.-M. Titirici, *Chemistry of Materials* **2010**, *22*, 6590-6597.

[250] A. V. Stanisheysky, C. Styres, H. Yockell-Lelievre, N. Yusuf, *J. Nanosci. Nanotechnol.* **2011**, *11*, 8705-8711.

[251] B. R. Selvi, D. Jagadeesan, B. S. Suma, G. Nagashankar, M. Arif, K. Balasubramanyam, M. Eswaramoorthy, T. K. Kundu, *Nano Letters* **2008**, *8*, 3182-3188.

[252] J. Gu, S. Su, Y. Li, Q. He, J. Shi, *Chemical Communications* **2011**, *47*, 2101-2103.

[253] G. Gao, H. Wu, Y. Zhang, K. Wang, P. Huang, X. Zhang, S. Guo, D. Cui, *Journal of Materials Chemistry* **2011**, *21*, 12224-12227.

[254] S. J. Son, X. Bai, S. B. Lee, *Drug Discovery Today* **2007**, *12*, 650-656.

[255] J. C. Yu, X. Hu, Q. Li, Z. Zheng, Y. Xu, *Chemistry – A European Journal* **2006**, *12*, 548-552.

[256] aG. R. Ley, C. P. Knapp, Cardiac Pacemakers, Inc., **2002**; bS. M. Janib, A. S. Moses, J. A. MacKay, *Advanced Drug Delivery Reviews* **2010**, *62*, 1052-1063.

[257] Y. F. Zhu, T. Ikoma, N. Hanagata, S. Kaskel, *Small* **2010**, *6*, 471-478.

[258] J. Guang, Z. Cuimiao, W. Liyong, D. Shiwen, Y. Hongpeng, *Journal of Alloys and Compounds* **2011**, *509*, 6418-64226422.

[259] G. Tian, Z. J. Gu, X. X. Liu, L. J. Zhou, W. Y. Yin, L. Yan, S. Jin, W. L. Ren, G. M. Xing, S. J. Li, Y. L. Zhao, *Journal of Physical Chemistry C* **2011**, *115*, 23790-23796.

[260] Z. A. Peng, X. Peng, *Journal of the American Chemical Society* **2000**, *123*, 183-184.

[261] Y.-P. Sun, B. Zhou, Y. Lin, W. Wang, K. A. S. Fernando, P. Pathak, M. J. Meziani, B. A. Harruff, X. Wang, H. Wang, P. G. Luo, H. Yang, M. E. Kose, B. Chen, L. M. Veca, S.-Y. Xie, *Journal of the American Chemical Society* **2006**, *128*, 7756-7757.

[262] L. Cao, X. Wang, M. J. Meziani, F. Lu, H. Wang, P. G. Luo, Y. Lin, B. A. Harruff, L. M. Veca, D. Murray, S.-Y. Xie, Y.-P. Sun, *Journal of the American Chemical Society* **2007**, *129*, 11318-11319.

[263] S.-T. Yang, L. Cao, P. G. Luo, F. Lu, X. Wang, H. Wang, M. J. Meziani, Y. Liu, G. Qi, Y.-P. Sun, *Journal of the American Chemical Society* **2009**, *131*, 11308-11309.

[264] J. Zhou, C. Booker, R. Li, X. Zhou, T.-K. Sham, X. Sun, Z. Ding, *Journal of the American Chemical Society* **2007**, *129*, 744-745.

[265] S. C. Ray, A. Saha, N. R. Jana, R. Sarkar, *Journal of Physical Chemistry C* **2009**, *113*, 18546-18551.

[266] S. R. Guo, J. Y. Gong, P. Jiang, M. Wu, Y. Lu, S. H. Yu, *Advanced Functional Materials* **2008**, *18*, 872-879.

[267] Y. H. Yang, J. H. Cui, M. T. Zheng, C. F. Hu, S. Z. Tan, Y. Xiao, Q. Yang, Y. L. Liu, *Chemical Communications* **2012**, *48*, 380-382.

[268] H.-W. Li, Y. Li, Y.-Q. Dang, L.-J. Ma, Y. Wu, G. Hou, L. Wu, *Chemical Communications* **2009**, 4453-4455.

[269] S. Chandra, P. Das, S. Bag, D. Laha, P. Pramanik, *Nanoscale* **2011**, *3*, 1533-1540.

[270] X. H. Wang, K. G. Qu, B. L. Xu, J. S. Ren, X. G. Qu, *Journal of Materials Chemistry* **2011**, *21*, 2445-2450.

[271] P. Hemstrom, K. Irgum, *Journal of Separation Science* **2006**, *29*, 1784-1821.

[272] H. A. Claessens, M. A. van Straten, *Journal of Chromatography A* **2004**, *1060*, 23-41.

[273] J. H. Knox, B. Kaur, G. R. Millward, *Journal of Chromatography* **1986**, *352*, 3-25.

[274] S. K. Hoekman, A. Broch, C. Robbins, *Energy & Fuels* **2011**, *25*, 1802-1810.

[275] C. Falco, N. Baccile, M.-M. Titirici, *Green Chemistry* **2011**, *13*, 3273-3281.

[276] W. Seifritz, *International Journal of Hydrogen Energy* **1993**, *18*, 405-407.

[277] aC. J. Atkinson, J. D. Fitzgerald, N. A. Hipps, *Plant and Soil* **2010**, *337*, 1-18; bA. Downie, P. Munroe, A. Cowie, L. Van Zwieten, D. M. S. Lau, *Critical Reviews in Environmental Science and Technology* **2012**, *42*, 225-250; cY. Gan, C. Liang, C. Hamel, H. Cutforth, H. Wang, *Agronomy for Sustainable Development* **2011**, *31*, 643-656; dC. Glasner, G. Deerberg, H. Lyko, *Chemie Ingenieur Technik* **2011**, *83*, 1932-1943; eS. Jeffery, F. G. A. Verheijen, M. van der Velde, A. C. Bastos, *Agriculture Ecosystems & Environment* **2011**, *144*, 175-187; fP. Jha, A. K. Biswas, B. L. Lakaria, A. S. Rao, *Current Science* **2010**, *99*, 1218-1225; gR. S. Kookana, A. K. Sarmah, L. Van Zwieten, E. Krull, B. Singh, in *Advances in Agronomy, Vol 112, Vol. 112* (Ed.: D. L. Sparks), **2011**, pp. 103-143; hJ. Lehmann, M. C. Rillig, J. Thies, C. A. Masiello, W. C. Hockaday, D. Crowley, *Soil Biology & Biochemistry* **2011**, *43*, 1812-1836; iS. P. Sohi, E. Krull, E. Lopez-Capel, R. Bol, in *Advances in Agronomy, Vol 105, Vol. 105* (Ed.: D. L. Sparks), **2010**, pp. 47-82.